GLOBAL MODELING AND ANALYSIS OF ANTHROPOGENIC COMBUSTION AND ASSOCIATED EMISSIONS

by

Wenfu Tang

A Dissertation Submitted to the Faculty of the

DEPARTMENT OF HYDROLOGY AND ATMOSPHERIC SCIENCES

In Partial Fulfillment of the Requirements

For the Degree of

DOCTOR OF PHILOSOPHY

WITH A MAJOR IN ATMOSPHERIC SCIENCES

In the Graduate College

THE UNIVERSITY OF ARIZONA

2019

THE UNIVERSITY OF ARIZONA
GRADUATE COLLEGE

As members of the Dissertation Committee, we certify that we have read the dissertation prepared by ***Wenfu Tang***, titled ***GLOBAL MODELING AND ANALYSIS OF ANTHROPOGENIC COMBUSTION AND ASSOCIATED EMISSIONS*** and recommend that it be accepted as fulfilling the dissertation requirement for the Degree of Doctor of Philosophy.

Avelino F. Arellano Date: (***Mar 29, 2019***)

Louisa K. Emmons Date: (***Mar 29, 2019***)

Xubin Zeng Date: (***Mar 29, 2019***)

Eric A. Betterton Date: (***Mar 29, 2019***)

Final approval and acceptance of this dissertation is contingent upon the candidate's submission of the final copies of the dissertation to the Graduate College.

I hereby certify that I have read this dissertation prepared under my direction and recommend that it be accepted as fulfilling the dissertation requirement.

Date: (***Mar 29, 2019***)

Dissertation Director: Avelino F. Arellano
Department of Hydrology and Atmospheric Sciences

ACKNOWLEDGEMENTS

Over the past five years, I have received enormous and generous support and encouragement from a great number of people.

First, I would like to express my deepest gratitude and appreciation to my advisor, Professor Avelino Arellano, who has been a great mentor and colleague. Time has indeed proved again and again that I made an excellent choice in 2014 for my career by working with Professor Avelino Arellano as his student. I am always grateful to have Professor Avelino Arellano being my PhD advisor, who has significantly contributed to my professional improvements and achievements during my PhD study. His tremendous support and patient guidance in the past five years have changed me from an undergraduate student who had no experience on research, to an early-career scientist who is ready to take challenges in the future. Without his support, I would not have come so far in atmospheric sciences.

I would also like to specially thank Dr. Louisa Emmons (also on my PhD dissertation committee), my host and mentor in the Atmospheric Chemistry Observations & Modeling Laboratory (ACOM) at the National Center for Atmospheric Research (NCAR). Dr. Louisa Emmons has been my NCAR host for almost two years. Her insightful and invaluable support and advice have been a great help to not only my PhD study but also my career. Her generous support and mentoring have made NCAR a caring and supportive working environment for me. I often feel lucky to have the opportunity to work with her for my last two years of PhD. And I am so happy and excited to continue working with her on new projects after my PhD.

I would like to express my sincere appreciation to other members of my PhD dissertation committee, Professor Xubin Zeng and Professor Eric Betterton, for their insightful comments and strong help. Professor Xubin Zeng has made significant contributions to my professional development as an early-career scientist. Professor Eric Betterton helped me to be more prepared for research in atmospheric chemistry through my comprehensive exam.

I thank all my collaborators who made contribution to my research and/or my career development, including Drs. Benjamin Gaubert, Helen Worden, Rebecca Buchholz, Kazuyuki Miyazaki, Joshua

DiGangi, and Yonghoon Choi. In particular, Dr. Benjamin Gaubert worked closely with me and generously helped and supported me in the past two years. I also thank my other colleagues at NCAR. I thank the NCAR Advanced Study Program (ASP) for all the wonderful opportunities they provide for early-career scientists, including summer colloquium, graduate student fellowship, and postdoctoral fellowship.

I thank all my fellow students and administrative and supporting staff in the Department of Hydrology and Atmospheric Sciences, University of Arizona, especially Sandy Holford who made me feel welcomed and cared during my first year in this country. I thank my dear friends who kept me company, brought me joy, and provided generous help, especially Fan Zhang, Xiaowei Zhang, Dr. Yang Cao, Kamini Joshi, Dr. Tim Lahmers, Wenjun Cui, Yiyi Huang, Shaoyue Qiu, Dr. Mengling Li and April Li.

I am extremely grateful to the organizers of the 2016 NCAR ASP summer colloquium and my advisor Professor Avelino Arellano for encouraging me to attend the colloquium. I met love of my life, my husband Dr. Cenlin He at this colloquium in the summer of 2016 at NCAR, Boulder. Cenlin is the best thing that ever happened to me in 2016, in my PhD, and in my entire life. His kind support, understanding, and encouragement have helped me get to this point. There are no words to convey how much I am grateful to have him in my life. His company has made the past few years a beautiful and wonderful journey. I thank Cenlin for everything.

I would also like to give my special thanks to my parents, who have been supporting and encouraging me to become a scientist since I was in elementary school. I would not have been here without the effort and sacrifice they made for me.

DEDICATION

To my husband

To my parents

For the endless love and support

TABLE OF CONTENTS

LIST OF TABLES

LIST OF FIGURES

ABSTRACT

Anthropogenic combustion and associated emissions have significant impacts on air quality and climate. However, current estimates of emissions from anthropogenic combustion are still subject to large uncertainties, especially in rapidly-developing regions. This hinders accurate assessments of their regional and global impacts on air quality and climate, which presents an urgent need to understand, assess, monitor, and predict anthropogenic combustion and associated emissions particularly at city-to-national scales. Combustion products co-emitted to the atmosphere and their relationships are typically related to characteristics of combustion processes. Thus, in order to understand anthropogenic combustion and associated emissions, my PhD study seeks to answer three major scientific questions: (1) To what extent could current observations of trace gases co-emitted from combustion be used to understand anthropogenic combustion, emissions, and related driving factors? (2) How well do present global climate-chemistry models simulate trace gases from combustion activities and could those models be used to study anthropogenic emissions? (3) To what extent could the current understanding of anthropogenic combustion and emissions be improved by jointly analyzing satellite, ground-based, aircraft measurements, and model simulations of trace gases co-emitted from combustion?

To address the first scientific question, I combine air pollution measurements from multiple satellite instruments across 2005-2014 to characterize emergent features of the ratios of carbon monoxide (CO) and sulfate dioxide (SO_2) to nitrogen dioxide (NO_2) enhancements from anthropogenic emissions over 36 cities in China. The resulting emission pattern is well-correlated with economic development and traces a common emission pathway that resembles the evolution of air pollution in more developed cities. The absence of this progression in the current IPCC Representative Concentration Pathway emission inventory is most likely due to its deficient representation of the shift towards cleaner combustion in more developed cities. The results highlight the usefulness of augmenting observational capabilities by exploiting relationships of combustion tracers in constraining the temporal variation of emissions for gaseous pollutants.

In addition, it is also desired to monitor and assess anthropogenic combustion and its impacts through modeling. Thus, to address the second scientific question, I evaluate simulations of two

important anthropogenic combustion products (carbon dioxide (CO_2) and CO) from a state-of-the-art high-resolution global prediction system, the Copernicus Atmosphere Monitoring Service (CAMS), by comparing with the Korea-United States Air Quality (KORUS-AQ) field measurements (May to June 2016) that aims to understand the factors controlling air quality over East Asia. The results show a slight overestimation for CAMS CO_2 and a moderate underestimation for CAMS CO. CAMS also captures the observed more efficient combustion over Seoul compared to China outflows.

Furthermore, to address both the second and third scientific questions, I combine observations and model simulations to uncover important combustion sources over East Asia, using the Community Atmosphere Model with chemistry (CAM-chem) with a CO tagging mechanism, where artificial CO tracers (i.e., tags) from specific sources are tracked as standard CO. With 17 CAM-chem tagged CO simulations using various model configurations, I quantify key regional sources of CO during KORUS-AQ. The results show that emissions from middle East Asia dominate continental outflows to Korea, while Korean emissions play an overall more important role for ground sites and plumes within the boundary layer in Korea. The CAM-chem tagging results are generally consistent with other source contribution approaches.

Following the CO modeling, together with newly developed CO_2 modeling and tagging mechanism in CAM-chem, I demonstrate the use of joint analysis of CO and CO_2 towards a multi-species inversion. I simulate atmospheric CO_2 as well as CO in CAM-chem using optimized carbon fluxes for CO_2. The model results generally agree with observations from satellite, aircraft, and ground-based observations during KORUS-AQ. Then, I implement a CO_2 tagging mechanism into the model. The modeled fossil fuel CO_2 tags agree well with fossil fuel CO_2 derived from radiocarbon samples during the field campaign. I also show that signatures of plume transport and sectoral emissions of CO_2 are enhanced in CO analyses. Overall, this work elucidates the use of jointly analyzing CO_2 and CO in tracking fossil fuel CO_2, quantifying regional sources, and understanding combustion efficiency of sources.

In my future work, I will (1) combine observations and model simulations of atmospheric gases to obtain improved estimates of their emissions from anthropogenic combustion based on inverse modeling techniques, and (2) use the improved emission estimates to quantify the impact of trace gases on air quality and climate.

CHAPTER 1

INTRODUCTION

1.1 BACKGROUND

Atmospheric composition and chemistry play an important role in our Earth system and our daily life (Charlson et al, 1992; Feely et al., 2004; Doney et al., 2007; Ohara et al., 2007; Shindell et al., 2011; Burnett et al., 2014; Lelieveld et al., 2015; Baklanov et al., 2016; Maher et al., 2016). Atmospheric composition and chemistry significantly impact air quality and public health. For example, it is estimated by World Health Organization (WHO) that exposure to fine particles in polluted air leads to about 7 million deaths per year through diseases such as stroke and lung cancer (World Health Organization, 2018). Atmospheric composition and chemistry also impact our climate and weather. Greenhouse Gases (GHG) such as carbon dioxide (CO_2) and methane (CH_4) and light-absorbing aerosols in the atmosphere such as black carbon (BC) influence our climate by impacting the Earth's radiation budget. Aerosols also play a critical role in weather through their influences on the formation and development of clouds and precipitation. Atmospheric composition and chemistry also influence agriculture and ecosystems. For example, air pollutants such as ozone (O_3) have been reported to cause damage to crops (Fuhrer and Booker, 2003; Van Dingenen et al., 2009), while airborne nitrogen pollutants have been reported to change species diversity in vegetation (Bobbink et al., 1998).

In response to the importance of atmospheric chemistry, research in atmospheric chemistry has been booming in the past decades. Atmospheric chemistry research has multiple foci including the atmospheric chemical composition, sources and emissions of gases and particles, fundamental chemical transformations in the atmosphere, and the response of atmospheric composition to anthropogenic and natural inputs (National Academies of Sciences, Engineering, and Medicine, 2016). Five priority research areas in atmospheric chemistry are suggested by the atmospheric chemistry community for the next decade in response to challenges in the field, including (1) advancing the fundamental atmospheric chemistry knowledge, (2) quantifying emissions and deposition of gases and particles, (3) advancing the integration of atmospheric chemistry within

weather and climate models, (4) understanding the sources and atmospheric processes controlling the species most deleterious to human health, and (5) understanding the feedbacks between atmospheric chemistry and the biogeochemistry of ecosystems (National Academies of Sciences, Engineering, and Medicine, 2016).

Sources and their emissions of gases and aerosols are a key component of atmospheric chemistry. Sources and emissions are usually divided into two kinds, namely natural (e.g., wildfire and biogenic sources) emissions and anthropogenic emissions. Fires have long been recognized as one of the major sources of radiatively and chemically active trace gases and aerosols in the atmosphere (Crutzen et al., 1979; Seiler and Crutzen, 1980; Crutzen and Andreae, 1990; Hao and Liu, 1994; Galanter et al., 2000; Andreae and Merlet, 2001; Duncan et al., 2003; Reid et al., 2005a, 2005b, 2009; van der Werf et al., 2006, 2010; Schultz et al., 2008; Lamarque et al., 2010; Wiedinmyer et al., 2011; Kaiser et al., 2012; Voulgarakis and Field, 2015; Tang and Arellano, 2017; Fourth National Climate Assessment, 2018). Biogenic emissions are important sources for some Volatile Organic Compounds (VOCs) to the atmosphere such as isoprene and monoterpenes (Guenther et al., 1995, 2006; Kesselmeier et al., 1999; Sindelarova et al., 2014). Anthropogenic combustion is generally fuel combustion that are related to human activities. For example, fuel burning in power plants, industrial processes, transport, and domestic activities are considered anthropogenic combustion. Emissions from agriculture and land cover and land use changes are also anthropogenic and related to human activities (e.g., Dobbie et al., 1999; Achard et al., 2004; Kaplan et al., 2011; Houghton et al., 2012; Reay et al., 2012; Tubiello et al., 2013), but are not considered in this dissertation.

Today, anthropogenic combustion and associated emissions play an increasingly important role in our changing world by significantly impacting air quality and climate at local to global scales (Charlson et al., 1992; Mage et al., 1996; Feely et al., 2004; Doney et al., 2007; Ohara et al., 2007; Shindell et al., 2008, 2011; Gaffney and Marley, 2009; Streets et al., 2013; Yang, 2013; Guo et al., 2014; Creutzig et al.,2015; Kennedy et al., 2015; Maher et al., 2016; National Academies of Sciences, Engineering, and Medicine, 2016). For example, in terms of impacts on climate, emissions from fossil fuel combustion and industry contribute 9.4 ± 0.5 gigatonnes of carbon annually to the atmosphere in the form of CO_2 during 2007-2016 (Le Quéré et al., 2018). In terms of impacts on air quality, anthropogenic combustion usually generates air pollutants that

degrade air quality such as carbon monoxide (CO), nitrogen monoxide (NO), nitrogen dioxide (NO_2), sulfur dioxide (SO_2), and aerosols.

In megacities, human activities are most intense, accompanied by immense energy consumption, mainly in the form of fossil-fuel combustion, which directly leads to enhanced emissions of air pollutants, GHG, and waste energy. In particular, cities in the Asian region that are rapidly developing in recent decades are subject to more frequent severe pollution conditions (Ohara et al., 2007; Shindell et al., 2008, 2011; Yang, 2013; Guo et al., 2014). **At present, estimates of city-to-national-scale emissions from fossil fuel combustion remain uncertain**, especially in rapidly developing regions where combustion is still poorly characterized due to the lack of detailed information on energy use, combustion practices, and pollution control strategies (*Streets* et al., 2013; Creutzig et al., 2015). This is also confounded by larger uncertainties on other sources of pollution that may be associated with urbanization (e.g., deforestation, agriculture, and fires). These alone preclude us to accurately assess the changes in atmospheric composition due to anthropogenic activities and emissions at scales that are relevant to air quality, energy, and environmental policy (National Academies of Sciences, Engineering, and Medicine, 2016).

1.2 OPPORTUNITY AND MOTIVATION

Direct measurements of fluxes or emissions from anthropogenic combustion activities are not often available. However, **we have observations of the abundance of these combustion products** (i.e., signatures of anthropogenic combustion and emissions in the atmosphere), such as CO_2, CO, NO, NO_2, SO_2, aerosols across different planforms (e.g., surface sites, aircrafts, ships, satellites). One complementary approach is to look at the relative abundance of these products. CO_2 is ultimately produced during any fossil-fuel combustion activity. Its emissions are stoichiometrically proportional to the total amount of carbon fuel burned (i.e., intensity of combustion). On the other hand, CO is a pollutant that produced during incomplete combustion and represents part of the carbon fuel that is not fully oxidized to CO_2. NO and NO_2 are produced from the oxidation of nitrogen from the fuel itself and from decomposition of N_2 in air at high temperatures (Flagan and Seinfeld, 2012). SO_2 is also produced when the fuel used in the combustion process contains sulfur (such is the case for low-grade fuels). Anthropogenic

combustion activities can also produce aerosols. SO_2, NO_2, and aerosols are measured from in-situ platforms (field campaigns and air quality stations) and space. For example, the Aura Ozone Monitoring Instrument measures both NO_2 and SO_2 (Krotkov et al., 2006, Boersma et al., 2011, 2017), and TROPOspheric Monitoring Instrument (TROPOMI) measures both NO_2 and Aerosol Optical Depth (AOD) (Veefkind et al., 2012). The NASA Moderate Resolution Imaging Spectroradiometer (MODIS) has been providing AOD measurements since 2000 (Levy et al., 2010). NO_2 has been used previously as a proxy of CO_2 for analyzing and understanding combustion characteristics when availability of CO_2 observations is limited (Parrish et al., 2002; Parrish, 2006; Reuter et al., 2014; Konovalov et al., 2016; Silva and Arellano, 2017; Tang and Arellano, 2017; Tang et al., 2019a).

Among these combustion products, CO_2 and CO are particularly important. The relative emissions of CO and CO_2 during an anthropogenic combustion event are typically associated with the 'efficiency' (or 'cleanness') of the process. As a result, the emission ratio of CO to CO_2 from combustion is higher when efficiency is low. This ratio, however, is not a constant as combustion efficiency changes with technology and practice. Determining the ratios of CO to CO_2 (and how these ratios change with time) can be beneficial to improving emission estimates of other combustion products (black carbon, nitrogen oxides) as these products vary with combustion 'efficiency' (or 'cleanness') as well (e.g., Raman and Arellano, 2017; Silva and Arellano, 2017). There is an opportunity to improve our understanding and estimates of anthropogenic combustion and emissions by monitoring atmospheric CO_2 and CO (e.g., Suntharalingam et al., 2004; Turnbull et al., 2006, 2011; Graven et al., 2009; Wunch et al., 2009; Djuricin et al., 2010; Wang et al., 2010; Brioude et al., 2013; Silva et al. 2013; Ammoura et al., 2016; Konovalov et al., 2016). Although a number of previous studies have investigated the combustion activity and associated emissions in the region, these studies are often limited by the availability, spatiotemporal coverage, and accuracy of CO_2 and CO measurements. Large uncertainties in combustion 'intensity' and 'efficiency' still exist in current emission estimates (Streets et al., 2006, 2013; Zhang et al., 2009; Li et al., 2017).

Observations of CO and CO_2 are available from different measuring platforms. In-situ measurements from the past and present NASA field campaigns (e.g., the Transport and Chemical Evolution over the Pacific field campaign; TRACE-P in 2001, and the Korea-United States Air

Quality; KORUS-AQ field study in 2016) provide accurate airborne measurements of CO and CO_2 concentrations. The Total Carbon Column Observing Network (TCCON) is a global ground-based network of to measure column abundances of CO_2, CO, CH_4, Dinitrogen monoxide (N_2O) as well as other species that also absorb in the near-infrared (Wunch et al., 2011). Besides the in-situ observations, satellite observations of CO and CO_2 are also helpful to the study of anthropogenic sources and emissions. For example, short-wavelength infrared observations measured by the Thermal And Near-infrared Sensor for carbon Observation (TANSO) aboard the Greenhouse gases Observing Satellite (GOSAT) are used to retrieve column-averaged dry-air mole fractions of CO_2 (XCO_2) (Morino et al., 2011; Crisp et al., 2012). The Orbiting Carbon Observatory-2 (OCO-2) has three specific near-infrared (NIR) wavelength bands to retrieve XCO_2 (Osterman et al., 2016; Wunch et al., 2017). As for CO, the Measurements Of Pollution In The Troposphere (MOPITT) aboard TERRA has been providing CO observations retrieved from multispectral (thermal-infrared/near-infrared) since 2000 (Worden et al., 2010; Deeter et al., 2014, 2017), while IASI is aboard MetOp-A and B satellites and uses Fast Optimal Retrievals on Layers for IASI (FORLI) to retrieve CO distributions from the TIR spectra (De Wachter et al., 2012). And now, with the new generation of satellite instruments, more and more satellite observations of CO and CO_2 are becoming available. For example, Greenhouse gases Observing SATellite-2 (GOSAT-2) will have both CO and CO_2 observations (http://global.jaxa.jp/projects/sat/gosat2/), while the TROPOMI (Veefkind et al., 2012) has high resolution CO observations (7km x 7km).

Modeling tools for atmospheric CO and/or CO_2 are also becoming available. For instance, for nearly a decade, CAMS has been operationally producing daily global near-real-time forecasts and analyses of reactive trace gases (e.g., CO), GHG (e.g., CO_2), and aerosols including global reanalyses and estimation of emissions of these atmospheric constituents (Benedetti et al., 2009; Morcrette et al., 2009; Kaiser et al., 2012; Flemming et al., 2015, 2017; Massart et al., 2016; Agustí-Panareda et al. 2014, 2017). The Community Earth System Model (CESM) is a state-of-the-art global earth system model including the atmosphere, land, ocean, and ice components (Hurrell et al., 2013). CESM has a biogeochemical version that online models global carbon cycle including atmospheric CO_2 (Keppel-Aleks et al., 2013). The Community Atmosphere Model with Chemistry (CAM-chem) is the atmospheric chemistry component of CESM, coupled with the land model (Lamarque et al., 2012; Tilmes et al., 2015). CAM-chem is used for simulations of global tropospheric and stratospheric atmospheric composition (e.g., CO). GEOS-Chem is also a widely

used global chemical transport model driven by meteorological input (Bey et al., 2001). Besides global models, regional models (usually with higher resolution) are also available to model CO and/or CO_2. For example, the Weather Research and Forecasting (WRF) model coupled with Chemistry (WRF-Chem) is widely used to model trace gases (e.g., CO) and aerosols simultaneously with the meteorology (Grell et al., 2005).

The complex nature of anthropogenic combustion activities poses challenges to understanding characteristics and estimates of anthropogenic combustion and emissions. **However, the observations and modeling tools in this decade have pointed towards a possible way** to understanding them.

CHAPTER 2

OBJECTIVES

In response to the challenges in the field of anthropogenic combustion and emissions research, **my PhD research focuses on characteristics of anthropogenic combustion and associated emissions of trace gases, by exploiting the direct and indirect constraints that can be inferred from observations and models.** Specifically, my PhD study seeks to answer three major scientific questions:

(1) To what extent could current observations of trace gases co-emitted from combustion be used to understand anthropogenic combustion, emissions, and related driving factors?

(2) How well do present global climate-chemistry models simulate trace gases from combustion activities and could those models be used to study anthropogenic emissions?

(3) To what extent could the current understanding of anthropogenic combustion and emissions be improved by jointly analyzing satellite, ground-based, aircraft measurements and model simulations of trace gases co-emitted from combustion?

To answer the first scientific question, and inspired by my previous work on wildfire characteristics in Amazon during my master-degree study (Tang and Arellano, 2017; Appendix A), **the first component of my PhD research is approaching characteristics of anthropogenic emissions through analyzing observational data**. This study is unique as it jointly analyzes relationships between multiple co-emitted species (CO, SO_2, and NO_2) with multiple satellite products. I took advantage of existing satellite remote sensing capabilities to study how pollutants produced during combustion processes vary within a city and across cities in China (Tang et al. 2019a; Chapter 3.1; Appendix B).

With observations being benchmark and constraints, we can use this knowledge to improve models. It is imperative and desired that we enhance our capability of simulating anthropogenic combustion and emissions, and predicting combustion signatures and impacts in global model.

The modeling system will allow us to monitor, verify, and assess anthropogenic combustion and its impacts as urban area across the globe is expected to rapidly grow in the following decades (Jalkanen, 2012; World Bank, 2015). Therefore, to address the second and the third scientific questions, **modeling is an important component of my PhD research**. **I evaluated an existing state-of-the-art model to acquire the current progress of the anthropogenic combustion and emission signature modeling in the field** (Tang et al., 2018; Chapter 3.2; Appendix C). In this study, I brought important model diagnostics beyond basic statistics such as Root Mean Square Error (RMSE). For example, I evaluated modeled CO-CO_2 relationships in addition to the separate evaluations of modeled CO and CO_2.

Based on evaluation of the state-of-the-art modeling system (CAMS), I also worked on enhancing modeling capabilities with a modeling system with flexibility based on an open-source community model with more flexibility in research (scientific question 3). **I explored the utility of CO tracer tagging in CAM-chem to study source contributions in the KORUS-AQ field campaign**, and tested robustness of the tagging results and compared the source analysis results from CAM-chem tags with other source analysis approaches (Tang et al. 2019b; Chapter 3.3; Appendix D).

In addition to the existing CO tagging in CAM-chem, **I developed and added CO_2 tagging mechanism in CAM-chem and validated the results against observations.** The developed model allows us to track fossil fuel CO_2 emissions from the regions of interest, study combustion efficiency and emission characteristics of the sources, and understanding the observed CO-CO_2 relationships. CO_2 and CO tagging in model are also useful to connect and interpret observations (Tang et al., 2019c; Chapter 3.4; Appendix E).

CHAPTER 3

PRESENT STUDY

3.1 SATELLITE DATA REVEALS A COMMON COMBUSTION EMISSION PATHWAY FOR MAJOR CITIES IN CHINA

Anthropogenic activities are most intense in megacities, accompanied by immense energy consumption mainly in the form of fossil fuel combustion (Mage et al., 1996; Kennedy et al., 2015). At present, estimates of city-to-national-scale emissions from fossil fuel combustion remain uncertain, especially in rapidly-developing regions where combustion is still poorly characterized due to the lack of detailed information on energy use, combustion practices, and pollution control strategies (Streets et al., 2013; Creutzig et al., 2015). Such is the case for cities in China even with the scientific attention the country has received in the past decades. As China grew into the world's second largest economy, its rapid development resulted in substantial emissions (Richter et al., 2005), and more frequent occurrences of most severe pollution events in many of its megacities, most notably Beijing (Guo et al., 2014). Along with the growth of these cities is a growing body of evidence of decreasing emissions and associated pollution levels in some cities in China. This points to important changes in air quality as a result of development, Air Quality management, and regional-to-national socioeconomic initiatives embodied within its Five-Year Plans (FYP) (Reuter et al., 2014; Krotkov et al., 2016; van der A et al., 2017; Koukouli et al., 2018; Sun et al., 2018). However, these changes in air quality as a result of efforts to control air pollution are still obfuscated at present by the increase in combustion activities, along with uncertainties in bottom-up emission inventories, and diversity in economic structure and growth across cities (Wang and Hao, 2012; Mi et al., 2017). Monitoring these reductions at city scale remains to be a challenge especially when narrowly viewed within the context of a single pollutant, and more so when attributing them to a particular emission sector.

Fossil fuel emissions from an evolving megacity follow a pattern that can be potentially monitored and refined, by combining observational constraints on combustion activity (abundance of combustion products) with efficiency and effectiveness of pollution control strategies or 'cleanness'

(enhancement ratios of these products) (Silva et al., 2013; Hassler et al., 2016; Silva and Arellano, 2017; Tang et al., 2018, 2019a), alongside information on the state of socio-economic development (e.g., gross domestic product (GDP) or income) and *a priori* estimates from bottom-up emission inventories. In this study, the goal is to uncover space-based evidence of dominant shifts in the cleanness of bulk combustion of large cities across the recent decade, associate these shifts to particular sectors, and identify a common emission pathway across these cities.

I analyzed the emergent patterns of the 'cleanness' of bulk combustion in the past decade (2005-2014), based on enhancement ratios between intermediate products of combustion ($\Delta CO/\Delta NO_2$ and $\Delta SO_2/\Delta NO_2$) observed within each megacity and urban agglomeration in China (Parrish et al., 2002, 2006). I used gridded monthly-averaged satellite retrievals of total columns of CO from Measurement of Pollution In The Troposphere (MOPITT), tropospheric columns of NO_2 from Ozone Monitoring Instrument (OMI), and planetary boundary layer (PBL) columns of SO_2 from OMI to derive monthly estimates of these ratios. I conducted spatial regression analysis and subsequently derived estimates of the decadal trends of these ratios using time series analysis, and then compared these trend estimates to inferred trends from a couple of model-derived abundance ratios and several emission ratios from current bottom-up emission inventories, including estimates based on the Representative Concentration Pathways scenario (RCP8.5) (Riahi et al., 2011). A simple inverse analysis was also used to update the contribution of major emission sectors in RCP8.5 to fit the estimates of decadal changes in enhancement ratios.

The results show a robust coherent progression of declining-to-growing $\Delta CO/\Delta NO_2$ relative to 2005 (-5.4±0.7%/year to +8.3±3.1%/year), and slowly-declining $\Delta SO_2/\Delta NO_2$ (-6.0±1.0%/year to -3.4±1.0%/year) across the four cities. The coherent progression I found is not evident in the trends of emission ratios reported in Representative Concentration Pathway (RCP8.5) inventory. This progression is likely due to a shift towards cleaner combustion from industrial and residential sectors in Shanghai and Shenzhen that is not yet seen in Shenyang and Beijing. This overall trend is presently obfuscated by China's still relatively higher dependence on coal. Such progression is well-correlated with economic development, and traces a common emission pathway that resembles evolution of air pollution in more developed cities.

This study highlights the utility of augmenting observing and modeling capabilities by exploiting enhancement ratios in constraining the time variation of emission ratios in current inventories. As cities and/or countries continue to socioeconomically develop, the ability to monitor combustion efficiency and effectiveness of pollution control becomes increasingly important in assessing sustainable control strategies (e.g., Saeki et al., 2017).

This study has been in press for publication in the *Atmosphere Chemistry and Physics*. For details of this study, please see Appendix B for this paper:

Tang, W., Arellano, A. F., Gaubert, B., Miyazaki, K., and Worden, H. M.: Satellite data reveal a common combustion emission pathway for major cities in China, *Atmosphere Chemistry and Physics*, 19, 4269-4288, https://doi.org/10.5194/acp-19-4269-2019, 2019.

3.2 EVALUATING HIGH-RESOLUTION FORECASTS OF ATMOSPHERIC CO AND CO_2 FROM A GLOBAL PREDICTION SYSTEM DURING KORUS-AQ FIELD CAMPAIGN

Accurate and consistent modeling capabilities of anthropogenic combustion are desired because of its significant health and environmental impacts, especially at city-to-regional scale. It is imperative therefore that we enhance our current capability to monitor, verify, and assess anthropogenic combustion and its impacts as the number of megacities across the globe is expected to rapidly grow in the following decades (United Nations, 2016). The modeling component of this dissertation starts with evaluating an existing state-of-the-art modeling system from the European Centre for Medium-Range Weather Forecasts (ECMWF), the Copernicus Atmosphere Monitoring Service (CAMS), which has a state-of-the-art global and integrated prediction system that is currently being implemented.

The KORUS-AQ field measurement campaign offers a unique opportunity to assess the accuracy and consistency of the high-resolution forecast and analysis system of CAMS and its skill in simulating atmospheric CO2 from anthropogenic combustion. During May to June 2016, the KORUS-AQ field campaign collected comprehensive measurements of air quality (including CO2 and tracers of fossil-fuel combustion) over the South Korean peninsula and its surrounding waters. KORUS-AQ is an international collaboration between the US and South Korea, led by the National Institute of Environmental Research (NIER) of Korea and the National Aeronautics and Space Administration (NASA) of the United States. The goal is to better understand the factors controlling air quality in the region across urban, rural, and coastal interfaces (Al-Saadi et al., 2014).

In this study, I evaluated the CAMS forecast and analysis of fossil-fuel combustion signatures over the KORUS-AQ spatial and temporal domain (South Korea and its surrounding waters; May to June 2016). In particular, I used measurements of the main products of combustion (i.e., CO and CO_2; Gamnitzer et al., 2006) from the NASA DC-8 aircraft, along with observations from five ground sites (Baengnyeong, Fukue, Olympic Park, Taehwa, and Yonsei University), two research vessels (Jangmok and Onnuri), and four satellites (MOPITT XCO, IASI XCO, OCO-2 XCO_2, and GOSAT XCO_2) to assess the capability of CAMS to monitor anthropogenic combustion.

Specifically, I evaluated the performance of CAMS 16-km forecasts, 9-km CO_2 forecasts, and analyses of CO_2, CO, and their relationships. Although CAMS CO and CO_2 forecasts and analyses have been evaluated previously (Agustí-Panareda et al., 2014, 2016, 2017; Claeyman et al., 2010; Massart et al., 2016; Flemming et al., 2009, 2015, 2017), this study is unique as (1) it is a joint evaluation of CO and CO_2 species, including their associated enhancement ratios which provide insights on CAMS representation of anthropogenic combustion processes; (2) it focuses on megacities provides an important baseline investigation.

The results show a slight overestimation of CAMS CO_2 with a mean bias against airborne CO_2 measurements of 2.2, 0.7, and 0.3 ppmv for 16-km and 9-km CO_2 forecasts, and analyses, respectively. The positive CO_2 mean bias in the 16-km forecast appears to be consistent across the vertical profile of the measurements. In contrast, I found a moderate underestimation of CAMS CO with an overall bias against airborne CO measurements of −19.2 (16-km), −16.7 (9-km), and −20.7 ppbv (analysis). This negative CO mean bias is mostly seen below 750 hPa for all three forecast/analysis configurations. Despite these biases, CAMS shows a remarkable agreement with observed enhancement ratios of CO with CO_2 over the Seoul metropolitan area and over the West (Yellow) Sea, where east Asian outflows were sampled during the study period. More efficient combustion is observed over Seoul (dCO/dCO_2 = 9 ppbv $ppmv^{-1}$) compared to the West Sea (dCO/dCO_2= 28 ppbv $ppmv^{-1}$). This "combustion signature contrast" is consistent with previous studies in these two regions. CAMS captured this difference in enhancement ratios (Seoul: 8–12 ppbv $ppmv^{-1}$, the West Sea: ~ 30 ppbv $ppmv^{-1}$) regardless of forecast/analysis con figurations. The correlation of CAMS CO bias with CO_2 bias is relatively high over these two regions (Seoul: 0.64–0.90, the West Sea: ~0.80), suggesting that the contrast captured by CAMS may be dominated by anthropogenic emission ratios used in CAMS. However, CAMS shows poorer performance in terms of capturing local-to-urban CO and CO_2 variability. Along with measurements at ground sites over the Korean Peninsula, CAMS produces too high CO and CO_2 concentrations at the surface with steeper vertical gradients (~ 0.4 ppmv hPa^{-1} for CO_2 and 3.5 ppbv hPa^{-1} for CO) in the morning samples than observed (~ 0.25 ppmv hPa^{-1} for CO_2 and 1.7 ppbv hPa^{-1} for CO), suggesting weaker boundary layer mixing in the model. I also found that analyses of CO show better agreement with satellite retrievals compared to the forecasts, while analyses of CO_2 are no better than the forecasts. I attributed this contrast to significant differences in the number of XCO

and XCO_2 satellite data potentially available for assimilation. Overall, the combination of CO analyses (i.e., improved initial condition) and the use of finer resolution (9-km vs. 16-km) generally produces better forecasts.

Finally, this study provides important implications on designing atmospheric composition and air quality modeling systems. Although CAMS captures the regional combustion signatures, it still has difficulty representing the variability at local-to-urban scales even at finer resolution. This suggests the need for improvements in both observational constraints and model representation of relevant processes (e.g., emissions and BL mixing).

This study has been published in the *Atmosphere Chemistry and Physics*. For details of this study, please see Appendix C for this paper:

Tang, W., Arellano, A. F., DiGangi, J. P., Choi, Y., Diskin, G. S., Agustí-Panareda, A., Parrington, M., Massart, S., Gaubert, B., Lee, Y., Kim, D., Jung, J., Hong, J., Hong, J.-W., Kanaya, Y., Lee, M., Stauffer, R. M., Thompson, A. M., Flynn, J. H., and Woo, J.-H., 2018. Evaluating high-resolution forecasts of atmospheric CO and CO_2 from a global prediction system during KORUS-AQ field campaign, *Atmosphere Chemistry and Physics*, 18, 11007-11030, https://doi.org/10.5194/acp-18-11007-2018.

3.3 SOURCE CONTRIBUTIONS TO CARBON MONOXIDE CONCENTRATIONS DURING KORUS-AQ BASED ON CAM-CHEM MODEL APPLICATIONS

In the previous study, I assessed a state-of-the-art global and integrated prediction system, the CAMS system from the ECMWF, in terms of its capability of simulating fossil-fuel combustion signatures during the KORUS-AQ. Even though CAMS performs remarkably in simulating the main products of combustion (CO and CO_2), it is an operational system that has limited availability and/or flexibility for research purpose. Therefore, I also worked with the Community Earth System Model (CESM)/Community Atmosphere Model (CAM-chem), which is an open-source community model with more flexibility (Lamarque et al., 2012; Hurrell et al., 2013).

In addition to being an open-source community model, the other major benefit of using CAM-chem is the potential tagging capability of tracking anthropogenic emissions (Emmons et al., 2012; Gaubert et al., 2016; Tang et al., 2019). The tagging method is particularly appropriate in chemistry by explicitly accounting for non-linearity in the sensitivity to change in emissions (Clappier et al. 2017). CO is a common pollutant in the atmosphere, being directly emitted from incomplete combustion sources, such as vehicles, industry, and biomass burning, as well as chemically produced from oxidation of methane and other hydrocarbons. CO is also a good tracer of pollution transport, with only one photochemical sink and an intermediate lifetime (approximately a month) (Li et al., 2002; Duncan and Bey, 2004; Gamnitzer et al., 2006). Such characteristics make tagging CO feasible and tagged CO relatively reliable as a tracer of pollution plumes from regional to hemispheric scales. Tagged CO has been widely used in previous studies for various research purposes such as source attribution (Granier et al., 1999; Staudt et al., 2001; Liu et al., 2003; Pfister et al., 2004, 2011; Chen et al. 2009; Park et al., 2009; Protonotariou et al., 2013; Buchholz et al., 2016; Fisher et al., 2017) and inverse modeling (Heald et al., 2004; Pétron et al., 2004; Arellano et al., 2004, 2006). The goal of this study is to elucidate the regional sources contributing to observed CO concentrations within the troposphere during the KORUS-AQ campaign over Korea using the tagged CO algorithm that is implemented in the Community Atmosphere Model with Chemistry (CAM-chem).

The KORUS-AQ field measurement campaign was conducted over South Korea and its surrounding waters in May-June 2016. During the campaign, observations from aircraft, ships,

ground sites, and satellites were integrated with models to help understand air quality and factors controlling air quality in the region. The campaign had three main research foci: (1) the opportunities and challenges for satellite observations of air quality; (2) the key factors governing ozone photochemistry and aerosol evolution; (3) model performance and needed improvements to better represent atmospheric composition over Korea and its connection to the larger global atmosphere (Al-Saadi et al., 2014). To better investigate these research topics, especially (2) and (3), it is critical to understand and quantify the influence of different pollution sources on the air quality in in the region.

I investigated regional sources contributing to CO during the KORUS-AQ campaign conducted over Korea (May 1st to June 10th 2016) using 17 tagged CO simulations from CAM-chem. The simulations use three spatial resolutions, three anthropogenic emission inventories, two meteorological fields, and nine emission scenarios. I also comprehensively evaluated these CO simulations by comparing with DC-8 aircraft measurements and MOPITT retrievals. I found that CAM-chem simulations with different spatial resolutions, bottom-up emissions anthropogenic CO emissions, and/or meteorological fields produce similar bias patterns and systematically underestimate CO vertical profiles by 30–40% (normalized mean bias) during the KORUS-AQ campaign, compared with DC-8 aircraft measurements. The simulations using bottom-up emissions anthropogenic CO emissions also have poorer performance (Taylor skill: 0.38–0.61) than simulations using alternative anthropogenic emissions (bias: -6~-33%; Taylor skill: 0.48–0.86), particularly for enhanced Asian CO and VOC emission scenarios (Taylor, 2001). I further analyzed the potential sources (transport, emission, resolution, and chemistry) of this underestimation and suggested that chemically produced CO may contribute to the underestimation in CO background in this region. I then compared the model simulations with MOPITT CO retrievals over East Asia during the KORUS-AQ period. The differences in CO vertical profiles between model simulations and MOPITT over Korea and its surrounding areas are much smaller, relative to the model biases against DC-8 airborne observations.

The results of CAM-chem tagged CO simulations show that direct Korean CO emissions overall contribute about 6-13% to modeled total CO concentrations throughout the DC-8 flight period. The Korean contribution is higher over the Seoul (10-22%) and Seoul-Jeju jetway (9-19%) of flight tracks due to the proximity to strong local emissions, but much lower over the West Sea

(<1%) due to the prevailing winds. The contribution of CO from direct Korean emissions to the DC-8 measurements is larger within the boundary layer (below 850 hPa; 8–19%) than free troposphere (above 850 hPa; ~1%). Contributions of direct CO emissions from Japan, Russia, Indonesia, and India together account for a smaller proportion (10-13%). The contributions of direct CO emissions from different parts of East Asia (southern, middle, and northern; EA-S, EA-M, and EA-S) show very different characteristics, with the largest and smallest overall contribution from EA-M (16–28%) and EA-S (~5%), respectively. I found that the contribution from EA-S CO emissions is higher in the free troposphere (8–11%) than in the boundary layer (~3%), while it is the opposite for contribution from EA-M (17–29% in the boundary layer and 14–26% in free troposphere) and EA-N (11–22% in the boundary layer and 5–10% in free troposphere) emissions. In particular, over the West Sea when Chinese outflow was expected, the contribution of CO emissions from EA-M along the DC-8 aircraft flight tracks is evidently larger (29-51%) than average, suggesting that the West Sea region is mainly impacted by the EA-M outflow. Other sources, including direct CO emissions from the rest of the world, biogenic CO, and CO chemical production, generally contribute more in the free troposphere (40–58%) than in the boundary layer (24–44%).

Finally, comparisons with the four following other source contribution approaches show general consistency with CAM-chem: (1) the Weather Research and Forecasting (WRF) inert NO2 tracers (Grell et al., 2005; Pfister et al., 2017); (2) the FLEXible PARTicle dispersion model (FLEXPART) back trajectory calculations driven by WRF (Stohl et al., 2005; Brioude et al., 2013), (3) VOCs signatures suggested by the Whole Air Sampling (WAS) group from the University of California, Irvine (Blake et al., 1996; Palmer et al., 2003; Blake et al., 2003, 2004; Wang et al., 2006; Barletta et al., 2009; Xue et al., 2011), and (4) observed CO to CO_2 enhancement ratios (Bakwin et al. 1994; Wang et al., 2010; Turnbull et al., 2011; Silva et al., 2013; Tang et al. 2018). The overall source contribution results from CAM-chem and FLEXPART-WRF simulations agree reasonably well. The correlation between CAM-chem CO tracers with WRF inert NO_2 tracers is higher for emissions from Korea (0.7) than from China (<0.5), which suggests a smaller contribution of Chinese emissions to short-lived air pollutants transported to Korea, relative to long-lived species. The comparisons with VOCs signatures suggested by the WAS group (CCl4, CFC-113, CFC-114, and OCS) from the University of California, Irvine show that modeled CO from direct EA emissions has higher correlations with the China signature VOCs, compared to CO from

elsewhere. Further comparisons with the China signature VOCs also imply that OCS could potentially be a more effective indicator of China outflows than the other three signature VOCs, while H-1211 is no longer a valid China signature VOC. Moreover, the different relationships between CO from EA sub-regions and different China signature VOCs might be a potential signal of the inhomogeneity in VOC emissions over EA. Finally, I found consistent results from CAM-chem tagged tracers and dCO/dCO_2 analysis, which shows that a higher-than-usual contribution of Korean CO emissions corresponds to a lower-than-usual dCO/dCO_2, with the opposite relationship for China. In summary, the source contribution results from CAM-chem tagged CO tracers are reasonably consistent with those from the other four methods.

This study has been published in the *Journal of Geophysical Research: Atmospheres*. For details of this study, please see Appendix D for this paper:

Tang, W., Emmons, L. K., Arellano, A. F., Gaubert, B., Knote, C., Tilmes, S., Buchholz, R. R., Pfister, G. G., Diskin, G. S., Blake, D. R., Blake, N. J., Meinardi, S., DiGangi, J P., Choi, Y., Woo, J., He, C., Schroeder, J. R., Suh, I., Lee, H., Jo, H., Kanaya, Y.,Jung, J., Lee, Y., and Kim, D., 2019. Source contributions to carbon monoxide concentrations during KORUS-AQ based on CAM-chem model applications, *J. Geophys. Res. Atmos*., 10.1029/2018JD029151.

3.4 ELUCIDATING THE UTILITY OF CO_2 AND CO ANALYSIS IN TRACKING FOSSIL FUEL CO_2

Increasing greenhouse gas (GHG) emissions from anthropogenic activities are projected to bring wide-ranging environmental changes, and impact regional air quality (AQ) through atmospheric feedback mechanisms. Understanding today's regional CO_2 sources and sinks, in particular, is a key focus area in carbon cycle science and atmospheric composition given the necessity for reliable projections of future atmospheric CO_2 concentrations (e.g., Le Quéré et al., 2018). Estimates of CO_2 emissions from fossil-fuel (FF) use and applications remain uncertain, especially in rapidly developing regions where combustion activity and efficiency and fuel-use mixtures are poorly characterized due to lack of detailed information on energy-use, combustion practices, and pollution control strategies (e.g., Ciais et al., 2010; Andres et al., 2012, 2016; Zhu et al., 2012; Creutzig et al., 2015; Gately and Hutyra et al. 2017). The uncertainty in tracking and quantifying $FFCO_2$ emissions is exacerbated by limited observations at the spatiotemporal scales necessary to resolve variations in combustion and fuel-use patterns (Duren and Miller, 2012; Hutyra et al., 2014; Shiga et al. 2014). Attributing the sources of these emissions is challenging due to the dearth of accurate CO_2 measurements with sufficient spatiotemporal coverage necessary to resolve variations in combustion and fuel-use patterns, the difficulty in teasing out the small anthropogenic signature from the large natural sources and sinks dominating the carbon cycle, and the uncertainties in modeling atmospheric transport (National Research Council, 2010; Ciais et al. 2014).

Recent studies have also demonstrated that chemical tracers of $FFCO_2$ (^{13}C, ^{14}C, ^{18}O) are significantly valuable in reducing these uncertainties and directly tracking $FFCO_2$ emissions by partitioning total CO_2 into fossil and terrestrial CO_2 as well as estimating its emissions (Levin et al., 2003, 2008; Djuricin et al. 2010; Turnbull et al., 2006, 2011, 2015; Graven et al., 2009, 2018; Miller et al. 2012; Newman et al. 2016; Basu et al., 2016; Nathan et al., 2018). However, these chemical tracers of $FFCO_2$ such as radiocarbon are expensive to obtain. Complementarily, carbon monoxide (CO) may be useful as a proxy of $FFCO_2$. The utility of CO in constraining $FFCO_2$ from the satellite perspective is three-fold. First, there is a larger number of retrievals for CO (and other AQ trace gases) than OCO-2 and/or GOSAT XCO_2. Second, CO retrievals provide enhanced spatial structure of combustion signature ($FFCO_2$) which cannot be easily identified with CO_2

retrievals without filtering and prior signal processing. Third, sectoral emissions can also be enhanced without the addition of tracers. This is particularly the case with fires where a strong CO enhancement can be observed.

We suggested in this study to augment this system with air quality observations particularly carbon monoxide (CO). Here, we elucidated the utility of a joint analysis of CO_2 and CO in tracking the abundance of $FFCO_2$ by simulating CO_2 and CO in CAM-chem using an ensemble of posterior fluxes from CarbonTracker 2017 (CT2017), CarbonTracker Europe 2018 (CTE2018), and CAMS greenhouse gases flux inversions (CAMSv17r1) for CO_2, and an emission scenario based on the Hemispheric Transport of Air Pollution version 2 inventory (HTAPv2) for CO. We evaluated these simulations (including regional tracers of $FFCO_2$ and FFCO) across observational platforms, namely the NOAA ESRL Carbon Cycle Cooperative Global Air Sampling Network (CCGG), the Total Carbon Column Observing Network (TCCON), aircraft measurements during the KORUS-AQ field campaign (May – June 2016) including $^{14}CO_2$, and the NASA Orbiting Carbon Observatory-2 (OCO-2) and the Measurements Of Pollution In The Troposphere onboard Terra (MOPITT) satellites. Overall, our simulation results are generally in agreement with these observations. Modeled CO_2 and CO are in good agreement with surface CO_2 and CO at the four CCGG sites (correlation ranges from 0.62-0.92 for CO_2 and 0.21 to 0.92 for CO; RMSE ranges from ~3 to 10 ppmv for CO_2 and ~59.0 to 178 ppbv for CO; Mean Bias ranges from ~ -3 to 1.5 ppmv for CO_2 and ~ -14 to 57 ppbv for CO). The use of posterior CO_2 fluxes has significantly improved CO_2 simulations over the Anmyeon-do and Lulin sites relative to the default CO_2 setting in CAM-Chem. The comparisons with observations from TCCON sites show about 2-4% (CO_2) and 11-16% (CO) errors. When compared the model results to the measurements from the NASA DC-8 aircraft, the systematic underestimation of CO_2 and CO near the surface suggests that either CO_2 and CO local sources are underestimated or that the sinks (and/or mixing) are overestimated in the region. When compared to satellite observations, the CAM-chem simulations using posterior CO_2 fluxes agree well with OCO-2 observations during the KORUS-AQ period (correlation=0.46~0.68, mean bias=-0.0~0.8 ppmv, and RMSE=1.3~1.7 ppmv). XCO derived from the CAM-chem simulation has higher correlation (0.76) with satellite observations compared to that for XCO_2 (0.46~0.68). The mean bias (6.40 ppbv) and RMSE (18.47 ppbv) are both reasonably small. Our results also show that the correlation between $FFCO_2$ derived from radiocarbon measurements and modeled $FFCO_2$ tags are surprisingly significant (r=0.82). We

found that $FFCO_2$ from East Asia and rest of the world needs to be scaled up (by a factor of 1.61 and 1.28, respectively), while $FFCO_2$ from Korea and Japan needs to be scaled down (by a factor of 0.84). Signatures of modeled $FFCO_2$ plume transport and sectoral emissions are enhanced if modeling analysis of CO is also considered. Lastly, we found that dCO/dCO_2 ratios can be more effectively used to diagnose inconsistencies in combustion efficiency using the associated tags especially with FFCO and $FFCO_2$. Specifically, we found that $dFFCO/dFFCO_2$ from Korea (6.7 ppbv/ppmv) is lower than from middle and northern East Asia (~52-55 ppbv/ppmv), indicating higher combustion efficiency over Korea. Our analyses suggest that constraints from CO through diagnosing consistency in $FFCO_2$ abundance and its associated regional and sectoral contributions, as well as quantifying combustion efficiencies from different sectors, can be exploited to complement current observational constraints in tracking $FFCO_2$.

This study is to be submitted to the *Atmosphere Chemistry and Physics*. For details of this study, please see Appendix E for this manuscript:

Tang, W., et al., 2019. Elucidating the Utility of CO_2 and CO Analysis in Tracking Fossil Fuel CO_2, *Atmosphere Chemistry and Physics*, to be submitted.

CHAPTER 4

CONCLUSIONS AND FUTURE RESEARCH

4.1 SUMMARY

Anthropogenic combustion and associated emissions significantly impact our air quality and climate. However, estimates of city-to-national-scale emissions from anthropogenic combustion remain uncertain, especially in rapidly developing regions. My PhD study mainly focuses on characteristics of anthropogenic combustion and associated emissions of trace gases. Observational data analysis and modeling are the two key components of my PhD research.

I analyzed observations of anthropogenic combustion and emissions in megacities in mainland China (Chapter 3.1). A new observational perspective on monitoring one of the major consequences of urbanization was introduced, not to replace existing observing capabilities but to further exploit the information that is already available. I found observational evidence of a common combustion emission pathway for major cities in China through satellite observations from space and reported observational evidence of decadal changes in the efficiency, and cleanness of bulk combustion over large cities in mainland China, which is well correlated with economic development. These trace a common emission pathway that resembles the evolution of air pollution in more developed cities in the United States which is characterized by transitions in energy use and subsequent implementation of pollution control and regulation. This implies information on combustion efficiency/effectiveness can in fact be monitored from space. This study proposed the use of these enhancement ratios derived from existing satellite retrievals to complement existing surface air quality networks, including carbon-related satellite observing systems in further constraining combustion efficiency and effectiveness of control technologies and policies. Augmenting existing capabilities is particularly relevant, especially with the aid of big data informatics and machine learning as well as the advent of activities focusing specifically on tracking fossil fuel emissions (like the CO_2 Human Emissions project; https://www.che-project.eu).

Based on observations, I also evaluated the capability of a state-of-the-art high-resolution global modeling system (CAMS 16-km forecasts, 9-km forecasts, and analyses) in simulating main products of anthropogenic combustion (CO and CO_2 and their relationships), using measurements from the NASA DC-8 aircraft, five ground sites, and two research vessels during the KORUS-AQ field campaign, along with four sets of satellite retrievals. The assessment of the overall CAMS performance against the DC-8 aircraft data shows that (1) the nominal background CO_2 in CAMS is slightly overestimated, which is further improved by CO_2 analysis. On the other hand, CO is generally underestimated by CAMS; and (2) among the three forecasts/analysis configurations, 9-km forecasts are more accurate and consistent overall than 16-km forecasts and analyses because of the finer model resolution and improved initialization. While analyses are coarser in resolution, they generally perform better than 16-km forecasts as the impact of initialization surpasses the impact of resolution. Even though CO_2, CO, and their relationships vary spatially, CAMS performs well in terms of simulating regional pattern of anthropogenic combustion. Comparisons with measurements from ground sites and two ships indicate that (1) the diurnal cycles of CO and CO_2 are stronger over urban environments and such periodic features are reasonably captured by CAMS; (2) vertical mixing near sources (such as Seoul) is too weak in CAMS and needs to be improved; and (3) in some cases, 9-km forecasts do not show improvements from 16-km forecasts, implying large spatiotemporal errors in emission inventories. In these cases, increasing the spatiotemporal resolution might even weaken the simulation results, whereas the lower resolution usually agrees better with observations as it "diffuses" the error of the emissions. This study has important implications on the design and implementation of current and future prediction systems for atmospheric composition and air quality.

In order to have more flexibility in developing and modifying a modeling system, I chose to base my further modeling work on another widely-used open-source state-of-the-art global climate-chemistry model, CESM/CAM-chem. Using tagged CO tracers in CAM-chem, I investigated CO source contributions during the KORUS-AQ field campaign. I conducted a set of model sensitivity test simulations by varying emissions, meteorology, and resolution, and evaluated the results with airborne measurements and satellite observations. Results show that simulations using bottom-up emissions are consistently lower (bias: -34~-39%) and poorer performing than simulations using alternative anthropogenic emissions (bias: -6~-33%; Taylor skill: 0.48–0.86), particularly for enhanced Asian CO and VOC emission scenarios, suggesting underestimation in modeled CO

background and emissions in the region. I then conducted source contribution analysis for the KORUS-AQ airborne and ground measurements by tagging CO tracers emitted from different source regions and chemical processes in CAM-chem simulations. The ranges of source contributions to modeled CO along the DC-8 aircraft flight track from Korea, EA-S, EA-M, and EA-N are 6–13%, ~5%, 16–28%, and 9–18%, respectively. CO emissions from middle and northern EA can reach Korea via transport within the boundary layer, whereas those from southern EA are transported to Korea mainly through the free troposphere. Emission contributions from middle EA dominate during continental outflow events (29–51%), while Korean emissions play an overall more important role for ground sites (up to 25–49%) and plumes within the boundary layer (up to 25–44%) in Korea. To further evaluate the robustness of the source contribution results by CAM-chem tagged CO, I compared the CAM-chem results with those from four other approaches to source contributions (FLEXPART-WRF back trajectories, WRF inert NO_2 tracers, China signature VOCs, and dCO/dCO_2). The comparisons show general consistency, implying the robustness of the CO source contribution from results of CAM-chem tagging.

Last but not least, I further demonstrated the value of a joint analysis of CO and CO_2 in tracking $FFCO_2$. Given the increasing importance in science and policy of accurately tracking and quantifying $FFCO_2$, this study is placed within the context of constraining transport models of CO_2 with observational and modeling information from CO. I used the recent KORUS-AQ field campaign as my test case region given extensive measurements during this campaign that are focused on sampling pollution plumes over Seoul and plumes entering Korea. This study focuses on directly investigating abundance rather than emissions as this is the most tractable and natural way to link CO_2 observations with identifiable CO constraints. First, I evaluated model simulations of CO and CO_2 based on observationally-constrained surface fluxes for CO_2 and a 'best emission scenario' for CO. I used various collocated CO_2 and CO measurements to encapsulate complementary information that can be derived from these observational platforms. I also introduced a tagging capability that I further developed for CO_2 and CO in CAM-Chem to help track sectoral and/or regional contributions to $FFCO_2$. I then used these $FFCO_2$ and FFCO tags to elucidate constraints from CO in terms of identifying relative combustion efficiencies of sampled air during KORUS-AQ (including inconsistencies in $FFCO_2$) and enhancing signatures of transport and mixing of atmospheric CO_2. The results show that the modeled CO_2, CO, and $FFCO_2$ reasonably consistent with measurements across platforms. Most notably, the modeled $FFCO_2$ is

in good agreement with observed $FFCO_2$ derived from radiocarbon measurements during KORUS-AQ. I found that simulations of regionally-tagged $FFCO_2$ and FFCO reveal significantly higher combustion efficiency in air samples from Korea than East Asia. This is consistent with previous studies. I highlighted the utility of using these tags to assess and quantify the contributions of different $FFCO_2$ sources to observed enhancement ratios. The use of these tags provides a means to calibrate the modeled abundances without needing to classify data into groups and to filter data for confounding factors. With this, I proposed that the community should start considering incorporating this type of analysis, especially to help in designing integrated observing systems for carbon monitoring. I am cognizant, however, on the limitations of incorporating these CO constraints in current inversion systems. I suggested augmenting the current carbon observing system to include AQ measurements. This is especially the case with the advent of new missions (Geo-Carb, TROPOMI, GOSAT-2 and 3). I also suggested that AQ-related field campaigns be exploited as I have shown in this study. All these, of course, should only complement the more pressing problem in carbon community, which is to better constrain our understanding of the biospheric and oceanic CO_2 flux and their carbon dynamics.

4.2 FINAL THOUGHTS

Overall, as mentioned previously in *Introduction*, anthropogenic combustion and emissions significantly impact our earth system. However, challenges still exist in the related research area. Through the four projects during my PhD study, I addressed the three scientific questions brought up in *Objectives* focusing on observations and/or modeling of anthropogenic combustion and emissions: (1) To what extent could current observations of trace gases co-emitted from combustion be used to understand anthropogenic combustion, emissions, and related driving factors? (2) How well do present global climate-chemistry models simulate trace gases from combustion activities and could those models be used to study anthropogenic emissions? (3) To what extent could the current understanding of anthropogenic combustion and emissions be improved by jointly analyzing satellite, ground-based, aircraft measurements and model simulations of trace gases co-emitted from combustion?

While working towards addressing these three questions, my PhD study is an attempt to understand anthropogenic combustion and emissions through atmospheric observations and modeling of their signatures (i.e., main combustion products). The main contribution of this dissertation is a step towards understanding characteristics of anthropogenic combustion and emissions. I explored the utility of the joint analysis of multi-species (especially the synergy of CO and CO_2) in constraining the time variation of emission ratios in current emission inventories, and evaluated and enhanced modeling capabilities of simulating and interpreting atmospheric signatures of anthropogenic combustion and associated emissions.

I recognize that this dissertation has limitations. (1) It mainly focuses on anthropogenic combustion and associated emissions in East Asia, where the human activities are most intense, accompanied by immense fossil-fuel combustion. The findings derived from the study over East Asia need to be validated over other regions across the world. (2) The modeling studies focus mainly on the period of the KORUS-AQ field campaign (May – June 2016). More work is needed to determine if these findings are valid over other time period. (3) Underestimation is a common issue for atmospheric CO modeling, which needs to be further and properly addressed before applying the methods to other regions and periods. (4) The tagging method in global models is particularly appropriate for tracers associated with complicated atmospheric processes (e.g., chemistry and deposition), which explicitly accounts for non-linearity in the sensitivity to changes in emissions. However, the spatial resolution of global models is not high enough to resolve some local features.

The knowledge and modeling tools gained through my PhD study contribute to three of the aforementioned five priority research topics in the atmospheric chemistry field (*Chapter 1*): quantifying emissions and deposition of gases and particles, advancing the integration of atmospheric chemistry within weather and climate models, and understanding the sources and atmospheric processes controlling the species most deleterious to human health. This dissertation is beneficial and informative to researchers in the field of anthropogenic combustion and emissions, related model developers, and policy makers. My PhD study is also in the context of the recently published decadal strategy for earth observation from space (National Academies of Sciences, Engineering, and Medicine. 2018), in which understanding processes that determine the spatio-temporal structure of important air pollutants and their concomitant adverse impact on human

health, agriculture, and ecosystems is suggested as one of the most important objectives for the next decade. The exploration towards characterizing and quantifying anthropogenic combustion and associated emissions is yet far from the end. Based on my PhD study, I will continue research on combustion and associated emissions, and study the following scientific topics in the future:

(1) As mentioned above, underestimation of atmospheric CO is a common issue in atmospheric chemistry models. I will work on addressing this issue in detail.

(2) As my modeling studies during PhD mainly focused on East Asia during the KORUS-AQ campaign period, in my next step, I will apply the methods and modeling tools to other spatial and temporal domains.

(3) Limitation in spatial resolutions of global models may prevent the tagging method from capturing local features at relatively small scale. I plan to use tagging in regional atmospheric chemistry models (e.g., WRF-Chem) and compare the results with those from global atmospheric chemistry models.

(4) This dissertation studies the characteristics of anthropogenic combustion and associated emissions. In the next step, I will apply this knowledge to anthropogenic emission estimates. I will work on combining observations of atmospheric gases with chemical transport models to obtain improved estimates of their emissions from anthropogenic as well as biomass combustion based on inverse modeling techniques.

(5) I will quantify the climatic and health impacts, using the improved CAM-chem model and estimates of emissions. Accurate predictions of climatic and health impacts of anthropogenic combustion and associated emissions are hindered by current model capability and uncertainties in estimates of emissions of atmospheric composition.

(6) Fires and associated emissions also play a critical role in our earth system. Previous studies have suggested an enhanced wildfire risk under climate change. However, fire chemical processes are still poorly understood and represented in current Earth-system models, and estimates of fire emissions and down-wind effects remain uncertain due to limited observational constraints. I plan to also work on understanding characteristics of and improving emission estimates of fires, and quantification and prediction of atmospheric impacts of fires.

REFERENCES

Achard, F., Eva, H.D., Mayaux, P., Stibig, H.J. and Belward, A., 2004. Improved estimates of net carbon emissions from land cover change in the tropics for the 1990s. *Global Biogeochemical Cycles*, 18(2).

Agustí-Panareda, A., Massart, S., Chevallier, F., Boussetta, S., Balsamo, G., Beljaars, A., Ciais, P., Deutscher, N. M., Engelen, R., Jones, L., Kivi, R., Paris, J.-D., Peuch, V.-H., Sherlock, V., Vermeulen, A. T., Wennberg, P. O., and Wunch, D., 2014. Forecasting global atmospheric CO_2, *Atmospheric Chemistry and Physics*, 14, 11959–11983, https://doi.org/10.5194/acp-14-11959-2014.

Agustí-Panareda, A., Massart, S., Chevallier, F., Balsamo, G., Boussetta, S., Dutra, E., and Beljaars, A., 2016. A biogenic CO_2 flux adjustment scheme for the mitigation of large-scale biases in global atmospheric CO_2 analyses and forecasts, *Atmospheric Chemistry and Physics*, 16, 10399–10418, https://doi.org/10.5194/acp-16-10399-2016.

Agustí-Panareda, A., Diamantakis, M., Bayona, V., Klappenbach, F., and Butz, A., 2017. Improving the inter-hemispheric gradient of total column atmospheric CO_2 and CH_4 in simulations with the ECMWF semi-Lagrangian atmospheric global model, *Geoscientific Model Development*, 10, 1–18, https://doi.org/10.5194/gmd-10-1-2017.

Al-Saadi, Jassim, Gregory Carmichael, James Crawford, Louisa Emmons, Saewung Kim, Chang-Keun Song, Lim-Seok Chang, Gangwoong Lee, Jhoon Kim, Rokjin Park, 2014. KORUS-AQ: An International Cooperative Air Quality Field Study in Korea, *the KORUS-AQ white paper* (https://espo.nasa.gov/korus-aq/content/KORUS-AQ_White_Paper).

Ammoura, L., Xueref-Remy, I., Vogel, F., Gros, V., Baudic, A., Bonsang, B., Delmotte, M., Té, Y. and Chevallier, F., 2016. Exploiting stagnant conditions to derive robust emission ratio estimates for CO_2, CO and volatile organic compounds in Paris. *Atmospheric Chemistry and Physics*, 16(24), pp.15653-15664.

Andreae, M. O., and Merlet, P., 2001. Emission of trace gases and aerosols from biomass burning, *Global biogeochemical cycles*, 15(4), 955–966, doi:10.1029/2000GB001382.

Andres, R.J., Boden, T.A., Bréon, F.M., Ciais, P., Davis, S., Erickson, D., Gregg, J.S., Jacobson, A., Marland, G., Miller, J. and Oda, T., 2012. A synthesis of carbon dioxide emissions from fossil-fuel combustion. *Biogeosciences*, 9(5), pp.1845-1871.

Andres, R. J., Boden, T. A., and Higdon, D. M., 2016. Gridded uncertainty in fossil fuel carbon dioxide emission maps, a CDIAC example, *Atmospheric Chemistry and Physics*, 16, 14979-14995, https://doi.org/10.5194/acp-16-14979-2016.

Arellano Jr, A. F., Kasibhatla, P. S., Giglio, L., Van Der Werf, G. R., & Randerson, J. T., 2004. Top-down estimates of global CO sources using MOPITT measurements. *Geophysical research letters*, 31(1).

Arellano, A.F., Kasibhatla, P.S., Giglio, L., Van der Werf, G.R., Randerson, J.T. and Collatz, G.J., 2006. Time-dependent inversion estimates of global biomass-burning CO emissions using Measurement of Pollution in the Troposphere (MOPITT) measurements. *Journal of Geophysical Research: Atmospheres*, 111(D9).

Baklanov, A., Molina, L.T. and Gauss, M., 2016. Megacities, air quality and climate. *Atmospheric Environment*, 126, pp.235-249, 25.

Bakwin, P.S.,.Tans, P.P, and Novelli, P.C., 1994. Carbon monoxide budget in the Northern hemisphere. *Geophysical research letters*, 21, 433-436.

Barletta, B., Meinardi, S., Simpson, I.J., Atlas, E.L., Beyersdorf, A.J., Baker, A.K., Blake, N.J., Yang, M., Midyett, J.R., Novak, B.J. and McKeachie, R.J., 2009. Characterization of volatile organic compounds (VOCs) in Asian and north American pollution plumes during INTEX-B: identification of specific Chinese air mass tracers. *Atmospheric Chemistry and Physics*, 9(14), pp.5371-5388.

Basu, S., Miller, J.B. and Lehman, S., 2016. Separation of biospheric and fossil fuel fluxes of CO_2 by atmospheric inversion of CO_2 and $^{14}CO_2$ measurements: Observation System Simulations. *Atmospheric Chemistry and Physics*, 16(9).

Benedetti, A., Morcrette, J.J., Boucher, O., Dethof, A., Engelen, R.J., Fisher, M., Flentje, H., Huneeus, N., Jones, L., Kaiser, J.W. and Kinne, S., 2009. Aerosol analysis and forecast in the European centre for medium-range weather forecasts integrated forecast system: 2. Data assimilation. *Journal of Geophysical Research: Atmospheres*, 114(D13).

Bey, I., Jacob, D.J., Yantosca, R.M., Logan, J.A., Field, B.D., Fiore, A.M., Li, Q., Liu, H.Y., Mickley, L.J. and Schultz, M.G., 2001. Global modeling of tropospheric chemistry with assimilated meteorology: Model description and evaluation. *Journal of Geophysical Research: Atmospheres*, 106(D19), pp.23073-23095.

Blake, D.R., Chen, T.Y., Smith Jr, T.W., Wang, C.J.L., Wingenter, O.W., Blake, N.J., Rowland, F.S. and Mayer, E.W., 1996. Three-dimensional distribution of nonmenthane hydrocarbons and halocarbons over the northwestern Pacific during the 1991 Pacific Exploratory Mission (PEM-West A). *Journal of Geophysical Research: Atmospheres*, 101(D1), pp.1763-1778.

Blake, N.J., Blake, D.R., Simpson, I.J., Meinardi, S., Swanson, A.L., Lopez, J.P., Katzenstein, A.S., Barletta, B., Shirai, T., Atlas, E. and Sachse, G., 2003. NMHCs and halocarbons in Asian continental outflow during the Transport and Chemical Evolution over the Pacific

(TRACE-P) Field Campaign: Comparison with PEM-West B. *Journal of Geophysical Research: Atmospheres*, 108(D20).

Blake, N.J., Streets, D.G., Woo, J.H., Simpson, I.J., Green, J., Meinardi, S., Kita, K., Atlas, E., Fuelberg, H.E., Sachse, G. and Avery, M.A., 2004. Carbonyl sulfide and carbon disulfide: Large-scale distributions over the western Pacific and emissions from Asia during TRACE-P. *Journal of Geophysical Research: Atmospheres*, 109(D15).

Bobbink, R., Hornung, M. and Roelofs, J.G., 1998. The effects of air-borne nitrogen pollutants on species diversity in natural and semi-natural European vegetation. *Journal of ecology*, 86(5), pp.717-738.

Boersma, K.F., Eskes, H.J., Dirksen, R.J., Veefkind, J.P., Stammes, P., Huijnen, V., Kleipool, Q.L., Sneep, M., Claas, J., Leitão, J. and Richter, A., 2011. An improved tropospheric NO 2 column retrieval algorithm for the Ozone Monitoring Instrument. *Atmospheric Measurement Techniques*, 4(9), pp.1905-1928.

Boersma, K.F., Eskes, H., Richter, A., De Smedt, I., Lorente, A., Beirle, S., Van Geffen, J., Peters, E., Van Roozendael, M. and Wagner, T., 2017. QA4ECV NO2 tropospheric and stratospheric vertical column data from OMI (Version 1.1) (data set), *Royal Netherlands Meteorological Institute* (KNMI).

Brioude, J., Arnold, D., Stohl, A., Cassiani, M., Morton, D., Seibert, P., Angevine, W., Evan, S., Dingwell, A., Fast, J.D. and Easter, R.C., 2013. The Lagrangian particle dispersion model FLEXPART-WRF version 3.1. *Geoscientific Model Development*, 6(6), pp.1889-1904.

Buchholz, R.R., Paton-Walsh, C., Griffith, D.W., Kubistin, D., Caldow, C., Fisher, J.A., Deutscher, N.M., Kettlewell, G., Riggenbach, M., Macatangay, R. and Krummel, P.B., 2016. Source and meteorological influences on air quality (CO, CH_4 & CO_2) at a Southern Hemisphere urban site. *Atmospheric Environment*, 126, pp.274-289.

Burnett, R.T., Pope III, C.A., Ezzati, M., Olives, C., Lim, S.S., Mehta, S., Shin, H.H., Singh, G., Hubbell, B., Brauer, M. and Anderson, H.R., 2014. An integrated risk function for estimating the global burden of disease attributable to ambient fine particulate matter exposure. *Environmental health perspectives*, 122(4), pp.397-403.

Charlson, R. J., Schwartz, S. E., Hales, J. M., Cess, R. D., Coakley, J. J., Hansen, J. E., & Hofmann, D. J., 1992. Climate forcing by anthropogenic aerosols. *Science*, 255(5043), 423-430.

Chen, D., Wang, Y., McElroy, M.B., He, K., Yantosca, R.M. and Sager, P.L., 2009. Regional CO pollution and export in China simulated by the high-resolution nested-grid GEOS-Chem model. *Atmospheric Chemistry and Physics*, 9(11), pp.3825-3839.

Claeyman, M., Attié, J.-L., El Amraoui, L., Cariolle, D., Peuch, V.-H., Teyssèdre, H., Josse, B., Ricaud, P., Massart, S., Piacentini, A., Cammas, J.-P., Livesey, N. J., Pumphrey, H. C., and Edwards, D. P., 2010. A linear CO chemistry parameterization in a chemistry-transport model: evaluation and application to data assimilation, *Atmospheric Chemistry and Physics*, 10, 6097–6115, https://doi.org/10.5194/acp-10-6097-2010.

Clappier, A., Belis, C.A., Pernigotti, D. and Thunis, P., 2017. Source apportionment and sensitivity analysis: two methodologies with two different purposes. Geoscientific Model Development, 10(11), pp.4245-4256.

Ciais, P., Paris, J.D., Marland, G., Peylin, P., Piao, S.L., Levin, I., Pregger, T., Scholz, Y., Friedrich, R., Rivier, L. and Houwelling, S., 2010. The European carbon balance. Part 1: fossil fuel emissions. *Global Change Biology*, 16(5), pp.1395-1408.

Ciais, P., Dolman, A.J., Bombelli, A., Duren, R., Peregon, A., Rayner, P.J., Miller, C., Gobron, N., Kinderman, G., Marland, G. and Gruber, N., 2014. Current systematic carbon-cycle observations and the need for implementing a policy-relevant carbon observing system. *Biogeosciences*, 11, pp.3547-3602.

Creutzig, F., Baiocchi, G., Bierkandt, R., Pichler, P.P. and Seto, K.C., 2015. Global typology of urban energy use and potentials for an urbanization mitigation wedge. *Proceedings of the National Academy of Sciences*, 112(20), pp.6283-6288.

Crisp, D., Fisher, B. M., O'Dell, C., Frankenberg, C., Basilio, R., Bösch, H., Brown, L. R., Castano, R., Connor, B., Deutscher, N. M., Eldering, A., Griffith, D., Gunson, M., Kuze, A., Mandrake, L., McDuffie, J., Messerschmidt, J., Miller, C. E., Morino, I., Natraj, V., Notholt, J., O'Brien, D. M., Oyafuso, F., Polonsky, I., Robinson, J., Salawitch, R., Sherlock, V., Smyth, M., Suto, H., Taylor, T. E., Thompson, D. R., Wennberg, P. O., Wunch, D., and Yung, Y. L., 2012. The ACOS CO_2 retrieval algorithm – Part II: Global XCO_2 data characterization, *Atmospheric Measurement Techniques*, 5, 687– 707, https://doi.org/10.5194/amt-5-687-2012.

Crisp, D., and Eldering, A., 2017. Comparisons of the Orbiting Carbon Observatory-2 (OCO-2) XCO_2 measurements with TCCON, *Atmospheric Measurement Techniques*, 10, 2209–2238, https://doi.org/10.5194/amt- 10-2209-2017.

Crutzen, P.J., Heidt, L.E., Krasnec, J.P., Pollock, W.H. and Seiler, W., 1979. Biomass burning as a source of atmospheric gases CO, H_2, N_2O, NO, CH_3Cl and COS. *Nature*, 282(5736), p.253.

Crutzen, P.J. and Andreae, M.O., 1990. Biomass burning in the tropics: Impact on atmospheric chemistry and biogeochemical cycles. *Science*, 250(4988), pp.1669-1678.

De Wachter, E., Barret, B., Le Flochmoën, E., Pavelin, E., Matricardi, M., Clerbaux, C., Hadji-Lazaro, J., George, M., Hurtmans, D., Coheur, P.-F., Nedelec, P., and Cammas, J. P., 2012. Retrieval of MetOp-A/IASI CO profiles and validation with MOZAIC data, *Atmospheric Measurement Techniques*, 5, 2843–2857, https://doi.org/10.5194/amt-5-2843-2012.

Deeter, M. N., Martínez-Alonso, S., Edwards, D. P., Emmons, L. K., Gille, J. C., Worden, H. M., Sweeney, C., Pittman, J. V., Daube, B. C., and Wofsy, S. C., 2014. The MOPITT Version 6 product: algorithm enhancements and validation, *Atmospheric Measurement Techniques*, 7, 3623–3632, https://doi.org/10.5194/amt-7-3623-2014.

Deeter, M. N., Edwards, D. P., Francis, G. L., Gille, J. C., Martínez-Alonso, S., Worden, H. M.,

& Sweeney, C., 2017. A climate-scale satellite record for carbon monoxide: the MOPITT Version 7 product. *Atmospheric Measurement Techniques*, 10(7), 2533-2555.

Djuricin, S., Pataki, D.E. and Xu, X., 2010. A comparison of tracer methods for quantifying CO_2 sources in an urban region. *Journal of Geophysical Research: Atmospheres*, 115(D11).

Dlugokencky, E.J., P.M. Lang, J.W. Mund, A.M. Crotwell, M.J. Crotwell, and K.W. Thoning. 2018. Atmospheric Carbon Dioxide Dry Air Mole Fractions from the NOAA ESRL Carbon Cycle Cooperative Global Air Sampling Network, 1968-2017, Version: 2018-07-31, Path: ftp://aftp.cmdl.noaa.gov/data/trace_gases/co2/flask/surface/.

Dobbie, K.E., McTaggart, I.P. and Smith, K.A., 1999. Nitrous oxide emissions from intensive agricultural systems: variations between crops and seasons, key driving variables, and mean emission factors. Journal of Geophysical Research: Atmospheres, 104(D21), pp.26891-26899.

Doney, S. C., Mahowald, N., Lima, I., Feely, R. A., Mackenzie, F. T., Lamarque, J. F., and Rasch, P. J., 2007. Impact of anthropogenic atmospheric nitrogen and sulfur deposition on ocean acidification and the inorganic carbon system, *Proceedings of the National Academy of Sciences,* USA, 104, 14580–14585.

Duncan, B. N., Martin, R. V., Staudt, A. C., Yevich, R., and Logan, J. A., 2003. Interannual and seasonal variability of biomass burning emissions constrained by satellite observations, *Journal of Geophysical Research: Atmospheres*, 108(D2), 4100, doi:10.1029/2002JD002378.

Duncan, B. N. and Bey, I., 2004. A modeling study of the export pathways of pollution from Europe: Seasonal and interannual variations (1987–1997). *Journal of Geophysical Research: Atmospheres*, 109(D8).

Duren, R.M. and Miller, C.E., 2012. Measuring the carbon emissions of megacities. *Nature Climate Change*, 2(8), p.560.

Emmons, L.K., Hess, P.G., Lamarque, J.F. and Pfister, G.G., 2012. Tagged ozone mechanism for MOZART-4, CAM-chem and other chemical transport models. *Geoscientific Model Development*, 5(6), p.1531.

Feely, R. A., Sabine, C. L., Lee, K., Berelson, W., Kleypas, J., Fabry, V. J., & Millero, F. J., 2004. Impact of anthropogenic CO_2 on the $CaCO_3$ system in the oceans. *Science*, 305(5682), 362-366.

Fisher, J. A., Murray, L. T., Jones, D. B. A., and Deutscher, N. M., 2017. Improved method for linear carbon monoxide simulation and source attribution in atmospheric chemistry models illustrated using GEOS-Chem v9, *Geoscientific Model Development*, 10, 4129-4144, https://doi.org/10.5194/gmd-10-4129-2017.

Flagan, R.C. and Seinfeld, J.H., 2012. Fundamentals of air pollution engineering. *Courier Corporation*.

Flemming, J., Inness, A., Flentje, H., Huijnen, V., Moinat, P., Schultz, M. G., and Stein, O., 2009. Coupling global chemistry transport models to ECMWF's integrated forecast system, *Geoscientific Model Development*, 2, 253–265, https://doi.org/10.5194/gmd-2-253- 2009.

Flemming, J., Huijnen, V., Arteta, J., Bechtold, P., Beljaars, A., Blechschmidt, A.-M., Diamantakis, M., Engelen, R. J., Gaudel, A., Inness, A., Jones, L., Josse, B., Katragkou, E., Marecal, V., Peuch, V.-H., Richter, A., Schultz, M. G., Stein, O., and Tsikerdekis, A., 2015. Tropospheric chemistry in the Integrated Forecasting System of ECMWF, *Geoscientific Model Development*, 8, 975–1003, https://doi.org/10.5194/gmd-8-975-2015.

Flemming, J., Benedetti, A., Inness, A., Engelen, R. J., Jones, L., Huijnen, V., Remy, S., Parrington, M., Suttie, M., Bozzo, A., Peuch, V.-H., Akritidis, D., and Katragkou, E., 2017. The CAMS interim Reanalysis of Carbon Monoxide, Ozone and Aerosol for 2003–2015, *Atmospheric Chemistry and Physics*, 17, 1945–1983, https://doi.org/10.5194/acp-17-1945-2017.

Fourth National Climate Assessment (NCA4), 2018. https://nca2018.globalchange.gov/.

Fuhrer, J. and Booker, F., 2003. Ecological issues related to ozone: agricultural issues. *Environment International*, 29(2-3), pp.141-154.

Gaffney, J.S. and Marley, N.A., 2009. The impacts of combustion emissions on air quality and climate–From coal to biofuels and beyond. *Atmospheric Environment*, 43(1), pp.23-36.

Galanter, M., Levy, H. and Carmichael, G.R., 2000. Impacts of biomass burning on tropospheric CO, NO_X, and O3. *Journal of Geophysical Research: Atmospheres*, 105(D5), pp.6633-6653.

Gamnitzer, U., Karstens, U., Kromer, B., Neubert, R.E., Meijer, H.A., Schroeder, H. and Levin, I., 2006. Carbon monoxide: A quantitative tracer for fossil fuel CO_2?. *Journal of Geophysical Research: Atmospheres*, 111(D22).

Gately, C.K. and Hutyra, L.R., 2017. Large uncertainties in urban-scale carbon emissions. *Journal of Geophysical Research: Atmospheres*, 122(20), pp.11-242.

Gaubert, B., Arellano, A. F., Barré, J., Worden, H. M., Emmons, L. K., Tilmes, S., … Jones, N., 2016. Toward a chemical reanalysis in a coupled chemistry climate model: An evaluation of MOPITT CO assimilation and its impact on tropospheric composition. *Journal of Geophysical Research: Atmospheres*, 121, 7310–7343. https://doi.org/10.1002/2016JD024863.

Granier, C., Mueller, J. F., Pétron, G., & Brasseur, G., 1999. A three-dimensional study of the global CO budget. *Chemosphere-Global Change Science*, 1(1-3), 255-261.

Graven, H.D., Stephens, B.B., Guilderson, T.P., Campos, T.L., Schimel, D.S., Campbell, J.E. and Keeling, R.F., 2009. Vertical profiles of biospheric and fossil fuel-derived CO_2 and fossil fuel CO_2: CO ratios from airborne measurements of Δ14C, CO_2 and CO above Colorado, USA. *Tellus B: Chemical and Physical Meteorology*, 61(3), pp.536-546.

Graven, H., Fischer, M.L., Lueker, T., Jeong, S., Guilderson, T.P., Keeling, R.F., Bambha, R., Brophy, K., Callahan, W., Cui, X. and Frankenberg, C., 2018. Assessing fossil fuel CO_2 emissions in California using atmospheric observations and models. *Environmental Research Letters*, 13(6), p.065007.

Grell, G. A., Peckham, S. E., Schmitz, R., McKeen, S. A., Frost, G., Skamarock, W. C., & Eder, B, 2005. Fully coupled "online" chemistry within the WRF model. *Atmospheric Environment*, 39(37), 6957-6975.

Guenther, A., Hewitt, C.N., Erickson, D., Fall, R., Geron, C., Graedel, T., Harley, P., Klinger, L., Lerdau, M., McKay, W.A. and Pierce, T., 1995. A global model of natural volatile organic compound emissions. *Journal of Geophysical Research: Atmospheres*, 100(D5), pp.8873-8892.

Guenther, A., Karl, T., Harley, P., Wiedinmyer, C., Palmer, P.I. and Geron, C., 2006. Estimates of global terrestrial isoprene emissions using MEGAN (Model of Emissions of Gases and Aerosols from Nature). *Atmospheric Chemistry and Physics*, 6(11), pp.3181-3210.

Guo, S., Hu, M., Zamora, M.L., Peng, J., Shang, D., Zheng, J., Du, Z., Wu, Z., Shao, M., Zeng, L. and Molina, M.J., 2014. Elucidating severe urban haze formation in China. *Proceedings of the National Academy of Sciences*, 111(49), pp.17373-17378.

Hao, W.M. and Liu, M.H., 1994. Spatial and temporal distribution of tropical biomass burning. *Global biogeochemical cycles*, 8(4), pp.495-503.

Hassler, B., McDonald, B.C., Frost, G.J., Borbon, A., Carslaw, D.C., Civerolo, K., Granier, C., Monks, P.S., Monks, S., Parrish, D.D. and Pollack, I.B., 2016. Analysis of long-term observations of NO_X and CO in megacities and application to constraining emissions inventories. *Geophysical research letters*, 43(18), pp.9920-9930.

Heald, C.L., Jacob, D.J., Jones, D., Palmer, P.I., Logan, J.A., Streets, D.G., Sachse, G.W., Gille, J.C., Hoffman, R.N. and Nehrkorn, T., 2004. Comparative inverse analysis of satellite (MOPITT) and aircraft (TRACE-P) observations to estimate Asian sources of carbon monoxide. *Journal of Geophysical Research: Atmospheres*, 109(D23).

Houghton, R.A., House, J.I., Pongratz, J., Van Der Werf, G.R., DeFries, R.S., Hansen, M.C., Quéré, C.L. and Ramankutty, N., 2012. Carbon emissions from land use and land-cover change. *Biogeosciences*, 9(12), pp.5125-5142.

Hurrell, J.W., Holland, M.M., Gent, P.R., Ghan, S., Kay, J.E., Kushner, P.J., Lamarque, J.F., Large, W.G., Lawrence, D., Lindsay, K. and Lipscomb, W.H., 2013. The community earth system model: a framework for collaborative research. *Bulletin of the American Meteorological Society*, 94(9), pp.1339-1360.

Hutyra, L.R., Duren, R., Gurney, K.R., Grimm, N., Kort, E.A., Larson, E. and Shrestha, G., 2014. Urbanization and the carbon cycle: Current capabilities and research outlook from the natural sciences perspective. *Earth's Future*, 2(10), pp.473-495.

Jalkanen, L., 2012. WMO/IGAC impacts of megacities on air pollution and climate. *Urban Climate*, 1, 67-68.

Kaiser, J.W., Heil, A., Andreae, M.O., Benedetti, A., Chubarova, N., Jones, L., Morcrette, J.J., Razinger, M., Schultz, M.G., Suttie, M. and Van Der Werf, G.R., 2012. Biomass burning emissions estimated with a global fire assimilation system based on observed fire radiative power. *Biogeosciences*, 9, 527-554, https://doi.org/10.5194/bg-9-527-2012.

Kaplan, J.O., Krumhardt, K.M., Ellis, E.C., Ruddiman, W.F., Lemmen, C. and Goldewijk, K.K., 2011. Holocene carbon emissions as a result of anthropogenic land cover change. *The Holocene*, 21(5), pp.775-791.

Kennedy, C.A., Stewart, I., Facchini, A., Cersosimo, I., Mele, R., Chen, B., Uda, M., Kansal, A., Chiu, A., Kim, K.G. and Dubeux, C., 2015. Energy and material flows of megacities. *Proceedings of the National Academy of Sciences*, 112(19), pp.5985-5990.

Keppel-Aleks, G., Randerson, J.T., Lindsay, K., Stephens, B.B., Keith Moore, J., Doney, S.C., Thornton, P.E., Mahowald, N.M., Hoffman, F.M., Sweeney, C. and Tans, P.P., 2013. Atmospheric carbon dioxide variability in the Community Earth System Model: Evaluation and transient dynamics during the twentieth and twenty-first centuries. *Journal of Climate*, 26(13), pp.4447-4475.

Kesselmeier, J. and Staudt, M., 1999. Biogenic volatile organic compounds (VOC): an overview on emission, physiology and ecology. *Journal of atmospheric chemistry*, 33(1), pp.23-88.

Konovalov, I.B., Berezin, E.V., Ciais, P., Broquet, G., Zhuravlev, R.V. and Janssens-Maenhout, G., 2016. Estimation of fossil-fuel CO_2 emissions using satellite measurements of" proxy" species. *Atmospheric Chemistry and Physics*, 16(21), p.13509.

Koukouli, M. E., Theys, N., Ding, J., Zyrichidou, I., Mijling, B., Balis, D., and van der A, R. J., 2018. Updated SO_2 emission estimates over China using OMI/Aura observations, *Atmospheric Measurement Techniques*, 11, 1817-1832, https://doi.org/10.5194/amt-11-1817-2018.

Krotkov, N.A., Carn, S.A., Krueger, A.J., Bhartia, P.K. and Yang, K., 2006. Band residual difference algorithm for retrieval of SO_2 from the aura ozone monitoring instrument (OMI). *IEEE Transactions on geoscience and remote sensing*, 44(5), pp.1259-1266.

Krotkov, N. A., McLinden, C. A., Li, C., Lamsal, L. N., Celarier, E. A., Marchenko, S. V., Swartz, W. H., Bucsela, E. J., Joiner, J., Duncan, B. N., Boersma, K. F., Veefkind, J. P., Levelt, P. F., Fioletov, V. E., Dickerson, R. R., He, H., Lu, Z., and Streets, D. G., 2016. Aura OMI observations of regional SO_2 and NO_2 pollution changes from 2005 to 2015, *Atmospheric Chemistry and Physics*, 2016, 4605-4629, https://doi.org/10.5194/acp-16-4605-2016.

Lamarque, J.F., Bond, T.C., Eyring, V., Granier, C., Heil, A., Klimont, Z., Lee, D., Liousse, C., Mieville, A., Owen, B. and Schultz, M.G., 2010. Historical (1850–2000) gridded anthropogenic and biomass burning emissions of reactive gases and aerosols: methodology and application. *Atmospheric Chemistry and Physics*, 10(15), pp.7017-7039.

Lamarque, J.F., Emmons, L.K., Hess, P.G., Kinnison, D.E., Tilmes, S., Vitt, F., Heald, C.L., Holland, E.A., Lauritzen, P.H., Neu, J. and Orlando, J.J., 2012. CAM-chem: Description and evaluation of interactive atmospheric chemistry in the Community Earth System Model. *Geoscientific Model Development*, 5(2), p.369.

Le Quéré, C., Andrew, R. M., Friedlingstein, P., Sitch, S., Pongratz, J., Manning, A. C., Korsbakken, J. I., Peters, G. P., Canadell, J. G., Jackson, R. B., Boden, T. A., Tans, P. P., Andrews, O. D., Arora, V. K., Bakker, D. C. E., Barbero, L., Becker, M., Betts, R. A., Bopp, L., Chevallier, F., Chini, L. P., Ciais, P., Cosca, C. E., Cross, J., Currie, K., Gasser, T., Harris, I., Hauck, J., Haverd, V., Houghton, R. A., Hunt, C. W., Hurtt, G., Ilyina, T., Jain, A. K., Kato, E., Kautz, M., Keeling, R. F., Klein Goldewijk, K., Körtzinger, A., Landschützer, P., Lefèvre, N., Lenton, A., Lienert, S., Lima, I., Lombardozzi, D., Metzl, N., Millero, F., Monteiro, P. M. S., Munro, D. R., Nabel, J. E. M. S., Nakaoka, S.-I., Nojiri, Y., Padin, X. A., Peregon, A., Pfeil, B., Pierrot, D., Poulter, B., Rehder, G., Reimer, J., Rödenbeck, C., Schwinger, J., Séférian, R., Skjelvan, I., Stocker, B. D., Tian, H., Tilbrook, B., Tubiello, F. N., van der Laan-Luijkx, I. T., van der Werf, G. R., van Heuven, S., Viovy, N., Vuichard, N., Walker, A. P., Watson, A. J., Wiltshire, A. J., Zaehle, S., and Zhu, D., 2018. Global Carbon Budget 2017, *Earth System Science Data*, 10, 405-448, https://doi.org/10.5194/essd-10-405-2018.

Lelieveld, J., Evans, J.S., Fnais, M., Giannadaki, D. and Pozzer, A., 2015. The contribution of outdoor air pollution sources to premature mortality on a global scale. *Nature*, 525(7569), p.367.

Levin, I., Kromer, B., Schmidt, M. and Sartorius, H., 2003. A novel approach for independent budgeting of fossil fuel CO_2 over Europe by $14CO_2$ observations. *Geophysical Research Letters*, 30(23).

Levin, I. and Karstens, U.T.E., 2007. Inferring high-resolution fossil fuel CO_2 records at continental sites from combined $^{14}CO_2$ and CO observations. Tellus B: Chemical and Physical Meteorology, 59(2), pp.245-250.

Levin, I., Hammer, S., Kromer, B. and Meinhardt, F., 2008. Radiocarbon observations in atmospheric CO_2: determining fossil fuel CO_2 over Europe using Jungfraujoch observations as background. *Science of the Total Environment*, 391(2-3), pp.211-216.

Levy, R.C., Remer, L.A., Kleidman, R.G., Mattoo, S., Ichoku, C., Kahn, R. and Eck, T.F., 2010. Global evaluation of the Collection 5 MODIS dark-target aerosol products over land. *Atmospheric Chemistry and Physics*, 10(21), pp.10399-10420.

Li, Q., Jacob, D.J., Bey, I., Palmer, P.I., Duncan, B.N., Field, B.D., Martin, R.V., Fiore, A.M., Yantosca, R.M., Parrish, D.D. and Simmonds, P.G., 2002. Transatlantic transport of pollution and its effects on surface ozone in Europe and North America. *Journal of Geophysical Research: Atmospheres*, 107(D13).

Li, M., Zhang, Q., Kurokawa, J.-I., Woo, J.-H., He, K., Lu, Z., Ohara, T., Song, Y., Streets, D. G., Carmichael, G. R., Cheng, Y., Hong, C., Huo, H., Jiang, X., Kang, S., Liu, F., Su, H., and Zheng, B., 2017. MIX: a mosaic Asian anthropogenic emission inventory under the

international collaboration framework of the MICS-Asia and HTAP, *Atmospheric Chemistry and Physics*, 17, 935-963, https://doi.org/10.5194/acp-17-935-2017.

Liu, H., Jacob, D.J., Bey, I., Yantosca, R.M., Duncan, B.N. and Sachse, G.W., 2003. Transport pathways for Asian pollution outflow over the Pacific: Interannual and seasonal variations. *Journal of Geophysical Research: Atmospheres*, 108(D20).

Mage, D., Ozolins, G., Peterson, P., Webster, A., Orthofer, R., Vandeweerd, V. and Gwynne, M., 1996. Urban air pollution in megacities of the world. *Atmospheric Environment*, 30(5), pp.681-686.

Maher, B. A., Ahmed, I. A., Karloukovski, V., MacLaren, D. A., Foulds, P. G., Allsop, D., Mann, D. M., Torres-Jardón, R., and Calderon-Garciduenas, L., 2016. Magnetite pollution nanoparticles in the human brain, *Proceedings of the National Academy of Sciences*, 113, 10797–10801.

Massart, S., Agustí-Panareda, A., Heymann, J., Buchwitz, M., Chevallier, F., Reuter, M., Hilker, M., Burrows, J. P., Deutscher, N. M., Feist, D. G., Hase, F., Sussmann, R., Desmet, F., Dubey, M. K., Griffith, D. W. T., Kivi, R., Petri, C., Schneider, M., and Velazco, V. A., 2016. Ability of the 4-D-Var analysis of the GOSAT BESD XCO_2 retrievals to characterize atmospheric CO_2 at large and synoptic scales, *Atmospheric Chemistry and Physics*, 16, 1653–1671, https://doi.org/10.5194/acp-16-1653-2016.

Mi, Z., Meng, J., Guan, D., Shan, Y., Liu, Z., Wang, Y., Feng, K. and Wei, Y.M., 2017. Pattern changes in determinants of Chinese emissions. *Environmental Research Letters*, 12(7), p.074003.

Miller, J.B., Lehman, S.J., Montzka, S.A., Sweeney, C., Miller, B.R., Karion, A., Wolak, C., Dlugokencky, E.J., Southon, J., Turnbull, J.C. and Tans, P.P., 2012. Linking emissions of fossil fuel CO_2 and other anthropogenic trace gases using atmospheric $^{14}CO_2$. *Journal of Geophysical Research: Atmospheres*, 117(D8).

Morcrette, J.J., Boucher, O., Jones, L., Salmond, D., Bechtold, P., Beljaars, A., Benedetti, A., Bonet, A., Kaiser, J.W., Razinger, M. and Schulz, M., 2009. Aerosol analysis and forecast in the European Centre for medium-range weather forecasts integrated forecast system: Forward modeling. *Journal of Geophysical Research: Atmospheres*, 114(D6).

Morino, I., Uchino, O., Inoue, M., Yoshida, Y., Yokota, T., Wennberg, P. O., Toon, G. C.,Wunch, D., Roehl, C. M., Notholt, J., Warneke, T., Messerschmidt, J., Griffith, D. W. T., Deutscher, N. M., Sherlock, V., Connor, B., Robinson, J., Sussmann, R., and Rettinger, M., 2011. Preliminary validation of column-averaged volume mixing ratios of carbon dioxide and methane retrieved from GOSAT short-wavelength infrared spectra, *Atmospheric Measurement Techniques*, 4, 1061–1076, https://doi.org/10.5194/amt-4-1061-2011.

Nathan, B., Lauvaux, T., Turnbull, J. and Gurney, K., 2018. Investigations into the use of multi-species measurements for source apportionment of the Indianapolis fossil fuel CO_2 signal. Elementa: *Science of the Anthropocene*, 6(1).

National Academies of Sciences, Engineering, and Medicine, 2016. The Future of Atmospheric Chemistry Research: Remembering Yesterday, Understanding Today, Anticipating Tomorrow. Washington, DC*: The National Academies Press*. doi: 10.17226/23573.

National Academies of Sciences, Engineering, and Medicine. 2018. Thriving on Our Changing Planet: A Decadal Strategy for Earth Observation from Space. Washington, DC: The National Academies Press. https://doi.org/10.17226/24938.

National Research Council, 2010. Verifying greenhouse gas emissions: methods to support international climate agreements. *National Academies Press*.

Newman, S., Xu, X., Gurney, K.R., Hsu, Y.K., Li, K.F., Jiang, X., Keeling, R., Feng, S., O'Keefe, D., Patarasuk, R. and Wong, K.W., 2016. Toward consistency between trends in bottom-up CO_2 emissions and top-down atmospheric measurements in the Los Angeles megacity. *Atmospheric Chemistry and Physics*, 16(6), pp.3843-3863.

Ohara, T., Akimoto, H., Kurokawa, J., Horii, N., Yamaji, K., Yan, X., and Hayasaka, T., 2007. An Asian emission inventory of anthropogenic emission sources for the period 1980–2020, *Atmospheric Chemistry and Physics*, 7, 4419–4444, https://doi.org/10.5194/acp-7-4419-2007.

Osterman, G. B., Eldering, A., Avis, C., Chafin, B., O'Dell, C. W., Frankenberg, C., Fisher, B. M., Mandrake, L., Wunch, D., Granat, R., and Crisp, D., 2016. Orbiting Carbon Observatory-2 (OCO-2) data product user's guide, operational L1 and L2 data versions 7 and 7R, *Jet Propulsion Laboratory*, Pasadena, CA, USA.

Palmer, P. I., Jacob, D. J., Mickley, L. J., Blake, D. R., Sachse, G. W., Fuelberg, H. E., & Kiley, C. M., 2003. Eastern Asian emissions of anthropogenic halocarbons deduced from aircraft concentration data. *Journal of Geophysical Research: Atmospheres*, 108(D24).

Park, M., Randel, W.J., Emmons, L.K. and Livesey, N.J., 2009. Transport pathways of carbon monoxide in the Asian summer monsoon diagnosed from Model of Ozone and Related Tracers (MOZART). *Journal of Geophysical Research: Atmospheres*, 114(D8).

Parrish, D.D., Trainer, M., Hereid, D., Williams, E.J., Olszyna, K.J., Harley, R.A., Meagher, J.F. and Fehsenfeld, F.C., 2002. Decadal change in carbon monoxide to nitrogen oxide ratio in US vehicular emissions. *Journal of Geophysical Research: Atmospheres*, 107(D12), pp.ACH-5.

Parrish, D. D., 2006. Critical evaluation of US on-road vehicle emission inventories. *Atmospheric Environment*, 40(13), 2288-2300.

Pétron, G., Granier, C., Khattatov, B., Yudin, V., Lamarque, J.F., Emmons, L., Gille, J. and Edwards, D.P., 2004. Monthly CO surface sources inventory based on the 2000–2001 MOPITT satellite data. *Geophysical research letters*, 31(21).

Petron, G., A.M. Crotwell, P.M. Lang, E. Dlugokencky (2018), Atmospheric Carbon Monoxide Dry Air Mole Fractions from the NOAA ESRL Carbon Cycle Cooperative Global Air

Sampling Network, 1988-2017, Version: 2018-10-17, Path: ftp://aftp.cmdl.noaa.gov/data/trace_gases/co/flask/surface/.

Pfister, G., Petron, G., Emmons, L.K., Gille, J.C., Edwards, D.P., Lamarque, J.F., Attie, J.L., Granier, C. and Novelli, P.C., 2004. Evaluation of CO simulations and the analysis of the CO budget for Europe. *Journal of Geophysical Research: Atmospheres*, 109(D19).

Pfister, G.G., Avise, J., Wiedinmyer, C., Edwards, D.P., Emmons, L.K., Diskin, G.D., Podolske, J. and Wisthaler, A., 2011. CO source contribution analysis for California during ARCTAS-CARB. *Atmospheric Chemistry and Physics*, 11(15), pp.7515-7532.

Pfister, G.G., Reddy, P.J., Barth, M.C., Flocke, F.F., Fried, A., Herndon, S.C., Sive, B.C., Sullivan, J.T., Thompson, A.M., Yacovitch, T.I. and Weinheimer, A.J., 2017. Using Observations and Source-Specific Model Tracers to Characterize Pollutant Transport During FRAPPÉ and DISCOVER-AQ. *Journal of Geophysical Research: Atmospheres*, 122(19).

Protonotariou, A. P., Kostopoulou, E., Tombrou, M., & Giannakopoulos, C., 2013. European CO budget and links with synoptic circulation based on GEOS-CHEM model simulations. *Tellus B: Chemical and Physical Meteorology*, 65(1), 18640.

Raman, A., & Arellano Jr, A. F., 2017. Spatial and Temporal Variations in Characteristic Ratios of Elemental Carbon to Carbon Monoxide and Nitrogen Oxides across the United States. *Environmental science & technology*, 51(12), 6829-6838.

Reay, D.S., Davidson, E.A., Smith, K.A., Smith, P., Melillo, J.M., Dentener, F. and Crutzen, P.J., 2012. Global agriculture and nitrous oxide emissions. *Nature climate change*, 2(6), p.410.

Reid, J. S., R. Koppmann, T. F. Eck, and D. P. Eleuterio, 2005a. A review of biomass burning emissions part II: Intensive physical properties of biomass burning particles, *Atmospheric Chemistry and Physics*, 5(3), 799–825.

Reid, J. S., T. F. Eck, S. A. Christopher, R. Koppmann, O. Dubovik, D. P. Eleuterio, B. N. Holben, E. A. Reid, and J. Zhang, 2005b. A review of biomass burning emissions part III: Intensive optical properties of biomass burning particles, *Atmospheric Chemistry and Physics*, 5(3), 827–849.

Reid, J.S., Hyer, E.J., Prins, E.M., Westphal, D.L., Zhang, J., Wang, J., Christopher, S.A., Curtis, C.A., Schmidt, C.C., Eleuterio, D.P. and Richardson, K.A., 2009. Global monitoring and forecasting of biomass-burning smoke: Description of and lessons from the Fire Locating and Modeling of Burning Emissions (FLAMBE) program. *IEEE Journal of Selected Topics in Applied Earth Observations and Remote Sensing*, 2(3), pp.144-162.

Reuter, M., Buchwitz, M., Hilboll, A., Richter, A., Schneising, O., Hilker, M., Heymann, J., Bovensmann, H. and Burrows, J.P., 2014. Decreasing emissions of NO_X relative to CO_2 in East Asia inferred from satellite observations. *Nature Geoscience*, 7(11), p.792.

Riahi, K., Rao, S., Krey, V., Cho, C., Chirkov, V., Fischer, G., Kindermann, G., Nakicenovic, N. and Rafaj, P., 2011. RCP 8.5—A scenario of comparatively high greenhouse gas emissions. *Climatic Change*, 109(1-2), p.33.

Richter, A., Burrows, J.P., Nü., H., Granier, C. and Niemeier, U., 2005. Increase in tropospheric nitrogen dioxide over China observed from space. *Nature*, 437(7055), p.129.

Saeki, T., Patra, P. K., 2017. Implications of overestimated anthropogenic CO2 emissions on East Asian and global land CO2 flux inversion. Geoscience Letters, 4(1), 9.

Schultz, M.G., Heil, A., Hoelzemann, J.J., Spessa, A., Thonicke, K., Goldammer, J.G., Held, A.C., Pereira, J.M. and van Het Bolscher, M., 2008. Global wildland fire emissions from 1960 to 2000. *Global biogeochemical cycles*, 22(2).

Seiler, W. and Crutzen, P.J., 1980. Estimates of gross and net fluxes of carbon between the biosphere and the atmosphere from biomass burning. *Climatic change*, 2(3), pp.207-247.

Shiga, Y.P., Michalak, A.M., Gourdji, S.M., Mueller, K.L. and Yadav, V., 2014. Detecting fossil fuel emissions patterns from subcontinental regions using North American in situ CO_2 measurements. Geophysical research letters, 41(12), pp.4381-4388.

Shindell, D., Lamarque, J.-F., Unger, N., Koch, D., Faluvegi, G., Bauer, S., Ammann, M., Cofala, J., and Teich, H.: Climate forcing and air quality change due to regional emissions reductions by economic sector, *Atmospheric Chemistry and Physics*, 8, 7101–7113, https://doi.org/10.5194/acp-8-7101-2008, 2008.

Shindell, D., Faluvegi, G., Walsh, M., Anenberg, S. C., Van Dingenen, R., Muller, N. Z., Austin, J., Koch, D., and Milly, G., 2011. Climate, health, agricultural and economic impacts of tighter vehicle-emission standards, *Nature Climate Change*, 1, 59–66.

Silva, S.J., Arellano, A.F. and Worden, H.M., 2013. Toward anthropogenic combustion emission constraints from space-based analysis of urban CO_2/CO sensitivity. *Geophysical research letters*, 40(18), pp.4971-4976.

Silva, S. and Arellano, A.F., 2017. Characterizing regional-scale combustion using satellite retrievals of CO, NO_2 and CO_2. *Remote Sensing*, 9(7), p.744.

Sindelarova, K., Granier, C., Bouarar, I., Guenther, A., Tilmes, S., Stavrakou, T., Müller, J.F., Kuhn, U., Stefani, P. and Knorr, W., 2014. Global data set of biogenic VOC emissions calculated by the MEGAN model over the last 30 years. *Atmospheric Chemistry and Physics*, 14(17), pp.9317-9341.

Staudt, A. C., Jacob, D. J., Logan, J. A., Bachiochi, D., Krishnamurti, T. N., & Sachse, G. W., 2001. Continental sources, transoceanic transport, and interhemispheric exchange of carbon monoxide over the Pacific. *Journal of Geophysical Research: Atmospheres*, 106(D23), 32571-32589.

Stohl, A., Forster, C., Frank, A., Seibert, P. and Wotawa, G., 2005. The Lagrangian particle

dispersion model FLEXPART version 6.2. *Atmospheric Chemistry and Physics*, 5(9), pp.2461-2474.

Streets, D.G., Zhang, Q., Wang, L., He, K., Hao, J., Wu, Y., Tang, Y. and Carmichael, G.R., 2006. Revisiting China's CO emissions after the transport and chemical evolution over the Pacific (TRACE-P) mission: synthesis of inventories, atmospheric modeling, and observations. *Journal of Geophysical Research: Atmospheres*, 111(D14).

Streets, D.G., Canty, T., Carmichael, G.R., de Foy, B., Dickerson, R.R., Duncan, B.N., Edwards, D.P., Haynes, J.A., Henze, D.K., Houyoux, M.R. and Jacob, D.J., 2013. Emissions estimation from satellite retrievals: A review of current capability. *Atmospheric Environment*, 77, pp.1011-1042.

Sun, W., Shao, M., Granier, C., Liu, Y., Ye, C.S. and Zheng, J.Y., 2018. Long-Term Trends of Anthropogenic SO_2, NO_X, CO, and NMVOCs Emissions in China. *Earth's Future*, 6(58), pp.1112-1133.

Suntharalingam, P., Jacob, D. J., Palmer, P. I., Logan, J. A., Yantosca, R. M., Xiao, Y. P., Evans, M. J., Streets, D. G., Vay, S. L., and Sachse, G. W., 2004. Improved quantification of Chinese carbon fluxes using CO_2/CO correlations in Asian outflow, *Journal of Geophysical Research: Atmospheres*, 109, D18S18, https://doi.org/10.1029/2003jd004362.

Tang. W., Arellano, A.F., 2017. Investigating dominant characteristics of fires across the Amazon during 2005–2014 through satellite data synthesis of combustion signatures. *Journal of Geophysical Research: Atmospheres*, 122(2), 1224-1245.

Tang, W., Arellano, A. F., DiGangi, J. P., Choi, Y., Diskin, G. S., Agustí-Panareda, A., Parrington, M., Massart, S., Gaubert, B., Lee, Y., Kim, D., Jung, J., Hong, J., Hong, J.-W., Kanaya, Y., Lee, M., Stauffer, R. M., Thompson, A. M., Flynn, J. H., and Woo, J.-H., 2018. Evaluating high-resolution forecasts of atmospheric CO and CO_2 from a global prediction system during KORUS-AQ field campaign, *Atmospheric Chemistry and Physics*, 18, 11007-11030, https://doi.org/10.5194/acp-18-11007-2018.

Tang, W., Arellano, A. F., Gaubert, B., Miyazaki, K., and Worden, H. M., 2019a. Satellite data reveal a common combustion emission pathway for major cities in China, Atmosphere Chemistry and Physics, 19, 4269-4288, https://doi.org/10.5194/acp-19-4269-2019.

Tang, W., Emmons, L.K., Arellano Jr, A.F., Gaubert, B., Knote, C., Tilmes, S., Buchholz, R.R., Pfister, G.G., Diskin, G.S., Blake, D.R. and Blake, N.J., 2019b. Source contributions to carbon monoxide concentrations during KORUS-AQ based on CAM-chem model applications. *Journal of Geophysical Research: Atmospheres*, https://doi.org/10.1029/2018JD029151.

Tang, W., et al., 2019. Elucidating the Utility of CO_2 and CO Analysis in Tracking Fossil Fuel CO_2, *Atmosphere Chemistry and Physics,* to be submitted.

Taylor, K. E., 2001. Summarizing multiple aspects of model performance in a single diagram,

Journal of Geophysical Research: Atmospheres, 106, 7183–7192.

Tilmes, S., Lamarque, J.F., Emmons, L.K., Kinnison, D.E., Ma, P.L., Liu, X., Ghan, S., Bardeen, C., Arnold, S.R., Deeter, M. and Vitt, F., 2015. Description and evaluation of tropospheric chemistry and aerosols in the Community Earth System Model (CESM1. 2). *Geoscientific Model Development*, 8, pp.1395-1426.

Tubiello, F.N., Salvatore, M., Rossi, S., Ferrara, A., Fitton, N. and Smith, P., 2013. The FAOSTAT database of greenhouse gas emissions from agriculture. *Environmental Research Letters*, 8(1), p.015009.

Turnbull, J.C., Miller, J.B., Lehman, S.J., Tans, P.P., Sparks, R.J. and Southon, J., 2006. Comparison of $14CO_2$, CO, and SF6 as tracers for recently added fossil fuel CO_2 in the atmosphere and implications for biological CO_2 exchange. *Geophysical research letters*, 33(1).

Turnbull, J. C., Tans, P. P., Lehman, S. J., Baker, D., Conway, T. J., Chung, Y. S., Gregg, J., Miller, J. B., Southon, J. R., and Zhou, L. X., 2011. Atmospheric observations of carbon monoxide and fossil fuel CO_2 emissions from East Asia, *Journal of Geophysical Research: Atmospheres*, 116, D24306, https://doi.org/10.1029/2011JD016691.

Turnbull, J.C., Sweeney, C., Karion, A., Newberger, T., Lehman, S.J., Tans, P.P., Davis, K.J., Lauvaux, T., Miles, N.L., Richardson, S.J. and Cambaliza, M.O., 2015. Toward quantification and source sector identification of fossil fuel CO_2 emissions from an urban area: Results from the INFLUX experiment. Journal of Geophysical Research: Atmospheres, 120(1), pp.292-312.

United Nations: Population Division, 2016. The World's Cities in 2016 – Data Booklet (ST/ESA/ SER.A/392), Department of Economic and Social Affairs, available at: http: //www.un.org/en/development/desa/population/publications/pdf/urbanization/the_worlds _cities_in_2016_data_booklet.pdf (last access: 4 August 2017).

van der A, R. J., Mijling, B., Ding, J., Koukouli, M. E., Liu, F., Li, Q., Mao, H., and Theys, N., 2017. Cleaning up the air: effectiveness of air quality policy for SO_2 and NO_X emissions in China, *Atmospheric Chemistry and Physics*, 17, 1775-1789, https://doi.org/10.5194/acp-2017-1775-2017.

van der Werf, G.R., Randerson, J.T., Giglio, L., Collatz, G.J., Kasibhatla, P.S. and Arellano Jr, A.F., 2006. Interannual variability in global biomass burning emissions from 1997 to 2004. *Atmospheric Chemistry and Physics*, 6(11), pp.3423-3441.

Van der Werf, G.R., Randerson, J.T., Giglio, L., Collatz, G.J., Mu, M., Kasibhatla, P.S., Morton, D.C., DeFries, R.S., Jin, Y.V. and van Leeuwen, T.T., 2010. Global fire emissions and the contribution of deforestation, savanna, forest, agricultural, and peat fires (1997–2009). *Atmospheric Chemistry and Physics*, 10(23), pp.11707-11735.

Van Dingenen, R., Dentener, F.J., Raes, F., Krol, M.C., Emberson, L. and Cofala, J., 2009. The global impact of ozone on agricultural crop yields under current and future air quality legislation. *Atmospheric Environment*, 43(3), pp.604-618.

Veefkind, J.P., Aben, I., McMullan, K., Förster, H., De Vries, J., Otter, G., Claas, J., Eskes, H.J., De Haan, J.F., Kleipool, Q. and Van Weele, M., 2012. TROPOMI on the ESA Sentinel-5 Precursor: A GMES mission for global observations of the atmospheric composition for climate, air quality and ozone layer applications. *Remote Sensing of Environment*, 120, pp.70-83.

Vogel, F., Hamme, S., Steinhof, A., Kromer, B. and Levin, I., 2010. Implication of weekly and diurnal ^{14}C calibration on hourly estimates of CO-based fossil fuel CO_2 ata moderately polluted site in southwestern Germany. *Tellus B: Chemical and Physical Meteorology*, 62(5), pp.512-520.

Voulgarakis, A. and Field, R.D., 2015. Fire influences on atmospheric composition, air quality and climate. *Current Pollution Reports*, 1(2), pp.70-81.

Ward, D. E., and C. C. Hardy (1991), Smoke emissions from wildland fires, *Environment International*, 17(2), 117–134.

Wang, Y., Choi, Y., Zeng, T., Ridley, B., Blake, N., Blake, D. and Flocke, F., 2006. Late-spring increase of trans-Pacific pollution transport in the upper troposphere. *Geophysical research letters*, 33(1).

Wang, Y., Munger, J. W., Xu, S., McElroy, M. B., Hao, J., Nielsen, C. P., and Ma, H., 2010. CO_2 and its correlation with CO at a rural site near Beijing: implications for combustion efficiency in China, *Atmospheric Chemistry and Physics*, 10, 8881–8897, https://doi.org/10.5194/acp-10-8881-2010.

Wang, S. and Hao, J., 2012. Air quality management in China: Issues, challenges, and options. *Journal of Environmental Sciences*, 24(1), pp.2-13.

Wiedinmyer, C., Akagi, S.K., Yokelson, R.J., Emmons, L.K., Al-Saadi, J.A., Orlando, J.J. and Soja, A.J., 2011. The Fire INventory from NCAR (FINN): A high resolution global model to estimate the emissions from open burning. *Geoscientific Model Development*, 4(3), p.625.

Worden, H.M., Deeter, M.N., Edwards, D.P., Gille, J.C., Drummond, J.R. and Nédélec, P., 2010. Observations of near-surface carbon monoxide from space using MOPITT multispectral retrievals. *Journal of Geophysical Research: Atmospheres*, 115(D18).

World Bank, 2015. East Asia's Changing Urban Landscape: Measuring a Decade of Spatial Growth. Urban Development Series. Washington, DC: *World Bank*. doi: 10.1596/978-1-4648-0363-5.

World Health Organization, 2018. WHO Global Ambient Air Quality Database (update 2018).

Wunch, D., Wennberg, P.O., Toon, G.C., Keppel-Aleks, G. and Yavin, Y.G., 2009. Emissions of greenhouse gases from a North American megacity. *Geophysical research letters*, 36(15).

Wunch, D., Toon, G. C., Blavier, J. F. L., Washenfelder, R. A., Notholt, J., Connor, B. J., Griffith, D. W., Sherlock, V., and Wennberg, P. O., 2011. The total carbon column observing network, *Philosophical Transactions of the Royal Society A*, 369, 2087–2112.

Wunch, D., Wennberg, P. O., Osterman, G., Fisher, B., Naylor, B., Roehl, C. M., O'Dell, C., Mandrake, L., Viatte, C., Kiel, M., Griffith, D. W. T., Deutscher, N. M., Velazco, V. A., Notholt, J., Warneke, T., Petri, C., De Maziere, M., Sha, M. K., Sussmann, R., Rettinger, M., Pollard, D., Robinson, J., Morino, I., Uchino, O., Hase, F., Blumenstock, T., Feist, D. G., Arnold, S. G., Strong, K., Mendonca, J., Kivi, R., Heikkinen, P., Iraci, L., Podolske, J., Hillyard, P. W., Kawakami, S., Dubey, M. K., Parker, H. A., Sepulveda, E., García, O. E., Te, Y., Jeseck, P., Gunson, M. R., Crisp, D., and Eldering, A., 2017. Comparisons of the Orbiting Carbon Observatory-2 (OCO-2) XCO_2 measurements with TCCON, *Atmospheric Measurement Techniques*, 10, 2209-2238, https://doi.org/10.5194/amt-10-2209-2017.

Xue, L., Wang, T., Simpson, I.J., Ding, A., Gao, J., Blake, D.R., Wang, X., Wang, W., Lei, H. and Jin, D., 2011. Vertical distributions of non-methane hydrocarbons and halocarbons in the lower troposphere over northeast China. *Atmospheric Environment*, 45(36), pp.6501-6509.

Yang, X. J., 2013. China's rapid urbanization, *Science*, 342, 310–310.

Zhang, Q., Streets, D.G., Carmichael, G.R., He, K.B., Huo, H., Kannari, A., Klimont, Z., Park, I.S., Reddy, S., Fu, J.S. and Chen, D., 2009. Asian emissions in 2006 for the NASA INTEX-B mission. *Atmospheric Chemistry and Physics*, 9(14), pp.5131-5153.

Zhu, Q., Peng, X. and Wu, K., 2012. Calculation and decomposition of indirect carbon emissions from residential consumption in China based on the input–output model. *Energy Policy*, 48, pp.618-626.

APPENDIX A

INVESTIGATING DOMINANT CHARACTERISTICS OF FIRES ACROSS THE AMAZON DURING 2005–2014 THROUGH SATELLITE DATA SYNTHESIS OF COMBUSTION SIGNATURES

(Published in the *Journal of Geophysical Research: Atmospheres*,
https://doi.org/10.1002/2016JD025216)

Wenfu Tang[1], Avelino F. Arellano[1]

[1]Department of Hydrology and Atmospheric Sciences, University of Arizona, Tucson, Arizona, USA.

Tang, W., & Arellano, A. F., 2017. Investigating dominant characteristics of fires across the Amazon during 2005–2014 through satellite data synthesis of combustion signatures. *Journal of Geophysical Research: Atmospheres*, 122(2), 1224-1245.

Abstract

Estimates of fire emissions remain uncertain due to limited constraints on the variations in fire characteristics. Here we demonstrate the utility of space-based observations of smoke constituents in addressing this limitation. We introduce a satellite-derived smoke index (***SI***) as an indicator of the dominant phase of large-scale fires. This index is calculated as the ratio of the geometric mean of observed fractional enhancements (due to fire) in carbon monoxide and aerosol optical depth to that of nitrogen dioxide. We assess the usefulness of this index on fires in the Amazon. We analyze the seasonal, regional, and interannual joint distribution of ***SI*** and fire radiative power (FRP) in relation to fire hotspots, land cover, drought severity index, and deforestation rate estimates. We also compare this index with an analogous quantity derived from field data or emission inventories. Our results show that ***SI*** changes from low (more flaming) to high (more smoldering) during the course of a fire season, which is consistent with the changes in observed maximum FRPs from high to low. We also find that flaming combustion is more dominant in areas where deforestation fires dominate, while smoldering combustion has a larger influence during drought years when understory fires are more likely enhanced. Lastly, we find that the spatiotemporal variation in ***SI*** is inconsistent with current emission inventories. Although we recognize some limitations of this approach, our results point to the utility of ***SI*** as a proxy for overall combustion efficiency in the parameterization of fire emission models.

1 Introduction

Fires have long been recognized as one of the major sources of radiatively- and chemically-active trace gases and aerosols in the atmosphere [Crutzen et al., 1979; Seiler and Crutzen, 1980; Crutzen and Andreae, 1990; Hao and Liu, 1994; Galanter et al. 2000; Andreae and Merlet, 2001; Duncan et al. 2003; Reid et al., 2005a and 2005b; van der Werf et al., 2006; Schultz et al. 2008; Reid et al., 2009; van der Werf et al., 2010; Lamarque et al., 2010; Wiedinmyer et al., 2011; Kaiser et al., 2012; Voulgarakis et al., 2015]. While highly variable across space and time, combustion products of biomass burning events across the globe constitute a significant fraction of the total direct anthropogenic emissions of CO_2, CO, CH_4, NO_x, OC, and BC according to current fire emission inventories such as Global Fire Emission Database (GFEDv3), Fire Inventory from NCAR (FINNv1), Fire Locating and Modeling of Burning Emissions (FLAMBE), and Global Fire Assimilation System (GFASv1). Regionally, enhancements in atmospheric abundance of these

smoke constituents are even more significant. Majority of CO_2, NO_X, and BC are released from savanna, grassland, and shrubland fires while a higher fraction of CO, CH_4, OC, and other particulate matter are contributed by tropical deforestation and degradation fires that mostly occur in southern South America, as well as peat fires that mostly occur in equatorial Asia. Fires contribute to significant perturbations in atmospheric composition causing substantial direct and/or indirect effects (and feedbacks) to air quality, weather, climate, ecosystem, agriculture, public health and safety [e.g., Andreae et al., 1991; Andreae, 1993; Christopher et al. 1996; Jacobson, 2004; Longo et al., 2009; Bowman et al., 2009; Langmann et al., 2009; Ward et al., 2012; Johnston et al., 2012; Keywood et al., 2013; Goldammer et al., 2013; Jacobson, 2014; Voulgarakis and Field, 2015; Saide et al., 2015; Pacifico et al., 2015; Reddington et al., 2015; Nazareno and Laurance, 2015]. A growing body of evidence also shows that the main drivers of these fire events (i.e., deforestation and drought) have been changing in the midst of rapidly transforming urban landscapes, and warmer and drier climate in these fire regions [e.g., Dennison et al., 2014; Golding and Betts, 2008; Westerling et al., 2006].

Smoke emissions can either be estimated using bottom-up or top-down approaches. Bottom-up estimates of the amount ($\boldsymbol{M_X}$, in g of $\boldsymbol{X}$ per fire) of trace gases and aerosols ($\boldsymbol{X}$) emitted from fires are traditionally derived from area burnt products ($\boldsymbol{A}$, in km^2), biomass available for burning per unit area or fuel load ($\boldsymbol{B}$, in kg of dry matter per km^2 or $\boldsymbol{FL}$ in other studies), combustion completeness ($\boldsymbol{C}$, in % or $\boldsymbol{CC}$ in other studies), and emission factors from laboratory and/or field data ($\boldsymbol{EF_X}$, in g of $\boldsymbol{X}$ per kg of dry matter) [Seiler and Crutzen 1980]. ($\boldsymbol{C}$) and ($\boldsymbol{EF_X}$) can be considered to be directly coupled and together signify fire combustion efficiency [Ward and Hardy, 1991; van Leeuwen and van der Werf, 2011; 2014]. Relatively higher combustion efficiency ($\boldsymbol{CE}$ or Modified Combustion Efficiency, $\boldsymbol{MCE}$) is related to flaming phase while relatively lower combustion efficiency is related to smoldering phase of a fire. Flaming combustion is associated with high levels of carbon, hydrogen, and nitrogen fuel oxidation to CO_2, H_2O, and NO_X, respectively. On the contrary, smoldering combustion is associated with high levels of incomplete combustion products such as CO and organic carbon aerosols [Ward and Hardy, 1991; Ferek et al., 1998; Andreae and Merlet, 2001; Bertschi et al., 2003; Yokelson et al., 2007; Akagi et al., 2011]. We note that whereas there have been studies on ($\boldsymbol{C}$) and ($\boldsymbol{EF_X}$), biomass

burning efficiency still remains to be fully understood and quantified [e.g., Andreae and Merlet, 2001; Schroeder et al., 2009; van Leeuwen and van der Werf, 2011; van Leeuwen et al., 2014].

Top-down observations also provide constraints on the estimates of these emissions. In particular, inverse analyses of smoke observations at or near a fire event have been conducted in the past to update prior emission estimates [e.g., Arellano et al., 2006; Chevalier et al., 2009; Kopacz et al., 2010; Hooghiemstra et al., 2012; Huneeus et al., 2012; Pechony et al., 2013; Mao et al., 2014; Konovalov et al., 2014]. A previous inter-comparison study of fire emission inventories showed reasonable consistency in large-scale temporal and spatial patterns but important differences (as large as a factor of 10) were found for monthly estimates [e.g., Al-Saadi et al., 2008; Urbanski et al., 2011]. While past inverse analyses have provided top-down constraints on these estimates, all of these analyses suffer from systematic issues such as mismatch in scales, errors in transforming emission to concentrations, and inconsistencies in emission estimates across species $\boldsymbol{X}$ [e.g., Stavrakou et al., 2015; Hyer et al., 2012]. Representativeness and model (transport, mixing, removal, chemistry) errors are difficult to address with a single modeling system and traditional methods/approximations. Moreover, despite the fact that multi-species inverse modeling studies have made progress using satellite and/or ground and/or airborne data [Kopacz et al., 2010; Hooghiemstra et al., 2012; Konovalov et al., 2014; Mao et al., 2014; Miyazaki et al., 2015], such studies have yet to directly connect and reconcile with emission inventories through improvements in understanding of combustion activity levels/fuel consumption ($\boldsymbol{A}$ and $\boldsymbol{B}$), and/or combustion efficiency and emission factors ($\boldsymbol{C}$ and $\boldsymbol{EF_X}$) [Streets et al., 2013].

A newer approach to quantifying fire emissions is through the use of satellite Fire Radiative Power ($\boldsymbol{FRP}$) or Fire Radiative Energy (FRE) retrievals [e.g., Wooster et al., 2005; Ichoku and Kaufman, 2005; Freeborn et al. 2008; Ichoku et al., 2008; Kaiser et al., 2012; Ichoku et al., 2014]. The amount of species $\boldsymbol{X}$ emitted during a fire can be estimated by the product of $\boldsymbol{FRE}$ and $\boldsymbol{C_e^X}$ (emission coefficient with unit of $\mathbf{kg\ MJ^{-1}}$). This has led to empirical approximations of 'combined' or 'bulk' combustion efficiency and regional emission coefficients and $\boldsymbol{EF_X}$ [e.g., Ichoku and Ellision, 2014; Schreir et al., 2014]. It is mostly applicable for large-scale fires in which satellite

products might most likely capture such events. However, both methods suffer from associated uncertainties in $\boldsymbol{EF_X}$ as well as undersampling due to clouds and aerosol contamination.

Overall, large uncertainties and inconsistencies remain to exist on our understanding of fire characteristics and associated smoke emissions. These uncertainties represent therefore a key challenge to understand and predict the impacts of fires and their strong interactions with other components of the Earth system [e.g., Kaiser and Keywood, 2015; Hyer et al., 2012; Knorr et al., 2012; Langmann et al., 2009]. These uncertainties are mainly due to the highly episodic and complex nature of fires across quite a variety of spatial and temporal scales, as well as ecological, environmental, and socio-economic conditions. This makes it very difficult to capture, study, and synthesize these fires and their consequences from a specific aspect of biomass burning, or particular observing, and/or modeling system alone [e.g., Schroeder et al., 2005]. An integrated approach to accurately and consistently monitor, quantify, assess, and predict fire emissions (and their impacts) is imperative at scales relevant to air quality, health, ecosystem services, and environmental policies [e.g., Goldammer, 2015; Kaiser and Keywood, 2015].

In light of decadal satellite-derived data on combustion products for CO (e.g., Measurements Of Pollution In The Troposphere, NASA Terra/MOPITT), NO_2 (e.g., Ozone Monitoring Instrument, NASA/Aura OMI), aerosols (e.g., in terms of Moderate Resolution Imaging Spectroradiometer – NASA Terra/Aqua MODIS Aerosol Optical Depth and OMI Aerosol Index), and CO_2 (e.g., Greenhouse gases Observing Satellite, JAXA/GOSAT and NASA Orbiting Carbon Observatory, OCO-2), there is a unique opportunity to explore and assess observational constraints on fire characteristics from these sets of retrievals. Observations of the relative abundance of these smoke constituents from space provide a means to assess and monitor the dominant smoldering/flaming properties of fires in the absence of field campaign data. This is especially the case given the availability of fire activity products from various satellite instruments (e.g., MODIS, Suomi National Polar-orbiting Partnership (NPP) satellite, Geostationary Operational Environmental Satellite (GOES)), which provide complementary information on fire emissions. Hence, in conjunction with fire activity data such as MODIS FRP, we present in this study a joint analysis of MOPITT CO, OMI NO_2 and MODIS AOD to investigate the potential utility of combining these retrievals in characterizing dominant combustion patterns during large-scale fire events. This is a proof-of-concept study, which is a direct extension of studies conducted by Konovalov et al.

[2014] on CO_2, CO, and AOD, Ichoku and Ellison [2014] on AOD and FRP, and Schreir et al. [2014] and Mebust and Cohen [2014] on NO_2 and FRP. Here we introduce a satellite-derived smoke index (***SI***), which is a combination of fire enhancements in CO, NO_2 and AOD, to indicate the integrated fire characteristics. This approach provides a synthesis on combustion efficiency, which to our knowledge has not been established for satellite retrievals. This index leverages on the complementary information of CO and AOD as indicators of incomplete combustion and NOx (and CO_2 when available) as an indicator of more complete combustion. This index can be used to diagnose the consistency of emission estimates for different constituents and consequently provide insights on combustion efficiency. This is especially useful when used within a data assimilation/inverse modeling framework (such as GFAS) as observational constraints on emission coefficients.

In this study, we focus on fires in the Amazon region. As previously mentioned, Amazon fires contribute significantly to global biomass burning emissions and have important influence on carbon budget and climate. There is also a unique opportunity in this region to test our approach in differentiating fire characteristics across different vegetation types (savanna versus tropical forest), fire types (deforestation versus non-deforestation/understory fires) as well as in identifying the influence of drought on fire characteristics. This is especially true given the relatively large number of studies including field campaigns conducted in the region.

The outline of this paper is as follows: In section 2, we describe the datasets and methods for analyzing the distribution of smoke variables. We investigate in section 3 the individual patterns of CO, NO_2, AOD, FRP, drought severity index, and deforestation rate across the recent decade (2005 to 2014) to provide a general overview of the average fire characteristics when viewed as separate smoke variables. We then introduce in section 4 a satellite-derived ***SI*** and analyze fire characteristics in the Amazon from the perspective of its joint statistical distribution. Here, we look at the spatiotemporal patterns of ***SI*** within the context of land cover, deforestation and drought to elucidate key factors influencing the observed smoke patterns. In section 5, we compare the ***SI*** to field measurements reported in literature and current fire emission inventories to further support our methodology. We discuss and summarize this study in section 6.

2 Data and Methods

2.1 Spatial Domain of Study

We select the study domain to coincide with the Large-Scale Biosphere-Atmosphere Experiment in Amazonia (LBA) Regional Boundary for the Amazon and Tocantins River Basins [Costa et al., 2003]. Spatial resolution of the LBA dataset is 0.083º (approximately 9 km). We convert it into 0.5º to coincide with the coarsest resolution among all datasets that we use in this study (e.g., MODIS Land Cover and Drought Severity Index). After regridding, the domain covers 70 half-degree grids in latitude and 110 half-degree grids in longitude and centered on the Amazon basin (about 200 km north of Porto Velho). All datasets described in the next section are re-gridded to 0.5º resolution (using simple averaging).

2.2 Satellite Retrievals and Ancillary Datasets

Table 1 is summary of the datasets used in this study. For CO, we use the NASA Terra Measurement of Pollution In The Troposphere (MOPITT) version 6, Level 2, multispectral (Thermal Infrared/Near Infrared) retrievals of carbon monoxide (CO) total columns. These retrievals exhibit an enhanced sensitivity to the lower tropospheric CO compared to thermal infrared only retrievals. In addition, this version of MOPITT has improved representation of CO variability on fine spatial scales. The geolocation bias has been characterized and eliminated in this version [Deeter et al., 2014]. For NO_2, we use tropospheric column retrievals from NASA Aura/OMI DOMINO v2.0. This version is an improvement of DOMINO v1.02 (in terms of air mass factor or AMF and sampling of a priori NO_2 profiles) and agrees better with independent measurements and model simulations [Boersma et al., 2011]. For aerosol abundance, we use MODIS aerosol optical depth (AOD) retrievals at 550 nm (Level 2 Collection 5.1 (dark target algorithm) from both NASA Terra (MOD04_L2) and Aqua (MYD04_L2) satellites [Levy et al., 2010, 2015].

To complement these smoke retrievals, we use MODIS FRP retrievals from Fire Information for Resource Management System (FIRMS) [Davies et al., 2009]. This provides information on fire intensity. We use fire counts based on thermal anomalies from MODIS Land Product Collection 5, Level 2 Thermal Anomalies from NASA Terra (MOD14_L2) and Aqua MYD14_L2 [Justice et

al., 2011] for fire detection. The fire counts have been used as part of the data filter (fire mask) to locate fires in the Amazon. The MODIS Land Cover Collection 5 [Friedl et al., 2010] is also used to classify the dominant land cover of the location where fires are detected. This product has a spatial resolution of 0.5º by 0.5º and is available for the year 2005 to 2012. The land cover class, which is based on IGBP, includes 4 forest subclasses, 2 woodlands (savannas), 1 grassland, 2 shrublands, 2 croplands, 1 wetland, and 4 unvegetated (urban, barren, water and snow). To better understand the two main drivers of fires in the Amazon, we use the data on deforestation from Program for the Estimation of Deforestation in the Brazilian Amazon (PRODES) and drought conditions from MODIS Global Terrestrial Drought Severity Index (DSI) [Mu et al., 2013]. Annual deforestation rates (km^2 $year^{-1}$) were directly taken from the PRODES website: http://www.obt.inpe.br/prodes/prodes_1988_2014.htm for 2005 to 2014. The PRODES deforestations maps (taken from the same website) has a resolution of 90m by 90m covering the Brazilian Amazon from 2005 to 2013. The PRODES project uses Landsat imageries to monitor the Amazon forest [Shimabukuro et al., 2012]. We use the annual MODIS DSI dataset at 0.5º by 0.5º resolution which is based from MODIS evapotranspiration (ET) and normalize difference vegetation index (NDVI) products (http://www.ntsg.umt.edu/project/dsi) spanning from 2000 to 2012. MODIS DSI provides an index of drought severity, with positive values corresponding to wetter than normal and negative values to drier than normal. We choose DSI because this provides temporally and spatially continuous information on vegetation and surface conditions and overcomes the limitations in using reanalysis data.

Table A1. Analysis datasets.

Instrument and Dataset **Website (download)** **Data Availability**	**Spatial Resolution** **Overpass Time** **Temporal Resolution**	**Relevance to Study** **(Main Product Reference)**
NASA Terra MOPITT CO version6, L2, TIR/NIR Retrieved CO Total Column https://www2.acom.ucar.edu/mopitt 2000 to present	22 km × 22 km 10:30 am daily	CO lower trop. concentration [Deeter et al., 2014]
Dutch OMI NO_2 (DOMINO) data product v2.0 Tropospheric Vertical Column http://www.temis.nl/airpollution/no2.html 2004 to present	13km × 25 km 1:45 pm daily	NO_2 trop. concentration [Boersma et al., 2011]
NASA Terra and Aqua MODIS AOD, C51, L2 Optical_Depth_Land_And_Ocean ladsweb.nascom.nasa.gov 2000 to present	10km × 10km 10:30 am and 1:30 pm daily	Aerosol abundance [Levy et al., 2010]
FIRMS MCD14ML Fire Radiative Power firms.modaps.eosdis.nasa.gov 2000 to present	~1 km × 1 km 10:30 am and 1:30 pm daily	Fire intensity [Davies et al., 2009]

NASA Terra and Aqua MODIS Thermal Anomalies, C5, L2 Fire Counts ladsweb.nascom.nasa.gov 2000 to present	~1 km × 1 km 10:30 am and 1:30 pm daily	Fire mask [Justice et al., 2010]
NASA MODIS Collection 5 Global Land Cover http://glcf.umd.edu/data/lc/ 2001 to 2012	0.5° × 0.5° annual	Land cover classification [Friedl et al., 2010]
PRODES deforestation http://www.obt.inpe.br/prodes/index.php	90m × 90m annual	Deforestation maps [Shimabukuro et al., 2012]
NASA MODIS Global Terrestrial Drought Severity Index http://www.ntsg.umt.edu/project/dsi 2000 to 2011	0.5° × 0.5° annual	Drought severity [Mu et al., 2013]

2.3 Spatiotemporal Filters

This study focuses on the LBA Amazon region defined in Costa et al. [2003]. We only consider fire season in this Amazon region from 2005 to 2014 corresponding to the months of June to November. While the dry (fire) season in this region typically occurs from July to October (with fires peaking in September), we include in the analysis the months of June, July and November to cover the entire evolution of fire season conditions and incorporate the possibility of modest changes in the growing season during drought years [e.g., Asner et al., 2000]. The total number of fire events during this period is shown in Figure A1a. We define a fire event for each half-degree grid cell to correspond to one or more fire counts on a given day. For each grid cell within the LBA regional domain, the total number of fire events can be interpreted as the total number of days of fire occurrence. If a fire event occurs every single day for a given grid cell, the maximum number would be 1830 days. But inherent sampling (revisit time, see Table 1) and associated retrieval issues from Terra/Aqua MODIS instrument limits this to a much lower number. We recognize that this approach does not distinguish the size and duration of individual fires. It represents, however, the aggregated (across the half-degree grid) information on when and where a fire has occurred. About 50 to 200 fire events have been registered for each grid, most of which are located in the southern and eastern part of the Amazon especially in Mato Grosso. Figure A1b shows the number of fire events we use in section 4 and later sections. This corresponds to the fire events for which CO, AOD, NO_2, and FRP data are all available. Although the number of fire events is reduced by a factor of 4, the spatial pattern of these fire events remains to be similar. The pair-wise (spatial) correlations between Figure A1a and 1b for each year and for the overall 10-year period vary from 0.6 to 0.9 (see Table AS1 of the supplementary material). The relatively high correlation reveals that our analysis represents the fire season consistently across the study period. We note that even though the samples maintain the spatial structure of fire activities across

the region, as indicated for example by high correlations (Table AS1), there is a large interannual variability in the fraction of fire counts used in this study that is not explicitly corrected in our estimates of ***SI*** and FRP. This may under-represent some of the years (e.g., 2009 and 2010) in the trend analysis. However, this issue is not expected to significantly influence our results.

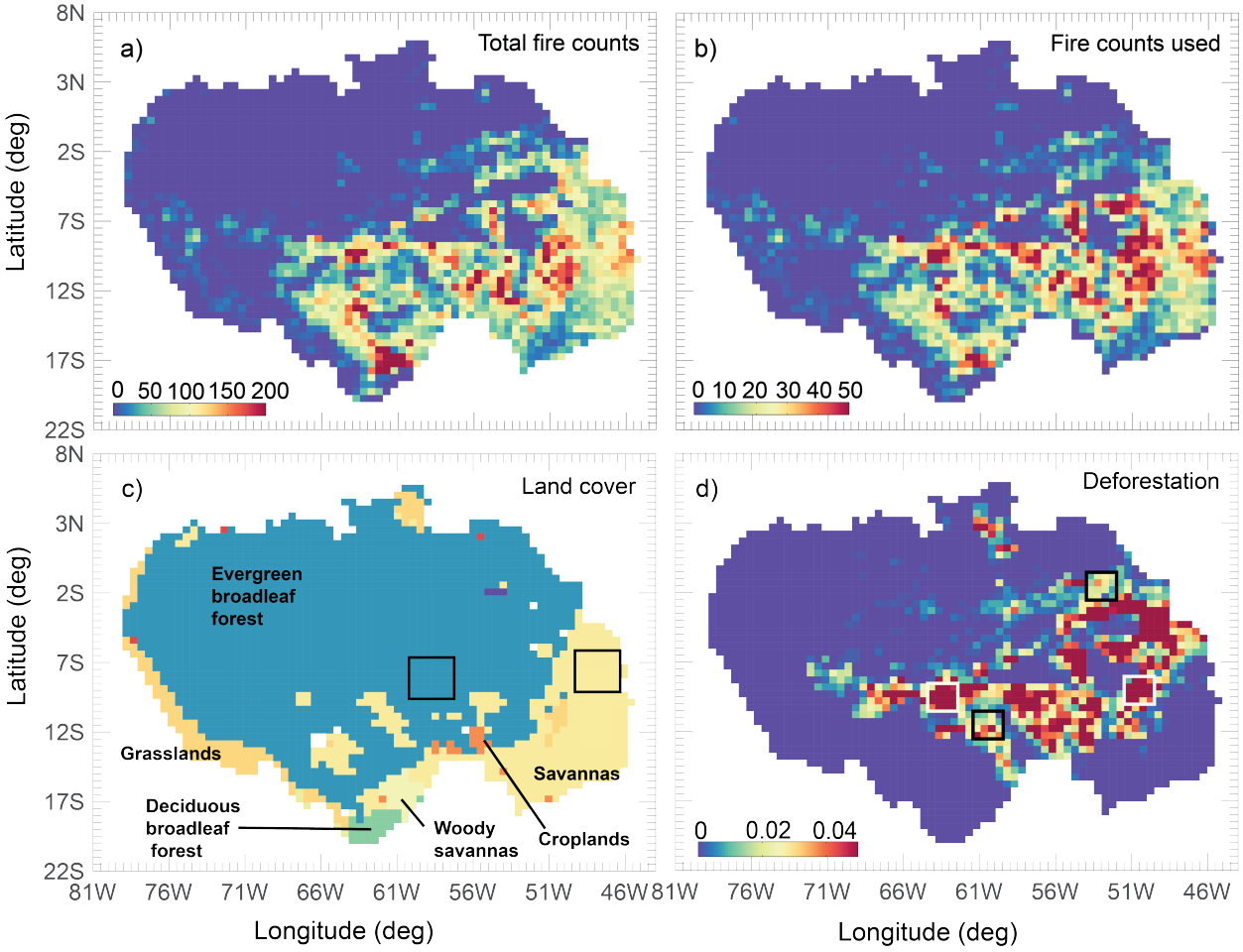

Figure A1. Maps of fire counts, land cover, and deforestation in Amazonia. Panels a) and b) correspond to total fire counts during fire seasons for 2005 to 2014 based on MODIS Thermal Anomaly and fire counts used in this study as fire mask, respectively. Panel c) is the dominant (mode) land cover classification for 2005 to 2012 from MODIS. We denote forest and non-forest locations for the sensitivity study in section 4.3.2 as black boxes in panel c). Panel d) is the total deforestation fraction in each grid during 2005-2013 based on PRODES. The white and black boxes correspond to regions used in our analysis of highly-deforested (A1) and barely-deforested areas (A2), respectively.

Dominant land cover across the study period within each half-degree grid cell is shown in Figure A1c. We use yearly MODIS dataset to identify the vegetation type of the fire events detected by

MODIS (section 4.3.2). For 2013 and 2014, we use the latest MODIS product for 2012 as there is no MODIS land cover dataset specific to these years available during the time of this study. Fire events occurred mostly along the edges of savanna, grassland, and tropical forest in the southeastern side of the Amazon basin. Deforestation activities in this region show a similar pattern. This is shown in Figure A1d as the accumulated fraction of deforested areas within the grid cell across the 2005-2013. Highly deforested areas in the Amazon (i.e., higher fraction) practically correspond to areas with larger number of fire events (arc-of-deforestation) [e.g., Malhi et al., 2008; Morton et al., 2008; Cardozo et al., 2014].

2.4 Field Campaign Data and Emission Inventories

We use enhancement ratios reported from field campaigns in the Amazon to assess the reasonableness of $\boldsymbol{SI}$ introduced in this study. We compile and summarize the data in Table AS2. This includes emission factors and/or ratios of CO_2, CO, NO_X, and particulate matter (PM) as well as MCE/CE and fire phases (when available). We note that different field campaigns provide different types of PM (e.g., PM2.5, PM4, PM10 and aerosol number (CN)). We derive average enhancement ratios from this compilation (when not available), which we then compare with $\boldsymbol{SI}$ (see section 5).

Since near-field enhancement ratios from field campaign are used by current emission inventories to parameterize $\boldsymbol{C}$ and $\boldsymbol{EF_x}$, we also examine a couple of emission inventories that follow a similar traditional methodology as described by Seiler and Crutzen [1980]. In particular, we calculated an analogous smoke index from GFED4s and FINNv1.5 to elucidate consistencies with our derived satellite-based $\boldsymbol{SI}$. Both GFED (http://www.globalfiredata.org, van der Werf et al., [2010]) and FINN (https://www2.acom.ucar.edu/modeling/finn-fire-inventory-ncar, Wiedinmyer et al., [2011]) use emission factors $\boldsymbol{EF_X}$ based on the compilation by Andreae and Merlet [2001] and Akagi et al. [2011].

3 Spatial and Temporal Distribution of Smoke Variables

In this section, we present the individual spatiotemporal patterns of CO, AOD, and NO_2 together with correlative datasets on fire counts, FRP, DSI, and deforestation rates. These patterns provide a general context of fires in this region similar to traditional analysis approaches done in the past.

We will further elaborate on the joint statistical distribution of these variables in section 4 where we introduce ***SI***.

For this analysis, we use all available data for each smoke variable. Temporally, we find overall decreasing trends on CO, NO_2, AOD and FRP which are well correlated with the trend on deforestation rate while the anomalies (especially for CO and AOD) are well correlated with drought. We also find strikingly similar spatial patterns between CO and AOD (R=0.72) as well as between NO_2 and FRP.

Anomaly Trends. For FRP, AOD, CO, and NO_2, we calculate the average cycle of the fire season for the entire domain using a Gaussian fit to the daily data (183 days x 10 years). We then subtract this seasonal cycle from the daily data to calculate daily anomalies. The anomalies are then concatenated across the entire study period. We estimate a linear trend to this resulting time series using a standard linear regression analysis on the mean anomalies. The results are shown in Figure A2 together with the annual average of MODIS DSI and total PRODES deforestation rates. We find that all variables decreased in the recent decade with CO and FRP decreasing faster than AOD and NO_2. The decreasing trends are well correlated with the trend on deforestation rate (R=0.45 to 0.70). This is consistent with Chen et al. [2013] who pointed out that fires in 2005-2012 have a small decrease in trend and large year-to-year variations. A decreasing trend after 2006 in AOD due to policy shift was also reported by Koren et al. [2007]. Drought, on the other hand, confounds this pattern by enhancing the anomalies during drier years (negative DSI) especially for well-correlated CO and AOD (R=0.68). We note that year 2006 is drier than usual although it is not directly considered to be ENSO-like drought year [e.g., Eduardo et al., 2007; Lewis et al., 2011]. This year also shows similar enhancement pattern on the anomalies with 2005, 2007, and 2010. It appears that drought enhances fires in the region which is consistent with literature [e.g., Alencar et al., 2006; Aragao et al., 2007; Chen et al., 2013]. The enhancements on CO and aerosol

abundance during drought years suggest that drought has a larger impact on smoldering fires which is associated with larger amounts of CO and aerosol emissions.

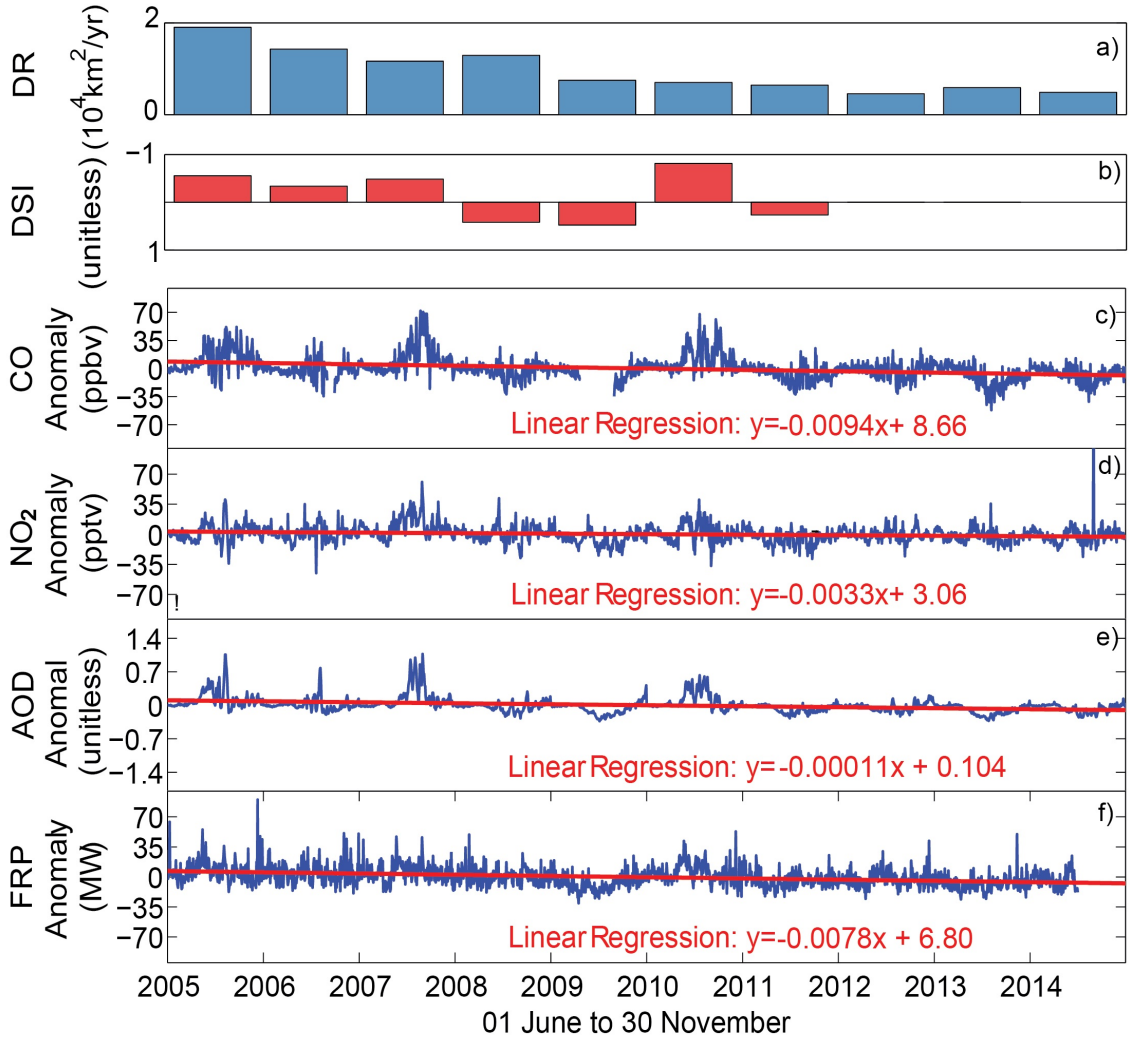

Figure A2. Temporal trends of smoke variables. The first two rows correspond to deforestation from PRODES and annual drought (negative value means drier than usual) from MODIS DSI, respectively. Remaining rows correspond to daily anomalies of CO (c), NO_2 (d), AOD (e), and FRP (f) over the fire season (June to November). Trends are represented as linear regression lines (red).

Spatial Patterns. Figure A3 shows the spatial distribution of DSI, CO, NO_2, AOD, and FRP. High loadings of CO and aerosols are centered in the south (Mato Grosso) while high NO_2 and more intense fires (higher FRP) are found in the eastern side of Amazonia (mostly in Para). While there

is a large inter-annual variability (as shown in the standard deviation), we find strikingly similar spatial patterns between CO and AOD (R = 0.72) as well as between NO_2 and FRP (R = 0.45). This is clearly shown in the average and anomaly plots. The differences in the typical lifetime of CO (1–2 months), NO_2 (hours to days), and aerosols (days to weeks) may partially contribute to the differences in spatial pattern in Figure A3 especially between CO and NO_2. Mesoscale to regional weather conditions (i.e., transport at weekly scale in time and in the order of hundred kilometers in space) can also play a role on the similarity between CO and AOD. On the other hand, there is also a possibility that the differences in spatial patterns observed are also due to differences in fire characteristics among these fire areas. Fires in the south are represented by higher CO and aerosol abundance, while fires in the eastern side of the basin are represented by higher NO_2 concentrations. We will investigate this further in section 4 by focusing on 'coincident' datasets of fire and loadings of fire constituents and their joint distribution.

Finally, we find good correspondence on drought (Figure A3) with the variability in CO and AOD anomalies (Figure A3) and on deforestation (Figure A1d) with the variability in NO_2 and FRP. This is consistent with the temporal trend of these anomalies (Figure A2). During drought years, positive anomalies of CO, NO_2, AOD, and FRP can be observed but mostly evident for CO and AOD. The spatial pattern of DSI, however, is not necessarily correlated with fires (R = -0.04) (e.g., the northern part of Amazon) and their combustion (smoke) signatures (for CO and AOD, R = -0.23; for NO_2, R = 0.15), in contrast to deforestation patterns shown in Figure A1.

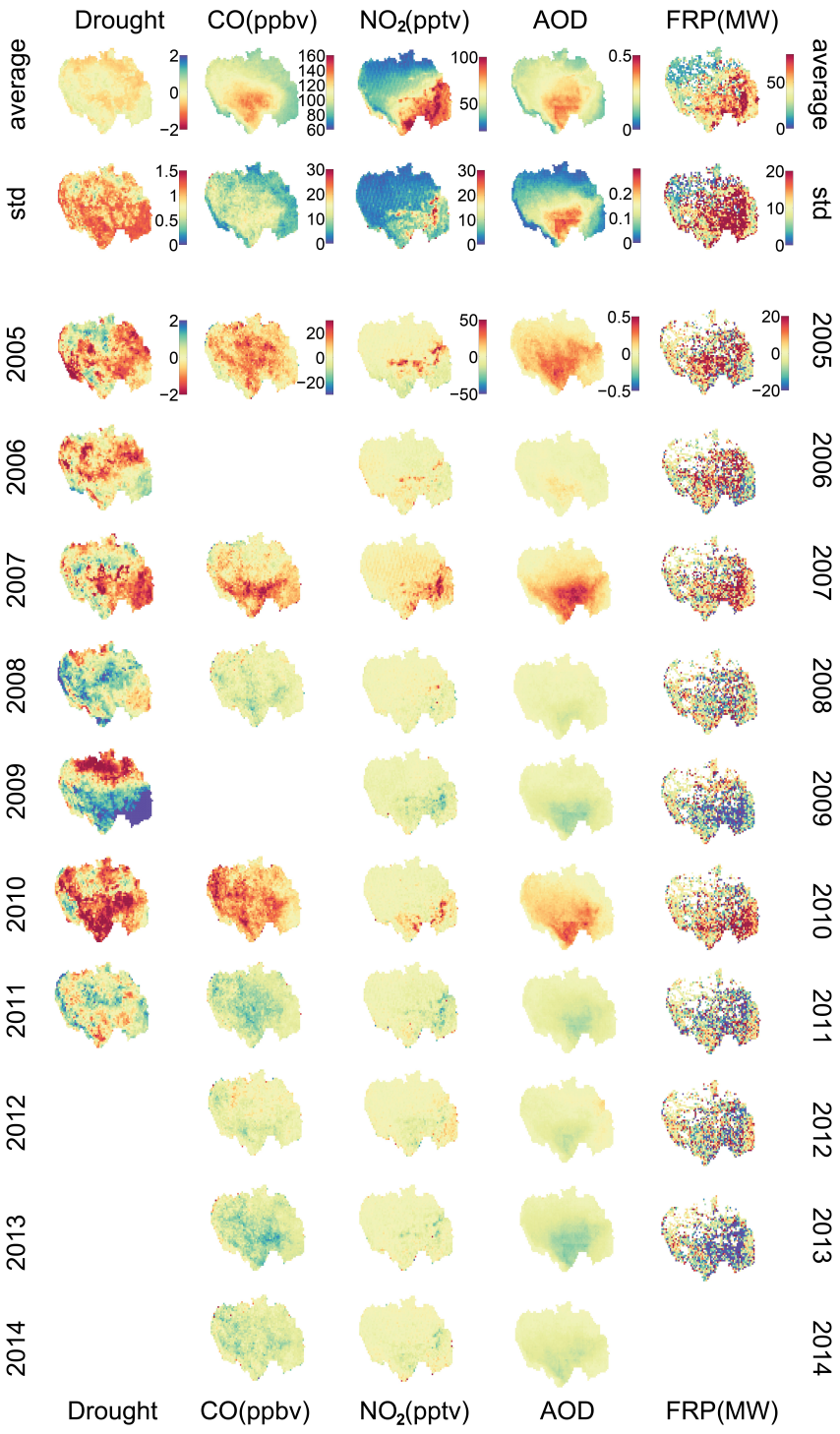

Figure A3. Spatial distribution of drought, CO, NO_2, AOD, and FRP. The first two rows correspond to decadal average and standard deviation (ca. 2005-2014), The remaining rows correspond to annual anomalies. Blank plots mean incomplete data across the fire season. Corresponding units are as follows: drought-unitless, CO-ppbv, NO_2-pptv, AOD-unitless, and FRP-MW.

4 Satellite-derived Smoke Index (*SI*)

Here, we introduce ***SI*** as an indicator of the dominant phase (smoldering/flaming) of large-scale fires. The joint distribution of smoke variables provides a means to glean on variations in fire properties. Thus, we carry out a series of analysis to separate key characteristics that influence fire emission and smoke profiles. We highlight here the strong relationship between **FRP** and ***SI***.

4.1 Multi-species Analysis

The combination of CO, AOD, and NO_2, in conjunction with FRP, can provide insights on combustion efficiency with CO and AOD as indicator of smoldering and NO_2 as an indicator of flaming combustion. Previous studies have shown, however, that there is a linear relationship between fire intensity (i.e., FRP) and NO_X over different biomass burning regions in the world, including central South America [Schreier et al., 2014]. The same linear relationship has been reported between FRP and the logarithm of MODIS AOD Level 3 over the Brazilian Amazon [Mishra et al., 2015]. With this, we carry out a similar regression analysis on monthly scales across our spatial domain. We find that at this resolution, the three smoke constituents are positively and linearly correlated with FRP (Figure A4), which is consistent with previous studies. The correlation coefficients between FRP and CO, NO_2, and AOD are 0.68, 0.83, and 0.68, respectively. This is expected since the dominant factor governing the relationship between FRP and emissions of fire products at a low spatiotemporal resolution could be combustion activity (see section 1). However, emissions also vary depending on combustion efficiency [Ward and Hardy, 1991; Andreae and Merlet, 2001; Akagi et al., 2011; Yokelson et al., 2007; Ferek et al., 1998], which could be dominant at a finer resolution.

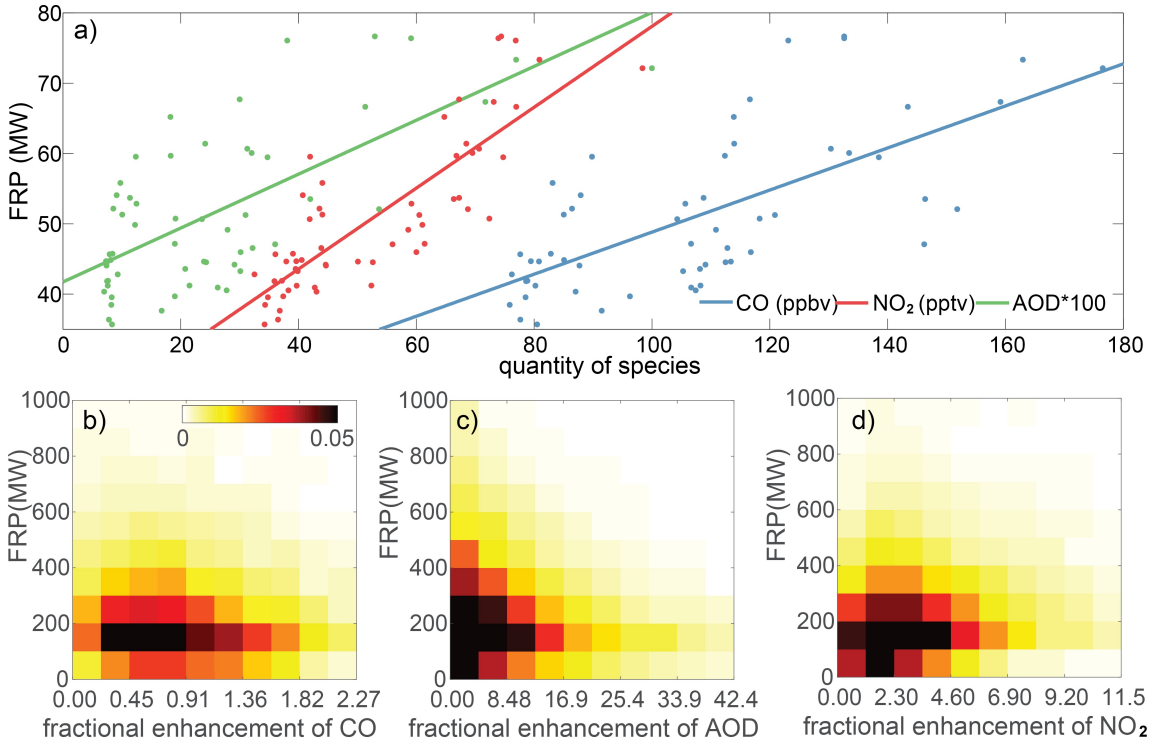

Figure A4. Average relationship of FRP and CO, NO_2, and AOD. Top panel corresponds to linear regression analysis of the corresponding monthly-mean across the entire study domain (CO in blue, NO_2 in red, and AOD scaled by 100 in green). Resulting coefficients and correlations are as follows: $\mathbf{FRP = 0.30 \times CO + 18.90, R = 0.68}$; $\mathbf{FRP = 0.58 \times NO_2 + 20.56, R = 0.83}$; $\mathbf{FRP = 38.34 \times AOD + 41.72, R = 0.68}$. Bottom panels correspond to the joint probability density function (pdf) of FRP and fractional enhancements of CO (left), NO_2 (center), and AOD (right).

We investigate these relationships at relatively finer scales to further distinguish the dominant fire characteristic. For every single fire event (see Figure A1b), we calculate the fractional enhancement in concentration for each smoke constituent due to fire. That is,

$$\boldsymbol{f}_{\Delta \boldsymbol{X}} = \frac{[\boldsymbol{X}] - [\boldsymbol{X}]_{\boldsymbol{b}}}{[\boldsymbol{X}]_{\boldsymbol{b}}} \qquad \text{(A1)}$$

where $[\boldsymbol{X}]$ is the smoke constituent's column abundance coincident with the fire event, and $[\boldsymbol{X}]_{\boldsymbol{b}}$ is the average background abundance. The background value is defined for each pixel (location), year (time), and constituent. In particular, we specify the background value of a constituent (see Figure AS1 in the supplementary material) on a particular grid in the study domain as the 25th percentile of the data for non-fire days across the fire season of a particular year. We have defined

a spatially and temporally explicit background to account for transported air mass contribution to the local fire enhancement. This contribution can be large for CO and aerosols which have relatively longer lifetime than the characteristic transport timescales in this region (see Figure AS1). This approach also accounts for the variations in lifetime of aerosols during drought conditions when dry season precipitation is reduced. Our choice of a specific percentile is a tradeoff between the use of a larger number of data points for robust analysis and having negative enhancements (e.g., higher percentile results in a higher background value increasing chances of negative daily enhancements). However, we note that the main results do not change with different percentile assumptions. We also recognize that we cannot completely eliminate the influence of transport and lifetime using this method alone. Nevertheless, our results consistently reflect the observed patterns of large-scale smoke signatures in view of different factors influencing fire characteristics.

Figure A4 (bottom panels) shows the joint probability density function (pdf) of FRP and fractional enhancement $\boldsymbol{f}_{\Delta X}$. Each bin corresponds to the joint probability that FRP and $\boldsymbol{f}_{\Delta X}$ are associated with particular bin values (>90th percentile of $\boldsymbol{f}_{\Delta X}$ are not shown). We find differences on the mode and shape of these pdfs, indicating that they provide different 'pieces of information' on fire characteristics. However, the relationship between FRP and $\boldsymbol{f}_{\Delta X}$ is non-linear for CO, NO_2, and AOD. FRP shows a negative relation with both CO and AOD and a positive relation with NO_2. As flaming fires are usually associated with higher temperature combustion, FRP for flaming fires is likely to be higher than that for smoldering fires, given the same amount of fuel loading [Wooster et al., 2005]. Stronger CO and AOD enhancements are related most likely to lower FRPs and smoldering combustion (lower combustion efficiency) while higher NO_2 enhancements are related to higher FRPs and most likely flaming combustion (higher combustion efficiency).

We propose a smoke index ($\boldsymbol{SI}$) which combines the information. $\boldsymbol{SI}$ is expressed as the geometric mean of fractional enhancement in CO and AOD divided by the fractional enhancement in NO_2.

$$\boldsymbol{SI} = \frac{\sqrt{f_{\Delta CO} \cdot f_{\Delta AOD}}}{f_{\Delta NO_2}} \qquad \text{(A2)}$$

We use fractional enhancements rather than absolute values so as to combine different constituents with different units (i.e., ppbv for CO, pptv for NO_2, and unitless for AOD). Also, $\boldsymbol{SI}$ is derived

using satellite data (integrated columns) and associated enhancements are not exactly emissions from fire. Our approach is to choose data quadruples (FRP, CO, NO_2, and AOD) that are coincident with fire events (within the half-degree grid cell and daily timescale) and to assume that the enhancements ($\Delta \boldsymbol{X}$) are strongly related to fire emissions ($\boldsymbol{M_X}$). The ratios of these enhancements correspond to the ratios of emission factors (i.e., $\boldsymbol{M_X/M_Y = EF_X/EF_Y}$). For example, when a fire event is registered on a given day, the combustion phase for that day will be characterized by $\boldsymbol{SI}$ and FRP. If a fire event lasts for two days, this is considered as two separate fire events (even though it is the same fire). Changes in the joint distribution of $\boldsymbol{SI}$ and FRP within this fire cycle will be associated with changes in combustion characteristics. This is especially useful as combustion phase may vary during a fire cycle. Although it is typical to have both flaming and smoldering in a given fire, a dominant combustion phase exists at any given time. In a fire cycle, the smoldering phase typically follows the flaming phase (residual smoldering combustion or RSC, Urbanski et al. [2008]). However, there are fires with low combustion efficiency (e.g., low temperature, high moisture conditions) throughout the cycle and barely reaching the flaming phase, and fires that are in smoldering phase transitioning to flaming phase [Rein, 2009]. The heat release in smoldering fires is also low compared to flaming fires [Rein, 2009], which is consistent with the information from maximum FRPs.

When viewed from a probabilistic approach, the satellite-derived $\boldsymbol{SI}$ represents an integrated (most likely or dominant) fire characteristic rather than specific to individual fire event. High $\boldsymbol{SI}$ (high CO and/or AOD and low NO_2) in low FRP condition corresponds to smoldering fires as dominant combustion phase while low $\boldsymbol{SI}$ (high NO_2, low CO and/or AOD) in high FRP condition corresponds to flaming fires as dominant combustion phase. $\boldsymbol{SI}$ is inversely related to CE or MCE, which is typically used to differentiate from flaming (higher CE) and smoldering (lower CE) fires in prescribing emission factors [Ward and Hardy, 1991; Ferek et al., 1998; Andreae and Merlet, 2001; Yokelson et al., 2007; Christian et al., 2007; Akagi et al., 2011]. We will compare this $\boldsymbol{SI}$ with field campaign data on fire combustion efficiency (and flaming versus smoldering property) in section 5.

Figure A5 shows the overall joint pdf of $\boldsymbol{SI}$ and FRP, similar to Figure A4. Also shown in Figure A5 are individual cumulative distribution functions (cdf) of $\boldsymbol{SI}$ and FRP for the entire domain and study period. The shape of the pdf suggests the following 3 scenarios: 1) high FRP and low $\boldsymbol{SI}$

indicative of flaming combustion; 2) low FRP and high ***SI*** indicative of smoldering combustion; 3) mixed combustion. High FRPs are more likely to occur with low ***SI*** values (relatively higher combustion efficiency), whereas high ***SI*** values are more likely to occur with low FRPs (relatively lower combustion efficiency). At 90th percentile, the ***SI*** and FRP values are about 2 and 300 MW, respectively.

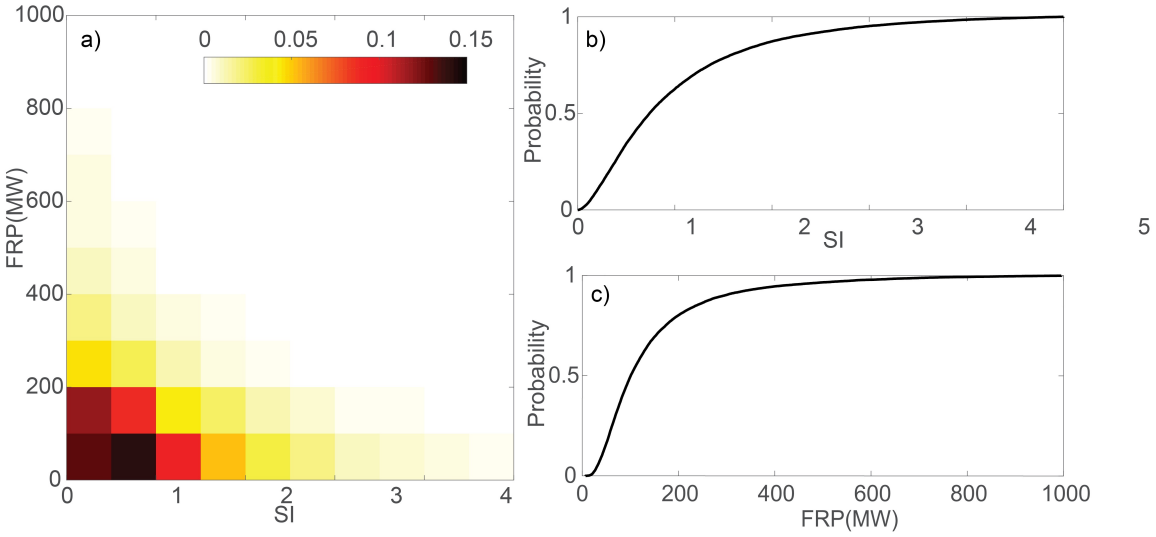

Figure A5. Average relationship of FRP and ***SI***. Left panel corresponds to joint probability density function (pdf) of FRP and ***SI*** while the right panel corresponds to cumulative distribution function (cdf) of ***SI*** (top) and FRP (bottom).

4.2 Spatial and Temporal Distribution of *SI*

Here, we elaborate on the spatiotemporal properties of ***SI***. We repeat our analysis on smoke patterns in section 3 for ***SI*** in the Amazon during its main fire season. We highlight the utility of ***SI*** in summarizing (as one index) the relationships that we saw earlier among the smoke retrievals of CO, NOx, and AOD. We find that (1) the overall ***SI*** shows a clear spatial distinction that is related to land cover and fire activity, and (2) ***SI*** increases within a fire season indicating an overall decreasing trend in combustion efficiency across the season. The observed variability in ***SI*** with

FRP across space and time implies a subsequent variability in the actual fire emissions which may not be reflected in current emission inventories.

Spatial Patterns. The average ***SI*** across the study period is shown in Figure A6. High ***SI*** can be seen in the southwestern side of the Amazon and close to the tropical forest and grassland/shrubland/savanna boundaries. ***SI*** values start low in the eastern edge and increase westward. This spatial pattern is fairly correlated with the pattern of land cover (Figure A1c) and deforestation (Figure A1d). It appears that fires in savanna tend to have higher ***SI*** compared to fires in tropical forest areas. Fires in highly deforested regions also show lower ***SI*** values than fires in barely deforested region. We infer from this pattern that fires in highly deforested region have relatively more flaming fires (higher combustion efficiency), whereas in the barely deforested region there are relatively more smoldering fires (lower combustion efficiency). This result implies that deforestation fires tend to have higher combustion efficiency and more likely to be dominated by flaming fires relative to other type of fires (e.g., understory fires). This result is consistent with

previous work by Rein [2009]. The high ***SI*** signature in the southeast corner of the Amazon basin can be associated with agricultural fires as has been suggested by Chen et al. [2013].

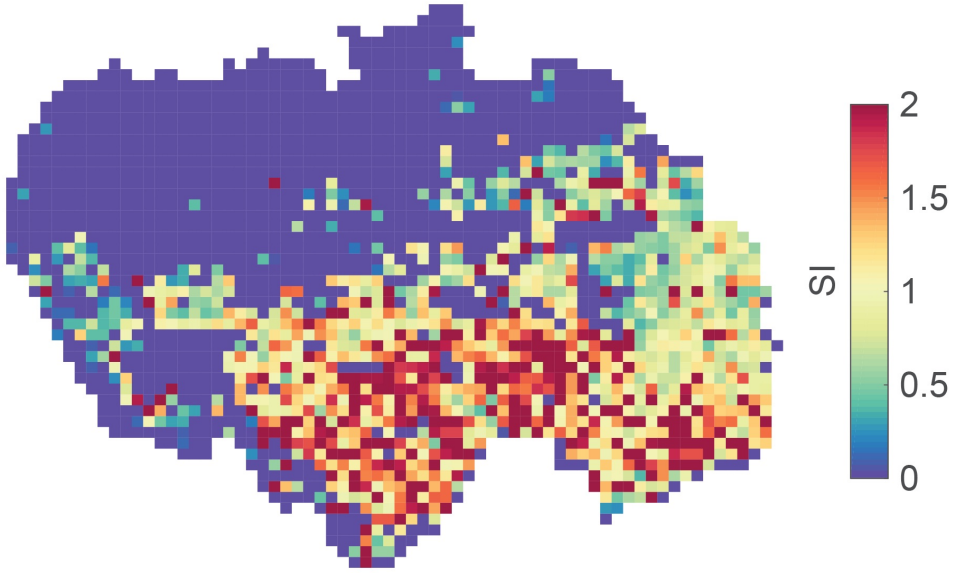

Figure A6. Spatial distribution of ***SI*** averaged across the study period (2005-2014).

Temporal Patterns. Figure A7 shows the fire seasonality of ***SI*** and FRP (June to November) along with the associated cdfs for each 10-day segment in the season. Here we only show segment 7 to 13, corresponding to 01 August to 10 October because this is the period when most of fires in the southern Amazon occur. The other 10-day segments do not have enough fire events. We show similar joint pdf plots as before but for different time segments. It is clear that the shape of the pdf is evolving from high FRP/low ***SI*** (mostly vertical) at the beginning of the main fire season to low FRP/high ***SI*** (mostly horizontal) at the end of the season. This is supported by the individual cdfs of ***SI*** showing lower 90th percentile ***SI*** value in earlier segments and higher in the end. The cdfs of FRP shows the opposite trend from higher to lower values. This is again consistent with our previous analysis that FRP is inversely related to ***SI***. We note that we find similar results when we

aggregate the first 90 days (start of fire season) and last 90 days (end of fire season) of the data in ***SI*** analysis.

We infer from this trend that on average the dominant fire combustion efficiency in the Amazon is decreasing with time. While flaming and smoldering occur during a fire event [Guyon et al., 2005], the associated smoke emissions are relatively dominated by flaming combustion at the beginning of the fire season and evolves to more dominant smoldering combustion in the end. This average pattern can be explained as follows: At the beginning of the fire season, deforestation fires (flaming conditions) are more dominant [Yokelson et al., 2007]. Even though there will still be new deforestation fires in flaming phase as time progresses, most flaming fires evolve to become residual smoldering combustion (RSC) fires. RSC can last for days or weeks after the end of flaming combustion [Urbanski et al., 2008]. As a result, the overall combustion efficiency decreases with time. Another possible scenario would be that during the fire season deforestation fires can lead to non-deforestation fires (mostly understory fires) with lower combustion efficiency [Rein, 2009; Morton et al., 2013]. The relative importance of non-deforestation fires increases with time, therefore the overall combustion efficiency decreases with time. Note that even with the careful definition of background value to minimize the impact of transport, it is possible that the sensitivity of ***SI*** to changes in fire properties decreases over time within the fire season due to the

accumulation of smoke constituents (especially longer-lived species) emitted from fires earlier in the season.

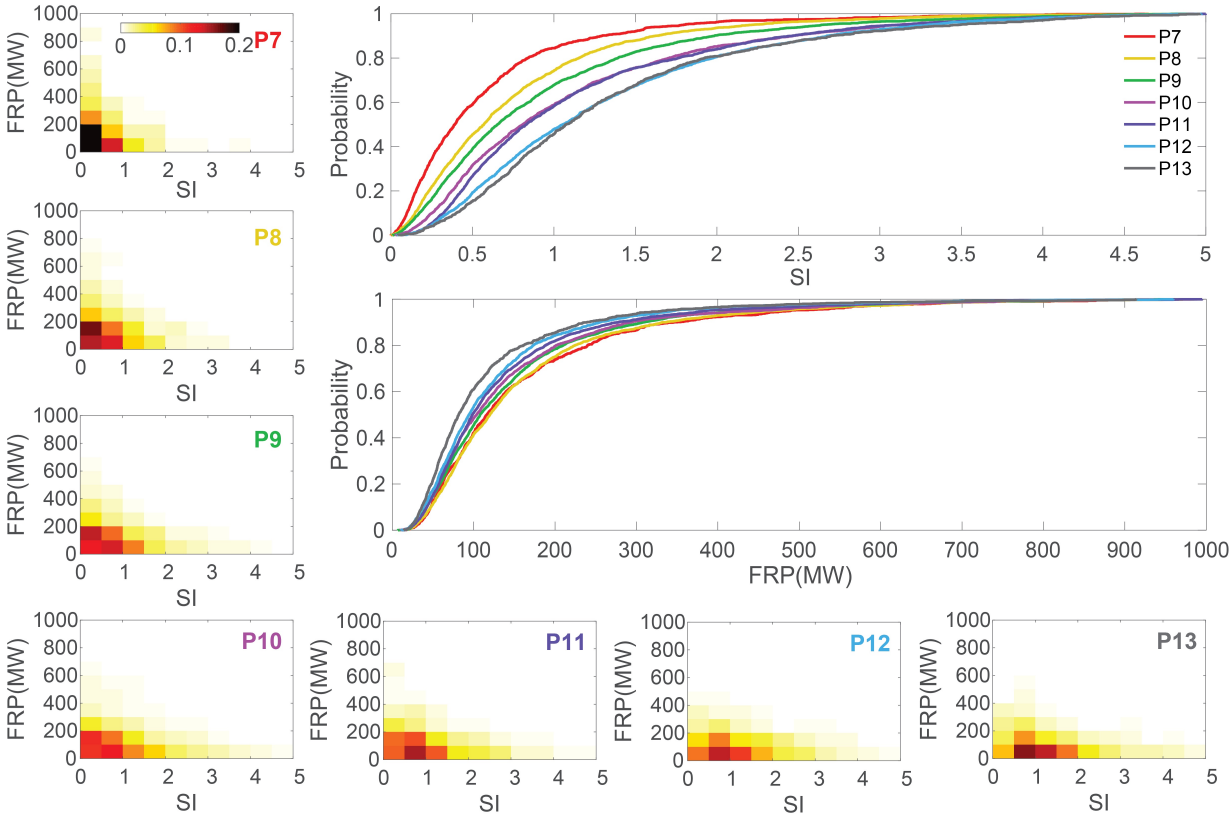

Figure A7. Intra-seasonal relationships of FRP and ***SI***. Outer panels correspond to joint pdfs of FRP and ***SI*** for seven 10-day segments (August 1 to October 10). The associated cdfs of ***SI*** and FRP are plotted in the top right panels. Colored lines represent each 10-day segment (red-P7, yellow-P8, green-P9, magenta-P10, violet-P11, blue-P12, and black-P13).

4.3 Key Factors of Smoke Index (*SI*)

We investigate the variations of ***SI*** with FRP across several key factors. We focus in particular on analyzing ***SI*** across location, land cover, drought, and deforestation to support our hypothesis that ***SI*** can be a useful indicator of integrated smoldering/flaming phase of fires in this region. Differences in ***SI*** across these stratifications provide insights on $\boldsymbol{M_X}$ by looking into the variations in fire properties ($\boldsymbol{C}$ and $\boldsymbol{EF_X}$). As discussed in the introduction, $\boldsymbol{C}$ and $\boldsymbol{EF_X}$ are difficult to measure or estimate. In many cases, these two most uncertain parameters in $\boldsymbol{M_X}$ are coupled and mainly influenced by environmental conditions such as land cover (e.g., fuel type), climate

conditions (e.g., drought), and fire type (deforestation and forest fires) as well as socio-economic-political drivers (e.g., fire practices, policies). We highlight the differences in the patterns of $\boldsymbol{SI}$ to further elucidate the linkages of $\boldsymbol{SI}$ to the drivers of $\boldsymbol{C}$ and $\boldsymbol{EF_X}$.

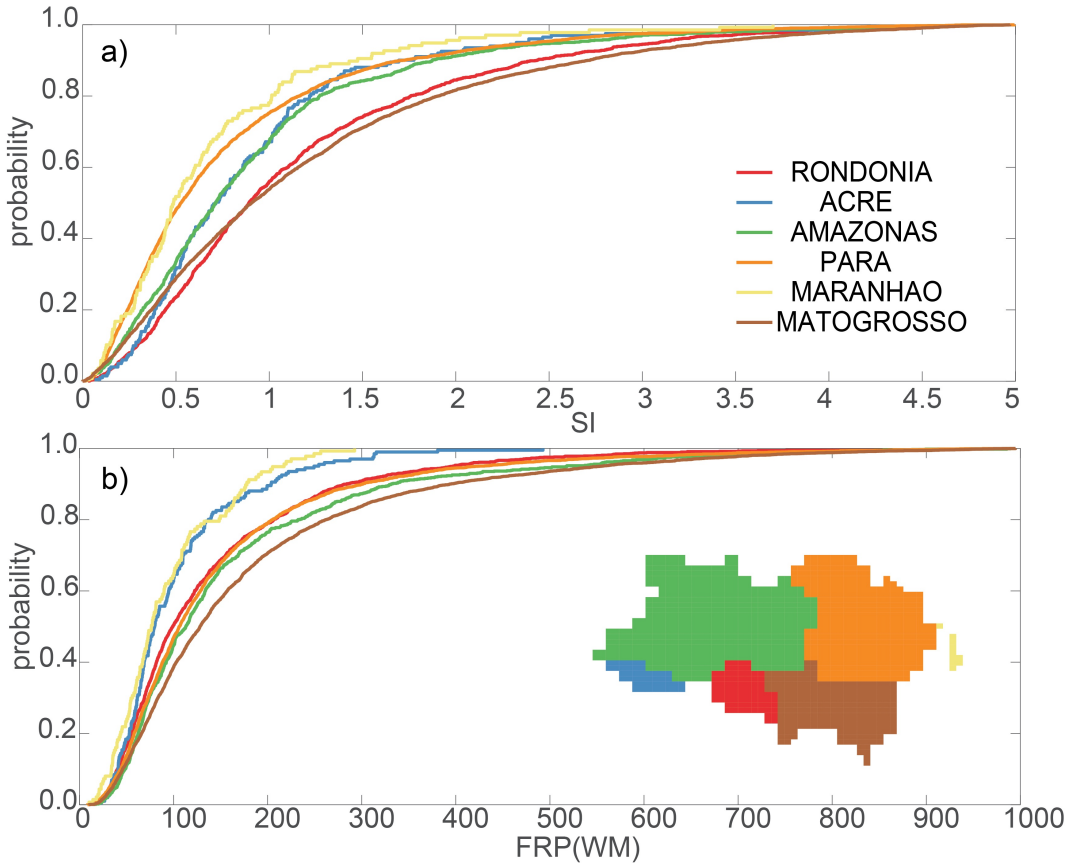

Figure A8. Variations in cumulative distribution functions of $\boldsymbol{SI}$(top panel) and FRP (bottom panel) across states in Amazonia (using all data for the entire study period). Colored lines to the states in the study domain (yellow-Maranhao, orange-Para, brown-Mato Grosso, red-Rondonia, green-Amazonas, and blue-Acre). See inset in bottom panel for relative location of these states within Amazonia.

4.3.1 Variations across Location

Figure A8 shows the difference in $\boldsymbol{SI}$ and FRP cdfs across several states in the region. We find that Mato Grosso has higher 90th percentile FRP (~450 MW) than in Para and Rondonia (~400

MW). These are the three states with most frequent fire occurrence. The higher 90th percentile ***SI*** values in Mato Grosso and Rondonia (~2.8), on the other hand, are higher than in Para (~2.0). This pattern corresponds well with differences in dominant land cover and fire practices across the states.

4.3.2 Variations in Land Cover

We stratify ***SI*** and FRP in terms of broad vegetation type (forest and non-forest) across the Amazon and compare the resulting joint pdfs and individual cdfs (Figure A9) to the overall ***SI*** and FRP shown in Figure A5. We select two sub-regions for this analysis. The choice on the size and location of these two sub-regions is motivated by the use of a coarser spatial resolution land cover map (0.5º). We choose specific locations that have relatively homogeneous land cover type but with similar number of fire events. Choosing generic locations is especially problematic in the southeast Amazon basin where fires are influenced by agricultural burning. Based on Figure A9, it appears that fires in non-forest areas (mostly savannas) has clearly higher overall combustion efficiency (***SI***~0.6) than fires in forested areas (***SI***~1.0). FRPs on the other hand are very similar. We note that the fuel types and associated emission factors for CO, NO_2, and aerosols are different for forests and non-forest [Andreae and Merlet, 2001]. It is difficult to tease out this confounding influence with combustion efficiency. With this in mind, our results appear to be consistent with

previous studies reporting higher combustion efficiency of fires in savannas than in forests [Urbanski, 2008; Yokelson et al., 2007].

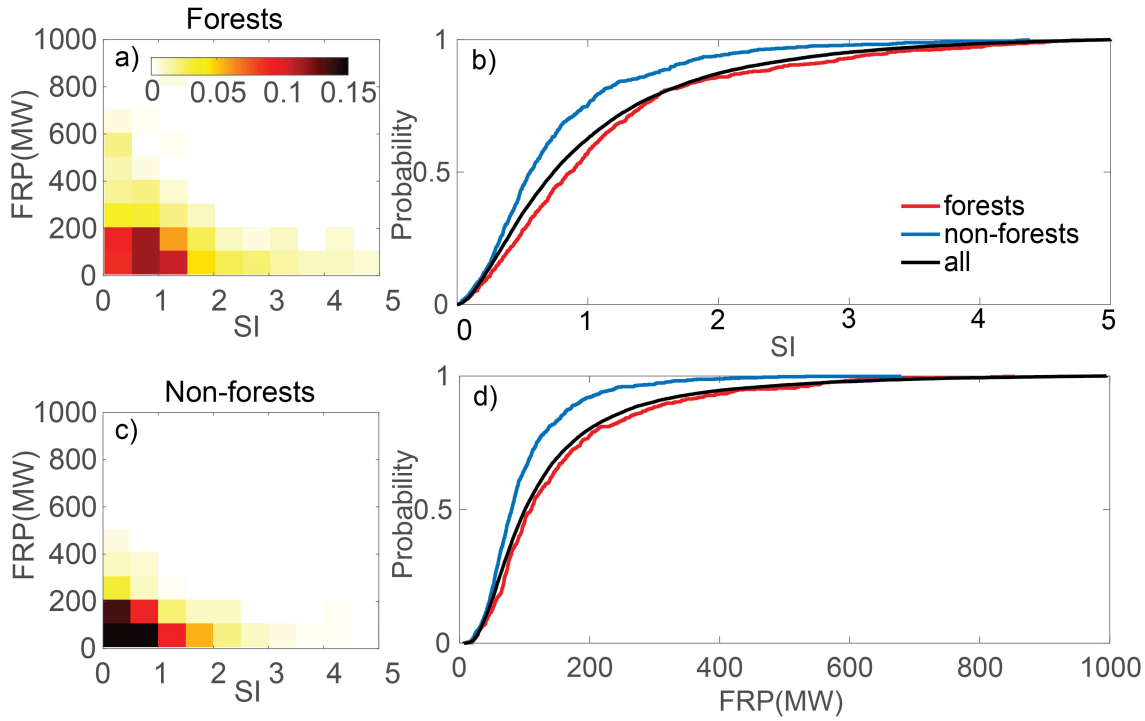

Figure A9. Average relationship of FRP and ***SI*** for fires in forest and non-forest regions in the Amazon. Left and right panels correspond to joint pdfs and cdfs of FRP and ***SI***, respectively. All data for the entire study period were used. Colored lines correspond to forest (red), non-forest (blue) and all types (black).

4.3.3 Variations during Drought

Figure A10 shows the differences of ***SI*** and FRP between drought and non-drought years. The joint pdf for drought years (2005, 2006, 2007, 2010) shows higher 90th percentile ***SI*** value compared to non-drought years (2008-2009, 2011-2014). This is not to say that during a drought year, fires can be characterized by smoldering fires alone. In fact, deforestation fires, which is a mixture of flaming and smoldering phase, occur every year regardless of drought. Flaming and smoldering combustion occurs simultaneously in deforestation fires [Guyon et al., 2005]. During drought years however, there is a high possibility that increasing number of deforestation fires can spread and increase the number of understory fires [Alencar et al., 2004; Alencar et al., 2006; Aragao et al., 2007; Chen et al., 2013]. Smoldering combustion are more likely to be present in

understory fires [Rein, 2009]. Another aspect of drought is its impact on combustion efficiency. Drier conditions provide higher chances of flaming than smoldering fires [Bloom et al., 2015]. Our results show however that there is a much larger spread to smoldering fires in non-deforested areas. This implies that drier conditions during drought years have relatively larger impact on non-deforestation than deforestation fires. Generally, although drought may increase combustion efficiency for each fire event, it decreases the overall combustion efficiency for the entire region through two possible mechanism: (1) introducing more low-efficiency fires directly, and/or (2) increasing duration of existing fires resulting to enhancement in smoldering phase. Again, the cdf of FRP does not show a clear difference between drought and non-drought years. While issues with FRP retrievals and sampling cannot be neglected, this pattern is consistent with Figure A2 that in drought years, smoke anomalies are more enhanced compared to FRP anomalies. It is also worth mentioning that the cdf for all fires (overall $\boldsymbol{SI}$) is closer to the cdf for drought than non-drought years. We suppose that this is more of a sampling issue since there are more fire events in drought than non-drought years, which again is fairly consistent with the finding in previous

studies concerning drought and understory fires [Alencar et al., 2004; Alencar et al., 2006; Aragao et al., 2007; Chen et al., 2013].

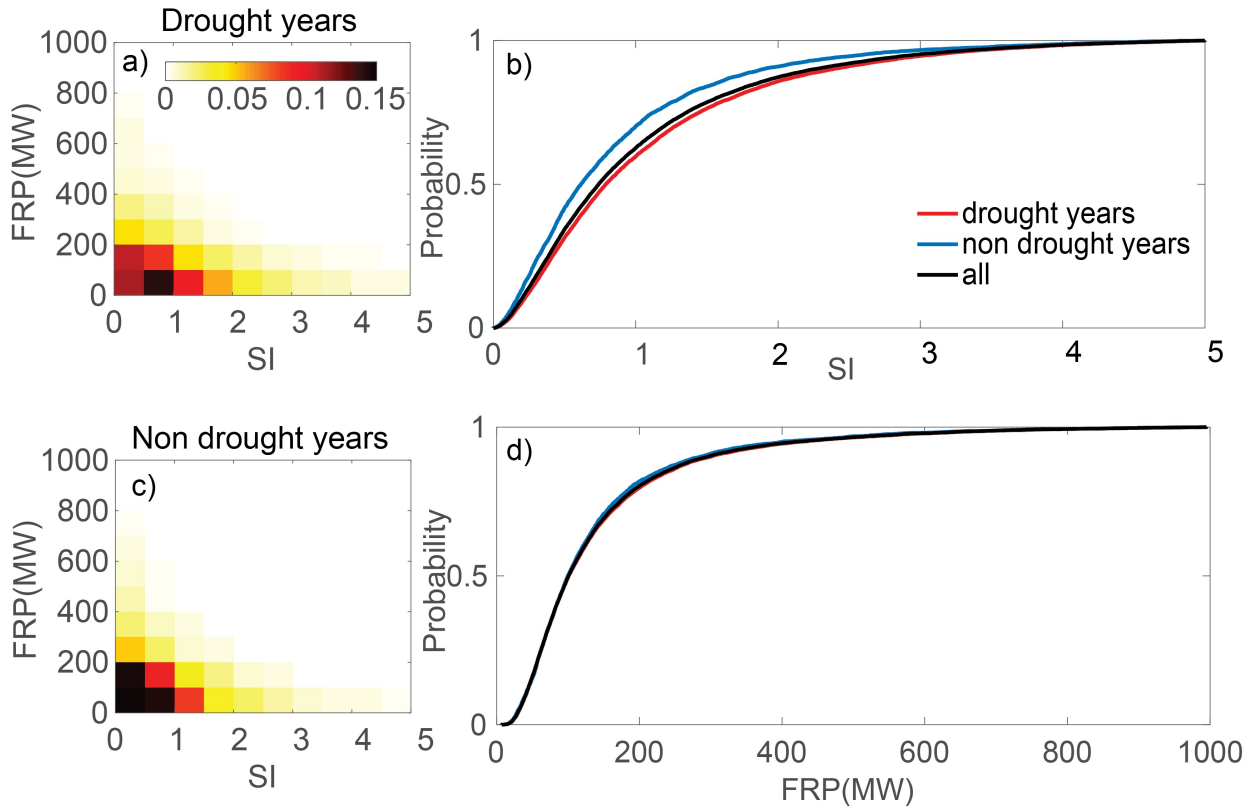

Figure A10. Average relationship of FRP and ***SI*** for fires during drought and non-drought years across the region. Left and right panels correspond to joint pdfs and cdfs of FRP and ***SI***, respectively. Colored lines correspond to drought (red), non-drought (blue) and all (black) years.

4.3.4 Variations in Fire Type

In section 4.2 we made an inference on the relationship between combustion phase (flaming/smoldering) and 'fire type' (deforestation/non-deforestation) based on similarity in spatiotemporal patterns. That is, fires in deforested areas have higher combustion efficiency than in non-deforested areas. Here, we support this finding by investigating ***SI*** and FRP in two sub-regions (A1 and A2) which we have denoted in Figure A1d. A1 and A2 correspond to highly deforested and barely deforested areas. To avoid potential sampling bias, these boxes were selected following three criteria: 1) There should be adequate fire events in the sub-regions; 2) The sizes of these boxes should be the same; 3) One sub-region for both A1 and A2 should be located in the

southern Amazon and one in the eastern Amazon. The average percent deforestation for A1 and A2 are 0.1 and 0.02, respectively. This differentiates between highly and barely deforested regions. The ensuing joint pdfs and individual cdfs are shown in Figure A11. There is a higher probability of high ***SI*** value and low FRP (most likely dominated by smoldering combustion) in A2 than in A1. The cdf of FRP for the entire region are similar to the cdf of A2 while the cdfs of ***SI*** for the entire region is between the cdfs of A1 and A2. It does not mean however that non-deforestation fires are dominant.

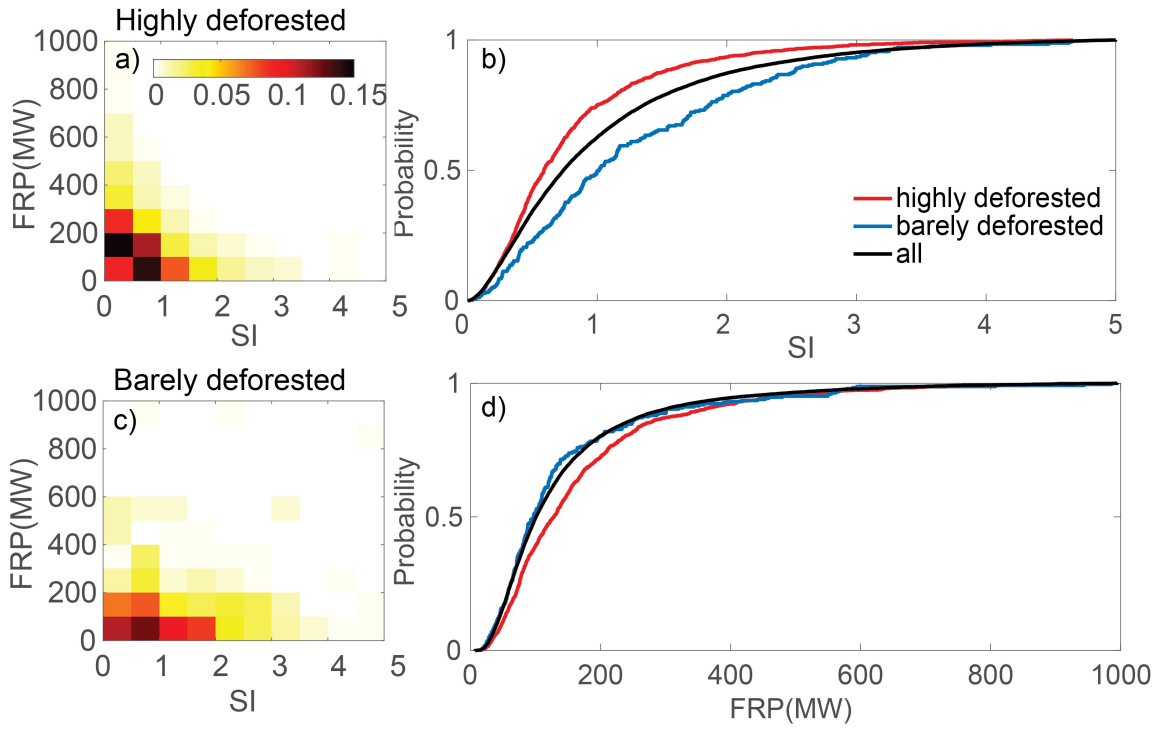

Figure A11. Average relationship of FRP and ***SI*** for fires in highly-deforested (A1) and barely-deforested regions (A2) (see Figure A1d for the location of A1 and A2). Left panels correspond to joint pdfs of ***SI*** and FRP of A1 (upper left) and A2 (lower left) data. Right panels correspond to cdfs of ***SI*** (upper right) and FRP (lower right). Colored lines correspond to A1 (red), A2 (blue) and all (black) data. All data for the entire study period corresponding to A1 and A2 were used.

5 Comparison with Analogous Smoke Indices

In the previous sections, we have introduced ***SI*** and analyzed its spatial and temporal joint distribution with FRP in relation to key factors that influence emissions. In this section, we compare ***SI*** with an analogous quantity derived from field campaign and existing emission

inventories. Our goal is to verify the robustness of the $\boldsymbol{SI}$ concept and demonstrate its potential application. This is our attempt to link $\boldsymbol{SI}$ to the parameters of $\boldsymbol{M_X}$ (i.e., $\boldsymbol{C}$ and $\boldsymbol{EF_X}$ as mentioned in the introduction). Our comparison shows that $\boldsymbol{SI}$ is reasonably consistent with the patterns of near-field observed enhancement ratios. Here we suggest that the variations in $\boldsymbol{SI}$ across space and time provide a useful diagnostic for current emission inventories where $\boldsymbol{C}$ and $\boldsymbol{EF_X}$ are typically prescribed as functions of land cover and/or fuel type.

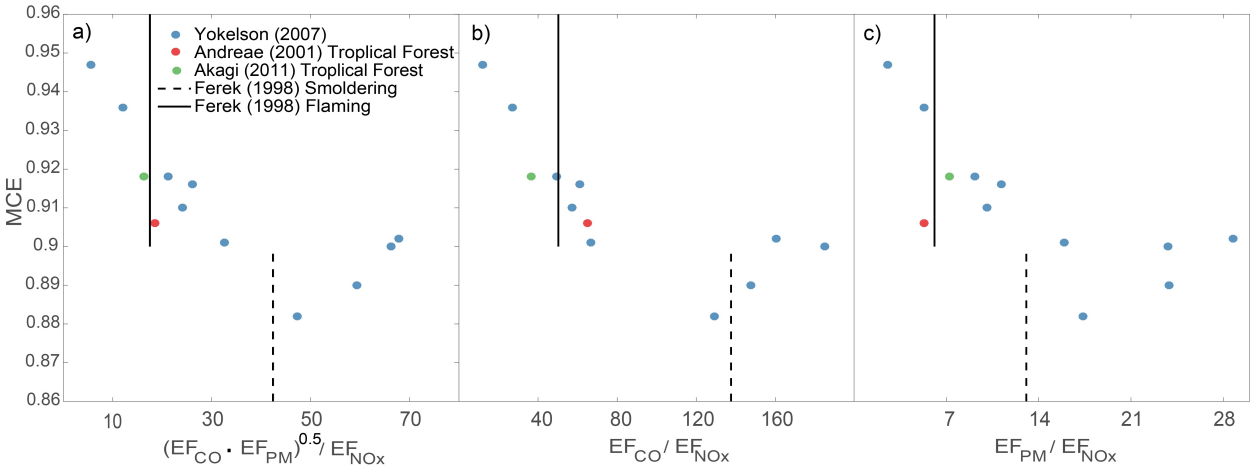

Figure A12. Relationship of MCE and $\boldsymbol{ASI_c}$ (left panel), emission ratios of CO and NO_X (center panel) and emission ratios of PM and NO_X from field campaigns in the Amazon (see Table AS2 for details on the data). Data from Ferek et al. [1998] (black solid and dashed lines) was only generally classified as flaming or smoldering (with MCE of 0.9 as cutoff). Colored markers correspond to data from Yokelson et al. [2007] (blue), Andreae and Merlet [2001] (red), and Akagi et al. [2011] (green).

5.1 Field Campaigns

We summarize the emission factors and emission ratios inferred from field campaigns that were carried out in the Amazon, along with previous compilation by Andreae and Merlet [2001] and Akagi et al. [2011]. We note that the study period and domain as well as observations of smoke constituents vary across these field campaigns. Combustion efficiencies are also reported as MCE or CE or labeled as flaming and smoldering based on a certain threshold. For comparision purposes, we define an analogous smoke index as: $\boldsymbol{ASI_c = \sqrt{(EF_{CO} \cdot EF_{PM})}/EF_{NOx}}$ where $\boldsymbol{c}$ corresponds to concentration-based $\boldsymbol{ASI}$. It is an identical expression to $\boldsymbol{SI}$ but using $\boldsymbol{EF_X}$ instead

of fractional enhancements $\boldsymbol{f_{\Delta X}}$ due to fires. We also use PM as surrogate for AOD and NO_X for NO_2 in the calculation of $\boldsymbol{ASI_c}$. Given that $\boldsymbol{ASI_c}$ is based on specific field campaign smoke observations while $\boldsymbol{SI}$ is based on satellite column retrievals, the magnitudes and units of these two indexes are not quantitatively comparable. Our comparison between $\boldsymbol{ASI_c}$ and $\boldsymbol{SI}$ focuses on identifying emerging patterns. The relationships between calculated $\boldsymbol{ASI_c}$ and reported MCE are shown in Figure A12. In general, $\boldsymbol{ASI_c}$ is non-linearly related to MCE. Higher $\boldsymbol{ASI_c}$ typically corresponds to lower MCE (smoldering) and vice versa (flaming). Qualitatively, this pattern is consistent with our hypothesis that higher $\boldsymbol{SI}$ is related to lower combustion efficiency.Several of these studies show consistently a clear distinction between flaming and smoldering fires in terms of $\boldsymbol{ASI_c}$ [Ferek et al., 1998; Yokelson et al., 2007]. This is especially the case with $\boldsymbol{ASI_c}$ from Ferek et al. [1998]. We also find that $\boldsymbol{ASI_c}$ shows a clearer distinction in MCE than using only the emission ratio of CO and NO_X (Figure A12b) or emission ratio of PM and NO_X (Figure A12c).

5.2 Fire Emission Inventories

Analogous $\boldsymbol{SI}$ from GFED4s and FINNv1.5 is calculated as $\boldsymbol{ASI_e = \sqrt{(M_{CO} \cdot M_{PM})}/M_{NOx}}$, where $\boldsymbol{e}$ corresponds to emission-based $\boldsymbol{ASI}$. For both GFED and FINN, the daily emitted amount of trace gas or aerosol species ($\boldsymbol{M_x}$) during the fire season in 2005-2014 are regridded into half-degree resolution. $\boldsymbol{ASI_e}$ is then calculated for each day and grid cell. As noted in Sections 1 and 4.1, $\boldsymbol{M_x}$ emitted from a fire is proportional to its emission factor, $\boldsymbol{EF_X}$. We expect to recover the effective ratio of emission factors applied in these inventories when calculating $\boldsymbol{ASI_e}$ since the ratio of $\boldsymbol{M_x}$ for different species $\boldsymbol{X}$ cancels out the activity term in $\boldsymbol{M_x}$. Hence, the spatial pattern of $\boldsymbol{ASI_e}$ can be associated with the treatment of $\boldsymbol{EF_X}$ in these inventories, which is typically calculated for a given grid cell as a weighted average of emission factors for broad vegetation and fuel types. We show in the left panels of Figure A13 the spatial distribution of $\boldsymbol{ASI_e}$ from GFED and FINN averaged across the study period (2005-2014). The spatial pattern of $\boldsymbol{ASI_e}$ from GFED closely resembles the pattern of deforestation in Figure A1d whereas $\boldsymbol{ASI_e}$ from FINN closely resembles the pattern of land cover in Figure A1c. This difference is also shown in the cdfs of $\boldsymbol{ASI_e}$ from FINN and GFED (Figure A13b) before applying the fire mask that we adopted in our $\boldsymbol{SI}$ analysis (Figure A1b). GFED appears to have a higher fraction of lower $\boldsymbol{ASI_e}$ than FINN. They also slightly differ in the minimum $\boldsymbol{ASI_e}$. The maximum and minimum value of $\boldsymbol{ASI_e}$ from GFED

is 20.5 and 5.9, respectively. These correspond to $\boldsymbol{ASI_e}$ values calculated using $\boldsymbol{EF_X}$ for temperate forest fires (maximum) and savanna fires (minimum) from an updated version of Andreae and Merlet [2001]. When we only considered the grid cells used in our $\boldsymbol{SI}$ analysis, the shape of the cdf has shifted to higher $\boldsymbol{ASI_e}$ (Figure A13d). This is more apparent in GFED than FINN. Now, the maximum value of $\boldsymbol{ASI_e}$ from GFED dropped to 13.6 which corresponds exactly to $\boldsymbol{ASI_e}$ calculated using $\boldsymbol{EF_X}$ for tropical forest fires. This represents a shift to a larger influence of deforestation and savanna fires across the domain of our $\boldsymbol{SI}$ analysis. This is also obviously consistent with GFED's and FINN's treatment of these $\boldsymbol{EF_X}$s, which vary only with broad vegetation and fuel type and highlights the dependencies in $\boldsymbol{M_x}$ to assumptions of land cover. We note that the shape of the cdf in $\boldsymbol{SI}$ is more continuous and monotonically increasing than $\boldsymbol{ASI_e}$ from both FINN and GFED. There appears to be an inconsistency in the overall combustion efficiency (i.e., product of $\boldsymbol{C}$ and $\boldsymbol{EF_X}$), between enhancement-based and emission-based analysis.We suggest that combustion efficiency should also vary in space and time (not just with land cover) and as a consequence fire emissions should have more variations in emission factors than what is implemented in current inventories. In particular, parameterization of fire emission models based on appropriate $\boldsymbol{SI}$ analogs for different conditions (deforestation/non-deforestation, drought/non-drought, tropical forest/savanna, flaming/smoldering) can be used to scale bottom-up fire emissions, which can then lead to more consistent emission estimates of these combustion products.

6 Summary and Discussions

There is a unique opportunity to utilize decadal satellite records of combustion products in improving the consistency and accuracy of current fire emission estimates. This is particularly the case in providing observational constraints on combustion efficiency, which is one of the most uncertain and difficult-to-observe emission model parameters at present time. While recent efforts to combine retrievals of fire combustion signatures have been made (Mishra et al. [2015], Schreier et al [2014]), none of these studies have established a synthesis analysis of MOPITT CO, OMI NO_2, and MODIS AOD in conjunction with MODIS FRP. In this study, we introduce $\boldsymbol{SI}$ that is derived from the combination of these retrievals as an indicator of overall combustion efficiency. This is based on our understanding that more efficient combustion (flaming) produces more oxidized products of carbon, hydrogen, and nitrogen from the biomass consumed (e.g., CO_2, H_2O,

and NO_X) and that less efficient combustion (smoldering) produces smoke, which is mostly CO and organic aerosols. The relative abundance of these smoke constituents provides a window to combustion efficiency and its variability. This study demonstrates the utility of these satellite retrievals to distinguish dominant fire characteristics consistent with the information that can be derived from these retrievals. We focus our initial study on the fires in the Amazon from 2005 to 2014.

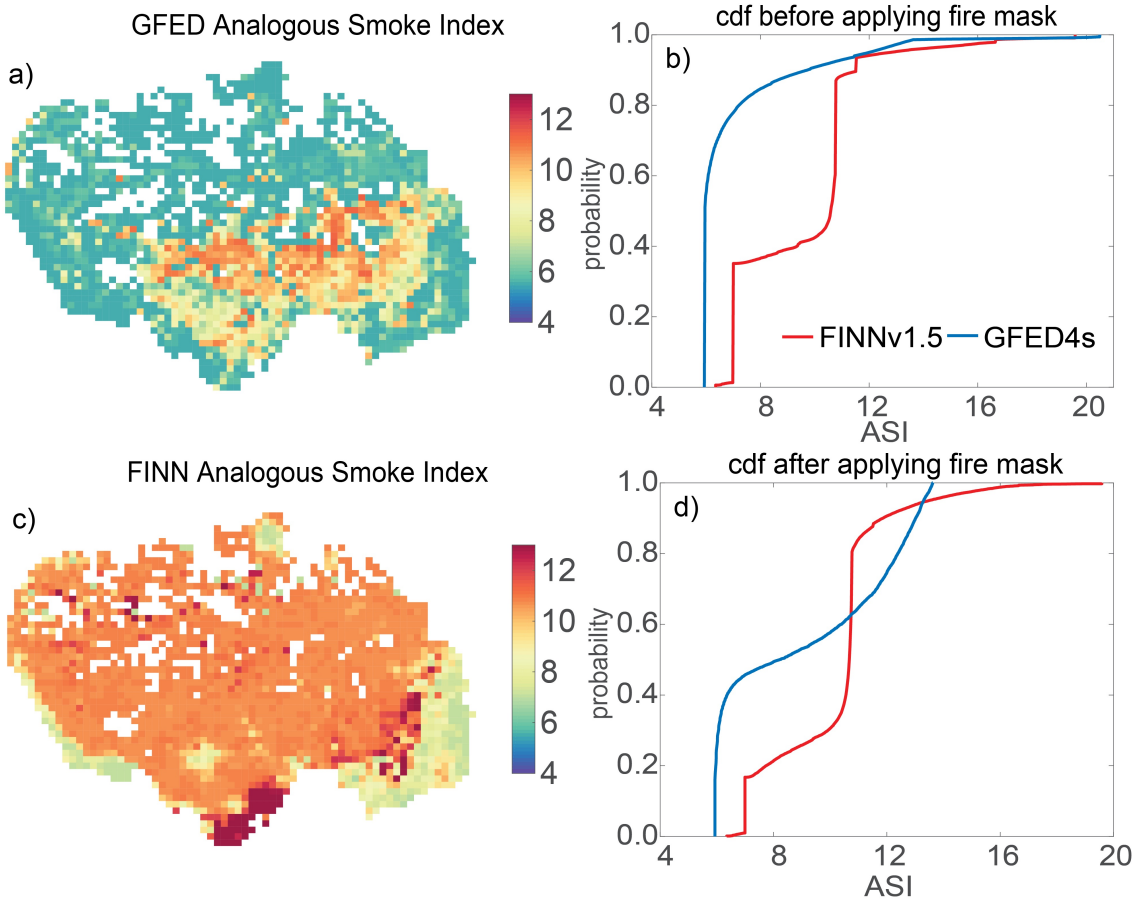

Figure A13. Analogous ***SI*** (***ASI$_e$***) for GFED4s and FINNv1.5 emission inventories. Left panels correspond to the average spatial distributions while the right panels correspond to the cdfs of ASI before (top right) and after (bottom right) our fire mask (Figure A1b) was applied. Blue and red lines correspond to GFED and FINN, respectively.

Anomalies of these combustion products, as well as FRP, show the influence of deforestation activities on the decreasing trend across the study period. Drought on the other hand enhances these anomalies, especially for CO and AOD, and has larger influence on the increase in the

number of smoldering fires. The patterns in FRP and NO_2 are well correlated with higher combustion efficiencies (flaming) and deforestation fires. In conjunction with FRP, we find that our satellite-derived ***SI***, which is calculated as the ratio of the geometric mean of observed enhancements due to fire in CO and AOD to that of NO_2, is able to distinguish variations in combustion efficiency during fire (dry) season in the Amazon. That is, the flaming phase dominates at the beginning (high FRP, low ***SI***) and smoldering phase (low FRP, high ***SI***) at the end of the fire season. We note that potential overestimation of OMI NO_2 due to aerosols [Castellanos et al., 2015] and underestimation of MODIS AOD and MOPITT CO in smoldering fires imply more enhanced ***SI*** under this condition. Consistent with our single-species analysis and past studies of fires in the region, we also find that flaming combustion is more dominant in areas mainly having deforestation fires while smoldering combustion has a larger influence during drought years when understory fires are more likely to occur. Our analysis is also consistent with field campaign data reported in the literature. The results show that the relation between analogous ***SI*** derived from field campaign and MCE supports the main patterns that we find in ***SI***. Furthermore, the differences in the patterns of analogous ***SI*** derived from emission inventories (GFED and FINN) and ***SI*** derived from enhancements highlight the need to incorporate observationally constrained variations in emission factors in current fire emission models.

Although we have carefully selected conditions on which issues in sampling (including clouds), retrieval algorithm, and implementation (saturation, contamination, biases), and sub-grid variations do not dominate our analysis, we also recognize that these issues still likely influence our data-driven analysis, especially when defining fire enhancements. It is difficult to isolate local from transported contribution and the influence of combustion efficiency from differences in lifetime merely based on the variations in ***SI***. While these issues are better handled by more advanced systems such as data assimilation and inverse modeling, we address these issues as follows: 1) We propose that the interpretation of ***SI*** should be in conjunction with FRP. This is analogous to looking at the joint phase of fire activity and efficiency. 2) We only calculate ***SI*** values for which fire hotspots are detected. We have also defined a spatially and temporally explicit background to minimize the influence due to transport and lifetime. 3) We present corroborating evidences (MCE from previous literature) and comparison with ***ASI*** to provide a broader picture of ***SI***. Overall, we propose that the interpretation of ***SI*** in this study be limited to large-scale

(dominant) features of fires in the Amazon, not on individual fires where the impacts of these issues are larger.

Our results point to the utility of ***SI*** as proxies for overall combustion efficiency in potentially parameterizing current fire emission models to better represent mesoscale-to-regional spatiotemporal variations. The application of ***SI*** to improve emissions hinges upon the use of models and data assimilation. This work complements recent studies on emission factors [e.g., van Leeuwen and van der Werf, 2011] and on emission coefficients [e.g., Ichoku and Ellison, 2014]. ***SI*** also presents an important diagnostic for emissions and chemistry transport models, especially when applied within the framework of multi-species state estimation with inverse modeling of emission parameters. In the future, we plan to refine and generalize this approach to other fire regions such as the boreal forests in Alaska/Canada/Siberia, and tropical forests in Africa and Indonesia.

Acknowledgements

This work was supported by NASA Terra/Aqua Grant NNX14AN47G. The authors would like to acknowledge all the teams developing and producing the datasets used in this study. We especially acknowledge the free use of tropospheric NO_2 column data from the OMI sensor (www.temis.nl). MOPITT CO, MODIS AOD, and MODIS DSI were obtained from the NASA Langley Research Center Atmospheric Science Data Center (LaRC ASDC), Level 1 and Atmospheric Archive and Distribution System (LAADS), and University of Montana (www.ntsg.umt.edu/project/dsi), respectively. We thank INPE / MCTI for PRODES deforestation data. All data used in this study are publicly available and can be accessed as stated in Table 1. We also thank Merritt Deeter and Sara Martinez-Alonso for initial insights on the manuscript and some of our peers for helpful edits. We thank Benjamin Gaubert and anonymous reviewers for their comments. The FIRMS data and imagery were taken from the Land, Atmosphere Near real-time Capability for EOS (LANCE) system operated by the NASA/GSFC/Earth Science Data and Information System (ESDIS) with funding provided by NASA/HQ.

References

Akagi, S. K., Yokelson, R. J., Wiedinmyer, C., Alvarado, M. J., Reid, J. S., Karl, T., ... & Wennberg, P. O. (2011). Emission factors for open and domestic biomass burning for use in atmospheric models. Atmospheric Chemistry and Physics, 11(9), 4039-4072.

Al-Saadi, J., Soja, A. J., Pierce, R. B., Szykman, J., Wiedinmyer, C., Emmons, L., ... & Bowman, K. (2008). Intercomparison of near-real-time biomass burning emissions estimates constrained by satellite fire data. Journal of Applied Remote Sensing, 2(1), 021504-021504.

Alencar, A. A., Solórzano, L. A., & Nepstad, D. C. (2004). Modeling forest understory fires in an eastern Amazonian landscape. Ecological Applications,14(sp4), 139-149.

Alencar, A., Nepstad, D., & Diaz, M. C. V. (2006). Forest understory fire in the Brazilian Amazon in ENSO and non-ENSO years: area burned and committed carbon emissions. Earth Interactions, 10(6), 1-17.

Andreae, M. O. (1991). Biomass burning: its history, use, and distribution and its impact on environmental quality and global climate. Global biomass burning: Atmospheric, climatic and biospheric implications, 3-21.

Andreae, M. O. (1993). The influence of tropical biomass burning on climate and the atmospheric environment. In Biogeochemistry of Global Change (pp. 113-150). Springer US.

Andreae, M. O., & Merlet, P. (2001). Emission of trace gases and aerosols from biomass burning. Global biogeochemical cycles, 15(4), 955-966.

Andreae, M. O., Artaxo, P., Beck, V., Bela, M., Freitas, S., Gerbig, C., ... & Wofsy, S. C. (2012). Carbon monoxide and related trace gases and aerosols over the Amazon Basin during the wet and dry seasons. Atmospheric Chemistry and Physics, 12(13), 6041-6065.

Aragao, L. E. O., Malhi, Y., Roman-Cuesta, R. M., Saatchi, S., Anderson, L. O., & Shimabukuro, Y. E. (2007). Spatial patterns and fire response of recent Amazonian droughts. Geophysical Research Letters, 34(7).

Arellano, A. F., Kasibhatla, P. S., Giglio, L., Van der Werf, G. R., Randerson, J. T., & Collatz, G. J. (2006). Time-dependent inversion estimates of global biomass-burning CO emissions using Measurement of Pollution in the Troposphere (MOPITT) measurements. Journal of Geophysical Research: Atmospheres, 111(D9).

Bertschi, I., Yokelson, R. J., Ward, D. E., Babbitt, R. E., Susott, R. A., Goode, J. G., & Hao, W. M. (2003). Trace gas and particle emissions from fires in large diameter and belowground biomass fuels. Journal of Geophysical Research: Atmospheres, 108(D13).

Bloom, A. A., Worden, J., Jiang, Z., Worden, H., Kurosu, T., Frankenberg, C., & Schimel, D. (2015). Remote-sensing constraints on South America fire traits by Bayesian fusion of atmospheric and surface data. Geophysical Research Letters, 42(4), 1268-1274.

Boersma, K. F., Eskes, H. J., Dirksen, R. J., Veefkind, J. P., Stammes, P., Huijnen, V., ... & Richter, A. (2011). An improved tropospheric NO2 column retrieval algorithm for the Ozone Monitoring Instrument. Atmospheric Measurement Techniques, 4(9), 1905-1928.

Bowman, D. M., Balch, J. K., Artaxo, P., Bond, W. J., Carlson, J. M., Cochrane, M. A., ... & Johnston, F. H. (2009). Fire in the Earth system. science, 324(5926), 481-484.

Câmara, G., Valeriano, D. M., & Soares, J. V. (2006). Metodologia para o Cálculo da Taxa Anual de Desmatamento na Amazônia Legal. INPE. (http://www.obt.inpe.br/prodes/ index.html)

Cardozo, F. D. S., Pereira, G., Shimabukuro, Y. E., & Moraes, E. C. (2014). Analysis and assessment of the spatial and temporal distribution of burned areas in the Amazon forest. Remote Sensing, 6(9), 8002-8025.

Castellanos, P., Boersma, K. F., Torres, O., & de Haan, J. F. (2015). OMI tropospheric NO 2 air mass factors over South America: effects of biomass burning aerosols. Atmospheric Measurement Techniques, 8(9), 3831-3849.

Channan, S., K. Collins, and W. R. Emanuel. 2014. Global mosaics of the standard MODIS land cover type data. University of Maryland and the Pacific Northwest National Laboratory, College Park, Maryland, USA.

Chen, Y., Morton, D. C., Jin, Y., Collatz, G. J., Kasibhatla, P. S., Van Der Werf, G. R., ... & Randerson, J. T. (2013). Long-term trends and interannual variability of forest, savanna and agricultural fires in South America. Carbon Management, 4(6), 617-638.

Chevallier, F., Fortems, A., Bousquet, P., Pison, I., Szopa, S., Devaux, M., & Hauglustaine, D. A. (2009). African CO emissions between years 2000 and 2006 as estimated from MOPITT observations. Biogeosciences, 6(1), 103-111.

Christopher, S. A., Kliche, D. V., Chou, J., & Welch, R. M. (1996). First estimates of the radiative forcing of aerosols generated from biomass burning using satellite data. Journal of Geophysical Research: Atmospheres, 101(D16), 21265-21273.

Christian, T. J., Yokelson, R. J., Carvalho, J. A., Griffith, D. W., Alvarado, E. C., Santos, J. C., ... & Hao, W. M. (2007). The tropical forest and fire emissions experiment: Trace gases emitted by smoldering logs and dung from deforestation and pasture fires in Brazil. Journal of Geophysical Research: Atmospheres (1984–2012), 112(D18).

Costa, M. H., C. H. C. Oliveira, R. G. Andrade, T. R. Bustamante, F. A. Silva, and M. T. Coe. 2003. LBA Regional Boundary for the Amazon and Tocantins River Basins, 5-min. Data set. Available on-line [http://www.daac.ornl.gov] from Oak Ridge National Laboratory Distributed Active Archive Center, Oak Ridge, Tennessee, U.S.A. doi:10.3334/ORNLDAAC/670.

Crutzen, P. J., Heidt, L. E., Krasnec, J. P., Pollock, W. H., & Seiler, W. (1979). Biomass burning as a source of atmospheric gases CO, H2, N2O, NO, CH3Cl and COS. Nature, 282, 253-256.

Crutzen, P. J., Delany, A. C., Greenberg, J., Haagenson, P., Heidt, L., Lueb, R., ... & Zimmerman, P. (1985). Tropospheric chemical composition measurements in Brazil during the dry season. Journal of Atmospheric Chemistry, 2(3), 233-256.

Crutzen, P. J., & Andreae, M. O. (1990). Biomass burning in the tropics: Impact on atmospheric chemistry and biogeochemical cycles. Science,250(4988), 1669-1678.

Davies, D. K., Ilavajhala, S., Wong, M. M., & Justice, C. O. (2009). Fire information for resource management system: archiving and distributing MODIS active fire data. Geoscience and Remote Sensing, IEEE Transactions on, 47(1), 72-79.

Deeter, M. N., Martínez-Alonso, S., Edwards, D. P., Emmons, L. K., Gille, J. C., Worden, H. M., ... & Wofsy, S. C. (2014). The MOPITT Version 6 product: algorithm enhancements and validation. Atmospheric Measurement Techniques, 7(11), 3623-3632.

Dennison, P. E., Brewer, S. C., Arnold, J. D., & Moritz, M. A. (2014). Large wildfire trends in the western United States, 1984–2011. Geophysical Research Letters, 41(8), 2928-2933.

Duncan, B. N., Martin, R. V., Staudt, A. C., Yevich, R., & Logan, J. A. (2003). Interannual and seasonal variability of biomass burning emissions constrained by satellite observations. Journal of Geophysical Research: Atmospheres, 108(D2).

Ferek, R. J., Reid, J. S., Hobbs, P. V., Blake, D. R., & Liousse, C. (1998). Emission factors of hydrocarbons, halocarbons, trace gases and particles from biomass burning in Brazil. Journal of Geophysical Research: Atmospheres (1984–2012), 103(D24), 32107-32118.

Freeborn, P. H., Wooster, M. J., Hao, W. M., Ryan, C. A., Nordgren, B. L., Baker, S. P., & Ichoku, C. (2008). Relationships between energy release, fuel mass loss, and trace gas and aerosol emissions during laboratory biomass fires. Journal of Geophysical Research: Atmospheres, 113(D1).

Friedl, M.A., D. Sulla-Menashe, B. Tan, A. Schneider, N. Ramankutty, A. Sibley and X. Huang (2010), MODIS Collection 5 global land cover: Algorithm refinements and characterization of new datasets, 2001-2012, Collection 5.1 IGBP Land Cover, Boston University, Boston, MA, USA.

Galanter, M., Levy, H., & Carmichael, G. R. (2000). Impacts of biomass burning on tropospheric CO, NO x, and O3. Journal of Geophysical Research: Atmospheres, 105(D5), 6633-6653.

Goldammer, J. G., (2015), Vegetation Fires and Global Change-Challenges for Concerted International Action: A White Paper directed to the United Nations and International Organizations. Planet@ Risk, 3(1).

Golding, N., & Betts, R. (2008). Fire risk in Amazonia due to climate change in the HadCM3 climate model: Potential interactions with deforestation. Global Biogeochemical Cycles, 22(4).

Gutiérrez-Vélez, V. H., & DeFries, R. (2013). Annual multi-resolution detection of land cover conversion to oil palm in the Peruvian Amazon. Remote Sensing of Environment, 129, 154-167.

Guyon, P., Frank, G. P., Welling, M., Chand, D., Artaxo, P., Rizzo, L., ... & Gatti, L. V. (2005). Airborne measurements of trace gas and aerosol particle emissions from biomass burning in Amazonia. Atmospheric Chemistry and Physics, 5(11), 2989-3002.

Hooghiemstra, P. B., Krol, M. C., Bergamaschi, P., Laat, A. T. J., Werf, G. R., Novelli, P. C., ... & Röckmann, T. (2012). Comparing optimized CO emission estimates using MOPITT or NOAA surface network observations. Journal of Geophysical Research: Atmospheres, 117(D6).

Huneeus, N., Chevallier, F., & Boucher, O. (2012). Estimating aerosol emissions by assimilating observed aerosol optical depth in a global aerosol model. Atmospheric Chemistry and Physics, 12(10), 4585-4606.

Hyer, E., Wang, J., & Arellano, A. (2012). Biomass burning: observations, modeling, and data assimilation. Bulletin of the American Meteorological Society, 93(1), ES10.

Ichoku, C., & Kaufman, Y. J. (2005). A method to derive smoke emission rates from MODIS fire radiative energy measurements. Geoscience and Remote Sensing, IEEE Transactions on, 43(11), 2636-2649.

Ichoku, C., Giglio, L., Wooster, M. J., & Remer, L. A. (2008). Global characterization of biomass-burning patterns using satellite measurements of fire radiative energy. Remote Sensing of Environment, 112(6), 2950-2962.

Ichoku, C., & Ellison, L. (2014). Global top-down smoke-aerosol emissions estimation using satellite fire radiative power measurements. Atmospheric Chemistry and Physics, 14(13), 6643-6667.

Instituto Nacional de Pesquisas Espaciais (INPE) (2002). Deforestation estimates in the Brazilian Amazon. São José dos Campos: INPE Available at: bhttp://www.obt.inpe.br/ prodes/.

Jacobson, M. Z. (2004). The short-term cooling but long-term global warming due to biomass burning. Journal of Climate, 17(15), 2909-2926.

Jacobson, M. Z. (2014). Effects of biomass burning on climate, accounting for heat and moisture fluxes, black and brown carbon, and cloud absorption effects. Journal of Geophysical Research: Atmospheres, 119(14), 8980-9002.

Johnston, F. H., Henderson, S. B., Chen, Y., Randerson, J. T., Marlier, M., DeFries, R. S., ... & Brauer, M. (2012). Estimated global mortality attributable to smoke from landscape fires. Environmental health perspectives, 120(5).

Justice, C. O., Giglio, L., Roy, D., Boschetti, L., Csiszar, I., Davies, D., ... & Morisette, J. (2010). MODIS-derived global fire products. In Land Remote Sensing and Global Environmental Change (pp. 661-679). Springer New York.

Kaiser, J. W., Heil, A., Andreae, M. O., Benedetti, A., Chubarova, N., Jones, L., ... & Van Der Werf, G. R. (2012). Biomass burning emissions estimated with a global fire assimilation system based on observed fire radiative power. Biogeosciences, 9(1), 527-554.

Kaiser, J. W., & Keywood, M. (2015). Preface for Atmos. Env. Special issue on IBBI. Atmospheric Environment, 121, 1-3.

Keywood, M., Kanakidou, M., Stohl, A., Dentener, F., Grassi, G., Meyer, C. P., ... & Burrows, J. (2013). Fire in the air: Biomass burning impacts in a changing climate. Critical Reviews in Environmental Science and Technology, 43(1), 40-83.

Knorr, W., Lehsten, V., & Arneth, A. (2012). Determinants and predictability of global wildfire emissions. Atmospheric Chemistry and Physics, 12(15), 6845-6861.

Konovalov, I. B., Berezin, E. V., Ciais, P., Broquet, G., Beekmann, M., Hadji-Lazaro, J., ... & Schulze, E. D. (2014). Constraining CO2 emissions from open biomass burning by satellite observations of co-emitted species: a method and its application to wildfires in Siberia. Atmospheric Chemistry and Physics, 14(19), 10383-10410.

Kopacz, M., Jacob, D. J., Fisher, J. A., Logan, J. A., Zhang, L., Megretskaia, I. A., ... & Buchwitz, M. (2010). Global estimates of CO sources with high resolution by adjoint inversion of multiple satellite datasets (MOPITT, AIRS, SCIAMACHY, TES). Atmospheric Chemistry and Physics, 10(3), 855-876.

Koren, I., Remer, L. A., & Longo, K. (2007). Reversal of trend of biomass burning in the Amazon. Geophysical Research Letters, 34(20).

Lamarque, J. F., Bond, T. C., Eyring, V., Granier, C., Heil, A., Klimont, Z., ... & Schultz, M. G. (2010). Historical (1850–2000) gridded anthropogenic and biomass burning emissions of reactive gases and aerosols: methodology and application. Atmospheric Chemistry and Physics, 10(15), 7017-7039.

Langmann, B., Duncan, B., Textor, C., Trentmann, J., & van der Werf, G. R. (2009). Vegetation fire emissions and their impact on air pollution and climate. Atmospheric Environment, 43(1), 107-116.

Levy, R. C., Remer, L. A., Kleidman, R. G., Mattoo, S., Ichoku, C., Kahn, R., & Eck, T. F. (2010). Global evaluation of the Collection 5 MODIS dark-target aerosol products over land. Atmospheric Chemistry and Physics, 10(21), 10399-10420.

Levy, R., Hsu, C., et al., 2015. MODIS Atmosphere L2 Aerosol Product. NASA MODIS Adaptive Processing System, Goddard Space Flight Center, USA: http://dx.doi.org/10.5067/MODIS/MOD04_L2.006.

Hao, W.M. and Liu, M-H. (1994). Spatial and temporal distribution of tropical biomass burning. Global biogeochemical cycles, 8(4), 495-503.

Longo, K. M., Freitas, S. R., Andreae, M. O., Yokelson, R., & Artaxo, P. (2009). Biomass Burning in Amazonia: Emissions, Long-Range Transport of Smoke and Its Regional and Remote Impacts. Amazonia and Global Change, 207-232.

Mao, Y. H., Li, Q. B., Chen, D., Zhang, L., Hao, W. M., & Liou, K. N. (2014). Top-down estimates of biomass burning emissions of black carbon in the Western United States. Atmospheric Chemistry and Physics, 14(14), 7195-7211.

Mebust, A. K., & Cohen, R. C. (2014). Space-based observations of fire NO x emission coefficients: a global biome-scale comparison. Atmospheric Chemistry and Physics, 14(5), 2509-2524.

Mishra, A. K., Lehahn, Y., Rudich, Y., & Koren, I. (2015). Co-variability of smoke and fire in the Amazon Basin. Atmospheric Environment, 109, 97-104.

Miyazaki, K., Eskes, H. J., & Sudo, K. (2015). A tropospheric chemistry reanalysis for the years 2005–2012 based on an assimilation of OMI, MLS, TES, and MOPITT satellite data. Atmospheric Chemistry and Physics, 15(14), 8315-8348.

Morton, D. C., Defries, R. S., Randerson, J. T., Giglio, L., Schroeder, W., & Van Der Werf, G. R. (2008). Agricultural intensification increases deforestation fire activity in Amazonia. Global Change Biology, 14(10), 2262-2275.

Morton, D. C., Le Page, Y., DeFries, R., Collatz, G. J., & Hurtt, G. C. (2013). Understorey fire frequency and the fate of burned forests in southern Amazonia. Philosophical Transactions of the Royal Society B: Biological Sciences, 368(1619), 20120163.

Mu, Q., Zhao, M., Kimball, J. S., McDowell, N. G., & Running, S. W. (2013). A remotely sensed global terrestrial drought severity index. Bulletin of the American Meteorological Society, 94(1), 83-98.

Nazareno, A. G., & Laurance, W. F. (2015). Brazil's drought: beware deforestation. Science (New York, NY), 347(6229), 1427.

Neto, T. S., Carvalho, J. A., Veras, C. A. G., Alvarado, E. C., Gielow, R., Lincoln, E. N., ... & Santos, J. C. (2009). Biomass consumption and CO 2, CO and main hydrocarbon gas emissions in an Amazonian forest clearing fire. Atmospheric Environment, 43(2), 438-446.

Pacifico, F., Folberth, G. A., Sitch, S., Haywood, J. M., Rizzo, L. V., Malavelle, F. F., & Artaxo, P. (2015). Biomass burning related ozone damage on vegetation over the Amazon forest: a model sensitivity study. Atmospheric Chemistry and Physics, 15(5), 2791-2804.

Pechony, O., Shindell, D. T., & Faluvegi, G. (2013). Direct top-down estimates of biomass burning CO emissions using TES and MOPITT versus bottom-up GFED inventory. Journal of Geophysical Research: Atmospheres, 118(14), 8054-8066.

Reddington, C. L., Butt, E. W., Ridley, D. A., Artaxo, P., Morgan, W. T., Coe, H., & Spracklen, D. V. (2015). Air quality and human health improvements from reductions in deforestation-related fire in Brazil. Nature Geoscience,8(10), 768-771.

Reid, J. S., Koppmann, R., Eck, T. F., & Eleuterio, D. P. (2005a). A review of biomass burning emissions part II: intensive physical properties of biomass burning particles. Atmospheric Chemistry and Physics, 5(3), 799-825.

Reid, J. S., Eck, T. F., Christopher, S. A., Koppmann, R., Dubovik, O., Eleuterio, D. P., ... & Zhang, J. (2005b). A review of biomass burning emissions part III: intensive optical properties of biomass burning particles. Atmospheric Chemistry and Physics, 5(3), 827-849.

Reid, J. S., Hyer, E. J., Prins, E. M., Westphal, D. L., Zhang, J., Wang, J., ... & Richardson, K. A. (2009). Global monitoring and forecasting of biomass-burning smoke: Description of and lessons from the Fire Locating and Modeling of Burning Emissions (FLAMBE) program. Selected Topics in Applied Earth Observations and Remote Sensing, IEEE Journal of, 2(3), 144-162.

Rein, G. (2009). Smouldering combustion phenomena in science and technology, Int. Rev. Chem. Eng., 1, 3–18.

Saide, P. E., Spak, S. N., Pierce, R. B., Otkin, J. A., Schaack, T. K., Heidinger, A. K., ... & Carmichael, G. R. (2015). Central American biomass burning smoke can increase tornado severity in the US. Geophysical Research Letters, 42(3), 956-965.

Schreier, S. F., Richter, A., Kaiser, J. W., & Burrows, J. P. (2014). The empirical relationship between satellite-derived tropospheric NO2 and fire radiative power and possible implications for fire emission rates of NOx. Atmospheric Chemistry and Physics, 14(5), 2447-2466.

Schroeder, W., Morisette, J. T., Csiszar, I., Giglio, L., Morton, D., & Justice, C. O. (2005). Characterizing vegetation fire dynamics in Brazil through multisatellite data: Common trends and practical issues. Earth Interactions, 9(13), 1-26.

Schroeder, W., Alencar, A., Arima, E., & Setzer, A. (2009). The spatial distribution and interannual variability of fire in Amazonia. Amazonia and Global Change, 43-60.

Schultz, M. G., A. Heil, J. J. Hoelzemann, A. Spessa, K. Thonicke, J. G. Goldammer, A. C. Held, J. M. C. Pereira, and M. van het Bolscher (2008), Global wildland fire emissions from 1960 to 2000, Global Biogeochem. Cycles, 22, GB2002, doi:10.1029/2007GB003031.

Seiler, W., & Crutzen, P. J. (1980). Estimates of gross and net fluxes of carbon between the biosphere and the atmosphere from biomass burning. Climatic change, 2(3), 207-247.

Shimabukuro, Y. E., dos Santos, J. R., Formaggion, A. R., Duarte, V., & Rudorff, B. F. T. (2012). The Brazilian Amazon monitoring program: PRODES and DETER projects. Global forest monitoring from earth observation, 153-169.

Stavrakou, T., Müller, J. F., Bauwens, M., Smedt, I. D., Van Roozendael, M., Mazière, M. D., ... & Coheur, P. F. (2015). How consistent are top-down hydrocarbon emissions based on formaldehyde observations from GOME-2 and OMI?. Atmospheric Chemistry and Physics, 15(20), 11861-11884.

Streets, D. G., Canty, T., Carmichael, G. R., de Foy, B., Dickerson, R. R., Duncan, B. N., ... & Jacob, D. J. (2013). Emissions estimation from satellite retrievals: A review of current capability. Atmospheric Environment, 77, 1011-1042.

Urbanski, S. P., Hao, W. M., & Baker, S. (2008). Chemical composition of wildland fire emissions. Developments in Environmental Science, 8, 79-107.

Urbanski, S. P., Hao, W. M., & Nordgren, B. (2011). The wildland fire emission inventory: western United States emission estimates and an evaluation of uncertainty. Atmospheric Chemistry and Physics, 11(24), 12973-13000.

van der Werf, G. R., Randerson, J. T., Giglio, L., Collatz, G. J., Kasibhatla, P. S., & Arellano Jr, A. F. (2006). Interannual variability in global biomass burning emissions from 1997 to 2004. Atmospheric Chemistry and Physics, 6(11), 3423-3441.

van der Werf, G. R., Randerson, J. T., Giglio, L., Collatz, G. J., Mu, M., Kasibhatla, P. S., ... & van Leeuwen, T. T. (2010). Global fire emissions and the contribution of deforestation, savanna, forest, agricultural, and peat fires (1997–2009). Atmospheric Chemistry and Physics, 10(23), 11707-11735.

Van Leeuwen, T. T., & Van Der Werf, G. R. (2011). Spatial and temporal variability in the ratio of trace gases emitted from biomass burning. Atmospheric Chemistry and Physics, 11(8), 3611-3629.

Van Leeuwen, T. T., Van der Werf, G. R., Hoffmann, A. A., Detmers, R. G., Rücker, G., French, N. H., ... & Hély, C. (2014). Biomass burning fuel consumption rates: a field measurement database.

Voulgarakis, A., & Field, R. D. (2015). Fire Influences on Atmospheric Composition, Air Quality and Climate. Current Pollution Reports, 1(2), 70-81.

Ward, D. E., & Hardy, C. C. (1991). Smoke emissions from wildland fires. Environment International, 17(2), 117-134.

Ward, D. E., Setzer, A. W., Kaufman, Y. J., & Rasmussen, R. A. (1991). Characteristics of smoke emissions from biomass fires of the Amazon region-BASE-A experiment. Global biomass burning: Atmospheric, climatic, and biospheric implications, 394-402.

Ward, D. E., Susott, R. A., Kauffman, J. B., Babbitt, R. E., Cummings, D. L., Dias, B., ... & Setzer, A. W. (1992). Smoke and fire characteristics for cerrado and deforestation burns in Brazil: BASE-B experiment. Journal of Geophysical Research: Atmospheres, 97(D13), 14601-14619.

Ward, D. S., Kloster, S., Mahowald, N. M., Rogers, B. M., Randerson, J. T., & Hess, P. G. (2012). The changing radiative forcing of fires: global model estimates for past, present and future. Atmospheric Chemistry and Physics, 12(22).

Westerling, A. L., Hidalgo, H. G., Cayan, D. R., & Swetnam, T. W. (2006). Warming and earlier spring increase western US forest wildfire activity. science, 313(5789), 940-943.

Wiedinmyer, C., Akagi, S. K., Yokelson, R. J., Emmons, L. K., Al-Saadi, J. A., Orlando, J. J., & Soja, A. J. (2011). The Fire INventory from NCAR (FINN): A high resolution global model to estimate the emissions from open burning. Geoscientific Model Development, 4, 625.

Wooster, M. J., Roberts, G., Perry, G. L. W., & Kaufman, Y. J. (2005). Retrieval of biomass combustion rates and totals from fire radiative power observations: FRP derivation and calibration relationships between biomass consumption and fire radiative energy release. Journal of Geophysical Research: Atmospheres (1984–2012), 110(D24).

Yokelson, R. J., Griffith, D. W., & Ward, D. E. (1996). Open-path Fourier transform infrared studies of large-scale laboratory biomass fires. Journal of Geophysical Research: Atmospheres, 101, 21067.

Yokelson, R. J., Karl, T., Artaxo, P., Blake, D. R., Christian, T. J., Griffith, D. W., ... & Hao, W. M. (2007). The Tropical Forest and Fire Emissions Experiment: overview and airborne fire emission factor measurements. Atmospheric Chemistry and Physics, 7(19), 5175-5196.

Yokelson, R. J., Christian, T. J., Karl, T. G., & Guenther, A. (2008). The tropical forest and fire emissions experiment: laboratory fire measurements and synthesis of campaign data. Atmospheric Chemistry and Physics, 8(13), 3509-3527.

Supporting Information

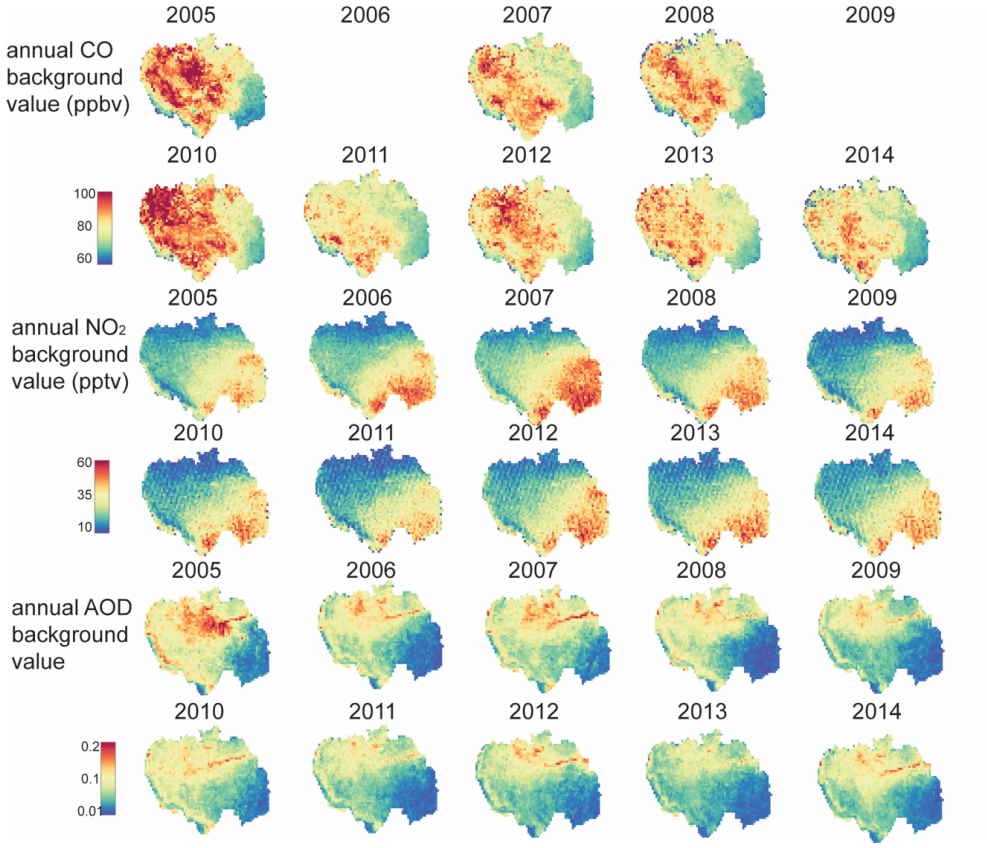

Figure AS1. Annual background field for CO, NO2 and AOD in Amazon.

Table AS1. Annual spatial correlations between fire events detected by MODIS hotspot and fire events used in this study (Figure A1a and Figure A1b).

year	2005	2006	2007	2008	2009	2010	2011	2012	2013	2014	all
correlation	0.93	0.89	0.91	0.87	0.58	0.82	0.61	0.85	0.67	0.60	0.92
P value	0	0	0	0	5.64E-212	0	1.98E-241	0	2.65E-305	1.64E-231	0
nx[a]	4434	2620	4669	2174	261	1942	537	1526	428	452	19043
ny[b]	11819	7919	12190	6799	3848	12403	4811	6443	3320	5279	74831

[a]nx is Fire events in the specific year used in this study.

[b]ny is Fire events in the specific year detected by MODIS hotspot.

Table AS2. Emission factors and ratios from literature.

Reference	meas. type	time	location/ vegetation type	EFs/ERs				
				MCE/CE	CO_2	CO	NO_x	PM
Crutzen (1985)[a]	Airborne	Aug-Sep 1979 &1980		–	–	CO/CO_2: 15.4%	NO_x/CO_2: 0.002	–
Ward (1991)[b] BASE-A	Airborne	Sep 1989	Cerrado	CE=0.972	1783 (g/kg)	24.5 (g/kg)	–	4.4 (g $PM_{2.5}$/kg)
			Deforestation	CE=0.908	1666 (g/kg)	97.7 (g/kg)	–	–
			Deforestation	CE=0.949	1741 (g/kg)	46.6 (g/kg)	–	2.48 (g $PM_{2.5}$/kg)
			Deforestation	CE=0.864	1586 (g/kg)	120.9 (g/kg)	–	15.6 (g $PM_{2.5}$/kg)
Ward (1992)[c] BASE-B	Ground		Cerrado	CE=0.93	1713 (g/kg)	63 (g/kg)	0.5 (g NO/kg)	4.5 (g $PM_{2.5}$/kg)
			Cerrado	CE=0.94	1732 (g/kg)	52 (g/kg)	–	4.4 (g $PM_{2.5}$/kg)
			Cerrado	CE=0.93	1705 (g/kg)	70 (g/kg)	0.4 (g NO/kg)	4.2 (g $PM_{2.5}$/kg)
			Cerrado	CE=0.92	1690 (g/kg)	68 (g/kg)	–	4.4 (g $PM_{2.5}$/kg)
			Cerrado	CE=0.95	1749 (g/kg)	46 (g/kg)	0.6 (g NO/kg)	1.4 (g $PM_{2.5}$/kg)
			Cerrado	CE=0.95	1740 (g/kg)	51 (g/kg)	–	2.7 (g $PM_{2.5}$/kg)
			Primary forest	CE=0.88	1612 (g/kg)	112 (g/kg)	0.6 (g NO/kg)	6.8 (g $PM_{2.5}$/kg)
			Primary forest	CE=0.85	1551 (g/kg)	142 (g/kg)	0.8 (g NO/kg)	8.9 (g $PM_{2.5}$/kg)
			Primary forest	CE=0.84	1531 (g/kg)	152 (g/kg)	0.8 (g NO/kg)	6.8 (g $PM_{2.5}$/kg)
			Second-growth forest	CE=0.92	1692 (g/kg)	73 (g/kg)	1.1 (g NO/kg)	10 (g $PM_{2.5}$/kg)
			Second-growth forest	CE=0.9	1652 (g/kg)	91 (g/kg)	0.8 (g NO/kg)	9.2 (g $PM_{2.5}$/kg)
			Second-growth forest	CE=0.89	1637 (g/kg)	94 (g/kg)	–	10.4 (g $PM_{2.5}$/kg)
			Second-growth forest	CE=0.89	1625 (g/kg)	107 (g/kg)	–	7.1 (g $PM_{2.5}$/kg)
Ferek (1998)[d] SCAR-B	Airborne	Aug-Sep 1995	Forest	Flaming (MCE>0.90)	913±34 (g C/kg C Burned)	60±28 (g C/kg C Burned)	1.1~1.5 (NO_x: g N/kg C Burned)	17.0±7.5 (g PM4 /kg C Burned)
			Forest	Smoldering (MCE<0.90)	831±22 (g C/kg C Burned)	120±13 (g C/kg C Burned)	0.8~1.1 (NO_x: g N/kg C Burned)	26.6±11.0 (g PM4 /kg C Burned)
Guyon (2005)[e] LBA-SMOCC	Airborne	Sep-Oct 2002	Amazonia/ forest & pasture	–	–	61; 90 (g kg^{-1} dm)	–	0.5-2(CN: 10^{15} kg^{-1} dm)
Yokelson (2007)[f] TROFFEE	Airborne	Aug-Sep 2004	Slash under partial canopy	MCE=0.916	1638 (g/kg)	95.72 (g/kg)	1.574 (g NO_x as NO/kg)	17.61 (g PM_{10}/kg)
			Pasture	MCE=0.900	1591 (g/kg)	112.08 (g/kg)	0.606 (g NO_x as NO/kg)	14.43 (g PM_{10}/kg)
			Grass & slash piles under partial canopy	MCE=0.882	1567 (g/kg)	133.45 (g/kg)	1.035 (g NO_x as NO/kg)	17.94 (g PM_{10}/kg)
			Mixed forest fuels	MCE=0.890	1579 (g/kg)	124.82 (g/kg)	0.846 (g NO_x as NO/kg)	20.18 (g PM_{10}/kg)
			Mixed forest fuels	MCE=0.902	1603 (g/kg)	110.7 (g/kg)	0.69 (g NO_x as NO/kg)	19.81 (g PM_{10}/kg)
			Mixed forest fuels	MCE=0.918	1636 (g/kg)	93.13 (g/kg)	1.883 (g NO_x as NO/kg)	17.27 (g PM_{10}/kg)
			Mixed forest fuels & source/fuels not observed from aircraft	MCE=0.901	1579 (g/kg)	110.52 (g/kg)	1.654 (g NO_x as NO/kg)	26.41 (g PM_{10}/kg)
			Mixed forest fuels	MCE=0.947	1679 (g/kg)	59.91 (g/kg)	4.926 (g NO_x as NO/kg)	12.53 (g PM_{10}/kg)
			Mixed forest fuels	MCE=0.936	1662 (g/kg)	72.36 (g/kg)	2.687 (g NO_x as NO/kg)	14.28 (g PM_{10}/kg)
			Study Average	MCE=0.910	1615 (g/kg)	101.41 (g/kg)	1.77 (g NO_x as NO/kg)	17.83 (g PM_{10}/kg)

Table AS2. Continued.

Reference	meas. type	time	location/ vegetation type	EFs/ERs				
				MCE/CE	CO_2	CO	NO_x	PM
			Study Average	MCE=0.910	1615 (g/kg)	101.41 (g/kg)	1.77 (g NO_x as NO/kg)	17.83 (g PM_{10}/kg)
Christian (2007)[g] TROFFEE	Ground	2004	Deforestation	RSC	1360 (g /kg dry fuel)	218 (g/kg)	–	–
			Deforestation	conv	1683 (g /kg dry fuel)	60 (g/kg dry fuel)	–	–
			Deforestation	total	1667 (g /kg dry fuel)	67.9 (g /kg dry fuel)	–	–
Yokelson (2008)[h] TROFFEE	Ground	2004	Laboratory fires	MCE=0.949	1677 (g/kg dry fuel)	57.46 (g/kg dry fuel)	NO 1.284; NO2 0.585 (g/kg dry fuel)	9.93 (g $PM_{2.5}$/kg dry fuel)
Neto (2009)[i]	Ground	Sep 2004		Flaming (MCE=0.945)	1690 (g/kg dm)	62.7 (g/kg dm)	–	7.45 (g $PM_{2.5}$/kg dm)
				Intermediate (MCE=0.911)	1625 (g/kg dm)	101.2 (g/kg dm)	–	4.21 (g $PM_{2.5}$/kg dm)
				Smoldering (MCE=0.874)	1540 (g/kg dm)	140.6 (g/kg dm)	–	3.85 (g $PM_{2.5}$/kg dm)
				Flaming (MCE=0.950)	1741 (g/kg dm)	58.9 (g/kg dm)	–	–
				Intermediate (MCE=0.890)	1631 (g/kg dm)	128.7 (g/kg dm)	–	–
				Smoldering (MCE=0.845)	1548 (g/kg dm)	181.3 (g/kg dm)	–	–
Andreae (2012)[j] BARCA	Airborne	Nov–Dec 2008 (A) & May–Jun 2009 (B)	Eastern and Central Amazon/ Mostly rainforest	–	–	$66\pm23\times10^{-3}$ CO/CO_2	–	53.1±22.6 (CN/CO $cm^{-3}ppb^{-1}$)
Andreae (2001)[k]	Literature review		Tropical forest	MCE=0.906	1580±90 (g/kg dm)	104±20 (g/kg dm)	1.6±0.7 (g NO_x as NO/kg dm)	6.5-10.5 (g TPM/kg dm)
			Savanna & Grassland	MCE=0.940	1613±95 (g/kg dm)	65±20 (g/kg dm)	3.9±2.4 (g NO_x as NO/kg dm)	8.3±3.2 (g TPM/kg dm)
Akagi (2011)[l]	Literature review		Tropical forest	MCE=0.918	1643±58 (g/kg)	93±27 (g/kg)	2.55±1.40 (g NO_x as NO/kg)	18.5±4.1(g PM_{10}/kg)
			Savanna	MCE=0.946	1686±38 (g/kg)	63±17 (g/kg)	3.9±0.80 (g NO_x as NO/kg)	–

a: CO/CO_2 comes from Table 1 and NO_x/CO_2 comes from text on Page 247.

b: BASE-A: the Biomass Burning Airborne and Spaceborne Experiment-Amazonia. Data comes from Table 48.2. Units are g emission per kg fuel consumed.

c: BASE-B: the Biomass Burning Airborne and Spaceborne Experiment-Brazil. Emission factors are on a mass of compound to mass of fuel-consumed basis except for NO it is mass of nitrogen per mass of fuel-consumed.

d: SCAR-B: the Smoke, Clouds, and Radiation-Brazil. CO_2 and CO data come from Table 1, PM4 comes from Table 4. The three species are for forests. NO_x comes from regression of all land cover in Fig 5.

e: LBA-SMOCC: Large-Scale Biosphere-Atmosphere Experiment in Amazonia – Smoke, Aerosols, Clouds, Rainfall, and Climate. CO comes from Table 1. CN stands for aerosol number. CN here is results from the Santa Lucia deforestation fire (SLF) in Table 5. 'dm' stands for dry matter. EFs of CO in this work: 61 is values from aircraft, online measurements while 90 is corrected value for residual smoldering combustion.

f: TROFFEE: the Tropical Forest and Fire Emissions Experiment. SC Fire is shifting cultivation fire. Data comes from Table 2.

g: FTIR (a mobile, Fourier transform infrared spectrometer) was used to measure the unlofted emissions. The values showed in this table are emissions of Deforestation fires in Table 4. 'conv' is convected emissions.

h: Data comes from Table 3 (average value of different tropical fuel types).

i: FASS (Fire Atmosphere Sampling System) is used in this work. Data comes from Table 6 and Table 7.

j: BARCA: the Balanco Atmosferico Regional de Carbono na Amazonia. BARCA-A and BARCA-B are two aircraft campaigns. CO to CO_2 ratio comes from Table. CN/CO comes from average of a few fire plume samples in Table 3.

k: EF values are calculated by averaging of previous literature. l: EF values are calculated by averaging of previous literature.

APPENDIX B

SATELLITE DATA REVEALS A COMMON COMBUSTION EMISSION PATHWAY FOR MAJOR CITIES IN CHINA

(Published in *Atmosphere Chemistry and Physics*,
https://doi.org/10.5194/acp-2018-1121)

Wenfu Tang[1], Avelino F. Arellano[1], Benjamin Gaubert[2], Kazuyuki Miyazaki[3], and Helen M. Worden[2]

[1]Department of Hydrology and Atmospheric Sciences, University of Arizona, Tucson, Arizona, USA.
[2]National Center for Atmospheric Research, Atmospheric Chemistry Observations and Modeling Laboratory, Boulder, Colorado, USA
[3]Japan Agency for Marine – Earth Science and Technology, Yokohama, Japan

Tang, W., Arellano, A. F., Gaubert, B., Miyazaki, K., and Worden, H. M., 2019a. Satellite data reveal a common combustion emission pathway for major cities in China, Atmos. Chem. Phys., 19, 4269-4288, https://doi.org/10.5194/acp-19-4269-2019.

Abstract

Extensive fossil fuel combustion in rapidly-developing cities severely affects air quality and public health. We report observational evidence of decadal changes in the efficiency, and cleanness of bulk combustion over large cities in mainland China. In order to estimate the trends in enhancement ratios of CO and SO_2 to NO_2 ($\Delta CO/\Delta NO_2$ and $\Delta SO_2/\Delta NO_2$) and infer emergent bulk combustion properties over these cities, we combine air quality retrievals from widely used satellite instruments across 2005-2014. We present results for four Chinese cities (Shenyang, Beijing, Shanghai, and Shenzhen) representing four levels of urban development. Our results show a robust coherent progression of declining-to-growing $\Delta CO/\Delta NO_2$ relative to 2005 (-5.4±0.7%/year to +8.3±3.1%/year), and slowly-declining $\Delta SO_2/\Delta NO_2$ (-6.0±1.0%/year to -3.4±1.0%/year) across the four cities. The coherent progression we found is not evident in the trends of emission ratios reported in Representative Concentration Pathway (RCP8.5) inventory. This progression is likely due to a shift towards cleaner combustion from industrial and residential sectors in Shanghai and Shenzhen that is not yet seen in Shenyang and Beijing. This overall trend is presently obfuscated by China's still relatively higher dependence on coal. Such progression is well-correlated with economic development, and traces a common emission pathway that resembles evolution of air pollution in more developed cities. Our results highlight the utility of augmenting observing and modeling capabilities by exploiting enhancement ratios in constraining the time variation of emission ratios in current inventories. As cities and/or countries continue to socioeconomically develop, the ability to monitor combustion efficiency and effectiveness of pollution control becomes increasingly important in assessing sustainable control strategies.

1 Introduction

Urban agglomeration, particularly megacities (i.e., cities with >10 million inhabitants), are expected to continue growing (in size and number) over the coming decades (Jalkanen, 2012; World Bank, 2015). Anthropogenic activities are most intense in megacities, accompanied by immense energy consumption mainly in the form of fossil fuel combustion (Mage et al., 1996; Kennedy et al., 2015). These lead to enhanced emissions of air pollutants, greenhouse gases, and waste energy, largely impacting air quality (AQ), climate, and ecosystems (Baklanov et al., 2016, Lelieveld et al., 2015). At present, estimates of city-to-national-scale emissions from fossil fuel

combustion remain uncertain, especially in rapidly-developing regions where combustion is still poorly characterized due to the lack of detailed information on energy use, combustion practices, and pollution control strategies (Streets et al., 2013; Creutzig et al., 2015). This is also confounded by larger uncertainties on other sources of pollution that may be associated with urbanization (e.g., deforestation, agriculture, and fires). These alone preclude us to accurately assess the changes in atmospheric composition due to anthropogenic activities at scales that are relevant to AQ, energy, and environmental policy (National Academies of Sciences, Engineering, and Medicine, 2016).

Such is the case for cities in China even with the scientific attention the country has received in the past decades. As China grew into the world's second largest economy, its rapid development resulted to substantial emissions (Richter et al., 2005), and more frequent occurrences of most severe pollution events in many of its megacities, most notably Beijing (Guo et al., 2014). These affect not only local AQ and public health but are reported to impact hemispheric-to-global atmospheric environment (Lin et al., 2014; Verstraeten et al., 2015). Along with the growth of these cities is a growing body of evidence of decreasing emissions and associated pollution levels in some cities in China. This points to important changes in AQ as a result of development, AQ management, and regional-to-national socioeconomic initiatives embodied within its Five-Year Plans (FYP) (Reuter et al., 2014; Krotkov et al., 2016; van der A et al., 2017; Sun et al., 2018; Koukouli et al., 2018). However, these changes in AQ as a result of efforts to control air pollution are still obfuscated at present by the increase in combustion activities, along with uncertainties in bottom-up emission inventories, and diversity in economic structure and growth across cities (Wang and Hao, 2012; Mi et al., 2017). Monitoring these reductions at city scale remains to be a challenge especially when narrowly viewed within the context of a single pollutant, and more so when attributing them to a particular emission sector.

Fossil fuel emissions from an evolving megacity follow a pattern that can be potentially monitored and refined, by combining observational constraints on combustion activity (abundance of combustion products) with efficiency and effectiveness of pollution control strategies or 'cleanness' (enhancement ratios of these products) (Silva et al., 2013; Hassler et al., 2016; Silva and Arellano, 2017; Tang et al., 2018, 2019), alongside information on the state of socio-economic development (e.g., gross domestic product (GDP) or income) and *a priori* estimates from bottom-up emission inventories. In particular, the 'cleanness' of combustion of a known fossil fuel type can be

determined stoichiometrically by measuring the relative abundance of intermediate products such as carbon monoxide (CO), nitrogen oxides (NO_X), sulfur dioxides (SO_2), and soot particles with final products like carbon dioxide (CO_2). Please see Methods section for more details. Most of these products are currently monitored as criteria pollutants by surface measurement networks and as tracers of pollution by satellite remote sensing (Streets et al., 2013; Duncan et al., 2014). In fact, these combustion products are revealed in space as very distinct bulk enhancements over a megacity metropolitan location in marked spatial contrast with the city's surroundings (Bechle et al., 2011; Lamsal et al., 2013). At a scale of a megacity being monitored from space, these enhancements are analogous to smoke plumes coming from a stationary smokestack. And so, observations of these megacity plumes enable us to monitor bulk anthropogenic activity and transboundary pollution. They have also been used in recent years to refine the spatiotemporal distribution of emissions (Lamsal et al., 2013; Hakkarainen et al., 2016; Ding et al., 2017), to indicate bulk combustion efficiency, inter-megacity differences and fire phase (Silva et al., 2013; Silva and Arellano, 2017; Tang and Arellano, 2017), and to infer fossil fuel CO_2 emissions (Konovalov et al., 2016) among others. From an annual to decadal standpoint, it is reasonable to interpret the long-term changes in spatial covariations between these observed pollutant enhancements within the megacity to reflect dominant shifts in bulk combustion characteristics (e.g., changes in fuel mixture and technology practice), which can then be indicative of an emission pathway for a given megacity (e.g., Parrish et al., 2002; Parrish, 2006; Russell et al., 2012; Silva et al., 2013; Hassler et al., 2016; Silva and Arellano, 2017). Data sampling and collocation issues, as well as retrieval information content and chemical nonlinearities between these pollutants, do not quite manifest at decadal scales more than emission changes, especially when treated as a smokestack in the analysis.

In this study, our goal is to uncover space-based evidence of dominant shifts in the cleanness of bulk combustion of large cities across the recent decade (through these ratios), associate these shifts to particular sectors, and identify a common emission pathway across these cities. Along the same line to studies on environmental Kuznets curves (EKC, Stern, 2004) and human development (Lamb et al., 2014), we attempt to connect this pathway to economic growth by finding a power law relationship between the ratios observed for each major city in China and the city's GDP per capita. As cities in China grow, emissions from fossil fuel combustion evolve accordingly depending on the rate and type of socioeconomic development, technological innovation, and

environmental policies (Chan and Yao, 2008; Bechle et al., 2011; Zhang et al., 2012; Wang et al., 2012; He and Wang, 2012; Luo et al., 2014; Koukouli et al., 2018; Sun et al., 2018). This evolution however cannot be reflected at shorter time scales. As a basis for comparison, pollution controls adopted in developed countries like United States and Europe, which followed a progression from first controlling SO_2, CO, and then NO_X (Crippa et al., 2016), reflect some aspects of decadal-scale sustainable development that can be brought to light in the case of China.

We analyze the emergent patterns of the 'cleanness' of bulk combustion in the past decade (2005-2014), based on enhancement ratios between intermediate products of combustion ($\Delta CO/\Delta NO_2$ and $\Delta SO_2/\Delta NO_2$) observed within each megacity and urban agglomeration in China. We use gridded monthly-averaged satellite retrievals of total columns of CO from Measurement of Pollution In The Troposphere (MOPITT), tropospheric columns of NO_2 from Ozone Monitoring Instrument (OMI), and planetary boundary layer (PBL) columns of SO_2 from OMI to derive monthly estimates of these ratios. We conduct spatial regression analysis and subsequently derive estimates of the decadal trends of these ratios using time series analysis. We then compare these trend estimates to inferred trends from a couple of model-derived abundance ratios and several emission ratios from current bottom-up emission inventories, including estimates based on the Representative Concentration Pathways scenario (RCP8.5) (Riahi et al., 2011). We also conducted a simple inverse analysis to update the contribution of major emission sectors in RCP8.5 to fit our estimates of decadal changes in enhancement ratios. Section 2 describes data and methods used in this study. Results and discussions are presented in Section 3. Section 4 is summary and implication of this study.

2 Data and Methods

2.1 Study Region

We considered all 31 provincial capitals and five special cities (Beijing, Shanghai, Shenzhen, Tianjin, and Chongqing) in mainland China for our analysis. These cities comprise the main urban agglomerations in the country (see Figure B1 for coverage). For purposes of finding long-term emergent patterns on its emission characteristics, we focused our analysis to 12 representative urban agglomerations. These 12 cities cover the four economic regions of China (i.e., East Coast: Beijing, Tianjin, Shanghai, Guangzhou, Shenzhen; Central China: Wuhan, Northeast China:

Harbin, Shenyang; and Western China: Chengdu, Chongqing, Xian, Hohhot). Based on prior information from RCP8.5 and National Bureau of Statistics of China (http://data.stats.gov.cn), these cities already exhibit largely diverse pollution and economic development attributes illustrated in Figure B1 as differences in magnitude, sectoral, and temporal distribution of emissions and GDP per capita for 2005 to 2014 between these cities. Our goal is to assess whether the long-term patterns that are seen in these *a priori* emission estimates are consistent with observations. We also considered Los Angeles and other large cities in the United States (New York City, Chicago, Houston, Phoenix, Boston, Seattle, and Miami) for comparison.

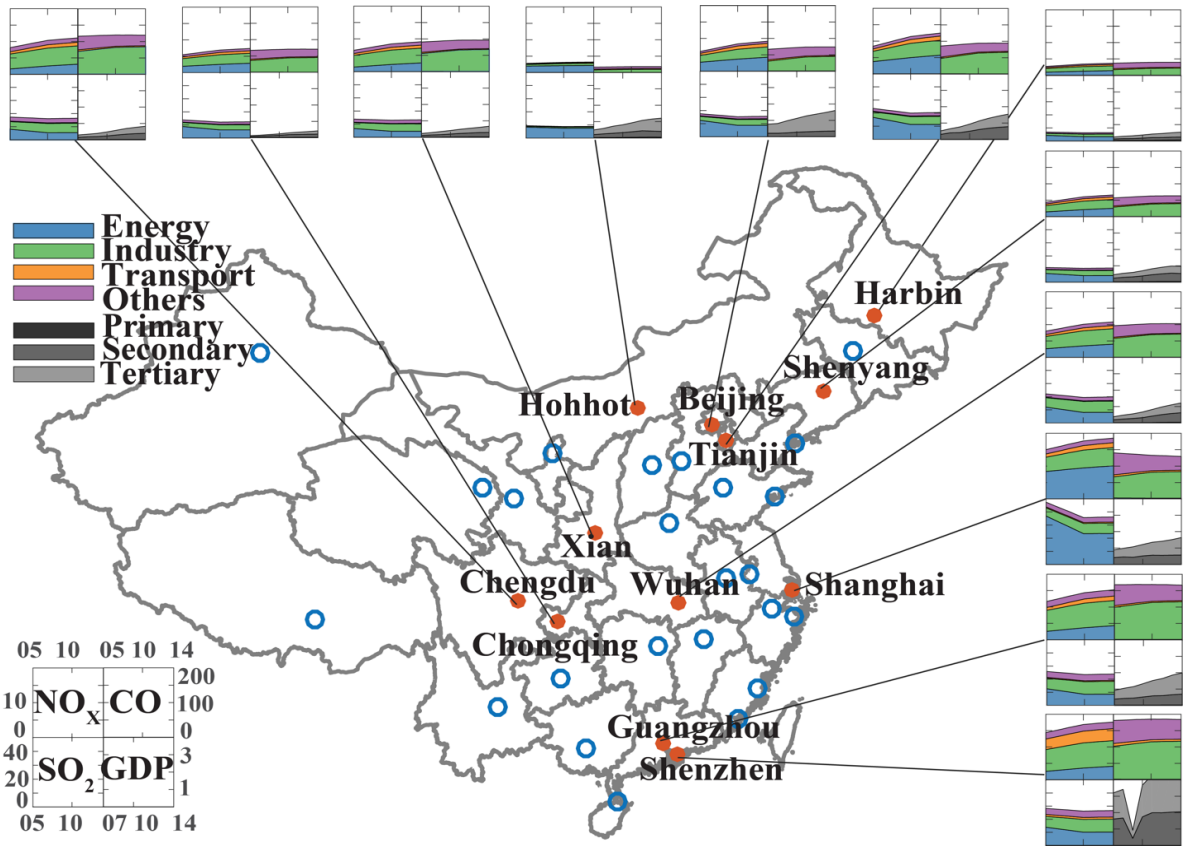

Figure B1: Time series (2005-2014) of RCP8.5 combustion-related emissions of NO_X (1st quad), CO (2nd quad) and SO_2 (3rd quad) all in units of g/year/m^2 and GDP per capita (4th quad) in units of 10^5RMB/capita/year for each of the 12 select major cities (red dots) in mainland China. The scales of each quadrant are indicated in the legend (lower-left of the map). The total emissions for each combustion product is broken down into 4 major sectors: energy, industry, land transport, and others which is the sum of agriculture, residential and commercial, and waste treatment and disposal). The GDP per capita is also broken down into primary (direct use of natural resources), secondary (industry and manufacturing), and tertiary (service) sectors. Each blue dot corresponds to one of the 36 designated provincial capital and special cities in mainland China.

2.2 Data

The main datasets used in this study are summarized in Table B1. This includes multiple satellite retrievals, representative emission inventories, and a couple of model simulations and chemical reanalysis.

2.2.1 Satellite Retrievals and Data Processing

We use the NASA Terra Measurement of Pollution In The Tropophere (MOPITT) version 6, Level 2, multispectral (Thermal Infrared/Near Infrared) retrievals of carbon monoxide (CO) total columns for CO (Deeter et al., 2014), tropospheric column retrievals from NASA Aura/ Dutch Ozone Monitoring Instrument NO_2 (DOMINO) v2.0 for NO_2 (Boersma et al., 2011), and Ozone Monitoring Instrument (OMI) Planetary Boundary Layer (PBL) SO_2, version 3, Level 2 (Krotkov et al., 2006). We collected daily MOPITT CO, OMI NO_2, and OMI SO_2 retrievals that are available within a $2^{\circ}\times2^{\circ}$ area around each city center. This radius was selected to cover the extent of each city based on NO_2 footprints (Bechle et al., 2011; Lamsal et al., 2013) and geopolitical maps of city boundaries. We grid each set of retrievals into $0.1^{\circ}\times0.1^{\circ}$ grids that commensurate to the finest retrieval resolution among MOPITT and OMI. We then average them across each month to minimize spatiotemporal collocation issues (see Table B1 for differences in sampling of MOPITT and OMI). As a result, there are 400 points for each species (CO, SO_2, NO_2) per city and month. We note that these retrievals have been used in the past to study decadal changes for individual (or a pair of) pollutants but not to derive enhancement ratios (e.g., Krotkov et al., 2016). While CO retrieved from thermal infrared (TIR) radiances are mostly sensitive to free tropospheric CO, it has also been reported to be capable of observing lower tropospheric CO, especially when retrieved jointly from TIR and near infrared (NIR) radiances (Worden et al., 2010; Deeter et al., 2014). We recognize however that retrievals of SO_2 from OMI have been reported to exhibit low sensitivity to weak SO_2 signals, in particular to less than 30 to 70 kTon per year of point source emissions (Krotkov et al., 2016). While our spatial and temporal smoothing, along with anchoring our SO_2 analysis with NO_2 data (please see later description of our regression analysis), should help in enhancing the SO_2 signal from cities with low SO_2 emissions, these SO_2 retrievals are useful as large SO_2 abundances are still observed across the majority of cities in China (Krotkov et al., 2016). We also used CO retrievals from the Infrared Atmospheric Sounding Interferometer (IASI), Level

2 (De Wachter et al., 2012), and tropospheric column NO_2 from FP7 QA4ECV OMI, v1 (Boersma et al., 2017) to verify consistency in our trend estimates.

We note that using 2˚×2˚ area to represent cities does lead to slight overlap over Guangzhou and Shenzhen, Beijing and Tianjin. This does not affect our analyses of emission inventories because we apply geopolitical maps of city boundaries to calculate emissions for each city (see Section 2.2.2). This does have an impact on our analyses of satellite observations because we use all the grids in the 2˚×2˚ area to conduct the spatial regression. However, we do not expect the overlap to significantly change our results because (1) the overlapped area is relatively small; (2) the overlapped cities are sometimes considered together as a whole region because of their similarities and connections (for example, the Jing-Jin-Ji megalopolis and the Pearl River Delta), and (3) the overlapped cities are in the same classes with similar patterns based on our analyses (i.e., Beijing and Tianjin are both in class 2, while Guangzhou and Shenzhen are both in class 4; Table B2).

2.2.2 Emission Inventories and Model Simulations

Multiple bottom-up emission inventories for CO, NO_2 and SO_2 are analyzed, namely Emission Database for Global Atmospheric Research (EDGAR, Crippa et al., 2016), Representative Concentration Pathways (RCP8.5, Riahi et al., 2011), Regional Emission inventory in ASia (REAS) version 2.1 (Kurokawa et al., 2013), and Hemispheric Transport of Air Pollution (HTAP, Janssens-Maenhout et al., 2015). We also use top-down emission estimates of CO and NO_2 from the Tropospheric Chemical Reanalysis (TCR) based on CHASER-LETKF assimilation system (Miyazaki et al., 2017). Since these emission inventories have different spatial resolutions (see details in Table B1) and are available in the form of fluxes (units in $kg/m^2/s$), we upscale/downscale them by simply regridding into 0.1˚ by 0.1˚ cells similar to our approach for satellite data to facilitate comparison. We then consider all cells within the 2˚ by 2˚ area around the city center. For annual emissions, we only take the sum of all cells within the geopolitical boundary of the city (see Figure B2). All of the cities extend to less than the 2˚ by 2˚ area that we set as our city domain.

We also use model data for CO and NO_2 from the Community Atmosphere Model with Chemistry (CAM-chem; Gaubert et al., 2016) and TCR to derive CO and NO_2 abundance ratios associated with the bottom-up emissions used in these models (i.e., RCP in CAM-Chem and EDGAR in

CHASER). The associated retrieval averaging kernels and prior information are applied to the daily-averaged model CO and NO_2 vertical profiles of mixing ratios from CAM-chem and CHASER, along with appropriate spatial interpolation and/or partial column integrations. Since the spatial resolution (about 2˚~3˚) of CAM-chem and CHASER outputs that we analyzed are far coarser than 0.1˚, we only considered the associated abundance ratio rather than deriving enhancement ratio across the month where non-stationarity and non-linearity issues are more likely to exist.

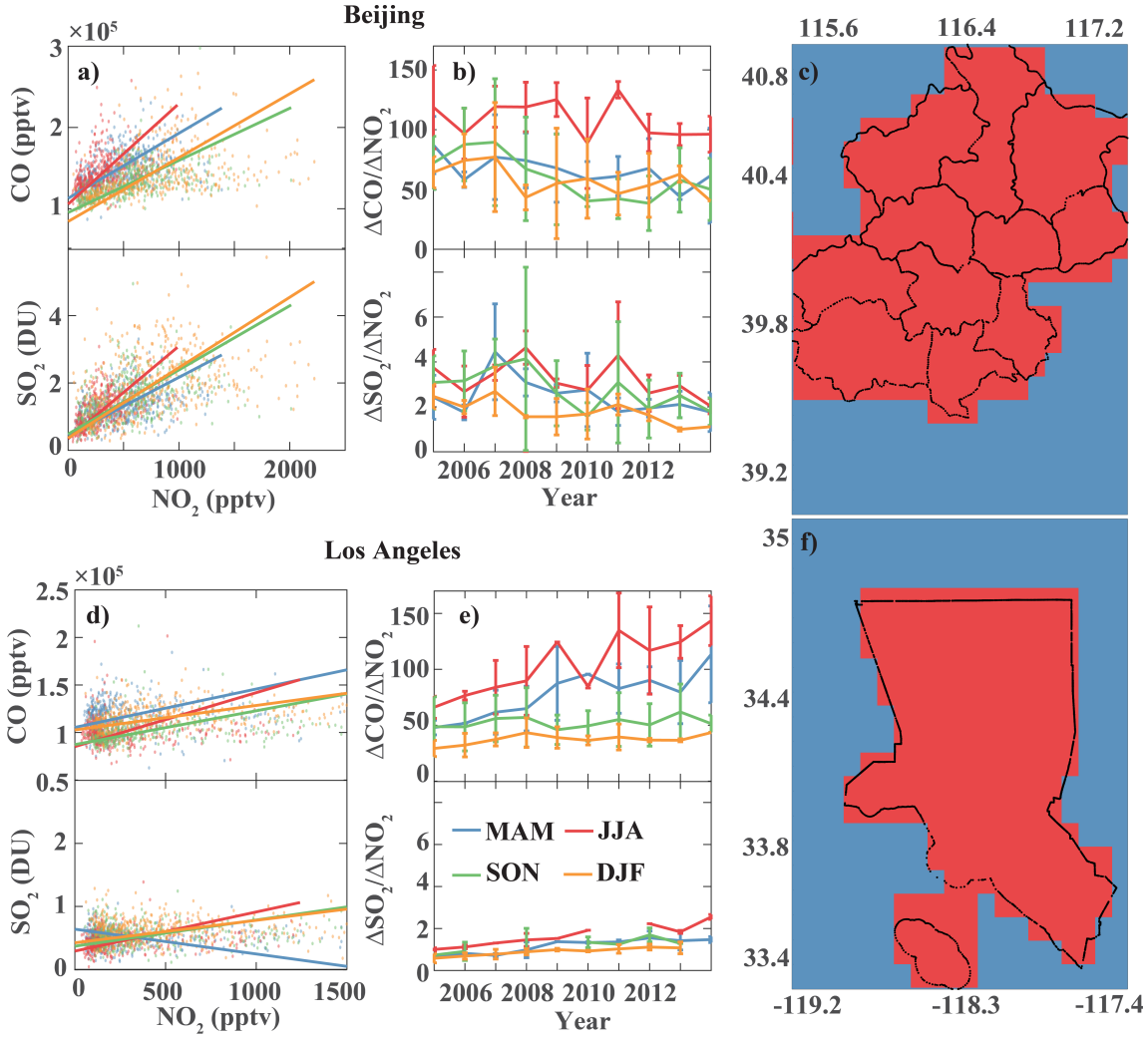

Figure B2: Spatial regression analysis of satellite retrievals of CO and SO_2 to NO_2 by season (blue: March-May (MAM); red: June-August (JJA); green: September-November (SON); orange: December-February (DJF)). The left column shows an example of scatter plots and linear regression for Beijing (top) and Los Angeles (bottom). The center column corresponds to the changes across 2005 to 2014 on the ratios calculated for a given season. The rightmost column panels show the city domain (2deg x 2deg) with the geopolitical extent of the city of Beijing and Los Angeles.

2.3 Deriving Enhancement Ratios using Spatial Regression Analysis

For each city, we regress the gridded monthly-average CO and SO_2 to NO_2 to calculate monthly enhancement ratios ($\Delta CO/\Delta NO_2$ and $\Delta SO_2/\Delta NO_2$). We use NO_2 as our control variable as NO_2 has the shortest lifetime (hours) among these products. Except for lightning, NO_X is mostly produced from high-temperature anthropogenic combustion processes. And because of its short lifetime, it is observed as distinctly and spatiotemporally local surface enhancements, with relatively very low background concentrations. Along with the availability of NO_2 retrievals from satellites at fine spatial scale and over long period, NO_2 allows us to effectively identify intra-megacity combustion activities and define the urban extent (Bechle et al., 2011; Lamsal et al., 2013; Hakkarainen et al., 2016). In other words, NO_2 is a good proxy for combustion activity. We use a reduce major axis regression (Smith, 2009) to estimate the slopes ($\Delta y/\Delta x$) representing enhancement ratio across the spatial extent of the megacity, and intercept (y^{bg}) for CO and SO_2 representing the background levels when there is no combustion (within the megacity and free-tropospheric contribution). This follows the approach introduced by (Fujita et al. (1992) and Parrish et al. (2002). However, we note that we use the spatial covariations of these species relative to NO_2 rather than their temporal covariations as in previous studies. Please see Section 3 for implications of this approach. We only consider statistically significant and positive slopes as we are focusing on sources and not sinks of these combustion products. These monthly ratios are then averaged across the year for analysis and archived for time series (decadal) analysis (see Section 3). Note that they can be considered to be comparable to emission ratios when observations are taken at or near the source and if they are normalized to account for air mass variations (Fujita et al., 1992; Parrish et al., 2002; Parrish, 2006; Hassler et al., 2016). Here, we normalize all ratios to year 2005 values.

It is important to note that we view each large city as a big smokestack that emits an aggregate of combustion products that can then be observed by satellite remote sensing as column-integrated quantities. The spatial (0.1˚) covariation of these aggregate within the 2˚ radius is interpreted as bulk characteristic of spatially heterogeneous combustion sources within the megacity. Monthly enhancement ratios are hence interpreted as the linear sensitivity in CO or SO_2 to intra-megacity spatial variations in combustion activity as defined by NO_2. We emphasize that these enhancement

ratios are not derived using time covariations but spatial covariations to minimize potential non-stationarities (e.g., differences in lifetimes between species), and influence of free-tropospheric signatures in MOPITT CO, which should be reflected as part of a larger scale contribution to CO^{bg} in this analysis given that we anchor the regression on OMI NO_2. Possible confounding factors such as biogenic sources of CO in a megacity is also minimized in our analysis by treating CO data only when NO_2 is observed since NO_2 is not largely co-emitted from CO biogenic sources. Although spatial and temporal smoothing can minimize the effect of lightning (NO_X) and fires (NO_X and CO) since they are emitted intermittently relative to anthropogenic combustion, our findings must be interpreted to represent changes in bulk combustion cleanness over a megacity rather than specific combustion cleanness.

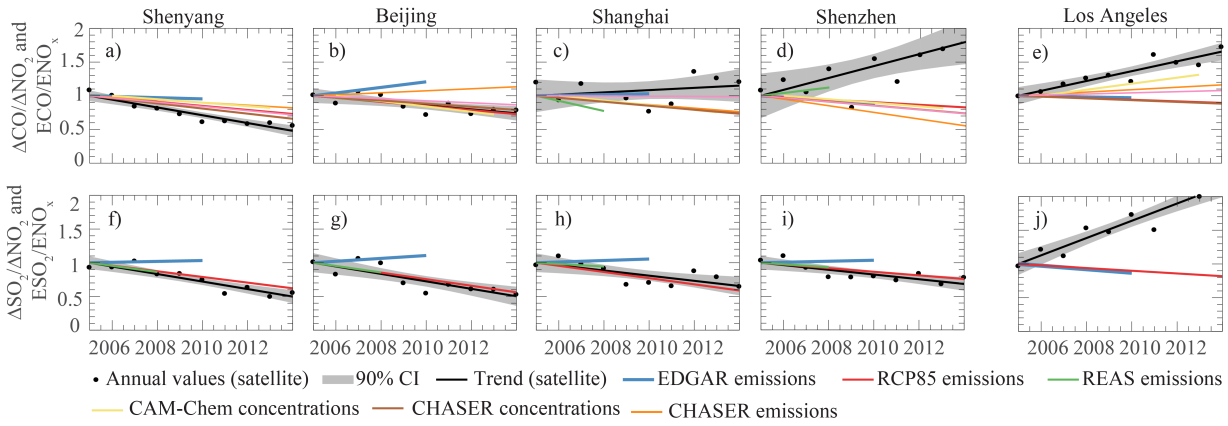

Figure B3: Changes in annual-mean enhancement ratios (black) from MOPITT and OMI retrievals of CO to NO_2 (top) and SO_2 to NO_2 (bottom) for select cities in China and U.S. relative to year 2005. Its associated emission ratios (ECO/ENO_X and ESO_2/ENO_X) from RCP8.5 (red), EDGAR4.2 (blue) and top-down estimate from CHASER (orange) and model-simulated abundance ratios from CHASER (purple) and CAM-Chem (green) chemistry transport models are superimposed. Grey areas are 90% confidence intervals of the linear fit (black lines). The four Chinese cities represent the four classes/levels of urban development across 12 selected cities in China.

2.4 Time Series Analysis and Curve Fitting

The focus of this work is to study the long-term changes in the spatial covariations of these monthly-averaged CO and SO_2 to NO_2, as expressed in terms of enhancement ratios. We hypothesized that at decadal scale the changes in covariations reflect the dominant changes in megacity emission characteristics. We use two approaches to calculate the decadal trend in our

normalized estimates of these ratios. For linear trend analyses, we use the Robust Regression Using Iteratively Reweighted Least-Squares (Holland and Welsch, 1977). This minimizes the influence of outliers relative to traditional least-squares fit especially when the relationship is not fully linear. We also use another trend analysis algorithm in our subsequent inverse analysis. Instead of using the annual mean values and estimate the linear trend across 2005-2014, we estimate the associated decadal trends in $\Delta CO/\Delta NO_2$ and $\Delta SO_2/\Delta NO_2$ using the seasonal trend decomposition with LOESS (locally weighted scatterplot smoothing) or STL algorithm (Cleveland et al., 1990). This algorithm separates the seasonal, inter-annual, and decadal contributions of monthly ratios. We use the smoothing windows for the decadal, inter-annual, and seasonal trends of 121 months, 25 months, and 5 months, respectively based on analysis of CO decadal trends in Jiang et al. (2018). As in Gaubert et al. (2017), we tested several other windows and found consistent temporal patterns across cities. For non-linear curve fitting, we use robust least square regressions with Least Absolute Residuals (LAR) method (within the cftool function in MATLAB) to fit a power law function to the annual-mean ratios and GDP per capita. This method also minimizes the influence of extreme values on the fit.

2.5 Inverse Analysis

We conduct an inverse analysis of the long-term trends in monthly enhancement ratios to further expound our findings by associating the overall changes to sectoral changes. In this case, we are interested in finding the decadal contribution of the time series (2005-2014) of monthly statistically-significant enhancement ratios that are derived from our previous regression and time series analysis. We decomposed the *a priori* estimate of monthly emission ratio of CO to NO_X (and SO_2 to NO_X) from RCP8.5 as a product of: a) ratio of effective emission factors for each of the four sectors (namely energy, industry, transport, and others); and b) fractional contribution of NO_2 emissions from each sector to the total NO_2 emissions for all four sectors. We then use a two-step Monte-Carlo-based Bayesian inversion method, to estimate effective emission factors and fractional contribution of NO_2 emissions from each sector. Please refer to Part 1 in Supporting Information (SI) for a short derivation of this decomposition, and Part 2 in SI for details in the inverse analysis.

3 Results and Discussions

3.1 Observed Patterns of Enhancement Ratios in Chinese and U.S. Cities

In this sub-section, we present observed patterns of enhancement ratios in Chinese and U.S. Cities. We firstly show spatial regression analysis of satellite retrievals of CO and SO_2 to NO_2 by season (taking Beijing and Los Angeles for demonstration) in Figure B2. Although naturally-produced CO and NO_2 like biogenic CO and lightning NO_X introduce a strong seasonality on these ratios even within the megacity, we find that when we average the monthly ratios using only the months corresponding to a particular season (i.e., more fires and lightning during the summer), we still find a similar temporal pattern (albeit different in magnitude) in derived $\Delta CO/\Delta NO_2$ and $\Delta SO_2/\Delta NO_2$ (see Figure B2). This is reasonable as these CO as well as SO_2 enhancements are dominantly from combustion-related processes that co-emit NO_2 by our study design, pointing to the robustness of analyzing annual-mean $\Delta CO/\Delta NO_2$ and $\Delta SO_2/\Delta NO_2$.

Shown in Figure B3 are linear trends of annual-mean $\Delta CO/\Delta NO_2$ and $\Delta SO_2/\Delta NO_2$ relative to year 2005 values in four Chinese cities. These cities are representative of a certain level of urban development across mainland China. The four levels in this study are defined using broad clustering between the average GDP per capita per year and the rate of change in $\Delta CO/\Delta NO_2$ that are derived from satellite observations. This is shown in Table B2, where a general rule resulting from this analysis would be a classification mainly based on GDP per capita per year, except Harbin and Wuhan. Combustion-related activities in Shenyang, Beijing, Shanghai, and Shenzhen can be characterized to follow a progression from heavy to light manufacturing, export processing, and service industries (Chan and Yao, 2008). For this analysis, Shenyang, Beijing, Shanghai, and Shenzhen represent the progression across the 12 select cities of increasing GDP per capita along with decreasing to increasing $\Delta CO/\Delta NO_2$ (-5.4±0.7%/year to +8.3±3.1%/year) and decreasing rate of $\Delta SO_2/\Delta NO_2$ reductions (-6.0±1.0%/year to -3.4±1.0%/year) relative to 2005 (Figure B3 and Table B2). This pattern in enhancement ratios is not evident in the rate of change of CO, SO_2, and NO_2 column abundance, for which we find increasing rate of decrease in CO (-0.1±0.3%/year to -1.0±0.2%/year) and SO_2 (-1.9±0.9%/year to -5.5±1.1%/year) abundance, along with decreasing rate of increase in NO_2 abundance from Shenyang (+5.2±1.4%/year) to Shenzhen (1.8±0.7%/year) (Table B2). This is consistent with previous studies of these species. In fact, we find a decreasing-

to-increasing pattern in the derived enhancements of CO due to combustion (i.e., $\Delta CO_{comb} = \langle \mathrm{CO} - \mathrm{CO}^{bg} \rangle$), across these four levels of development.

We have minimized the influence of inter-annual variations due to meteorology (e.g., changes in air mass) by analyzing molar ratios (e.g., mole CO/mole NO_2) rather than absolute molar concentrations (e.g., mole CO/mole air; Parrish et al., 2002, 2006). As the co-emitted species (i.e., CO, SO_2, and NO_2) are subject to the same meteorological conditions (affecting transport, dilution, and lifetime), their enhancement ratios are expected to be less sensitive to meteorology compared to the absolute molar concentrations. This is supported by the fact that decadal $\Delta\mathrm{CO}/\Delta\mathrm{NO}_2$ as well as $\Delta\mathrm{SO}_2/\Delta\mathrm{NO}_2$ for different seasons have similar trends (Figure B2). Previous studies have also proven that the ratios compared to the concentrations themselves are relatively immune to changing meteorological conditions, and can provide insights into the magnitude and temporal trends of the emissions (Parrish et al, 2002, 2006, 2009, Silva et al., 2013, Hassler et al. 2016). In addition, they can be directly compared to the corresponding emission ratios under certain circumstances. However, we note that even though the ratios derived from satellite observations are relatively less sensitive to meteorology, the methodology cannot eliminate all the impacts from meteorology. The enhancement ratios may be impacted by the meteorological conditions because lifetimes of different air pollutants may respond to meteorological conditions differently. Nevertheless, we believe such impact should not influence our main conclusions for the following two reasons: (1) Our analysis focuses on decadal trends instead of short-term trends. As shown by previous study, meteorology also plays an important role on relatively short time scales, but meteorology probably plays a lesser role in the longer-term trends (Krotkov et al. 2016); (2) The satellite retrieval samples are taken over the megacities (right above strong emission sources) instead of downwind of the pollution sources, making them more representative of megacity sources.

Normalizing these ratios to 2005 values should have also minimized the impact of the differences in the magnitude of these ratios between these cities. The impact of meteorology on inferred decadal trends through variations in columnar abundance is more evident when absolute magnitudes of single species are analyzed. In addition, potential drifts of biases in time (caused by systematic errors in the instrument and/or retrieval algorithm) cannot account for the differences in the temporal pattern that we find across these cities. Such biases should be commonly reflected

in all cities, yet we see differences between cities. In fact, we find very similar progression pattern when we use the Infrared Atmospheric Sounding Interferometer (IASI) CO retrievals (De Wachter et al., 2012) instead of MOPITT, or OMI QA4ECV (Boersma et al., 2017) instead of OMI DOMINO. Interestingly, we find that the increasing enhancement ratio of CO to NO_2 in Shenzhen (and to a lesser extent in Shanghai) remarkably resembles the relative changes in CO to NO_2 ratios in more developed megacities (Los Angeles and New York) and several urban agglomerations in the United States (see Figure B3e for Los Angeles and Table B2 and Figure BS1 for all other select cities). More importantly, the increasing pattern that we see in Los Angeles (~ +7±1%/year) relative to 2005 is generally consistent to the increasing trend (~ +4%/year) after 2007 of ground-based CO to NO_X enhancement ratio in Los Angeles as reported by Hassler et al. (2016). It is a common understanding that modernization brings about larger energy use coupled with higher economic productivity, but poorer environmental quality (i.e., increasing abundance of pollutants). However, the changes in lifestyle concomitant with human development results in a shift to fewer activities (including increase use of renewable energy), along with more efficient and cleaner combustion and changes in fuel types (coal to natural gas) (Mazur and Rosa, 1974). This eventually leads to increases in relative sensitivities of CO and SO_2 to NO_2. Along the same line as previous studies suggesting emissions of CO, SO_2, NO_2, and their ratios can be indicators of modernization to some extent (Krotkov et al., 2006; Russell et al., 2012; Luo et al., 2014; Hassler et al., 2016), our finding on this progression in $\Delta CO/\Delta NO_2$ serves as a satellite-based evidence of a dominant shift in the cleanness of bulk combustion in more economically developed city within a developing country like China.

On the other hand, there is no clear difference in the observed enhancement ratios ($\Delta SO_2/\Delta NO_2$) and derived enhancements of SO_2 due to combustion ($\Delta SO_{2_{comb}}$) between cities. The sensitivity of SO_2 to NO_2 relative to 2005 in Shenzhen does not follow the increasing pattern in Los Angeles (Figure B3b). Unlike ΔCO_{comb}, $\Delta SO_{2_{comb}}$ in all four Chinese cities still show a decreasing trend relative to 2005 while $\Delta SO_{2_{comb}}$ in Los Angeles show an increasing pattern consistent with its ΔCO_{comb}. On one hand, there is a striking difference in absolute magnitudes in SO_2 abundance between these cities (as has been reported), reflecting large-scale differences in combustion practice. Yet, the low SO_2 abundance in Los Angeles makes it also difficult to detect possibly large SO_2 point sources (Krotkov et al., 2016). Enhanced SO_2 signal can still be detected as the spatial

first-order derivatives of SO_2 with NO_2 at megacity-scale should not be largely (non-linearly) influenced by its absolute magnitude. We find that there is a tighter correspondence between SO_2 and NO_2 abundance in Chinese cities than in U.S. cities. This might suggest differences in fuel use as SO_2 is mainly produced within a megacity from burning of sulfur-containing fossil fuel (mostly coal, oil, and natural gas) and to a smaller extent from industrial processes (e.g., smelting). Here, we postulate that the absence of an apparent shift in $\Delta SO_2/\Delta NO_2$ across the four Chinese cities is due to continuing heavier reliance of these cities (and China) on coal burning relative to United States (Wang and Hao, 2012; Bhattacharya et al., 2015; Qi et al., 2016; Yang et al., 2016; Sun et al., 2018; Zheng et al., 2018). In terms of the sectoral share, the majority of NOx emissions over Los Angeles basin is from transport according to a recent fuel-based inventory (Hassler et al., 2016), whereas fossil fuel combustion (from power generation and industry) is the most dominant NOx source in China (Sun et al., 2018). In terms of the energy share, it was estimated that coal accounts for about 69% and 23% of the total primary energy consumption in China and U.S. in 2005, respectively. Actions including usage of low-sulfur coals, installation of flue gas desulfurization (FGD) facilities, and closing of small units, have been taken to reduce coal-related emissions in China. The aforementioned de-SO_2 procedure in China is most likely to be the dominant driving factor of the declining $\Delta SO_2/\Delta NO_2$ (Li et al., 2018; Zheng et al., 2018). While there are on-going activities regulating coal-related emissions, coal consumption in China remains to increase in the past decade (Qi et al., 2016; Yang et al., 2016). In terms of mass, it has increased by 70% from 2005 to 2014 (Korsbakken et al., 2016). On the other hand, the use of coal in U.S. has been found to be slightly decreasing along with previous adoption of SO_2 control technologies (Taylor et al., 2005). In addition, previous studies have reported recent reduction in NOx emissions over China since 2011 based on satellite observations and emission inventories (Liu et al., 2016; van der A., et al, 2017). The installation of selective catalytic reduction (SCR) equipment at power plants and new emissions standards for vehicles both contribute to the NOx emission reduction (Liu et al., 2016; van der A., et al, 2017; Wu et al., 2017). On the other hand, based on our analysis of decadal trends (2005-2014), only NO_2 over Shenzhen overall decreased in the decade, while 10-year average changes of NO_2 over Shenyang, Beijing, and Shanghai were overall positive (Table B2). Intradecadal changes as reported in Liu et al. 2016 (from increasing to decreasing NOx emissions around 2011) do not contradict the derived 10-year trend in this work, especially over Shenyang, and Beijing where NOx emissions are still rapidly increasing during the first half of the

decade (2005-2011). The changes in SO_2 emissions and NO_2 emissions together contribute to the trends of $\Delta SO_2/\Delta NO_2$ that we found. Positive ΔNO_2 and negative ΔSO_2 produce negative $\Delta SO_2/\Delta NO_2$ over the three cities; while negative ΔSO_2 and negative ΔNO_2 (albeit smaller in magnitude) still produce negative $\Delta SO_2/\Delta NO_2$ but smaller magnitude over Shenzhen than $\Delta SO_2/\Delta NO_2$ over the other cities (Table B2). This indicates a stronger influence of the changes in SO_2 emissions (as reflected in ΔSO_2) in the decreasing trends of these ratios.

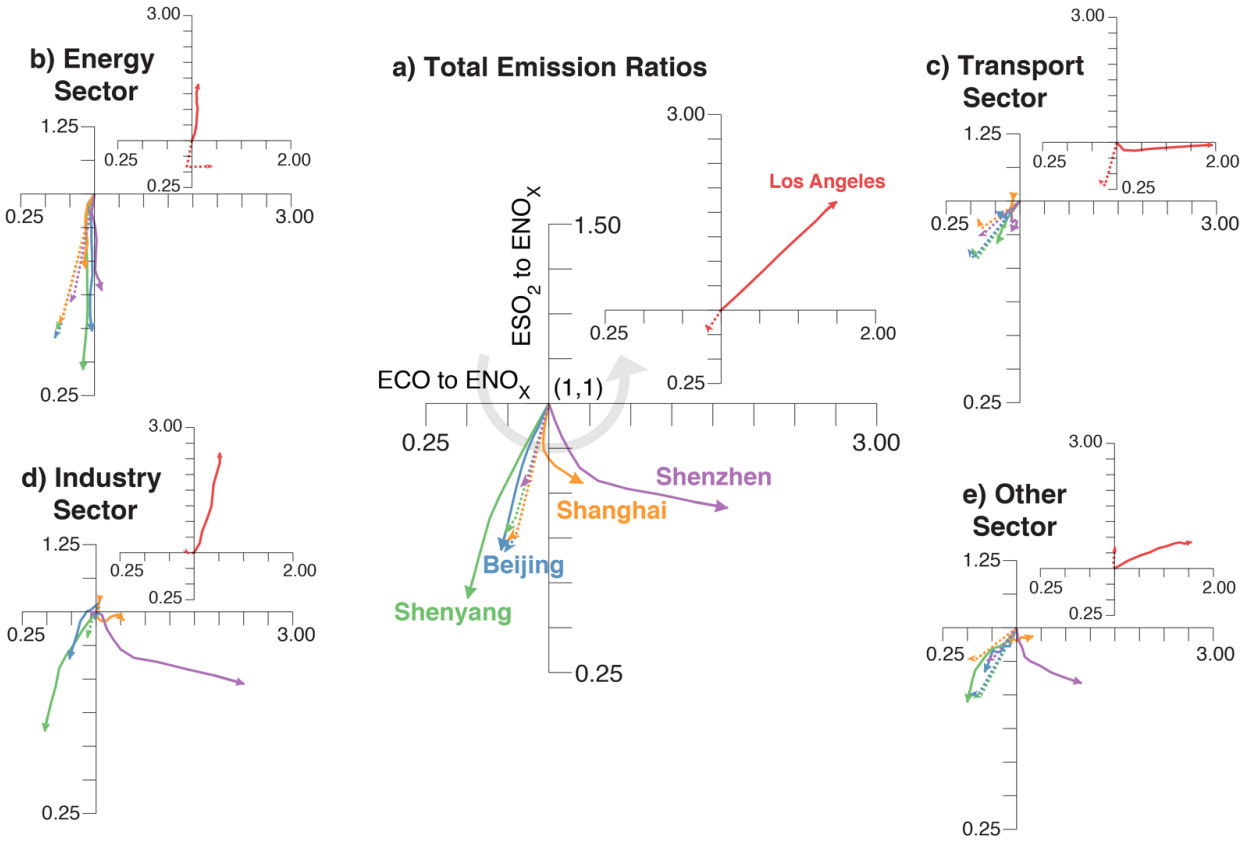

Figure B4: Joint traces of the annual changes in *a priori* (dotted line) and *a posteriori* (solid line) estimates of ECO/ENO_X (x-axis) and ESO_2/ENO_X (y-axis) relative to year 2005 for four select Chinese cities (Shenyang: green, Beijing: blue, Shanghai: orange, and Shenzhen: purple) representing four levels of urban development. These traces are presented as line arrows (with origin at x=1, y=1 and endpoint corresponding to year 2005 and 2014, respectively) for total emission ratios (panel a) and four sectoral ratios (panels b to e). Other sector is the sum of mostly residential/commercial along with agriculture, and waste treatment and disposal. The inset for each panel represents the associated traces for Los Angeles, which is added as basis for comparison. The lower-left, lower-right, and upper-right quadrants correspond to decreasing ECO/ENO_X and ESO_2/ENO_X, increasing ECO/ENO_X but decreasing ESO_2/ENO_X, and increasing ECO/ENO_X and ESO_2/ENO_X relative to year 2005, respectively. The gray semi-circular arrow in panel a) represents our suggested common combustion emission pathway for Chinese cities.

3.2 Inconsistencies with A Priori Estimates

The satellite-based $\Delta CO/\Delta NO_2$ patterns are inconsistent with emission- and model-based ratios (Figures 3 and S1, Table B2). As previously introduced, estimates of the ratios of emissions can be related to observed ratios of enhancements when these observations are taken at or near the source. In this case, we assume that a megacity is a big smokestack emitting mostly combustion-related pollutants (i.e., CO, NO_2, and SO_2) that can be observed from space with MOPITT and OMI. In addition, NO_2 is considered to be the dominant form of NO_X that can be observed at this scale. From a global atmospheric chemistry modeling (CTMs) perspective, the associated abundance over megacities is represented as one to four discrete vertical column(s) assuming spatial resolution of these CTMs of one to two degrees. While recognizing the associated month-to-month variability in $\Delta CO/\Delta NO_2$ and expected differences on how these ratios should be compared, the trends in emission ratios relative to 2005 of CO to NO_X from bottom-up emission inventories (EDGAR4.2 and RCP8.5) and top-down emission estimates (CHASER, Miyazaki et al., 2017) do not appear to follow the progression (i.e., decreasing to increasing $\Delta CO/\Delta NO_2$ relative to 2005 from Shenyang to Shenzhen; Figure B3). This is also true for the ratios of CO to NO_2 abundance from CAM-Chem and CHASER CTMs, which are mostly consistent (except in Los Angeles) with the trends of their associated emission ratios (i.e., CAM-Chem and CHASER emissions are based on RCP8.5 and EDGARv4.2 inventories, respectively). The *a posteriori* emission ratios in Beijing from Miyazaki et al. (2017), which uses CHASER-LETKF to assimilate MOPITT CO and OMI NO_2 retrievals among other retrievals, also appear to initially follow the emission ratios from EDGAR. Furthermore, the ratios of SO_2 to NO_X emissions from RCP8.5 follow the trend of $\Delta SO_2/\Delta NO_2$ in Chinese cities but tend to diverge in Los Angeles, whereas the emission ratios from EDGAR exhibit a lack of trend in China and Los Angeles. A closer look at linear trends of the ratios for each sector in RCP8.5 (Figure BS2) reveals inconsistencies in the trends, which cannot be addressed by simple scaling of activity levels in bottom-up inventories (Zheng et al., 2018). All these differences underscore the need to reduce uncertainties in representing time-varying emission activity and emission factors in CTM inputs. There is also a need to quantify errors in model physics and dynamics in transforming emissions to abundance, as well as in data assimilation and inverse methods in integrating observations into models including representativeness of these retrievals. We highlight here the need to improve not only

the accuracy but also the consistency of AQ predictions across pollutants in megacities. Initial results from an improved set of multi-species data assimilation runs using CHASER-LETKF show better agreements with the trends in $\Delta CO/\Delta NO_2$ (Miyazaki et al., 2017). Such improvements highlight an under-explored utility of available observational constraints on the changes in emission ratios. We emphasize here that while these differences are expected and have been previously reported, our findings highlight the need to focus on improving model treatments of the dynamic nature of emission factors in these megacities.

Table B1. List of satellite products and emission inventories used in this study. All these datasets are re-gridded into 0.1˚ × 0.1˚ if the original resolutions are not. This version of CHASER-LETKF does not provide emissions of SO_2.

Dataset and Data Availability	Spatial and Temporal Resolution	Relevance to Study & Main Reference
NASA Terra MOPITT CO version6, L2, TIR/NIR https://www2.acom.ucar.edu/mopitt 2000 to present	22 km × 22 km 10:30 AM daily	CO total column (Deeter et al., 2014)
Aura/OMI SO2 Total Column 1-orbit L2 v003 NRT https://aura.gsfc.nasa.gov/omi.html 2004 - present	13km × 25 km 1:45 PM daily	PBL Column Amount SO_2 (Krotkov et al., 2006)
Dutch OMI NO_2 (DOMINO) data product v2.0 http://www.temis.nl/airpollution/no2.html 2004 to present	13km × 25 km 1:45 PM daily	NO_2 trop. column (Boersma et al., 2011)
QA4ECV OMI NO_2 data product version 1 http://temis.nl/qa4ecv/no2col/no2regioomimonth_v2.php 2004 to present	13km × 25 km 1:45 PM daily	NO_2 trop. column (Boersma et al., 2017)
IASI Level 2 FORLI XCO https://navigator.eumetsat.int/product/ EO:EUM:DAT:METOP:IASSND02 2007 to present	12km × 12 km 9:30 AM daily	CO total column (De Wachter et al., 2012)
European Commission EDGAR version 4.3.1 http://edgar.jrc.ec.europa.eu/overview.php?v=431 1970 to 2010	0.1˚ × 0.1˚ sectorial annual	CO, SO_2, NO_X emissions (Crippa et al., 2016)
IIASA RCPs http://accmip-emis.iek.fz- juelich.de/data/accmip/gridded_netcdf/ 1850 to 2100	0.5˚ × 0.5˚ sectorial monthly	CO, SO_2, NO_X emissions (Riahi et al., 2011)
REAS v2.1 https://www.nies.go.jp/REAS/ 2000 to 2008	0.25˚ × 0.25˚ sectorial monthly	CO, SO_2, NO_X emissions (Kurokawa et al., 2013)
HTAP v2 http://edgar.jrc.ec.europa.eu/htap_v2/ 2008 and 2010	0.1˚ × 0.1˚ sectorial monthly	CO, SO_2, NO_X emissions (Janssens-Maenhout et al., 2015)
CHASER-LETKF https://ebcrpa.jamstec.go.jp/~miyazaki/tcr/ 2005 to 2014	2.8˚ for longitude and the T42 Gaussian grid for latitude daily	CO and NO_X emissions (Miyazaki et al., 2017)

3.3 Combustion Emission Pathway for Chinese Cities

We define combustion emission pathway as a trajectory in time of the overall changes in emissions due to combustion with respect to socioeconomic development (e.g., Riahi et al., 2011; Steinberger et al., 2012; Li et al., 2016; Marangoni et al., 2017). In this section, we identify a common combustion emission pathway across these four levels of development and associate them to sectoral changes through inverse analysis. We will briefly describe the inverse analysis of the ratios in section 3.3.1, present our findings on combustion emission pathway in section 3.3.2, and elucidate the driving factors by means of time traces in sectoral emission ratios in section 3.3.3.

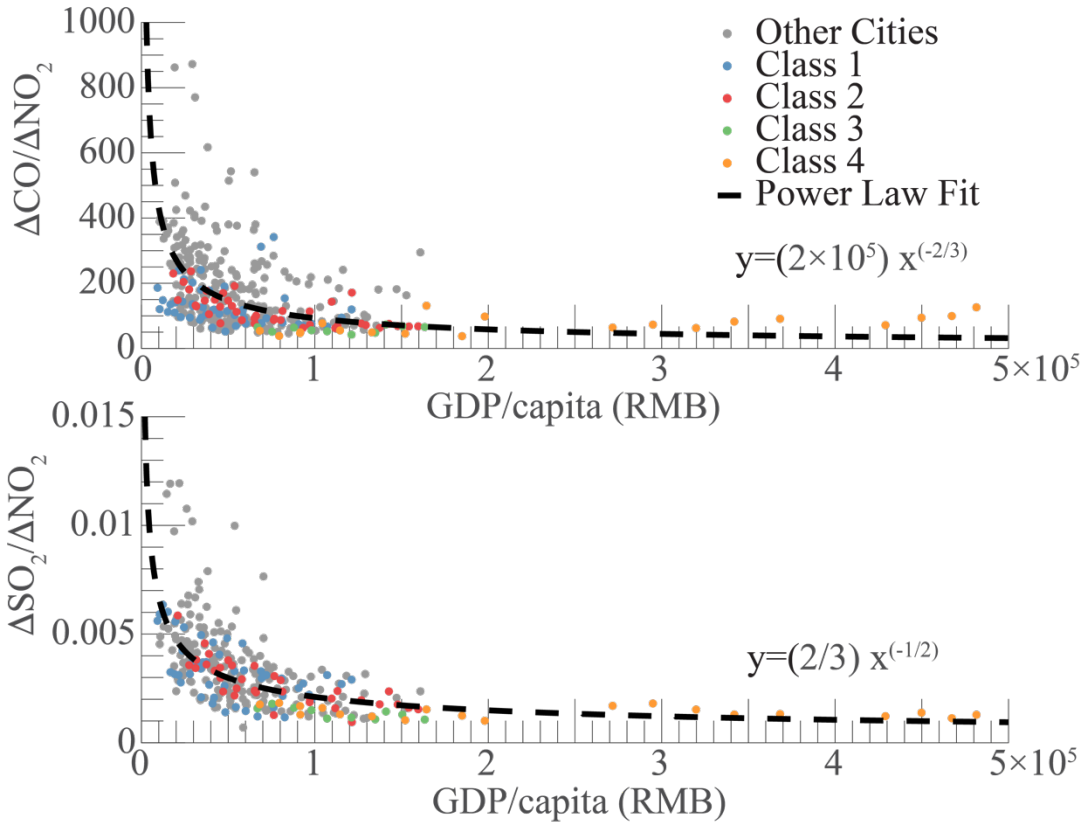

Figure B5: Annual-mean enhancement ratios (in units of mole/mole) of CO to NO_2 (panel a) and SO_2 to NO_2 (panel b) for all 36 provincial capitals and cities (2005 to 2014) as a function of its corresponding annual GDP/capita (in units of RMB/year/capita). The 12 select cities analyzed in this study are plotted in color, where each color represents four increasing levels or classes of urban development (e.g., Shenyang: Class 1, Beijing: Class 2, Shanghai: Class 3 and Shenzhen: Class 4). The rest of the 36 cities are plotted in gray. Superimposed on panel a) and b) is a fitted curve (black dashed line) based on power-law relationship of the data which is indicated in the plot by its corresponding equation.

3.3.1 Inverse Analysis of the Ratios

We conduct an inverse analysis of the ratios shown in Figure B3 to further expound on these patterns, by associating them to sectoral changes. Please see details of the matrix-vector product and inversion methodology in Section 2.5 and Part 2 in SI. The result of this inversion is a set of *a posteriori* time series estimates of sectoral CO to NO_X and SO_2 to NO_X ratios, such that the corresponding time series estimates of the total CO to NO_X and SO_2 to NO_X ratios match the decadal trends of $\Delta CO/\Delta NO_2$ and $\Delta SO_2/\Delta NO_2$ inferred from these satellite retrievals. Again, we note that we use the STL-inferred decadal trend as the data to fit (not the monthly-mean ratios nor the linear trend in Figure B3), as this is the most appropriate data for analyzing long-term changes in emission sectors.

3.3.2 Combustion Emission Pathway

The results of our inverse analysis are presented in Figure B4. This figure consists of five 2-D line plots of *a posteriori* (solid) and *a priori* (dashed) time series of SO_2 to NO_X emission ratios (ESO_2/ENO_X) in y-axis versus corresponding values of CO to NO_X emission ratios (ECO/ENO_X) in x-axis. The five plots correspond to the annual total (center panel, Figure B4a) and sectoral emission ratios (four side panels, Figures 4b to 4e) of each of the four cities selected in Figure B3. The time series, which is normalized to 2005 values, starts at the origin (1,1) and ends at the arrow tip of the line. Each 2-D plot also contains an inset showing the corresponding emission trajectory for Los Angeles. The center panel of Figure B4 is similar to Figure B3 but plotted jointly and with the *a posteriori* time series of emission ratios now corresponding to the time series of enhancement ratios (i.e., STL-inferred decadal trend). We find that the progression in combustion characteristics across these four cities is clearly evident from this diagram and very consistent with the linear trends in Figure B3. In Shenyang, both ESO_2/ENO_X and ECO/ENO_X are decreasing relative to 2005 at a faster rate (as represented by the length of the line) than in Beijing. On the other hand, we see a clear shift in Shanghai and most notably in Shenzhen to a slightly decreasing ESO_2/ENO_X and increasing ECO/ENO_X leading their emission trajectories toward a different state of 'combustion cleanness'. The combustion emission ratios in Los Angeles (and other cities in U.S.) lies however at a different state than Shanghai and Shenzhen. In particular, we find ESO_2/ENO_X and ECO/ENO_X in Los Angeles to be both linearly increasing relative to 2005 values. And so,

there exists a progression of decreasing-to-increasing sensitivities of CO and SO_2 to NO_2 from Shenyang to Shenzhen to Los Angeles (gray semi-circular trace in Figure B4a) relative to 2005, that appears to be related to socioeconomic development consistent with the current understanding of human development pathways (Lamb et al., 2014). In this case, it may be a consequence of air quality management practice and improved efficiency in China (Sun et al., 2018; van der A et al., 2017) and U.S. (Hassler et al., 2016; Russell et al., 2012). Altogether, this leads us to suggest a common combustion emission pathway for the megacities in mainland China, that begins with a reduction in SO_2, followed by CO, and continues with a reduction in NO_X and potentially on volatile organic compounds (VOCs) later on. To illustrate, we still see increases in NO_X abundance in Shenyang although CO and SO_2 are already decreasing, whereas in Shenzhen, we see NO_X starting to decrease (at a faster rate) along with decreasing CO and SO_2 abundance. The rate at which SO_2, CO, and NO_2 are decreasing is not at a level that is observed in Los Angeles. And so, while the satellite data reveals a combustion emission pathway in these Chinese megacities, these cities are yet to reach conditions that is at par with megacities in more developed cities in U.S. and Europe. It is worth noting that the *a priori* estimates from RCP8.5 do not follow this pathway, even for Los Angeles, suggesting inconsistencies and necessary updates on temporal changes in emission factors, effectiveness in pollution control technologies, and/or more information on fuel use mixtures in this emission inventory. It also appears that the pathway represented in RCP is similar to all cities and more resembling the emission pathway for Beijing.

3.3.3 Traces in Sectoral Emission Ratios

Furthermore, the traces in sectoral emission ratios from RCP8.5 all point to decreasing ratios relative to 2005 and are primarily driven by the energy (transportation) sector, which constitute more than one-third of NO_X emissions in Chinese (U.S.) cities (Figure B4b to 4e). Our inversion results to slight adjustments in Chinese energy emission pathway towards little to no changes in CO to NO_X emission ratios (Figure B4b). Adjustments from the transportation sector are also small in terms of direction and slower in terms of its rate of change relative to 2005 RCP values (Figure B4c). This is certainly not the case in Los Angeles where CO to NO_X and SO_2 to NO_X ratios follow quite the opposite pathway of increasing ratios from the energy sector and increasing CO to NO_X, with no change in SO_2 to NO_X from the transportation sector. This is expected in United States because of cleaner fuel standards (Shindell et al., 2011; Zhang et al., 2012; Kheirbek et al., 2014;

Yang et al., 2016; Paulot et al., 2017). Significant shifts on these ratios relative to 2005 are clearly evident from the industry and other (i.e., agriculture, residential, and waste) sectors in the cities in China (Figure B4d and 4e). Shanghai and most notably Shenzhen show a shift to increasing CO to NO_X with slightly decreasing SO_2 to NO_X that are not reflected in RCP8.5. The emission ratios from industry and other (mostly residential) sectors need to be adjusted significantly in our inversion to match the shifts in observed $\Delta CO/\Delta NO_2$ and $\Delta SO_2/\Delta NO_2$ in these two cities. As earlier mentioned, tertiary (service) industries including export processing activities are dominant in Shanghai and Shenzhen than in Shenyang. The shift in recent years to increasing CO to NO_X reflects a larger rate of decrease in NO_X levels than CO from the industrial and residential sectors of these cities. While a more detailed investigation is warranted to narrowly identify the activities and/or policies driving this shift (van der A et al., 2017), it is clear that changes in combustion activity alone cannot account for these shifts, and that updates on emission factors for these sectors in RCP8.5 are needed. We find that these findings are robust across a suite of error assumptions in the inverse analysis. This update applies all the more to all sectors in RCP emissions for Los Angeles. Again, this is well supported by studies like Hassler et al. (2016). where they reported increasing CO to NO_X enhancement ratio after 2007 in Los Angeles along with a 45% decline of NO_X emissions based on their fuel-based inventory. This is in contrast to decreasing RCP8.5-based MACCity emission ratios that they also reported for Los Angeles. This increase in enhancement ratios (similar to this work) is attributed to a combination of factors such as the decrease in NO_X from freight traffic activity during U.S. recession and implementation of new NO_X emission control technologies and regulations to meet Tier two emission standards on U.S. light-duty vehicles. They also noted that differences in the trends of $\Delta CO/\Delta NO_2$ are still observed even between cities from developed countries like U.S. and Europe, as these cities differ in terms of transportation practices and lifestyles (e.g., increase in light duty diesel vehicles). It is also now conceivable that $\Delta CO/\Delta NO_2$ can be further influenced by shifts in relative importance of emission sectors (e.g., VOCs in petrochemical and pharmaceutical industries) as activity decreases with efficiency, pollution is controlled, and lifestyle changes whenever cities evolve (McDonald et al., 2018). A recent study (Jiang et al., 2018) revealing an over-estimation in the decrease of USEPA NO_X emissions based on OMI NO_2 and MOPITT CO retrievals with USEPA ground station measurements of NO_2, also suggests potential changes in 'bulk' combustion characteristics in urban regions of the United States. Along with these studies, our results suggest that regional to

global emission inventories, which are used as input to predictive models of atmospheric composition, have to reflect: a) the evolution of air pollution for a given city (sectoral shifts) and b) the differences in combustion practices from city to city, in order to capture these observed magnitudes and variations in enhancement ratios.

Table B2: Summary of Percent Rate of Change for Select Cities in China and United States. Numbers that follow the ± sign are standard errors.

				Satellite Observations				
		Average GDP (RMB/cap/yr for China and USD/cap/yr for USA)	Annual Rate of Change (RMB/cap/yr for China and USD/cap/yr for USA)	Annual Rate of Change (%/year)				
city	class			CO	NO_2	SO_2	$\Delta CO/\Delta NO_2$	$\Delta SO_2/\Delta NO_2$
Shenyang	1	66293	8279	-0.13±0.25	5.16±1.40	-1.92±0.93	-5.35±0.74	-6.03±1.02
Xian	1	39594	5854	-0.61±0.22	7.45±2.21	-4.68±1.78	-4.73±1.44	-7.55±1.06
Chengdu	1	48722	7221	-1.18±0.52	6.93±1.33	-4.45±1.99	-4.44±2.25	-9.58±3.67
Hohhot	1	77744	10315	-0.21±0.23	7.49±3.71	-2.41±1.29	-3.47±1.78	-5.68±1.12
Chongqing	1	23706	3848	-0.58±0.41	5.65±1.20	-7.79±2.18	-3.11±1.49	-7.67±1.40
Tianjin	2	91503	13723	-0.18±0.28	6.09±1.43	-2.91±1.44	-3.36±1.61	-5.46±2.08
Beijing	2	106474	11820	-0.37±0.28	3.15±1.70	-2.04±1.16	-2.86±1.07	-5.49±1.42
Harbin	2	35578	4079	0.07±0.25	2.82±1.73	-0.35±1.13	-2.69±2.05	-6.51±1.75
Wuhan	2	67785	10940	-0.70±0.16	6.87±1.90	-4.19±1.53	-1.83±2.14	-7.23±1.19
Shanghai	3	115027	10809	-0.34±0.22	2.58±1.50	-4.32±1.23	1.40±2.03	-3.99±1.44
Guangzhou	4	129455	14741	-1.26±0.31	-3.07±0.76	-7.00±1.01	7.61±6.30	-4.80±1.24
Shenzhen	4	352018	25958	-1.01±0.20	-1.77±0.72	-5.50±1.09	8.26±3.08	-3.40±0.98
Los Angeles	/	59943	215	-0.47±0.18	-4.00±0.60	0.23±0.29	7.34±1.31	13.3±1.69
New York	/	60760	516	-0.44±0.19	-3.67±0.72	-1.42±0.54	4.98±1.64	7.97±1.39
Chicago	/	57078	-137	-0.28±0.18	-3.30±0.55	-0.67±0.51	7.88±1.84	1.48±2.63

		RCP85 Emissions				
		Annual Rate of Change (%/year)				
city	class	ECO	ENO_X	ESO_2	ECO/ENO_X	ESO_2/ENO_X
Shenyang	1	1.28±0.17	5.85±0.39	-0.40±0.15	-2.90±0.24	-3.94±0.49
Xian	1	0.75±0.11	4.54±0.31	-0.47±0.16	-2.63±0.21	-3.45±0.43
Chengdu	1	0.33±0.07	4.10±0.28	-0.58±0.17	-2.69±0.22	-3.32±0.42
Hohhot	1	1.14±0.14	1.72±0.12	-0.69±0.14	-0.50±0.03	-2.06±0.25
Chongqing	1	0.65±0.10	3.99±0.27	-1.21±0.25	-2.41±0.18	-3.73±0.49
Tianjin	2	1.22±0.17	5.38±0.34	-1.54±0.31	-2.73±0.20	-4.49±0.60
Beijing	2	1.23±0.18	5.83±0.38	-1.30±0.28	-2.93±0.22	-4.50±0.59
Harbin	2	0.89±0.11	4.07±0.29	-0.72±0.18	-2.28±0.18	-3.41±0.43
Wuhan	2	0.74±0.11	3.96±0.27	-1.21±0.25	-2.33±0.17	-3.71±0.48
Shanghai	3	-0.87±0.04	2.63±0.19	-2.73±0.46	-2.79±0.22	-4.25±0.60
Guangzhou	4	-0.06±0.04	3.44±0.23	-0.87±0.20	-2.63±0.21	-3.22±0.41
Shenzhen	4	0.20±0.06	2.54±0.19	-0.69±0.17	-1.89±0.14	-2.58±0.33
Los Angeles	/	-5.56±0.30	-4.91±0.19	-5.96±0.54	-1.17±0.10	-1.95±0.41
New York	/	-6.00±0.29	-5.77±0.25	-6.60±0.52	-0.50±0.05	-1.80±0.33
Chicago	/	-5.50±0.32	-4.99±0.27	-6.53±0.66	-0.94±0.05	-2.89±0.46

3.4 Socioeconomic Dependence of Urban Enhancement Ratios in China

Here, we attempt to connect these emission pathways to the larger pattern of economic growth across the 31 capital cities and five special cities in mainland China. We find in particular a power law relationship between the observed annual-mean $\Delta CO/\Delta NO_2$ (and $\Delta SO_2/\Delta NO_2$) and GDP per capita. This is not to derive an overall EKC for China, as this in fact requires a very long record of environmental quality, but specifically to investigate how economic development shapes how 'clean' the bulk combustion in Chinese cities would be. These enhancement ratios complement abundance and/or emissions of pollutants as traditional measures of air pollution. Unlike Figure B3 and 4, our focus is to illustrate the larger dependence of enhancement ratios on GDP per capita. As discussed in the Methods section, we relate the enhancement ratio of a megacity to the ratio of the product of emission factor ($EF_{species}$) and effectiveness of control technology ($1 - CE_{species}$) for CO and NO_X species in the case of $\Delta CO/\Delta NO_2$ for example. We use a robust least-squares regression with least absolute residuals method to fit a curve of the form: $y = ax^k$, where y is $\Delta CO/\Delta NO_2$ or $\Delta SO_2/\Delta NO_2$ and x is GDP per capita. Our results are presented in Figure B5a and 5b for $\Delta CO/\Delta NO_2$ and $\Delta SO_2/\Delta NO_2$, respectively. The 12 cities considered in our analysis of emission pathways are marked with colors corresponding to its level of urban development described in previous section. Note that the magnitudes of enhancement ratios derived from this work is a factor of 10 higher than ratios derived from ground-based networks. We attribute this discrepancy to differences in air mass and volume, representativeness, and vertical sensitivity between abundance retrieved as total or tropospheric columns and in-situ and point samples in units of mixing ratios. Nevertheless, we find a strong power law relationship with GDP per capita having k coefficients (R^2=0.98) of negative two-thirds and negative one-half for $\Delta CO/\Delta NO_2$ and $\Delta SO_2/\Delta NO_2$, respectively. Likely, the coefficients in $\Delta SO_2/\Delta NO_2$ will converge to that in $\Delta CO/\Delta NO_2$ as changes in fuel type and SO_2 controls should decrease SO_2 abundance. While each city is unique and that the evolution of air pollution may be different from city to city, there also exist a clear signature of urbanization at national level that reflects the influence of economic growth on the cleanness of bulk combustion. Similar power law relationships (albeit different coefficients) have been reported in studies of urban growth and development (Bechle et al., 2011; Lamsal et al., 2013; Bettencourt et al., 2013), energy flows (Creutzig et al., 2015) and carbon

emissions (Fragkias et al., 2013). Our results suggest that enhancement ratios scale with GDP per capita, with lower GDP per capita like Shenyang and other cities (gray dots) having higher enhancement ratios, while Shenzhen and other cities (yellow dots) with highest GDP per capita in China lie among cities with the lowest enhancement ratios. As we have shown in Figure B4 (and Table B2), the ratios in Shenzhen tend to increase with time (and GDP) but this increase has its limits and appears to be dwarfed by cities with highest enhancement ratios. We note, however, that identifying a mechanistic rationale of these negative scaling coefficients is beyond the scope of this work and hence is not proposed. A unified relationship cannot also be established across countries as there are obvious differences in socioeconomic and air pollution conditions in China and U.S. that cannot be accounted for (Figure B6). Nevertheless, we suggest incorporating this observable along with estimates of emissions to future scaling studies, especially as we move past RCPs and toward recent developments in building more realistic emission scenarios that integrate socioeconomic and environmental development pathways like the Shared Socioeconomic Pathways (SSPs; O'Neil et al., 2014).

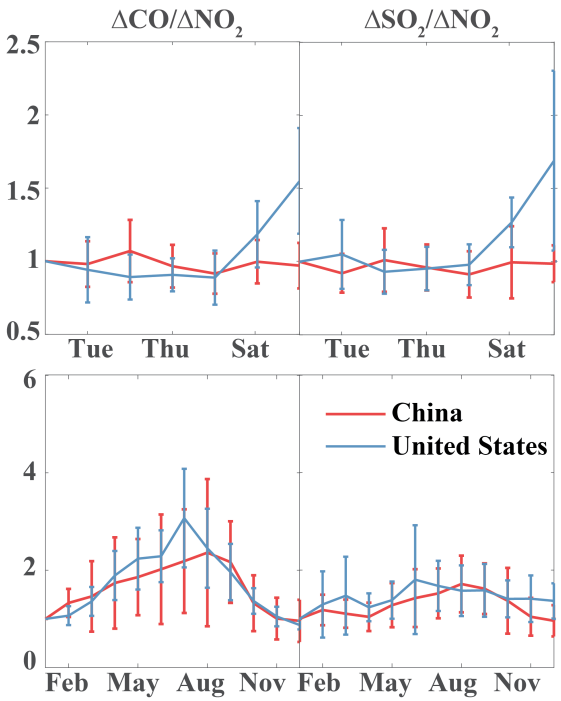

Figure B6: Weekly (top) and seasonal cycle (bottom) of the satellite-based enhancement ratios averaged for the 12 cities in China (red) and for 8 cities in U.S. (blue). The error bars stand for standard deviation across cities.

4 Summary and Implications

The main goal of this work is to provide observational evidence from Earth observing satellites of emission pathways of combustion-related air pollutants, as a result of urban growth in economically developing countries like China. A new observational perspective on monitoring one of the major consequences of urbanization is introduced, not to replace existing observing capabilities but to further exploit the information that is already available. Following the pioneering work by Parrish et al. (2002), the sensitivities of intermediate products of combustion can be derived from existing satellite retrievals of air quality (AQ), to inform changes in bulk combustion characteristics (and consequently emissions) of a megacity. This is especially relevant as the number of megacities continue to grow in the coming decades, mostly at locations that lack sufficient AQ monitoring capabilities. Enhancement ratios of CO to NO_2 and SO_2 to NO_2 over megacities in mainland China that are derived from MOPITT and OMI satellite instruments show a coherent long-term progression in recent years of decreasing to increasing ratios relative to 2005. This is well correlated with economic development. These trace a common emission pathway that resembles the evolution of air pollution in more developed cities in the United States which is characterized by transitions in energy use and subsequent implementation of pollution control and regulation. Although we find cleaner combustion as cities in China develop consistent with their Five Year Plans, this is presently obfuscated by increasing fuel use particularly its heavy reliance on coal. We propose the use of these enhancement ratios derived from existing satellite retrievals to complement existing surface AQ networks, including carbon-related satellite observing systems in further constraining combustion efficiency and effectiveness of control technologies and policies. Augmenting existing capabilities (Saeki et al., 2017) is particularly relevant, especially with the aid of big data informatics and machine learning as well as the advent of activities focusing specifically on tracking fossil fuel emissions (like the CO_2 Human Emissions project; https://www.che-project.eu). While we recognize the current limitations of these retrievals (e.g., collocation, sensitivity), our findings appear to be robust across retrievals and methods, and are supported by previous studies using these retrievals in a different way (Krotkov et al., 2016; Jiang et al., 2018) or ground measurements (Hassler et al., 2016). We strongly suggest that the capability to monitor relatively long-term changes in atmospheric composition has to be supported and continued with complementary new satellite and field missions and deployments (Streets et al., 2013; National Academies of Sciences, Engineering, and Medicine, 2016).

The relative importance of monitoring combustion efficiency and effectiveness of pollution control increases as a city and country continue to socioeconomically develop and become sustainable. Despite past and present studies (Mazur and Rosa, 1974; Lamb et al., 2014), it is only in most recent years that we have developed comprehensive and integrated monitoring and prediction systems, which paved new measures of air pollution and new developments in emission scenarios like SSPs. For China, more detailed information on energy use and improved emission inventories are increasingly becoming available for assessment (Li et al., 2017; Zhong et al., 2017). As we also recognize some of the challenges to quantify socioeconomic variables such as the impact of international trade on air pollution (Lin et al., 2014), economic structural upgrading (Mi et al., 2017), greater utilization of renewable energy, and even metrics of performance (Ramaswami et al., 2013), from a physical science perspective, our results strongly support these new developments. We find inconsistencies between the long-term spatiotemporal patterns of emission ratios from RCP8.5 and model predictions of abundance ratios, and the corresponding patterns derived from observed enhancement ratios. Scientific improvements in representing the evolution of air pollution (Lewis, 2018) and emission pathways (Mitchell et al., 2017) can be made by (1) considering observationally-constrained time-varying emission factors, and (2) confronting emissions and physical models with available data not only for their accuracy, but also for their consistency in representing both carbon and AQ-related combustion products.

Data Availability

The raw data used in this study are available online (links to satellite data and emission inventories can be found in Table B1; Socioeconomic Data: Annual GDP and population are directly taken from China Statistical Yearbook compiled by National Bureau of Statistics of China (http://www.stats.gov.cn/)). Model outputs and reanalysis data are available upon request from the authors.

Acknowledgements

This study is supported by NASA ACMAP Grant NNX17AG39G. K.M's reanalysis is supported by JSPS KAKENHI Grant 15K05296 and 18H01285. We acknowledge MOPITT, IASI, and OMI retrieval teams for CO, NO_2, SO_2, data, respectively. We also thank EDGAR, HTAP, REAS, RCPs

data teams for the emission inventories. All the satellite data and emission inventories are available to the public online. We thank Kevin Bowman, Cenlin He, and Sam Silva for insightful discussions.

Author contributions

The initial idea was provided by AFA. and WT. CHASER-LETKF experiments were performed and provided by KM. CAM-chem modeling experiments were performed and provided by BG. Data analyses and results interpretation were performed by WT. and AFA. HW provided key expert guidance on MOPITT CO. The manuscript was written by AFA. and WT.

References

Baklanov, A., Molina, L.T. and Gauss, M.: Megacities, air quality and climate. Atmospheric Environment, 126, pp.235-249, 2016.

Bechle, M.J., Millet, D.B. and Marshall, J.D.: Effects of income and urban form on urban NO2: Global evidence from satellites. Environmental science & technology, 45(11), pp.4914-4919, 2011.

Bettencourt, L.M.: The origins of scaling in cities. science, 340(6139), pp.1438-1441, 2013.

Bhattacharya, M., Rafiq, S., & Bhattacharya, S.: The role of technology on the dynamics of coal consumption–economic growth: New evidence from China. Applied Energy, 154, 686-695, 2015.

Boersma, K.F., Eskes, H.J., Dirksen, R.J., Veefkind, J.P., Stammes, P., Huijnen, V., Kleipool, Q.L., Sneep, M., Claas, J., Leitão, J. and Richter, A.: An improved tropospheric NO2 column retrieval algorithm for the Ozone Monitoring Instrument. Atmospheric Measurement Techniques, 4(9), pp.1905-1928, 2011.

Boersma, K.F., Eskes, H., Richter, A., De Smedt, I., Lorente, A., Beirle, S., Van Geffen, J., Peters, E., Van Roozendael, M. and Wagner, T.: QA4ECV NO2 tropospheric and stratospheric vertical column data from OMI (Version 1.1)(data set), Royal Netherlands Meteorological Institute (KNMI), 2017.

Chan, C.K. and Yao, X.: Air pollution in mega cities in China. Atmospheric environment, 42(1), pp.1-42, 2008.

Cleveland, R.B., Cleveland, W.S., McRae, J.E. and Terpenning, I.: STL: A seasonal-trend decomposition. Journal of official statistics, 6(1), pp.3-73, 1990.

Creutzig, F., Baiocchi, G., Bierkandt, R., Pichler, P.P. and Seto, K.C.: Global typology of urban energy use and potentials for an urbanization mitigation wedge. Proceedings of the National Academy of Sciences, 112(20), pp.6283-6288, 2015.

Crippa, M., Janssens-Maenhout, G., Dentener, F., Guizzardi, D., Sindelarova, K., Muntean, M., Van Dingenen, R. and Granier, C.: Forty years of improvements in European air quality: regional policy-industry interactions with global impacts. Atmospheric Chemistry and Physics, 16(6), pp.3825-3841, 2016.

De Wachter, E., Barret, B., Le Flochmoën, E., Pavelin, E., Matricardi, M., Clerbaux, C., Hadji-Lazaro, J., George, M., Hurtmans, D., Coheur, P.-F., Nedelec, P., and Cammas, J. P.: Retrieval of MetOp-A/IASI CO profiles and validation with MOZAIC data, Atmos. Meas. Tech., 5, 2843–2857, https://doi.org/10.5194/amt-5-2843-2012, 2012.

Deeter, M.N., Martínez-Alonso, S., Edwards, D.P., Emmons, L.K., Gille, J.C., Worden, H.M., Sweeney, C., Pittman, J.V., Daube, B.C. and Wofsy, S.C.: The MOPITT Version 6 product: algorithm enhancements and validation. Atmospheric Measurement Techniques, 7(11), pp.3623-3632, 2014.

Ding, J., Mijling, B. and Levelt, P.F.: Space-based NOx emission estimates over remote regions improved in DECSO. Atmospheric Measurement Techniques, 10(3), pp.925-938, 2017.

Duncan, B.N., Prados, A.I., Lamsal, L.N., Liu, Y., Streets, D.G., Gupta, P., Hilsenrath, E., Kahn, R.A., Nielsen, J.E., Beyersdorf, A.J. and Burton, S.P.: Satellite data of atmospheric pollution for US air quality applications: Examples of applications, summary of data end-user resources, answers to FAQs, and common mistakes to avoid. Atmospheric environment, 94, pp.647-662, 2014.

Flagan, R.C. and Seinfeld, J.H.: Fundamentals of air pollution engineering. Courier Corporation, 2012.

Fragkias, M., Lobo, J., Strumsky, D. and Seto, K.C.: Does size matter? Scaling of CO2 emissions and US urban areas. PLoS One, 8(6), p.e64727, 2013.

Fujita, E.M., Croes, B.E., Bennett, C.L., Lawson, D.R., Lurmann, F.W. and Main, H.H.: Comparison of emission inventory and ambient concentration ratios of CO, NMOG, and NOx in California's South Coast Air Basin. Journal of the Air & Waste Management Association, 42(3), pp.264-276, 1992.

Gaubert. B, Arellano, A. F., Barré, J.,Worden, H. M., Emmons, L. K., Tilmes, S., Buchholz, R. R., Vitt, F., Raeder, K., Collins, N., Anderson, J. L., Wiedinmyer, C., Martinez Alonso, S., Edwards, D. P., Andreae, M. O., Hannigan, J. W., Petri, C., Strong, K., and Jones, N.: Toward a chemical reanalysis in a coupled chemistry-climate model: An evaluation of MOPITT CO assimilation and its impact on tropospheric composition, J. Geophys. Res. Atmos., doi:10.1002/2016JD024863, http://dx.doi.org/10.100/2016JD024863, 2016JD024863, 2016.

Gaubert, B., Worden, H.M., Arellano, A.F.J., Emmons, L.K., Tilmes, S., Barré, J., Alonso, S.M., Vitt, F., Anderson, J.L., Alkemade, F. and Houweling, S.: Chemical feedback from decreasing carbon monoxide emissions. Geophysical Research Letters, 44(19), pp.9985-9995, 2017.

Guo, S., Hu, M., Zamora, M.L., Peng, J., Shang, D., Zheng, J., Du, Z., Wu, Z., Shao, M., Zeng, L. and Molina, M.J.: Elucidating severe urban haze formation in China. Proceedings of the National Academy of Sciences, 111(49), pp.17373-17378, 2014.

Hakkarainen, J., Ialongo, I. and Tamminen, J.: Direct space-based observations of anthropogenic CO2 emission areas from OCO-2. Geophysical Research Letters, 43(21), pp.11-400, 2016.

Hassler, B., McDonald, B.C., Frost, G.J., Borbon, A., Carslaw, D.C., Civerolo, K., Granier, C., Monks, P.S., Monks, S., Parrish, D.D. and Pollack, I.B.: Analysis of long-term observations of NOx and CO in megacities and application to constraining emissions inventories. Geophysical Research Letters, 43(18), pp.9920-9930, 2016.

He J., Wang, H.: Economic structure, development policy and environmental quality: An empirical analysis of environmental Kuznets curves with Chinese municipal data. Ecological Economics, 76, 49-59, 2012.

Holland, P. W., Welsch, R. E.: Robust regression using iteratively reweighted least-squares. Communications in Statistics-theory and Methods, 6(9), 813-827, 1977.

Jalkanen, L.: WMO/IGAC impacts of megacities on air pollution and climate. Urban Climate, 1, 67-68, 2012.

Janssens-Maenhout, G., Crippa, M., Guizzardi, D., Dentener, F., Muntean, M., Pouliot, G., Keating, T., Zhang, Q., Kurokawa, J., Wankmüller, R., Denier van der Gon, H., Kuenen, J. J. P., Klimont, Z., Frost, G., Darras, S., Koffi, B., and Li, M.: HTAP_v2.2: a mosaic of regional and global emission grid maps for 2008 and 2010 to study hemispheric transport of air pollution, Atmos. Chem. Phys., 15, 11411-11432, https://doi.org/10.5194/acp-15-11411-2015, 2015.

Jiang, Z., McDonald, B.C., Worden, H., Worden, J.R., Miyazaki, K., Qu, Z., Henze, D.K., Jones, D.B., Arellano, A.F., Fischer, E.V. and Zhu, L.: Unexpected slowdown of US pollutant emission reduction in the past decade. Proceedings of the National Academy of Sciences, 115(20), pp.5099-5104, 2018.

Kennedy, C.A., Stewart, I., Facchini, A., Cersosimo, I., Mele, R., Chen, B., Uda, M., Kansal, A., Chiu, A., Kim, K.G. and Dubeux, C.: Energy and material flows of megacities. Proceedings of the National Academy of Sciences, 112(19), pp.5985-5990, 2015.

Kheirbek, I., Haney, J., Douglas, S., Ito, K., Caputo Jr, S. and Matte, T.: The public health benefits of reducing fine particulate matter through conversion to cleaner heating fuels in New York City. Environmental science & technology, 48(23), pp.13573-13582, 2014.

Konovalov, I.B., Berezin, E.V., Ciais, P., Broquet, G., Zhuravlev, R.V. and Janssens-Maenhout, G.: Estimation of fossil-fuel CO2 emissions using satellite measurements of" proxy" species. Atmospheric Chemistry and Physics, 16(21), p.13509, 2016.

Korsbakken, J.I., Peters, G.P. and Andrew, R.M.: Uncertainties around reductions in China's coal use and CO2 emissions. Nature Climate Change, 6(7), p.687, 2016.

Koukouli, M. E., Theys, N., Ding, J., Zyrichidou, I., Mijling, B., Balis, D., and van der A, R. J.: Updated SO2 emission estimates over China using OMI/Aura observations, Atmos. Meas. Tech., 11, 1817-1832, https://doi.org/10.5194/amt-11-1817-2018, 2018.

Krotkov, N.A., Carn, S.A., Krueger, A.J., Bhartia, P.K. and Yang, K.: Band residual difference algorithm for retrieval of SO/sub 2/from the aura ozone monitoring instrument (OMI). IEEE Transactions on geoscience and remote sensing, 44(5), pp.1259-1266, 2006.

Krotkov, N. A., McLinden, C. A., Li, C., Lamsal, L. N., Celarier, E. A., Marchenko, S. V., Swartz, W. H., Bucsela, E. J., Joiner, J., Duncan, B. N., Boersma, K. F., Veefkind, J. P., Levelt, P. F., Fioletov, V. E., Dickerson, R. R., He, H., Lu, Z., and Streets, D. G.: Aura OMI observations of regional SO2 and NO2 pollution changes from 2005 to 2015, Atmos. Chem. Phys., 16, 4605-4629, https://doi.org/10.5194/acp-16-4605-2016, 2016.

Kurokawa, J., Ohara, T., Morikawa, T., Hanayama, S., Janssens-Maenhout, G., Fukui, T., Kawashima, K., and Akimoto, H.: Emissions of air pollutants and greenhouse gases over Asian regions during 2000–2008: Regional Emission inventory in ASia (REAS) version 2, Atmos. Chem. Phys., 13, 11019-11058, https://doi.org/10.5194/acp-13-11019-2013, 2013.

Lamb, W.F., Steinberger, J.K., Bows-Larkin, A., Peters, G.P., Roberts, J.T. and Wood, F.R.: Transitions in pathways of human development and carbon emissions. Environmental Research Letters, 9(1), p.014011, 2014.

Lamsal, L.N., Martin, R.V., Parrish, D.D. and Krotkov, N.A.: Scaling relationship for NO2 pollution and urban population size: a satellite perspective. Environmental science & technology, 47(14), pp.7855-7861, 2013.

Lelieveld, J., Evans, J.S., Fnais, M., Giannadaki, D. and Pozzer, A.: The contribution of outdoor air pollution sources to premature mortality on a global scale. Nature, 525(7569), p.367, 2015.

Lewis, A.C.: The changing face of urban air pollution. Science, 359(6377), pp.744-745, 2018.

Li, G., Fang, C., Wang, S. and Sun, S.: The effect of economic growth, urbanization, and industrialization on fine particulate matter (PM2. 5) concentrations in China. Environmental science & technology, 50(21), pp.11452-11459, 2016.

Li, M., Zhang, Q., Kurokawa, J.-I., Woo, J.-H., He, K., Lu, Z., Ohara, T., Song, Y., Streets, D. G., Carmichael, G. R., Cheng, Y., Hong, C., Huo, H., Jiang, X., Kang, S., Liu, F., Su, H., and Zheng, B.: MIX: a mosaic Asian anthropogenic emission inventory under the international collaboration framework of the MICS-Asia and HTAP, Atmos. Chem. Phys., 17, 935-963, https://doi.org/10.5194/acp-17-935-2017, 2017.

Lin, J., Pan, D., Davis, S.J., Zhang, Q., He, K., Wang, C., Streets, D.G., Wuebbles, D.J. and Guan, D.: China's international trade and air pollution in the United States. Proceedings of the National Academy of Sciences, 111(5), pp.1736-1741, 2014.

Luo, Y., Chen, H., Peng, C., Yang, G., Yang, Y. and Zhang, Y.: Relationship between air pollutants and economic development of the provincial capital cities in China during the past decade. PLoS One, 9(8), p.e104013, 2014.

Mage, D., Ozolins, G., Peterson, P., Webster, A., Orthofer, R., Vandeweerd, V. and Gwynne, M.: Urban air pollution in megacities of the world. Atmospheric Environment, 30(5), pp.681-686, 1996.

Mazur, A. and Rosa, E.: Energy and life-style. Science, 186(4164), pp.607-610, 1974.

Marangoni, G., Tavoni, M., Bosetti, V., Borgonovo, E., Capros, P., Fricko, O., Gernaat, D.E., Guivarch, C., Havlik, P., Huppmann, D. and Johnson, N.: Sensitivity of projected long-term CO2 emissions across the Shared Socioeconomic Pathways. Nature Climate Change, 7(2), p.113, 2017.

McDonald, B.C., De Gouw, J.A., Gilman, J.B., Jathar, S.H., Akherati, A., Cappa, C.D., Jimenez, J.L., Lee-Taylor, J., Hayes, P.L., McKeen, S.A. and Cui, Y.Y.: Volatile chemical products emerging as largest petrochemical source of urban organic emissions. Science, 359(6377), pp.760-764, 2018.

McLinden, C.A., Fioletov, V., Shephard, M.W., Krotkov, N., Li, C., Martin, R.V., Moran, M.D. and Joiner, J.: Space-based detection of missing sulfur dioxide sources of global air pollution. Nature Geoscience, 9(7), p.496, 2016.

Mi, Z., Meng, J., Guan, D., Shan, Y., Liu, Z., Wang, Y., Feng, K. and Wei, Y.M.: Pattern changes in determinants of Chinese emissions. Environmental Research Letters, 12(7), p.074003, 2017.

Mitchell, L.E., Lin, J.C., Bowling, D.R., Pataki, D.E., Strong, C., Schauer, A.J., Bares, R., Bush, S.E., Stephens, B.B., Mendoza, D. and Mallia, D.: Long-term urban carbon dioxide observations reveal spatial and temporal dynamics related to urban characteristics and growth. Proceedings of the National Academy of Sciences, 115(12), pp.2912-2917, 2018.

Miyazaki, K., Eskes, H., Sudo, K., Boersma, K. F., Bowman, K., and Kanaya, Y.: Decadal changes in global surface NOx emissions from multi-constituent satellite data assimilation, Atmos. Chem. Phys., 17, 807-837, https://doi.org/10.5194/acp-17-807-2017, 2017.

National Academies of Sciences, Engineering, and Medicine: The Future of Atmospheric Chemistry Research: Remembering Yesterday, Understanding Today, Anticipating Tomorrow. Washington, DC: The National Academies Press. doi: 10.17226/23573, 2016.

O'Neill, B.C., Kriegler, E., Riahi, K., Ebi, K.L., Hallegatte, S., Carter, T.R., Mathur, R. and van Vuuren, D.P.: A new scenario framework for climate change research: the concept of shared socioeconomic pathways. Climatic change, 122(3), pp.387-400, 2014.

Parrish, D.D., Trainer, M., Hereid, D., Williams, E.J., Olszyna, K.J., Harley, R.A., Meagher, J.F. and Fehsenfeld, F.C.: Decadal change in carbon monoxide to nitrogen oxide ratio in US

vehicular emissions. Journal of Geophysical Research: Atmospheres, 107(D12), pp.ACH-5, 2002.

Parrish, D. D.: Critical evaluation of US on-road vehicle emission inventories. Atmospheric Environment, 40(13), 2288-2300, 2006.

Paulot, F., Fan, S. and Horowitz, L.W.: Contrasting seasonal responses of sulfate aerosols to declining SO2 emissions in the Eastern US: Implications for the efficacy of SO2 emission controls. Geophysical Research Letters, 44(1), pp.455-464, 2017.

Qi, Y., Stern, N., Wu, T., Lu, J. and Green, F.: China's post-coal growth. Nature Geoscience, 9(8), p.564, 2016.

Ramaswami, A., Chavez, A.: What metrics best reflect the energy and carbon intensity of cities? Insights from theory and modeling of 20 US cities. Environmental Research Letters, 8(3), 035011, 2013.

Reuter, M., Buchwitz, M., Hilboll, A., Richter, A., Schneising, O., Hilker, M., Heymann, J., Bovensmann, H. and Burrows, J.P.: Decreasing emissions of NOx relative to CO2 in East Asia inferred from satellite observations. Nature Geoscience, 7(11), p.792, 2014.

Riahi, K., Rao, S., Krey, V., Cho, C., Chirkov, V., Fischer, G., Kindermann, G., Nakicenovic, N. and Rafaj, P.: RCP 8.5—A scenario of comparatively high greenhouse gas emissions. Climatic Change, 109(1-2), p.33, 2011.

Richter, A., Burrows, J.P., Nüß, H., Granier, C. and Niemeier, U.: Increase in tropospheric nitrogen dioxide over China observed from space. Nature, 437(7055), p.129, 2005.

Russell, A. R., Valin, L. C., and Cohen, R. C.: Trends in OMI NO2 observations over the United States: effects of emission control technology and the economic recession, Atmos. Chem. Phys., 12, 12197-12209, https://doi.org/10.5194/acp-12-12197-2012, 2012.

Saeki, T., Patra, P. K.: Implications of overestimated anthropogenic CO2 emissions on East Asian and global land CO2 flux inversion. Geoscience Letters, 4(1), 9, 2017.

Shindell, D., Faluvegi, G., Walsh, M., Anenberg, S.C., Van Dingenen, R., Muller, N.Z., Austin, J., Koch, D. and Milly, G.: Climate, health, agricultural and economic impacts of tighter vehicle-emission standards. Nature Climate Change, 1(1), p.59, 2011.

Silva, S.J., Arellano, A.F. and Worden, H.M.: Toward anthropogenic combustion emission constraints from space-based analysis of urban CO2/CO sensitivity. Geophysical Research Letters, 40(18), pp.4971-4976, 2013.

Silva, S. and Arellano, A.: Characterizing regional-scale combustion using satellite retrievals of CO, NO2 and CO2. Remote Sensing, 9(7), p.744, 2017.

Smith, R. J.: Use and misuse of the reduced major axis for linefitting, Am. J. Phys. Anthropol., 140, 476–486, 2009.

Steinberger, J.K., Roberts, J.T., Peters, G.P. and Baiocchi, G.: Pathways of human development and carbon emissions embodied in trade. Nature Climate Change, 2(2), p.81, 2012.

Stern, D. I.: The rise and fall of the environmental Kuznets curve. World development, 32(8), 1419-1439, 2004.

Streets, D.G., Canty, T., Carmichael, G.R., de Foy, B., Dickerson, R.R., Duncan, B.N., Edwards, D.P., Haynes, J.A., Henze, D.K., Houyoux, M.R. and Jacob, D.J.: Emissions estimation from satellite retrievals: A review of current capability. Atmospheric Environment, 77, pp.1011-1042, 2013.

Sun, W., Shao, M., Granier, C., Liu, Y., Ye, C.S. and Zheng, J.Y.: Long-Term Trends of Anthropogenic SO2, NOx, CO, and NMVOCs Emissions in China. Earth's Future, 6(8), pp.1112-1133, 2018.

Tang. W., Arellano, F. A.: Investigating dominant characteristics of fires across the Amazon during 2005–2014 through satellite data synthesis of combustion signatures. Journal of Geophysical Research: Atmospheres, 122(2), 1224-1245, 2017.

Tang, W., Arellano, A. F., DiGangi, J. P., Choi, Y., Diskin, G. S., Agustí-Panareda, A., Parrington, M., Massart, S., Gaubert, B., Lee, Y., Kim, D., Jung, J., Hong, J., Hong, J.-W., Kanaya, Y., Lee, M., Stauffer, R. M., Thompson, A. M., Flynn, J. H., and Woo, J.-H.: Evaluating high-resolution forecasts of atmospheric CO and CO2 from a global prediction system during KORUS-AQ field campaign, Atmos. Chem. Phys., 18, 11007-11030, https://doi.org/10.5194/acp-18-11007-2018, 2018.

Tang, W., Emmons, L. K., Arellano, A. F., Gaubert, B., Knote, C., Tilmes, S., Buchholz, R. R., Pfister, G. G., Diskin, G. S., Blake, D. R., Blake, N. J., Meinardi, S., DiGangi, J P., Choi, Y., Woo,J., He, C., Schroeder, J. R., Suh, I., Lee, H., Jo, H., Kanaya, Y.,Jung, J., Lee, Y., and Kim, D.: Source contributions to carbon monoxide concentrations during KORUS-AQ based on CAM-chem model applications, J. Geophys. Res. Atmos., 10.1029/2018JD029151, 2019.

Taylor, M.R., Rubin, E.S. and Hounshell, D.A.: Control of SO2 emissions from power plants: A case of induced technological innovation in the US. Technological Forecasting and Social Change, 72(6), pp.697-718, 2005.

van der A, R. J., Mijling, B., Ding, J., Koukouli, M. E., Liu, F., Li, Q., Mao, H., and Theys, N.: Cleaning up the air: effectiveness of air quality policy for SO2 and NOx emissions in China, Atmos. Chem. Phys., 17, 1775-1789, https://doi.org/10.5194/acp-17-1775-2017, 2017.

Verstraeten, W.W., Neu, J.L., Williams, J.E., Bowman, K.W., Worden, J.R. and Boersma, K.F.: Rapid increases in tropospheric ozone production and export from China. Nature geoscience, 8(9), p.690, 2015.

Wang, S. and Hao, J.: Air quality management in China: Issues, challenges, and options. Journal of Environmental Sciences, 24(1), pp.2-13, 2012.

Worden, H.M., Deeter, M.N., Edwards, D.P., Gille, J.C., Drummond, J.R. and Nédélec, P.: Observations of near-surface carbon monoxide from space using MOPITT multispectral retrievals. Journal of Geophysical Research: Atmospheres, 115(D18), 2010.

World Bank: East Asia's Changing Urban Landscape: Measuring a Decade of Spatial Growth. Urban Development Series. Washington, DC: World Bank. doi: 10.1596/978-1-4648-0363-5, 2015.

Wu, Y., Zhang, S., Hao, J., Liu, H., Wu, X., Hu, J., Walsh, M.P., Wallington, T.J., Zhang, K.M. and Stevanovic, S.: On-road vehicle emissions and their control in China: A review and outlook. Science of The Total Environment, 574, pp.332-349, 2017.

Yang, X., Wang, S., Zhang, W., Li, J., & Zou, Y.: Impacts of energy consumption, energy structure, and treatment technology on SO2 emissions: A multi-scale LMDI decomposition analysis in China. Applied energy, 184, 714-726, 2016.

Zhang, Q., He, K. and Huo, H.: Policy: cleaning China's air. Nature, 484(7393), p.161, 2012.

Zheng, B., Chevallier, F., Ciais, P., Yin, Y., Deeter, M.N., Worden, H.M., Wang, Y., Zhang, Q. and He, K.: Rapid decline in carbon monoxide emissions and export from East Asia between years 2005 and 2016. Environmental Research Letters, 13(4), p.044007, 2018.

Zhong, Q., Huang, Y., Shen, H., Chen, Y., Chen, H., Huang, T., Zeng, E.Y. and Tao, S.: Global estimates of carbon monoxide emissions from 1960 to 2013. Environmental Science and Pollution Research, 24(1), pp.864-873, 2017.

Supporting Information

Part 1: Combustion Emission Ratios and their Decomposition

In a combustion process using a hydrocarbon fuel, CO and elemental carbon (e.g., soot or BC) are produced when combustion is incomplete; otherwise carbon in the fuel is oxidized to CO_2 (Eq. 1). In addition, NO and NO_2 are produced from the oxidation of nitrogen from the fuel itself and from decomposition of N_2 in air at high temperatures (Flagan and Seinfeld, 2012). Sulfur dioxide (SO_2) is also produced when the fuel used in the combustion process contains sulfur (such is the case for low-grade fuels).

$$C_{x_1}H_{x_2}O_{x_3}N_{x_4}S_{x_5} + n_1(1+e)(O_2 + 3.76N_2) \rightarrow$$
$$n_2CO_2 + n_3H_2O + n_4O_2 + n_5N_2 + n_6CO + n_7NO + n_8NO_2 + n_9SO_2 + n_{10}C + \cdots \quad \text{Eq. (A1)}$$

Emissions of these intermediate product are typically expressed as:

$$E_x = \sum_s \left[A_s \cdot EF_{x,s} \cdot \left(1 - CE_{x,s}\right)\right] = \sum_s \left[A_s \cdot EEF_{x,s}\right] \quad \text{Eq. (A2)}$$

where E_x is the total mass of emissions for species x, $EF_{x,s}$ is its associated emission factor for a specific source/sector s, A_s is the activity level of the source. $CE_{x,s}$ corresponds to effectiveness of control measure and $EEF_{x,s} = EF_{x,s} \cdot \left(1 - CE_{x,s}\right)$ is the effective emission factor. When we take the ratio of emissions (Eq. 2) of co-emitted species x and y,

$$\frac{E_y}{E_x} = \frac{\sum_s \left[A_s \cdot EEF_{y,s}\right]}{\sum_s \left[A_s \cdot EEF_{x,s}\right]} = \sum_s \left(\frac{EEF_{y,s}}{EEF_{x,s}}\right)\left(\frac{E_{x,s}}{E_{x,total}}\right) \quad \text{Eq. (A3)}$$

this ratio can be expressed as the sum of the products of the ratio of effective emission factors ($R_{x,y,s}^{EEF}$) and the fractional contribution of emission sector f for species x ($f_{x,s}$) (Eq. A3).

Part 2: Inverse Analysis

We decomposed the *a priori* estimate of monthly emission ratio of CO to NO_X (and SO_2 to NO_X) from RCP8.5 as a product of: a) ratio of effective emission factors for each of the four sectors namely energy, industry, transport, and others ($R^{EEF}_{x,y,s}$); and b) fractional contribution of NO_2 emissions from each sector to the total NO_2 emissions ($f_{x,s}$) for all four sectors s (s_1: energy, s_2:industry, s_3:transport, s_4:others). In matrix-vector form, this can be expressed as:

$$\begin{bmatrix} ECO/ENO_X \\ ESO_2/ENO_X \end{bmatrix} = \begin{bmatrix} R^{EEF}_{CO/NO_X,s_1} & R^{EEF}_{CO/NO_X,s_2} & R^{EEF}_{CO/NO_X,s_3} & R^{EEF}_{CO/NO_X,s_4} \\ R^{EEF}_{SO_2/NO_X,s_1} & R^{EEF}_{SO_2/NO_X,s_2} & R^{EEF}_{SO_2/NO_X,s_3} & R^{EEF}_{SO_2/NO_X,s_4} \end{bmatrix} \begin{bmatrix} f_{NO_X,s_1} \\ f_{NO_X,s_2} \\ f_{NO_X,s_3} \\ f_{NO_X,s_4} \end{bmatrix} \quad \text{Eq. (B1)}$$

or

$$\mathbf{y} = \mathbf{Hx} \quad \text{Eq. (B2)}$$

We use a two-step Monte-Carlo-based Bayesian inversion method to estimate both **H** and **x** of the following cities: Shenyang, Beijing, Shanghai, Shenzhen, and Los Angeles. We focus our analysis on the decadal trends of the RCP8.5 CO to NO_X and SO_2 to NO_X emission ratios using the decadal trends of $\Delta CO/\Delta NO_2$ and $\Delta SO_2/\Delta NO_2$ as observational data (**y**). We use the decadal trend of enhancement ratios of CO to NO_2 and SO_2 to NO_2 (derived using STL), calculate their annual averages and normalized to 2005 values, and then take these as our observational (fitting) data. Our goal is to estimate **H** and **x** given **y** subject to the following constraints: a) errors in **H** and **x** are 10% and 25% of their values, b) errors in **y** is 5% of its value, c) error covariances of **y** and **x** are uncorrelated and diagonal ($\mathbf{S_e}$, $\mathbf{S_a}$) and d) sum of **x** is unity. Since this is an under-determined inverse problem, we apply prior information on **H** and **x** using the RCP emissions ($\mathbf{H_a}$, $\mathbf{x_a}$). We conduct our inverse analysis into two-step: 1) estimate the most likely **H** that results to estimates of **x** best fitting the decadal trend, 2) estimate **x** using the new estimate of **H**. For Step 1, first, we draw n=10,000 samples of **H** assuming its errors are normally distributed with mean to be its prior

and covariance to be the diagonal of its squared errors. Second, we use the *maximum a posteriori* (MAP) solution to the Bayesian problem to estimate $\mathbf{x}$ for every sample. i.e.,

$$\hat{\mathbf{x}} = \mathbf{x_a} + \left(\mathbf{H_a}^{\mathrm{T}}\mathbf{S_e}^{-1}\mathbf{H_a} + \mathbf{S_a}^{-1}\right)^{-1}\mathbf{H_a}^{\mathrm{T}}\mathbf{S_e}^{-1}(\mathbf{y} - \mathbf{H_a}\mathbf{x_a}),$$

$$\hat{\mathbf{S}} = \left(\mathbf{H_a}^{\mathrm{T}}\mathbf{S_e}^{-1}\mathbf{H_a} + \mathbf{S_a}^{-1}\right)^{-1} \qquad \text{Eq. (B3)}$$

We draw a new sample if any of the elements in $\hat{\mathbf{x}}$ is negative. Third, we take the mean of 100 $\mathbf{H}$ samples resulting to the lowest root-mean-square errors relative to the data. We use this mean as our new estimate of $\mathbf{H}$ ($\widehat{\mathbf{H}}$). For Step 2, we apply the same MAP solution using $\mathbf{x_a}$ and $\mathbf{H_a} = \widehat{\mathbf{H}}$ to estimate $\hat{\mathbf{x}}$ and $\hat{\mathbf{S}}$. Similar to a Kalman filter, we cycle this procedure for each year starting from 2006 to 2014. We use the new estimates of $\hat{\mathbf{x}}$, $\widehat{\mathbf{H}}$, and $\hat{\mathbf{S}}$ for a given year as priors for the succeeding cycle with fix inflation on the covariance of 1.25 to minimize filter divergence. We note that the additional constraints (positive $\hat{\mathbf{x}}$, sum of $\hat{\mathbf{x}}$ is unity) minimizes the underdeterminacy of the problem. This is supported by post-inverse analysis diagnostics (i.e., averaging kernels) showing that elements of $\hat{\mathbf{x}}$ are resolved by the trend data. Since $\mathbf{H}$ is drawn based on Monte-Carlo sampling, we do not have a diagnostic for the relative contributions of the prior and the data on $\mathbf{H}$. We chose the mean across 100 $\mathbf{H}$ values resulting to estimates of $\mathbf{H}\hat{\mathbf{x}}$ with the lowest RMSEs relative to the data. The changes in $\widehat{\mathbf{H}}$ relative to the $\mathbf{H_a}$ can be explored in the sectoral changes shown in Figure B4. This is especially the case for Shanghai and Shenzhen where the change in $\mathbf{H}$ is larger than the change in $\mathbf{x}$.

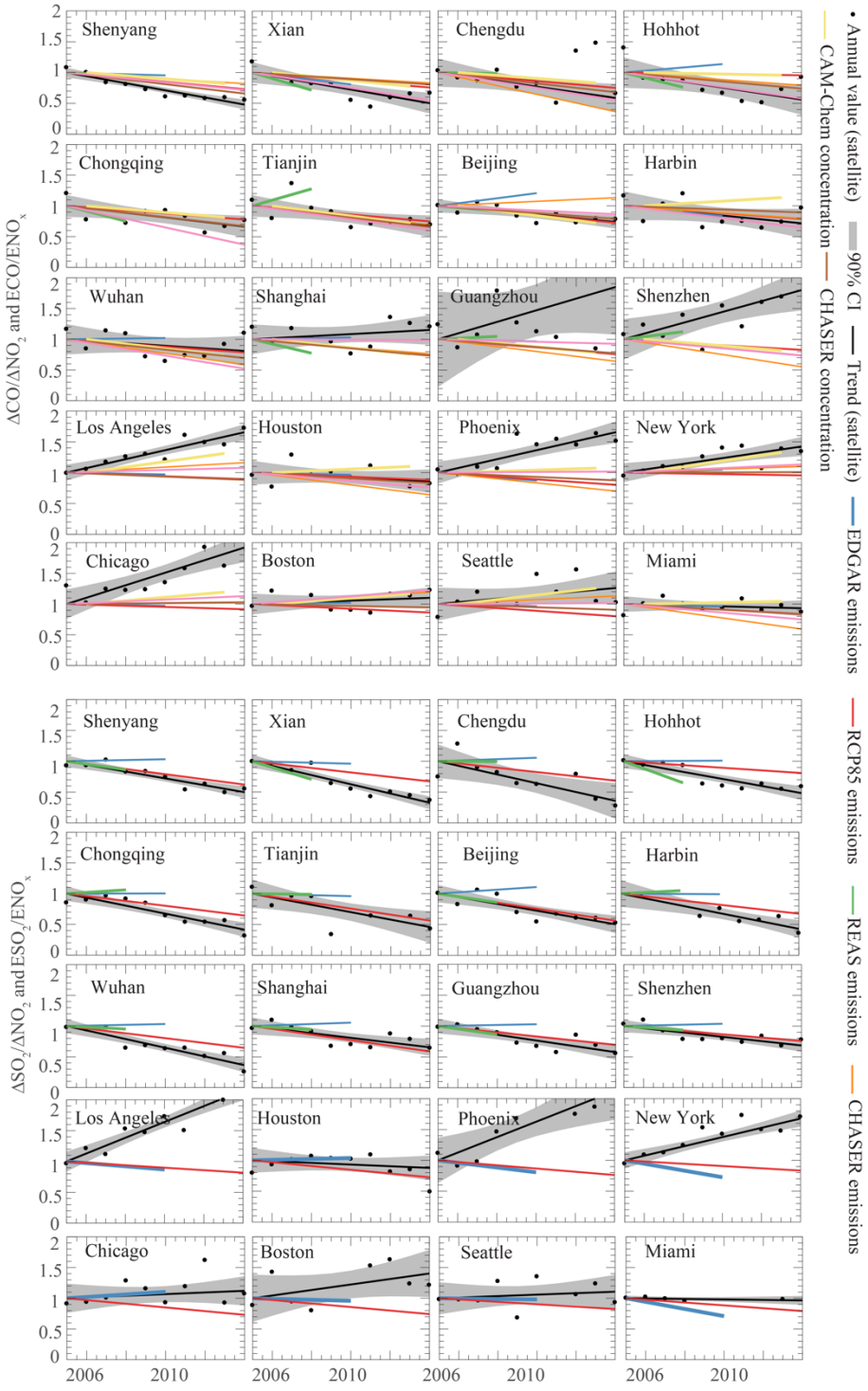

Figure. BS1. Same as Figure 3 but for all the 12 Chinese cities and 8 U.S. cities.

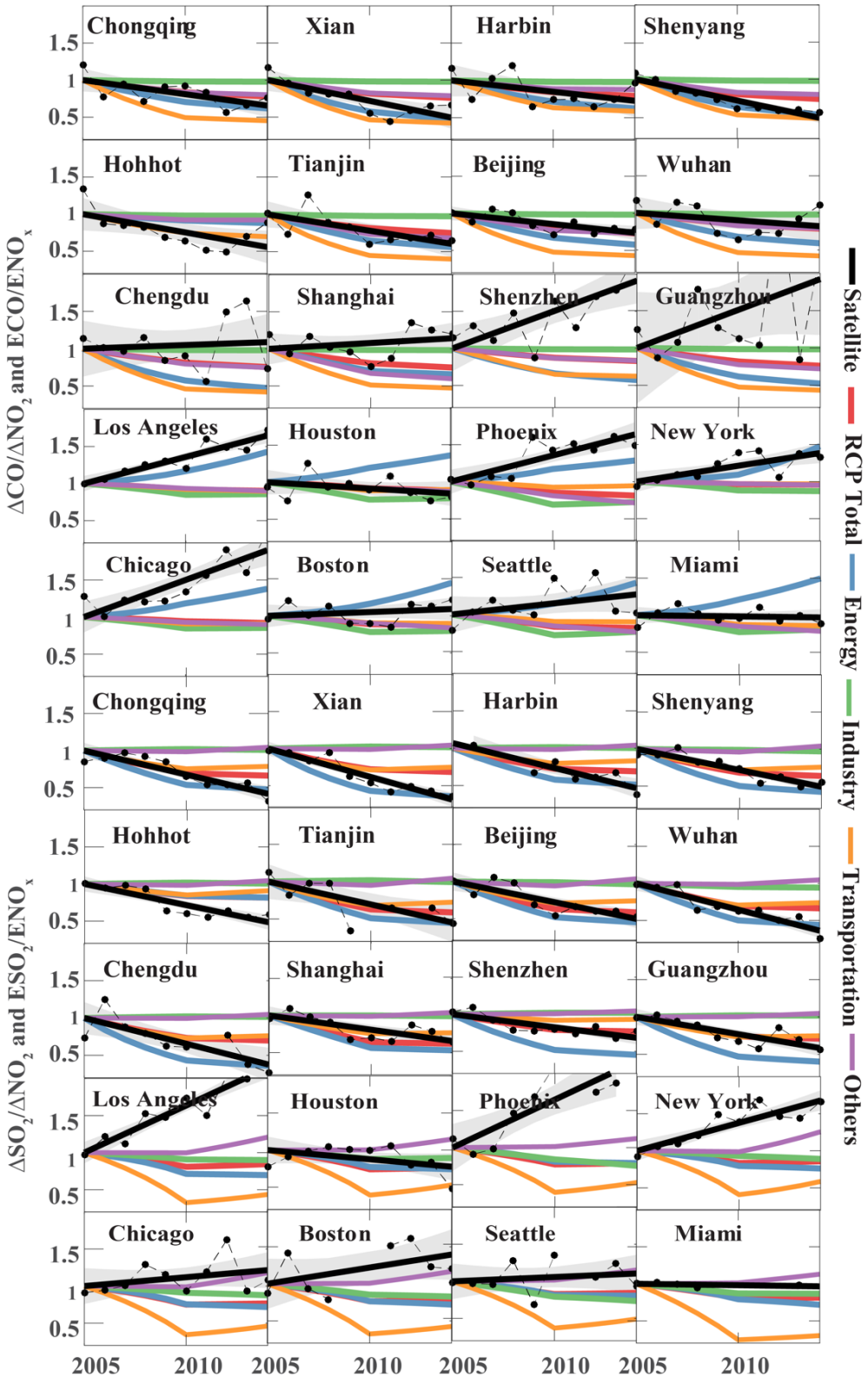

Figure. BS2. Comparisons between satellite-based ratios and sectoral emission ratios from RCP85 in 2005-2014. Gray shade corresponds to the seasonal variability of the satellite-based ratios.

APPENDIX C

EVALUATING HIGH-RESOLUTION FORECASTS OF ATMOSPHERIC CO AND CO2 FROM A GLOBAL PREDICTION SYSTEM DURING KORUS-AQ FIELD CAMPAIGN

(Published in *Atmosphere Chemistry and Physics*,
https://doi.org/10.5194/acp-2018-1121)

Wenfu Tang[1], Avelino F. Arellano[1], Joshua P. DiGangi[2], Yonghoon Choi[2,3], Glenn S. Diskin[2], Anna Agustí-Panareda[4], Mark Parrington[4], Sebastien Massart[4], Benjamin Gaubert[5], Youngjae Lee[6], Danbi Kim[6], Jinsang Jung[7], Jinkyu Hong[8], Je-Woo Hong[8], Yugo Kanaya[9], Mindo Lee[6], Ryan M. Stauffer[10,11], Anne M. Thompson[11], James H. Flynn[12], and Jung-Hun Woo[13]

[1]Dept. of Hydrology and Atmospheric Sciences, University of Arizona, Tucson, AZ, USA
[2]NASA Langley Research Center, Hampton, VA, USA
[3]Science Systems and Applications, Inc., Hampton, VA, USA
[4]European Centre for Medium-Range Weather Forecasts, Reading, UK
[5]Atmospheric Chemistry Observations and Modeling Laboratory, National Center for Atmospheric Research, Boulder, CO, USA
[6]National Institute of Environmental Research, Korea
[7]Korea Research Institute of Standards and Science, Korea
[8]Department of Atmospheric Sciences, Yonsei University, Korea
[9]Japan Agency for Marine-Earth Science and Technology, Japan
[10]Universities Space Research Association, Columbia, MD, USA
[11] Earth Sciences Division, NASA Goddard Space Flight Center, Greenbelt, MD, USA
[12]Department of Earth and Atmospheric Sciences, University of Houston, Houston, TX, USA
[13]Dept. of Advanced Technology Fusion, Konkuk University, Korea

Tang, W., Arellano, A. F., DiGangi, J. P., Choi, Y., Diskin, G. S., Agustí-Panareda, A., Parrington, M., Massart, S., Gaubert, B., Lee, Y., Kim, D., Jung, J., Hong, J., Hong, J.-W., Kanaya, Y., Lee, M., Stauffer, R. M., Thompson, A. M., Flynn, J. H., and Woo, J.-H., 2018. Evaluating high-resolution forecasts of atmospheric CO and CO2 from a global prediction system during KORUS-AQ field campaign, *Atmospheric Chemistry and Physics*, 18, 11007-11030, https://doi.org/10.5194/acp-18-11007-2018.

Abstract

Accurate and consistent monitoring of anthropogenic combustion is imperative because of its significant health and environmental impacts, especially at city-to-regional scale. Here, we assess the performance of the Copernicus Atmosphere Monitoring Service (CAMS) global prediction system using measurements from aircraft, ground sites, and ships during the Korea United States Air Quality (KORUS-AQ) field study in May to June 2016. Our evaluation focuses on CAMS CO and CO_2 analyses plus two higher resolution forecasts (16-km and 9-km horizontal resolution), to assess their capability in predicting combustion signatures over East Asia. Our results show a slight overestimation of CAMS CO_2 with a mean bias against airborne CO_2 measurements of 2.2, 0.7, and 0.3 ppmv for 16-km and 9-km CO_2 forecasts, and analyses, respectively. The positive CO_2 mean bias in the16-km forecast appears to be consistent across the vertical profile of the measurements. In contrast, we find a moderate underestimation of CAMS CO with an overall bias against airborne CO measurements of -19.2 (16-km), -16.7 (9-km), and -20.7 ppbv (analysis). This negative CO mean bias is mostly seen below 750 hPa for all three forecast/analysis configurations. Despite these biases, CAMS shows a remarkable agreement with observed enhancement ratios of CO with CO_2 over the Seoul metropolitan area and over the West Sea, where East Asian outflows were sampled during the study period. More efficient combustion is observed over Seoul (dCO/dCO_2 = 9 ppbv/ppmv) compared to the West Sea (dCO/dCO_2 = 28 ppbv/ppmv). This 'combustion signature contrast' is consistent with previous studies in these two regions. CAMS captured this difference in enhancement ratios (Seoul: 8-12 ppbv/ppmv, the West Sea: ~30 ppbv/ppmv) regardless of forecast/analysis configurations. The correlation of CAMS CO bias with CO_2 bias is relatively high over these two regions (Seoul: 0.64-0.90, the West Sea: ~0.80) suggesting that the contrast captured by CAMS may be dominated by anthropogenic emission ratios used in CAMS. However, CAMS shows poorer performance in terms of capturing local-to-urban CO and CO_2 variability. Along with measurements at ground sites over the Korean peninsula, CAMS produces too high CO and CO_2 concentrations at the surface with steeper vertical gradients (~0.4 ppmv/hPa for CO_2 and 3.5 ppbv/hPa for CO) in the morning samples than observed (~0.25 ppmv/hPa for CO_2 and 1.7 ppbv/hPa for CO), suggesting weaker boundary layer mixing in the model. Lastly, we find that the combination of CO analyses (i.e., improved initial condition) and use of finer resolution (9-km vs 16-km) generally produce better forecasts.

1. Introduction

Anthropogenic combustion significantly impacts air quality, climate, ecosystem, agriculture, and public health at local to global scales (Charlson et al, 1992; Doney et al., 2007; Feely et al., 2004; Heald et al., 2006; Maher et al., 2016). This is especially the case in megacities where human activities are most intense, accompanied by immense energy consumption, mainly in the form of fossil-fuel combustion, which directly leading to enhanced emissions of air pollutants, greenhouse gases, and waste energy. In particular, cities in the Asian region that are rapidly developing in recent decades are subject to more frequent severe pollution conditions (Yang et al., 2013; Guo et al., 2014; Ohara et al., 2007; Shindell et al., 2008, 2011). It is imperative therefore that we enhance our current capability to monitor, verify, and assess anthropogenic combustion and its impacts as the number of megacities across the globe is expected to rapidly grow in the following decades (United Nations, 2016). The Copernicus Atmosphere Monitoring Service (CAMS) has a state-of-art global and integrated prediction systems that is currently being implemented to meet this need. The Service is funded by the European Union and it builds upon a legacy of projects such as the Monitoring Atmospheric Composition and Climate (MACC) and GEMS (Hollingsworth et al, 2008).

For nearly a decade, CAMS has been operationally producing daily global near-real-time forecasts and analyses of reactive trace gases, greenhouse gases, and aerosols including global reanalyses and estimation of emissions of these atmospheric constituents (Morcrette et al., 2009; Benedetti et al., 2009; Kaiser et al., 2012; Flemming et al., 2015; Flemming et al., 2017; Massart et al., 2016; Agustí-Panareda et al. 2014, Agustí-Panareda et al. 2017). CAMS global forecasts and analyses are based on the Integrated Forecasting System (IFS) of the European Centre for Medium-Range Weather Forecasts (ECMWF), which is also used for Numerical Weather Prediction (NWP). CAMS recently developed 2 forecasts at higher resolution, which have potential advantages compared to lower resolution analysis and/or forecast, in terms of local-to-regional air quality (Table C1).

The Korea United States Air Quality (KORUS-AQ) field measurement campaign offers a unique opportunity to assess the accuracy and consistency of the high resolution forecast and analysis system of CAMS and its skill in simulating atmospheric CO_2 from anthropogenic combustion.

During May to June 2016, the KORUS-AQ field campaign collected comprehensive measurements of air quality (including CO_2 and tracers of fossil-fuel combustion) over the South Korean peninsula and its surrounding waters. KORUS-AQ is an international collaboration between U.S. and South Korea to better understand the factors controlling air quality in the region across urban, rural, and coastal interfaces (Kim and Park, 2014, KORUS-AQ White Paper). This field campaign follows several NASA-led sub-orbital missions in the past focusing on air quality in the United States (e.g., DISCOVER-AQ, SEAC^{4}RS), and pollution outflows from Asia (e.g., TRACE-P, INTEX-B, ARCTAS) and integrating the measurements from these campaigns to satellite retrievals and air quality models (Crawford et al., 2014; Toon et al., 2016; Jacob et al., 2003; Singh et al., 2009; Jacob et al., 2010). Local measurements over the West Sea, often representative of Chinese pollution outflow, and over the Seoul metropolitan area provide a rich dataset that is very useful in evaluating global prediction and analysis systems like CAMS at city-to-regional scale.

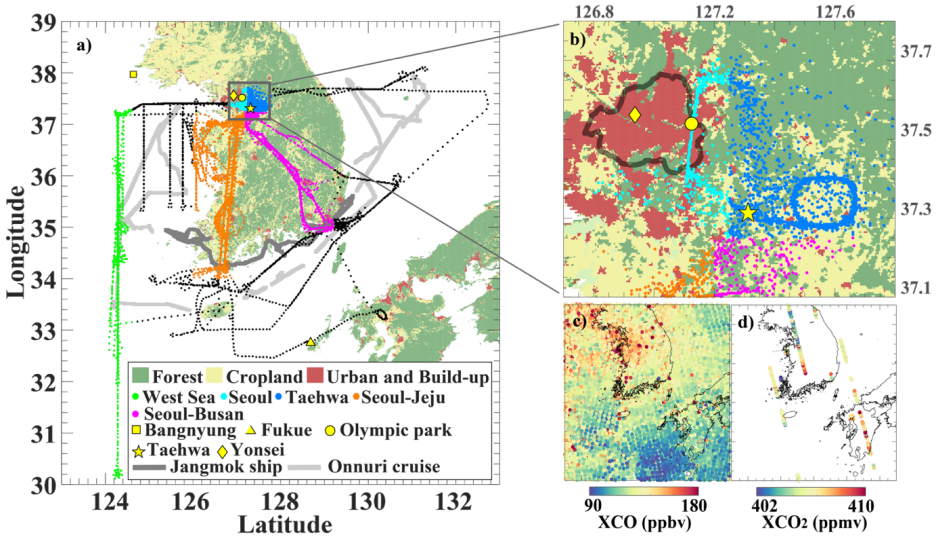

Figure C1. Domain of the study and KORUS-AQ measurements used in this study. Panel (a) shows land cover of the domain (Broxton et al., 2014), DC-8 aircraft tracks, ship tracks, and location of ground sites. The airborne measurements are classified into 5 groups (the West (Yellow) Sea, Seoul, Taehwa, Seoul-Jeju jetway, and Seoul-Busan jetway), as marked in bright green, bright blue, mazarine blue, orange, and magenta. The ground sites are labelled with bright yellow markers. Olympic Park and Yonsei sites are located in urban regions (Seoul) while Baengnyeong and Fukue (Kanaya et al., 2016) site are located in remote regions. Taehwa (Kim et al., 2013) site is located in a forest nearby Seoul. Tracks of the two ships are marked in dark grey (Jangmok ship) and light grey (Onnuri ship). Also shown in (b) is the zoomed-in version of the grey box in panel (a). Panel (c) shows a composite MOPITT XCO retrievals during KORUS-AQ campaign while panel (d) shows OCO-2 XCO_2 retrievals in the same time period.

In this study, we evaluate CAMS forecast and analysis of fossil-fuel combustion signatures over the KORUS-AQ spatial and temporal domain. In particular, we use measurements of the main products of combustion (i.e., CO and CO_2) from the NASA DC-8 aircraft, along with observations from five ground sites, two research ships, and four satellites to assess the capability of CAMS to monitor anthropogenic combustion. Although CAMS CO and CO_2 forecasts and analyses have been evaluated previously (Agustí-Panareda et al., 2014; Agustí-Panareda et al., 2016; Agustí-Panareda et al., 2017; Claeyman et al., 2010; Massart et al., 2016; Flemming et al., 2009; Flemming et al., 2015; Flemming et al., 2017), this study is unique for the following reasons: (1) This study is a joint evaluation of CO and CO_2 species, including their associated enhancement ratios which provide insights on CAMS representation of anthropogenic combustion processes; (2) A focus on megacities provides an important baseline investigation. This is especially the case in East Asia where there is still lack of detailed information and measurements to constrain emission inventories; (3) KORUS-AQ provides a unique opportunity to evaluate the new high resolution global CAMS forecasts of CO and CO_2 at local-to-regional scale. This paper begins with a brief description of CAMS and KORUS-AQ (Section 2), followed by an evaluation of CAMS with airborne measurements (Section 3) and with ground sites, ships, and satellites (Section 4). We provide a summary of our findings in Section 5.

2. Descriptions of CAMS and KORUS-AQ CO and CO_2

2.1 CAMS CO and CO_2 Forecasts and Analysis

The Copernicus Atmosphere Monitoring Service (CAMS) has been providing global forecasts and analysis of atmospheric composition on a daily basis at ECMWF for nearly a decade with applications on air quality and monitoring of long-lived greenhouse gases. CAMS uses the Integrated Forecasting System (IFS) for Numerical Weather Prediction (NWP) to assimilate a wealth of meteorological observations plus satellite products of atmospheric composition to produce atmospheric analysis of reactive gases (e.g. CO, O_3, NO_2, SO_2), aerosols and long-lived greenhouse gases (e.g. CO_2, CH_4) on the NWP model grid which are then used as initial conditions to forecast the atmospheric composition with a 5-day lead time. The IFS simulates transport of the chemical species (Flemming et al. 2009, Agusti-Panareda et al. 2017) and includes the on-line integration of modules for atmospheric chemistry (Flemming et al. 2015, 2017) and biogenic CO_2

fluxes from terrestrial vegetation (Boussetta et al., 2013) to model atmospheric composition in conjunction with an assimilation system based on four-dimensional variational (4D-VAR) data assimilation (Rabier et al., 2000; Inness et al., 2015). The CAMS global atmospheric analysis and prediction system runs at different resolutions and at a different lag times for the various atmospheric species depending on the use of chemistry in the model and the timeliness of the satellite retrievals used in the analysis. The system providing reactive trace gases and aerosols runs at approximately 80 km horizontal resolution with 60 vertical levels and its analysis is available less than 1-day behind real time. While higher horizontal and vertical resolution is used for the analysis and forecasts of greenhouse gases, the analysis of CO_2 and CH_4 is available at around 40 km in the horizontal and 137 vertical levels. Currently the forecasts of CO_2 and CH_4 have the same resolution as the operational weather forecast at ECMWF (137 levels with 9 km horizontal resolution) but previously their resolution was 16 km (from 2015 to 2016). A CO tracer with simplified chemistry based on a linear CO scheme (Massart et al., 2015) is also available in the high resolution forecasts. However, the CO_2 and CH_4 analysis is only available four days behind real time as the satellite retrievals are not available closer to real time. Because of this, in the 16-km resolution forecast, CO_2, CH_4 and linear CO are free running and only the meteorology is initialised with the meteorological operational analysis (see Agusti-Panareda et al. (2014) for further details on the free-running forecast configuration). Following a recent improvement in the timeliness of the satellite retrievals, the linear CO is initialised with CO analysis, while CO_2 and CH_4 are initialised with a 4-day forecast from the CO_2 and CH_4 40 km analysis in the 9-km forecasts. In order not to lose the small-scale features in the initialization process, a spectral filter is applied to only adjust the large scales in the initial conditions of the forecast (Massart, 2016, personal communication). Table C1 (as well as Fig. CS1) provides a summary of the three CAMS configurations and five resulting CAMS products evaluated in this paper and Fig. CS2 depicts the different vertical and horizontal resolutions used in the different CAMS configurations.

For this study, we focus on evaluating the three CO and CO_2 forecasts and analysis products listed above, namely, CO_2 and CO 16-km forecast (FC16s), analyses (ANs) of CO_2 (at 40 km) and CO (at 80 km), and a relatively recent CAMS 9-km CO_2 and CO forecast product (FC9s) which are initialized from its respective analysis. The FC9s are different from FC16s in terms of both resolution and initialization as described above (e.g. the FC16s are produced from a free-running simulation of CO_2 and CO). The near-real time ANs of CO and CO_2 are also different from FC16s

and FC9s as these ANs continuously assimilate satellite retrievals of CO total column from Measurements Of Pollution In The Troposphere (MOPITT V5-TIR) and the Infrared Atmospheric Sounding Interferometer (IASI) (Inness et al., 2015), and column averaged dry-air mole fractions of CO_2 (XCO_2) from the Greenhouse gases Observing Satellite (GOSAT) (Massart et al., 2016), in addition to the available meteorological data. Observations of both CO and CO_2 are assimilated in 12-hour assimilation windows. Inness et al. (2015) found that CO total column field, vertical distribution, and concentrations in the lower troposphere are improved by assimilating the CO total column from MOPITT. Assimilation of the GOSAT XCO_2 lead to improvements in mean absolute error and bias variability in XCO_2 fields during the year 2013 (Massart et al., 2016). FC9s CO are initialized from MOPITT and IASI CO analysis at a previous time, which are then downscaled from 80 km to 9 km by a spectral filtering scheme. Due to observational and computing constraints, FC9s of CO_2 are initialized and downscaled from a 96-hour forecast of CO_2 initialized by GOSAT analysis 4 days earlier.

The IFS contains several components, including an atmospheric general circulation model, a land surface model, an ocean wave model, an ocean general circulation model, and perturbation models for the data assimilation and forecast (Persson, 2001). Model dynamics and numerical procedures, and physical processes are documented in IFS documentation-Cy43r3 (ECMWF, 2017, https://www.ecmwf.int/search/elibrary/part?title=part&year=2017&secondary_title=IFS).
Detailed cloud and precipitation physics of the IFS benefits the calculation of wet deposition (Flemming et al., 2017). As for emissions and surface fluxes, CAMS uses the Global Fire Assimilation System (GFAS) for biomass burning fluxes of CO_2 (Kaiser et al., 2012). CAMS uses the anthropogenic CO_2 fluxes that are based on the annual mean of the Emission Database for Global Atmospheric Research version 4.2 (EDGARv4.2). As the most recent year available for EDGARv4.2 is 2008, estimated and climatological trends are used to extrapolate to the years after 2008. The land vegetation fluxes for CO_2 are calculated online by the carbon module of the land surface model in IFS CTESSEL (Boussetta et al., 2013). A biogenic flux adjustment scheme (BFAS) is employed in CAMS to improve the continental budget of CO_2 fluxes (Agustí-Panareda et al., 2014; Agustí-Panareda et al., 2015; Agustí-Panareda et al., 2016). Specifically, (1) BFAS computes the scaling factors for the model net ecosystem exchange (NEE) based on reference (NEE climatology from the optimized fluxes); (2) the scaling factors are used to adjust biogenic CO_2 fluxes from the land surface model (i.e., flux bias correction); (3) the bias-corrected fluxes

are then used to simulate the atmospheric CO_2. According to Agustí-Panareda et al. (2016), in Northern Asia, the employment of BFAS slightly decreases NEE in May and has negligible impacts on NEE in June. CO_2 overestimation by CAMS over the Northern Hemisphere (NH) in winter and spring is enhanced by BFAS. For CO, CAMS uses anthropogenic and biogenic emissions that are based on the MACC/CityZEN EU projects (MACCity) (Granier et al., 2011), and a climatology of the Model of Emissions of Gases and Aerosols from Nature developed under the MACC (MEGAN-MACC) emission inventories (Sindelarova et al., 2014). GFAS is also used for fire emissions. ANs for CO use the on-line implemented chemical mechanism (C-IFS-CB05, Flemming et al., 2015) that is an extended version of the Carbon Bond mechanism 5 (CB05, Yarwood et al., 2005). Because hydroxyl radical (OH) is an important sink for CO, modeled OH is critical for the simulation of CO (Gaubert et al., 2016, 2017). In the ANs for CO, the global and NH means of air mass-weighted OH are 0.98×10^{-6} molecules/cm^3 and 1.20×10^{-6} molecules/cm^3 during May 2016, respectively (calculated following recommendations from Lawrence et al. (2001)). The mean OH from the ANs for CO is consistent with previous studies (e.g., Lawrence et al., 2001; Lelieveld et al., 2016; Gaubert et al., 2016, 2017). A linear chemistry scheme is (C-IFS-LINCO) used in FC16s and FC9s for CO for computationally expediency (Claeyman et al., 2010; Flemming et al., 2012; Massart et al. 2015; Eskes et al., 2017). C-IFS-LINCO computes CO sources and sinks using the approach developed by Cariolle and Déqué (1986) and updated by Cariolle and Teyssèdre (2007), without direct use of modeled OH. C-IFS-LINCO is less computationally demanding than the full chemistry, permitting simulations at higher resolutions (Massart et al. 2015). Key aspects of the three CAMS configurations evaluated in this study are listed in Table C1.

2.2 CO and CO_2 Measurements during KORUS-AQ

KORUS-AQ is a comprehensive field campaign based on international collaboration between U.S. and South Korea (https://espo.nasa.gov/korus-aq). The goal is to better understand the factors controlling air quality (AQ) in the region across urban, rural, and coastal interfaces. The field campaign was conducted over the South Korean peninsula and surrounding waters from May to June 2016. the South Korean peninsula and its surrounding waters is a desirable region to conduct the campaign because: (1) Korea's urban/rural sectors are distinct, which is advantageous for distinguishing anthropogenic and natural emissions; (2) Korea is embedded in a rapidly changing

region; (3) the region allows studies of local versus trans-boundary pollution; and (4) air quality monitoring and ground-based measurements are provided by Korea. AQ measurements (including CO_2) from aircrafts, ships, and ground sites were obtained during this period. The campaign was designed to answer three scientific questions: (1) what are the challenges and opportunities for satellite observations of air quality; (2) what are the factors governing ozone photochemistry and aerosol evolution; (3) how well do models perform and what improvements are needed to better represent atmospheric composition over Korea and its connection to the larger global atmosphere (Kim and Park, 2014, KORUS-AQ White Paper). Fig. C1 shows the study domain ($30°\mathrm{N}-39°\mathrm{N}, 123°\mathrm{E}-133°\mathrm{E}$) along with the tracks from DC-8 aircraft flights and research ship deployments. The locations of ground sites are also added in Fig. C1. Satellite retrievals from MOPITT CO and Orbiting Carbon Observatory-2 (OCO-2) CO_2 are shown in Fig. C1 to provide spatial context and coverage of remote sensing measurements during the campaign. All the observational data used in this study are summarized in Table C2.

2.2.1 Airborne CO and CO_2 Measurements

We use measurements of CO_2 and CO from the DC-8 aircraft. CO_2 was measured by Atmospheric Vertical Observations of CO_2 in the Earth's Troposphere (AVOCET) using a modified LI-COR model 6252 non-dispersive infrared spectrometer (NDIR). This instrument provides CO_2 concentrations with high precision by sensing the difference in light absorption between the continuously flowing sample and reference gases (Vay et al., 2003, 2011; https://airbornescience.nasa.gov/instrument/AVOCET). CO_2 1 Hz 1σ precision and accuracy are ±0.1 ppm and ±0.25 ppm, respectively. CO was measured by the Differential Absorption CO Measurement (DACOM) instrument via infrared wavelength modulation spectroscopy. The system uses three tunable diode lasers providing 4.7, 4.5, and 3.3 μm radiation for accessing absorption lines of CO, N_2O, and CH_4. The time response for CO measurements is 1 s; the precision is < 1% or 0.1 ppbv; the accuracy is 2% (Warner et al., 2010; https://airbornescience.nasa.gov/instrument/DACOM). Calibrations for both instruments were performed during flight at regular intervals using gas standards traceable to the WMO scale (CO_2: x2012; CO: x2008) and certified by NOAA ESRL. Details about the two instruments are listed in Table C2. Note that we use the 1 min (60 s) merged DC-8 data in this study. The data are available at NASA Langley Research Center archive (www-air.larc.nasa.gov/missions/korus-aq/).

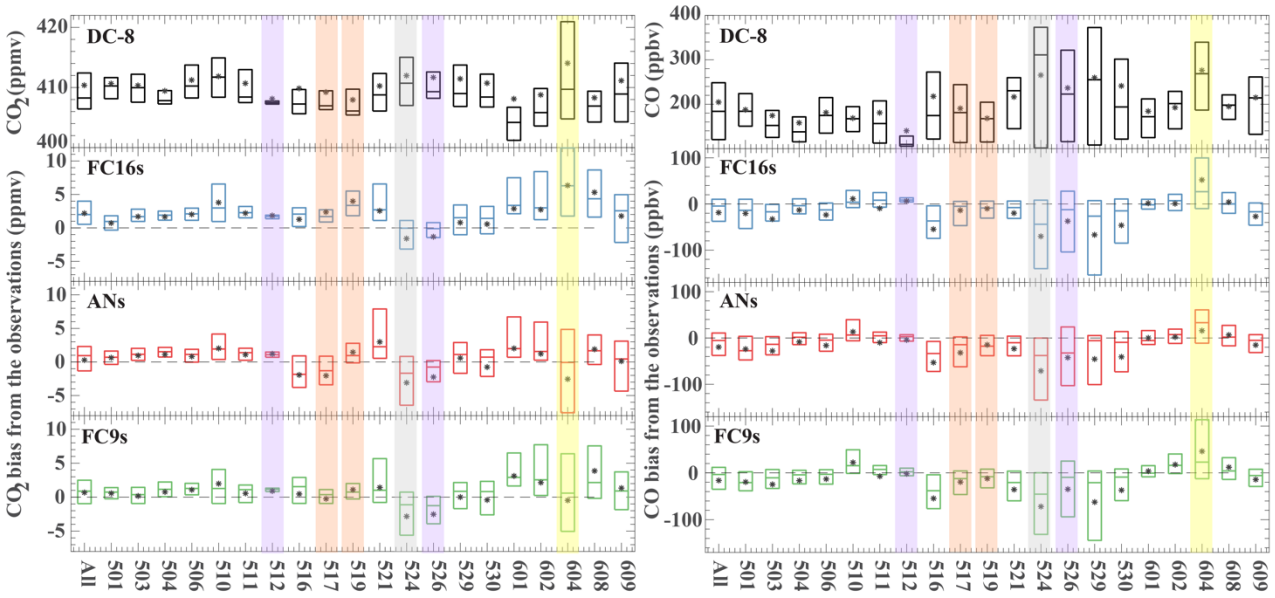

Figure C2. Boxplot for each individual flight. The flight date (MDD) for each boxplot is indicated in the bottom x-axis. Note that the dates here are in UTC time instead of Korea time. The left panel is for CO_2 and the right panel is for CO. The first row corresponds to the boxplot of the abundances measured by DC-8 aircraft. The second, third, and fourth rows correspond to the boxplot of the bias of FC16s, ANs, and FC9s relative to the DC-8 aircraft data, respectively. The purple shade marks the flights with frontal passage, and orange shade marks the flights that may possibly be affected by biomass burning. The grey shade marks the flight measuring China outflow while yellow shade marks the flight surveying point emission sources.

There were 20 formal DC-8 science flights. Note that for time reference, the 'Date' in this paper refers to the day on which the flight started in UTC time instead of Korean local time, unless the term 'Local time' is explicitly used. This 'date' in UTC time is one day behind Korea local time as all flights typically start at 8am local time. We also divide the flight measurements into five groups based on the land cover below the flight tracks and types of pollution sources with which they can be broadly associated with. These groups are classified as: Seoul metropolitan, Taehwa, the West (Yellow) Sea, Seoul-Jeju jetway and Seoul-Busan jetway (Please refer to Fig. C1 for an illustration of these flight groups). The Seoul metropolitan represents air samples over the large city of Seoul which can have a dominant signature from anthropogenic combustion processes. On the other hand, Taehwa represents air samples over a forest area near Seoul, which can be influenced by both surface carbon fluxes from the local forest as well as anthropogenic emissions from Seoul. Measurements over the West Sea were designed to capture China pollution outflows. The flight tracks over the West Sea were typically zonal tracks forming a 'wall' between China

and Korea (see Fig. C1). These flights are conducted only when a China outflow is expected to be present based on weather and AQ forecasts during the campaign. These measurements enable us to investigate combustion signatures from China and differentiate them from Seoul. The Seoul-Jeju jetway and Seoul-Busan jetway groups are two jetway flights on which the DC-8 aircraft frequently obtain measurements. The two jetways are both above the Korean peninsula, connecting Seoul to Jeju and Busan, respectively. Flights in Seoul-Busan jetway is designed to capture activities in forest, rural, and Busan urban regions. The flights in Seoul-Jeju jetway, on the other hand, sample air over local power plants, transported air from the West Sea, and over nearby croplands. We will discuss our evaluation CAMS for each of these five groups in Section 3.

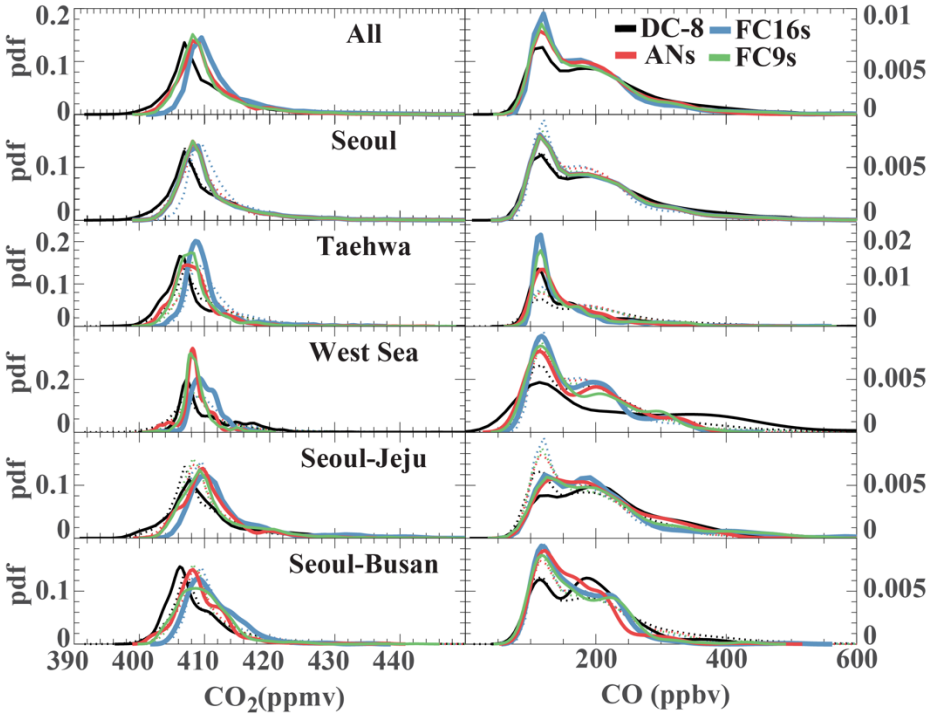

Figure C3. Probability density functions (pdfs) of CO_2 and CO for each flight group. Solid lines are pdfs for each group while the dashed lines are pdfs for all groups.

2.2.2 Ground-based CO and CO_2 measurements

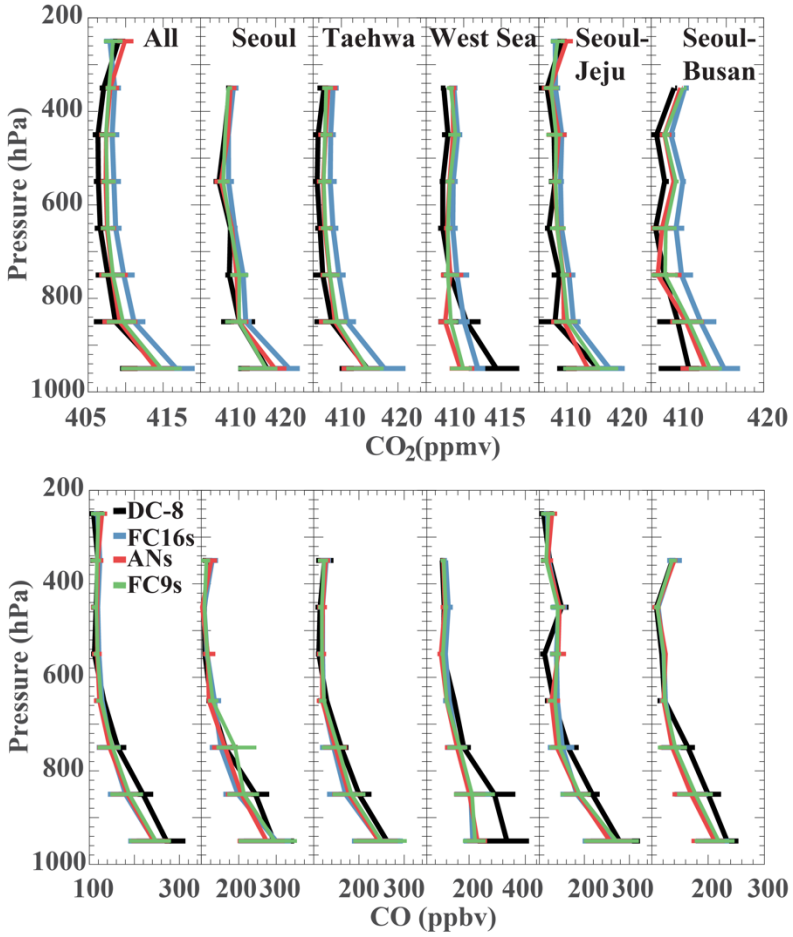

Figure C4. Averaged vertical profiles of CO_2 and CO mixing ratios from the DC-8 aircraft data and CAMS for each flight group. Horizontal bars correspond to the interquartile ranges (between 25th and 75th percentiles) of the layer bin.

Observations from the following ground sites are used for comparison with CAMS CO and CO_2: Baengnyeong, Fukue, Olympic Park, Taehwa, and Yonsei University (see Fig. C1 for the site locations). The sites in Baengnyeong and Taehwa are managed by the National Institute of Environmental Research (NIER). The Baengnyeong site is located on the sparsely populated Baengnyeong Island, Incheon, northwest of Seoul. The Fukue site belongs to the Japan Agency for Marine-Earth Science and Technology (JAMSTEC) and is located on the remote island of Fukue, Japan (Kanaya et al., 2016). The Olympic Park and Yonsei University sites belong to Korea Research Institute of Standards and Science and Yonsei University, respectively. Both sites are located within the Seoul Metropolitan area. These five ground sites cover different environments,

which allows us to differentiate between urban (Olympic Park and Yonsei University) and remote (Baengnyeong and Fukue) air quality conditions during the campaign. The sites in Baengnyeong, Fukue, and Olympic Park provide measurements of CO (in ppbv), while the site in Yonsei University provides measurements of CO_2 (in ppmv). Only the site in Taehwa provides measurements of both CO (in ppbv) and CO_2 (in mg/m^3) (Kim et al., 2013). Locations of the five sites, and corresponding instruments and data intervals are provided in the Table C2. Note that we use data from these sites taken during the KORUS-AQ campaign period to provide the ground context of our evaluation.

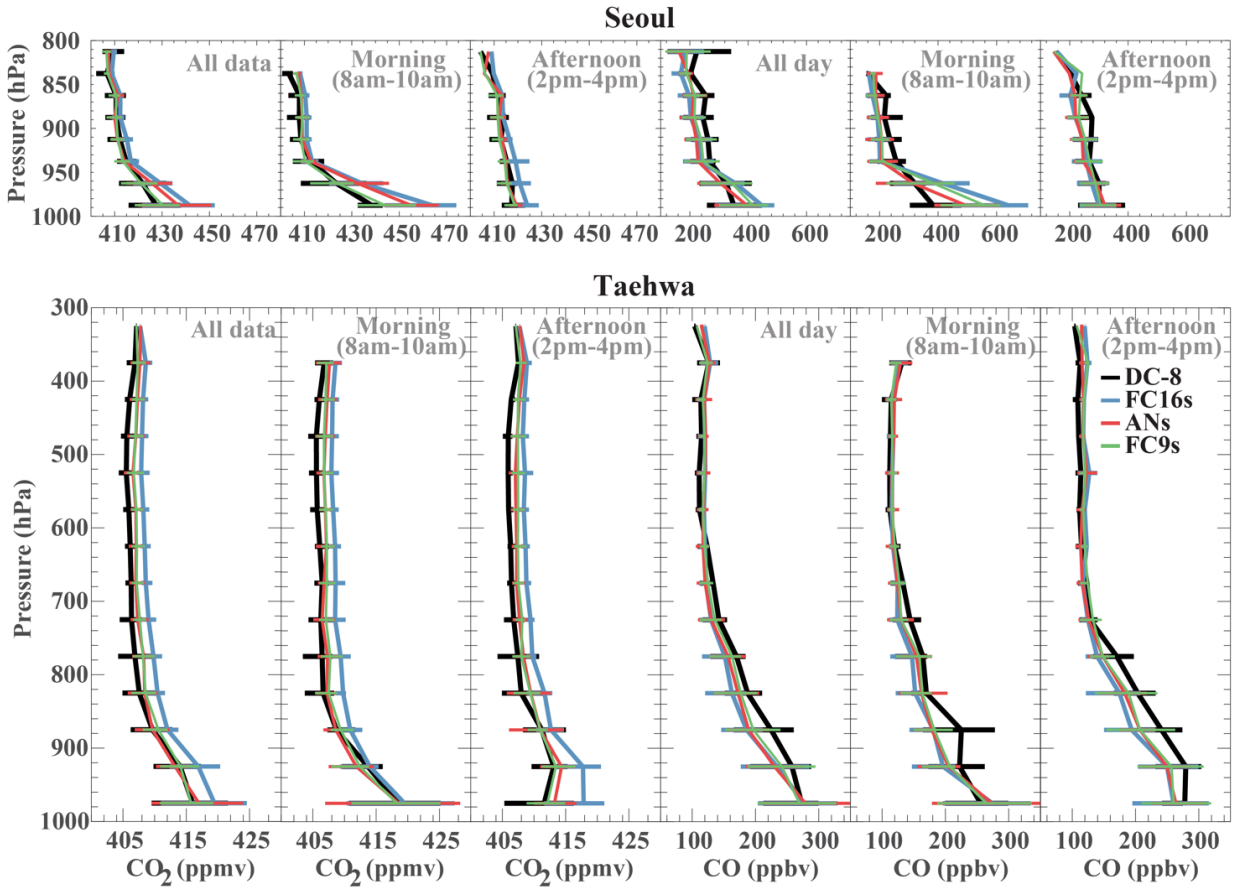

Figure C5. Temporal variation of averaged vertical profiles of CO_2 and CO mixing ratios from the DC-8 aircraft data and CAMS over Seoul and Taehwa flight groups. The first, second, and third columns are averaged CO_2 profiles for all day, morning (8-10am), and afternoon (2-4pm), respectively. Horizontal bars correspond to interquartile ranges (between 25th and 75th percentiles) of the profiles. The fourth, fifth, and sixth column are the same as the first three columns but for CO.

2.2.3 Ship Observations

We use ship measurements of CO from Jangmok and Onnuri. Both of them are research vessels owned by Korea Institute of Ocean Science and Technology. The ship deployments are part of the Korea-United States Ocean Color (KORUS-OC) field study coinciding with KORUS-AQ. KORUS-OC was led by NASA and the Korean Institute of Ocean Science and Technology, focusing on the ocean color, biology and biogeochemistry as well as atmospheric composition in coastal waters adjacent to Korea (https://www.asp.ucar.edu/sites/default/files/4_Emmons_07_27_2016.pdf). The two ships sailed along the Korean coast from May 20th to June 5th. Tracks of the two ships are shown in Fig. C1 by dark grey (Jangmok) and light grey (Onnuri). CO measurements in Jangmok and Onnuri were taken from the Thermo 48i-TLE CO analyzer and Thermo 48C CO analyser, respectively (http://www.kiost.ac.kr/kor.do), and are provided every minute.

2.2.4 Satellite-derived CO and CO_2 Retrievals

We use four sets of satellite-derived measurements for comparison with CAMS CO and CO_2. We use retrievals of CO_2 column-averaged dry air mole fraction (XCO_2) from NASA OCO-2, version 7, Level 2 (L2) full product with the standard quality flag and warn level ≤15 (Crisp et al. 2004; Boesch et al., 2011; Wunch et al. 2011a, 2011b, 2017; Osterman et al., 2015; Mandrake et al., 2015; https://oco.jpl.nasa.gov/). and from Japan Aerospace Exploration Agency (JAXA) GOSAT, Level 2 (L2), version 2 (Yokota et al., 2004, 2009; Morino et al., 2011; Crisp et al. 2012; http://global.jaxa.jp/projects/sat/gosat/). Short-wavelength Infrared observations measured by the Thermal And Near-infrared Sensor for carbon Observation (TANSO) onboard the GOSAT satellite are used to retrieve XCO_2. OCO-2 also has three specific Near Infrared (NIR) wavelength bands to retrieve XCO_2 (https://oco.jpl.nasa.gov/). For CO, we use the NASA Terra MOPITT version 6, Level 2, multispectral (Thermal Infrared/Near Infrared; TIR/NIR) total column retrievals (MOP02J, L2, V6) with the standard quality flag. Compared to thermal infrared only retrievals (TIR), these retrievals have an enhanced sensitivity to the lower tropospheric CO (Deeter et al., 2014; https://www2.acom.ucar.edu/mopitt). In addition, we also use total column mole fractions of CO from IASI, Level 2 data with the standard quality flag (George et al., 2009; Clerbaux et al., 2009). IASI is on board MetOp-A and B satellites and uses Fast Optimal Retrievals

on Layers for IASI (FORLI) to retrieve CO distributions from the thermal infrared (TIR) spectra. We applied the associated averaging kernels from MOPITT and IASI to CAMS CO before comparison as these retrievals exhibit large sensitivities in the free troposphere. We also note that both IASI and MOPITT have significantly more observations than OCO-2 and GOSAT. As summarized in Table C2, the resolutions of OCO-2, GOSAT, MOPITT, and IASI are 2.25×1.29 km, 10.5×10.5 km, 22×22 km, and 12×12 km, respectively. The overpass times for the four satellites are also different. OCO-2 overpasses at 1:18 - 1:33 pm, GOSAT overpasses at around 1 pm. Overpass time is 10:30 am for MOPITT, and 9:30 am for IASI. Uncertainties have also been reported for these satellite products. OCO-2 XCO_2 has uncertainties of 1-2 ppm (Boesch et al., 2011) while GOSAT XCO_2 has retrieval errors of 2 ppm (Griffith et al. 2011; Crisp et al. 2012). Deeter et al. (2014) reported 0.09×10^{18} molecules/cm^2 for total column retrieval for MOPITT. Wachter et al. (2012) reported uncertainties to be <13% for IASI FORLI.

3. Comparison with Airborne Measurements

Here, we evaluate CAMS forecasts and analysis of CO and CO_2 with NASA DC-8 aircraft observations. We interpolate the 4-D fields of CAMS CO and CO_2 model output to collocate with flight measurements in both space and time. The equivalent model data for all flights and for the three configurations (FC16s, FC9s, ANs) are made available in the same file format as the 1-min merged DC-8 dataset to facilitate model to observation comparison. We also estimate enhancement ratios of CO and CO_2 from both airborne and model data and analyse its spatial and temporal variations across different flights. We present in the following subsections the summary statistics of our comparison of CAMS data with the DC-8 aircraft data.

3.1 Performance across All Flights

Across all flight data, CAMS overestimates CO_2, with mean biases of 2.2, 0.7, and 0.3 ppmv for FC16s, FC9s, and ANs, respectively. Agusti-Panareda et al. (2016) also suggested CO_2 is overestimated by CAMS in the NH at the end of winter and throughout spring. In contrast, CAMS underestimates CO with mean biases for FC16s, FC9s, and ANs against the DC-8 aircraft data of -19.2, -16.7, and -20.7 ppbv, respectively. The mean bias is calculated as the average across all data of CAMS minus the DC-8 aircraft data. We also find that the overall pairwise correlation between the DC-8 aircraft data and CAMS is moderately high (CO_2: 0.52–0.57, CO: 0.65–0.73)

while the root-mean-square-errors (RMSEs) in CAMS relative to the DC-8 aircraft data are about 7 ppmv for CO_2 and 80 ppbv for CO. These statistics can be summarized using a Taylor diagram as shown in Fig. CS3 and Fig. CS4 of the supplementary material. We also calculated the associated Taylor scores to summarize the skill of CAMS in capturing the observed CO_2 or CO variations. Taylor score (Taylor, 2001) is defined by

$$S = \frac{4(1+R)}{(\hat{\sigma}_f + 1/\hat{\sigma}_f)^2(1+R_0)} \quad (C1)$$

where $\hat{\sigma}_f$ is the ratio of σ_f (standard deviation of the model) and σ_r (standard deviation of observations), R is correlation between model and observations, and R_0 is the maximum potentially realizable correlation (= 0.9 in this study).

We find that CAMS has relatively good skill regardless of configuration: for CO_2, the skill scores are 0.82 (FC16s), 0.82 (FC9s), and 0.75 (ANs); while for CO, the skill scores are 0.85 (FC16s), 0.86 (FC9s), and 0.83 (ANs). However, it is important to note that these statistics can vary from flight to flight and the skill for CO_2 is not necessarily related to that of CO. For instance, for the May 10th flight, where a southern peninsula outflow was expected, CAMS ANs show higher skill than those from FC9s in terms of both CO_2 and CO, while the scores of FC16s are higher than those of FC9s in terms of CO (Fig. CS5). Yet, for the May 3rd flight, where a weak Chinese influence was expected, the scores of FC16s and FC9s are higher for CO_2 than CO, while we find the opposite for the June 2nd flight, where the DC-8 aircraft sampled local influences. Lastly, we note that the skill of CAMS during the June 4th flight is not high for either species. This flight was designed to measure local point sources with large variations at much finer scales.

3.2 Performance across Individual Flights

We present in Fig. C2 the summary statistics of CAMS against the DC-8 aircraft data for all 20 individual flights. This is shown in the second to fourth rows of Fig. C2 as boxplots of the bias for FC16s, ANs and FC9s, respectively. We also show the boxplot of the airborne measurements of CO_2 (first row left column) and CO (first row right column) for each flight as points of comparison. The overall mean, median, interquantile range (IQR), and standard deviation (sigma) of the airborne measurements of CO_2 mixing ratios (in ppmv) are 410.37, 408.25, 5.97, and 7.73 respectively. The overall mixing ratio, which varies within 1 to 2 percent, are slightly higher than

the month median observed in Mauna Loa (NOAA https://www.esrl.noaa.gov/gmd/ccgg) for May 2016 (408±1 ppmv). For the airborne measurements of CO mixing ratios (in ppbv), the corresponding statistics (mean: 204.59, median:183.90, IQR:127.97, sigma: 101.74) show enhanced CO (and larger variance) than the background value observed in Mauna Loa (100±24 ppbv). In general, CAMS overestimates CO_2 and underestimates CO for most flights. Differences also exist among the 20 flights in terms of both measured mixing ratios and model biases from the DC-8 aircraft. For flights with higher observed variances, CAMS biases and the corresponding variance of the biases tend to be also larger. This is related to variations in weather conditions during the campaign along with variations in sampling goals of the science flights. For example, parts of flight tracks on May 3rd, May 17th, May 24th, May 29th, and May 30th were specifically designed to capture Chinese pollution outflow. In these days, the variances in CAMS biases for CO (but not CO_2) are generally larger than the average except for the flight tracks on May 3rd when Chinese influences were expected to be weak. The colored shades in Fig. C2 indicate flights for 'special conditions'. The grey and yellow shades indicate two special cases that we study in detail in later sections. In particular, DC-8 flew a 'wall' over the West Sea on May 24th to investigate the transport of Chinese pollution. On June 4th, DC-8 flew near Seoul to measure pollution from local point sources (e.g., power plants). The other shades indicate that the flights were conducted during a frontal passage (purple) and that the flights may possibly be affected by fires in Siberia (orange). These flights were not further analyzed in this study since for example the May 26th flight (with frontal passage influence) and the May 17th and May 19th flights (with possible fire influence) do not clearly stand out from the other flights (see Fig. C2).

3.3 Performance across Flight Groups

Here, we evaluate CAMS per flight group as described in section 2.2.1. We show in Fig. C3 the probability density functions (pdfs) of CO and CO_2 for the DC-8 aircraft data and CAMS per flight group. The pdf of CAMS CO_2 (which exhibits a longer tail to higher values) show a general offset to higher values relative to the DC-8 aircraft data (except for the West Sea). There is a systematic overestimation of CAMS CO_2 against the DC-8 aircraft data. Accordingly, the 'apparent local background' of CO_2 (lower tails of the pdfs) is relatively high in CAMS than the DC-8 aircraft data. In contrast, CO is underestimated in CAMS across all of the five groups. The pdfs of CO in CAMS show a bi-modal distribution (except in Taehwa and the West Sea) indicative of two

dominant AQ conditions sampled by DC-8 over this region. The shapes of the CO pdfs of CAMS largely differ from those of the DC-8 aircraft data (except in Taehwa). We see a higher frequency of occurrence of the two to three modes in the West Sea in CAMS that is not apparent in the DC-8 aircraft data while the opposite is the case in Seoul-Busan. This suggests that the underestimation of CO in CAMS may not be systematic or may be caused by biases in CO background values. The pdf over the West Sea also show that CAMS underestimates (or even misses) the more elevated CO observed by the DC-8 aircraft.

Table C1. Configuration of CAMS global atmospheric composition products valid during the period of the KORUS-AQ Field Campaign (May to June 2016). The tracers evaluated in this paper are highlighted in bold face. Time availability is in number of days with respect to real time.

CAMS product	Atmospheric composition tracers	Horizontal resolution	Number vertical levels	Initial conditions: Meteorology	Initial conditions: Atmospheric composition	Time availability observations/analysis of atmospheric composition	Time availability of product
AN_CHEM	Reactive gases (**CO**,O3,NO_2, etc) and aerosols	80 km	L60	Own analysis	Own analysis	<1day	<1day
FC_CHEM	Reactive gases (**CO**,O3,NO_2, etc) and aerosols	80 km	L60	AN_CHEM	AN_CHEM	<1day	0 days (real time)
AN_GHG	**CO_2**, CH_4	40 km	L137	Own analysis	Own analysis	2-4 days	4 days
FC16s	**CO_2**, CH_4 and **linCO**	16 km	L137	ECMWF operational analysis	Previous 1-day forecast	N/A	1 day
FC9s	**CO_2**, CH_4, **linCO** and tagged tracers	9 km	L137	ECMWF operational analysis	AN_GHG 4-day fc for CO_2/CH_4 and AN_CHEM for linCO	4 day for AN_GHG; <1day for AN_CHEM	1 day

We further investigate the differences between CAMS and the DC-8 aircraft data by looking at the bias in the mean profiles. We show in Fig. C4 the mean profiles for all data and each individual

group. We find that the overall bias in CAMS CO_2 is systematic and close to uniform across all layers (FC16s: ~2.2 ppmv, FC9s: ~1 ppmv, and ANs: ~0.8 ppmv). This overestimation is true for all flight groups except over the West Sea. On the other hand, for CO, the overall bias in CAMS is mostly evident in the lower troposphere (about -20 to 25 ppbv below 700 hPa). This underestimation is especially the case over the West Sea and is consistent with the pdfs in Fig. C3.

3.3.1 The Seoul Metropolitan and Taehwa

The airborne measurements over the Seoul metropolitan area were mostly during frequent aborted landing maneuvers (i.e. missed approaches) over the Seoul Air Base. More than 90% of the measurements in this group are taken below 850 hPa. Fig. C3 shows that the performance of FC16s, FC9s, and ANs are alike over Seoul for both CO and CO_2, in contrast to the other four flight groups. Given that the measurements over Seoul are dominated by boundary layer (BL) and anthropogenic emissions in Seoul, the model performance over Seoul are most likely to be driven by local emissions. We show in Fig. C5 the mean vertical profiles over Seoul below 800hPa. For CO_2, FC9s profiles agree well with the observations. This is not the case for CO, where FC16s, FC9s, and ANs do not agree well with the DC-8 aircraft data, but with the bias in ANs being relatively smaller. However, the near surface temporal variations (changes in the profile from morning to afternoon) observed by the DC-8 aircraft are captured by FC16s, FC9s, and ANs. It is worth noting that over Seoul, there is an abrupt change in the profile at around 925 hPa for both CO and CO_2 of the morning samples. Accordingly, CO is overestimated below 925 hPa and underestimated above 925 hPa. This vertical gradient below 925 hPa (i.e., change in mixing ratios divided by change in pressure) in the averaged profiles of the DC-8 aircraft data CO_2 and CO are about 0.25 ppmv/hPa and 1.7 ppbv/hPa, respectively. In contrast, the gradients of CO_2 in CAMS are 0.50 ppmv/hPa for FC16s, 0.34 ppmv/hPa for FC9s, and 0.45 ppmv/hPa for ANs while the gradients of CO in CAMS are 4.2 ppbv/hPa for FC16s, 3.4 ppbv/hPa for FC9s, and 3.3 for ANs. It is evident that these gradients (CO and CO_2) regardless of CAMS configuration are significantly steeper than observed. While in part this may be attributed to overestimation of emissions during rush hours (and night-time) in Seoul along with model representativeness errors in the BL, we attribute this steep gradient to a possible weaker BL mixing in CAMS since there is an important contrast between near surface CO (overestimation) and CO aloft (underestimation) which cannot be explained by emissions alone. This is not very apparent in CO_2 since there is an overestimation

of background CO_2 superimposed on this difference. In addition, given the air traffic over the Seoul Air Base (where the DC-8 aircraft frequently conducted missed approaches), emissions from airplanes may also contribute to the model biases (Boschetti et al., 2015).

In Taehwa, the differences between morning and afternoon samples are not as large compared to the Seoul metropolitan. The CO_2 profiles from ANs and FC9s are apparently closer to the DC-8 aircraft data than from FC16s. However, this difference is not obvious for the CO profiles. Note that in the afternoon (2-4pm), measured CO_2 mixing ratio near surface (at 975 hPa) becomes lower than the layer above, indicating a possible drawdown of CO_2 by underlying vegetation in Taehwa. This change is captured by CAMS, especially in FC9s. We further find that compared with the Seoul metropolitan, the observed vertical gradient of CO_2 over Taehwa (~0.03 ppmv/hPa) below 925 hPa is smaller, which is relatively better captured by CAMS (0.02–0.12 ppmv/hPa). This again implies the possible inefficient BL mixing in CAMS over the Seoul urban environment. CO over Taehwa is more likely to be due to regional transport, as Taehwa is not a strong CO source region. Thus, the vertical gradient of CO over Taehwa does not necessarily reflect the impact of BL mixing over Taehwa. We further compared the mixing layer (ML) height derived from the KORUS-AQ airborne DIAL-HSRL measurements of aerosol backscatter following the technique from Brooks et al. (2003), and the BL heights from CAMS. We note that ML height is only approximately equal to BL height. We find that CAMS generally underestimates BL heights during KORUS-AQ (Fig. CS6). The model underestimation of BL over the Seoul metropolitan (-761.3±39.7 m) is stronger than that over Taehwa (721.7±38.6 m) which is covered by forests instead of urban. This is consistent with the CAMS's relatively better capability of capturing vertical gradient of CO_2 over Taehwa compared to that over Seoul, supporting our previous implication of the possible inefficient BL mixing in CAMS over the Seoul urban environment.

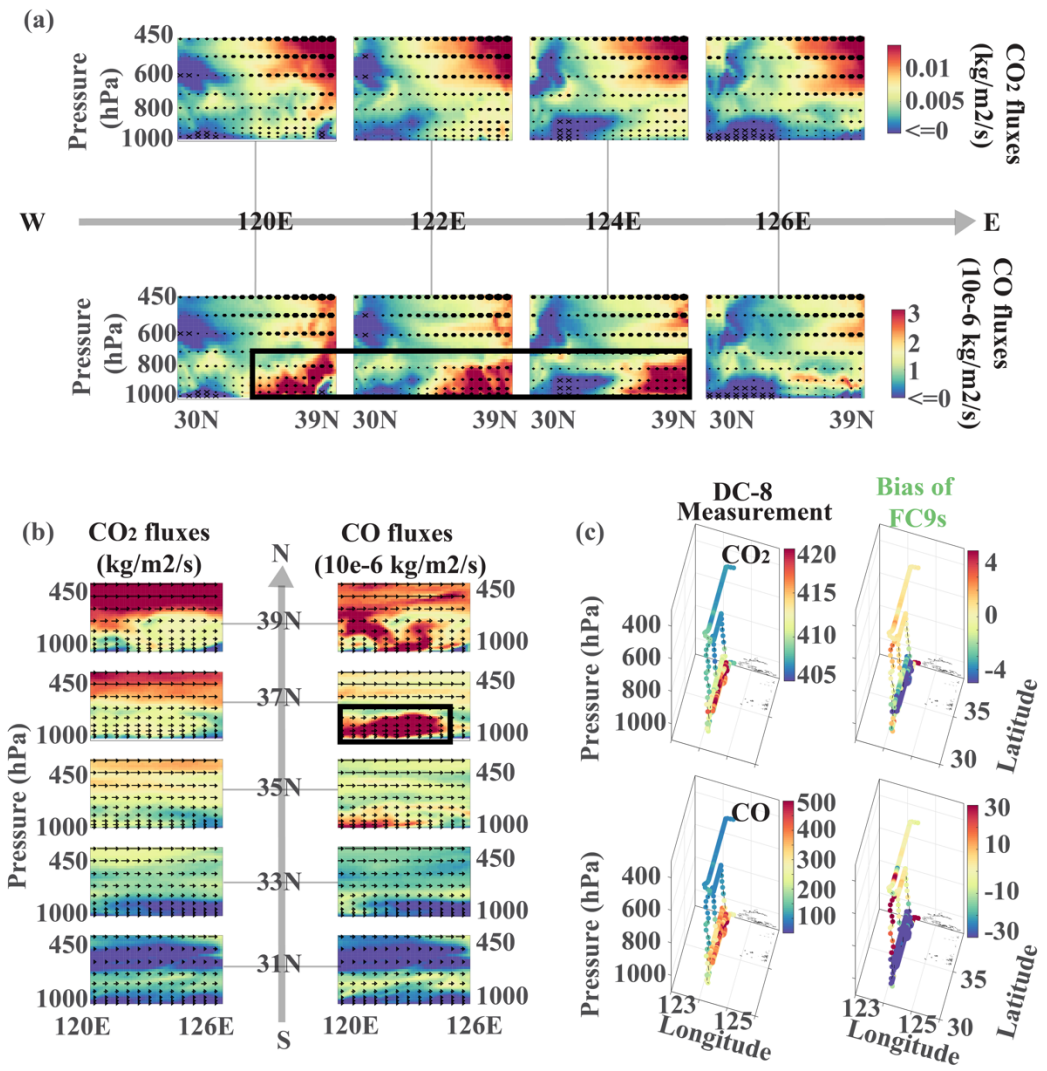

Figure C6. Case study for the flight on May 24th (UTC time). (a) Vertical distributions (hereafter denoted as 'sections') of fluxes (kg/m^2/s) at 9:00 am on May 25th (Korea time) in meridional direction. Dots represent meridional winds going from west to east (i.e., from China to Korea) and crosses represent meridional winds with the opposite direction. Sizes of the dots and crosses are proportional to the wind speed. 'Sections' on the top are for CO_2 fluxes and the bottom are for CO fluxes. (b) 'Sections' of fluxes (kg/m2/s) at 9:00 am on May 25th (Korea time) in zonal direction. Arrows represent meridional winds. 'Sections' in panel (b) share the same colorbar as panel (a). (c) the DC-8 aircraft measurements (left column) and bias of CAMS along the flight track over the West Sea (right column). The top row is for CO_2 and bottom row is for CO.

3.3.2 West (Yellow) Sea

As previously mentioned, the flights over the West (Yellow) Sea are focused on capturing pollution outflow from China. Both CO and CO_2 in this flight group are underestimated by CAMS

below 900 hPa (Fig. C4). It is the only group in which near surface CO_2 is underestimated by all the three CAMS configuration. In addition, the underestimation of CAMS CO over the West Sea is more significant than that over the other groups. We list two possible reasons for this unique model performance over the West Sea considering that the Chinese outflows constitute the dominant influence of CO and CO_2 samples in this group. First, the transport of surface pollution from China to the West Sea is not well represented in CAMS. Second, emissions in China may not be as well quantified as in Korea. During the May 24th flight, a strong outflow from China was expected, so DC-8 aircraft flew an extended sampling "wall" over the West Sea to sample transport from China. We show in Fig. C6 some of the details of this flight. In particular, we show the vertical cross sections of meridional (panel a) and zonal (panel b) fluxes of CO and CO_2 in CAMS FC9s. These fluxes are calculated as the product of meridional (from west to east) or zonal (from south to north) wind speed with simulated species density (i.e. in terms of units, $\frac{\mathrm{m}}{\mathrm{s}} \times \frac{\mathrm{kg}}{\mathrm{m}^3} = \frac{kg}{m^2 \cdot s}$). The China outflow moving towards the West Sea and Seoul is well demonstrated in the fluxes of CO in panel (a) and (b) especially in the region marked by the black rectangles. This outflow is not apparent in the fluxes of CO_2. This is because the variations in CO_2 density are very low relative to CO_2 background in contrast to CO variations. We also show in Fig. C6 panel (c) the measurements from the DC-8 aircraft and the bias of FC9s over the West Sea on that day. As can be seen in Fig. C6, CAMS CO_2 and CO are largely underestimated (CO_2: 2-4 ppmv, CO: 86-88 ppbv) for this flight. This underestimation in both species is consistent with Fig. C4. Note that the underestimation of CO_2 over the West Sea is not consistent with other flights and the overall results. This underestimation could be associated with an underestimation of anthropogenic emissions in China, and/or transport from China to the West Sea. This is discussed in Section 3.4 in more details. In summary, the transport pattern of China outflow (CO and CO_2) to the West Sea is captured but the abundances of both CO and CO_2 are underestimated by CAMS especially near the surface.

3.3.3 Seoul-Jeju and Seoul-Busan Jetways

Measurements in the Seoul-Jeju and Seoul-Busan jetways are both above the South Korean peninsula, connecting Seoul to Jeju and Busan, respectively. While both flight groups share some common features, they are treated here as two distinct groups for the following reasons: (1) Seoul-Jeju jetway is close to the west coast of South Korea, whereas Seoul-Busan jetway sampled air

southeast of Seoul and more inland; (2) There are more croplands, urban, and build-up areas along Seoul-Jeju jetway while there are more forested areas along Seoul-Busan jetway; (3) There are some important point sources along Seoul-Jeju jetway such as power plants and the Daesan chemical facility. In fact, the June 4th flight was designed to survey point sources west of Seoul and focused more to the Seoul-Jeju jetway. Details of the June 4th flight are summarized in Fig. C7. In contrast to the overall statistics across all flight groups, FC16s, FC9s, and ANs for this flight clearly overestimate CO near point sources. We also note that measurements for this flight are mostly taken below 900 hPa. As such, the spatial variations are larger near point sources than in other conditions. Nevertheless, these variations are not well captured by CAMS, especially by ANs. This may be due to its coarser grid representation (i.e., 40 km for CO_2 and 80 km for CO). In addition, we find a difference in terms of mean bias in CO_2 between CAMS FC9s and FC16s. This difference is not apparent in CO. This implies there might be large spatiotemporal errors existing in CO emission inventories in the region, since higher emission resolution does not result in an improvement. In this case, increasing the spatiotemporal resolution might even weaken the simulation results, whereas lower resolution usually agrees better with observations as it "diffuses" the error of the emissions.

Table C2. Measurements during KORUS-AQ.

			CO_2	CO
Airborne measurements	NASA DC-8 aircraft	Instrument	LI-COR	DACOM
		Time Response	1 second	1 second
		Precision	< 0.1 ppmv	< 1% or 0.1 ppbv
		Accuracy	0.25 ppmv (Vay et al., 2003)	2% (Warner et al., 2010)
Ground site measurements	Baengnyeong (37.97N,124.63E)	Instrument	/	Teledyne Gas analyzer
		Data intervals	/	1 hour
	Fukue (32.75N,128.68E)	Instrument	/	Thermo 48C
		Data intervals	/	1 hour
	Olympic Park (37.52N,127.12E)	Instrument	/	KENTEK CO analyzer
		Data intervals	/	5 minutes
	Taehwa (37.31N,127.31E)	Instrument	LI-COR LI-7500	Thermo 48i
		Data intervals	1 hour	1 hour

	Yonsei (37.56N, 126.94E)	Instrument	G2201-I CO_2/CH_4 carbon stable isotope analyzer	/
		Data intervals	30 minutes	/
Ship measurements	R/V Jangmok	Instrument	/	Thermo 48i-TLE
		Data intervals	/	1 minute
	R/V Onnuri	Instrument	/	Thermo Scientific, Inc., Model 48C
		Data intervals	/	1 minute
Satellite measurements			OCO-2	/
	OCO-2	Date product	Level 2 v7 Full Product XCO_2	/
		Resolution	2.25x1.29-km	/
			Global coverage	
			~16 days	
		Revisit time	1:18 - 1:33 pm	/
		Uncertainty	1-2 ppm XCO_2 (Wunch et al. 2017; Osterman et al., 2015)	/
	GOSAT	Date product	Level 2 V02	/
		Resolution	10.5 x 10.5 km ~12 days	/
		Revisit time	~1:00 pm	/
		Uncertainty	2 ppm for retrieval errors of XCO_2	/
			Griffith et al. 2011; Crisp et al. 2012	
	MOPITT	Date product	/	TIR/NIR Level 2 v6 XCO
		Resolution	/	22 x 22 km
				~3-4 days
		Revisit time	/	10:30 am
		Uncertainty	/	0.09e18 molecules/cm^2 for total column retrieval; (Deeter et al., 2014)
	IASI	Date product	/	Level 2 FORLI XCO
		Resolution	/	12 km x 12 km twice a day
		Revisit time	/	
		Uncertainty	/	<13% for FORLI (Wachter et al., 2012)

3.4 Enhancement Ratios of CO to CO_2

We also evaluate the three CAMS configuration against the DC-8 aircraft data in terms of enhancement ratios of CO to CO_2 (dCO/dCO_2) for all flights and for each flight group. We conduct a reduced major axis (RMA) regression to estimate the sensitivity of CO to CO_2 (i.e., dCO/dCO_2) with the 1 minute merges. We use RMA instead of ordinary least squares (OLS) regression as the two variables (CO and CO_2) are both subject to error (Smith, 2009). The estimated regression slope in the RMA corresponds to enhancement ratio of CO and CO_2. This ratio can reflect the emission ratios of a particular area especially when using near field data (Parrish et al. 2002). Despite its limitations (Yokelson et al., 2013), such analysis has been used in previous studies for surface CO and NO_X (Parrish et al. 2002), emission factors for biomass burning (Wofsy et al., 1992; Lefer et al., 1994), flask samples of CO and CO_2 in East Asia (Turnbull et al., 2011), airborne measurements of CO and CO_2 during TRACE-P (Suntharalingam et al. 2004), surface CO and CO_2 in rural Beijing (Wang et al. 2010) and more recently with satellite retrievals of CO (MOPITT) and CO_2 (GOSAT) (Silva et al., 2013). We present our estimates of dCO/dCO_2 (with units of ppbv/ppmv) from the DC-8 aircraft data and CAMS FC16s, FC9s and ANs in Table C3. Overall, the observed dCO/dCO_2 during the KORUS-AQ campaign is ~13 ppbv/ppmv (or ~1.3%). This is a relatively low value compared to reported ratios in more polluted megacities such as Beijing. The lowest dCO/dCO_2 among the five flight groups is observed over Seoul (~9 ppbv/ppmv). The observed dCO/dCO_2 for other groups within Korea ranges from ~10 ppbv/ppmv (Seoul-Jeju) to ~16 ppbv/ppmv (Seoul-Busan and Taehwa). Taehwa is close to and sometimes downwind of Seoul, but has higher observed dCO/dCO_2 than Seoul. We attribute this difference to biogenic CO sources and biospheric influence on CO_2 over Taehwa. The highest dCO/dCO_2 (~28 ppbv/ppmv) is observed over the West Sea. This ratio is a sharp contrast to Seoul and other flight groups over Korea. This indicates that the bulk combustion efficiency over Seoul is higher in Seoul than in the China pollution outflows over the West Sea. The ratio over the West Sea is very consistent with dCO/dCO_2 observed over China (upwind of the West Sea) during KORUS-AQ by ARIAs (20-100 ppbv/ppmv (REF). Such 'combustion signature contrast' is consistent with previous studies in the region. During TRACE-P in 2001, the observed ratio over Japan is ~12-17 ppbv/ppmv and ~50-100 ppbv/ppmv over northern China (Suntharalingam et al. 2004). Over Shangdianzi, China and Tae-Ahn Perninsula (TAP), Korea, Turnbull et al. (2011) reported

CO: CO_2ff ratios (which are derived from measurements of CO and $\Delta^{14}CO_2$ in flask samples taken during winter 2009/2010), of ~47 and ~44 ppbv/ppmv, respectively. They also reported that the South Korea samples from TAP have CO: CO_2ff of ~13 ppbv/ppmv. Wang et al. (2010) reported a change in observed dCO/dCO_2 near Beijing from 34-42 ppbv/ppmv in 2005-2007 to 22 ppbv/ppmv in 2008. Finally, dCO/dCO_2 derived from satellite retrievals in 2010 indicate a similar contrast between Beijing/Tianjin (~25-50 ppbv/ppmv) and Seoul (~7-9 ppbv/ppmv). Despite the differences in the data sources (satellites, airborne measurements, flask samples) and time period, these dCO/dCO_2 values are consistent and all point to a 'combustion signature contrast' between Korea and China. We expect that this contrast may be decreasing over time as Chinese combustion activities become more efficient.

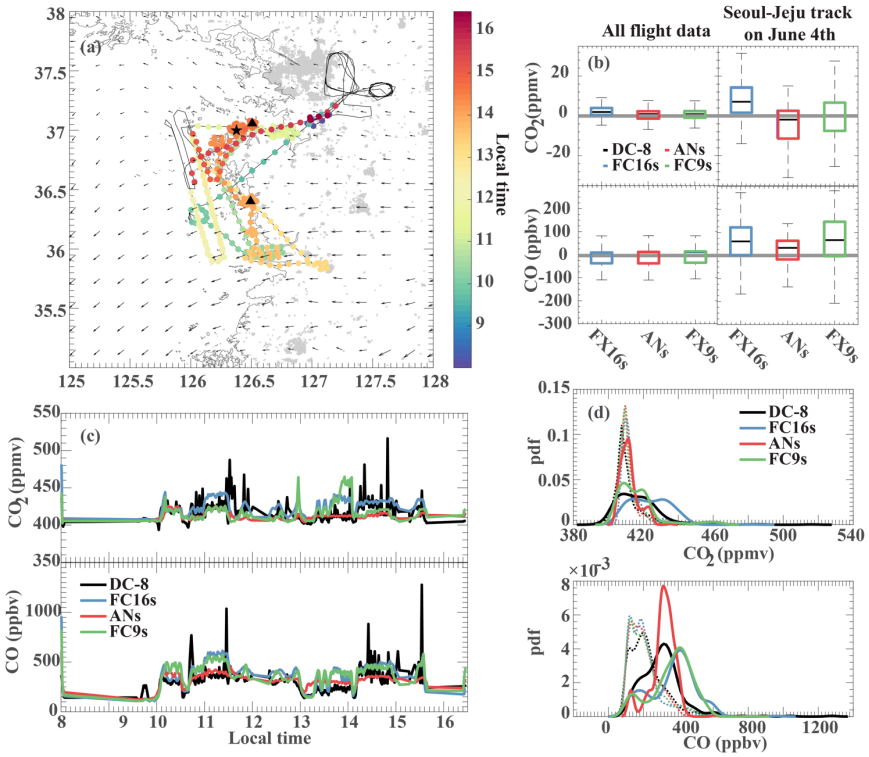

Figure C7. Case study for the flight on June 4th (UTC time). (a) Flight track of DC-8 aircraft in the Seoul-Jeju jetway group for this day. The Daesan chemical facility is marked as black pentagram and two power plants are marked as black triangles. Arrows correspond to 950 hPa wind field at 12:00pm local time. (b) Boxplot of CAMS bias from all the DC-8 aircraft measurements during the campaign (left), and from measurements on June 4th in the Seoul-Jeju jetway group (right). Top row is for CO_2 and bottom row is for CO. (c) Time series of the DC-8 aircraft measurements and CAMS during the flight. (d) pdfs of CO and CO_2 for measurements on June 4th of the Seoul-Jeju jetway group (solid) and for all groups (dashed).

These observed ratios are remarkably consistent with dCO/dCO_2 from CAMS (see Table C3). The three CAMS configurations have dCO/dCO_2 over Seoul metropolitan of ~8 to 12 ppbv/ppmv and over the West Sea of ~31-32 ppbv/ppmv. Our rough estimates of CO to CO_2 emission ratios in CAMS over Seoul and China during KORUS-AQ also show marked similarity with CAMS enhancement ratios. The CO to CO_2 emission ratios over China is about 28 (1000 mole/mole) and about 10 (1000 mole/mole) over Korea. Our results suggest that CAMS emission ratios reflect this contrast and that the modeled dCO/dCO_2 is indicative of emissions of Seoul and China. To further understand the skill of CAMS in capturing this contrast, we compare the observed correlation between CO and CO_2 and the correlation from CAMS FC16s, FC9s, and ANs. This corr(CO_2,CO) is presented in the second row of Table C3. Over Seoul, the observed corr(CO_2,CO) is moderately high (~0.8), which is likely driven by common CO and CO_2 sources (mostly local anthropogenic emissions from Seoul). This correlation is well captured by ANs and FC9s but not FC16s. We attribute this difference to a better initialization in ANs and FC9s due to assimilation. The observed corr(CO_2,CO) over the West Sea is even higher (0.89), indicating that CO and CO_2 comes from common sources in China. However, this corr(CO_2,CO) is not captured by any of the three configurations (0.25-0.42). A few factors may contribute to this low corr(CO_2,CO) over the West Sea. First, the flight on May 12th is a noteworthy source of low corr(CO_2,CO) in CAMS. We have shown in Fig. C2 that the major goal of this flight is to study AQ conditions during a frontal passage instead of sampling China outflows. Even though part of the track during May 12th is located in the West Sea, the AQ features of that day are evidently different from China outflow events. After excluding measurements during May 12th, the corr(CO_2,CO) in CAMS (FC16s-0.51, FC9s-0.43, and ANs-0.29) are now higher albeit still lower than observed (0.9). Uncertainties in model transport can be a likely cause as the corr(CO_2,CO) can be subject to transport errors even though dCO/dCO_2 may not necessarily be affected. Performance of CAMS over the Baengnyeong site (discussed in Section 4.1) also implies possible issues with transport of China pollution towards the West Sea. Furthermore, the difference in temporal representation of China emissions in CAMS may contribute to this mismatch in timing and hence resulting to low correlation. As mentioned in Section 2, CAMS uses prescribed monthly emission for CO while the diurnal cycle of CO_2 fluxes is calculated online in CAMS. In fact, there is a strong diurnal cycle in the spatial correlations between CO emissions and CO_2 fluxes in CAMS caused by diurnal cycles of the CO_2

NEE (Fig. CS8). The diurnal cycle of spatial correlations between CO emissions and CO_2 fluxes over Korea in CAMS peaks (~0.7) in daytime when measurements over Korea were made. On the other hand, during the nighttime, the correlations between CO emissions and CO_2 fluxes in CAMS are relatively low over East China (<0.4). This implies that the relatively low correlations between the CO and CO_2 abundances over the West Sea in CAMS may reflect the effect of nighttime emissions from East China in CAMS. Lastly, the corr(CO_2,CO) in FC16s and FC9s are closer to observed corr(CO_2,CO) than in ANs suggesting that resolution may also play a role. For the other three flight groups, the observed corr(CO_2,CO) are not as high as those over Seoul and the West Sea. This implies that CO_2 and CO observed over these three flight groups may not come from common sources and/or have been mixed with the environment. CAMS corr(CO_2,CO) do not always agree with observed corr(CO_2,CO). Overall, corr(CO_2,CO) from FC16s is higher than observed while corr(CO_2,CO) from FC9s and ANs agree well with observed corr(CO_2,CO). Again, this may be related to the fact that FC16s is generated from a free running simulation (i.e., not initialized with analyses).

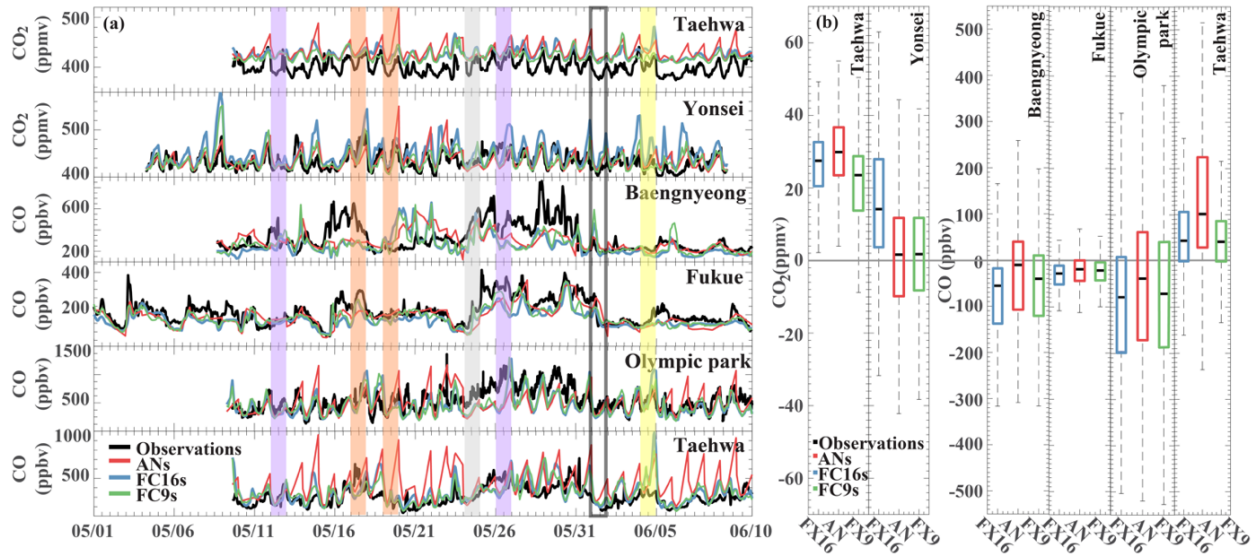

Figure C8. Comparisons of CAMS against ground site measurements. Values of CAMS are averages across layers with pressure higher than 95% of the surface pressure. (a) Time series of measured and CAMS CO_2 from the Taehwa and Yonsei sites, and CO from the Bangnyung, Fukue, Olympic Park, and Taehwa sites. Shades denote same events as they do in Fig. C2. (b) Boxplot of CAMS bias for CO_2 at the Taehwa and Yonsei site measurements, and for CO at the Bangnyung, Fukue, Olympic Park, and Taehwa sites.

Finally, we present the correlation between the biases of CAMS for the two species ($\mathrm{corr}(\mathrm{Bias}_{CO},\mathrm{Bias}_{CO_2})$) (please see the third row of Table C3). This correlation provides another piece of information on whether the performance of CAMS in CO_2 and CO are related. We find that $\mathrm{corr}(\mathrm{Bias}_{CO},\mathrm{Bias}_{CO_2})$ are high over Seoul and the West Sea, indicating that the performance of CAMS in CO and CO_2 are related for the two groups. Over the West Sea, FC16s, FC9s, and ANs perform similarly. However, the $\mathrm{corr}(\mathrm{Bias}_{CO},\mathrm{Bias}_{CO_2})$ are lower in the other three groups relative to Seoul and the West Sea. In addition, our results show that ANs and FC9s usually have lower $\mathrm{corr}(\mathrm{Bias}_{CO},\mathrm{Bias}_{CO_2})$ than FC16s, especially over Seoul. This implies that FC16s performance in CO_2 and CO are more strongly related than in FC9s and ANs performance, which could be associated again with the fact that FC16s comes from a free running simulation while FC9s and ANs are both initialized from analyses. The assimilation of CO and CO_2 satellite retrievals may reduce the interdependence of CAMS CO_2 and CO performance.

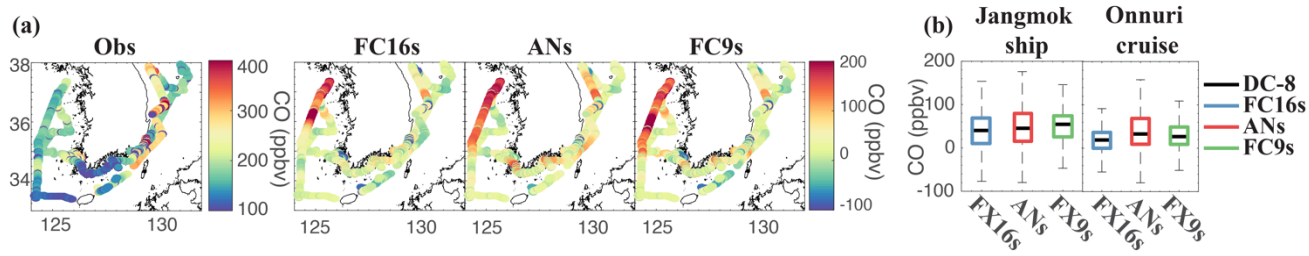

Figure C9. Comparisons of CAMS CO against ship measurements. Values of CAMS are averages across layers with pressure higher than 95% of the surface pressure. (a) Bias of CAMS CO against ship measurements along the ship track. (b) Boxplot of CAMS bias for CO compared with ship measurements.

4 Comparison with Other Measurements

In this section, we evaluate CAMS FC16s and FC9s, and ANs against CO and/or CO_2 measurements from five ground sites, two ships, and four satellites. Unlike the data from the DC-8 aircraft, data on CO_2 or CO in these cases may not be jointly available. In particular, each ground site (except Taehwa) only measures one of the two species. The ships also provide measurements for CO only while the four sets of satellite retrievals of CO_2 and CO are from four different instruments on board four different satellites. Therefore, in this section, CO_2 and CO are evaluated separately, and relationships between CO_2 and CO inferred from some of these sites are only indicative of a larger pattern that we see in the DC-8 aircraft data.

4.1 Comparison with Ground Observations

Here, we focus our evaluation on CAMS performance in capturing surface conditions and diurnal cycle of CO_2 and/or CO. Data from the following five ground sites are used in this study: Baengnyeong, Fukue, Olympic Park, Taehwa, and Yonsei University (Fig. C1 and Table C2). It can be seen in Fig. C8 that CO from Olympic Park and CO_2 from Yonsei and Taehwa clearly show a diurnal cycle during KORUS-AQ. This feature is well captured by CAMS. CO at Taehwa on the other hand, exhibits a very weak diurnal cycle that is not captured by CAMS. At this site, CO in CAMS (especially ANs) shows a strong diurnal cycle. Variations of CO in the remote sites of Baengnyeong and Fukue also appears to be irregular and episodic. Signatures of elevated CO can also be seen at these sites, some of which coinciding with pollution transport from China sampled by the DC-8 aircraft. The mean diurnal cycle for these five ground sites can be found in Fig. CS9.

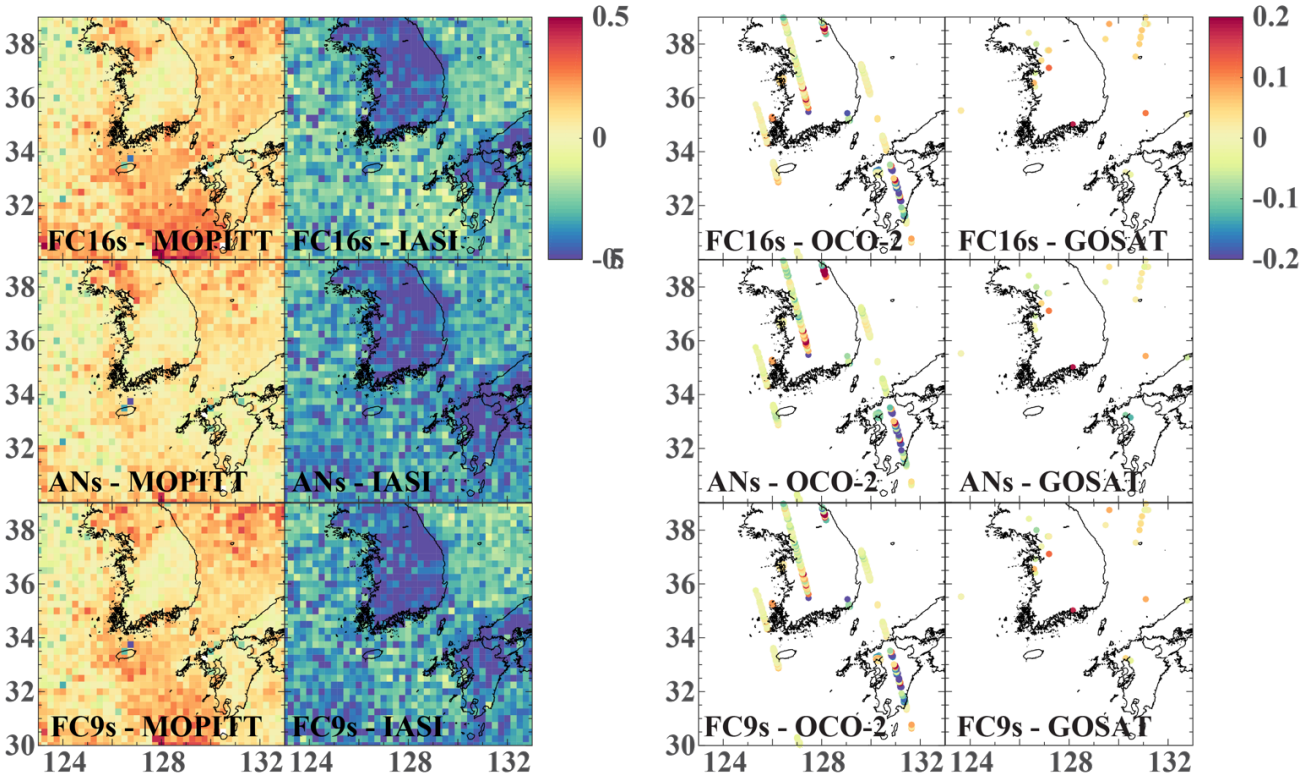

Figure C10. Spatial distributions of CAMS bias against satellite retrievals. For XCO, the unit is 10^{18} molecules/cm^2 while for XCO_2, the unit is 10^{21} molecules/cm^2.

While CAMS is able to get the observed timing of CO_2, the modelled magnitudes of CO_2 (and CO) at these sites from CAMS are too high (especially for the sites in and nearby Seoul). We took the average value across a few layers near the model surface in CAMS to provide a reasonable comparison at these sites. We use model vertical layers below 95% of the model surface pressure (i.e., if surface pressure is 1000hPa, we average the layers below 950 hPa) to account for potential weak BL mixing (especially near source regions). This feature in CAMS has been discussed in section 3.3.1. Since this averaging may introduce errors in our comparison, we only evaluate CAMS in terms of relative patterns (diurnal cycle and spatial variability across sites). Note that CAMS CO along the ship tracks (to be discussed in the succeeding section) are also averaged across a few layers in the same way for consistency. We show in Fig. C8 the summary statistics of the bias in CAMS relative to ground observations. The boxplots show that the variability of model bias in CO is in general smaller for remote sites and larger for the two sites in Seoul metropolitan. The bias in CAMS is also smaller in Fukue than in Baengnyeong, where a larger influence of pollution transport from China is observed but not well captured in CAMS. It is also worth mentioning that relative to other sites, CAMS significantly overestimates both CO and CO_2 at Taehwa. This may be due to the proximity of Taehwa to Seoul. The model grid spacing may not be able to resolve well the subgrid-scale processes (emissions) and variations between Seoul and Taehwa. This overestimation is most apparent in CAMS ANs which has a coarser grid spacing (40 km for CO_2 and 80 km for CO) than FC16s and FC9s. In the case of CO_2 at Yonsei, we find lower bias in CAMS FC9s and ANs than FC16s suggesting improvements of CAMS due to better initialization.

We take advantage of the location of the sites in Olympic Park (CO) and Yonsei University (CO_2) which are within Seoul metropolitan and the collocated measurements of CO and CO_2 in Taehwa to investigate patterns of ground-based dCO/dCO_2 in Seoul and Taehwa. Here, we only discuss observed dCO/dCO_2 since the modeled dCO/dCO_2 at these ground sites may not be accurate given CAMS issues with vertical mixing near the surface and representativeness errors. Following similar analysis with the dCO/dCO_2 of the DC-8 aircraft data, regressions of CO to CO_2 at these sites can represent emission ratios of CO to CO_2 in Seoul metropolitan. Our estimate of dCO/dCO_2 from Olympic Park and Yonsei sites is 11.32 ppbv/ppmv. This is consistent with dCO/dCO_2 calculated from the DC-8 aircraft data which sampled air closely above these sites (~9

ppbv/ppmv). Our estimate of dCO/dCO_2 from the Taehwa site is 6.57 ppbv/ppmv. This is different from our estimate of 15.3 ppbv/ppmv based on the DC-8 aircraft data. Unlike Seoul, 70% of the airborne measurements over Taehwa are taken above 800 hPa, Over Taehwa, airborne dCO/dCO_2 varies with altitude from 8.92 ppbv/ppmv below 950 hPa, 10.28 ppbv/ppmv below 900 hPa, and 14.74 ppbv/ppmv above 400 hPa.

4.2 Comparison with Ship Observations

Table C3. Enhancement ratios of CO to CO_2 (ppbv/ppmv), CO and CO_2 correlations, and bias of CO to bias of CO_2 correlations from airborne measurements, CAMS FC16s, ANs, and FC9s.

		Seoul	Taehwa	the West Sea	Seoul-Jeju jetway	Seoul-Busan jetway	All
dCO/dCO_2 (ppbv/ppmv)	DC-8 measurement	9.09±0.48	15.3±0.56	28.17±0.75	10.37±0.31	15.86±0.73	13.29±0.21
	FC16s	9.84±0.29	14.31±0.40	30.86±1.64	13.00±0.27	13.39±0.51	12.28±0.15
	ANs	8.21±0.45	13.71±0.48	30.60±1.73	14.98±0.45	12.68±0.47	12.60±0.2
	FC9s	11.56±0.62	16.06±0.57	32.44±1.77	11.68±0.35	13.87±0.54	12.52±0.2
Correlation of CO and CO_2	DC-8 measurement	0.78	0.68	0.89	0.62	0.60	0.66
	FC16s	0.94	0.83	0.42	0.83	0.74	0.82
	ANs	0.77	0.71	0.25	0.61	0.76	0.63
	FC9s	0.78	0.70	0.36	0.60	0.73	0.65
Correlation of $Bias_{CO}$ and $Bias_{CO_2}$	FC16s	0.90	0.61	0.80	0.46	0.55	0.61
	ANs	0.66	0.59	0.82	0.36	0.63	0.51
	FC9s	0.64	0.52	0.82	0.33	0.54	0.49

Two research vessels (Jangmok and Onnuri) were deployed during KORUS-OC. The two ships travelled along the Korean coast and measured CO from May 20th to June 5th (as marked in Fig. C1). Measurements of CO from ships, and biases of CAMS FC16s, ANs, and FC9s are shown in

Fig. C9. Note that CAMS values along ship tracks are also averaged across a few layers near surface in the same way CAMS at ground sites were processed. CAMS at three (out of four) ground sites tend to underestimate CO, while CAMS overestimates CO relative to ship measurements. This seems to be inconsistent with our findings with airborne measurements (i.e., CO is underestimated by CAMS at lowermost troposphere (Fig. C4 and Fig. C6). This is likely due to the differences in sampling between the airborne and ship measurements. Over sea, the DC-8 aircraft often sampled air from China outflow while the two ships continuously sampled air over the waters regardless of the presence of China outflows. The ship measurements reflect surface conditions over waters which may also be different from what is observed by the DC-8 aircraft along the vertical profile. This inconsistency is further discussed in the next section with satellite data.

4.3 Comparison with Satellite Retrievals

The total column dry air mole fractions of CO_2 and CO (XCO_2 and XCO) derived from CAMS are compared here to XCO_2 from OCO-2 and GOSAT, and XCO from MOPITT and IASI. It is worth noting that satellite retrievals may have associated bias and uncertainties, which are generally larger than those of ground and airborne measurements. Slight inconsistencies also exist between MOPITT XCO and IASI XCO (George et al., 2009; 2015). We show in Fig. C10 the spatial distribution of CAMS biases against these retrievals. We also summarize the statistics in Table C4. Overall, ANs tend to agree better with satellite observations than the forecasts. For CO, CAMS XCO tends to be higher than MOPITT but lower than IASI. In addition, CAMS XCO agrees better with MOPITT than IASI. For CO_2, CAMS XCO_2 tend to be higher than GOSAT but lower than OCO-2. FC16s, FC9s, and ANs differ from each other in terms of bias when compared to any of the four satellite retrievals although there is no clear difference in terms of RMSE. For XCO, when compared to MOPITT, ANs are better than the two forecasts in terms of bias, RMSE, and correlation. When compared to IASI, ANs are better in terms of RMSE and correlation, but not its bias. For XCO_2, ANs do not show improvements from the two forecasts when compared to both OCO-2 and GOSAT retrievals. For both XCO and XCO_2, FC9s is not necessarily better than FC16s. In summary, ANs XCO show better agreement with satellite retrievals but this is not the case for XCO_2. Differences in the resolution and amount of satellite data of XCO and XCO_2 could be two possible causes. The spatial and temporal resolutions of FC16s and FC9s are higher than

those of ANs while ANs assimilate observational data from these satellite retrievals (except OCO-2). These two factors compete against each other. Because the amount of CO data (13612 retrievals for MOPITT and 25509 for IASI over our study domain during KORUS-AQ) is much larger than that of CO_2 (42 for GOSAT over our domain during KORUS-AQ), there are more observational constraints for CO in CAMS resulting to better performance of ANs CO (Fig. C9 and Table C4). The opposite is the case for CO_2. The model resolution dominates for CAMS CO_2 performance especially with regards to capturing spatiotemporal variability. Scatter plots of CAMS XCO and XCO_2 against satellite observations are also presented in Fig. CS10 of the supplementary material.

Table C4. Statistics of CAMS performance compared against satellite observations.

		CO		CO2	
		MOPITT	IASI	OCO-2	GOSAT
Total observations during campaign		13612	25509	4591	42
Bias (molecules cm^{-2})	FC16s	-9.53×10^{16}	2.53×10^{17}	9.30×10^{18}	-2.64×10^{19}
	ANs	-5.29×10^{16}	3.00×10^{17}	4.48×10^{19}	1.05×10^{19}
	FC9s	-8.67×10^{16}	2.83×10^{17}	-1.31×10^{19}	-1.28×10^{19}
RMSE (molecules cm^{-2})	FC16s	2.84×10^{17}	4.53×10^{17}	7.11×10^{19}	5.67×10^{19}
	ANs	2.74×10^{17}	4.64×10^{17}	8.48×10^{19}	6.42×10^{19}
	FC9s	2.97×10^{17}	4.76×10^{17}	8.29×10^{19}	5.49×10^{19}
Correlation	FC16s	0.72	0.57	0.88	0.78
	ANs	0.72	0.63	0.85	0.63
	FC9s	0.69	0.56	0.85	0.75

We note that CAMS overestimates XCO when compared with MOPITT XCO over the West Sea (Fig. C10). This appears to be contradictory to our conclusions in section 3 and the similar inconsistency also exists when we compare CAMS CO with ship measurements (as mentioned in Section 4.2). To further explain this inconsistency, we compare CAMS FC9s with ship measurements and satellite XCO. Because the West Sea flight group in the DC-8 aircraft data forms a zonal 'wall' and such measurements over the West Sea are only conducted when a China

outflow is expected, we separate the days when China outflows are present. The following are the days during the campaign when China outflows were expected to occur and DC-8 flights measured walls over the West Sea: May 3rd, May 17th, May 24th, May 29th, and May 30th On May 3rd, May 17th, May 24th, and May 29th, there are no MOPITT observations over the West Sea (Fig. CS11). Therefore, the overall differences between CAMS FC9s and MOPITT observations are driven by the non-outflow days. On May 30th, however, there are MOPITT observations over the West Sea. Unlike the overall picture (Fig. C10), we find that CAMS actually underestimates the outflows over the West Sea on that day, which is consistent with our findings in Section 3. On June 1st (a non-China outflow day), comparison with ship measurements indicates that CAMS FC9s overestimates CO near the Korean coast. It is also consistent with MOPITT XCO in June 1st (Fig. CS11). This overestimation in CAMS FC9s is also captured in our comparison with Baengnyeong (highlighted by a black box in Fig. C9). We find similar overestimation using CAMS FC16s and ANs. Hence, during 'normal' conditions, CAMS tend to overestimate CO over the West Sea, whereas during China outflow events, CAMS tend to underestimate CO. More elaborate analysis of source contributions during KORUS-AQ is beyond the scope of this study and can be found in Tang et al. (2018), which suggested that during China outflow events, the contribution from Chinese direct emissions to CO over the West Sea is largely enhanced and dominant.

5 Discussions and Conclusions

We use measurements from the NASA DC-8 aircraft, five ground sites (Baengnyeong, Fukue, Olympic Park, Taehwa, and Yonsei University), and two ships (Jangmok and Onnuri) during the KORUS-AQ field campaign, along with four sets of satellite retrievals (MOPITT XCO, IASI XCO, OCO-2 XCO_2, and GOSAT XCO_2) to evaluate the capability of a high-resolution global modeling system (CAMS) in simulating anthropogenic combustion. Specifically, we evaluate the performance of CAMS FC16s, FC9s, and ANs of CO_2, CO, and their relationships. Our assessment of the overall performance of CAMS against the DC-8 aircraft data show that: (1) The nominal background CO_2 in CAMS is slightly overestimated (bias is 2.2 ppmv for FC16s, 0.7 ppmv for FC9s, and 0.3 ppmv for ANs), which is further improved by CO_2 analysis. On the other hand, CO is generally underestimated by CAMS (bias is -19.2 ppbv for FC16s, -16.7 ppbv for FC9s, and -20.7 ppbv for ANs); and (2) Among the three forecasts/analysis configurations, FC9s are more accurate and consistent overall than FC16s and ANs because of the finer model resolution and

improved initialization. While ANs are coarser in resolution, they generally perform better than FC16s as the impact of initialization surpasses the impact of resolution (Fig. CS3). We also classify the airborne measurements into five groups based on land cover below the flight tracks and associated pollution sources. While CO_2, CO, and their relationships vary across these five groups, CAMS perform well in terms of simulating regional pattern of anthropogenic combustion. This is because: 1) CAMS simulations of both species have relatively low bias; and 2) CAMS reproduces dCO/dCO_2 observed by the DC-8 aircraft. Both CAMS and the DC-8 aircraft data show more efficient combustion (low dCO/dCO_2) over Seoul than over the West Sea which is representative of Chinese outflows. Our case study on the May 24th flight over the West Sea indicates that the Chinese outflow is captured by CAMS. However, the modeled CO and CO_2 concentrations are significantly underestimated (by -2 to -4 ppmv for CO_2 and -86 to -88 ppbv for CO) especially within the lowermost troposphere. This suggests that, although CAMS emission ratios are relatively consistent with dCO/dCO_2, the absolute magnitude of China emissions are still underestimated. CAMS also show poorer performance at local-to-urban scales as exemplified by our case study in the June 4th flight where larger variations near point sources were not represented in CAMS. Our comparisons with measurements from ground sites and two ships indicate that: (1) the diurnal cycle of CO and CO_2 are stronger over urban environments and such periodic features are reasonably captured by CAMS; (2) vertical mixing near sources (such as Seoul) is too weak in CAMS and needs to be improved; and (3) in some cases, FC9s do not show improvements from FC16s (such as over Seoul and the point sources during the June 4th flight), implying large spatiotemporal errors in emission inventories. In these cases, increasing the spatiotemporal resolution might even weaken the simulation results, whereas lower resolution usually agrees better with observations as it "diffuses" the error of the emissions. We also compared XCO and XCO_2 derived from CAMS to satellite retrievals from four instruments (MOPITT CO, IASI CO, OCO-2 CO_2, and GOSAT CO_2). We find that ANs XCO show better agreement with satellite retrievals compared to the forecasts, while ANs CO_2 is no better than the forecasts. We attribute this contrast to significant differences in the number of XCO and XCO_2 satellite data potentially available for assimilation.

We recognize the following limitations of this work. (1) The temporal distribution of airborne measurements are not completely independent from their spatial distributions. For example, most of the measurements in the West Sea group are conducted before noon, whereas measurements in

Seoul-Busan jetway are concentrated in the afternoon. (2) CAMS is only evaluated over the South Korean peninsula and surrounding waters during the campaign (May 1st to June 10th). More work is needed to determine if our findings are valid over other regions. For example, Agusti-Panareda et al. (2014) reported the overall overestimation of CO_2 in spring over the whole NH and it is enhanced by biogenic flux correction. (3) Inconsistencies exist even among different satellite products (George et al., 2009; 2015), thus limiting our comparisons with CAMS to relative differences; and 4) Our comparison of CAMS with ground and ship measurements are only qualitative and indicative as CAMS surface concentrations are significantly higher than surface observations and not comparable.

Finally, this study has important implications on the design and implementation of current and future prediction system for atmospheric composition and air quality. Although CAMS captured the regional combustion signatures, it still has difficulty representing the variability at local-to-urban scales even at finer resolution. This suggests both improvements in observational constraints and model representation of relevant processes (e.g., emissions and BL mixing).

Data Availability

CAMS 16-km forecasts, and analyses are available online (http://apps.ecmwf.int/datasets/data/cams-nrealtime/levtype=sfc/). CAMS 9-km forecasts are available upon request. Observational data from KORUS-AQ will be open to public soon (https://www-air.larc.nasa.gov/cgi-bin/ArcView/korusaq). All the satellite data used in this study are available online. MOPITT CO and OCO-2 CO_2 can be downloaded at https://reverb.echo.nasa.gov/reverb/. IASI CO can be found at http://ether.ipsl.jussieu.fr/ether/pubipsl/iasi_CO_uk.jsp. GOSAT CO_2 data after 2014 is available at http://www.gosat.nies.go.jp/en/.

Acknowledgements

This work is supported by NASA KORUSAQ NNX16AE16G and NNX16AD96G. We thank the KORUS-AQ team for observational data, the CAMS global production team for the model products of CO and CO_2, MOPITT, IASI, OCO-2, and GOSAT data teams for satellite data. IASI CO is provided by LATMOS/CNRS and ULB. We acknowledge NASA and the OCO-2 project

for OCO-2 CO_2 data. We thank the DIAL/HSRL team for the Mixed Layer Heights product. The authors thank Dr. Cenlin He and Dr. Kazuyuki Miyazaki for helpful comments on improving the paper. NCAR is sponsored by the National Science Foundation. Yugo Kanaya was supported by the Environment Research and Technology Development Fund (2-1505 and 2-1803) of the Ministry of the Environment, Japan. The authors thank the anonymous reviewers for their comments and suggestions. The CAMS data was generated using Copernicus Atmosphere Monitoring Service Information [2016].

References

Agustí-Panareda, A., Massart, S., Chevallier, F., Bousetta, S., Balsamo, G., Beljaars, A., Ciais, P., Deutscher, N. M., Engelen, R., Jones, L. and Kivi, R.: Forecasting global atmospheric CO_2. Atmospheric Chemistry and Physics, 14(21), 11959-11983, 2014.

Agusti-Panareda, A., Monitoring upgrades of analysis/forecast system, MACC-III Deliverable D44.04, June 2015.

Agustí-Panareda, A., Massart, S., Chevallier, F., Balsamo, G., Boussetta, S., Dutra, E., and Beljaars, A.: A biogenic CO 2 flux adjustment scheme for the mitigation of large-scale biases in global atmospheric CO 2 analyses and forecasts. Atmospheric Chemistry and Physics, 16(16), 10399-10418, 2016.

Agusti-Panareda, A., Diamantakis, M., Bayona, V., Klappenbach, F., and Butz, A.: Improving the inter-hemispheric gradient of total column atmospheric CO 2 and CH 4 in simulations with the ECMWF semi-Lagrangian atmospheric global model. Geoscientific Model Development, 10(1), 1, 2017.

Andreae, M. O., and Merlet, P.: Emission of trace gases and aerosols from biomass burning. Global biogeochemical cycles, 15(4), 955-966, 2001.

Benedetti, A., Morcrette, J.J., Boucher, O., Dethof, A., Engelen, R.J., Fisher, M., Flentje, H., Huneeus, N., Jones, L., Kaiser, J.W. and Kinne, S.: Aerosol analysis and forecast in the European centre for medium-range weather forecasts integrated forecast system: 2. Data assimilation. Journal of Geophysical Research: Atmospheres, 114(D13), 2009.

Boesch, H., Baker, D., Connor, B., Crisp, D., and Miller, C.: Global characterization of CO2 column retrievals from shortwave-infrared satellite observations of the Orbiting Carbon Observatory-2 mission. Remote Sensing, 3(2), 270-304, 2011.

Boschetti, F., Chen, H., Thouret, V., Nedelec, P., Janssens-Maenhout, G., & Gerbig, C. (2015). On the representation of IAGOS/MOZAIC vertical profiles in chemical transport models: contribution of different error sources in the example of carbon monoxide. Tellus B: Chemical and Physical Meteorology, 67(1), 28292.

Boussetta, S., Balsamo, G., Beljaars, A., Panareda, A. A., Calvet, J. C., Jacobs, C., Hurk, B., Viterbo, P., Lafont, S., Dutra, E. and Jarlan, L. (2013). Natural land carbon dioxide exchanges in the ECMWF Integrated Forecasting System: Implementation and offline validation. Journal of Geophysical Research: Atmospheres, 118(12), 5923-5946.

Brooks, I. M.: Finding boundary layer top: Application of wavelet covariance transform to Lidar backscatter profiles, J. Atmos. Ocean. Tech., 20, 1092–1105, 2003.

Cariolle, D., & Déqué, M. (1986). Southern Hemisphere medium-scale waves and total ozone disturbances in a spectral general circulation model. Journal of Geophysical Research: Atmospheres, 91(D10), 10825-10846.

Cariolle, D., & Teyssedre, H. (2007). A revised linear ozone photochemistry parameterization for use in transport and general circulation models: multi-annual simulations. Atmospheric chemistry and physics, 7(9), 2183-2196.

Charlson, R. J., and Schwartz, S. E: Climate forcing by anthropogenic aerosols. Science, 255(5043), 423, 1992.

Claeyman, M., Attié, J. L., El Amraoui, L., Cariolle, D., Peuch, V. H., Teyssèdre, H., Josse, B., Ricaud, P., Massart, S., Piacentini, A. and Cammas, J. P.: A linear CO chemistry parameterization in a chemistry-transport model: evaluation and application to data assimilation. Atmospheric Chemistry and Physics, 10(13), 6097, 2010.

Clerbaux, C., Boynard, A., Clarisse, L., George, M., Hadji-Lazaro, J., Herbin, H., Hurtmans, D., Pommier, M., Razavi, A., Turquety, S. and Wespes, C. (2009). Monitoring of atmospheric composition using the thermal infrared IASI/MetOp sounder. Atmospheric Chemistry and Physics, 9(16), 6041-6054.

Crawford, J.H. and Pickering, K.E.: DISCOVER-AQ: Advancing strategies for air quality observations in the next decade. Environ. Manage, pp.4-7, 2014.

Crisp, D., Atlas, R.M., Breon, F.M., Brown, L.R., Burrows, J.P., Ciais, P., Connor, B.J., Doney, S.C., Fung, I.Y., Jacob, D.J. and Miller, C.E.: The orbiting carbon observatory (OCO) mission. Advances in Space Research, 34(4), pp.700-709, 2004.

Crisp, D., Fisher, B., O'Dell, C., Frankenberg, C., Basilio, R., Bosch, H., Brown, L. R., Castano, R., Connor, B., Deutscher, N. M. and Eldering, A.: The ACOS CO2 retrieval algorithm-Part II: Global XCO2 data characterization, 2012.

Deeter, M. N., Martínez-Alonso, S., Edwards, D. P., Emmons, L. K., Gille, J. C., Worden, H. M., Sweeney, C., Pittman, J.V., Daube, B.C. and Wofsy, S. C.: The MOPITT Version 6 product: algorithm enhancements and validation. Atmospheric Measurement Techniques, 7(11), 3623-3632, 2014.

Doney, S. C., Mahowald, N., Lima, I., Feely, R. A., Mackenzie, F. T., Lamarque, J. F., and Rasch, P. J.: Impact of anthropogenic atmospheric nitrogen and sulfur deposition on ocean

acidification and the inorganic carbon system. Proceedings of the National Academy of Sciences, 104(37), 14580-14585, 2007.

ECMWF: IFS Documentation CY43R3. European Centre for Medium-Range Weather Forecasts: Reading, UK, 2017.

Eskes, H.J., Wagner, A., Schulz, M., Christophe, Y., Ramonet, M., Basart, S., Benedictow, A., Blechschmidt, A.-M., Chabrillat, S., Clark, H., Cuevas, E., Flentje, H., Hansen, K.M., Im, U., Kapsomenakis, J., Langerock, B., Petersen, K., Richter, A., Sudarchikova, N., Thouret, V., Warneke, T., Zerefos, C.: Validation report of the CAMS near-real-time global atmospheric composition service: Period June - August 2017. Copernicus Atmosphere Monitoring Service (Cams) Report, Cams84_2015sc2_D84.1.1.7_2017djf_V1.Pdf, May 2017.

Feely, R. A., Sabine, C. L., Lee, K., Berelson, W., Kleypas, J., Fabry, V. J., and Millero, F. J.: Impact of anthropogenic CO2 on the CaCO3 system in the oceans. Science, 305(5682), 362-366, 2004.

Flemming, J., Inness, A., Flentje, H., Huijnen, V., Moinat, P., Schultz, M. G., and Stein, O.: Coupling global chemistry transport models to ECMWF's integrated forecast system. Geoscientific Model Development, 2, 253-265, 2009.

Flemming, J., Peuch, V. H., Engelen, R., and Kaiser, J. W.: A European global-to-regional air pollution forecasting system that combines modeling with satellite observations. EM Magazine, November, 610, 2013.

Flemming, J., Huijnen, V., Arteta, J., Bechtold, P., Beljaars, A., Blechschmidt, A. M., Diamantakis, M., Engelen, R. J., Gaudel, A., Inness, A. and Jones, L.: Tropospheric chemistry in the Integrated Forecasting System of ECMWF. Geoscientific model development, 8(4), 975-1003, 2015.

Flemming, J., Benedetti, A., Inness, A., Engelen, R. J., Jones, L., Huijnen, V., Remy, S., Parrington, M., Suttie, M., Bozzo, A. and Peuch, V. H.: The CAMS interim Reanalysis of Carbon Monoxide, Ozone and Aerosol for 2003–2015. Atmospheric Chemistry and Physics, 17(3), 1945-1983, 2017.

Gamnitzer, U., Karstens, U., Kromer, B., Neubert, R. E., Meijer, H. A., Schroeder, H., and Levin, I.: Carbon monoxide: A quantitative tracer for fossil fuel CO_2? Journal of Geophysical Research: Atmospheres, 111(D22), 2006.

Gaubert, B., Arellano, A. F., Barré, J., Worden, H. M., Emmons, L. K., Tilmes, S., … Jones, N. (2016). Toward a chemical reanalysis in a coupled chemistry climate model: An evaluation of MOPITT CO assimilation and its impact on tropospheric composition. Journal of Geophysical Research: Atmospheres, 121, 7310–7343. https://doi.org/10.1002/2016JD024863.

Gaubert, B., Worden, H. M., Arellano, A. F. J., Emmons, L. K., Tilmes, S., Barré, J., ... & Houweling, S. (2017). Chemical Feedback From Decreasing Carbon Monoxide Emissions. Geophysical Research Letters, 44(19), 9985-9995.

George, M., Clerbaux, C., Hurtmans, D., Turquety, S., Coheur, P. F., Pommier, M., Hadji-Lazaro, J., Edwards, D. P., Worden, H., Luo, M. and Rinsland, C.: Carbon monoxide distributions from the IASI/METOP mission: evaluation with other space-borne remote sensors. Atmospheric chemistry and physics, 9(21), 8317-8330, 2009.

George, M., Clerbaux, C., Bouarar, I., Coheur, P.F., Deeter, M.N., Edwards, D.P., Francis, G., Gille, J.C., Hadji-Lazaro, J., Hurtmans, D. and Inness, A.: An examination of the long-term CO records from MOPITT and IASI: comparison of retrieval methodology. Atmospheric Measurement Techniques, 8, pp.4313-4328, 2015.

Granier, C. et al.: Evolution of anthropogenic and biomass burning emissions of air pollutants at global and regional scales during the 1980–2010 period. Climatic Change (109), 2011.

Griffith, D. W., Toon, G. C., Connor, B., Sussmann, R., Warneke, T., Deutscher, N. M., Wennberg, P.O., Notholt, J., Sherlock, V., Robinson, J. and Uchino, O.: Preliminary validation of column-averaged volume mixing ratios of carbon dioxide and methane retrieved from GOSAT short-wavelength infrared spectra, 2011.

Guan, D., Liu, Z., Geng, Y., Lindner, S. and Hubacek, K.: The gigatonne gap in China/'s carbon dioxide inventories. Nature Climate Change, 2(9), pp.672-675, 2012.

Guo, S., Hu, M., Zamora, M. L., Peng, J., Shang, D., Zheng, J., Du, Z., Wu, Z., Shao, M., Zeng, L. and Molina, M. J. (2014). Elucidating severe urban haze formation in China. Proceedings of the National Academy of Sciences, 111(49), 17373-17378.

Heald, C. L., Jacob, D. J., Park, R. J., Alexander, B., Fairlie, T. D., Yantosca, R. M., and Chu, D. A.: Transpacific transport of Asian anthropogenic aerosols and its impact on surface air quality in the United States. Journal of Geophysical Research: Atmospheres, 111(D14), 2006.

Hollingsworth, A., Engelen, R. J., Benedetti, A., Dethof, A., Flemming, J., Kaiser, J. W., Morcrette, J.J., Simmons, A.J., Textor, C., Boucher, O. and Chevallier, F.: Toward a monitoring and forecasting system for atmospheric composition: The GEMS project. Bulletin of the American Meteorological Society, 89(8), 1147-1164, 2008.

Inness, A., Blechschmidt, A. M., Bouarar, I., Chabrillat, S., Crepulja, M., Engelen, R. J., ... & Huijnen, V. (2015). Data assimilation of satellite-retrieved ozone, carbon monoxide and nitrogen dioxide with ECMWF's Composition-IFS. Atmospheric chemistry and physics, 15(9), 5275-5303.

Jacob, D. J., Crawford, J. H., Kleb, M. M., Connors, V. S., Bendura, R. J., Raper, J. L., Sachse, G.W., Gille, J.C., Emmons, L. and Heald, C. L.: Transport and Chemical Evolution over the Pacific (TRACE-P) aircraft mission: Design, execution, and first results. Journal of Geophysical Research: Atmospheres, 108(D20), 2003.

Jacob, D. J., Crawford, J. H., Maring, H., Clarke, A. D., Dibb, J. E., Emmons, L. K., Ferrare, R. A., Hostetler, C. A., Russell, P. B., Singh, H. B. and Thompson, A. M.: The Arctic Research of the Composition of the Troposphere from Aircraft and Satellites (ARCTAS) mission: design, execution, and first results. Atmospheric Chemistry and Physics, 10(11), 5191-5212, 2010.

Kaiser, J.W., Heil, A., Andreae, M.O., Benedetti, A., Chubarova, N., Jones, L., Morcrette, J.J., Razinger, M., Schultz, M.G., Suttie, M. and Van Der Werf, G.R.: Biomass burning emissions estimated with a global fire assimilation system based on observed fire radiative power. Biogeosciences, 9(1), p.527, 2012.

Kanaya, Y., Pan, X., Miyakawa, T., Komazaki, Y., Taketani, F., Uno, I., & Kondo, Y. (2016). Long-term observations of black carbon mass concentrations at Fukue Island, western Japan, during 2009–2015: constraining wet removal rates and emission strengths from East Asia. Atmospheric Chemistry and Physics, 16(16), 10689-10705.

Kim, S. Y., Jiang, X., Lee, M., Turnipseed, A., Guenther, A., Kim, J. C., ... & Kim, S. (2013). Impact of biogenic volatile organic compounds on ozone production at the Taehwa Research Forest near Seoul, South Korea. Atmospheric environment, 70, 447-453.

Kim, S., and Park, R. KORUS-AQ: An International Cooperative Air Quality Field Study in Korea, the KORUS-AQ white paper, 2014.

Lawrence M. G., J¨ockel P., and von Kuhlmann R., What does the global mean OH concentration tell us, Atmos. Chem. Phys., 1, 37–49, 2001.

Lefer, B. L., Talbot, R. W., Harriss, R. H., Bradshaw, J. D., Sandholm, S. T., Olson, J. O., ... & Klemm, K. I. (1994). Enhancement of acidic gases in biomass burning impacted air masses over Canada. Journal of Geophysical Research: Atmospheres, 99(D1), 1721-1737.

Lelieveld, J., Gromov, S., Pozzer, A., & Taraborrelli, D. (2016). Global tropospheric hydroxyl distribution, budget and reactivity. Atmospheric Chemistry and Physics, 16, 12,477–12,493. https://doi.org/10.5194/acp-16-12477-2016.

Maher, B. A., Ahmed, I. A., Karloukovski, V., MacLaren, D. A., Foulds, P. G., Allsop, D., Mann, D. M., Torres-Jardón, R. and Calderon-Garciduenas, L.: Magnetite pollution nanoparticles in the human brain. Proceedings of the National Academy of Sciences, 113(39), 10797-10801, 2016.

Mandrake, L., O'Dell, C. W., Wunch, D., Wennberg, P. O., Fisher, B., Osterman, G. B., & Eldering, A. (2015). Orbiting Carbon Observatory-2 (OCO-2) Warn Level, Bias Correction, and Lite File Product Description. Jet Propulsion Laboratory: Pasadena, CA, USA.

Massart, Flemming J., Cariolle, D., Jones,L.: High resolution CO tracer forecasts, MACC-III Deliverable D022.04, 2015.

Massart, S., Agustí-Panareda, A., Heymann, J., Buchwitz, M., Chevallier, F., Reuter, M., Hilker, M., Burrows, J. P., Deutscher, N. M., Feist, D. G. and Hase, F.: Ability of the 4-D-Var

analysis of the GOSAT BESD XCO 2 retrievals to characterize atmospheric CO 2 at large and synoptic scales. Atmospheric Chemistry and Physics, 16(3), 1653-1671, 2016.

Morcrette, J.J., Boucher, O., Jones, L., Salmond, D., Bechtold, P., Beljaars, A., Benedetti, A., Bonet, A., Kaiser, J.W., Razinger, M. and Schulz, M.: Aerosol analysis and forecast in the European Centre for medium-range weather forecasts integrated forecast system: Forward modeling. Journal of Geophysical Research: Atmospheres, 114(D6), 2009.

Morino, I., Uchino, O., Inoue, M., Yoshida, Y., Yokota, T., Wennberg, P., Toon, G.C., Wunch, D., Roehl, C.M., Notholt, J. and Warneke, T.: Preliminary validation of column-averaged volume mixing ratios of carbon dioxide and methane retrieved from GOSAT short-wavelength infrared spectra, 2011.

OCO-2 Science Team/Michael Gunson, Annmarie Eldering (2015), OCO-2 Level 2 bias-corrected XCO2 and other select fields from the full-physics retrieval aggregated as daily files, Retrospective processing V7r, Greenbelt, MD, USA, Goddard Earth Sciences Data and Information Services Center (GES DISC), Accessed 07/2016 https://disc.gsfc.nasa.gov/datacollection/OCO2_L2_Lite_FP_7r.html.

Ohara, T. A. H. K., Akimoto, H., Kurokawa, J. I., Horii, N., Yamaji, K., Yan, X., and Hayasaka, T.: An Asian emission inventory of anthropogenic emission sources for the period 1980–2020. Atmospheric Chemistry and Physics, 7(16), 4419-4444, 2007.

Parrish, D. D., Trainer, M., Hereid, D., Williams, E. J., Olszyna, K. J., Harley, R. A., Meagher, J. F. and Fehsenfeld, F. C.: Decadal change in carbon monoxide to nitrogen oxide ratio in US vehicular emissions. Journal of Geophysical Research: Atmospheres, 107(D12), 2002.

Persson, A. User Guide to ECMWF forecast products, 2001.

Rabier F, Jarvinen H, Klinker E, Mahfouf J-F, Simmons, A.: The ECMWF operational implementation of four-dimensional variational assimilation. I: Experimental results with simplified physics. Q. J. R. Meteorol. Soc. 126, 1143 – 1170, 2000.

Shindell, D., Faluvegi, G., Walsh, M., Anenberg, S. C., Van Dingenen, R., Muller, N. Z., Austin, J., Koch, D. and Milly, G.: Climate, health, agricultural and economic impacts of tighter vehicle-emission standards. Nature Climate Change, 1(1), 59-66, 2011.

Shindell, D., Lamarque, J. F., Unger, N., Koch, D., Faluvegi, G., Bauer, S., Ammann, M., Cofala, J. and Teich, H.: Climate forcing and air quality change due to regional emissions reductions by economic sector. Atmospheric Chemistry and Physics, 8(23), 7101-7113, 2008.

Silva, S. J., Arellano, A. F., and Worden, H.: Toward anthropogenic combustion emission constraints from space-based analysis of urban CO_2/CO sensitivity, Geophys. Res. Lett., 40, 4971–4976, doi:10.1002/grl.50954, 2013.

Singh, H. B., Brune, W. H., Crawford, J. H., Flocke, F., and Jacob, D. J.: Chemistry and transport of pollution over the Gulf of Mexico and the Pacific: spring 2006 INTEX-B campaign overview and first results. Atmospheric Chemistry and Physics, 9(7), 2301-2318, 2009.

Sindelarova, K., Granier, C., Bouarar, I., Guenther, A., Tilmes, S., Stavrakou, T., Müller, J.-F., Kuhn, U., Stefani, P., and Knorr, W.: Global data set of biogenic VOC emissions calculated by the MEGAN model over the last 30 years, Atmos. Chem. Phys., 14, 9317-9341, doi:10.5194/acp-14-9317-2014, 2014.

Smith, R.J.: Use and misuse of the reduced major axis for line-fitting. American journal of physical anthropology, 140(3), pp.476-486, 2009.

Streets, D.G., Bond, T.C., Carmichael, G.R., Fernandes, S.D., Fu, Q., He, D., Klimont, Z., Nelson, S.M., Tsai, N.Y., Wang, M.Q. and Woo, J.H.: An inventory of gaseous and primary aerosol emissions in Asia in the year 2000. Journal of Geophysical Research: Atmospheres, 108(D21), 2003.

Streets, D.G., Zhang, Q., Wang, L., He, K., Hao, J., Wu, Y., Tang, Y. and Carmichael, G.R.: Revisiting China's CO emissions after the transport and chemical evolution over the Pacific (TRACE-P) mission: synthesis of inventories, atmospheric modeling, and observations. Journal of Geophysical Research: Atmospheres, 111(D14), 2006.

Tang, W. et al., KORUS-AQ Carbon Monoxide Source Attribution using CAM-chem Tagged Tracers, JGR, 2018, in revision.

Taylor, K. E.: Summarizing multiple aspects of model performance in a single diagram. Journal of Geophysical Research: Atmospheres, 106(D7), 7183-7192, 2001.

Toon, O.B., Maring, H., Dibb, J., Ferrare, R., Jacob, D.J., Jensen, E.J., Luo, Z.J., Mace, G.G., Pan, L.L., Pfister, L. and Rosenlof, K.H.: Planning, implementation, and scientific goals of the Studies of Emissions and Atmospheric Composition, Clouds and Climate Coupling by Regional Surveys (SEAC4RS) field mission. Journal of Geophysical Research: Atmospheres, 121(9), pp.4967-5009, 2016.

Turnbull, J. C., Tans, P. P., Lehman, S. J., Baker, D., Conway, T. J., Chung, Y. S., Gregg, J., Miller, J. B., Southon, J. R., and Zhou, L. X.: Atmospheric observations of carbon monoxide and fossil fuel CO2 emissions from East Asia. Journal of Geophysical Research: Atmospheres, 116(D24), 2011.

United Nations, Department of Economic and Social Affairs, Population Division: The World's Cities in 2016 – Data Booklet (ST/ESA/ SER.A/392), 2016.

Van Leeuwen, T. T., and Van Der Werf, G. R.: Spatial and temporal variability in the ratio of trace gases emitted from biomass burning. Atmospheric Chemistry and Physics, 11(8), 3611-3629, 2011.

Vay, S.A., Woo, J.H., Anderson, B.E., Thornhill, K.L., Blake, D.R., Westberg, D.J., Kiley, C.M., Avery, M.A., Sachse, G.W., Streets, D.G. and Tsutsumi, Y.: Influence of regional-scale

anthropogenic emissions on CO2 distributions over the western North Pacific. Journal of Geophysical Research: Atmospheres (1984–2012), 108(D20), 2003.

Vay, S.A., Choi, Y., Vadrevu, K.P., Blake, D.R., Tyler, S.C., Wisthaler, A., Hecobian, A., Kondo, Y., Diskin, G.S., Sachse, G.W. and Woo, J.H.: Patterns of CO2 and radiocarbon across high northern latitudes during International Polar Year 2008. Journal of Geophysical Research: Atmospheres, 116(D14), 2011.

Wachter, E. D., Barret, B., Flochmoën, E. L., Pavelin, E., Matricardi, M., Clerbaux, C., Hadji-Lazaro, J., George, M., Hurtmans, D., Coheur, P. F. and Nedelec, P.: Retrieval of MetOp-A/IASI CO profiles and validation with MOZAIC data. Atmospheric Measurement Techniques, 5(11), 2843-2857, 2012.

Wang, Y., Munger, J. W., Xu, S., McElroy, M. B., Hao, J., Nielsen, C. P., and Ma, H.: CO 2 and its correlation with CO at a rural site near Beijing: implications for combustion efficiency in China. Atmospheric Chemistry and Physics, 10(18), 8881-8897, 2010.

Ward, D. E., and Hardy, C. C.: Smoke emissions from wildland fires. Environment International, 17(2-3), 117-134, 1991.

Wunch, D., Wennberg, P. O., Toon, G. C., Connor, B. J., Fisher, B., Osterman, G. B., Frankenberg, C., Mandrake, L., O'Dell, C., Ahonen, P. and Biraud, S. C. A method for evaluating bias in global measurements of CO 2 total columns from space. Atmospheric Chemistry and Physics, 11(23), 12317-12337, 2011.

Warner, J.X., Wei, Z., Strow, L.L., Barnet, C.D., Sparling, L.C., Diskin, G. and Sachse, G.: Improved agreement of AIRS tropospheric carbon monoxide products with other EOS sensors using optimal estimation retrievals. Atmospheric Chemistry and Physics, 10(19), pp.9521-9533, 2010.

Wofsy, S. C., Sachse, G. W., Gregory, G. L., Blake, D. R., Bradshaw, J. D., Sandholm, S. T., ... & Shipham, M. A. (1992). Atmospheric chemistry in the Arctic and Subarctic: Influence of natural fires, industrial emissions, and stratospheric inputs. Journal of Geophysical Research: Atmospheres, 97(D15), 16731-16746.

Wunch, D., Toon, G. C., Blavier, J. F. L., Washenfelder, R. A., Notholt, J., Connor, B. J., Griffith, D.W., Sherlock, V. and Wennberg, P. O.: The total carbon column observing network. Philosophical Transactions of the Royal Society of London A: Mathematical, Physical and Engineering Sciences, 369(1943), 2087-2112, 2011.

Yang, X. J.: China's rapid urbanization. Science, 342(6156), 310-310, 2013.

Yarwood, G., Rao, S., Yocke, M., & Whitten, G. (2005). Updates to the carbon bond chemical mechanism: CB05. Final report to the US EPA, EPA Report Number: RT-0400675.

Yokelson, R. J., Andreae, M. O., & Akagi, S. K. (2013). Pitfalls with the use of enhancement ratios or normalized excess mixing ratios measured in plumes to characterize pollution sources and aging. Atmospheric Measurement Techniques, 6, 2155.

Yokota, T., Oguma, H., Morino, I., and Inoue, G.: A nadir looking SWIR FTS to monitor CO2 column density for Japanese GOSAT project, Proc. Twenty-fourth Int. Sympo. on Space Technol. And Sci. (Selected Papers), 887–889, 2004.

Yokota, T., Yoshida, Y., Eguchi, N., Ota, Y., Tanaka, T., Watanabe, H. and Maksyutov, S. Global concentrations of CO2 and CH4 retrieved from GOSAT: First preliminary results. Sola, 5, pp.160-163, 2009.

Supporting Information

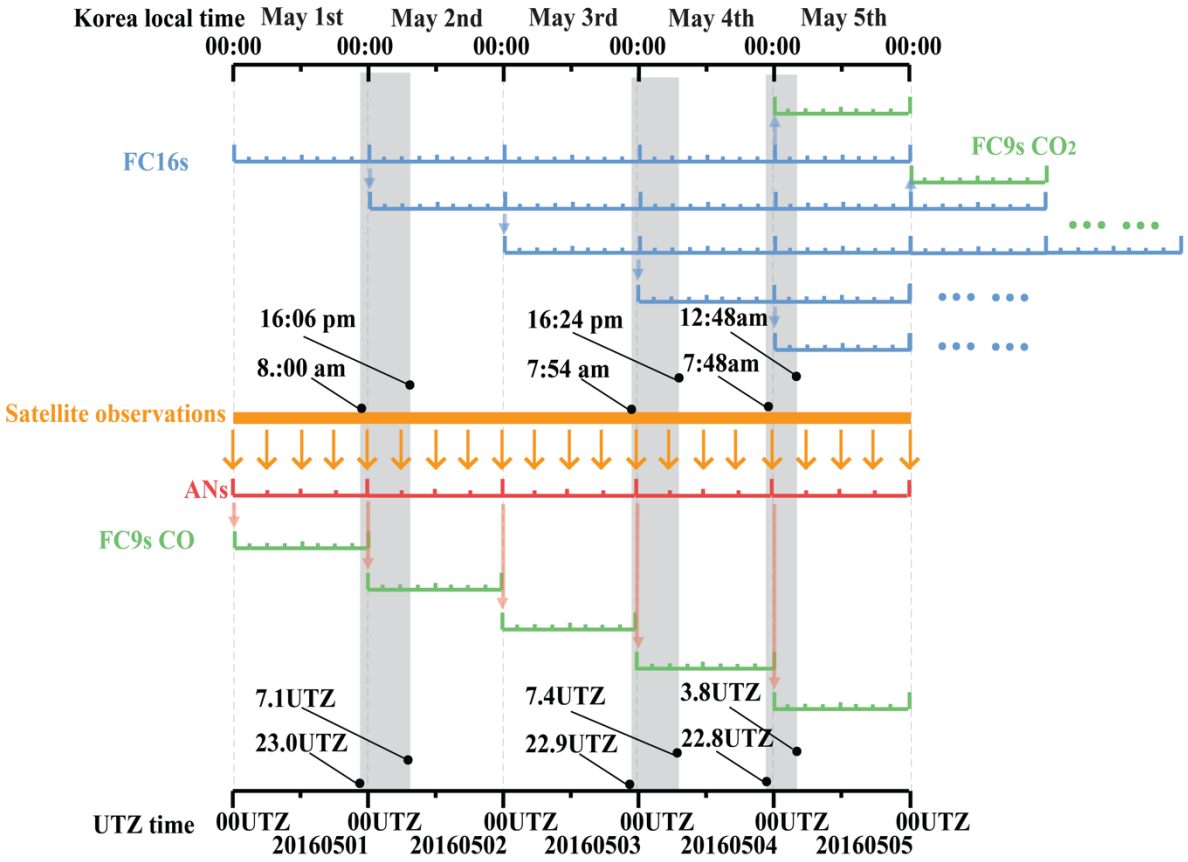

Figure S1. CAMS configuration. Left panel corresponds to the time configuration of the CAMS CO and CO2 evaluated in this study. The black lines represent Korea local time (on the top) and UTC time (on the bottom). The blue lines represent CAMS 5-day FC16s. FC16s are initialized with forecasts from the previous day. The orange line represents satellite observations (i.e., CO from MOPITT and IASI, CO2 from GOSAT) assimilated in CAMS (ANs). Gray shade denotes campaign time of the DC-8 aircraft. A typical DC-8 flight starts at 8am Korea time (23 UTC of previous day) and ends at 4pm Korea time (7 UTC).

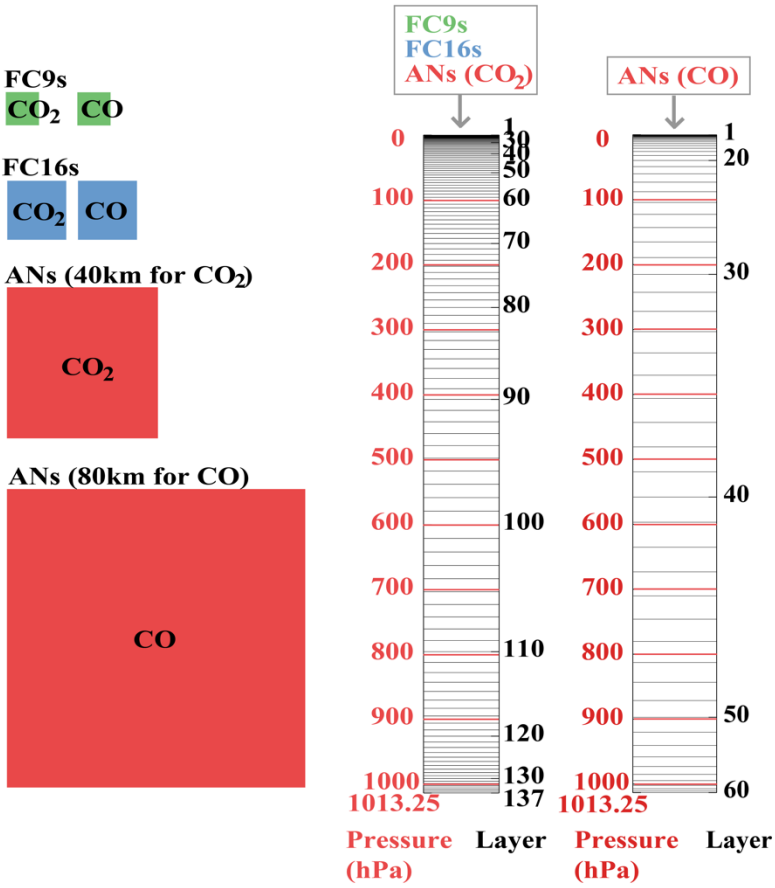

Figure S2. Model grid sizes of the CAMS and vertical structures of the model layers assuming the surface pressure being 1013.25hPa. FC9s, FC16s, and ANs for CO_2 (40 km) have 137 vertical layers. ANs for CO (80 km) have 60 vertical layers.

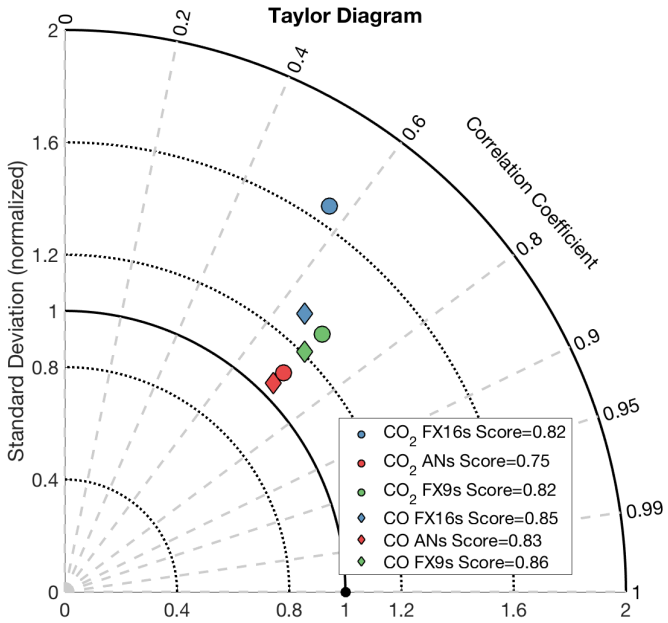

Figure S3. Taylor diagram for CAMS CO (diamonds) and CO_2 (circles) from FC9s (green), FC16s (blue), and ANs (red). Also shown are the Taylor scores.

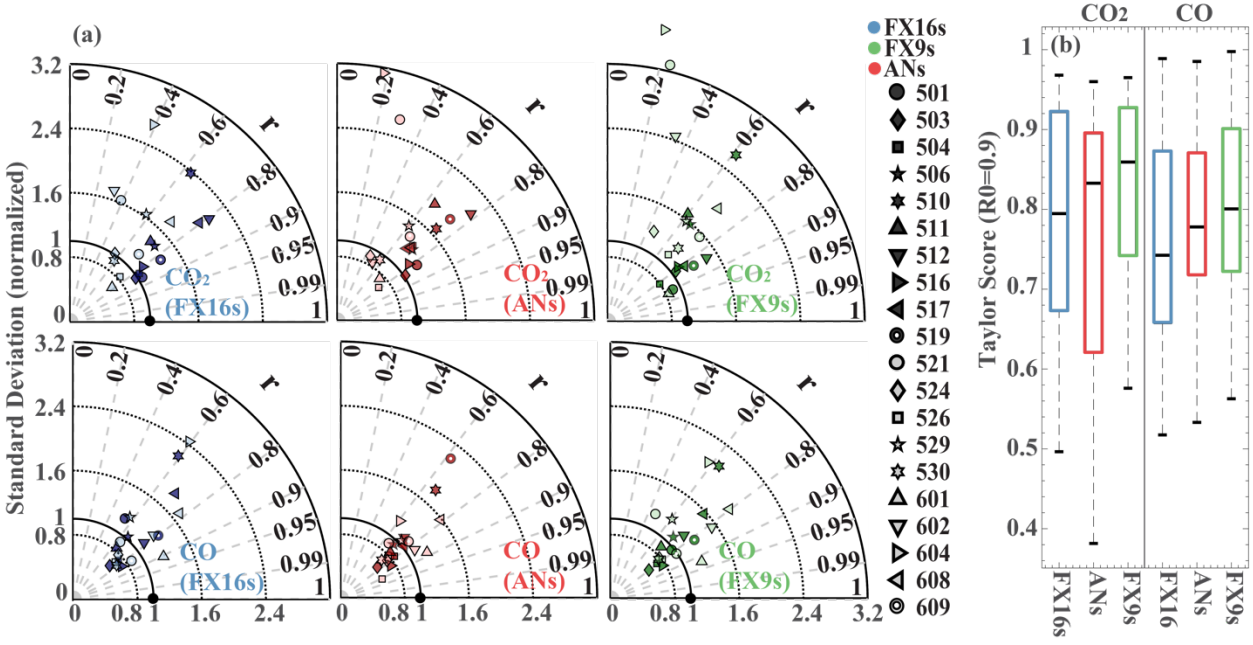

Figure S4. (a) Taylor diagrams for CAMS CO_2 (first row) and CO (second row) from 16-km forecasts (FC16s, left column), analyses (ANs, middle column), and 9-km forecasts (FC9s, right column) for individual flights (different symbols). (b) Boxplot of Taylor scores for CAMS CO_2 (left panel) and CO (right panel) from FC16s (blue), ANs (red), and FC9s (green).

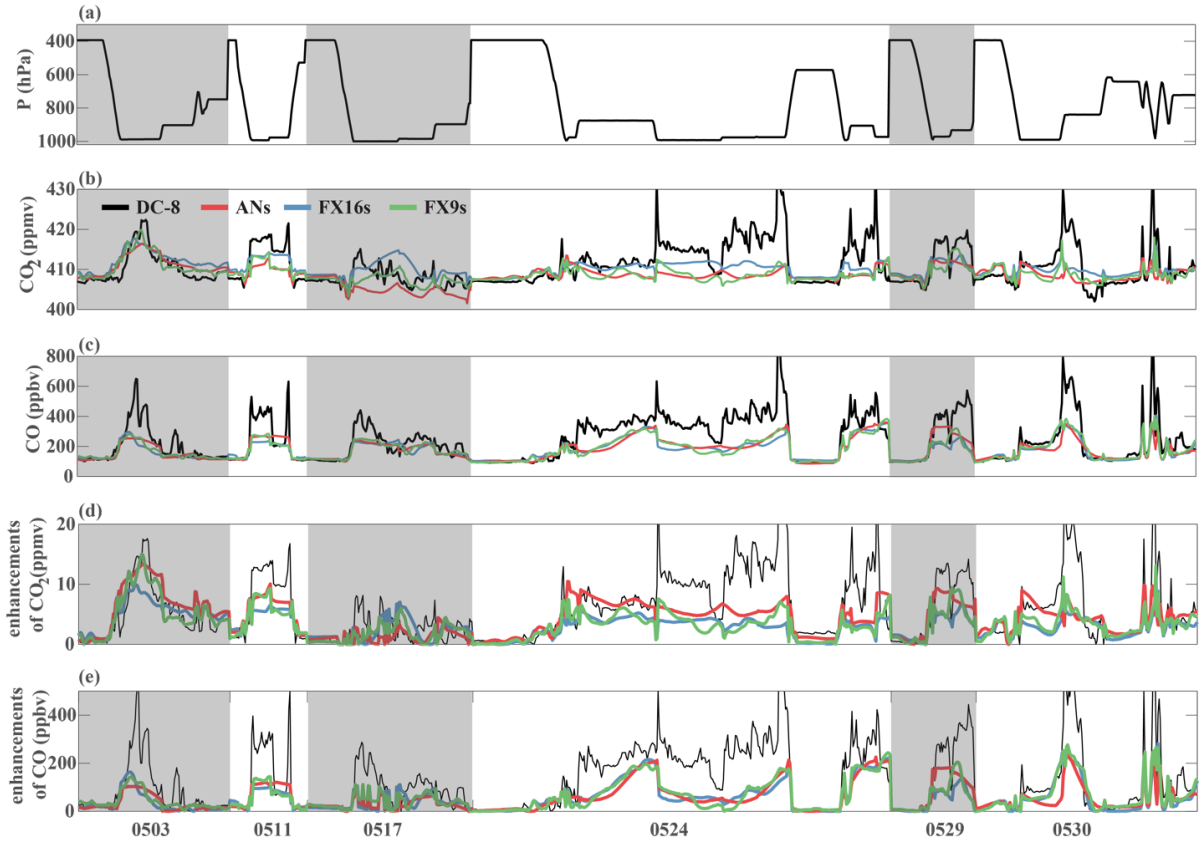

Figure S5. Time series of (a) pressure levels, (b) CO_2 concentrations and (d) their enhancements relative to background values, (c) CO concentrations and (e) their enhancements relative to background values along DC-8 aircraft tracks over the West Sea from measurements (black), 16-km forecasts (FC16s, blue), analyses (ANs, red), and 9-km forecasts (FC9s, green).

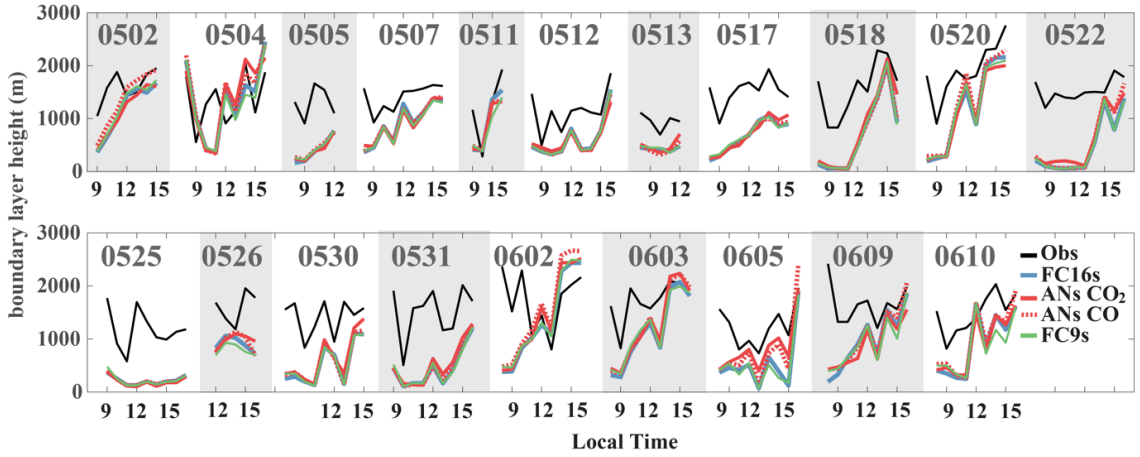

Figure S6. Hourly-average time series of the mixing layer heights derived from the airborne DIAL-HSRL measurements of aerosol backscatter (black) and corresponding boundary layer heights from the four CAMS configurations (colored) along the DC-8 flight track during KORUS-AQ.

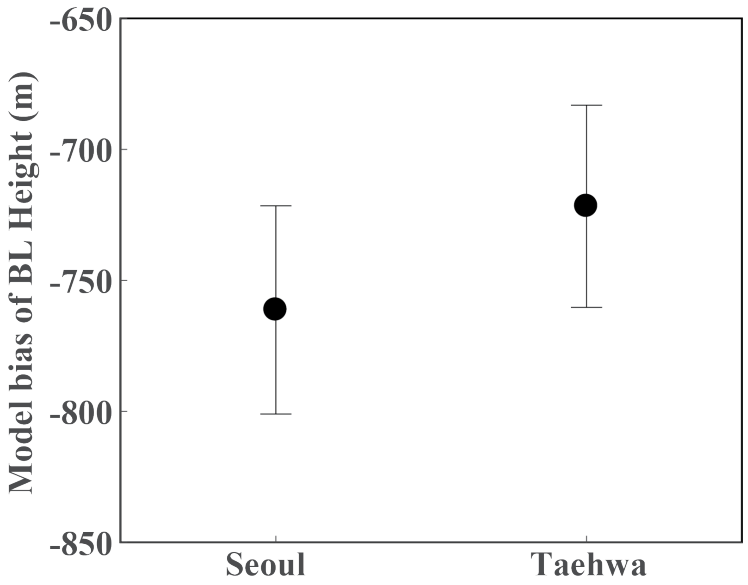

Figure S7. Model bias of boundary layer heights against boundary layer heights derived from the airborne DIAL-HSRL measurements of aerosol backscatter. Error bars represent standard deviations among the four CAMS configurations (i.e., FC16s, 80km ANs for CO, 40km ANS for CO_2, and FC9s).

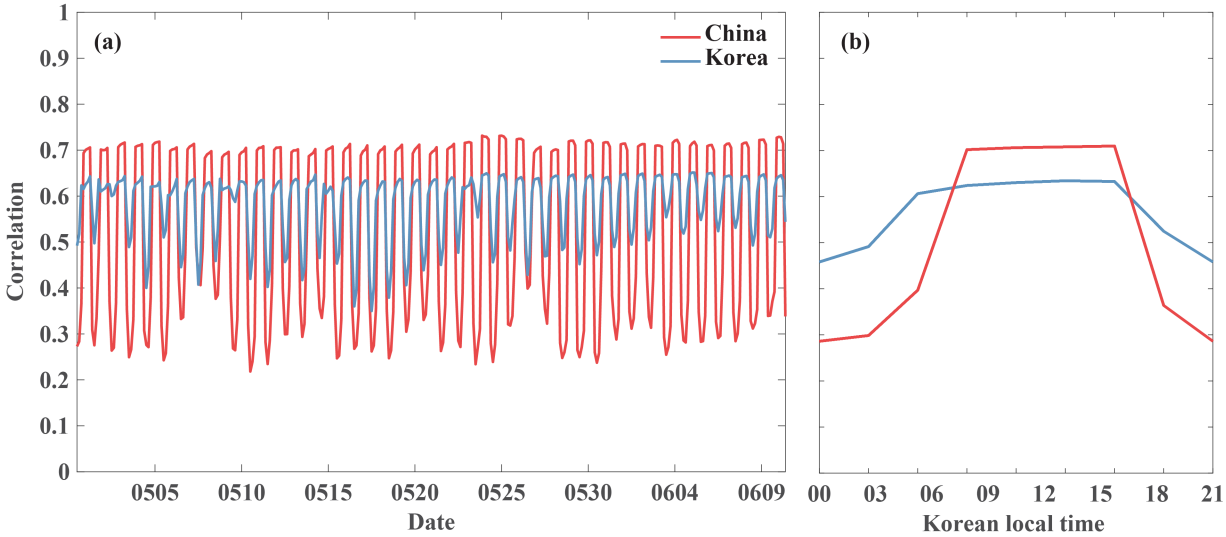

Figure S8. (a) Time series of spatial correlations between CO emissions and CO2 fluxes din CAMS over East China (which dominates Chinese contribution to the West Sea (Tang et al., 2018)) and Korea. (b) Averaged diurnal cycle of spatial correlations between CO emissions and CO2 fluxes in CAMS over East China and Korea.

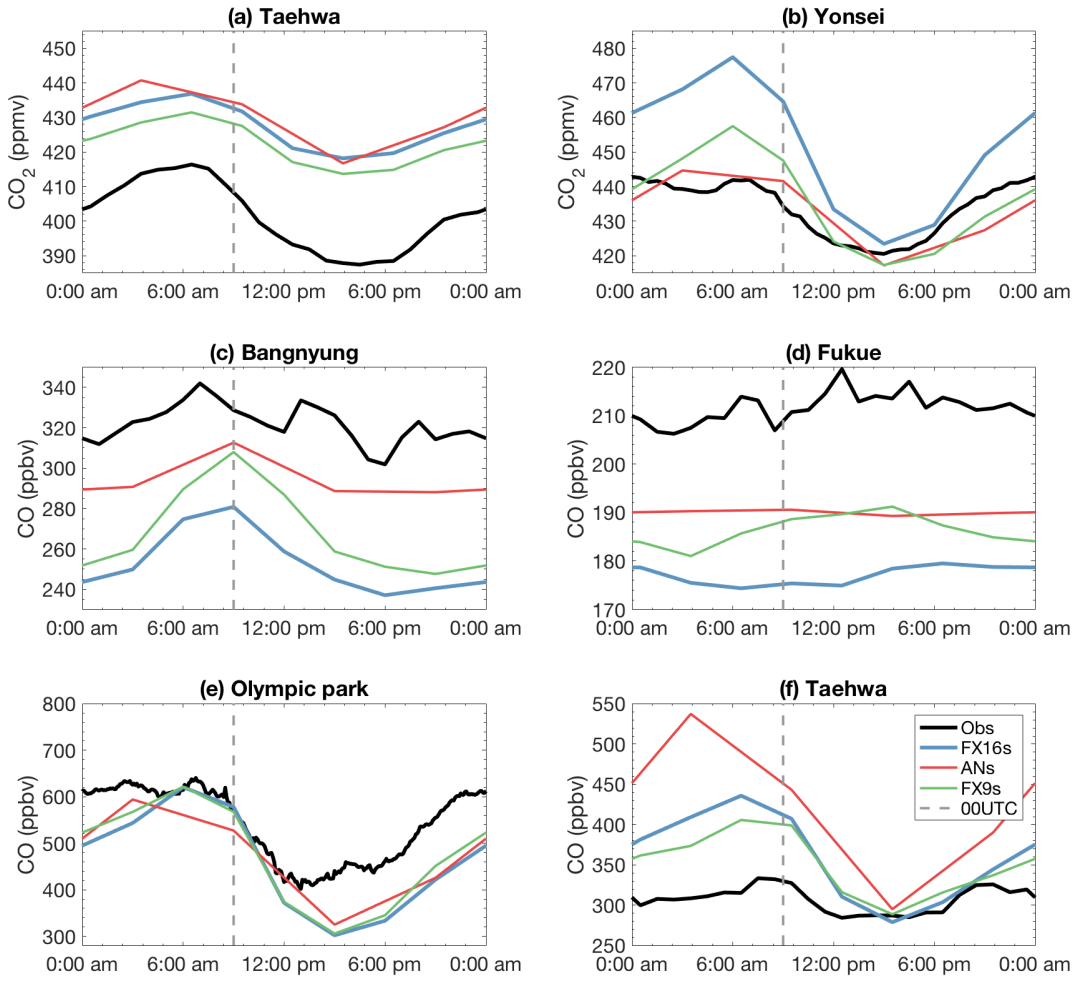

Figure S9. Diurnal cycles of CO_2 (a–b) and CO (c–f) concentrations averaged over days with available data during the KORUS-AQ period from observations (black), 16-km forecasts (FC16s, blue), analyses (ANs, red), and 9-km forecasts (FC9s, green) at fix ground sites, including (a, f) Taehwa, (b) Yonsei, (c) Bangnyung, (d) Fukue, and (e) Olympic park. CAMS values are averages across layers with pressure higher than 95% of the surface pressure.

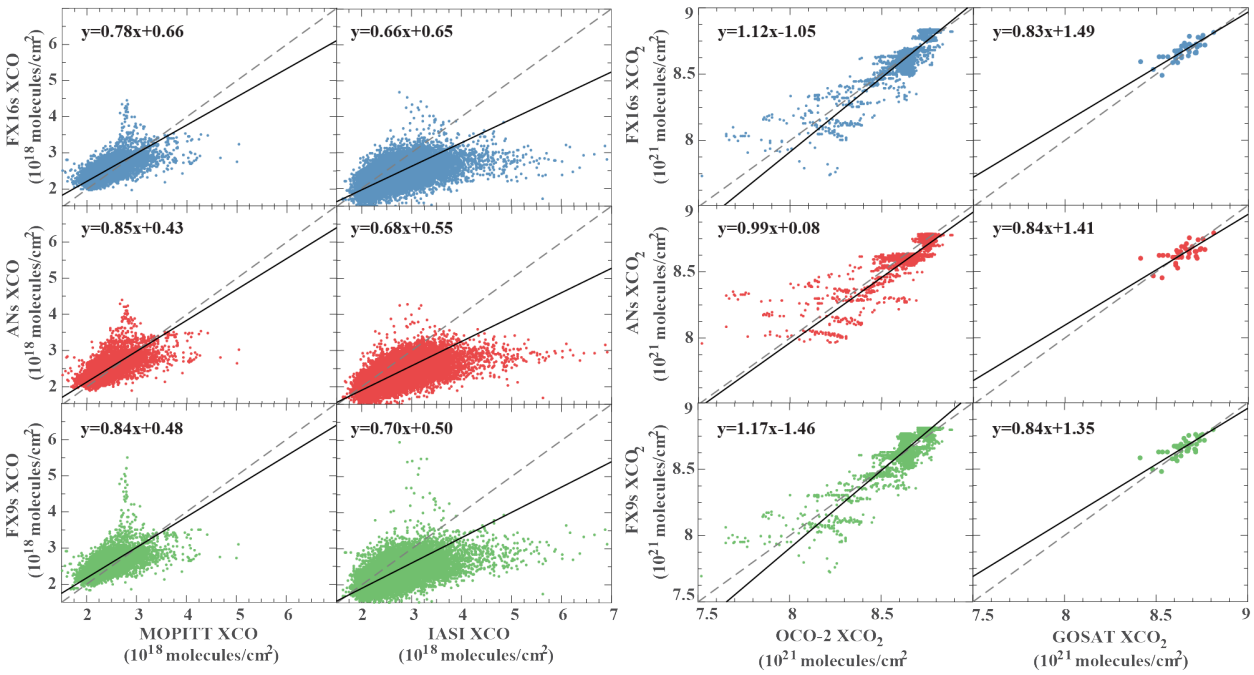

Figure S10. Comparisons between satellite observations and CAMS XCO and XCO2 from 16-km forecasts (FC16s, blue, 1st row), analyses (ANs, red, 2nd row), and 9-km forecasts (FC9s, green, 3rd row). The columns from left to right correspond to MOPITT XCO, IASI XCO, OCO-2 XCO2, and GOSAT XCO2, respectively.

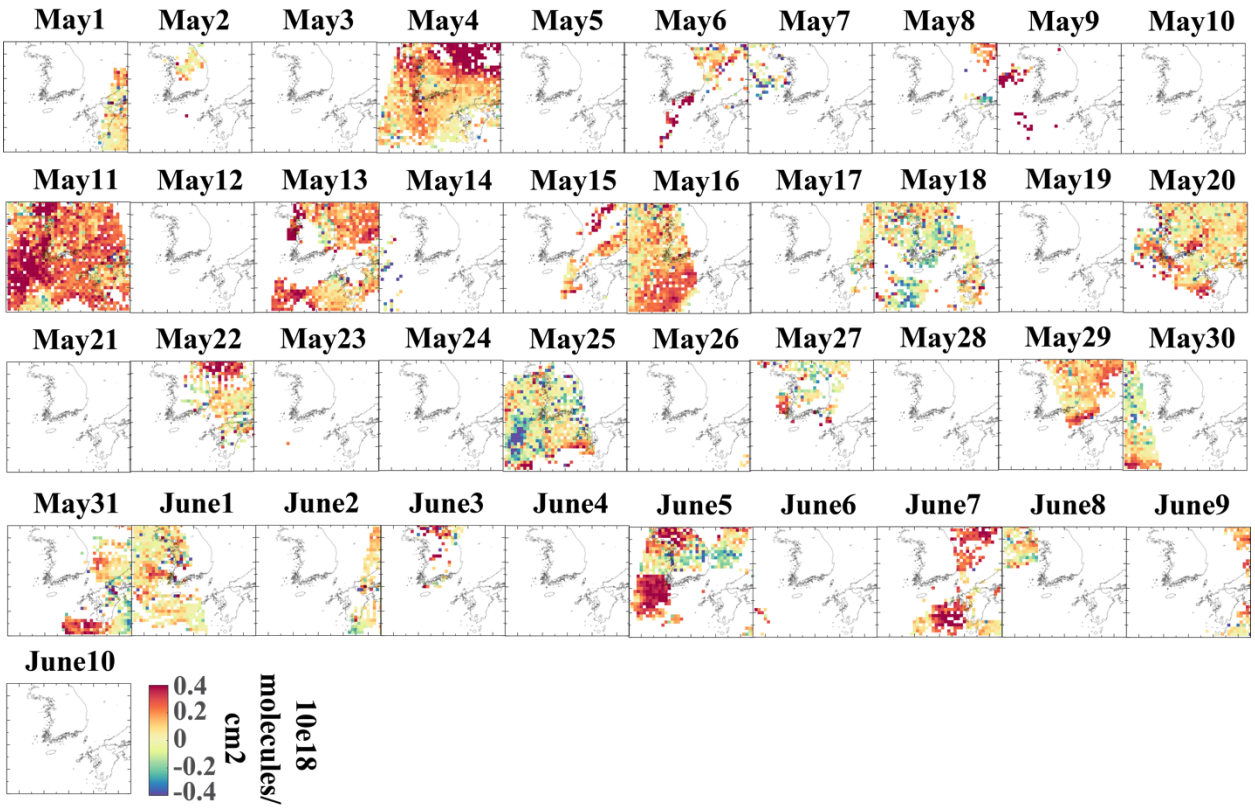

Figure S11. Daily spatial distributions of XCO biases in CAMS 9-km forecasts compared with MOPITT observations during the KORUS-AQ period (May 1 to June 10, 2016).

APPENDIX D

SOURCE CONTRIBUTIONS TO CARBON MONOXIDE CONCENTRATIONS DURING KORUS-AQ BASED ON CAM-CHEM MODEL APPLICATIONS

(Published in the *Journal of Geophysical Research: Atmospheres*,
https://doi.org/10.1029/2018JD029151)

Wenfu Tang[1], Louisa K. Emmons[2], Avelino F. Arellano[1], Benjamin Gaubert[2], Christoph Knote[3], Simone Tilmes[2], Rebecca R. Buchholz[2], Gabriele G. Pfister[2], Glenn S. Diskin[4], Donald R. Blake[5], Nicola J. Blake[5], Simone Meinardi[5], Joshua P. DiGangi[4], Yonghoon Choi[4,6], Jung-Hun Woo[7], Cenlin He[8], Jason R. Schroeder[4], Inseon Suh[9], Hyo-Jung Lee[10], Hyun-Young Jo[10], Yugo Kanaya[11], Jinsang Jung[12], Youngjae Lee[13], Danbi Kim[13]

[1]Department of Hydrology and Atmospheric Sciences, University of Arizona, Tucson, AZ, USA
[2]Atmospheric Chemistry Observations and Modeling Laboratory, National Center for Atmospheric Research, Boulder, CO, USA
[3]Meteorologisches Institut, Ludwig-Maximilians-Universität München, Munich, Germany
[4]NASA Langley Research Center, Hampton, VA, USA
[5]Department of Chemistry, University of California, Irvine, CA, USA
[6]Science Systems and Applications, Inc., Hampton, VA, USA
[7]Dept. of Advanced Technology Fusion, Konkuk University, Korea
[8]Research Applications Laboratory, National Center for Atmospheric Research, Boulder, CO, USA
[9]Dept. of Earth & Environmental Sciences, Korea University, Korea
[10]Pusan National University, Korea
[11]Japan Agency for Marine-Earth Science and Technology, Japan
[12]Korea Research Institute of Standards and Science, Korea
[13]National Institute of Environmental Research, Korea

Tang, W., Emmons, L. K., Arellano, A. F., Gaubert, B., Knote, C., Tilmes, S., Buchholz, R. R., Pfister, G. G., Diskin, G. S., Blake, D. R., Blake, N. J., Meinardi, S., DiGangi, J P., Choi, Y., Woo,J., He, C., Schroeder, J. R., Suh, I., Lee, H., Jo, H., Kanaya, Y.,Jung, J., Lee, Y., and Kim, D., 2019. Source contributions to carbon monoxide concentrations during KORUS-AQ based on CAM-chem model applications*, J. Geophys. Res. Atmos.*, 10.1029/2018JD029151.

Abstract

We investigate regional sources contributing to CO during the KORUS-AQ campaign conducted over Korea (May 1st to June 10th 2016) using 17 tagged CO simulations from the Community Atmosphere Model with chemistry (CAM-chem). The simulations use three spatial resolutions, three anthropogenic emission inventories, two meteorological fields, and nine emission scenarios. These simulations are evaluated against measurements from DC-8 and MOPITT. Results show that simulations using bottom-up emissions are consistently lower (bias: -34~-39%) and poorer performing (Taylor skill: 0.38–0.61) than simulations using alternative anthropogenic emissions (bias: -6~-33%; Taylor skill: 0.48–0.86), particularly for enhanced Asian CO and VOC emission scenarios, suggesting underestimation in modeled CO background and emissions in the region. The ranges of source contributions to modeled CO along DC-8 from Korea and southern (90°E–123°E, 20°N–29°N), middle (90°E–123°E, 29°N–38.5°N), and northern (90°E–131.5°E, 38.5°N–45°N) East Asia (EA) are 6–13%, ~5%, 16–28%, and 9–18%, respectively. CO emissions from middle and northern EA can reach Korea via transport within the boundary layer, whereas those from southern EA are transported to Korea mainly through the free troposphere. Emission contributions from middle EA dominate during continental outflow events (29–51%), while Korean emissions play an overall more important role for ground sites (up to 25–49%) and plumes within the boundary layer (up to 25–44%) in Korea. Finally, comparisons with four other source contribution approaches (FLEXPART-WRF back trajectories, WRF inert tracer, China signature VOCs, CO to CO_2 enhancement ratios) show general consistency with CAM-chem.

1. Introduction

Air pollutants and emissions have significant impacts on environment, climate, ecosystem, agriculture, public health and safety [Charlson et al, 1992; Feely et al., 2004; Doney et al., 2007; Ohara et al., 2007; Shindell et al., 2011; Maher et al., 2016; Gao et al., 2017]. This is especially the case in East Asia, where human activities are most intense, accompanied by immense energy consumption [Kennedy et al., 2015]. Previous studies have shown that anthropogenic combustion and emissions in East Asia have impacts at both local and hemispheric scales, including long-range transport to North America [Jaffe et al., 1999; Jacob et al., 1999; Heald et al., 2006; Jiang et al., 2016]. This highlights an urgent need to better understand emissions and air quality in East Asia.

Field campaigns provide valuable measurements. For example, the NASA Pacific Exploratory Mission in the Western Pacific Ocean (PEM-West) Phase B in 1994 studied chemical processes and long-range transport of trace species in Asian outflow over the Northwest Pacific Ocean [Hoell et al., 1997]. The NASA Transport and Chemical Evolution over the Pacific (TRACE-P) was conducted over the Northwest Pacific in 2001 to investigate Asian chemical outflow and its sources, and chemical evolution [Jacob et al., 2003]. The Asian Pacific Regional Aerosol Characterization Experiments (ACE-Asia) in 2001 aimed to understand the properties and controlling factors of aerosols in the atmosphere of East Asia and the Northwest Pacific [Huebert et al., 2003].

Recently, the Korea United States Air Quality (KORUS-AQ) field measurement campaign, was performed based on an international collaboration between U.S. and South Korea, led by the National Institute of Environmental Research (NIER) of Korea and the National Aeronautics and Space Administration (NASA) of the United States. The campaign was conducted over South Korea and its surrounding waters in May-June 2016. During the campaign, observations from aircraft, ships, ground sites, and satellites were integrated with models to help understand air quality and factors controlling air quality in the region. The campaign had three main research foci: (1) the opportunities and challenges for satellite observations of air quality; (2) the key factors governing ozone photochemistry and aerosol evolution; (3) model performance and needed improvements to better represent atmospheric composition over Korea and its connection to the larger global atmosphere [Al-Saadi et al., 2014]. To better investigate these research topics, especially (2) and (3), it is critical to understand and quantify the influence of different pollution sources on the air quality in in the region.

Tagging in chemical transport models (CTM) is a powerful tool to investigate source contributions to air pollutants' concentrations levels [Granier et al., 1999; Emmons et al., 2012]. The tagging method is particularly appropriate in chemistry by explicitly accounting for non-linearity in the sensitivity to change in emissions [Clappier et al. 2017]. CO is a common pollutant in the atmosphere, being directly emitted from incomplete combustion sources, such as vehicles, industry, and biomass burning, as well as chemically produced from oxidation of methane and other hydrocarbons. CO is also a good tracer of pollution transport, with only one photochemical sink and an intermediate lifetime (approximately a month) [Li et al., 2002; Duncan and Bey, 2004;

Gamnitzer et al., 2006]. Such characteristics make tagging CO feasible and tagged CO relatively reliable as a tracer of pollution plumes from regional to hemispheric scales. Tagged CO has been widely used in previous studies for various research purposes such as source attribution [Granier et al., 1999; Staudt et al., 2001; Liu et al., 2003; Pfister et al., 2004, 2011; Chen et al. 2009; Park et al., 2009; Protonotariou et al., 2013; Buchholz et al., 2016; Fisher et al., 2017] and inverse modeling [Heald et al., 2004; Pétron et al., 2004; Arellano et al., 2004, 2006]. Our goal in this study is to elucidate the regional sources contributing to observed CO concentrations within the troposphere during the KORUS-AQ campaign over Korea using the tagged CO algorithm that is implemented in the Community Atmosphere Model with Chemistry (CAM-chem).

Despite its wide use in the community, the reliability of source contribution analysis through tagged tracers in CTMs needs further evaluation. Sources apportioned by tagged CO are sensitive to many parameters such as emissions, transport, chemistry, and resolution in the CTM. These factors are important sources of model errors [Naik et al., 2013; Strode et al. 2015; Gaubert et al., 2016; Yan et al., 2016; Müller et al., 2018], which could lead to CO underestimation commonly seen in most global chemistry transport models (CTMs) but have not been fully understood yet [Shindell et al., 2006; Stein et al., 2014; Tilmes et al., 2015; Fisher et al., 2017]. To provide insights on the sensitivity of our findings on source contributions to the aforementioned factors, we conduct an ensemble of model simulations with different model configurations and report the range of estimates of the source contributions from these simulations. In addition, we compare these results with four other source contribution approaches to examine the rigor of our findings using CAM-chem. KORUS-AQ is a desirable testbed to evaluate and validate the source contribution analysis from tagged CO tracers in CAM-chem, as there are extensive observations and additional modeling tools used for source contribution analysis in this campaign. Here, we compare the ensemble of tagged source contribution results with other analyses from: (1) the Weather Research and Forecasting (WRF) inert NO_2 tracers [Grell et al., 2005; Pfister et al., 2017]; (2) the FLEXible PARTicle dispersion model (FLEXPART) back trajectory calculations driven by WRF [Stohl et al., 2005; Brioude et al., 2013], (3) Volatile Organic Compounds (VOCs) signatures suggested by the Whole Air Sampling (WAS) group from the University of California, Irvine (UCI), and (4) observed CO to CO_2 enhancement ratios.

This paper is organized as follows. We introduce models and observations in Section 2. In Section

3, we evaluate the performance of CAM-chem simulations of CO during KORUS-AQ. In Section 4, we provide the source contribution analysis using a set of CAM-chem simulations with tagged CO for the KORUS-AQ field campaign. In Section 5, results of the source contribution analysis by tagged tracers in CAM-chem are compared with four other approaches. Section 6 concludes the study.

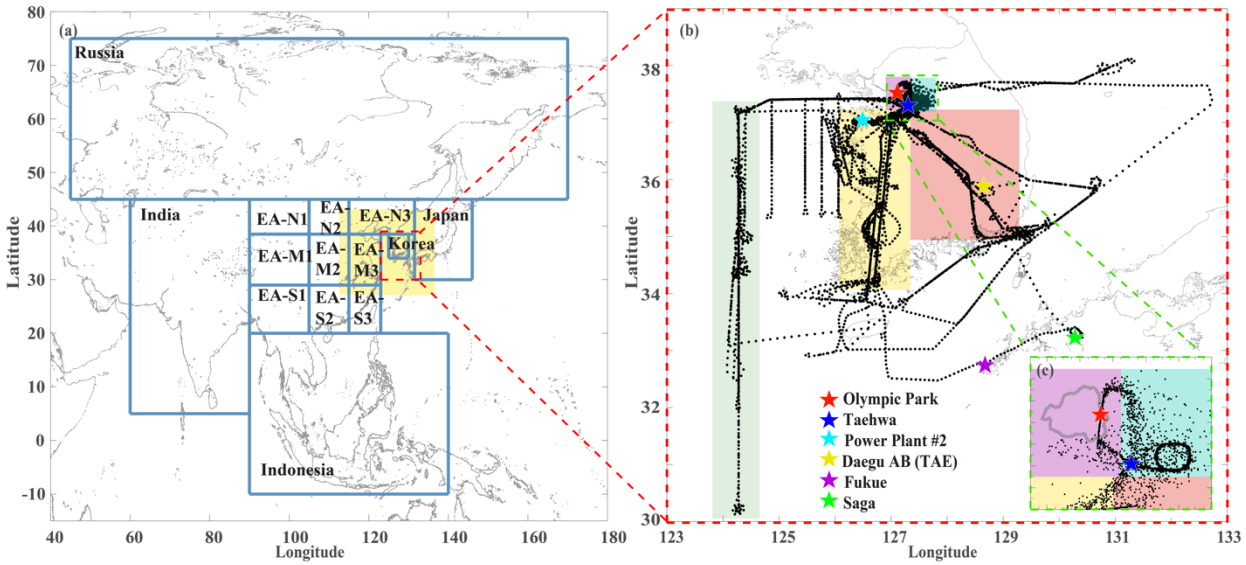

Figure D1. Tagged regions in CAM-chem, domain of FLEXPART-WRF, and DC-8 flight tracks and locations of ground sites during the KORUS-AQ campaign (May 1st – June 10th, 2016). (a) Blue rectangles denote 14 tagged source regions in CAM-chem: Korea, Russia, India, Indonesia, Japan, East Asia-North1 (EA-N1), East Asia-North2 (EA-N2), East Asia-North3 (EA-N3), East Asia-Middle1 (EA-M1), East Asia-Middle2 (EA-M2), East Asia-Middle3 (EA-M3), East Asia-South1 (EA-S1), East Asia-South2 (EA-S2), and East Asia-South3 (EA-S3). We assign areas outside these 14 tagged regions as the rest of the world. Yellow shaded area represents FLEXPART-WRF domain used in this study. (b) DC-8 flight tracks during KORUS-AQ are shown as dotted lines. The DC-8 aircraft measurements are classified into five groups (Seoul, Taehwa, West Sea, Seoul-Jeju jetway, Seoul-Busan jetway) shown as purple, blue, green, yellow, and red shaded areas, respectively. Colored stars represent 6 ground sites involved in the KORUS-AQ campaign. Also shown in (c) is the zoomed-in version of the green box in panel (b). Grey line denotes political boundary of Seoul.

2. Observations and Model Descriptions

2.1 Observations during KORUS-AQ

The KORUS-AQ campaign (May 1st – June 10th, 2016) provides comprehensive observations from aircraft, ships, and ground sites. Three aircraft (NASA DC-8, NASA B200 King Air, and Hanseo

King Air) were involved in the campaign. The NASA Langley B200 King Air was outfitted with only remote sensing instruments, so there were no onboard CO measurements for analysis, while Hanseo King Air flight tracks were usually at a relatively smaller scale. However, the NASA DC-8 aircraft flights covered Korea and its surrounding waters during KORUS-AQ, sampling the lower and mid-troposphere (see Figures 1 and S1). Thus, we use the measurements from the NASA DC-8 aircraft in this study. We also use the CO measurements from 3 ground sites involved in the KORUS-AQ campaign and the Measurements Of Pollution In The Troposphere (MOPITT) satellite retrievals. Depending on our analysis, model results are shown at all or part from the 6 sites presented in Fig.D1. The date and time in this paper are based on Korean local time.

Table D1. Model configurations for the 14 CAM-chem simulations. The simulations are named according to their configurations. Specifically, the naming follows the format of: C2TK<resolution>_<meteorology>_<emissions inventories>, where "C2TK" represents CESM2 Tags for KORUS-AQ. <Resolution> takes values of "05", "1", "2", corresponding to 0.47°×0.63°, 0.9°×1.25°, and 1.9°×2.5°. "G" and "M" in <meteorology> correspond to GEOS-FP and MERRA-2, respectively. <Emissions inventories> includes "HF" (HTAP + FINN), "CF" (CREATE +FINN), and "CMIP6" (CMIP6+FINN). The 9 additional simulations are based on C2TK1_G_HF, with doubled anthropogenic CO and/or VOC emissions over the globe or different regions.

Simulation name	Resolution	Meteorology	Emissions
C2TK1_G_HF	f09_f09 (0.9´1.25)	GEOS-FP	HTAP (anthro) + FINN (bb)
C2TK1_G_CF	f09_f09 (0.9´1.25)	GEOS-FP	CREATE (anthro) + FINN (bb)
C2TK1_G_CMIP6	f09_f09 (0.9´1.25)	GEOS-FP	CMIP6 (anthro) + FINN (bb)
C2TK1_M_HF	f09_f09 (0.9´1.25)	MERRA-2	HTAP (anthro) + FINN (bb)
C2TK1_M_CF	f09_f09 (0.9´1.25)	MERRA-2	CREATE (anthro) + FINN (bb)
C2TK1_M_CMIP6	f09_f09 (0.9´1.25)	MERRA-2	CMIP6 (anthro) + FINN (bb)
C2TK2_G_HF	f19_f19 (1.9´2.5)	GEOS-FP	HTAP (anthro) + FINN (bb)
C2TK05_G_HF	f05_g16 (0.47´0.63 and gx1v6 mask)	GEOS-FP	HTAP (anthro) + FINN (bb)
Global CO ×2	f09_f09 (0.9´1.25)	GEOS-FP	HTAP (anthro) + FINN (bb), with doubled global anthro CO emissions
EA CO ×2	f09_f09 (0.9´1.25)	GEOS-FP	HTAP (anthro) + FINN (bb), with doubled EA anthro CO emissions
Korea CO ×2	f09_f09 (0.9´1.25)	GEOS-FP	HTAP (anthro) + FINN (bb), with doubled Korea anthro CO emissions
EA-N CO ×2	f09_f09 (0.9´1.25)	GEOS-FP	HTAP (anthro) + FINN (bb), with doubled EA-N anthro CO emissions
EA-M CO ×2	f09_f09 (0.9´1.25)	GEOS-FP	HTAP (anthro) + FINN (bb), with doubled EA-M anthro CO emissions
EA-S CO ×2	f09_f09 (0.9´1.25)	GEOS-FP	HTAP (anthro) + FINN (bb), with doubled EA-S anthro CO emissions
EA & Korea CO ×2	f09_f09 (0.9´1.25)	GEOS-FP	HTAP (anthro) + FINN (bb), with doubled EA and Korea anthro CO emissions
EA & Korea VOC ×2	f09_f09 (0.9´1.25)	GEOS-FP	HTAP (anthro) + FINN (bb), with doubled EA and Korea anthro VOC emissions
EA & Korea CO & VOC ×2	f09_f09 (0.9´1.25)	GEOS-FP	HTAP (anthro) + FINN (bb), with doubled EA and Korea anthro CO and VOC emissions

2.1.1 Observations of CO

Onboard the DC-8 aircraft, CO concentrations were measured by the DACOM/DLH team (Differential Absorption CO Measurement and Diode Laser Hygrometer from Langley Research Center). The DACOM/DLH team used the in-situ diode laser spectrometer system (which measured absorption lines of several species including CO with three tunable diode lasers) to take CO measurements with a time response of 1 second, precision of 0.1 ppbv (or < 1%), and accuracy of 2% (https://airbornescience.nasa.gov/instrument/DACOM) [Warner et al., 2010]. In addition, we use *in-situ* CO measurements available from 3 KORUS-AQ ground sites, including Taehwa (127.311°E, 37.312°N), Fukue (128.682°E, 32.752°N), and Olympic Park (127.124°E, 37.522°N). Taehwa is managed by NIER and uses the Thermo 48i instrument for CO measurements. Fukue is managed by the Japan Agency for Marine-Earth Science and Technology (JAMSTEC) and uses the Thermo 48C instrument (Kanaya et al., 2016). Olympic Park is managed by Korea Research Institute of Standards and Science and employs a KENTEK CO analyzer. To provide a broader spatial context for this study, we also utilize the MOPITT version 7, multispectral TIR/NIR, Level 3 retrievals of daytime CO total column density [Deeter et al., 2017a]. Onboard the NASA Terra satellite, these retrievals have a spatial resolution at nadir of about 22 km with satellite overpass time around 10:30 am. The retrieval qualities can be surface dependent with the effects of geophysical noise generally stronger over land than over the ocean, especially over mountainous regions [Deeter et al., 2015]. In MOPITT version 7, meteorological fields from the Modern-Era Retrospective analysis for Research and Applications, Version 2 (MERRA-2), and Moderate-Resolution Imaging Spectroradiometer (MODIS) Collection 6 cloud mask product (instead of Collection 5) are used for retrieving CO. MOPITT version 7 products show generally smaller retrieval biases and reduced bias variability compared to previous versions [Deeter et al., 2017a]. The multispectral TIR/NIR products have larger degrees of freedom for signal and higher sensitivity to CO, especially over land and near the surface, compared to the TIR-only products [Worden et al., 2010]. The Level 3 products are produced by averaging on a one-degree latitude/longitude grid and are less affected by random retrieval errors compared to level 2 products [Deeter, 2017b].

2.1.2 Observations of CO_2 and VOCs

In addition to CO measurements, we also use measurements of CO_2 collected aboard the DC-8 aircraft for another source analysis approach. The AVOCET team (Atmospheric Vertical Observations of CO_2 in the Earth's Troposphere from Langley Research Center) measured CO_2 with high precision using a modified LI-COR model 6252 non-dispersive infrared spectrometer (NDIR). The AVOCET team provided CO_2 concentrations by sensing the difference in light absorption between the continuously flowing sample and reference gases (https://airbornescience.nasa.gov/instrument/AVOCET) [Vay et al., 2011]. The ratio of emitted CO and CO_2 is a measure of combustion efficiency, since incomplete combustion produces CO. The CO to CO_2 enhancement ratios (as proxy of emission ratios) have proven to be a useful indicator of anthropogenic combustion efficiency [e.g., Bakwin et al. 1994; Wang et al., 2010; Turnbull et al., 2011; Silva et al., 2013; Tang et al. 2018], despite that the ratios are impacted by various factors including air mass aging and reaction with hydroxyl radical (OH). Besides, we also assume that the potential ocean sink of CO_2 between China and Korea does not significantly influence the source contribution analysis, because of the short transport time of Chinese pollution to the KORUS-AQ domain. We conduct the reduced major axis regression [Smith, 2009] using the DC-8 CO and CO_2 measurements (every 1 second) to compute the regression slope (dCO/dCO_2) for every minute of each flight data series. The regression slopes (dCO/dCO_2) correspond to the enhancement ratios [Parrish et al., 2002].

VOCs measurements and analysis made by the UC-Irvine Whole Air Sampler (WAS) group is also used to corroborate our findings derived from the tagged CO simulations. The WAS group (https://espo.nasa.gov/korus-aq/content/WAS_%E2%80%93_UCI) collected whole air samples during the DC-8 flights and analyzed them at the UC Irvine laboratory using Gas Chromatography for about 90 species of VOCs. The WAS group, as well as previous studies, suggests four China signature VOCs, including CCl_4, CFC-113, CFC-114, and carbonyl sulfide (OCS) [Blake et al., 1996; Palmer et al., 2003; Blake et al., 2003, 2004; Wang et al., 2006; Barletta et al., 2009; Xue et al., 2011]. Based on the VOC measurements and analyses, the WAS group also find that H-1211 (CF_2ClBr), which was previously used as an indicator of Chinese air masses [Blake et al., 2001, 2003], can no longer be used as an indicator during the KORUS-AQ period. We test the consistency between our source contribution results and their conclusions (see Section 5.2).

2.2 Global Model with Tagged CO

2.2.1 Model Description

The Community Earth System Model (CESM) is a global earth system model including the atmosphere, land, ocean, and ice components [Hurrell et al., 2013]. CAM-chem is the atmospheric component of CESM with chemistry, coupled with the land model [Lamarque et al., 2012]. In this study, we use a development version of CESM (cesm2_0_alpha07c). CESM can be configured with various component sets (http://www.cesm.ucar.edu/models/cesm2.0/cesm/compsets.html). Our simulations use the component set of FCSD which includes CAM6 physics with chemistry and the meteorology is relaxed to specified dynamics (SD). Tropospheric and stratospheric chemistry are included, with a volatility basis set secondary organic aerosol scheme and modal aerosols. In our CAM-chem simulations, we use a significantly updated tropospheric chemistry mechanism: Model for OZone and Related chemical Tracers, version T1 (MOZART-T1). MOZART-T1 includes an expansion of the isoprene oxidation scheme, splits lumped aromatics and terpenes to individual species, and has a more detailed representation of organic nitrates (https://www2.acom.ucar.edu/gcm/mozart). The model meteorology (including winds, surface pressure, and temperature) is nudged towards prescribed meteorological fields on their native levels, which is the lower 56 of 72 levels ranging from the surface to ~2 hPa [Morrison et al., 2008; Bogenschutz et al., 2012, 2018; Liu et al., 2016]. In terms of the land component (LND), our configuration uses the Community Land Model Version 5.0 (CLM5.0). In addition, FCSD also uses the prescribed ocean mode (DOCN%DOM) as well as prescribed sea ice (CICE).

We use three model resolutions, including 0.9°×1.25° (1-degree; f09_f09), 1.9°×2.5° (2-degree; f19_f19), and 0.47°×0.63° (half-degree; f05_g16). For the 1-degree and 2-degree configurations, ATM, LND, OCN, and CICE use the finite volume grid with the same resolutions of 0.9°×1.25° and 1.9°×2.5°, respectively. For the half-degree configuration, ATM and LND use finite volume grid and both have resolutions of 0.47°×0.63°, while OCN and ICE use the displaced Greenland pole grid of approximately 1-degree resolution (gx1v6 mask). The displaced Greenland Pole grid is a latitude/longitude grid with the North Pole displaced over Greenland to avoid singularity problems in the OCN and ICE models.

2.2.2 Emissions

We employ three anthropogenic emission inventories with monthly time resolution, including the Hemispheric Transport of Air Pollution (HTAP) version 2 inventory [Janssens-Maenhout et al., 2015], the Community Emissions Data System (CEDS) for Coupled Model Intercomparison Project Phase 6 (CMIP6) [Hoesly et al., 2017], and the Comprehensive Regional Emissions Inventory for Atmospheric Transport Experiment (CREATE) embedded in HTAPv2 [Woo et al., 2013]. HTAPv2 provides monthly and annual emissions for CO, SO_2, NO_X, non-methane volatile organic compounds (NMVOCs), NH_3, PM_{10}, $PM_{2.5}$, black carbon (BC), and organic carbon (OC) for the years 2008 and 2010 at a resolution of 0.1°×0.1°, by compiling regional inventories (e.g., the MIX inventory for Asian anthropogenic emissions; Li et al., 2017). The uncertainties in HTAPv2 CO emissions are 35%~70% for the energy and industry sectors, and 70%~150% for the residential and transportation sectors [Janssens-Maenhout et al., 2015]. CMIP6, developed with CEDS, provides anthropogenic emissions of CO, CH_4, NH_3, NO_X, SO_2, NMVOCs, and carbonaceous aerosols (BC and OC) from 1750 to 2014 at a resolution of 0.5°×0.5°. The CMIP6 inventory incorporates regional and country-specific inventories and existing energy consumption datasets. Despite the advantageous features in the CMIP6 emission inventory such as usage of updated emission factors and wide span of time, it has some limitations, including disaggregation of key non-combustion sectors and static gridding proxies for residential (and related) emissions. The uncertainties of CMIP6 have not been as well quantified as HTAP [Hoesly et al., 2017]. Due to the unavailability of data for year 2016, the HTAP 2010 and CMIP6 2014 emissions are used in this study, with the awareness that using the 2010 or 2014 inventory may not match actual 2016 emissions. CREATE version 1 is a regional inventory developed specifically for the KORUS-AQ campaign (covering China and Korea). We embed CREATE in HTAP because CAM-chem requires a global emission inventory as input.

For biomass burning emissions, we use the Fire INventory from NCAR version 1.5 (FINNv1.5 [Wiedinmyer et al., 2011]. The FINN inventory is gridded to the CAM-chem resolutions to generate global daily biomass burning emissions for input to CAM-chem. Major uncertainties of FINN come from missed fires (including small fires) and overestimation of the size of detected small fires. However, the two factors tend to cancel each other [Wiedinmyer et al., 2011]. Tang and Arellano [2017] suggested that treatment of emission factors in FINN (as well as other biomass

burning emission inventories) introduce uncertainties into the emission estimates. Monks et al. [2015] showed that CO emissions in FINN are overestimated over Siberia and Myanmar. We find that biomass burning emissions of CO are much lower than anthropogenic CO emissions over Korea and China, but are high in Russia and Indonesia during KORUS-AQ (Fig. DDS2d).

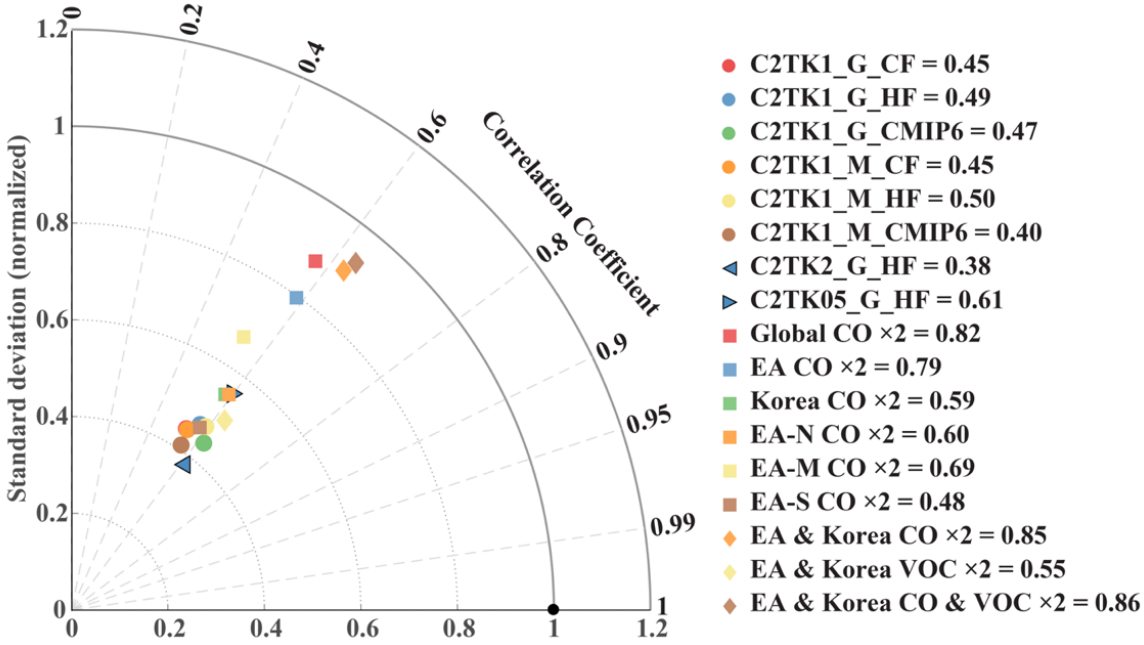

Figure D2. Taylor diagram of CO concentrations during the KORUS-AQ campaign from 17 CAM-chem CO simulations (colored symbols) and airborne CO observations by the DC-8 aircraft (black circle). Circles denote 6 simulations using the same resolution (0.9°×1.25°) but 2 different meteorological (GEOS-FP and MERRA-2) and 3 different emissions (HTAP+FINN, CREATE+FINN, and CMIP6+FINN). Triangles denote simulations using 2 different resolutions (0.47°×0.63° and 1.9°×2.5°). Squares and diamonds denote 9 simulations by doubling anthropogenic CO and/or VOC emissions over the globe or different regions. See Table D1 for definitions of different CAM-chem simulations. Also shown are Taylor scores (S).

We combine the three anthropogenic emission inventories with the biomass burning emission inventory (hereinafter HTAP+FINN, CREATE+FINN, and CMIP6+FINN) as input into CAM-chem. Spatial correlations between the combined inventories are 0.80 (HTAP+FINN and CREATE+FINN) and 0.96 (HTAP+FINN and CMIP6+FINN) over Korea, and 0.80 (HTAP+FINN and CREATE+FINN) and 0.68 (HTAP+FINN and CMIP6+FINN) over East Asia, respectively. Overall, the spatial distributions of total CO emissions from these combined inventories are consistent in the region (Fig. DDS2). The total CO emissions during the KORUS-

AQ period (May 1st –June 10th) derived from the CREATE+FINN, CMIP6+FINN, and HTAP +FINN are 3.08×10^{13}g, 3.38×10^{13}g, and 3.42×10^{13}g, respectively over East Asia (75°E–145°E, 15°N–55°N), while they are 1.89×10^{11}g, 2.72×10^{11}g, and 3.66×10^{11}g over Korea and its surrounding waters (123°E–133°E, 30°N–39°N), respectively.

2.2.3 Meteorological Fields

Our simulations use the meteorological fields generated by the NASA Goddard Global Modeling and Assimilation Office using the operational forecast model Goddard Earth Observing System (GEOS) Model, namely the GEOS Forward Processing (GEOS-FP) near real time forecast [Molod et al., 2015], and MERRA-2 [Gelaro et al., 2017]. MERRA-2 assimilates more observations and includes updates to the GEOS model and analysis scheme [Rienecker et al., 2011]. In this study, we prescribed wind fields, surface pressure, and temperature from either GEOS-FP or MERRA-2. The original spatial resolutions of GEOS-FP and MERRA-2 used by CAM-chem are 0.3125°×0.25° and 0.625°×0.5°, respectively. They are both regridded to the CAM-chem model resolutions before simulations. Currently, CAM-chem does not run with a nested grid, however, a regional refinement version of CAM-chem is under development based on the CAM model with a spectral element dynamical core (CAM-SE; Dennis et al., 2012). Because CO transport is mainly affected by winds (Heald et al., 2003; Liang et al., 2004), we compare CAM-chem wind fields over East Asia when the dynamic is nudge to GEOS-FP or MERRA-2. The differences in the wind patterns averaged over the KORUS-AQ period between the two datasets at 850 hPa, 500 hPa, and 200 hPa are small and negligible to some extent (Fig. DS3). We also compare time series of wind speeds at the surface layer from the two datasets over two large Korean cities (Seoul and Busan; Fig. DS3). In addition, we compare spatial distributions of temperature at the surface layer and surface pressure over East Asia (Fig. DS4). The surface-layer temperature and surface pressure from MERRA-2 are generally consistent with those from GEOS-FP, except in the western and northeastern China, where MERRA-2 tends to have higher temperature and pressure than GEOS-FP (e.g., differences of temperature at the surface layer are typically less than 12% while differences of surface pressure are typically less than 1%). GEOS-FP and MERRA-2 are the two external meteorological fields currently available to CAM-chem (Lamarque et al., 2012). We recognize that the differences between the two are small, hence may not fully represent uncertainties in the model transport. This is one of the limitation of our study. However, we note that even though the differences between

GEOS-FP and MERRA-2 wind, temperature, and pressure fields are small at synoptic-to-meso scale, they can still be different at meso-to-local scale, for example, over Seoul and Busan (Fig. DS3g-h). Meteorological fields assimilated by NCAR Data Assimilation Research Testbed (DART) is currently available (Gaubert et al., 2016, 2017). In our further study with CAM-chem, we will also use meteorological fields from DART.

Table D2. CAM-chem simulated source contributions to CO concentrations along the DC-8 flight tracks during KORUS-AQ. See text and Fig. D1 for definitions of tagged sources and five groups of DC-8 flight tracks.

		Seoul	Taehwa	West Sea	Seoul–Jeju jetway	Seoul–Busan jetway	All
Korea	All	10-22%	3-6%	0-1%	9-19%	4-8%	6-13%
	above 850 hPa	1-2%	1-3%	0-0%	1-1%	1-2%	1-1%
	below 850 hPa	11-24%	6-14%	0-2%	11-25%	5-11%	8-19%
Japan + Russia	All	7-10%	6-8%	4-5%	7-9%	9-12%	7-9%
	above 850 hPa	4-5%	5-7%	2-3%	4-5%	5-7%	4-5%
	below 850 hPa	7-10%	9-12%	4-7%	7-10%	12-15%	8-11%
Indonesia + India	All	2-3%	5-7%	4-5%	3-4%	5-6%	4-5%
	above 850 hPa	5-7%	6-8%	7-9%	7-10%	8-10%	7-9%
	below 850 hPa	2-3%	3-4%	2-3%	2-3%	3-4%	2-3%
EA–S	All	3-3%	6-8%	4-5%	4-5%	5-6%	5-5%
	above 850 hPa	5-7%	7-9%	7-10%	10-15%	7-10%	8-11%
	below 850 hPa	2-3%	3-3%	3-3%	2-3%	3-4%	3-3%
EA–M	All	16-29%	12-24%	29-51%	15-27%	10-19%	16-28%
	above 850 hPa	18-35%	12-23%	17-37%	14-26%	8-15%	14-26%
	below 850 hPa	15-29%	14-26%	36-58%	15-27%	11-21%	17-29%
EA–N	All	12-24%	8-16%	6-13%	10-20%	10-19%	9-18%
	above 850 hPa	7-14%	7-13%	4-8%	5-10%	5-10%	5-10%
	below 850 hPa	13-26%	13-25%	7-17%	12-23%	12-24%	11-22%
The rest + Ocean	All	7-9%	10-14%	8-11%	7-10%	11-15%	9-11%
	above 850 hPa	9-13%	11-15%	11-15%	10-14%	13-18%	11-15%
	below 850 hPa	6-8%	8-11%	6-9%	6-8%	9-13%	7-10%
CH4 oxidation	All	8-12%	12-19%	10-15%	9-14%	12-18%	10-15%
	above 850 hPa	12-19%	13-20%	14-20%	13-19%	15-22%	14-20%
	below 850 hPa	7-12%	9-14%	8-13%	8-12%	10-15%	8-13%
Biogenic	All	1-2%	1-2%	1-2%	1-2%	2-2%	1-2%
	above 850 hPa	1-2%	1-2%	1-2%	1-2%	2-2%	1-2%
	below 850 hPa	1-2%	1-2%	1-1%	1-2%	1-2%	1-2%
Chemical production besides CH_4	All	4-19%	7-24%	5-20%	6-22%	6-23%	6-22%
	above 850 hPa	8-24%	8-25%	8-25%	7-25%	10-26%	8-25%
	below 850 hPa	4-19%	5-21%	3-17%	6-21%	4-21%	5-21%

2.2.4 Tagging Approach

We tag CO emitted from different source regions as well as CO produced from chemical processes. Each of these tracers are treated in the model in the same way as the prognostic CO. In particular, the time evolution of the abundance of a specific tracer is calculated in the model from the same continuity equation that includes dynamic (e.g., advection, convection) and physico-chemical processes (e.g., dry deposition, CO+OH reaction) but only taking into account specific emissions from a particular region or sector or chemical production. The change in the tracer abundance however does not affect the interactive chemistry in the model [Emmons et al., 2010; Gaubert et al., 2016]. We note that the OH fields are calculated online and are not prescribed from previous simulations. Here, we tagged CO tracers from 14 source regions shown in Fig. D1, which includes Korea, Russia, India, Indonesia, Japan, East Asia-North1 (EA-N1), East Asia-North2 (EA-N2), East Asia-North3 (EA-N3), East Asia-Middle1 (EA-M1), East Asia-Middle2 (EA-M2), East Asia-Middle3 (EA-M3), East Asia-South1 (EA-S1), East Asia-South2 (EA-S2), and East Asia-South3 (EA-S3). We assign areas outside these 14 tagged regions as the rest of the world (ROW). In addition to these source regions, we also tagged 3 megacities (Beijing, Shanghai, and Seoul) for the purpose of matching and comparing with the WRF tracers (see Section 2.3). For each source region or megacity, biomass burning and anthropogenic emissions of CO are tagged separately. We note that biomass burning emissions are significantly lower than anthropogenic emissions for the tagged regions during the campaign, so biomass burning and anthropogenic emissions of CO are analyzed together even though they are tagged separately. Besides direct anthropogenic and biomass burning emissions, we also have tags for global biogenic CO, CO from the ocean, CO from CH_4 oxidation using a yield of 0.75 for CH_4 molecule loss by reaction with OH [Gaubert et al., 2016], and CO from other chemical production besides CH_4. We spin up the model for one year before simulations for the KORUS-AQ period. To compare model results with observations, we linearly interpolate the simulated CO concentrations along the location and time of each observational data. The sensitivity of simulation results to model resolution (see Section 3) provides insights on how model resolutions contribute to the representation errors introduced by interpolation.

2.2.5 Model Experiments

To explore the uncertainty of CAM-Chem CO simulations, we conducted 17 sets of CAM-Chem full chemistry with tagged CO tracer simulations. In particular, eight sensitivity test simulations were carried out with varying spatial resolutions, prescribed meteorological fields, or emission inventories. In addition, we conducted nine sensitivity test simulations based on nine emissions scenarios . That is, we increased (e.g., doubled) magnitude of CO emissions for a particular sector or region consistent with reported uncertainties of the bottom-up emission inventories and top-down estimates to further elucidate the influence of emissions to model underestimation of CO in the region. Table D1 shows the definitions and details of the 17 model experiments for this study.

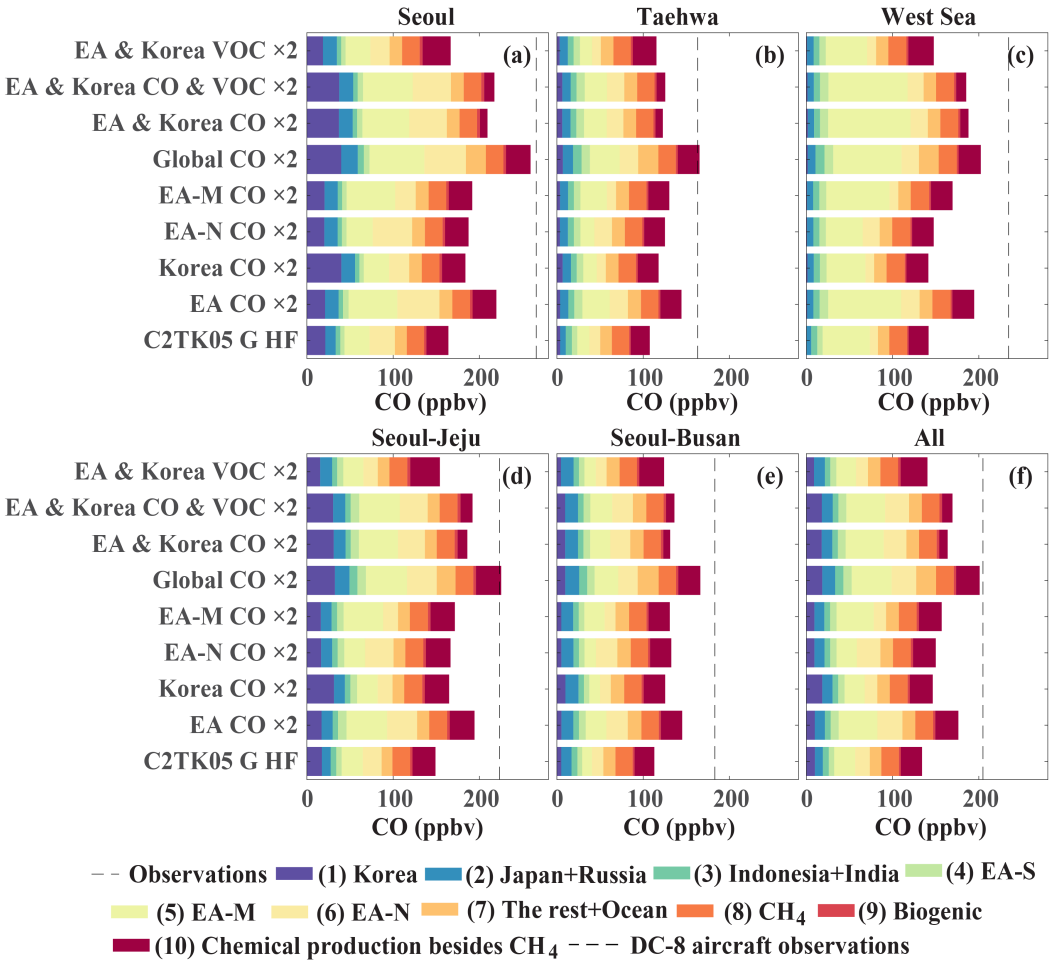

Figure D3. Ensemble of mean estimates of CAM-chem source contributions to CO concentrations along the DC-8 flight tracks during the KORUS-AQ period for all tracks and five track groups defined in Fig. D1. Different colors indicate tagged CO sources (see text for details). Dashed lines represent DC-8 observations.

2.3 Regional Models

2.3.1 WRF

Forecasts of inert tracers were provided by NCAR during KORUS-AQ using WRFv3.3.1 with inert tracers similar to the approach employed in Pfister et al. [2017]. The outer WRF domain (115.3°E–138.7°E, 27.7°N–46.2°N) covers East Asia with a resolution of 15 km ×15 km, and the inner domain (122.4°E–133.1°E, 31.6°N–40.6°N) covers Korea with a resolution of 3 km×3 km. Meteorological fields from the National Centers for Environmental Prediction (NCEP) Global Forecast System (GFS) at a resolution of 0.5 degree were used as the initial and boundary conditions. The WRF tracers are scaled to NO_2 emissions from CREATE and defined to have a 2-day lifetime for Korean sources and a 4-day lifetime for three selected China regions. More details on model configurations are described in Pfister et al. [2017]. In this study, we compare our tagged tracer results from directly emitted CO simulated by CAM-chem (section 2.2) with the WRF inert NO_2 tracers. We note that the CAM-Chem CO and WRF NO_2 tracers are very different since the CO tracers in CAM-chem undergo chemical transformation and exhibit a longer lifetime, whereas the NO_2 tracers in WRF are inert with a prescribed lifetime much shorter than CO. We also note that our tagged regions (‘Korea’, ‘Beijing’, ‘Shanghai’, and ‘EA-M3’) are not exactly equivalent to the counterparts in WRF due to differences in definition and resolution. For these reasons, the comparisons can only be analyzed qualitatively.

2.3.2 FLEXPART

The FLEXible PARTicle dispersion model (FLEXPART) is a Lagrangian transport and particle dispersion model (Stohl et al., 2005), which can be run either forward or backward in time [Seibert and Frank, 2004]. FLEXPART can also work with limited-area models such as WRF [Brioude et al., 2013]. Here we use FLEXPART 9.1 back trajectory calculations driven by WRF (FLEXPART-WRF) meteorology at 3km×3 km horizontal resolution similar to the inner domain described in section 2.3.1. For each DC-8 aircraft observation (every 1 minute along the flight track), back trajectories are calculated following the air mass for 5 days back in time [Stohl et al., 2002]. In order to estimate contributions to the observed CO concentrations, we fold the surface sensitivity function calculated by FLEXPART (defined as the sensitivity below 100 m above ground level) with the CO emissions for each region of interest. We assume that CO tracers are inert in the

atmosphere and do not account for photochemical loss or production of CO. The FLEXPART-WRF domain is shown in Fig. D1a (roughly 115°E–136°E, 27°N–43°N). Two of the CAM-chem tags (Korea and EA-M3) are covered entirely by the FLEXPART-WRF domain.

3. Evaluation and Sensitivity Study of CAM-chem CO Simulations

We first evaluate our CAM-chem simulations of CO by comparing with the DC-8 aircraft measurements supplemented with MOPITT retrievals during KORUS-AQ. A summary of this evaluation is shown in Figure D2, DS5, DS6 and Table DS1. We will first focus the discussion of our results on simulations using bottom-up emission inventories followed by our results on simulations using alternative emissions.

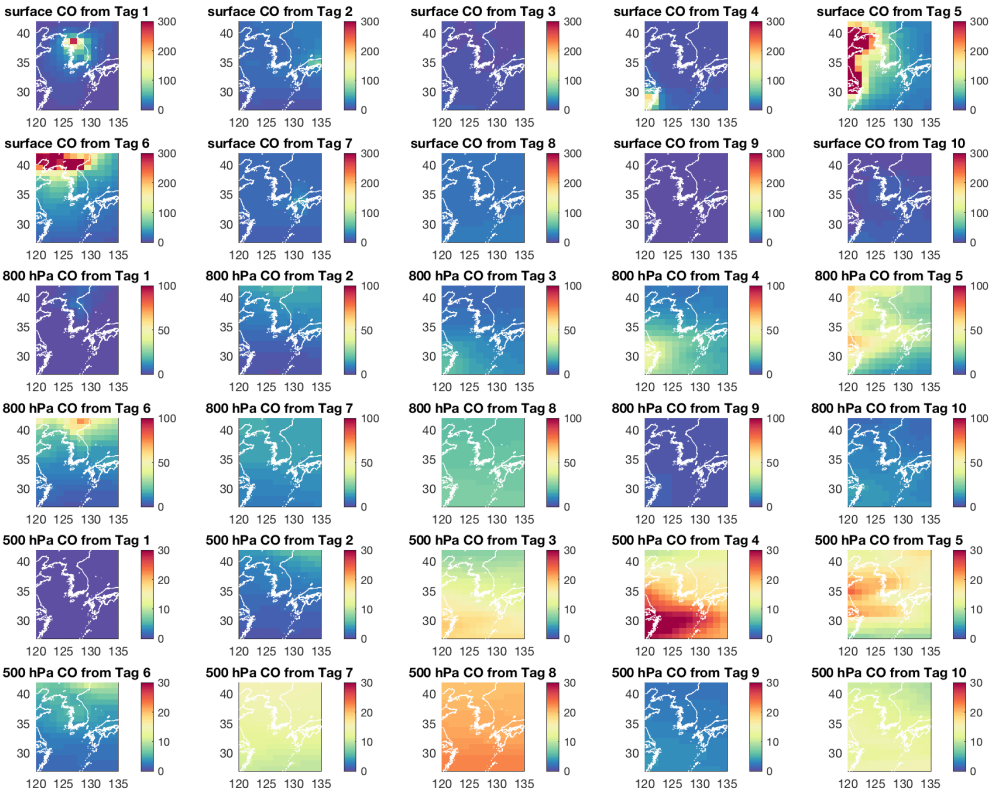

Figure D4. Spatial distributions of the tagged CO (ppbv) averaged across the KORUS-AQ period at model surface, 800 hPa, and 500 hPa. Tag 1: Korea; Tag 2: Japan+Russia; Tag 3: Indonesia+India; Tag 4: EA-S; Tag 5: EA-M; Tag 6: EA-N; Tag 7: ROW+ocean; Tag 8: CH_4 oxidation; Tag 9: biogenic; Tag 10: chemical production besides CH_4.

Figure DS5a–c shows the mean vertical profiles of the observed CO concentrations and the modeled-observed CO concentration differences. Overall, we find that the simulations with a 1-degree resolution and/or different meteorological fields using bottom-up emission inventories all underestimate CO concentrations across the profile by up to 50 and 130 ppbv above and below 700 hPa, respectively. The use of different meteorological fields (GEOS-FP and MERRA-2) and emission inventories (HTAP+FINN, CREATE+FINN, and CMIP6+FINN) have relatively small effects (differences < 20 ppbv) on modeled mean CO profiles (Fig. DS5b). This is due to the small differences among the meteorological or emission datasets (see Section 2.2). However, using 1-degree (0.9°×1.25°) model resolution, instead of 2-degree (1.9°×2.5°), improves simulation results by up to ~20 ppbv across most of the levels in the mean vertical profile, particularly below 500 hPa. The use of finer resolution (0.47°×0.63°) only slightly reduces model biases below 950 hPa yet increases the underestimation above 850 hPa relative to the 1-degree simulation results (Fig. DS5c), likely due to the enhanced impact of spatiotemporal errors in emissions by using a finer resolution and/or the uncertainty in model vertical transport. Previous studies also suggested that higher spatial resolutions may not improve model simulations [Wild and Prather, 2006; Valari and Menut, 2008; Yu et al., 2016]. However, more accurate and quantitative evaluations of the reasons require further investigation (see also discussions below). From these results, we find that the 1-degree simulation performs better than the other two in terms of mean vertical profiles. Nevertheless, simulations with the three resolutions all show large negative biases especially near the surface (~100 ppbv). Lastly, these model simulations with different meteorological fields, emission inventories, and resolutions show similar bias patterns (Figs. DS5b–c). In addition to the mean of model biases, profiles of standard deviation (std) of observed CO from DC-8 aircraft and model biases (dashed lines) are also shown in Fig. DS5a-c. This provides information on the high variability of CO (and model biases) during the KORUS-AQ campaign. As we can expect, overall, the large variability in modeled CO surface concentrations can be attributed to local emission and/or boundary layer mixing uncertainties. An increase in variability around 850 hPa is most likely a result of intermittent advection of CO plumes to Korea.

We present in Figure DS6a–b the probability density functions (pdfs) of the DC-8 airborne observations and aforementioned eight model simulations to show the domain scale statistics (i.e., data across spatial and temporal domain), which is complementary to Figure DS5's overall vertical

profile statistics (Figure DS5a-b). First, the pdf for observed CO exhibits a bimodal distribution peaking at around 100 ppbv and 200 ppbv. It is also skewed to the right with a long tail at high CO values. The pdfs of the modeled CO are also bimodal but tend to be centered towards the lower values and more importantly exhibit significant underestimation at higher (>200 ppbv) CO values (Figs. DS6a–b), consistent with the negative biases in mean vertical profiles. Among the three simulations with the same emissions (HTAP+FINN) and meteorological fields (GEOS-FP) but different resolutions, the 1-degree simulation gives a slightly lower normalized mean bias (NMB, -35%) and root-mean-square-error (RMSE, 110 ppbv) than the half-degree simulation (-37% and 112 ppbv) and the 2-degree simulation (-38% and 114 ppbv). The 1-degree simulations using HTAP+FINN emissions show the lowest biases (34–35%) and RMSE (108–110 ppbv) among the eight simulations (please see Table DS1). On average, all these simulations lead to consistent underestimates of CO by 69–79 ppbv (34–39%), attributed most likely due to persistent underestimation of CO emissions (Bey et al., 2001; Streets et al., 2006; Stein et al, 2014; Miyazaki et al., 2018), and will be elaborated further in the following sections.

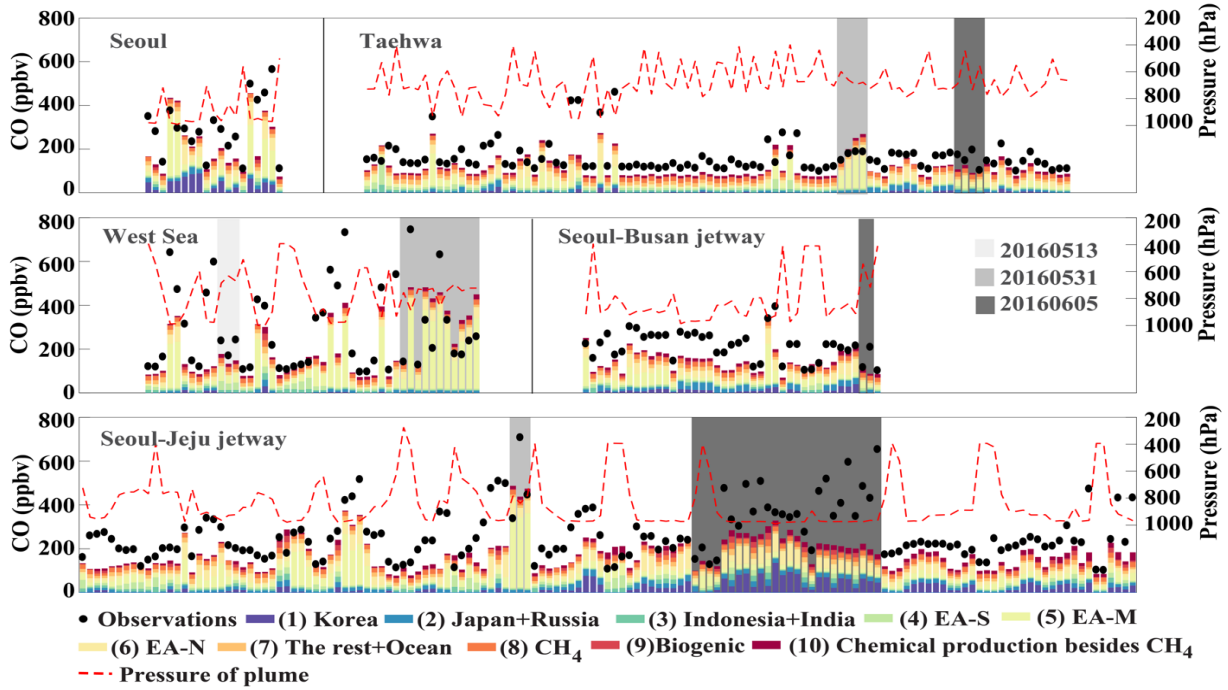

Figure D5. CAM-chem source contributions to all identified CO plumes captured by DC-8 aircraft measurements during KORUS-AQ. The results are from the EA_&_Korea_CO_&_VOC_×2 simulation only for demonstration purpose. Different colors indicate tagged CO sources (see text for details). Black dots represent DC-8 observations. Red dashed lines represent pressures at which the plumes were encountered. Grey shades are used to highlight plumes on three specific days. Note that the x-axis represents the plume ID.

Indeed, the above analysis revealed that small changes in meteorological inputs (MERRA-2 and GEOS-FP) to CAM-chem result in slight differences in overall model performance (Fig. DS5b) This is somewhat expected since GEOS-FP and MERRA-2 produced similar large-scale meteorological patterns in this region despite MERRA-2 being a reanalysis product which ingests more observational constraints than GEOS-FP [Gelaro et al., 2017] (see Section 2.23). As the DC-8 CO samples represent more of local to regional pollution, the changes that we see (albeit small) suggest that large-scale (hemispheric to continental) transport errors should play a relatively insignificant role. This is further supported by the model ability in capturing observed plumes and its consistency with results of other source contribution approaches (see Section 5). We note however that errors in the model representation of boundary layer mixing, diurnal patterns of convection, land-sea breeze, as well as ventilation and uplift processes cannot be ruled out as local-to-regional scale sources of errors.

Increasing the model resolution (1.9°×2.5°, 0.9°×1.25°, 0.47°×0.63°) has relatively small effect on overall CO simulations (Fig. DS5c) relative to DC-8 CO samples. Specifically, increasing the resolution from 2-degree (1.9°×2.5°) to 1-degree (0.9°×1.25°) slightly reduces the mean biases by 3%, whereas increasing the resolution from 1-degree (0.9°×1.25°) to half-degree (0.47°×0.63°) slightly increases the mean biases by 2% (Table DS1). The better performance of 1-degree is also expected as the domain statistics represent a large-scale rather than local feature, washing away the impact of higher resolution. In addition, the impact of large spatiotemporal errors in emissions are potentially enhanced in higher resolution simulations leading to relatively larger bias. However, improvements in model performance using higher resolution can be evident in the modeled versus observed CO correlations (see Fig. D2 and later discussion). Our finding is consistent with Tang et al. [2018] who found that increasing resolution from 16 km to 9 km generally produce better CO forecasts in the Copernicus Atmosphere Monitoring Service (CAMS) global prediction system, although in some cases particularly over Seoul and point sources, the 9 km did not show improvements from 16 km. We note however that previous studies suggested that increasing model resolution does not necessarily improve model simulations [Wild and Prather, 2006; Valari and Menut, 2008; Yu et al., 2016]. Here, we use the 1-degree (0.9°×1.25°) resolution in the subsequent analysis of source contribution as it provides a compromise between performance and computational expediency.

With regards to model chemistry, we compare the modeled OH to measured OH from Airborne Tropospheric Hydrogen Oxides Sensor based on LIF onboard the DC-8 aircraft (Table DS2). As described earlier, reaction of CO with OH serves as the main chemical loss pathway for CO [e.g., Gaubert et al., 2016, 2017]. Overall, the modeled OH mixing ratios from the aforementioned eight simulations agree with observations. The normalized mean biases and RMSE ranges from -1%–+9% and 0.14–0.15 pptv, respectively (Table DS2). However, even a small relative overestimation of OH can have a significant impact on the CO loss on one hand and on the chemical production of CO on the other hand. Uncertainties in CO chemical production from oxidation of CH_4 and NMVOC may also contribute to the model underestimation of CO [Stein et al., 2014]. The investigation on the model error due to chemistry and oxidants levels will be investigated in future work.

Uncertainties in emission inputs to CAM-Chem are likely to play an important role in the underestimation of modeled CO concentrations relative to those collected by the DC-8 aircraft, given that the airborne measurements of CO are made close to the sources. As noted before, Janssens-Maenhout et al. [2015] reported, for example, that uncertainties in HTAP CO emissions are relatively large (i.e., 35–70% for energy and industry sectors and 70–150% for residential and transportation sectors). To investigate how the uncertainties in CO emissions as well as chemical production influence CAM-chem CO results, we conduct 9 additional sensitivity test simulations based on the base case configuration with a resolution of 0.9°×1.25°, GEOS-FP meteorology fields, and HTAP+FINN emissions (hereinafter the C2TK1_G_HF simulation). Correspondingly, 9 additional emissions scenarios are considered, where the anthropogenic CO and/or VOC emissions from the globe or major source regions (e.g., EA, Korea, EA-N, EA-M, EA-S; see also Fig. D1) are doubled. Even though they still fall in the uncertainty range provided by HTAP, we note that doubled anthropogenic CO and/or VOC emissions over EA and/or Korea are arbitrary and likely to be overestimated [e.g., Jiang et al., 2017; Yin et al., 2015]. In addition, doubling the emissions is not expected to improve the model results in the case that source emissions are missing in the inventory. The simulation with doubled global anthropogenic CO emissions is only used as one of the sensitivity test simulations. It does not necessarily indicate that global or regional anthropogenic CO emissions are underestimated by 50%. In fact, the contribution of direct emissions from regions outside of EA and Korea is rather small, therefore the differences between

doubling global anthropogenic CO emissions from doubling only EA and Korean CO anthropogenic emissions reflect impacts of chemical processes. This is supported by the OH simulations of the ensembles (Table DS2). The scenario of doubling the global anthropogenic CO emissions (hereinafter Global_CO_×2) changes the OH mean bias compared to the base case C2TK1_G_HF from 3% to -8%, while the OH mean bias of the simulation when CO emissions from only EA and Korea are doubled (hereafter EA_&_Korea_CO_×2) is ~0%.

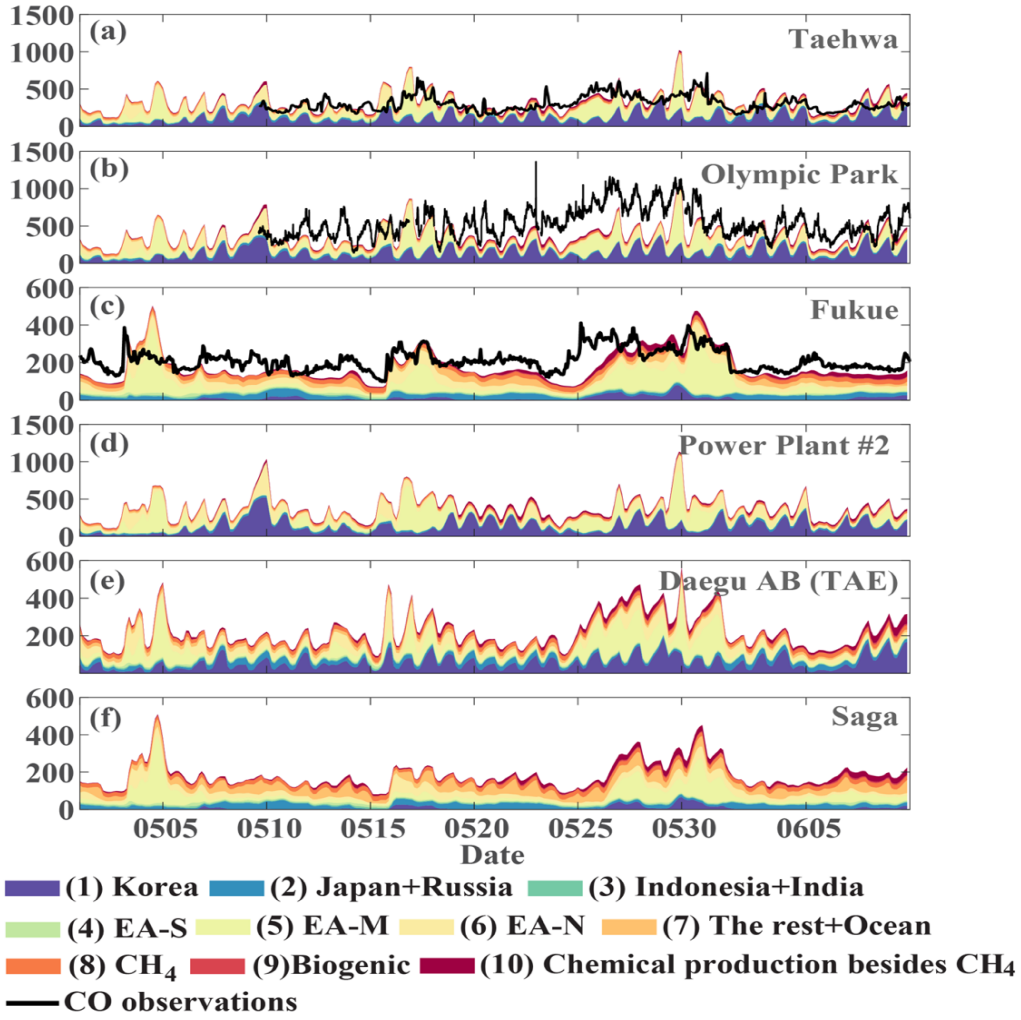

Figure **D6.** Time series of CAM-chem source contributions to CO concentrations at the 6 ground sites during KORUS-AQ. The results are from the EA_&_Korea_CO_&_VOC_×2 simulation only for demonstration purpose. Model results are interpolated to the station locations. Colored areas indicate tagged CO sources (see text for details). Black lines represent corresponding in-situ observations.

In Figure DS5d-e, we show the improvements in model performance for the nine alternative simulations scenarios. The model biases decrease substantially (slightly) when CO (VOC) emissions are increased, particularly near the surface. Among the nine simulations, the CO vertical profiles from the Global_CO_×2 agree the best (mean bias of -6%) with the mean profiles of the DC-8 aircraft observations, followed by the simulation with doubled anthropogenic CO and VOC emissions in EA and Korea (hereinafter EA_&_Korea_CO_&_VOC_×2) with model mean biases of -12% (Table DS1). EA_&_Korea_CO_&_VOC_×2, however, has the lowest RMSE (87.60 ppbv) and highest correlation among the 17 simulations (0.63). Correlation with the DC-8 observations is not improved by Global_CO_×2 compared to the base case configuration (0.57). In addition, the pdf of the Global_CO_×2 simulation misses the peak at higher CO concentrations (~200 ppbv) and is not able to reproduce the bimodal pdf structure of the DC-8 aircraft observations (Fig. DS6c). This implies that the significantly reduced mean bias by Global_CO_×2 is likely to be due to increased background values instead of better representation of CO pattern in the region.

The model performance for all 17 simulations is summarized in Fig. D2 as a Taylor diagram (Taylor, 2001). We also estimate the corresponding Taylor scores for these simulations (see Fig. D2 and Table DS1). These scores provide indications of model skill in representing the amplitude and pattern of observational variability (see Equation S1 for the definition of Taylor score). Among the six 1-degree simulations using different meteorological fields and/or emissions, the simulations using HTAP+FINN still have slightly higher Taylor scores than the others, consistent with our previous findings. We find the Taylor scores increases from 0.38 to 0.49 and further to 0.61 as the model resolution increases from 1.9°×2.5° to 0.9°×1.25° and further to 0.47°×0.63° (Fig. D2). This indicates that while increasing resolutions from 0.9°×1.25° to 0.47°×0.63° slightly increases model biases (Table DS1), the model skill in representing the pattern of observational variability are improved. EA_&_Korea_CO_&_VOC_×2 has the highest Taylor score (0.86) among all the 17 simulations, followed by EA_&_Korea_CO_×2 (0.85) and Global_CO_×2 (0.82), indicating that anthropogenic CO emissions play a more important role than anthropogenic VOC emissions in the region in terms of performance of CAM-chem CO. It is also worth noting that even though doubling anthropogenic CO emissions in Korea does not significantly reduce the model bias compared with the C2TK1_G_HF simulation (Table DS1), it increases the representation of the

pattern in modeled CO variability with the Taylor score increasing from 0.49 to 0.59. In summary, our results show that simulations using bottom-up emission scenarios are consistently low (bias: -34 to -39%) and poorly perform (skill: Taylor 0.38 to 0.61) than simulations using alternative emissions (bias: -6 to -33%; Taylor skill: 0.48 to 0.86).

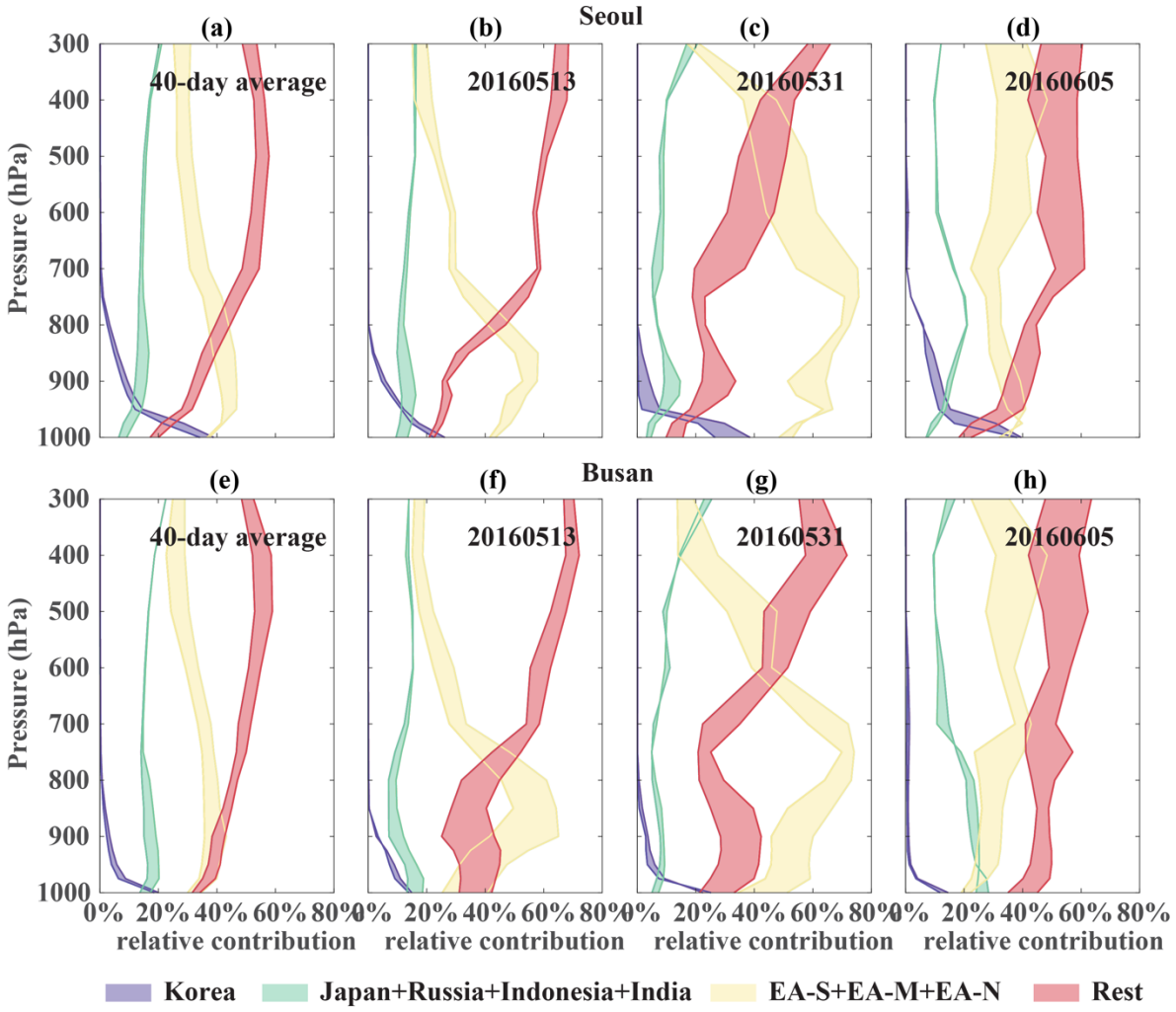

Figure D7. CAM-chem source contributions to CO concentrations at different altitudes over Seoul and Busan during KORUS-AQ for (a, e) 40-day averaged profiles and (b–d, f–h) daily averages of three days (20160513, 20160531, and 20160605). The shaded area corresponds to the range of estimates from top 50% of Taylor scores across the ensemble of simulations.

We also compare all 17 simulations with MOPITT retrieved CO vertical profiles by interpolating CAM-chem CO onto the MOPITT level 3 grid and pressure levels, and further applying the MOPITT averaging kernels to model results to make quantitative comparisons. Figure DS5f–j show CO vertical profiles from MOPITT averaged over Korea and its surrounding waters (123°E–

133°E, 30°N–39°N) during the KORUS-AQ period and corresponding differences between observations and CAM-chem simulations. Overall, even without doubling the anthropogenic emissions, the differences between model and MOPITT are relatively small (<40 ppbv), compared to the model biases against airborne observations (Fig. DS5b–e). The bias patterns for different model simulations in comparison with MOPITT are similar to those in comparison with airborne observations. For example, using different meteorological fields and emission inventories have small effects on simulated CO vertical distributions (Fig. DS5g), with the C2TK1_G_HF simulation performing slightly better than the others. Figure DS5h shows that the results using resolutions of 0.9°×1.25° and 1.9°×2.5° are very close, with negative biases of <30 ppbv, while the simulation using the resolution of 0.47°×0.63° gives slightly larger negative biases. Figure DS5i-j indicates that doubling anthropogenic CO and VOC emissions over East Asia and Korea (EA_&_Korea_CO_&_VOC_×2), doubling anthropogenic CO emissions over East Asia and Korea(EA_&_Korea_CO_×2), and doubling anthropogenic CO emissions over East Asia (hereafter EA_CO_×2) leads to slight (≤ 6%) overestimates in the lower and middle troposphere, while Global_CO_×2 has stronger overestimates (≤ 20%). This is different from the results of comparisons with airborne observations, where Global_CO_×2 agrees best with DC-8 profiles, which is partially due to differences in sampling time and regions between MOPITT and DC-8 measurements. Furthermore, the spatial distributions of MOPITT and modeled CO total column density (Fig. DS7) indicate that all the 17 simulations tend to overestimate in the southern part of East Asia (EA-S; see also Fig. D1) and most of the simulations underestimate in the northern part of East Asia (EA-N). Global_CO_×2 shows the lowest underestimate in EA-N but the highest overestimate in EA-S (Fig. DS7). We note that a comprehensive evaluation of MOPITT CO over the region against KORUS-AQ airborne observations requires further study and is beyond the scope of this work.

Overall, the simulations with increased anthropogenic CO and/or VOC emissions results in a substantial model improvement compared with the default simulation (C2TK1_G_HF) during the KORUS-AQ campaign. This also implies that the underestimated anthropogenic CO emissions as well as chemical production is likely to be the main cause of CO underestimation by CAM-chem during KORUS-AQ in this study. This is consistent with Gaubert et al. [2016] and other data assimilation and inverse modeling studies (Flemming et al. 2017; Miyazaki et al. 2017; Jiang et al.

2017; Yin et al. 2015). We note that although doubling anthropogenic CO emissions may not be the optimized solution, the model improvements obtained by increasing these emissions could still shed light on understanding CO underestimates in global models, particularly considering the large uncertainties in current emission inventories. Here, the sensitivity study also implies that more future work needs to be done on refining CO emissions in different source regions.

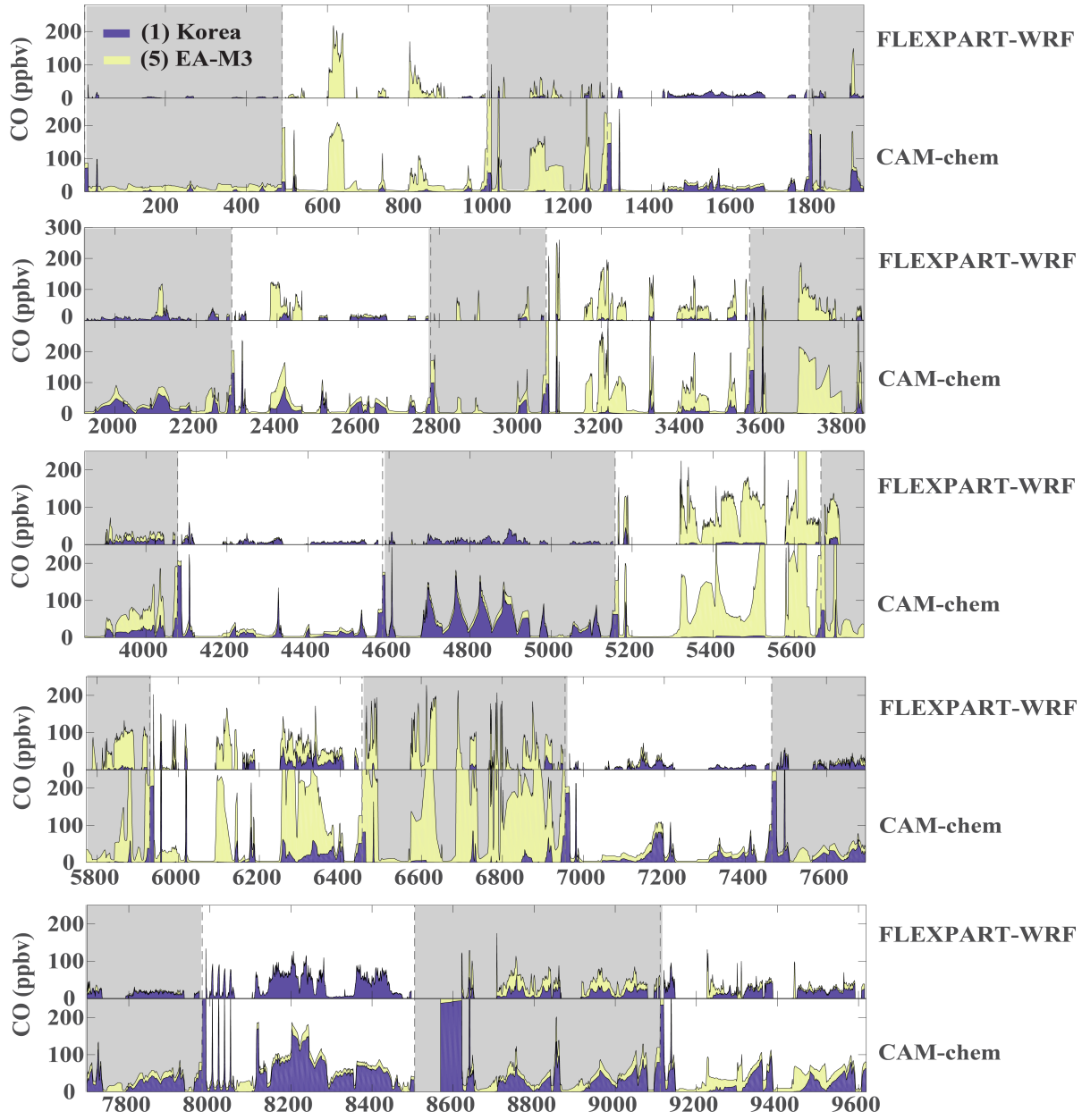

Figure D8. Contributions from Korea (blue) and EA-M3 (yellow) direct CO emissions to CO concentrations along the DC-8 flight tracks derived from FLEXPART-WRF back trajectories (upper part of each panel) and CAM-chem (lower part of each panel) during KORUS-AQ. The time series are separated into five panels.

To emphasize the uncertainties in our source contribution analysis and to take advantage of the ensemble, we provide ranges derived from the top 50% performed ensemble members (based on Taylor score) for the following source contribution analysis (see Sections 4 and 5).

4. Analysis of Source Contributions to Observed CO

In this section, we present analyses of source contribution to CO concentrations collected from DC-8 aircraft and at ground sites and cities during KORUS-AQ. The results are based on the top 50% well performed CAM-chem simulations with CO tags. To this aim, we use the Taylor skill scores presented in Section 3 to rank the 17 simulations in terms of model performance (Table DS1). We note that the model-observation discrepancies, albeit reduced by adjusting CO and/or VOC emissions, translate into uncertainties in our results which are estimated source contributions to the CAM-chem modeled CO concentrations that are spatiotemporally collocated with the DC-8 aircraft and ground-based measurements. Nevertheless, CAM-chem tagged CO is still a powerful tool to analyze source contribution for the observations, and the uncertainties in our source contribution analysis are addressed by the range derived from the ensemble.

4.1 Modeled Source Contributions to DC-8 CO

Flight tracks of the DC-8 aircraft during KORUS-AQ and their grouping (Seoul, Taehwa, the West (Yellow) Sea, Seoul-Jeju jetway, and Seoul-Busan jetway) are shown in Fig. D1. These five groups are defined based on the land cover below the flight tracks and the sources of pollution following Tang et al. [2018]. The Seoul group contains air samples over the metropolitan area of Seoul, while the Taehwa group contains air samples over a forest area near Seoul. Measurements in the West Sea group were designed to capture pollution outflow from China and Korea to the West Sea. Measurements in the Seoul–Jeju jetway and Seoul–Busan jetway groups were both made above the Korean Peninsula. Strong local point sources (such as power plants and industrial regions) are located below the Seoul-Jeju jetway, whereas flights in the Seoul–Busan jetway are designed to capture activities in forest, rural, and Busan urban regions. Figure D3 show the contributions of different source regions to CO mixing ratios along the DC-8 flight tracks from the top 50% well-performed simulations, including EA & Korea CO & VOC ×2, EA & Korea CO ×2, Global CO ×2, EA CO ×2, EA-M CO ×2, C2TK05_G_HF, EA-N CO ×2, Korea CO ×2, and EA & Korea VOC ×2. The differences between Global_CO_×2 and EA_&_Korea_CO_×2 is significantly

attributed to the CO chemical production besides CH_4. Note that because CH_4 surface mixing ratios are prescribed in CAM-chem, CO production from CH_4 remains similar between the simulations while only CO chemical production from NMVOCs is impacted by doubling anthropogenic CO emissions outside of EA and Korea. This indicates that doubling anthropogenic CO emissions outside of EA and Korea indirectly impacts CO background significantly through secondary CO processes. Here, uncertainties in chemical processes of CO is reflected coincidentally via increase in CO direct emissions outside of KORUS-AQ domain. Figure D4 shows the spatial distributions of the tagged CO averaged across the KORUS-AQ period. We also provide modeled contributions from different sources for the plumes encountered by the DC-8 aircraft (Fig. D5). These plumes were identified by the KORUS-AQ Plume Flagging Team (https://www-air.larc.nasa.gov/cgi-bin/ArcView/korusaq). First, they normalized the DC-8 CO measurements by median vertical profiles. These normalized CO measurements are then marked as plumes when they are above the respective 98th percentile. In many of these plumes, the modeled contributions from one or two sources are usually dominant and hence regarded as the major source/s for these plumes. However, in some plumes (such as plumes during the May 20th aircraft flight), there is no dominant signature associated with these plumes. Below, we discuss in some detail our key findings which we organized by major source categories.

Table D3. Correlations between CO concentrations contributed from 9 East Asia source regions derived from CAM-chem and VOCs measured by the WAS group along the DC-8 flight tracks during KORUS-AQ. Shaded cells indicate the corresponding correlations are not significant (α=0.05).

Measured VOC	EA-N1	EA-N2	EA-N3	EA-M1	EA-M2	EA-M3	EA-S1	EA-S2	EA-S3
CCl_4	-0.09	0.18	0.30	-0.14	0.15	0.55	-0.17	-0.08	-0.03
CFC-113	-0.06	0.10	0.17	-0.08	0.08	0.32	-0.09	-0.03	0.01
CFC-114	-0.06	0.06	0.21	-0.04	0.01	0.23	-0.04	0.02	0.04
OCS	0.00	0.30	0.24	-0.07	0.25	0.60	-0.10	-0.05	-0.02
H-1211	-0.08	0.03	0.20	-0.09	0.01	0.18	-0.10	-0.07	-0.06

4.1.1 Contribution of Direct Korean CO Emissions

Throughout the campaign period, direct anthropogenic and biomass burning emissions of CO from Korea varies significantly among the five groups of DC-8 flights. The contribution of direct

Korean CO emissions to modeled CO concentrations over Seoul (10-22%) is the highest among the groups (Fig. D3). This is quite expected as Seoul is a megacity and has larger local emissions than its neighboring cities. The Korean emissions also contribute to the modeled CO concentrations over the Seoul-Jeju jetway (9-19%) but only slightly to CO over the Seoul-Busan jetway group (4-8%). This is related to the fact that some strong local point sources (such as power plants and Daesan Chemical Facility) are located in the domain of the Seoul-Jeju jetway (Fig. D1). The contribution of Korean CO emissions to CO over Taehwa group (3-6%) is lower than that over Seoul, although Taehwa is near Seoul. CO concentrations observed over Seoul represents CO from urban areas while over Taehwa CO concentrations are more likely coming from biogenic CO sources over the forest, which may explain the difference between the two groups. We also note that the DC-8 measurements over Seoul are mostly made below 850 hPa, while more than half of the measurements are made above 850 hPa over Taehwa, which can also contribute to the difference. Over the West Sea, the contribution from direct Korean emissions is very small (~0-1%). This is reasonable since the wind direction on average in this area is from west to east (Fig. DS3), leading to negligible transport from Korea to the West Sea (although from time to time there are CO outflow albeit near the coast due to land-sea breeze). Moreover, measurements in this group of flights were usually made when Chinese outflow was expected, resulting to rather small Korean contributions to modeled CO. On average, direct Korean CO emissions to modeled CO concentrations only contribute about 6-13% to modeled CO along the DC-8 flight tracks throughout the campaign period (Table D2).

We further analyzed this source contribution by separately analyzing airborne measurements below and above 850 hPa to investigate the overall differences between boundary layer and free tropospheric contributions. Here, we approximate the boundary layer height to reach on average to about 850 hPa although we recognize that the height varies over time. The results suggest that the Korean contribution to modeled CO along the DC-8 tracks mainly concentrates in the boundary layer. This is especially the case for the flight tracks over the local sources (Table D2). For example, over Seoul the Korean CO emissions contribute 11-24% and 1-2% below and above 850 hPa, respectively; over Seoul-Jeju jetway, the contributions are 11-25% and ~1%, respectively. Overall, the contribution of Korean CO emissions to modeled total CO is 8-19% below 850 hPa, and ~1% above 850 hPa.

The flight on June 5th was designed to sample a number of point sources such as industrial sites, chemical facility, and power plants, thus the contributions of Korean CO emissions to the DC-8 observations are higher (11–20%) compared to usual (4–7%; see also Fig. D5 and Fig. DS8). During this flight, the contribution of direct CO emissions from Korea to modeled CO along the tracks is significant, particularly when the flight is close to the surface (~1000 hPa), as strong local point sources dominate rather than transported CO. We note that CAM-chem generally captures the plumes throughout the KORUS-AQ period (Fig. D5), suggesting that transport is well represented in CAM-chem. However, we note that the model tends to underestimate CO concentrations for the plumes that are associated with strong contributions of Korean CO emissions. This indicates that the CO emissions for these point sources may be underestimated and/or the relatively coarse resolution (1-degree) is unable to resolve the local scale emission and dynamic features of these point sources.

4.1.2 Contribution of Direct CO Emissions from East Asia

We divided East Asia (EA) source regions into three sub-regions, including the northern (EA-N), middle (EA-M), and southern (EA-S) parts as shown in Fig 1. We find that the source contribution of the three sub-regions have different characteristics. During the measurement period, direct CO emissions from EA-S, EA-M, and EA-N overall contribute ~5%, 16-28%, and 9-18% to modeled total CO along the flight tracks, respectively. Over Seoul, contributions of CO emissions from EA-S, EA-M, and EA-N are about ~3%, 16-29%, and 12-24%, respectively, revealing a much smaller influence from EA-S emissions. Over Taehwa, EA emissions generally contribute less than those over Seoul (Table D2). Over the West Sea, CO concentrations are dominated by CO emissions from EA-M (29-51%), whereas EA-N and EA-S emissions only contribute to 6-13% and 4-5%. Considering that the measurements in this group of flights were usually conducted when Chinese outflow was expected, our result indicates that the East Asian outflow to the West Sea and further to Korea is mainly from the middle part of East Asia (EA-M). We cannot rule out however the possibility that EA-N emissions are underestimated and EA-M emissions are overestimated in CAM-chem. Initial results from a separate study on CO Bayesian synthesis inversions, where aggregated tagged CO emissions are optimized using DC-8 CO concentrations, point to this possibility (personal communications with Avelino F. Arellano, 2018). On the other hand, we find that contributions of direct CO emissions from both EA-M and EA-N for the Seoul-Jeju jetway

group (15-27% and 10-20%, respectively) are higher than those for the Seoul-Busan jetway group (10-19% and 10-19%, respectively). This is because the Seoul-Jeju jetway is along the west coast of Korea and is closer to EA than the Seoul-Busan jetway.

Along the flight tracks below 850 hPa, direct CO emissions from EA-S, EA-M, and EA-N contribute ~3%, 17-29%, and 11-22% to modeled total CO, respectively. Compared with the results below 850 hPa, the contribution of EA-S emissions is higher above 850 hPa (8-11%). However, the contributions of EA-M (14-26%) and EA-N (5-10%) emissions are lower above 850 hPa than below 850 hPa. This suggests that a large portion of CO emissions from EA-M and EA-N can reach Korea and surrounding areas via transport in the boundary layer, whereas CO emissions from EA-S are likely to be transported to Korea mainly through the free troposphere (particularly during frontal passage periods; see the following analysis). Previous studies (e.g., Liu et al., 2003) also have shown that air pollutants can be lifted from the boundary layer to the free troposphere by fronts in Asian outflows.

In terms of contribution to the plumes, we find that direct CO emissions from EA-M are dominant in the plumes on May 31st (Fig. D5 and Fig. DS9). On May 31st, direct transport of Chinese emissions to the Korean peninsula was expected, so the DC-8 flew offshore between China and Korea in the morning, and then along the Seoul-Jeju jetway in the afternoon. During this flight, CO over the West Sea and along the Seoul-Jeju jetway are dominated by direct emissions from EA-M. These CO source contribution results using CAM-chem tagged tracers support the expected conditions during the science flights. During the two flights in which a frontal passage occurred, the contribution of direct EA-S CO emissions is enhanced. For example, during the May 13th flight, a frontal passage with a cloud band occurred over the Korean peninsula (from the southwest to the northeast), and the DC-8 aircraft aimed to sample the frontal cloud during the flight. During this measurement period, the EA-S contribution to modeled CO is higher than that during most of the other flights (Fig. D5 and Fig. DS10).

4.1.3 Contribution of Direct CO Emissions from Other Neighboring Regions

Direct CO emissions from Japan, Russia, Indonesia, and India in total only contribute a small proportion to CO mixing ratios along the flight tracks, with contributions of 7-9% from Japan and Russia and 4-5% from Indonesia and India. The contribution of CO from Japan and Russia reaches

the maximum (9-12%) for the Seoul-Busan jetway group and the minimum (4-5%) for the West Sea group. For CO from Indonesia and India, the contribution is the highest for the Taehwa group (5-7%) and the lowest for the Seoul group (2-3%). This is likely due to the different altitudes at which measurements were taken by these groups of flights. We further find that the contribution of Japan and Russia is higher below 850 hPa than above 850 hPa, whereas it is the opposite for Indonesia and India (Table D2). This is reasonable, considering that the flight tracks are closer to Japan and Russia than Indonesia and India. As such, it requires strong uplift and subsequent long-range transport of pollution from Indonesia and India to Korea in the free troposphere, consistent with the mesoscale dynamics in this region during this period [Fuelberg et al., 2003; Woo et al., 2003]. The differences of the emission response in the vertical between EA-N/EA-M and EA-S/Indonesia/India are also consistent with the results of our doubled emission simulation experiments discussed in section 3.

4.1.4 Contribution from Other Sources

Direct CO emissions from the ROW (including ocean) contribute 9-11% to modeled total CO during the entire flight period. Overall, biogenic CO sources have a small contribution (1-2%), whereas CO chemical production plays a relatively important role (10-15% from CH_4 oxidation and 6-22% from chemical production besides CH_4 oxidation) in representing the background CO abundance. One common feature of these sources is that they contribute more to CO in the free troposphere where background CO dominate than in the boundary layer where direct CO emissions from the aforementioned regions dominate. However, we recognize the uncertainties in these estimates as discussed in the previous section (Sections 3, 4.1) and elucidated in Figure D3 (Global_CO_×2 versus EA_&_Korea_CO_×2).

4.2 Source Contribution to Ground Sites and Cities

We also investigated source contributions to surface CO concentrations at 6 ground sites and to vertical profiles of CO concentrations over Seoul and Busan in Korea during KORUS-AQ. For the ground sites, the patterns of contributions from different sources generally agree with those along the DC-8 flight tracks (Section 4.1). However, direct Korean CO emissions play an obviously more important role at ground sites, especially at sites that are close to large local sources (Fig. D6). For example, at the Olympic Park site (located in Seoul), direct CO emissions from Korea contribute

more (25-49%) compared to EA-S (~2%), EA-M (11-25%), and EA-N (11-25%) to modeled total CO concentrations, respectively. At Power plant #2 site, the contribution of Korean CO emissions (22-45%) is also higher than those from other source regions (e.g., 1-2% from EA-S, 15-33% from EA-M, and 11-23% from EA-N). Fukue and Saga are two ground sites in Japan. Thus, at these two sites, the Korean contribution is small, whereas the contribution from East Asia and the rest of the world is relatively large. Fukue is a remote site and does not have a strong diurnal cycle, and it captures Asian outflows especially of EA-M and EA-N.

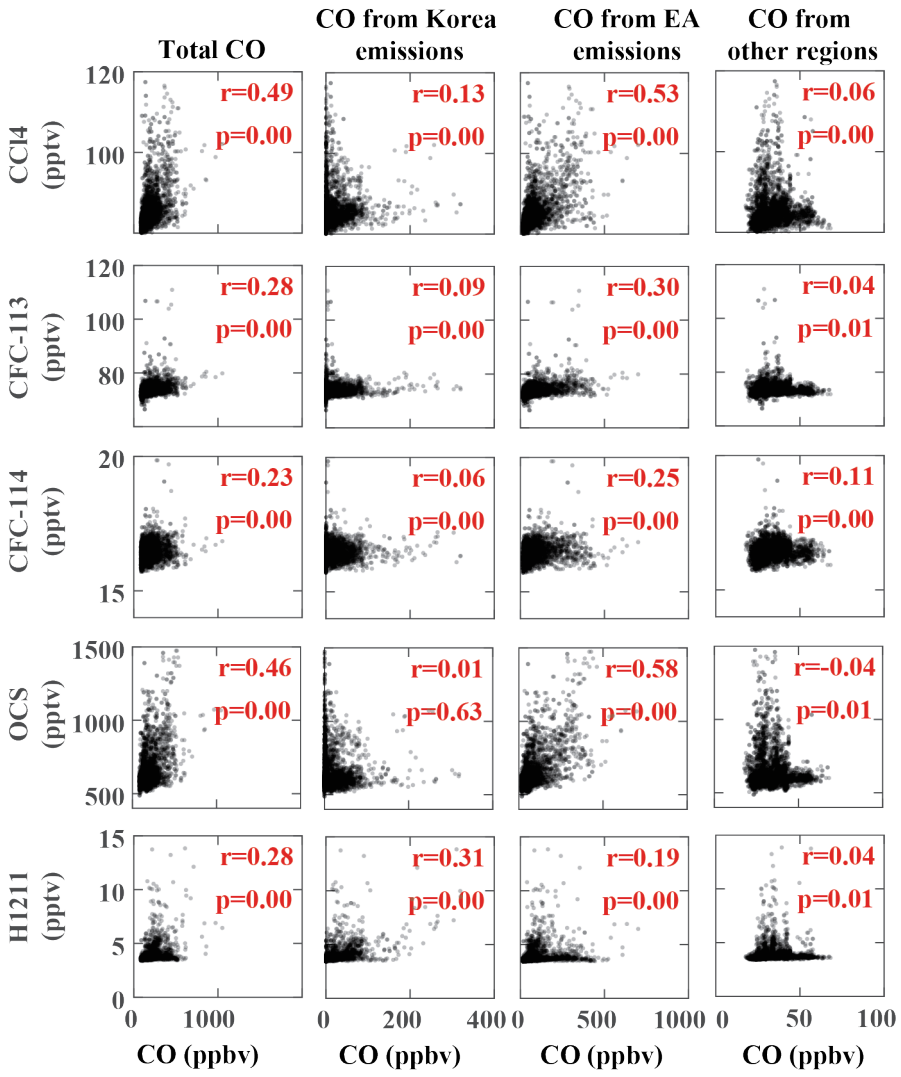

Figure D9. Relationships between CO concentrations contributed from different source regions derived from CAM-chem (EA_&_Korea_CO_&_VOC_×2) and VOCs measurements provided by the WAS group along the DC-8 flight tracks during KORUS-AQ. Correlation coefficients (r) and p-values (p) are also shown as red.

Figure D7 shows the averaged source contributions to CO vertical profiles over Seoul and Busan (in the southeastern South Korea) during KORUS-AQ period (from May 1st 2016 to June 9th 2016). Direct CO emissions from Korea have a much higher contribution to CO concentrations in the two cities near the surface (34–39% for Seoul and 19–20% for Busan) compared to the middle and upper troposphere (<1% for both Seoul and Busan; see also Figs. D7a and D7e). We find that due to the larger contribution of Korean CO emissions, the averaged CO concentrations over Seoul are much higher than those over Busan by up to 200 ppbv near the surface. We also show daily averaged profiles of relative contributions on three characteristic days (May 13th, 31st, and June 5th, 2016). As mentioned in Section 4.1, a frontal passage occurred on May 13th. On this day, the contribution of direct Korean CO emissions is lower than usual for both Seoul and Busan, whereas a higher contribution from EA emissions is seen, particularly at 800-900 hPa (Figs. D7b and D7f). Similar features are also seen on May 26th (another day with a frontal passage; see Figs. DS11 and DS12). On May 31st, direct China outflow was expected. During this period, the contribution of direct CO emissions from EA are much higher than usual, especially in the middle troposphere (Figs. D7c and D7g). The EA impact is also strong near the surface over Seoul, that is not seen over Busan. On June 5th, Chinese emissions were expected to have a smaller impact. Over Seoul and Busan, the CO vertical profiles on this day are similar to those averaged over the KORUS-AQ period. It is worth noticing that, on this day, contributions of Japan and Russia to CO in Seoul are higher than usual because of the prevailing winds.

5. Comparisons with Other Approaches to Source Contributions

In this section, we compare the source contribution results from the CAM-chem tagged CO (derived from EA & Korea CO & VOC ×2 as it is the best-performed simulation, unless stated otherwise) with those from the analysis of FLEXPART-WRF back trajectory, WRF-Chem NO_2 tracer, China signature VOCs, and CO to CO_2 enhancement ratios. All the source contribution results from different methods discussed in this section are referred to as contributions of CO emitted from different source regions to modeled total CO along the DC-8 flight tracks during KORUS-AQ, unless stated otherwise.

5.1 Comparisons with FLEXPART-WRF Back Trajectory and WRF Inert Tracer Analysis

Figure D8 shows the contributions from Korea and EA-M3 CO emissions to CO concentrations along the DC-8 flight tracks simulated by FLEXPART-WRF and CAM-chem. These are the two source regions (Korea and EA-M3) that overlapped between the two models. The correlations between the results from FLEXPART-WRF and CAM-chem are 0.77 and 0.56 for the source regions of Korea and EA-M3, respectively. Both FLEXPART-WRF back trajectory and WRF inert tracer analysis are compared to C2TK_G_HF so that they will have same emissions. Although CAM-chem has a coarser resolution than FLEXPART-WRF, the results from the two approaches agree reasonably well. Note that in this comparison, the CAM-chem simulation uses the same CO emissions (HTAP+FINN) as the FLEXPART-WRF back trajectory simulation for consistency.

We also qualitatively compare our CAM-chem results with the WRF inert tracer forecasts during the KORUS-AQ campaign (Fig. DS13). For contributions from Korean anthropogenic CO emissions along the DC-8 flight tracks, the correlation between the WRF inert tracer result and CAM-chem tagged CO result is 0.69. This correlation is higher than those for contributions from China anthropogenic source regions (0.47 for Beijing, 0.21 for Shanghai, and 0.49 for Shandong). Because CO in CAM-chem has a longer lifetime than the WRF inert tracer, the higher correlation for tracer contributions from Korean emissions and lower correlations for contributions from Chinese emissions indicate that the WRF inert tracer may be removed more quickly during transport. Therefore, even though East Asia contributes significantly to CO over Korea and surrounding areas during KORUS-AQ, it is possible that its contribution for short-lived species (such as NO_2) is not as significant.

5.2 Comparisons with Analysis of Signature VOCs

Figure D9 shows observations of five anthropogenic VOCs (CCl_4, CFC-113, CFC-114, OCS, and H-1211) that are indicators of pollution from China along the flight tracks during KORUS-AQ and the corresponding CAM-chem simulated CO, including directly emitted CO from Korea, EA, and other regions. We find that CO from direct EA emissions has relatively high correlations with the four suggested China signature VOCs (0.53 for CCl_4, 0.30 for CFC-113, 0.25 for CFC-114, and 0.58 for OCS), which are all statistically significant. However, the correlations for CO directly emitted from Korea (0.01–0.13) and other regions (-0.04–0.11) are much smaller. In addition, the correlation of OCS with CO from direct EA emissions (0.58) is the highest among the four China

signature VOCs, while its correlation with CO emitted from Korea (0.01) are the lowest. This implies that OCS could potentially be a more effective indicator of air from China than the other anthropogenic VOC tracers [Qin, 2007]. We also show relationships between H-1211 and CO tracers from different sources, which have very weak correlations (r=0.19 and 0.31 for EA and Korea, respectively). This agrees with the conclusion from the WAS group that H-1211 is no longer a valid China signature VOC during the KORUS-AQ campaign (Section 2.1.2).

Given the large area and potential heterogeneity over EA, we further analyzed the relationships between the five VOCs and CO from nine tagged EA sub-regions and the results are given in Table D3). EA-N1, EA-N2, EA-M1, EA-M2, EA-S1, EA-S2, and EA-S3 do not have strong correlations ($r \leq 0.3$) with the four China signature VOCs (CCl_4, CFC-113, CFC-114, and OCS), whereas EA-M3 has the highest correlation. Correlations of OCS and CCl_4 with CO from EA-N3 (0.24 and 0.30, respectively) are much lower than those with EA-M3 (0.60 and 0.55, respectively), whereas correlations between CFCs and CO from EA-N3 are similar to that for EA-M3 (0.2–0.3). For H-1211 and tagged CO, however, the correlation for EA-N3 (0.20) is higher than that for EA-M3 (0.18). The differences among the nine EA sub-regions in terms of their relationships with the five VOCs are related with the fact that contributions of CO from some EA regions (such as EA-N1, EA-M1, and EA-S1) are smaller than others (such as EA-N3 and EA-M3). However, it could also be a potential signal of the heterogeneity in anthropogenic VOC emissions over EA.

5.3 Comparisons with Analysis of CO to CO_2 Enhancement Ratios

Previous studies found that dCO/dCO_2 (i.e., CO to CO_2 enhancement ratio; see Section 2.1 for definition) are significantly higher for China than Korea, since Korea tends to have overall higher combustion efficiency than China [Tang et al. 2018; Silva et al., 2013; Turnbull et al., 2011; Wang et al., 2010]. Thus, a higher dCO/dCO_2 should correspond to a larger China contribution. We compare the dCO/dCO_2 derived from DC-8 aircraft measurements and the corresponding source contributions to CO derived from CAM-chem. Compared with the mean condition (averaged throughout the measurement period), Korean contribution increases from 6-13% to 10-22% over the Seoul group (Table DS3), with the corresponding dCO/dCO_2 decreasing from 15.6 ppbv/ppmv to 11.8 ppbv/ppmv. On the other hand, over the West Sea, the contribution from EA increases from 31-49% to 44-67% (Table DS3), with the corresponding dCO/dCO_2 increasing from 15.6 ppbv/ppmv to 21.8 ppbv/ppmv. This difference in dCO/dCO_2 indicates that Korea has overall

higher combustion efficiency than China. Albeit limited in scope, this is qualitatively consistent with our previous findings for CAMS CO and CO_2 forecast and analysis products [Tang et al., 2018] and corroborates our new findings of source contributions to this region from CAM-chem tagged CO tracers.

6. Summary and Conclusions

In this study, we investigated CO source contributions for the KORUS-AQ campaign using CAM-chem tagged tracers. We first conducted a set of model sensitivity test simulations by varying emissions, meteorology, and resolution, and comprehensively evaluated these CO simulations by comparing with DC-8 aircraft measurements and MOPITT retrievals. We then conducted source contribution analysis for the KORUS-AQ airborne and ground measurements by tagging CO tracers emitted from different source regions and chemical processes in CAM-chem simulations. To further assess the robustness of our analyses of source contributions, we compared the CAM-chem results with the results from four other approaches to source contributions (FLEXPART-WRF back trajectory, WRF inert NO_2 tracer, China signature VOCs, and dCO/dCO_2).

We found that CAM-chem simulations with different spatial resolutions (0.9°×1.25°, 1.9°×2.5°, and 0.47°×0.63°), anthropogenic CO emissions (HTAP, CREATE, and CMIP6), and/or meteorological fields (GEOS-FP and MERRA-2) produce similar bias patterns and systematically underestimate CO vertical profiles by 30–40% (normalized mean bias) during the KORUS-AQ campaign, compared with DC-8 aircraft measurements. We further analyzed the potential sources (transport, emission, resolution, and chemistry) of this underestimation and suggested that chemically produced CO may contribute to the underestimation in CO background in this region. We conducted nine additional sensitivity test simulations by varying anthropogenic CO emissions based on C2TK1_G_HF, which used GEOS-FP meteorology fields, HTAP+FINN emissions, and the resolution of 0.9°×1.25°. We emphasize that there are limitations for this approach. We note that doubling anthropogenic CO and/or VOC emissions may not be the optimized solution, and more future work is needed to refine CO emissions and chemistry processes in different source regions. Further studies on the isoprene oxidation, and on explaining the biases in the modelled OH values also need to be done. We are also using a smooth and prescribed CH_4 fields that may not explain local industrial and oil and gas point sources.

In these nine additional sensitivity test simulations, the anthropogenic CO and/or VOC emissions from the globe or a specific source region (i.e., EA, Korea, EA-N, EA-M, EA-S) were doubled. We find that simulations using bottom-up emission inventories (HTAP, CREATE, CMIP6) are consistently low (bias: -34 to -39%) and perform more poorly (Taylor skill: 0.38 to 0.61) than simulations using alternative emissions (bias: -6 to -33%; Taylor skill: 0.48 to 0.86), particularly for simulations with doubled East Asian and Korean anthropogenic CO and VOC emissions, suggesting underestimation in modeled background CO (Global_CO_x2) and bottom-up emissions (EA_&_Korea_CO_&_VOC_x2) in the region. We further compared all the aforementioned model simulations with MOPITT CO retrievals over East Asia during the KORUS-AQ period. The differences in CO vertical profiles between model simulations and MOPITT over Korea and its surrounding areas are much smaller, relative to the model biases against DC-8 airborne observations. EA_&_Korea_CO_&_VOC_×2 also agrees better with MOPITT compared to Global CO ×2. We also found that all the model simulations tend to overestimate (underestimate) CO total column density in the southern (northern) part of East Asia. We note that a systematic evaluation of MOPITT CO over the region using the KORUS-AQ airborne observations requires further work and is beyond the scope of this work.

To emphasize the uncertainties in our source contribution analysis and to take advantage of the ensemble of model simulations, we provide ranges derived from the top 50% performed ensemble members (based on Taylor score) for our source contribution analysis. We elucidate the contributions of different tagged emissions to CO concentrations along DC-8 flight tracks and across several ground sites.

The results of CAM-chem tagged CO simulations showed that direct Korean CO emissions overall contribute about 6-13% to modeled total CO concentrations throughout the DC-8 flight period. The Korean contribution is higher for the Seoul (10-22%) and Seoul-Jeju jetway (9-19%) groups of flight tracks due to the proximity to strong local emissions, but much lower for the West Sea group (≤1%) due to the prevailing winds. The contribution of CO from direct Korean emissions to the DC-8 measurements is larger within the boundary layer (below 850 hPa; 8–19%) than free troposphere (above 850 hPa; ~1%). Contributions of direct CO emissions from Japan, Russia, Indonesia, and India together account for a smaller proportion (10-13%). The contributions of direct CO emissions from different parts of East Asia (EA-S, EA-M, and EA-S) show very

different characteristics, with the largest and smallest overall contribution from EA-M (16–28%) and EA-S (~5%), respectively. We found that the contribution from EA-S CO emissions is higher in the free troposphere (8–11%) than in the boundary layer (~3%), while it is the opposite for contribution from EA-M (17–29% in the boundary layer and 14–26% in free troposphere) and EA-N (11–22% in the boundary layer and 5–10% in free troposphere) emissions. In particular, for the West Sea group of DC-8 flights when Chinese outflow was expected, the contribution of CO emissions from EA-M is evidently larger (29-51%) than average, suggesting that the West Sea region is mainly impacted by the EA-M outflow. Other sources, including direct CO emissions from the rest of the world, biogenic CO, and CO chemical production, generally contribute more in the free troposphere (40–58%) than in the boundary layer (24–44%).

We also analyzed source contributions to the plumes encountered by the DC-8 aircraft. The results are consistent with the source contribution analysis for the general airborne measurements. During the frontal passage days, contribution of EA-S CO emissions to the plumes is enhanced (11–16% to plumes captured on May 13th) compared to the average (6–8%). During the China outflow days, the plumes are dominated by EA-M CO emissions (44–64% to plumes captured on May 31st). For the plumes expected to be dominated by Korea local emissions, the contribution of Korean CO emissions (11–20% to plumes captured on June 5th) is evidently higher than usual (4–7%). Further source contribution analyses for 6 ground sites and 2 cities during KORUS-AQ indicated that the results generally agree with those for the airborne measurements, except that direct Korean CO emissions play an obviously more important role, especially at sites close to large local sources.

To further evaluate the robustness of the source contribution results by CAM-chem tagged CO, we compared the CAM-chem results with those from four other approaches to source contributions (FLEXPART-WRF back trajectories, WRF inert NO_2 tracers, China signature VOCs, and dCO/dCO_2). The overall source contribution results from CAM-chem and FLEXPART-WRF simulations agree reasonably well. The correlation between CAM-chem CO tracers with WRF inert NO_2 tracers is higher for emissions from Korea (0. 7) than from China (<0.5), which suggests a smaller contribution of Chinese emissions to short-lived air pollutants transported to Korea, relative to long-lived species. Further comparisons with four China signature VOCs (CCl_4, CFC-113, CFC-114, and OCS) showed that modeled CO from direct EA emissions has higher correlations with the China signature VOCs, compared to CO from elsewhere. The results also

suggested that OCS could potentially be a more effective indicator of China outflows than the other three signature VOCs, while H-1211 is no longer a valid China signature VOC. Moreover, the different relationships between CO from EA sub-regions and different China signature VOCs might be a potential signal of the inhomogeneity in VOC emissions over EA. Finally, we found consistent results from CAM-chem tagged tracers and dCO/dCO_2 analysis, which shows that a higher -than-usual contribution of Korean CO emissions corresponds to a lower-than-usual dCO/dCO_2, with the opposite relationship for China. In summary, the source contribution results from CAM-chem tagged CO tracers are reasonably consistent with those from the other four methods.

We note that the CAM-chem CO tagged tracers as well as the other four approaches have advantages and limitations. The tagging method is particularly appropriate for tracers associated with complicated atmospheric processes (e.g., chemistry and deposition), which explicitly accounts for non-linearity in the sensitivity to changes in emissions. Besides, CAM-chem has a global coverage and represents CO from global emissions, chemistry, and other sources such as biogenic production, but its spatial resolution is not high enough to resolve some local features. On the contrary, FLEXPART-WRF back trajectories and WRF-Tracer used in this study have higher resolutions but cover a much smaller domain and do not include chemistry. VOCs can be reliable pollution tracers but using VOCs to analyze sources of air is strongly dependent on *a priori* knowledge. For example, H-1211 was often used as a China signature VOC previously, but during KORUS-AQ it has been found to be no longer a useful indicator for Chinese plumes. The dCO/dCO_2 regression ratio may contain valuable information on combustion efficiency, but a careful analysis along with other supporting datasets and tools (such as radiocarbon and tagged fossil fuel CO_2 tracers) is necessary for a more rigorous interpretation, since this approach can be affected by other confounding factors such as air mass aging and chemical reactions. More quantitative and comprehensive evaluations and comparisons of different source contribution methods are needed in future work. We also note that this study is conducted for the time period of the KORUS-AQ experiment (May-June 2016), and do not necessarily represent the source contributions throughout the year.

Acknowledgements

We thank the KORUS-AQ team for observational data (including the WAS group from UCI for VOC data, the DACOM/DLH team for CO data, the AVOCET team for CO_2 data, Dr. W. Brune and team for the ATHOS measurements, and Dr. J. Hair and the DIAL team for the ozone data). We also thank the CESM and CAM-chem team for technical support. CESM is sponsored by the National Science Foundation (NSF) and the U.S. Department of Energy (DOE). Administration of the CESM is maintained by the Climate and Global Dynamics Division (CGD) at the National Center for Atmospheric Research (NCAR). We thank MOPITT teams for satellite retrievals of CO. The NCAR MOPITT project is supported by the National Aeronautics and Space Administration (NASA) Earth Observing System (EOS) Program. The authors thank the anonymous reviewers for their constructive comments and suggestions. W. Tang thanks the NCAR Advanced Study Program's Graduate Visitor Program. C. He is supported by the NCAR Advanced Study Program Postdoctoral Fellowship. The authors thank Dr. Jean-Francois Lamarque and Dr. Helen Worden for helpful discussions. Yugo Kanaya was supported by the Environment Research and Technology Development Fund (2-1505 and 2-1803) of the Ministry of the Environment, Japan. Computing resources were provided by the Climate Simulation Laboratory at NCAR's Computational and Information Systems Laboratory (CISL), sponsored by the National Science Foundation and other agencies. We would like to acknowledge high-performance computing support from Cheyenne (doi:10.5065/D6RX99HX) provided by NCAR's Computational and Information Systems Laboratory, sponsored by the National Science Foundation. NCAR is sponsored by the National Science Foundation. This work is supported by NASA grant NNX16AD96G and NNX16AE16G. Observational data, modeling results of WRF, FLEXPART-ERF during KORUS-AQ are available at https://www-air.larc.nasa.gov/cgi-bin/ArcView/korusaq. MOPITT data are available at https://www2.acom.ucar.edu/mopitt. CAM-chem modeling results are available at https://github.com/EarthSciData/Modeloutput.git.

References

Al-Saadi, Jassim, Gregory Carmichael, James Crawford, Louisa Emmons, Saewung Kim, Chang-Keun Song, Lim-Seok Chang, Gangwoong Lee, Jhoon Kim, Rokjin Park, KORUS-AQ: An International Cooperative Air Quality Field Study in Korea, the KORUS-AQ white paper, 2014 (https://espo.nasa.gov/korus-aq/content/KORUS-AQ_White_Paper).

Arellano, A. F., Kasibhatla, P. S., Giglio, L., Van Der Werf, G. R., & Randerson, J. T. (2004). Top-down estimates of global CO sources using MOPITT measurements. Geophysical research letters, 31(1).

Arellano, A.F., Kasibhatla, P.S., Giglio, L., Van der Werf, G.R., Randerson, J.T. and Collatz, G.J.: Time-dependent inversion estimates of global biomass-burning CO emissions using Measurement of Pollution in the Troposphere (MOPITT) measurements. Journal of Geophysical Research: Atmospheres, 111(D9), 2006.

Bakwin, P.S.,.Tans, P.P, and Novelli, P.C.: Carbon monoxide budget in the Northern hemisphere. Geophysical Research Letters. 21, 433-436, 1994.

Barletta, B., Meinardi, S., Simpson, I.J., Atlas, E.L., Beyersdorf, A.J., Baker, A.K., Blake, N.J., Yang, M., Midyett, J.R., Novak, B.J. and McKeachie, R.J.: Characterization of volatile organic compounds (VOCs) in Asian and north American pollution plumes during INTEX-B: identification of specific Chinese air mass tracers. Atmospheric Chemistry and Physics, 9(14), pp.5371-5388, 2009.

Bey, I., Jacob, D. J., Yantosca, R. M., Logan, J. A., Field, B. D., Fiore, A. M., ... & Schultz, M. G. (2001). Global modeling of tropospheric chemistry with assimilated meteorology: Model description and evaluation. Journal of Geophysical Research: Atmospheres, 106(D19), 23073-23095.

Blake, D.R., Chen, T.Y., Smith, T.W., Wang, C.J.L., Wingenter, O.W., Blake, N.J., Rowland, F.S. and Mayer, E.W.: Three-dimensional distribution of nonmenthane hydrocarbons and halocarbons over the northwestern Pacific during the 1991 Pacific Exploratory Mission (PEM-West A). Journal of Geophysical Research: Atmospheres, 101(D1), pp.1763-1778, 1996.

Blake, N.J., Blake, D.R., Simpson, I.J., Lopez, J.P., Johnston, N.A., Swanson, A.L., Katzenstein, A.S., Meinardi, S., Sive, B.C., Colman, J.J. and Atlas, E.: Large-scale latitudinal and vertical distributions of NMHCs and selected halocarbons in the troposphere over the Pacific Ocean during the March-April 1999 Pacific Exploratory Mission (PEM-Tropics B). Journal of Geophysical Research: Atmospheres, 106(D23), pp.32627-32644, 2001.

Blake, N.J., Blake, D.R., Simpson, I.J., Meinardi, S., Swanson, A.L., Lopez, J.P., Katzenstein, A.S., Barletta, B., Shirai, T., Atlas, E. and Sachse, G.: NMHCs and halocarbons in Asian continental outflow during the Transport and Chemical Evolution over the Pacific (TRACE-P) Field Campaign: Comparison with PEM-West B. Journal of Geophysical Research: Atmospheres, 108(D20), 2003.

Blake, N.J., Streets, D.G., Woo, J.H., Simpson, I.J., Green, J., Meinardi, S., Kita, K., Atlas, E., Fuelberg, H.E., Sachse, G. and Avery, M.A.: Carbonyl sulfide and carbon disulfide: Large-scale distributions over the western Pacific and emissions from Asia during TRACE-P. Journal of Geophysical Research: Atmospheres, 109(D15), 2004.

Bogenschutz, P.A., Gettelman, A., Morrison, H., Larson, V.E., Schanen, D.P., Meyer, N.R. and Craig, C., 2012. Unified parameterization of the planetary boundary layer and shallow convection with a higher-order turbulence closure in the Community Atmosphere Model: Single-column experiments. Geoscientific Model Development, 5(6), p.1407.

Bogenschutz, P. A., Gettelman, A., Hannay, C., Larson, V. E., Neale, R. B., Craig, C., and Chen, C.-C.: The path to CAM6: coupled simulations with CAM5.4 and CAM5.5, Geosci. Model Dev., 11, 235-255, https://doi.org/10.5194/gmd-11-235-2018, 2018.

Brioude, J., Arnold, D., Stohl, A., Cassiani, M., Morton, D., Seibert, P., Angevine, W., Evan, S., Dingwell, A., Fast, J.D. and Easter, R.C.: The Lagrangian particle dispersion model FLEXPART-WRF version 3.1. Geoscientific Model Development, 6(6), pp.1889-1904, 2013.

Buchholz, R.R., Paton-Walsh, C., Griffith, D.W., Kubistin, D., Caldow, C., Fisher, J.A., Deutscher, N.M., Kettlewell, G., Riggenbach, M., Macatangay, R. and Krummel, P.B.: Source and meteorological influences on air quality (CO, CH4 & CO2) at a Southern Hemisphere urban site. Atmospheric Environment, 126, pp.274-289, 2016.

Chen, D., Wang, Y., McElroy, M.B., He, K., Yantosca, R.M. and Sager, P.L.: Regional CO pollution and export in China simulated by the high-resolution nested-grid GEOS-Chem model. Atmospheric Chemistry and Physics, 9(11), pp.3825-3839, 2009.

Clappier, A., Belis, C.A., Pernigotti, D. and Thunis, P., 2017. Source apportionment and sensitivity analysis: two methodologies with two different purposes. Geoscientific Model Development, 10(11), p.4245.

Computational and Information Systems Laboratory. 2017. Cheyenne: SGI ICE XA System (University Community Computing). Boulder, CO: National Center for Atmospheric Research. doi:10.5065/D6RX99HX.

Deeter, M. N., Edwards, D. P., Gille, J. C., & Worden, H. M. (2015). Information content of MOPITT CO profile retrievals: Temporal and geographical variability. Journal of Geophysical Research: Atmospheres, 120(24), 12723-12738.

Deeter, M.N., Edwards, D.P., Francis, G.L., Gille, J.C., Martínez-Alonso, S., Worden, H.M. and Sweeney, C.: A climate-scale satellite record for carbon monoxide: the MOPITT Version 7 product. Atmospheric Measurement Techniques, 10(7), p.2533, 2017a.

Deeter, M. N.: MOPITT (Measurements of Pollution in the Troposphere) Version 7 Product User's Guide. National Center for Atmospheric Research, 2017b.

Dennis, J. M., Edwards, J., Evans, K. J., Guba, O., Lauritzen, P. H., Mirin, A. A., ... & Worley, P.

H. (2012). CAM-SE: A scalable spectral element dynamical core for the Community Atmosphere Model. The International Journal of High Performance Computing Applications, 26(1), 74-89.

Duncan, B.N. and Bey, I.: A modeling study of the export pathways of pollution from Europe: Seasonal and interannual variations (1987–1997). Journal of Geophysical Research: Atmospheres, 109(D8), 2004.

Emmons, L.K., Hess, P.G., Lamarque, J.F. and Pfister, G.G.: Tagged ozone mechanism for MOZART-4, CAM-chem and other chemical transport models. Geoscientific Model Development, 5(6), p.1531, 2012.

Fisher, J. A., Murray, L. T., Jones, D. B. A., and Deutscher, N. M.: Improved method for linear carbon monoxide simulation and source attribution in atmospheric chemistry models illustrated using GEOS-Chem v9, Geosci. Model Dev., 10, 4129-4144, https://doi.org/10.5194/gmd-10-4129-2017, 2017.

Flemming, J., Benedetti, A., Inness, A., Engelen, R. J., Jones, L., Huijnen, V., ... & Peuch, V. H. (2017). The CAMS interim Reanalysis of Carbon Monoxide, Ozone and Aerosol for 2003-2015. Atmospheric Chemistry and Physics, 17(3), 1945.

Fuelberg, H. E., Kiley, C. M., Hannan, J. R., Westberg, D. J., Avery, M. A., & Newell, R. E. (2003). Meteorological conditions and transport pathways during the Transport and Chemical Evolution over the Pacific (TRACE-P) experiment. Journal of Geophysical Research: Atmospheres, 108(D20).

Gamnitzer, U., Karstens, U., Kromer, B., Neubert, R.E., Meijer, H.A., Schroeder, H. and Levin, I.: Carbon monoxide: A quantitative tracer for fossil fuel CO2?. Journal of Geophysical Research: Atmospheres, 111(D22), 2006.

Gao, M., Saide, P. E., Xin, J., Wang, Y., Liu, Z., Wang, Y., ... & Carmichael, G. R. (2017). Estimates of health impacts and radiative forcing in winter haze in eastern China through constraints of surface PM2. 5 predictions. Environmental science & technology, 51(4), 2178-2185.

Gaubert, B., Arellano, A. F., Barré, J., Worden, H. M., Emmons, L. K., Tilmes, S., … Jones, N. .: Toward a chemical reanalysis in a coupled chemistry climate model: An evaluation of MOPITT CO assimilation and its impact on tropospheric composition. Journal of Geophysical Research: Atmospheres, 121, 7310–7343. https://doi.org/10.1002/2016JD024863, 2016.

Gaubert, B., Worden, H. M., Arellano, A. F. J., Emmons, L. K., Tilmes, S., Barré, J., Martínez Alonso, S., Vitt, F., Anderson, J.L., Alkemade, F., Houweling, S., and Edwards D.P.: Chemical feedback from decreasing carbon monoxide emissions, Geophys. Res. Lett., 44, doi:10.1002/2017GL074987, 2017.

Gelaro, R., McCarty, W., Suárez, M.J., Todling, R., Molod, A., Takacs, L., Randles, C.A., Darmenov, A., Bosilovich, M.G., Reichle, R. and Wargan, K.: The modern-era

retrospective analysis for research and applications, version 2 (MERRA-2). Journal of Climate, 30(14), pp.5419-5454, 2017.

Granier, C., Mueller, J.F., Pétron, G. and Brasseur, G.: A three-dimensional study of the global CO budget. Chemosphere-Global Change Science, 1(1), pp.255-261, 1999.

Grell, G. A., Peckham, S. E., Schmitz, R., McKeen, S. A., Frost, G., Skamarock, W. C., & Eder, B: Fully coupled "online" chemistry within the WRF model. Atmospheric Environment, 39(37), 6957-6975, 2005.

Heald, C. L., Jacob, D. J., Fiore, A. M., Emmons, L. K., Gille, J. C., Deeter, M. N., ... & Sachse, G. W. (2003). Asian outflow and trans-Pacific transport of carbon monoxide and ozone pollution: An integrated satellite, aircraft, and model perspective. Journal of Geophysical Research: Atmospheres, 108(D24).

Heald, C. L., Jacob, D. J., Park, R. J., Alexander, B., Fairlie, T. D., Yantosca, R. M., and Chu, D. A.: Transpacific transport of Asian anthropogenic aerosols and its impact on surface air quality in the United States. Journal of Geophysical Research: Atmospheres, 111(D14), 2006.

Heald, C. L., Jacob, D. J., Jones, D., Palmer, P. I., Logan, J. A., Streets, D. G., ... & Nehrkorn, T. (2004). Comparative inverse analysis of satellite (MOPITT) and aircraft (TRACE-P) observations to estimate Asian sources of carbon monoxide. Journal of Geophysical Research: Atmospheres, 109(D23).

Hoell, J. M., Davis, D. D., Liu, S. C., Newell, R. E., Akimoto, H., McNeal, R. J., & Bendura, R. J. (1997). The Pacific Exploratory Mission-West Phase B: February-March, 1994. Journal of Geophysical Research: Atmospheres, 102(D23), 28223-28239.

Hoesly, R.M., Smith, S.J., Feng, L., Klimont, Z., Janssens-Maenhout, G., Pitkanen, T., Seibert, J.J., Vu, L., Andres, R.J., Bolt, R.M. and Bond, T.C.: Historical (1750-2014) anthropogenic emissions of reactive gases and aerosols from the Community Emission Data System (CEDS). Geoscientific Model Development Discussions, pp.1-41, 2017.

Huebert, B. J., Bates, T., Russell, P. B., Shi, G., Kim, Y. J., Kawamura, K., ... & Nakajima, T. (2003). An overview of ACE-Asia: Strategies for quantifying the relationships between Asian aerosols and their climatic impacts. Journal of Geophysical Research: Atmospheres, 108(D23).

Hurrell, J.W., Holland, M.M., Gent, P.R., Ghan, S., Kay, J.E., Kushner, P.J., Lamarque, J.F., Large, W.G., Lawrence, D., Lindsay, K. and Lipscomb, W.H.: The community earth system model: a framework for collaborative research. Bulletin of the American Meteorological Society, 94(9), pp.1339-1360, 2013.

Jacob, D. J., Logan, J. A., & Murti, P. P. (1999). Effect of rising Asian emissions on surface ozone in the United States. *Geophysical Research Letters*, 26(14), 2175-2178.

Jacob, D. J., Crawford, J. H., Kleb, M. M., Connors, V. S., Bendura, R. J., Raper, J. L., ... & Heald,

C. L. (2003). Transport and Chemical Evolution over the Pacific (TRACE-P) aircraft mission: Design, execution, and first results. Journal of Geophysical Research: Atmospheres, 108(D20).

Jaffe, D., Anderson, T., Covert, D., Kotchenruther, R., Trost, B., Danielson, J., ... & Harris, J. (1999). Transport of Asian air pollution to North America. Geophysical Research Letters, 26(6), 711-714.

Janssens-Maenhout, G., Crippa, M., Guizzardi, D., Dentener, F., Muntean, M., Pouliot, G., Keating, T., Zhang, Q., Kurokawa, J., Wankmüller, R. and Denier van der Gon, H., 2015. HTAP_v2. 2: a mosaic of regional and global emission grid maps for 2008 and 2010 to study hemispheric transport of air pollution. Atmospheric Chemistry and Physics, 15(19), pp.11411-11432, 2015.

Jiang, Z., Worden, J. R., Payne, V. H., Zhu, L., Fischer, E., Walker, T., & Jones, D. (2016). Ozone export from East Asia: The role of PAN. Journal of Geophysical Research: Atmospheres, 121(11), 6555-6563.

Jiang, Z., J. Worden, H. Worden, M. Deeter, D. Jones, A. Arellano, and D. Henze (2017), Fifteen-year CO emission estimates constrained with MOPITT CO measurements, Atmospheric Chemistry and Physics, 17, 4565-4583, doi:10.5194/acp-17-4565-2017.

Kanaya, Y., Pan, X., Miyakawa, T., Komazaki, Y., Taketani, F., Uno, I., & Kondo, Y. (2016). Long-term observations of black carbon mass concentrations at Fukue Island, western Japan, during 2009–2015: constraining wet removal rates and emission strengths from East Asia. Atmospheric Chemistry and Physics, 16(16), 10689-10705.

Lamarque, J.F., Emmons, L.K., Hess, P.G., Kinnison, D.E., Tilmes, S., Vitt, F., Heald, C.L., Holland, E.A., Lauritzen, P.H., Neu, J. and Orlando, J.J.: CAM-chem: Description and evaluation of interactive atmospheric chemistry in the Community Earth System Model. Geoscientific Model Development, 5(2), p.369, 2012.

Li, Q., Jacob, D.J., Bey, I., Palmer, P.I., Duncan, B.N., Field, B.D., Martin, R.V., Fiore, A.M., Yantosca, R.M., Parrish, D.D. and Simmonds, P.G.: Transatlantic transport of pollution and its effects on surface ozone in Europe and North America. Journal of Geophysical Research: Atmospheres, 107(D13), 2002.

Li, M., Zhang, Q., Kurokawa, J.-I., Woo, J.-H., He, K., Lu, Z., Ohara, T., Song, Y., Streets, D. G., Carmichael, G. R., Cheng, Y., Hong, C., Huo, H., Jiang, X., Kang, S., Liu, F., Su, H., and Zheng, B.: MIX: a mosaic Asian anthropogenic emission inventory under the international collaboration framework of the MICS-Asia and HTAP, Atmos. Chem. Phys., 17, 935-963, doi:10.5194/acp-17-935-2017,2017.

Liang, Q., Jaeglé, L., Jaffe, D. A., Weiss-Penzias, P., Heckman, A., & Snow, J. A. (2004). Long-range transport of Asian pollution to the northeast Pacific: Seasonal variations and transport pathways of carbon monoxide. Journal of Geophysical Research: Atmospheres, 109(D23).

Liu, H., Jacob, D.J., Bey, I., Yantosca, R.M., Duncan, B.N. and Sachse, G.W.: Transport pathways for Asian pollution outflow over the Pacific: Interannual and seasonal variations. Journal of Geophysical Research: Atmospheres, 108(D20), 2003.

Liu, X., Ma, P.-L., Wang, H., Tilmes, S., Singh, B., Easter, R. C., Ghan, S. J., and Rasch, P. J.: Description and evaluation of a new four-mode version of the Modal Aerosol Module (MAM4) within version 5.3 of the Community Atmosphere Model, Geosci. Model Dev., 9, 505-522, https://doi.org/10.5194/gmd-9-505-2016, 2016.

Miyazaki, K., Eskes, H., Sudo, K., Boersma, K. F., Bowman, K., and Kanaya, Y.: Decadal changes in global surface NOx emissions from multi-constituent satellite data assimilation, Atmos. Chem. Phys., 17, 807-837, doi:10.5194/acp-17-807-2017, 2017.

Miyazaki, K., Sekiya, T., Fu, D., Bowman, K. W., Kulawik, S. S., Sudo, K., ... & Eskes, H. (2018). Balance of emission and dynamical controls on ozone during KORUS-AQ from multi-constituent satellite data assimilation. Journal of Geophysical Research: Atmospheres.

Molod, A., Takacs, L., Suarez, M., & Bacmeister, J. (2015). Development of the GEOS-5 atmospheric general circulation model: Evolution from MERRA to MERRA2. Geoscientific Model Development, 8(5), 1339.

Monks, S. A., Arnold, S. R., Emmons, L. K., Law, K. S., Turquety, S., Duncan, B. N., ... & Mao, J. (2015). Multi-model study of chemical and physical controls on transport of anthropogenic and biomass burning pollution to the Arctic. Atmospheric Chemistry and Physics, 15(6), 3575-3603.

Morrison, H. and Gettelman, A. A new two-moment bulk stratiform cloud microphysics scheme in the Community Atmosphere Model, version 3 (CAM3). Part I: Description and numerical tests. Journal of Climate, 21(15), pp.3642-3659, 2008.

Müller, J. F., Stavrakou, T., Bauwens, M., George, M., Hurtmans, D., Coheur, P. F., ... & Sweeney, C. (2018). Top-Down CO Emissions Based On IASI Observations and Hemispheric Constraints on OH Levels. Geophysical Research Letters, 45(3), 1621-1629.

Naik, V., Voulgarakis, A., Fiore, A.M., Horowitz, L.W., Lamarque, J.F., Lin, M., Prather, M.J., Young, P.J., Bergmann, D., Cameron-Smith, P.J. and Cionni, I.: Preindustrial to present-day changes in tropospheric hydroxyl radical and methane lifetime from the Atmospheric Chemistry and Climate Model Intercomparison Project (ACCMIP). Atmospheric Chemistry and Physics, 13(10), pp.5277-5298, 2013.

Palmer, P.I., Jacob, D.J., Mickley, L.J., Blake, D.R., Sachse, G.W., Fuelberg, H.E. and Kiley, C.M.: Eastern Asian emissions of anthropogenic halocarbons deduced from aircraft concentration data. Journal of Geophysical Research: Atmospheres, 108(D24), 2003.

Park, M., Randel, W.J., Emmons, L.K. and Livesey, N.J.: Transport pathways of carbon monoxide in the Asian summer monsoon diagnosed from Model of Ozone and Related Tracers (MOZART). Journal of Geophysical Research: Atmospheres, 114(D8), 2009.

Parrish, D. D., Trainer, M., Hereid, D., Williams, E. J., Olszyna, K. J., Harley, R. A., Meagher, J. F. and Fehsenfeld, F. C.: Decadal change in carbon monoxide to nitrogen oxide ratio in US vehicular emissions. Journal of Geophysical Research: Atmospheres, 107(D12), 2002.

Pétron, G., Granier, C., Khattatov, B., Yudin, V., Lamarque, J.F., Emmons, L., Gille, J. and Edwards, D.P.: Monthly CO surface sources inventory based on the 2000–2001 MOPITT satellite data. Geophysical Research Letters, 31(21), 2004.

Pfister, G., Petron, G., Emmons, L.K., Gille, J.C., Edwards, D.P., Lamarque, J.F., Attie, J.L., Granier, C. and Novelli, P.C.: Evaluation of CO simulations and the analysis of the CO budget for Europe. Journal of Geophysical Research: Atmospheres, 109(D19), 2004.

Pfister, G.G., Avise, J., Wiedinmyer, C., Edwards, D.P., Emmons, L.K., Diskin, G.D., Podolske, J. and Wisthaler, A.: CO source contribution analysis for California during ARCTAS-CARB. Atmospheric Chemistry and Physics, 11(15), pp.7515-7532, 2011.

Pfister, G.G., Reddy, P.J., Barth, M.C., Flocke, F.F., Fried, A., Herndon, S.C., Sive, B.C., Sullivan, J.T., Thompson, A.M., Yacovitch, T.I. and Weinheimer, A.J.: Using Observations and Source-Specific Model Tracers to Characterize Pollutant Transport During FRAPPÉ and DISCOVER-AQ. Journal of Geophysical Research: Atmospheres, 122(19), 2017.

Protonotariou, A., Kostopoulou, E., Tombrou, M., and Giannakopoulos, C.. "European CO budget and links with synoptic circulation based on GEOS-CHEM model simulations" Tellus B, 2013, 65, 18640, http://dx.doi.org/10.3402/tellusb.v65i0.18640.

Rienecker, M. M., Suarez, M. J., Gelaro, R., Todling, R., Bacmeister, J., Liu, E., Bosilovich, M. G., Schubert, S. D., Takacs, L., Kim, G.-K., Bloom, S., Chen, J., Collins, D., Conaty, A., da Silva, A., Gu, W., Joiner, J., Koster, R. D., Lucchesi, R., Molod, A., Owens, T., Pawson, S., Pegion, P., Redder, C. R., Reichle, R., Robertson, F. R., Ruddick, A. G., Sienkiewicz, M., and Woollen, J.: MERRA: NASA's Modern-Era Retrospective Analysis for Research and Application, J. Climate, 24, 3624–3648. doi:10.1175/JCLI-D-11-00015.1, 2011.

Qin, D.: Decline in the concentrations of chlorofluorocarbons (CFC-11, CFC-12 and CFC-113) in an urban area of Beijing, China. Atmospheric Environment, 41(38), pp.8424-8430, 2007.

Seibert, P. and Frank, A.: Source-receptor matrix calculation with a Lagrangian particle dispersion model in backward mode. Atmospheric Chemistry and Physics, 4(1), pp.51-63, 2004.

Shindell, D.T., Faluvegi, G., Stevenson, D.S., Krol, M.C., Emmons, L.K., Lamarque, J.F., Petron, G., Dentener, F.J., Ellingsen, K., Schultz, M.G. and Wild, O.: Multimodel simulations of carbon monoxide: Comparison with observations and projected near-future changes. Journal of Geophysical Research: Atmospheres, 111(D19), 2006.

Silva, S.J., Arellano, A.F. and Worden, H.M.: Toward anthropogenic combustion emission constraints from space-based analysis of urban CO2/CO sensitivity. Geophysical Research Letters, 40(18), pp.4971-4976, 2013.

Smith, R.J.: Use and misuse of the reduced major axis for line-fitting. American journal of physical

anthropology, 140(3), pp.476-486, 2009.

Staudt, A.C., Jacob, D.J., Logan, J.A., Bachiochi, D., Krishnamurti, T.N. and Sachse, G.W.: Continental sources, transoceanic transport, and interhemispheric exchange of carbon monoxide over the Pacific. Journal of Geophysical Research: Atmospheres, 106(D23), pp.32571-32589, 2001.

Stein, O., Schultz, M.G., Bouarar, I., Clark, H., Huijnen, V., Gaudel, A., George, M. and Clerbaux, C.: On the wintertime low bias of Northern Hemisphere carbon monoxide found in global model simulations. Atmospheric chemistry and physics, 14(17), pp.9295-9316, 2014.

Streets, D.G., Bond, T.C., Carmichael, G.R., Fernandes, S.D., Fu, Q., He, D., Klimont, Z., Nelson, S.M., Tsai, N.Y., Wang, M.Q. and Woo, J.H.: An inventory of gaseous and primary aerosol emissions in Asia in the year 2000. Journal of Geophysical Research: Atmospheres, 108(D21), 2003.

Streets, D.G., Zhang, Q., Wang, L., He, K., Hao, J., Wu, Y., Tang, Y. and Carmichael, G.R.: Revisiting China's CO emissions after the transport and chemical evolution over the Pacific (TRACE-P) mission: synthesis of inventories, atmospheric modeling, and observations. Journal of Geophysical Research: Atmospheres, 111(D14), 2006.

Stohl, A., Eckhardt, S., Forster, C., James, P., Spichtinger, N. and Seibert, P.: A replacement for simple back trajectory calculations in the interpretation of atmospheric trace substance measurements. Atmospheric Environment, 36(29), pp.4635-4648, 2002.

Stohl, A., Forster, C., Frank, A., Seibert, P. and Wotawa, G.: The Lagrangian particle dispersion model FLEXPART version 6.2. Atmospheric Chemistry and Physics, 5(9), pp.2461-2474, 2005.

Strode, S. A., Duncan, B. N., Yegorova, E. A., Kouatchou, J., Ziemke, J. R., & Douglass, A. R. (2015). Implications of carbon monoxide bias for methane lifetime and atmospheric composition in chemistry climate models. Atmospheric Chemistry and Physics, 15(20), 11789-11805.

Tang, W., & Arellano, A. F. (2017). Investigating dominant characteristics of fires across the Amazon during 2005–2014 through satellite data synthesis of combustion signatures. Journal of Geophysical Research: Atmospheres, 122(2), 1224-1245.

Tang, W., Arellano, A. F., DiGangi, J. P., Choi, Y., Diskin, G. S., Agustí-Panareda, A., ... & Kim, D. (2018). Evaluating high-resolution forecasts of atmospheric CO and CO 2 from a global prediction system during KORUS-AQ field campaign. Atmospheric Chemistry and Physics, 18(15), 11007-11030.

Taylor, K. E. (2001). Summarizing multiple aspects of model performance in a single diagram. Journal of Geophysical Research: Atmospheres, 106(D7), 7183-7192.

Tilmes, S., Lamarque, J.F., Emmons, L.K., Kinnison, D.E., Ma, P.L., Liu, X., Ghan, S., Bardeen, C., Arnold, S.R., Deeter, M. and Vitt, F., 2015. Description and evaluation of tropospheric

chemistry and aerosols in the Community Earth System Model (CESM1. 2). Geoscientific Model Development, 8, pp.1395-1426.

Turnbull, J. C., Tans, P. P., Lehman, S. J., Baker, D., Conway, T. J., Chung, Y. S., Gregg, J., Miller, J. B., Southon, J. R., and Zhou, L. X.: Atmospheric observations of carbon monoxide and fossil fuel CO2 emissions from East Asia. Journal of Geophysical Research: Atmospheres, 116(D24), 2011.

Valari, M., & Menut, L. (2008). Does an increase in air quality models' resolution bring surface ozone concentrations closer to reality?. Journal of Atmospheric and Oceanic Technology, 25(11), 1955-1968.

Vay, S.A., Choi, Y., Vadrevu, K.P., Blake, D.R., Tyler, S.C., Wisthaler, A., Hecobian, A., Kondo, Y., Diskin, G.S., Sachse, G.W. and Woo, J.H.: Patterns of CO2 and radiocarbon across high northern latitudes during International Polar Year 2008. Journal of Geophysical Research: Atmospheres, 116(D14), 2011.

Wang, Y., Choi, Y., Zeng, T., Ridley, B., Blake, N., Blake, D. and Flocke, F.: Late-spring increase of trans-Pacific pollution transport in the upper troposphere. Geophysical Research Letters, 33(1), 2006.

Wang, Y., Munger, J. W., Xu, S., McElroy, M. B., Hao, J., Nielsen, C. P., and Ma, H.: CO 2 and its correlation with CO at a rural site near Beijing: implications for combustion efficiency in China. Atmospheric Chemistry and Physics, 10(18), 8881-8897, 2010.

Warner, J.X., Wei, Z., Strow, L.L., Barnet, C.D., Sparling, L.C., Diskin, G. and Sachse, G.: Improved agreement of AIRS tropospheric carbon monoxide products with other EOS sensors using optimal estimation retrievals. Atmospheric Chemistry and Physics, 10(19), pp.9521-9533, 2010.

Wiedinmyer, C., Akagi, S.K., Yokelson, R.J., Emmons, L.K., Al-Saadi, J.A., Orlando, J.J. and Soja, A.J.: The Fire INventory from NCAR (FINN): a high resolution global model to estimate the emissions from open burning. Geoscientific Model Development, 4(3), p.625, 2011.

Wild, O., & Prather, M. J. (2006). Global tropospheric ozone modeling: Quantifying errors due to grid resolution. Journal of Geophysical Research: Atmospheres, 111(D11).

Woo, J.-H., et al (2013), Development of the Asia Emission Inventory in Support of Integrated Modeling of Climate and Air Quality(Ⅲ), National Institute of Environmental Research, NIER-SP2013-1, Incheon, Korea.

Worden, H. M., Deeter, M. N., Edwards, D. P., Gille, J. C., Drummond, J. R., & Nédélec, P.: Observations of near-surface carbon monoxide from space using MOPITT multispectral retrievals. Journal of Geophysical Research: Atmospheres, 115(D18), 2010.

Woo, J. H., Streets, D. G., Carmichael, G. R., Tang, Y., Yoo, B., Lee, W. C., ... & Fu, Q. (2003). Contribution of biomass and biofuel emissions to trace gas distributions in Asia during the

TRACE-P experiment. Journal of Geophysical Research: Atmospheres, 108(D21).

Xue, L., Wang, T., Simpson, I.J., Ding, A., Gao, J., Blake, D.R., Wang, X., Wang, W., Lei, H. and Jin, D.: Vertical distributions of non-methane hydrocarbons and halocarbons in the lower troposphere over northeast China. Atmospheric environment, 45(36), pp.6501-6509, 2011.

Yan, Y., Lin, J., Chen, J., and Hu, L.: Improved simulation of tropospheric ozone by a global-multi-regional two-way coupling model system, Atmos. Chem. Phys., 16, 2381-2400, https://doi.org/10.5194/acp-16-2381-2016, 2016.

Yin, Y., Chevallier, F., Ciais, P., Broquet, G., Fortems-Cheiney, A., Pison, I., & Saunois, M. (2015). Decadal trends in global CO emissions as seen by MOPITT. Atmospheric Chemistry & Physics Discussions, 15(10).

Yu, K., Jacob, D. J., Fisher, J. A., Kim, P. S., Marais, E. A., Miller, C. C., ... & Cohen, R. C. (2016). Sensitivity to grid resolution in the ability of a chemical transport model to simulate observed oxidant chemistry under high-isoprene conditions. Atmospheric Chemistry and Physics, 16(7), 4369-4378.

Supporting Information

Taylor score (Taylor, 2001) is defined by

$$S = \frac{4(1+R)}{(\hat{\sigma}_f+1/\hat{\sigma}_f)^2(1+R_0)} \quad \text{(DS1)}$$

where $\hat{\sigma}_f$ is the ratio of σ_f (standard deviation of the model) and σ_r (standard deviation of observations), R is correlation between model and observations, and R_0 is the maximum potentially realizable correlation (= 0.9 in this study).

Table DS1. Statistics for performance of CAM-chem CO simulations comparing with DC-8 aircraft observations during KORUS-AQ.

Simulation	mean bias (ppbv)	normalized mean bias	RMSE (ppbv)	correlation	Taylor score	Rank of Taylor score
C2TK1_G_HF	-71.40	-35%	110.34	0.57	0.49	11
C2TK1_G_CF	-74.66	-36%	114.12	0.54	0.45	14
C2TK1_G_CMIP6	-75.86	-37%	111.48	0.63	0.47	13
C2TK1_M_HF	-69.11	-34%	107.90	0.59	0.50	10
C2TK1_M_CF	-77.01	-38%	115.48	0.54	0.45	14
C2TK1_M_CMIP6	-79.08	-39%	116.74	0.56	0.40	16
C2TK05_G_HF	-76.04	-37%	111.66	0.60	0.61	6
C2TK2_G_HF	-77.36	-38%	113.97	0.62	0.38	17
Global CO ×2	-11.45	-6%	89.77	0.57	0.82	3
EA CO ×2	-33.92	-17%	91.80	0.59	0.79	4
Korea CO ×2	-64.14	-31%	104.86	0.58	0.59	8
EA-N CO ×2	-59.20	-29%	101.35	0.59	0.60	7
EA-M CO ×2	-52.71	-26%	101.85	0.53	0.69	5
EA-S CO ×2	-67.92	-33%	108.06	0.58	0.48	12
EA & Korea CO ×2	-29.67	-14%	89.21	0.63	0.85	2
EA & Korea VOC ×2	-68.54	-33%	105.46	0.63	0.55	9
EA & Korea CO & VOC ×2	-24.22	-12%	87.60	0.63	0.86	1

Table DS2. Statistical analysis of CAM-chem OH and ozone simulations by comparing with DC-8 aircraft observations. See Table D1 for definitions of different model simulations.

	OH				Ozone			
Simulation	mean bias (ppbv)	normalized mean bias	RMSE (ppbv)	correlation	mean bias (ppbv)	normalized mean bias	RMSE (ppbv)	correlation
C2TK1_G_HF	0.01	3%	0.15	0.37	-12.86	-16%	22.75	0.38
C2TK1_G_CF	0.01	3%	0.15	0.39	-13.62	-17%	22.83	0.38
C2TK1_G_CMIP6	0.00	-1%	0.14	0.42	-13.02	-16%	22.46	0.38
C2TK1_M_HF	0.01	4%	0.15	0.39	-12.70	-15%	21.56	0.44
C2TK1_M_CF	0.01	5%	0.15	0.40	-13.55	-16%	22.84	0.40
C2TK1_M_CMIP6	0.00	1%	0.14	0.47	-13.68	-17%	22.67	0.36
C2TK05_G_HF	0.01	4%	0.15	0.39	-9.15	-11%	20.27	0.41
C2TK2_G_HF	0.03	9%	0.15	0.40	-14.79	-18%	24.34	0.34
Global CO ×2	-0.02	-8%	0.15	0.38	-9.55	-12%	19.46	0.48
EA CO ×2	-0.01	-5%	0.15	0.38	-11.12	-14%	20.59	0.47
Korea CO ×2	0.00	0%	0.15	0.39	-12.20	-15%	21.47	0.45
EA-N CO ×2	0.00	0%	0.15	0.40	-12.16	-15%	21.43	0.44
EA-M CO ×2	0.00	0%	0.15	0.40	-12.26	-15%	21.92	0.43
EA-S CO ×2	0.00	0%	0.15	0.38	-12.15	-15%	21.25	0.45
EA & Korea CO ×2	0.00	0%	0.14	0.41	-6.30	-8%	17.98	0.51
EA & Korea VOC ×2	0.00	-1%	0.14	0.41	-5.01	-6%	17.10	0.54
EA & Korea CO & VOC ×2	-0.02	-7%	0.14	0.43	-4.11	-5%	16.89	0.55

Table DS3. dCO/dCO_2 and corresponding source contributions to total CO over the Seoul and West Sea group.

		Seoul	West Sea	All
dCO/dCO_2 (ppbv/ppmv)		11.8	21.8	15.6
Contribution to total CO	EA	32-51%	44-67%	31-49%
	Korea	10-22%	1%	6-13%
	regions other than Korea and EA	7-9%	8-11%	9-11%

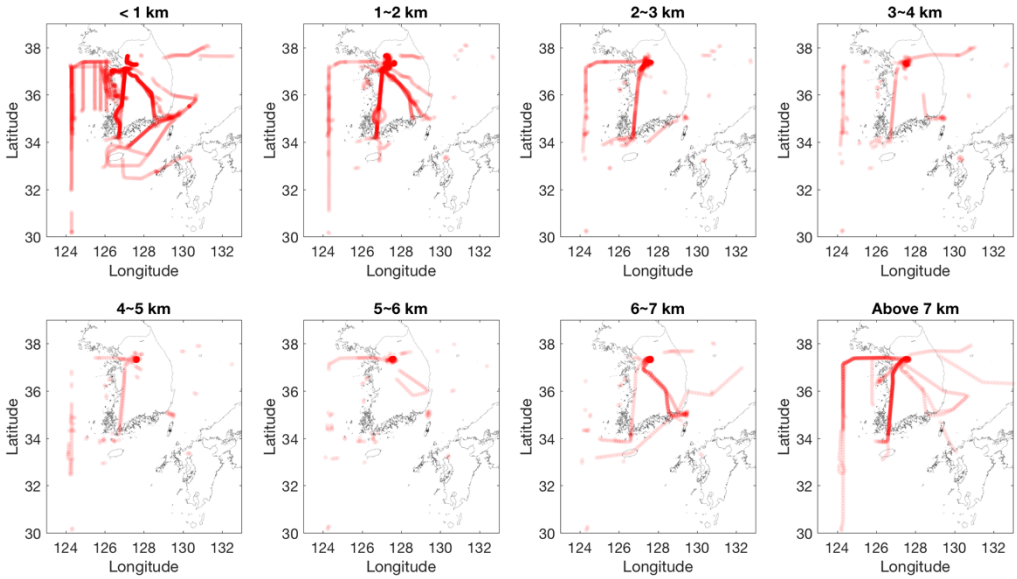

Figure DS1. DC-8 aircraft measurements at different altitude levels during KORUS-AQ. Stronger red color represents higher measurement density.

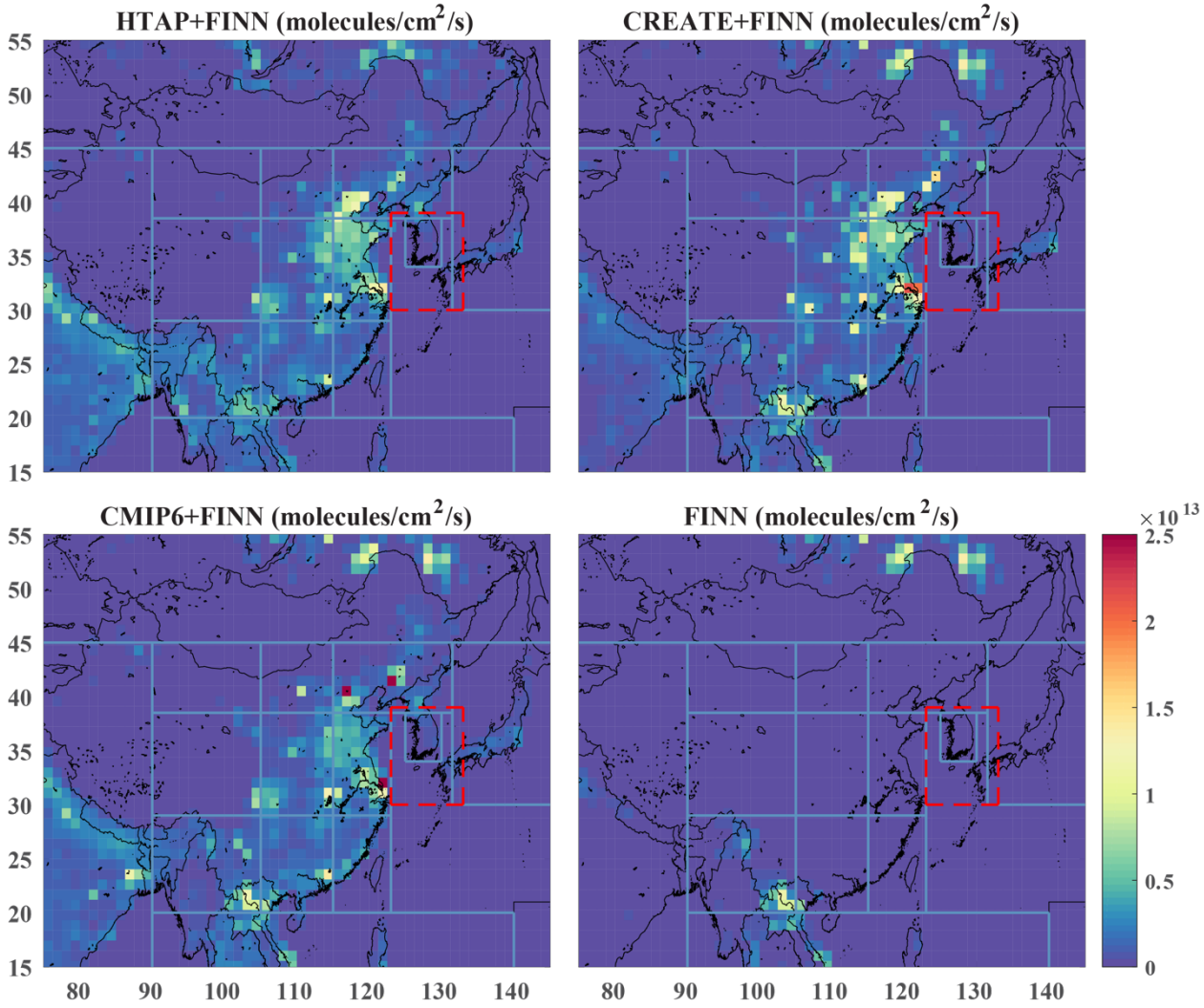

Figure DS2. Spatial distributions of direct CO emissions over East Asia averaged over the KORUS-AQ period (May 1st – June 10th, 2016). The blue rectangles represent our tagged regions (see also Fig. D1). Korea and surrounding waters (123°E-133°E, 30°N-39°N) covered by KORUS-AQ aircraft and ground measurements are highlighted by red dashed rectangles. Anthropogenic emissions are from the Hemispheric Transport of Air Pollution (HTAP) version 2 inventory, the Community Emissions Data System (CEDS) for Coupled Model Intercomparison Project Phase 6 (CMIP6), and the Comprehensive Regional Emissions Inventory for Atmospheric Transport Experiment (CREATE) embedded in HTAP. Biomass burning emissions are from the Fire INventory from NCAR (FINN) version 1.5. See text for details.

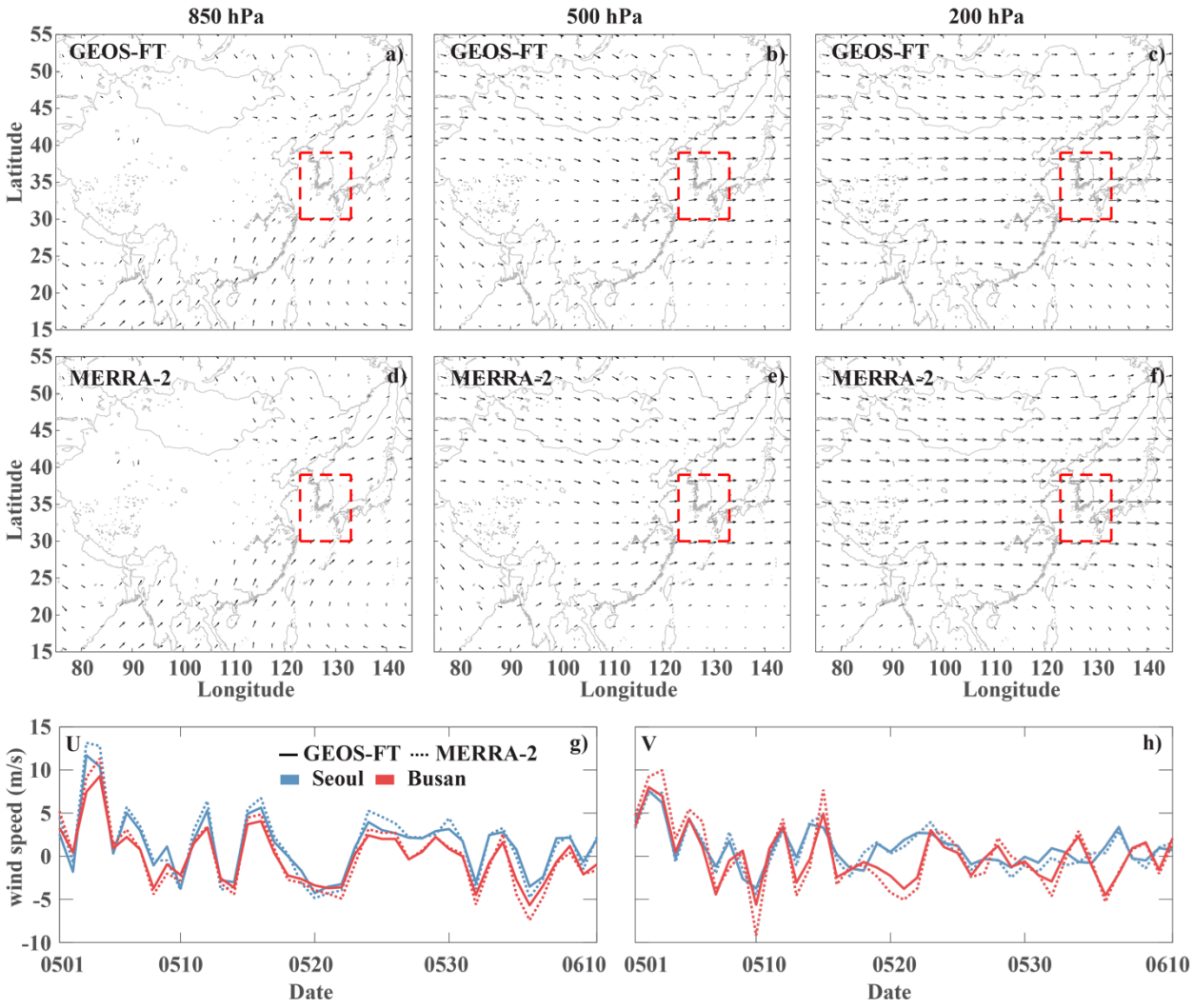

Figure DS3. (a–f) Spatial distributions of wind fields over East Asia at (a, d) 850 hPa, (b, e) 500 hPa, and (c, f) 200 hPa obtained from (a–c) GEOS-FT and (d–f) MERRA-2 datasets averaged through the KORUS-AQ period (May 1st – June 10th, 2016). (g–h) Time series of daily surface (g) meridional (U) and (h) zonal (V) wind speeds over Seoul (blue) and Busan (red) obtained from GEOS-FT (solid lines) and MERRA-2 (dashed lines) datasets.

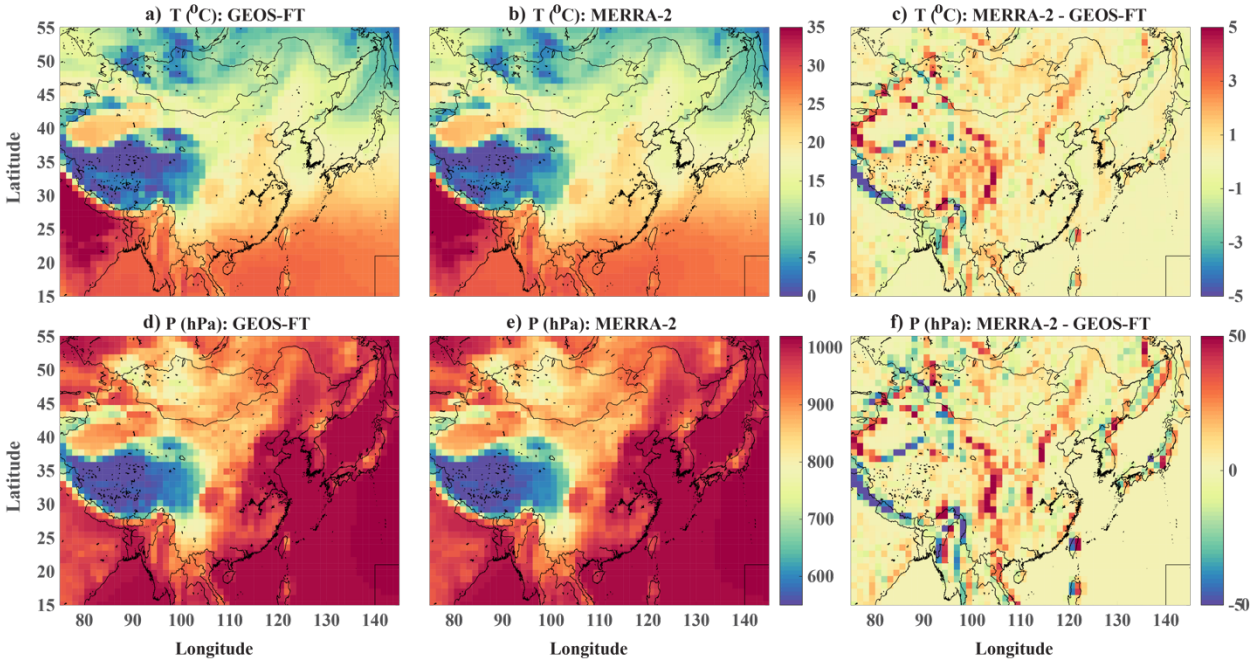

Figure DS4. Spatial distributions of (a–c) surface-layer temperature (T) and (d–f) surface pressure (P) over East Asia obtained from (a, d) GEOS-FT and (b, e) MERRA-2 datasets averaged through the KORUS-AQ period (May 1st – June 10th, 2016) as well as (c, f) their differences.

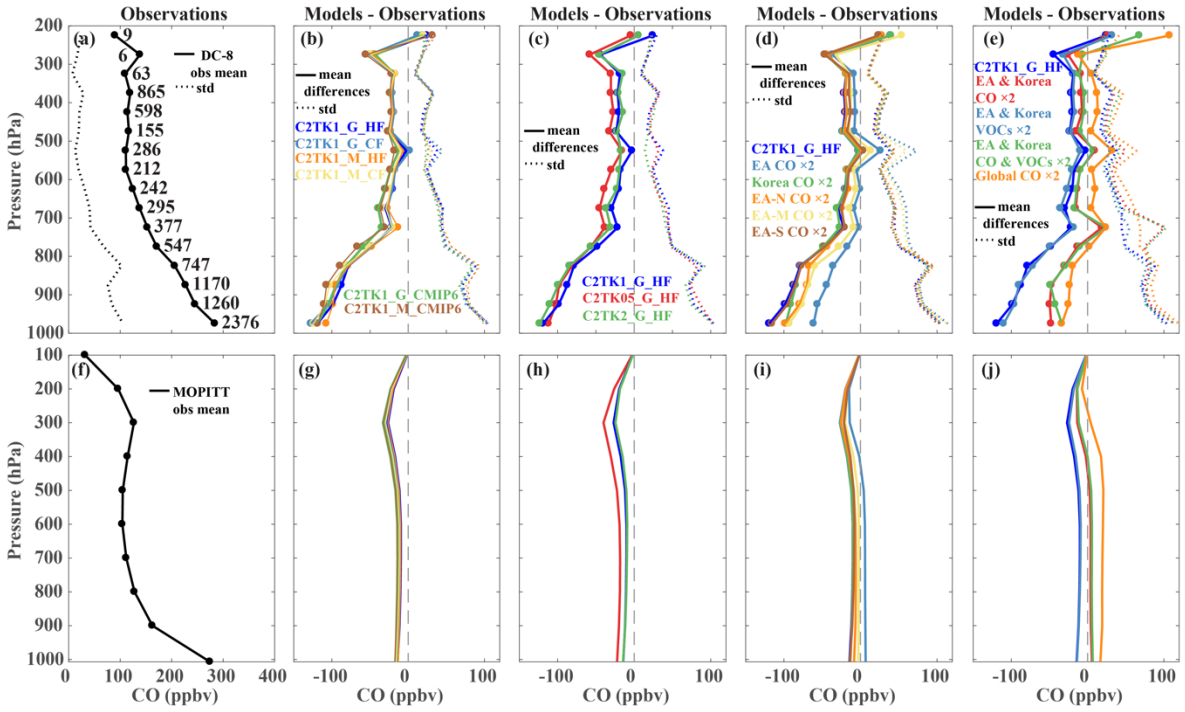

Figure DS5. (a–e) Vertical profiles of the observed (black) and CAM-chem simulated (colored) CO concentrations during the KORUS-AQ campaign. (a) Mean (solid line) and standard deviation (std; dashed line) of CO vertical profiles (averaged over 50-hPa altitude bins) obtained from the DC-8 aircraft measurements. Numbers of observations within each 50-hPa altitude bin are labeled in the panel. (b) Vertical profiles of mean (solid line) and std (dashed line) of differences in CO between airborne observations (shown in a) and 6 CAM-chem simulations using the same resolution ("C2TK1" for 0.9°×1.25°) but 2 different meteorological fields ("G" for GEOS-FP and "M" for MERRA-2) and 3 different emissions ("HF" for HTAP+FINN, "CF" for CREATE+FINN, and "CMIP6" for CMIP6+FINN). Panel c shows mean and std of model biases of 3 simulations that uses same meteorological fields (GEOS-FP) and emissions (HTAP+FINN) but different resolutions ("C2TK05", "C2TK1", and "C2TK2" denote resolutions of 0.47°×0.63°, 0.9°×1.25°, and 1.9°×2.5°). (d-e) Same as (b), but for the additional simulations and their control simulation (C2TK1_G_HF). The additional simulations employ same meteorological fields (GEOS-FP), emissions (HTAP+FINN), and resolutions (0.9°×1.25°) as their control simulation. However, in these additional simulations, the global anthropogenic CO emissions (Global CO ×2) or anthropogenic CO and/or VOC emissions from different source regions ("<the region> ×2") are doubled. See Table D1 for detailed definitions of different CAM-chem simulations. (f) Mean CO vertical profiles obtained from MOPITT (black) averaged over Korea and its surrounding waters (123°E–133°E, 30°N–39°N) and KORUS-AQ period. (g–j) Same as (b-e), but corresponding to MOPITT-model comparisons.

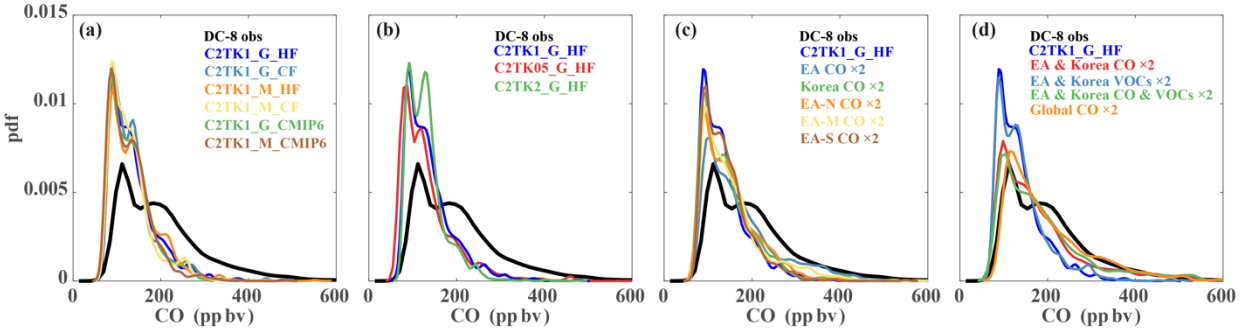

Figure DS6. Probability density functions (pdfs) of DC-8 aircraft observations (black) and model simulations (colored). The pdfs (colored) in (a–d) correspond to the simulations in (Figs. D2b–e), respectively. See Table D1 for detailed definitions of different CAM-chem simulations.

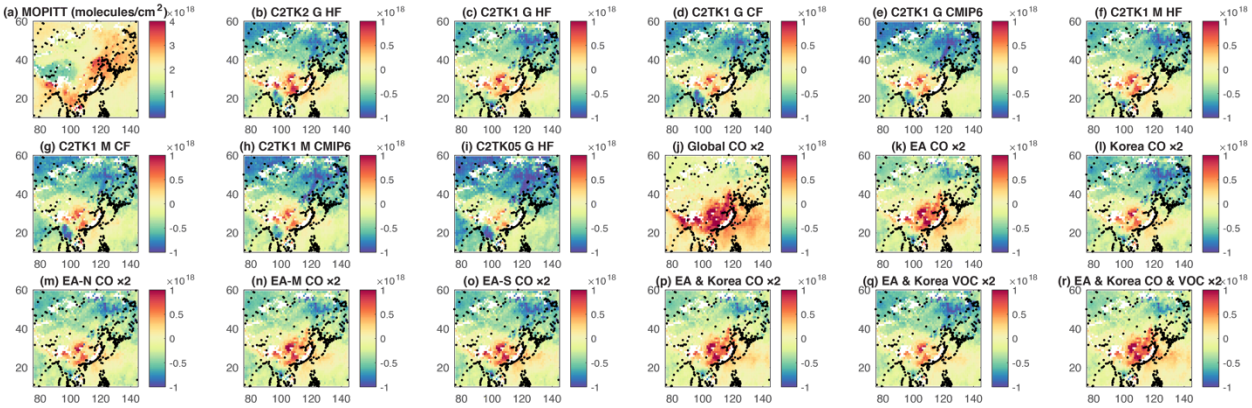

Figure DS7. (a) MOPITT CO total column density and (b–r) differences between CAM-chem simulations and MOPITT retrievals averaged through the KORUS-AQ period (May 1st – June 10th, 2016). Model results have been smoothed with MOPITT averaging kernels and *a priori* information before comparing. Units are molecules/cm^2. See Table D1 for definitions of different model simulations.

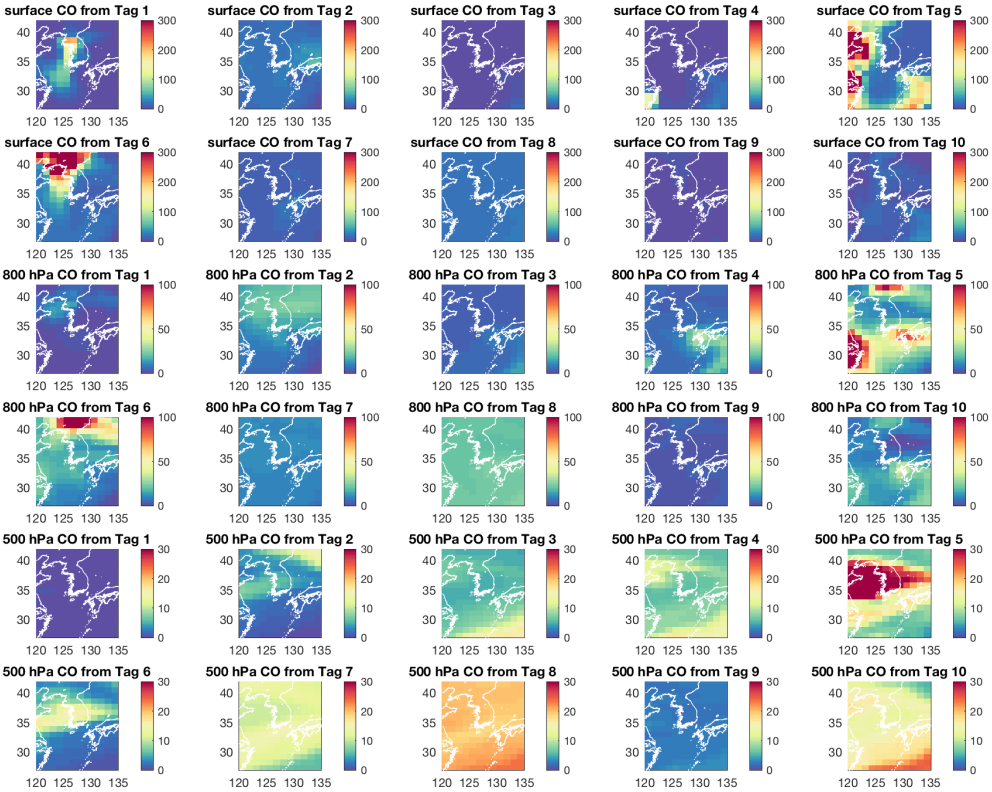

Figure DS8. Same as Fig. D4 but for June 5th, 2016.

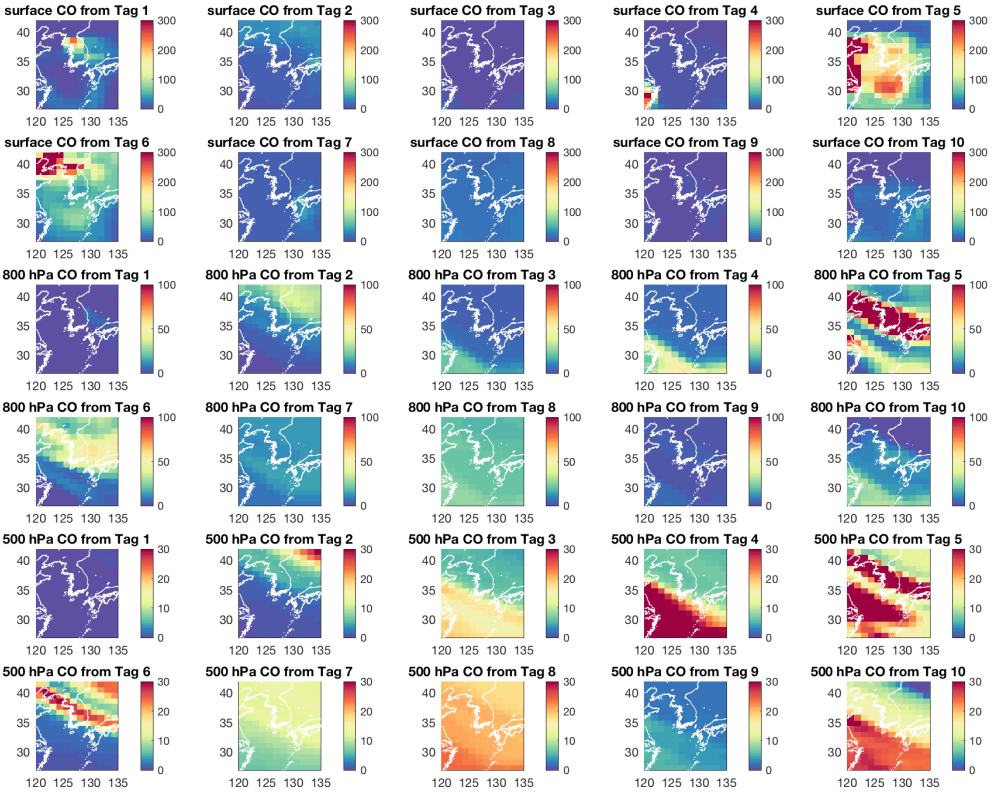

Figure DS9. Same as Fig. D4 but for May 31st, 2016.

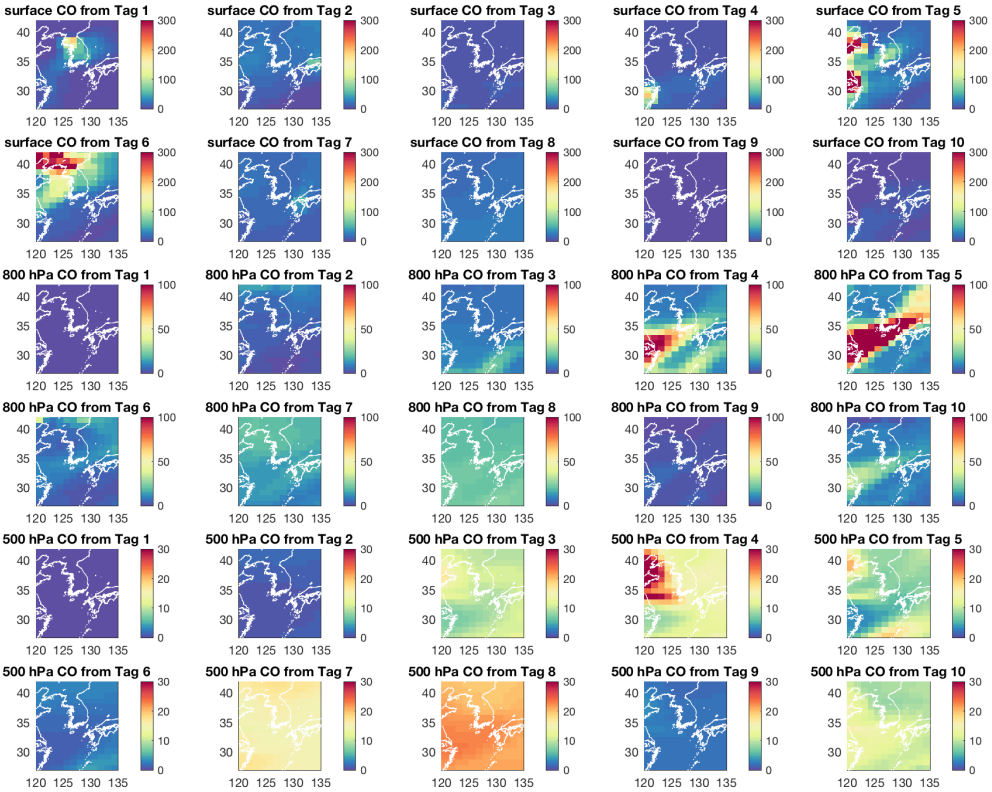

Figure DS10. Same as Fig. D4 but for May 13th, 2016.

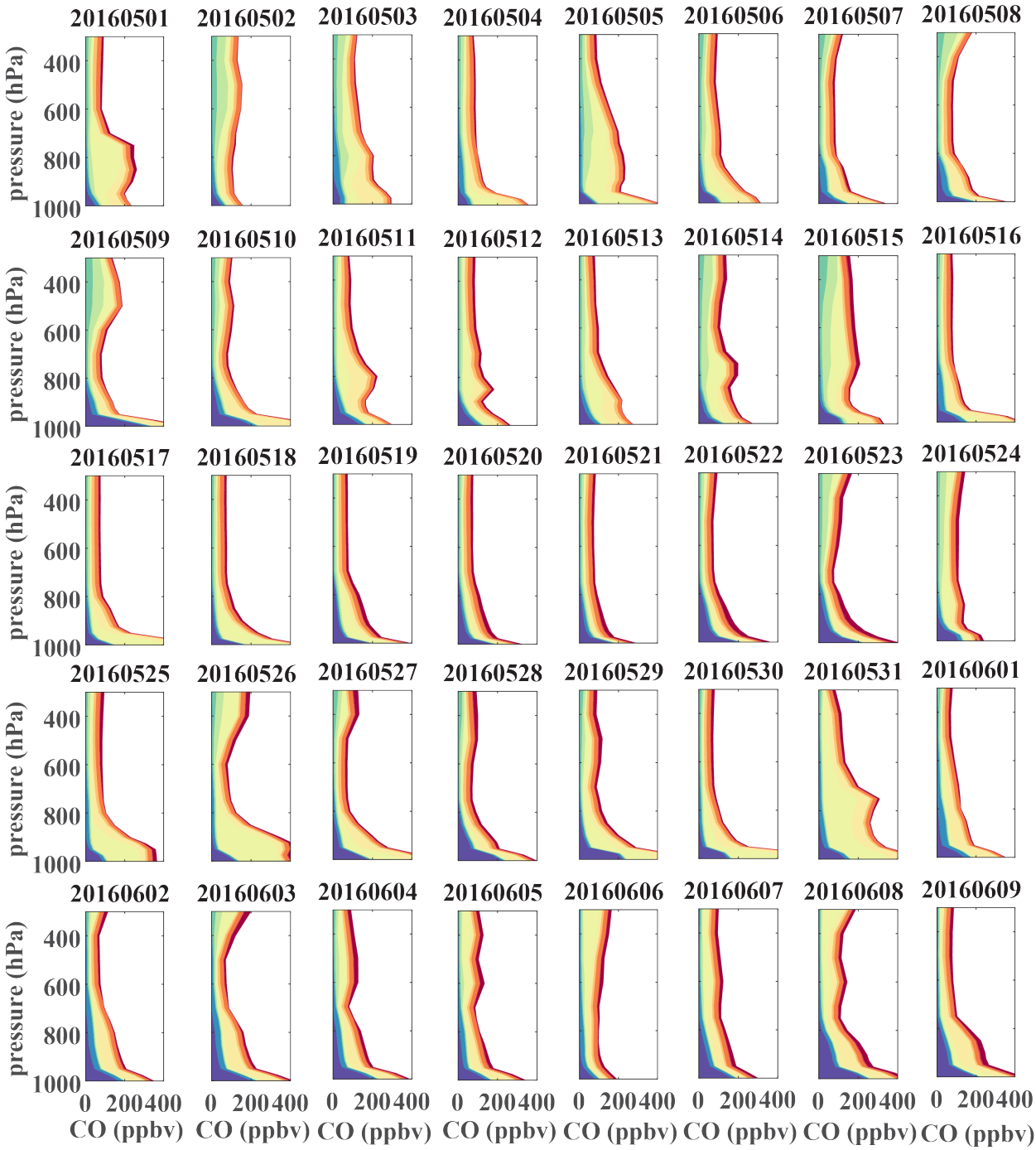

Figure DS11. Daily averaged vertical profiles of source contributions to CO concentrations over Seoul based on CAM-chem tag-tracer simulations during the KORUS-AQ period (May 1st – June 10th, 2016). See Fig. D1 and text for definitions of different source regions.

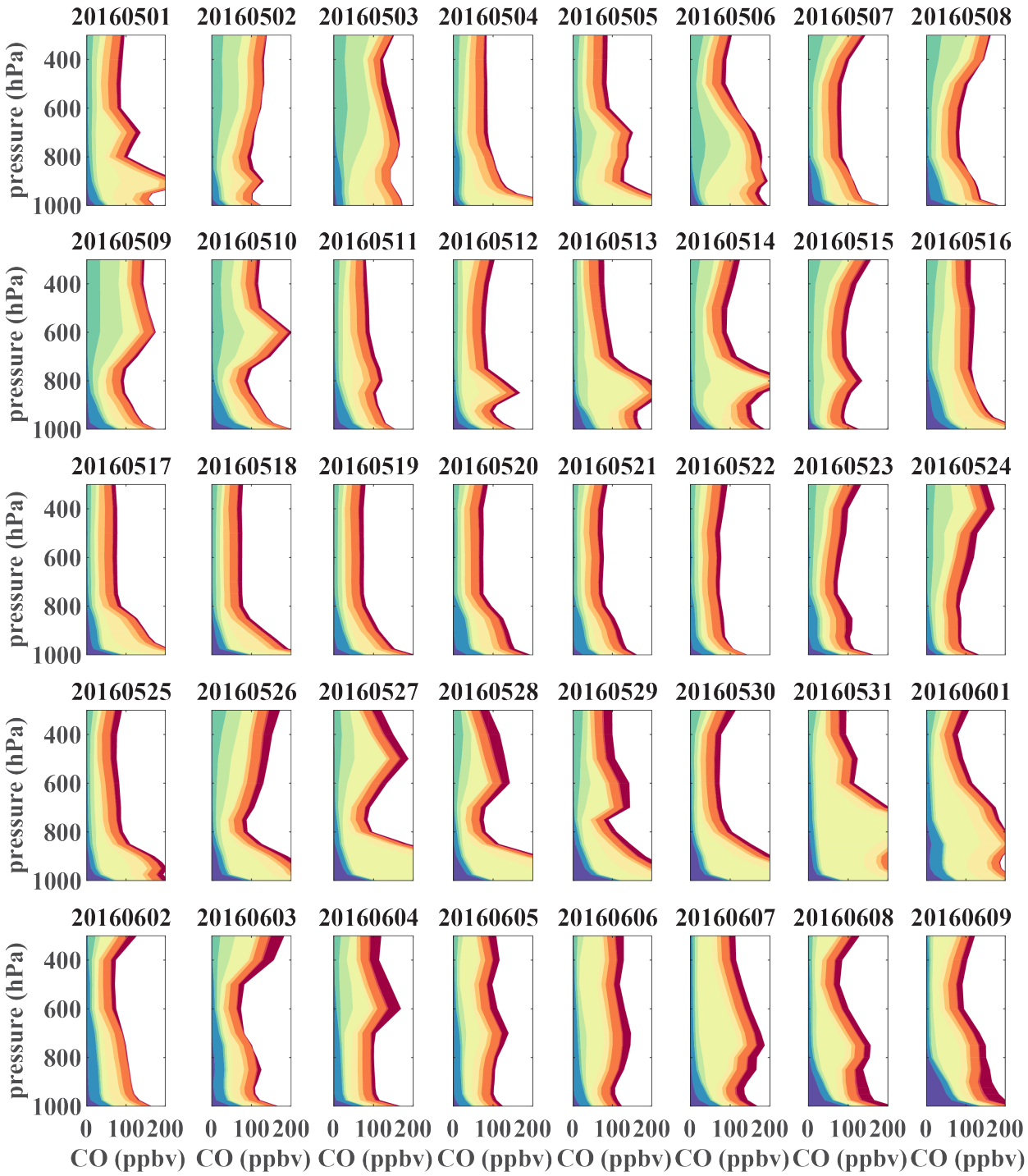

Figure DS12. Same as Fig. DS11, but over Busan.

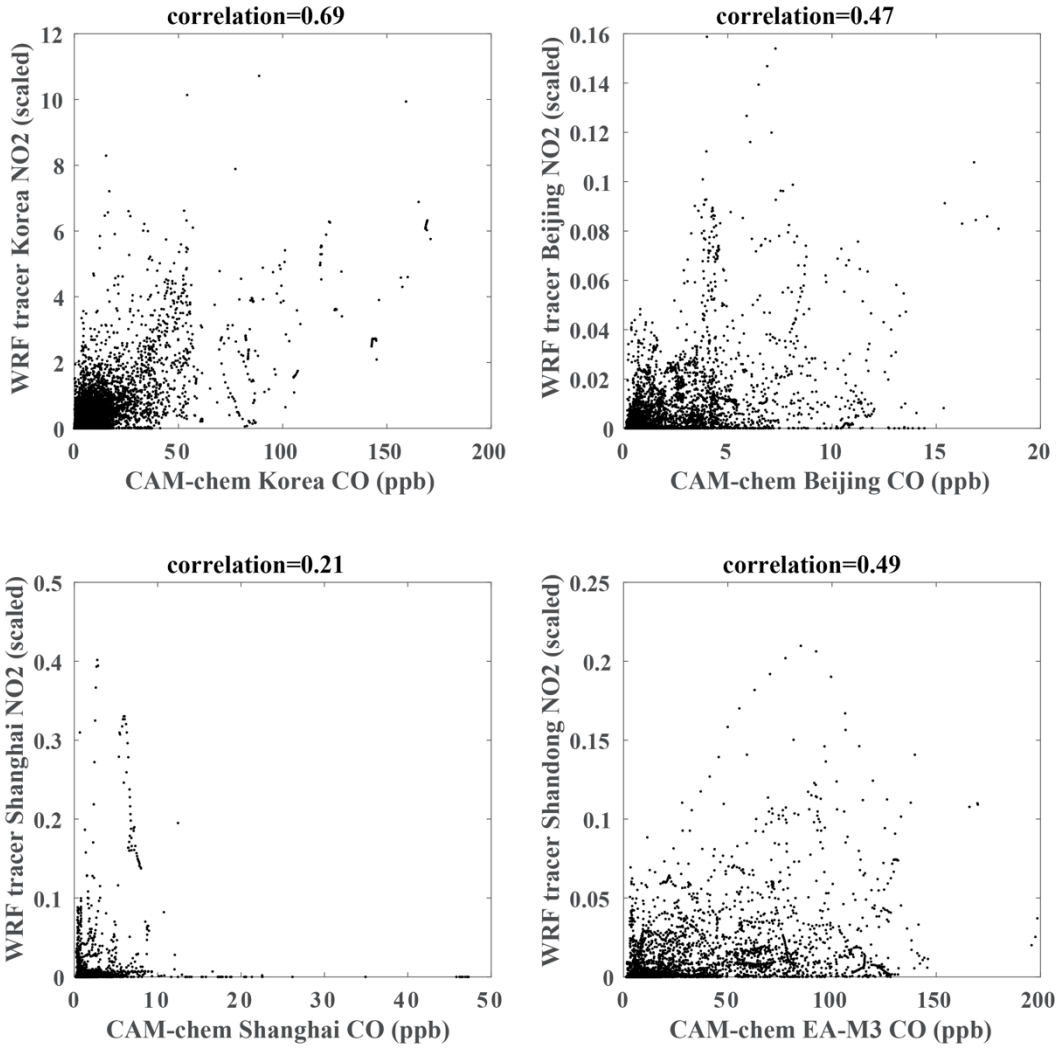

Figure DS13. Scatter plots of CAM-chem CO source contributions versus WRF NO2 source contributions from Korea, Beijing, Shanghai, and Shandong. Also shown are the correlations between the CO and NO_2 results.

APPENDIX E

Elucidating the Utility of CO_2 and CO Analysis in Tracking Fossil Fuel CO_2

(To be submitted to *Atmosphere Chemistry and Physics*)

Wenfu Tang[1], Benjamin Gaubert[2], Avelino F. Arellano[1], Louisa K. Emmons[2], Yonghoon Choi[3,4] et al

[1]Department of Hydrology and Atmospheric Sciences, University of Arizona, Tucson, Arizona, USA.

[2]Atmospheric Chemistry Observations and Modeling Laboratory, National Center for Atmospheric Research, Boulder, CO, USA

[3]NASA Langley Research Center, Hampton, VA, USA

[4]Science Systems and Applications, Inc., Hampton, VA, USA

Tang, W., et al., 2019. Elucidating the Utility of CO_2 and CO Analysis in Tracking Fossil Fuel CO_2, *Atmosphere Chemistry and Physics,* to be submitted.

Abstract

The current carbon observing system remains to be limited in constraining emissions of carbon dioxide from fossil-fuel combustion ($FFCO_2$) especially over rapidly developing regions. Networks of radiocarbon measurements, while significantly valuable, are still prohibitive to be implemented at continental scales. We suggest in this study to augment this system with air quality observations particularly carbon monoxide (CO). Here, we elucidate the utility of a joint analysis of CO_2 and CO in tracking the abundance of $FFCO_2$ by simulating CO_2 and CO in CAM-chem using an ensemble of posterior fluxes from CarbonTracker 2017 (CT2017), CarbonTracker Europe 2018 (CTE2018), and CAMS greenhouse gases flux inversions (CAMSv17r1) for CO_2, and an emission scenario based on the Hemispheric Transport of Air Pollution version 2 inventory (HTAPv2) for CO. We evaluate these simulations (including regional tracers of $FFCO_2$ and FFCO) across observational platforms, namely the NOAA ESRL Carbon Cycle Cooperative Global Air Sampling Network (CCGG), the Total Carbon Column Observing Network (TCCON), aircraft measurements during the KORUS-AQ field campaign (May – June 2016) including $^{14}CO_2$, and the NASA Orbiting Carbon Observatory-2 (OCO-2) and the Measurements Of Pollution In The Troposphere onboard Terra (MOPITT) satellites. Overall, our simulation results are generally in agreement with these observations. Modeled CO_2 and CO are in agreement with surface CO_2 and CO at the four CCGG sites (correlation ranges from 0.62-0.92 for CO_2 and 0.21 to 0.92 for CO; Mean Bias ranges from ~ -3 to 1.5 ppmv for CO_2 and ~ -14 to 57 ppbv for CO). The comparisons with observations from TCCON sites show about 2-4% (CO_2) and 11-16% (CO) errors. When the model results are compared to the measurements from the NASA DC-8 aircraft, the systematic underestimation of CO_2 and CO near the surface suggests that either CO_2 and CO local sources are underestimated or that the sinks (and/or mixing) are overestimated in the region. When compared to satellite observations, the CAM-chem simulations using posterior CO_2 fluxes agree well with OCO-2 observations during the KORUS-AQ period (correlation=0.46~0.68, mean bias=-0.0~0.8 ppmv, and RMSE=1.3~1.7 ppmv). Our results also show that the correlation between $FFCO_2$ derived from radiocarbon measurements and modeled $FFCO_2$ tags is surprisingly significant (r=0.82). We find that $FFCO_2$ from East Asia and rest of the world needs to be scaled up (1.61 and 1.28, respectively), while $FFCO_2$ from Korea and Japan needs to be scaled down (0.84). Signatures of modeled $FFCO_2$ plume transport and sectoral emissions are enhanced if modeling analysis of CO is also considered. Lastly, we find that dCO/dCO_2 ratios can be more effectively use to

diagnose inconsistencies in CE using the associated tags especially with FFCO and $FFCO_2$. Specifically, we find that $dFFCO/dFFCO_2$ from Korea (6.7 ppbv/ppmv) is lower than from middle and northern East Asia (~52-55 ppbv/ppmv), indicating higher CE over Korea. Our analyses suggest that constraints from CO through diagnosing consistency in $FFCO_2$ abundance and its associated regional and sectoral contributions as well as quantifying combustion efficiencies from different sectors, can be exploited to complement current observational constraints in tracking $FFCO_2$.

1 Introduction

Increasing greenhouse gas (GHG) emissions from anthropogenic activities are projected to bring wide-ranging environmental changes, and impact regional air quality (AQ) through atmospheric feedback mechanisms. Understanding today's regional CO_2 sources and sinks, in particular, is a key focus area in carbon cycle science and atmospheric composition given the necessity for reliable projections of future atmospheric CO_2 concentrations (e.g., Le Quéré et al., 2018). As majority of the world's population lives in urban areas, the intensity of sustainable development challenges will be especially felt in regions with fastest pace of urbanization like Africa and Asia (United Nations, 2014). Urban agglomeration, particularly megacities, are expected to continue growing (in size and number) over the coming decades. These megacities have nearly tripled since 1990. This is especially problematic since it is in these megacities where human (anthropogenic) activities are most intense. These activities are associated with immense energy consumption, mainly in the form of fossil-fuel combustion from power generating and industrial plants as well as transportation sectors (Kennedy et al., 2015). These directly lead to enhanced emissions of air pollutants, GHG, and waste energy and as a consequence, these emissions largely impact AQ, public health, and ecosystems (e.g., Lawrence et al., 2007; Duren and Miller, 2012; Zhu et al., 2012; Folberth et al., 2015; Lelieveld et al., 2015; Baklanov et al., 2016). As nations seek to develop strategies to manage their carbon emissions, capabilities of quantifying, verifying, monitoring, and reporting local-to-regional carbon sources and sinks are necessary for informed policy decisions.

1.1 $FFCO_2$ Emissions

Estimates of CO_2 emissions from fossil-fuel (FF) use and applications remain uncertain, especially in rapidly developing regions where combustion activity and efficiency and fuel-use mixtures are poorly characterized due to lack of detailed information on energy-use, combustion practices, and pollution control strategies (e.g., Ciais et al., 2010; Andres et al. 2012, 2016; Zhu et al., 2012; Creutzig et al., 2015; Gately and Hutyra et al. 2017; Quilcaille et al., 2018). As discussed in detail by Andres et al. (2012), the uncertainty in current global fossil fuel CO_2 ($FFCO_2$) emission inventories is about 10% globally and ranges from a few percent to greater than 50% regionally (or nationally). These bottom-up inventories are produced by organizations such as CDIAC:

Carbon Dioxide Information Analysis Center, EIA: International Energy Agency, EIA: Energy Information Administration of the United States Department of Energy, EDGAR: Emission Database for Global Atmospheric Research, which is a joint effort of the Joint Research Centre of the European Commission and PBL Netherlands Environmental Assessment Agency, and UNFCC: United Nations Framework Convention on Climate Change. The uncertainties of these inventories, which continue to increase with scale and time, arose from inconsistencies in: a) accounting and reporting (both energy production and consumption) especially in countries with rapidly developing economy, and b) in spatial and temporal distribution of these emissions that are heavily based on proxies like population densities (CDIAC, EDGAR), specific point source location maps (EDGAR), and nightlights (ODIAC: Open Source Data Inventory of Anthropogenic CO_2 Emissions), which may not be exactly the direct representation (in terms of location and time) of $FFCO_2$ emitted to the atmosphere (e.g., Andres et al. 2016; Hogue et al. 2016). Data assimilation techniques are also employed in more recent emission modeling systems that combine these proxies with bottom-up inventories like the Vulcan and Hestia projects (Gurney et al. 2009; 2012) to downscale (disaggregate) national emissions and provide high resolution global $FFCO_2$ emissions (FFDAS: Rayner et al., 2010; Asefi-Najafabady et al., 2014). Differences between ODIAC with Hestia $FFCO_2$ emissions in four U.S. cities are reported to range from -1.5% to 20.8% (whole city) and 47-84% at a 1-km^2 grid scale (Gurney et al. 2019), suggesting that these $FFCO_2$ inventories still do not accurately represent the spatial distribution of emissions at urban scales. Recent estimates of uncertainties in $FFCO_2$ emissions have also been reported by Gately and Hutyra, (2017). They have shown large differences in $FFCO_2$ emissions from EDGAR, ODIAC, and FFDAS ranging from 20% (at regional scale) to 50-250% (at city scales when compared to a 1-km hourly resolution emission inventory (Anthropogenic Carbon Emissions System or ACES) across the northeastern United States.

The uncertainty in tracking and quantifying $FFCO_2$ emissions is exacerbated by limited observations at the spatiotemporal scales necessary to resolve variations in combustion and fuel-use patterns (Duren and Miller, 2012; Hutyra et al., 2014; Shiga et al. 2014). Attributing the sources of these emissions is challenging due to the dearth of accurate CO_2 measurements with sufficient spatiotemporal coverage necessary to resolve variations in combustion and fuel-use patterns, the difficulty in teasing out the small anthropogenic signature from the large natural

sources and sinks dominating the carbon cycle, and the uncertainties in modeling atmospheric transport (Pacala et al., 2010; Ciais et al. 2014, 2015). This is especially true in estimating CO_2 fluxes using top-down approaches, despite the addition of aircraft and satellite measurements of CO_2 abundance in recent years (e.g., Chevallier et al., 2014; Hutyra et al., 2014; Houweling et al. 2015). Inferences on $FFCO_2$ emissions are made based on limited observational constraints against the backdrop of uncertainties in prior CO_2 fluxes and more importantly uncertainties in transport models that translate these fluxes to abundances (Gurney et al., 2002, 2003, 2004; Stephens et al., 2007; Peylin et al., 2013). Global atmospheric CO_2 inversions typically use observations of surface in-situ and mixing ratio profiles from NOAA ESRL Carbon Cycle Cooperative Global air sampling network (CCGG; Sweeney et al., 2015; Dlugokencky et al., 2018), vertical mixing ratio profiles from HIAPER Pole-to-Pole Observations (HIPPO; Wofsy, 2011), and column-average dry air mole fraction XCO_2 retrievals from Orbiting Carbon Observatory 2 (OCO-2; Eldering et al., 2017) and Greenhouse Gases Observing Satellite (GOSAT; Kuze et al., 2009); among other constraints such as CO_2 partial pressure (pCO_2) from Surface Ocean CO_2 Atlas (SOCAT; Pfeil et al., 2012) and XCO_2 retrievals from ground-based Total Carbon Column Observing Network (TCCON; Wunch et al., 2011). State-of-the-art inverse modeling systems employ data assimilation techniques (e.g., variational methods like 4DVar, Bayesian synthesis or matrix methods, and ensemble Kalman filtering) to infer posterior CO_2 fluxes from a combination of these datasets and atmospheric transport models (e.g., LMDz, TM3/5) (Le Quéré et al., 2018). Several of these inverse studies have demonstrated the importance of fossil-fuel emission uncertainties on their estimates, suggesting the importance of temporally defined emission inventory and representativeness (e.g., Gurney et al., 2005; Peylin et al., 2011; Saeki and Patra, 2017; Wang et al., 2017; Brophy et al., 2019). Most recently, Gaubert et al. (2019) raises this importance even more by suggesting that while global atmospheric CO_2 inverse models are converging on neutral tropical land exchange, they are diverging on fossil-fuel and atmospheric growth rate.

1.2 Tracers of $FFCO_2$

Recent studies have also demonstrated that chemical tracers of $FFCO_2$ (^{13}C, ^{14}C, ^{18}O) are significantly valuable in reducing these uncertainties and directly tracking $FFCO_2$ emissions by partitioning total CO_2 into fossil and terrestrial CO_2 as well as estimating its emissions (Levin et al., 2003, 2010; Choi and Wang, 2004; Turnbull et al., 2006, 2009, 2011, 2015; Graven et al., 2009,

2018; Djuricin et al. 2010; Vay et al., 2011; Miller et al. 2012; Basu et al., 2016; Newman et al. 2016; Niu et al., 2016; Berhanu et al., 2017; Nathan et al., 2018). Fossil is defined by depleted ^{14}C due to the shorter half-life of ^{14}C (~5,700 years) than the age of the fossil (~10^6 years). Hence, measurements of radiocarbon content of atmospheric CO_2 strongly indicate FF additions to the air sample when $\Delta^{14}C$ is low (delta value of -1000 ‰). For example, a $\Delta^{14}C$ of ~2.7 ‰ is a result of one ppm of fossil CO_2 addition to an atmospheric burden of 390 ppm given an atmosphere that is observed to have +50 ‰ (Miller et al., 2012). Since ^{14}C measurements tend to be expensive, one approach is to use these measurements to calibrate other $FFCO_2$ proxies (like CO), which can be measured at a lesser cost (Vogel et al., 2010; Turnbull et al. 2011).

It is particularly appealing and logical to consider synergies between AQ and GHG emission monitoring over megacities since in an urban environment, AQ pollutants and GHG share the same dominant source category. Both are co-emitted during carbonaceous-fuel (FF) generation, combustion, and distribution processes. In particular, CO and elemental carbon (e.g., soot or BC) are produced when combustion is incomplete; otherwise carbon in the fuel is oxidized to CO_2 at equilibrium levels of CO. In addition, NO and NO_2 are produced from the oxidation of nitrogen from the fuel itself and from decomposition of N_2 in air at high temperatures. CO_2 is also produced, along with FF combustion, during the calcination process in cement manufacturing. And so, observing the relative abundance of $FFCO_2$ and CO over megacities should provide useful synergistic information on their associated emissions. Here, CO serves as an indirect tracer of $FFCO_2$ which can complement ^{14}C (e.g., Levin et al., 2007). This information is confounded however by: a) sharp differences in their associated sinks (chemical transformation and/or biospheric uptake) downwind, and hence differences in lifetimes, b) biogenic sources within the megacity, and c) inter-species variations in the effectiveness of pollution control strategies. Nevertheless, with an appropriate analysis framework, these synergies can be exploited to enhance current observing system for $FFCO_2$ and to provide consistent monitoring, assessment, and source attribution.

This is the case for carbon monoxide (CO), and nitrogen dioxide (NO_2), for which larger number of observations are available from ground network, airborne, and satellite-derived measurements. Such datasets have been utilized by atmospheric chemistry and AQ community and have been shown as useful constraints on combustion-related emission patterns in urban regions and biomass

burning activities at local to global scales. They have been extended to provide insights on FF and fire CO_2 (e.g., Suntharalingam et al., 2004; Palmer et al. 2006; Parrish et al., 2009; Wang et al., 2010; Beirle et al., 2011; Turnbull et al., 2011; Berezin et al., 2013; Brioude et al., 2013; Fioletov et al., 2013; Lopez et al., 2013; Nassar et al., 2013; Pollack et al. 2013; Pommier et al., 2013; Reuter et al., 2014, 2019; Silva et al., 2013; Streets et al., 2013 and references therein; Yang et al., 2013; Konovalov et al., 2014; Lindenmaier et al. 2014; Ammoura et al., 2016; Hakkarainen et al., 2016; Silva and Arellano, 2017). From spatiotemporal sampling perspective, these datasets are strongly complementary especially in the absence or lack of CO_2 and ^{14}C measurements. In addition, identifiable physico-chemical constraints from CO on anthropogenic CO_2 emissions and their transformations can also be exploited (Suntharalingam et al., 2005; Nassar et al., 2010).

1.3 Constraints from CO

Although chemical processes can influence atmospheric CO, it can be a good chemical tracer of anthropogenic combustion and biomass burning sources (Gamnitzer et al., 2006). Direct emissions of AQ and GHG from fossil fuel, biofuel, and/or biomass combustion are typically calculated using information on combustion efficiency (CE), which is the ratio of CO to CO_2. Differences in CE across different source sectors (e.g., power plant: high CE, domestic heating: low CE, flaming fire: high CE, smoldering fire: low CE) can be distinguished with measurements of CO and CO_2. In fact, emission factors are usually based on CO and/or CO_2. Both information is particularly useful when examining long-term changes in a megacity where CE (and its associated EF) may change due to pollution control and/or changes in fuel usage (e.g., shift from coal to natural gas, gasoline to diesel) as the city evolve socio-economically (Gately et al., 2017; Quilcaille et al., 2018; Tang et al., 2019). Because of its medium lifetime, CO is a useful tracer of pollution transport (e.g., Edwards et al., 2004, 2006). Tracking megacity plumes using CO can help enhance horizontal and vertical transport signatures of CO_2 plumes, which may be difficult with CO_2 measurements alone due to its longer lifetime and influence of large biospheric signal. In fact, measurements of CO (especially profiles) can help quantify uncertainties in anthropogenic CO_2 top-down estimates due to errors in model transport (Peylin et al., 2011).

1.4 Objectives

The main goal of this study is to further demonstrate the value of a joint analysis of CO and CO_2 in tracking $FFCO_2$ within the context of constraining transport models of CO_2 with information from CO. We propose that this type of analysis should be considered in designing integrated observing systems for carbon monitoring as has been suggested in previous studies (e.g., Ciais et al., 2015). This study is a continuation of our evaluation of the Copernicus Atmosphere Monitoring Service (CAMS) CO and CO_2 high resolution forecast and analysis products during Korea-United States Air Quality (KORUS-AQ) field campaign (Tang et al. 2018). This also serves as a complementary study to our recent work on quantifying the source contributions of CO over Seoul during KORUS-AQ using regional tags or tracers in the Community Atmosphere Model with Chemistry or CAM-Chem (Tang et al. 2019).

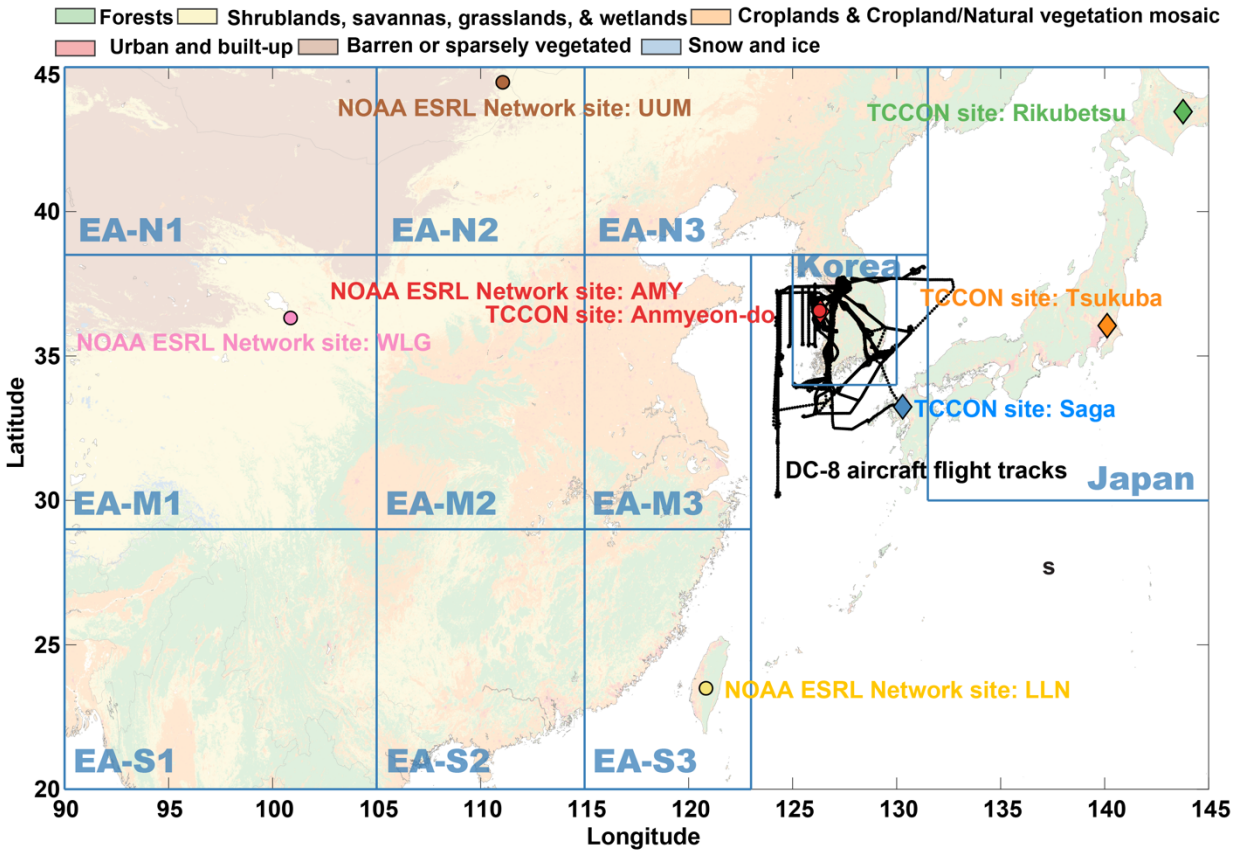

Figure E1. Map of the study domain including: land cover (colored map; Broxton et al., 2014), definition of tag (basis) regions (blue rectangles), location of four East Asia sites from the NOAA ESRL Carbon Cycle Cooperative Global Air Sampling Network (colored dots), location of East Asia TCCON sites (colored rhombus), and the DC-8 aircraft flight tracks during KORUS-AQ (black lines).

Here, we focus on: a) evaluating the simulated abundance of CO and CO_2 in CAM-Chem, based on observationally-constrained surface fluxes for CO_2 from global inversions and a 'best emission scenario' for CO from our previous work; b) tagging the regional sources of FFCO and $FFCO_2$; and c) elucidating constraints from CO in terms of identifying relative combustion efficiencies of sampled air during KORUS-AQ and enhancing signatures of transport and mixing of atmospheric CO_2. The CO_2 fluxes are taken from CAMS GHG flux inversion (CAMSv17r1; Chevallier et al., 2005, 2010, 2013, 2018), CarbonTracker 2017 (CT2017; Peters et al., 2007), and CarbonTracker Europe 2017 Fast Track (CTE2018; van der Laan-Luijkx et al., 2017). Emissions of CO, on the other hand, are taken from Hemispheric Transport of Air Pollution (HTAP) version 2 inventory (Janssens-Maenhout et al., 2015) which are scaled to match observations of CO during KORUS-AQ (i.e., doubled anthropogenic CO and VOCs from East Asia and Korea). Our goal is to have a CO and CO_2 abundance that are already in reasonable agreement with observations. We emphasize that this is not an inversion study of $FFCO_2$ emissions. In fact, we assume here that a large portion of the biospheric flux component of CO_2 has been constrained by these inversions; thereby facilitating the treatment of $FFCO_2$ as tracers in CAM-Chem with the biospheric flux serving as its sink. The CO_2 variable has been added in CAM-Chem to facilitate the joint analysis of CO and CO_2 abundance while simulating full chemistry to estimate interactively the hydroxyl radical (OH) concentrations for the CO sink and chemical production (i.e., CH_4 to CO and VOCs to CO). We evaluate these simulations (including its consistency) with CO and CO_2 datasets from NOAA CCGG, TCCON, OCO-2/GOSAT and Measurement of Pollution In The Troposphere (MOPITT; Deeter et al. 2017), and KORUS-AQ field campaign including ^{14}C measurements.

This paper is structured as follows. In Sections 2 and 3, we describe the model and datasets used in this study. In Section 4 and 5, we evaluate CO and CO_2 across different observing platforms,

and demonstrate the utility of joint CO and CO2 analysis on tracking $FFCO_2$. We conclude in Section 6.

2 CESM/CAM-chem

In this section, we briefly introduce Community Earth System Model (CESM) and CAM-chem, present the implementation of CO_2 simulation and tagging mechanism within CAM-chem, and describe the design of our ensemble simulation experiments.

Table E1. CO_2 fluxes used in this study.

CO_2 fluxes	Spatial Res.	Temporal Res.	Period	Transport Model	Fossil Fuel Priors	Biosphere and Fires Priors	Ocean Priors	Main Reference
CAMS (v17r1)	3.75° lon 1.875 ° lat	3-hourly	1979-2017	LMDz	EDGAR scaled to CDIAC	ORCHIDEE (climatology) + GFEDv4	Landschüster et al. (2014)	Chevallier et al. (2018) http://apps.ecmwf.int/datasets/data/cams-ghg-inversions
CT2017	1° lon 1° lat	3-hourly monthly	2000-2017	TM5	"Miller" (EDGAR scaled to CDIAC) & "ODIAC"	CASA w/ GFED 4.1s GFED_CMS	Jacobson et al. (2007) Takahashi et al. (2009)	Peters et al. (2007) https://www.esrl.noaa.gov/gmd/ccgg/carbontracker
CTE2018 (CTE2017-FT)	1° lon 1° lat	monthly	2000-2016	TM5	EDGAR+ IER scaled to CDIAC	SiBCASA-GFED4	Jacobson et al. (2007)	van der Laan-Luijkx et al. (2017) http://www.carbontracker.eu

The Community Earth System Model version 2 (CESM2) is an open-source, community, fully-coupled global earth system model (Hurrell et al., 2013). The model is being developed and maintained by the National Center for Atmospheric Research (NCAR). CESM2 includes the atmosphere (Community Atmosphere Model version 6; CAM6), land (Community Land Model version 5; CLM5), ocean (Parallel Ocean Program version 2; POP2), and land ice (Community Ice Sheet Model version 2.1; CISM2.1), sea ice (Los Alamos National Laboratory Sea Ice Model version 5.1.2; CICE5.1.2), and river (Model for Scale Adaptive River Transport; MOSART) components, all of which are connected by a coupler. CESM supports various model resolutions (e.g., 0.23°×0.31°, 0.9°×1.25°, 1.9°×2.5°, 4°×5°, and 10°×15°) and component sets for different research objectives (http://www.cesm.ucar.edu/models/cesm2.0/cesm/compsets.html). The

component sets represent combinations of the aforementioned components being either actively or not actively coupled. In some CESM component sets, the atmosphere, ocean, and land are actively coupled to simulate the biogeochemical cycle (Keppel-Aleks et al., 2013; Moore et al., 2013; Lindsay et al., 2014; Lehner et al., 2015). These CESM BGC simulations usually does not run with CAM-chem where complex atmospheric chemistry is also simulated.

Table E2. Global budget of CO_2 (in 10^{15} g C) and CO (in 10^{12} g C) during KORUS-AQ (May 2016).

			CO_2 (PgC)			CO (TgC)
		Region	CT	CTE2018	CAMS	
Sources	fossil fuel or anthropogenic	Korea	0.01	0.01	/	0.11
		Japan	0.02	0.03	/	0.13
		EA-S	0.07	0.07	/	1.68
		EA-M	0.11	0.11	/	2.71
		EA-N	0.05	0.04	/	1.05
		the rest	0.53	0.53	/	18.44
	fire		0.11	0.11	/	9.69
	biosphere		/	/	/	3.25
	ocean		/	/	/	0.61
	chemical production		/	/	/	58.40
	source total		0.90	0.89	/	96.07
Sinks	biosphere		0.63	0.90	/	/
	ocean		0.26	0.18	/	/
	chemical loss*		/	/	/	102.76
	sink total		0.88	1.08	/	102.76
Net (Sources-Sinks)			0.01	-0.19	-0.04	-6.69
Initial Burden			854.83	854.37	853.98	156.82
Final Burden			854.93	854.19	853.93	145.10
Initial-Final			-0.10	0.18	0.05	11.72
Budget delta			-0.08	-0.01	0.01	5.03

The Community Atmosphere Model with Chemistry (CAM-chem) is the atmospheric chemistry component of CESM, coupled with the land model (Lamarque et al., 2012). Emission files for chemical species are needed as input for CAM-chem simulations, and can be defined and changed in the namelist for the atmosphere component. CAM-chem can either run with the online model meteorology (calculated by CAM) or be nudged towards external meteorological fields (specified

dynamics), such as the Modern-Era Retrospective analysis for Research and Applications, Version 2 (MERRA-2) and Goddard Earth Observing System Forward Processing (GEOS-FP) near real time forecast (Molod et al., 2015; Gelaro et al., 2017). The nudged meteorological fields include horizontal wind components, air temperature, surface temperature, surface pressure (Lamarque et al., 2012). The amount of nudging towards external meteorological fields (relaxation time) can be customized by the user in the namelist. A strong nudging (e.g., relaxation time equals to 5 hours) or loose nudging (e.g., relaxation time equals to 50 hours) can be chosen depending on the research objectives. The relaxation time of infinite hours is the same as online model meteorology. CAM-chem can also run with an assimilation of meteorology using NCAR Data Assimilation Research Testbed (DART; Anderson et al., 2009). This has been tested previously by Arellano et al., (2007), Barré et al., (2015), and Gaubert et al., (2016). In CESM2, CAM-chem includes a significantly updated tropospheric chemistry mechanism (MOZART-T1), coupled to a VBS (volatility basis set) scheme for the formation Secondary Organic Aerosols (SOA). This allows to simulate explicitly the tropospheric and stratospheric composition. The Troposphere and Stratosphere (TS1) chemical mechanism represent 221 species with 528 reactions (Emmons et al., in preparation for JAMES; https://www2.acom.ucar.edu/gcm/mozart).

2.1 Simulating Global CO_2 and CO in CAM-chem

As mentioned earlier, we use an ensemble of posterior fluxes from CarbonTracker 2017 (CT2017), CarbonTracker Europe 2018 (CTE2018), and CAMS (CAMSv17r1). CarbonTracker is a global modeling system of CO_2 developed by NOAA with a focus on North America (Peters et al., 2007). The estimates of fluxes are provided 3-hourly and monthly. We use both 3-hourly and monthly fluxes in CAM-chem to investigate the impact of temporal resolution in the fluxes on our simulation results. CarbonTracker Europe is developed based on CarbonTracker (van der Laan-Luijkx et al., 2017). We use the monthly fluxes of CTE2018 in our study. Both CT2017 and CTE2018 provide fluxes of fossil fuel, fire, land, and ocean components, which we use for our tagging of regional sources of $FFCO_2$. CAMSv17r1 is produced by the inversion system called PyVAR (Chevallier, 2018). It does not provide (however) the fluxes for the aforementioned

components. We regridded all these fluxes (with resolution of 1°×1° and 3.75°×1.875°) to match our CAM-Chem resolution (1.25°×0.95°). Details of the fluxes are listed in the Table E1.

For the emissions of CO (as well as other species such as NMVOCs), we use the Fire INventory from Ncar (FINN; Wiedinmyer et al., 2011) for biomass burning, and the Hemispheric Transport of Air Pollution version 2 inventory (HTAPv2; Janssens-Maenhout et al., 2015) (see Table E1 for details). HTAPv2 provides monthly anthropogenic emissions for CO and NMVOCs at a resolution of 0.1°×0.1° by compiling regional inventories. These emissions are also regridded to 1.25°×0.95° similar to the CO_2 fluxes. As previously mentioned, we doubled CO and VOCs in this inventory following our evaluation of CO over KORUS-AQ in Tang et al. (2019).

In CAM-chem, concentrations of greenhouse gases such as CO_2 and CH_4 are prescribed with smooth fields at the model surface layer. The CO_2 concentrations at surface layer are based on zonal averaged CO_2 from NOAA CCGG. To add the online CO_2 simulation, we firstly define a new species called "CO2_online" in the model. CAM-chem employs a chemical preprocessor (named chem_mech.in by default) to generate CAM Fortran source code to solve chemistry, which provides flexibility in defining and changing the chemical mechanism (Lamarque et al., 2012). We define "CO2_online" in the chemical preprocessor to be explicitly solved. The CO_2 fluxes described in Section 2.1 are used as prescribed sources and sinks for the "CO2_online" variable at the surface. We do not explicitly solve the dry deposition and chemical production of CO_2 to total CO_2 in these simulations. Although we added a capability to track the chemical contribution to CO_2 from CH_4 and NMVOCs (including CO) by adding an independent variable called "CO2_chem" in CAM-Chem, we are not investigating this variable for this study. For initial conditions, we use the CT2017 mole fraction fields to avoid long spin-up. We also note that the "CO2_online" is a newly added chemical species in CAM-chem with no impact to model chemistry or physics (such as radiative effect) yet.

Table E3. Observations used in this study

			CO_2	CO
Satellite Retrievals	Orbiting Carbon Observatory-2 (OCO-2)	Date product	Level 2 v8 Lite XCO2	/
		Resolution	2.25x1.29 km Global coverage 2x/month	
		Revisit time	1:18 - 1:33 pm	
		Uncertainty	1-2 ppm XCO_2 (Boesch et al., 2011 and references therein)	
	Measurements Of Pollution In The Troposphere (MOPITT)	Date product	/	TIR/NIR Level 2 v7 XCO
		Resolution		22 x 22 km ~3-4 days
		Revisit time		10:30 AM
		Uncertainty		0.09e18 molec/cm^2 for total column retrieval; (Deeter et al., 2014)
NOAA ESRL Carbon Cycle Cooperative Global (CCGG) Air Sampling Network	Anmyeon-do (AMY) 36.54°N, 126.33°E 85.12 masl	Available period Measuring method Data size	2013.12 - now Surface flask air sampling 119 measurements in 2016	
	Lulin (LLN) 23.47°N, 120.87°E 2862.00 masl	Available period Measuring method Data size	2006.08 - now Surface flask air sampling 98 measurements in 2016	
	Ulaan Uul (UUM) 44.45°N, 111.10°E 1007.00 masl	Available period Measuring method Data size	1992.01 - now Surface flask air sampling 104 measurements in 2016	
	Mt. Waliguan (WLG) 36.29°N, 100.90°E 3810.00 masl	Available period Measuring method Data size	1990.08 - now Surface flask air sampling 102 measurements in 2016	
Total Carbon Column Observing Network (TCCON)	Anmyeon-do 36.54°N, 126.33°E 30 masl	Available period Instrument Data size reference	2015.02 - 2016.11 ground-based Fourier Transform Spectrometers 3081 measurements in 2016 Goo et al., 2017	
	Saga 33.24°N, 130.29°E 7 masl	Available period Instrument Data size reference	2011.07 - 2018.08 ground-based Fourier Transform Spectrometers 7177 measurements in 2016 Shiomi et al., 2017	
	Tsukuba 36.05°N, 140.12°E 31 masl	Available period Instrument Data size reference	2011.08 - 2017.12 ground-based Fourier Transform Spectrometers 16499 measurements in 2016 Morino et al., 2017a	
	Rikubetsu 43.46°N, 143.77°E, 380 masl	Available period Instrument Data size reference	2013.11 - 2017.12 ground-based Fourier Transform Spectrometers 6127 measurements in 2016 Morino et al., 2017b	
Measurements during KORUS-AQ	NASA DC-8 aircraft	Team Instrument Time Response Precision Accuracy	AVOCET LI-COR 1 second < 0.1 ppmv 0.25 ppmv	DACOM/DLH DACOM 1 second < 1% or 0.1 ppbv 2%
	Taehwa ground site 37.31°N,127.31°E	Instrument Data intervals	LI-COR LI-7500 1 hour	Thermo 48i 1 hour

2.2 Tagging $FFCO_2$ and FFCO in CAM-chem

We developed tagging capabilities in CAM-chem for CO and CO_2. Tagging CO has been developed in the past by treating CO from a particular basis function as tracers. That is, we solve the continuity equation for every tagged CO in the same way as the default CO variable in the model but making sure that each tagged CO does not interact with model chemistry (i.e., by treating it as a passive tracer). This mechanism is mentioned in Emmons et al. (2010) and previously used in Bayesian synthesis inversion studies (e.g., Arellano and Hess, 2006) and chemical budget studies (Gaubert et al., 2016). A similar approach (albeit in an offline mode) is also used by Fisher et al. (2017) with GEOS-Chemv9 model. This tagging capability is further illustrated in Eq. 1 for a particular tag CO (*itag*).

$$\frac{\partial [X]^{itag}}{\partial t} = \frac{\partial [X]^{itag}}{\partial t}\Big|_{transport} + \frac{\partial [X]^{itag}}{\partial t}\Big|_{sources} - \frac{\partial [X]^{itag}}{\partial t}\Big|_{sinks} \quad \text{Eq. 1}$$

The temporal evolution of a tracer $[X]^{itag}$ for each grid cell in the model is calculated using the same continuity equation for species $[X]$. This includes transport (dynamics and physics incl. advection, diffusion, mixing, convection to represent CO flux convergence/divergence), all sources (emissions and chemical production), and all sinks (CO+OH reaction, and deposition). These tags or basis can be either disaggregated sectoral components and/or regional source components of CO depending on the problem to be addressed. Here, we use FFCO emitted from a few regions around Korea as our basis. All these regions are defined in Figure E1. The response of this basis or the contribution of this source region to overall abundance in CO is estimated by integrating Eq. 1. Hence, the simulated $[CO]^{itag}$ for example corresponds to $[CO]$ mixing ratio for a given mass of CO emitted to the atmosphere by this *itag* region. The CO tags added in CAM-chem consists of the following edits to the code: (1) The CO tags are defined in the chemical preprocessor (variable names are usually defined as "CO01", "CO02" …); (2) emission files for the tags of emissions from specific regions are prepared and defined in the namelist; (3) chemical production of CO for CO tags of chemical sources are defined by adding related chemical reactions in chemical preprocessor; (4) chemical loss of all tags are defined in chemical preprocessor without changing the OH field (e.g., COtag + OH = OH); (5) dry deposition for the CO tags is calculated and applied in the same way for the default CO variable. Detailed evaluation and validation of

CAM-chem CO tags can be found in Tang et al. (2018b) and https://wiki.ucar.edu/display/camchem/.

We apply a similar approach in tagging $FFCO_2$ (Eq. 1). However, we do not account for chemical production in the source term nor deposition in the sink term. The sink of each $FFCO_2$ tags is derived from the negative surface flux $f_{CO_2}^{itag}$, which we define as the product of the negative surface flux of CO_2 (f_{CO_2}) at a given time and the ratio of the associated CO_2 mixing ratio of the tag ($[CO_2]_{srf}^{itag}$) at the surface and the modeled CO_2 mixing ratio $[CO_2]_{srf}$ at the surface; i.e.,

$$f_{CO_2}^{itag} = f_{CO_2} \cdot \left({[CO_2]_{srf}^{itag}} \Big/ {[CO_2]_{srf}} \right) \quad \text{Eq. 2}$$

In this manner, the sink of model CO_2 can be disaggregated into the sum of the sinks for all tags. This ensures that mass is conserved when solving the continuity equation. Edits to the model include: 1) The CO_2 tags are defined in the chemical preprocessor similarly as "CO2_online" (named "CO2_online_anthro", "CO2_online_fire", "CO2_online01", "CO2_online02", …); (2) positive flux (source) files for the tags from specific regions are prepared and defined in the namelist; (4) sinks of all tags are defined using Eq. 2. The routines, mo_srf_emissions.F90 and chemistry.F90 codes inside the MOZART scripts are modified for this development. The modified CAM-chem version could potentially serve as a convenient tool for tracking CO_2 from customized sources (i.e., fossil fuel emissions from a megacity or a country, or biomass burning emissions from a wildfire event) in the atmosphere and its sink in land and ocean. The modified CAM-chem source codes and chemical preprocessor are accessible through Github (See data availability for details).

For $FFCO_2$, we only consider $FFCO_2$ emitted during 2016 for each of the 12 tagged regions. The initial conditions for $FFCO_2$ from these regions are set to zero since $FFCO_2$ from these regions are only used to study specifically FF emissions during the campaign. $FFCO_2$ before 2016, which can be considered to represent the background $FFCO_2$ for these tags, is not directly addressed in our analysis.

Table E4. Summary statistics of CO and CO_2 from surface (in-situ/CCGG, column/TCCON), aircraft (DC-8), and remote sensing (OCO-2, MOPITT) measurements. Model equivalent and model evaluation against CO and CO_2 data are also shown. Units are ppmv for CO_2 and ppbv for CO.

		NOAA/ESRL CCGG				TCCON				NASA DC-8 KORUS-AQ					OCO-2 MOPITT
		AMY	LLN	UUM	WLG	Amy	Sag	Tsu	Rik	Seoul	Taehwa	West Sea	Seoul Jeju	Seoul Busan	Study Domain
Obs Mean	CO_2	415	407	406	405	403	406	403	403	415	408	411	411	408	405
	CO	217	124	142	130	109	108	103	99	266	163	234	223	183	111
Obs Std	CO_2	12	3	6	3	3	2	2	3	13	5	5	10	4	2
	CO	67	55	26	26	8	15	14	15	113	73	143	101	64	19
Obs $R_{CO2,CO}$		0.32	0.31	0.48	0.36	0.59	0.52	0.37	0.28	0.79	0.68	0.89	0.62	0.60	0.22
Obs dCO/dCO_2		5.90	18.90	4.53	9.42	2.86	7.40	5.63	4.81	9.13	15.28	28.20	10.37	15.92	11.90
Model Mean	CO_2	414	405	405	406	403	405	404	403	411	407	408	411	408	405
	CO	239	142	129	187	105	111	102	93	237	143	202	213	155	118
Model Std	CO_2	6-8	2	6-8	5-7	2-3	~2	~2	3-4	6-11	2-4	2-4	7-10	2-6	1-2
	CO	124	103	52	173	12	19	17	20	133	70	119	117	62	27
Model $R_{CO2,CO}$ (min/max)		-0.12	0.46	0.16	0.40	-0.2	0.51	0.33	0.05	0.56	0.21	-0.10	0.65	0.25	0.25
		0.18	0.70	0.27	0.71	-0.1	0.54	0.44	0.29	0.73	0.60	0.76	0.81	0.66	0.41
Model dCO/dCO_2 (min/max)		21.01	48.85	6.64	33.88	NaN	9.53	7.43	5.57	12.61	16.56	33.66	11.54	10.68	16.96
		26.17	59.80	8.68	44.47		11.24	8.67	7.53	20.91	30.91	48.28	16.08	26.79	27.05
Bias Model minus Obs	CT3h	-0.2	-1.4	-0.6	-0.1	-0.6	-1.0	0.9	-0.1	-3.3	0.1	-1.9	-1.3	1.2	0.8
	CTm	-0.2	-1.4	-0.7	0.3	-0.2	-1.0	1.1	0.2	-3.5	-0.2	-1.5	-1.4	0.4	0.5
	CTE2018	1.4	-1.2	-0.3	1.5	0.5	-0.6	1.6	0.6	-2.7	0.0	-1.6	-0.7	1.1	0.2
	CAMS	-3.4	-1.6	-1.0	0.1	-0.9	-1.5	0.3	-0.5	-7.4	-2.5	-4.4	-5.3	-2.5	0.0
	CO	22.0	18.1	-13.7	57.1	-4.3	2.3	-0.9	-6.1	-29.2	-20.4	-32.6	-34.5	-27.9	6.4
R Model versus Obs	CT3h	0.74	0.46	0.84	0.83	0.92	0.85	0.87	0.94	0.60	0.46	0.38	0.41	0.10	0.46
	CTm	0.70	0.71	0.86	0.81	0.92	0.87	0.86	0.94	0.72	0.64	0.54	0.53	0.60	0.68
	CTE2018	0.81	0.62	0.88	0.69	0.91	0.86	0.84	0.91	0.71	0.58	0.60	0.50	0.55	0.60
	CAMS	0.67	0.67	0.92	0.82	0.92	0.86	0.89	0.95	0.65	0.46	0.06	0.35	0.60	0.63
	CO	0.68	0.92	0.21	0.22	0.40	0.63	0.61	0.66	0.63	0.64	0.67	0.59	0.72	0.76
RMSE	CT3h	8.1	3.0	4.5	4.4	1.3	1.5	1.5	1.2	10.9	4.7	5.3	9.1	6.8	1.7
	CTm	8.6	2.5	3.3	2.8	1.2	1.4	1.6	1.1	9.7	3.8	4.6	8.4	3.4	1.3
	CTE2018	7.4	2.6	3.0	4.0	1.4	1.2	2.1	1.4	9.3	3.9	4.4	8.5	3.8	1.3
	CAMS	9.7	2.7	2.7	2.6	1.5	1.8	1.2	1.1	12.0	5.0	7.1	10.5	4.2	1.4
	CO	94.6	59.0	54.7	177.9	12.1	15.5	14.1	16.2	111.5	64.0	113.6	90.3	55.2	18.5

2.3 Design of Model Sensitivity Experiments

We run four CAM-chem simulations with "CO2_online" as well as full tropospheric chemistry (e.g., CO, O_3) for the KORUS-AQ period (May 1 – June 10, 2016). The four simulations use 4 sets of CO_2 fluxes (including CT2017 3-hourly fluxes, CT2017 monthly fluxes, CTE2018 fluxes, and CAMS fluxes). In addition to the four simulations with "CO2_online" that use external CO_2 fluxes, we have a fifth simulation that uses the prescribed smooth CO_2 fields at the surface which is the default setting of CAM-Chem. In terms of meteorology, we run CAM-chem with specified dynamics (i.e., the component set of FCSD) with the model meteorological fields nudging towards MERRA-2 on its native levels, which is the lower 56 of 72 vertical model levels ranging from the surface to ~2 hPa. The "CO2_online" and CO variables are initialized with CT2017 mole fraction fields on January 1st 2016 and with previous CAM-Chem (without CO_2) simulations for CO_2 and CO, respectively.

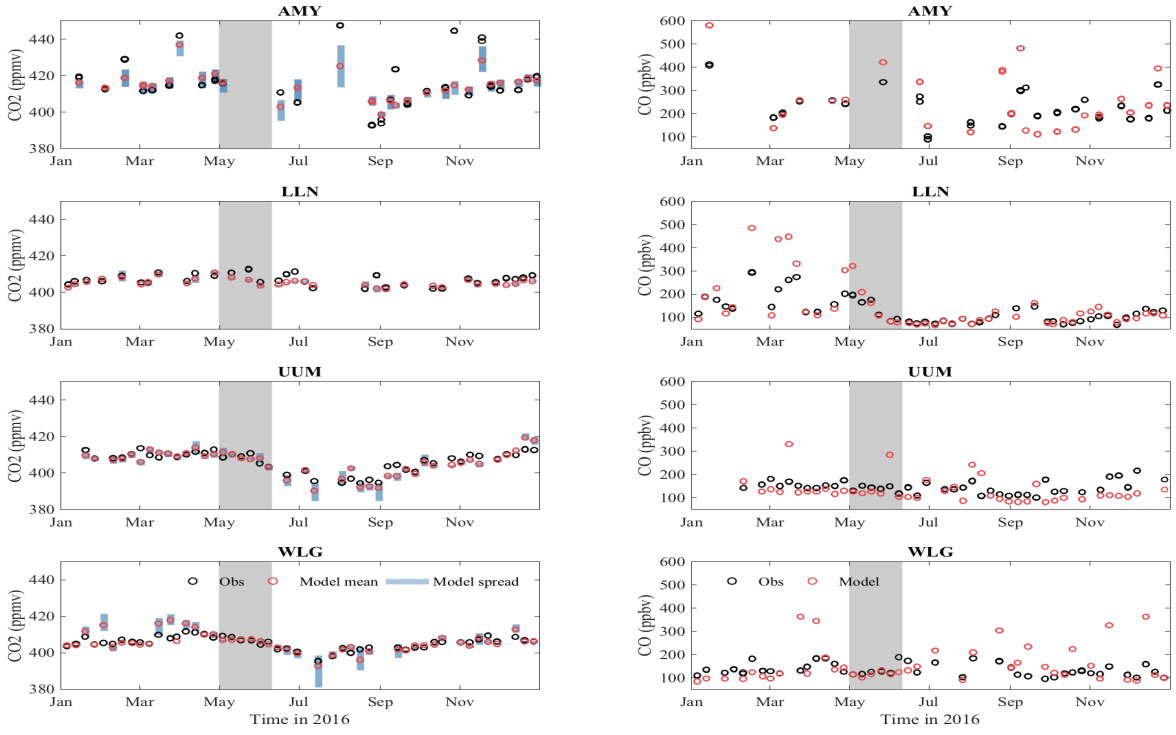

Figure E2. Time series of CO_2 data (left column) and CO data (right column) in black dots superimposed with the corresponding model results (red dots) at four East Asia sites from the NOAA ESRL Carbon Cycle Cooperative Global (CCGG) Air Sampling Network in 2016. The equivalent modeled CO_2 is represented as the mean of four model simulations with the blue bars representing the spread (min/max) of the four model simulations) The KORUS-AQ period (May 1 – June 10) is indicated in gray shade.

We also have an additional simulation for the KORUS-AQ period using the same configuration but with CO_2 and CO tags (i.e., using CT2017 3-hourly fluxes for CO2 and the aforementioned emissions scenario for CO as well as NMVOCs). Simulation with tagged tracers is more computationally expensive. Due to limitation in computational resources, we run one CAM-chem simulation with tagging of both CO and CO_2 using the 3-hourly CT fluxes for CO_2. We tag $FFCO_2$ from 11 regions in East Asia (shown in Figure E1) with one additional tag that accounts for fossil fuel emissions from the rest of the world, following our previous study (Tang et al., 2019), to show the results during KORUS-AQ. The CO_2 and CO tags are initialized with zero fields on Jan 1, 2016 so that only the emissions in 2016 are accounted when analyzing the relationships between CO and CO_2 tags during KORUS-AQ.

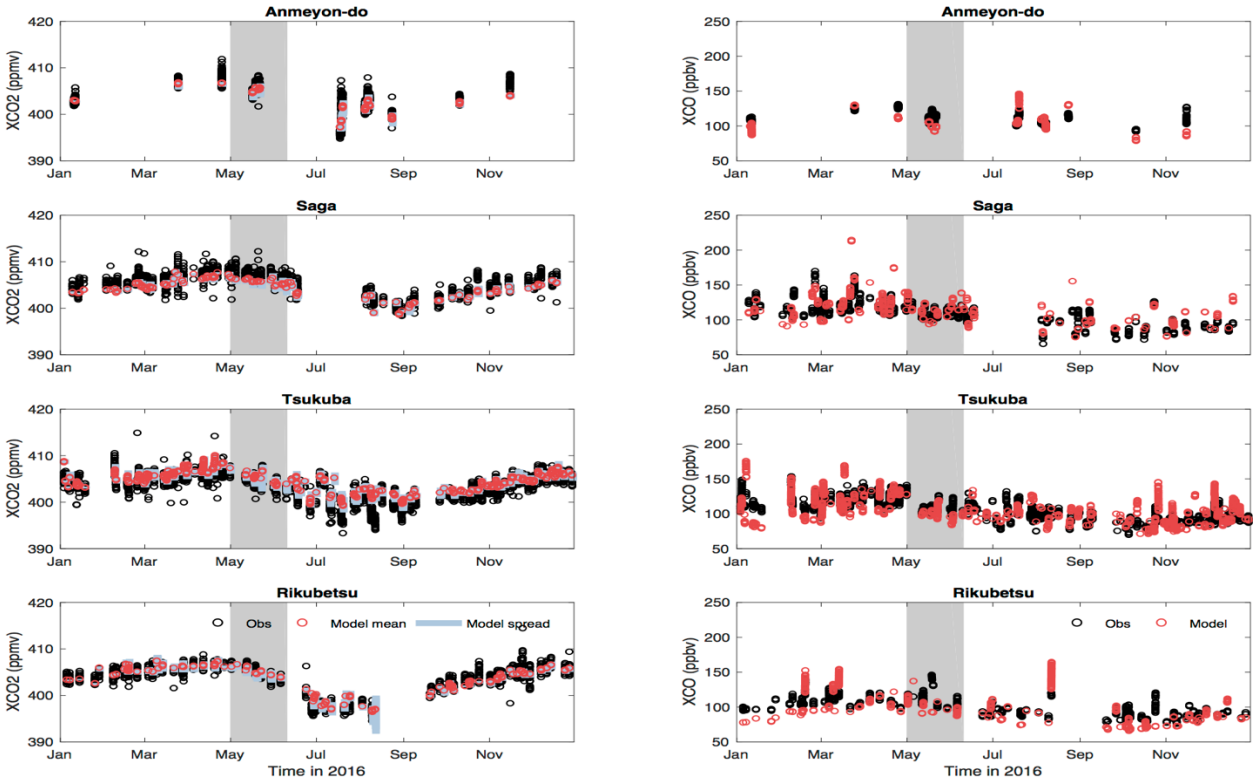

Figure E3. Time series of observations (black dots) and corresponding model results (red dots) The equivalent modeled CO_2 is represented as the mean of four model simulations with the blue bars representing the spread (min/max) of the four model simulations at four TCCON sites in 2016. KORUS-AQ period (May 1 – June 10) is indicated in gray shade.

The associated global budgets for our CO and CO_2 simulations are presented in Table E2. We also show in the supplementary material (Figure ES1) the corresponding CO_2 abundance for each flux product that we used and the concentration fields from Carbon Tracker (CT2017). This summary and comparison for CO_2 are intended to ensure that: a) CAM-Chem reasonably reproduces the CO_2 fields from CT2017; b) appropriate accounting of each tag is carried out; and c) mass is conserved. Overall, our simulation results produce CO_2 fields comparable to current CO_2 analyses while carbon is reasonably accounted for. The small differences may be attributed to unaccounted losses due to dry deposition (for CO, ~3% of the burden), and a cutoff of model top at ~2 hPa. Differences in CO_2 mass is ~0.001% of initial burden.

3. Observational Datasets

In Table E3, we provide a list of datasets that we used for model evaluation. Our intention is to investigate the consistency of simulated CO and CO_2 (incl. their relationships) across observing platforms and compare the model results with these observations. We note that each dataset has complementary information that we would like to highlight below within the context of tracking $FFCO_2$.

3.1 Surface Flask Air Sampling

The NOAA ESRL Carbon Cycle Cooperative Global Air Sampling Network is an international effort that includes samples from the NOAA ESRL/GMD baseline observatories, cooperative fixed sites, as well as commercial ships. The air samples are analyzed for species including CO_2, CH_4, CO, N_2O, many Volatile Organic Compounds (VOCs), and stable isotopes of CO_2 and CH_4 (https://www.esrl.noaa.gov/gmd/ccgg/flask.php). We use the flask measurements of atmospheric CO_2 and CO dry air mole fractions from four ground sites in East Asia that are part of the NOAA ESRL Carbon Cycle Cooperative Global Air Sampling Network (Dlugokencky et al., 2018; Petron et al., 2018), namely Anmyeon-do (AMY; 36.54°N, 126.33°E, 85.12 masl), Lulin (LLN; 23.47°N, 120.87°E, 2862.00 masl), Ulaan Uul (UUM; 44.45°N, 111.10°E, 1007.00 masl), and Mt. Waliguan (WLG; 36.29°N, 100.90°E, 3810.00 masl). The AMY surface flask air sampling site, operated by Korea Meteorological Administration, is co-located with one of the aforementioned TCCON Anmyeondo site. LLN is a high-elevation baseline station situated at the peak of Mt. Front Lulin in central Taiwan Island, 2 km away from the nearest major road (Hsiao et al., 2017). UUM is

located in the Gobi Desert in southeast Mongolia, operated by Mongolian Hydrometeorological Research Institute. WLG is a remote site, located on the top of Mt. Waligaun, on the Tibetan plateau, and is away from major industrial sources (https://www.esrl.noaa.gov/gmd/dv/site/WLG.html). WLG is operated by Chinese Academy of Meteorological Sciences and Qinghai Meteorological Bureau (QMB), China Meteorological Administration. For comparison, model results are interpolated to the four sites. These datasets serve as the data for baseline comparison and providing seasonal context of the model simulations.

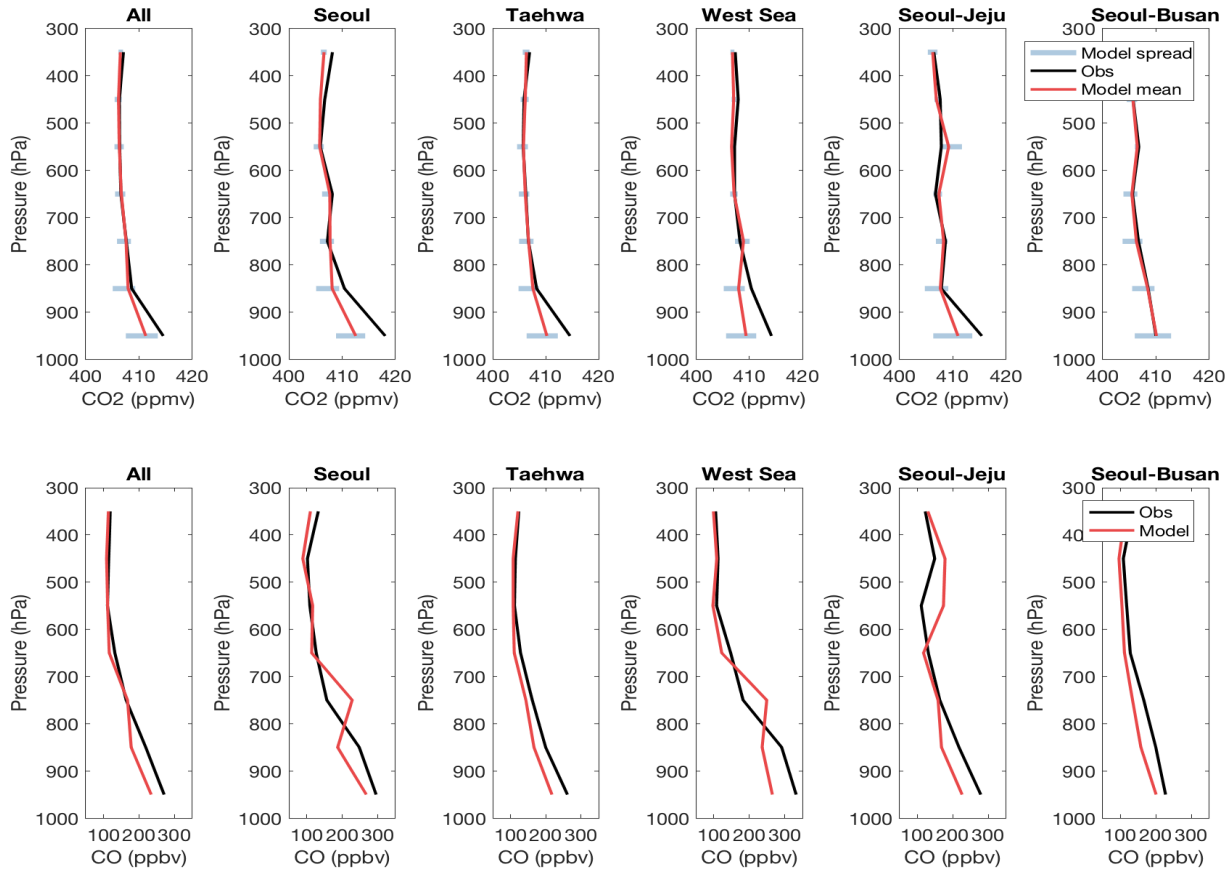

Figure E4. Averaged vertical profiles of CO_2 and CO volume mixing ratios from DC-8 aircraft measurements (black lines) and equivalent model results during KORUS-AQ. The equivalent modeled CO_2 is represented as the mean of four model simulations with the blue bars representing the spread (min/max) of the four model simulations).

3.2 Ground-based Remote Sensing

The Total Carbon Column Observing Network (TCCON) is a global ground-based network of to measure column abundances of CO_2, CO, CH_4, N_2O as well as other species that also absorb in the near-infrared (Wunch et al., 2011; https://tccon-wiki.caltech.edu/). TCCON data have been widely used previously for evaluation and validation of satellite retrievals and model performance (Basu et al., 2011; Butz et al., 2011; Reuter et al., 2011; Cogan et al., 2012; Schneising et al., 2012; Kulawik et al., 2016; Wunch et al., 2017; Jing et al., 2018). In this study, XCO_2 and XCO measurements from four TCCON sites in East Asia (Release GGG2014) are used (Wunch et al., 2015), including Anmyeon-do (36.54°N, 126.33°E, 30 masl; Goo et al., 2017), Saga (33.24°N, 130.29°E, 7 masl; Shiomi et al., 2017), Tsukuba (36.05°N, 140.12°E, 31 masl; Morino et al., 2017a), and Rikubetsu (43.46°N, 143.77°E, 380 masl; Morino et al., 2017b). Anmyeon-do is the sixth largest island in the country (area is ~87.96 km^2), with ~1.25 million residents. The Anmyeon-do site is located on the west coast of the Korean Peninsula, and 180 km away from Seoul (https://tccon-wiki.Anmyeondo.edu; Oh et al., 2018). The Saga site, located on the Kyushu Island, became operational since June 2011 at Saga University and is managed by Japan Aerospace Exploration Agency (https://tccon-wiki.caltech.edu/Sites/Saga). The Tsukuba site is operated by the National Institute for Environmental Studies (NIES), and is located about 50 km north of Tokyo in the Japan main island (https://tccon-wiki.caltech.edu/Sites/Tsukuba; Ishizawa et al., 2016). The Rikubetsu site is also operated by NIES, located in Hokkaido, Japan (https://tccon-wiki.caltech.edu/Sites/ Rikubetsu). For comparison, model results are interpolated to TCCON locations and smoothed with TCCON *a priori* profiles and averaging kernels (AKs). These datasets also serve as our data for baseline comparison and consistency check with the corresponding satellite retrievals.

3.3 Aircraft Measurements during KORUS-AQ

The Korea United States Air Quality (KORUS-AQ) field campaign was conducted over South Korea and its surrounding waters from May to June 2016. KORUS-AQ was based on an international collaboration between U.S. and South Korea, led by the National Institute of Environmental Research (NIER) of Korea and the National Aeronautics and Space Administration (NASA) of the United States. The campaign aimed to recognize the opportunities and challenges

for satellite observations of air quality, study the key factors governing ozone photochemistry and aerosol evolution, and evaluate model performance in representing atmospheric composition over Korea and its connection to the larger global atmosphere (Kim and Park, 2014, KORUS-AQ White Paper). During the campaign, the NASA DC-8 aircraft flights sampled the lower and mid-troposphere (https://www-air.larc.nasa.gov/missions/korus-aq/). The flight tracks are shown in Figure E1. Two instruments (Atmospheric Vertical Observations of CO_2 in the Earth's Troposphere and Differential Absorption CO Measurement; AVOCET and DACOM) were onboard the NASA DC-8 aircraft to measure CO and CO_2. AVOCET provided CO2 concentrations by sensing the difference in light absorption between the continuously flowing sample and reference gases with precision less than 0.1 ppmv and accuracy of 0.25 ppmv (https://airbornescience.nasa.gov/instrument/AVOCET; Vay et al., 2011). The DACOM measured absorption lines of several species including CO with three tunable diode lasers to take CO measurements with precision of 0.1 ppbv (or < 1%), and accuracy of 2% (https://airbornescience.nasa.gov/instrument/DACOM; Warner et al., 2010). In this study, the airborne CO and CO_2 measurements from KORUS-AQ is used in in Section 4 and 5 to demonstrate and validate the tagging mechanism in CAM-chem. In addition, radiocarbon has also been measured onboard the DC-8 aircraft. $FFCO_2$ from radiocarbon ($FFCO_2$_from_radiocarbon) is calculated based on the approach by Turnbull et al. (2011). Values of ΔCO_2 are taken from Accelerator Mass Spectrometer (AMS). Details regarding derivation of $FFCO_2$ from $^{14}CO_2$ along with in-situ CO_2 measurements can be found in Choi and Wang (2004). In this study, we use $FFCO_2$_from_radiocarbon to evaluate our anthropogenic CO_2 tags.

3.4 Satellite-derived Measurements

We use retrievals of CO_2 column-averaged dry-air mole fraction (XCO_2) from the NASA Orbiting Carbon Observatory-2 (OCO-2), version 8, level 2 (L2) Lite product with the recommended quality flag (i.e., xco2 quality flag equals to 0). Overall, the version 8 data reduces regional-scale biases compare to the previous version (O'Dell et al., 2018). The Lite product contains quality screen data extracted from the Level 2 Standard product, with bias correction applied (Boesch et al., 2011; Osterman et al., 2017; Wunch et al., 2017). OCO-2 has spatial resolution of 2.25×1.29 km. It covers the globe every 16 days and its revisit time is about 13:30 (local time). The uncertainty of XCO_2 retrievals is about 1-2 ppmv (Wunch et al., 2017). For CO, we use total

column retrievals (XCO) of the Measurements Of Pollution In The Troposphere onboard Terra, version 7, Level 2, multispectral (thermal infrared/near infrared; TIR/NIR) (MOP02J, L2, V7) with the recommended quality flag (i.e.: cloud mask from MOPITT and Moderate Resolution Imaging Spectroradiometer agree on clear for Cloud Description; sum of Retrieval Anomaly Diagnostics equals to 0; solar zenith angle is less than 80). Compared to the TIR retrievals, the TIR/NIR retrievals have are more sensitive to the lower tropospheric CO (Worden et al., 2010; Deeter et al., 2017). MOPITT has spatial resolution of 22×22 km and global coverage every 3~4 days. The revisit time is around 10:30 (local time) and the uncertainty is about 0.09×10^{18} molecules cm^{-2} for total column retrieval (Deeter et al., 2014). We use these retrievals to look at spatial patterns of CO and CO_2 within the KORUS-AQ domain (see Figure E1).

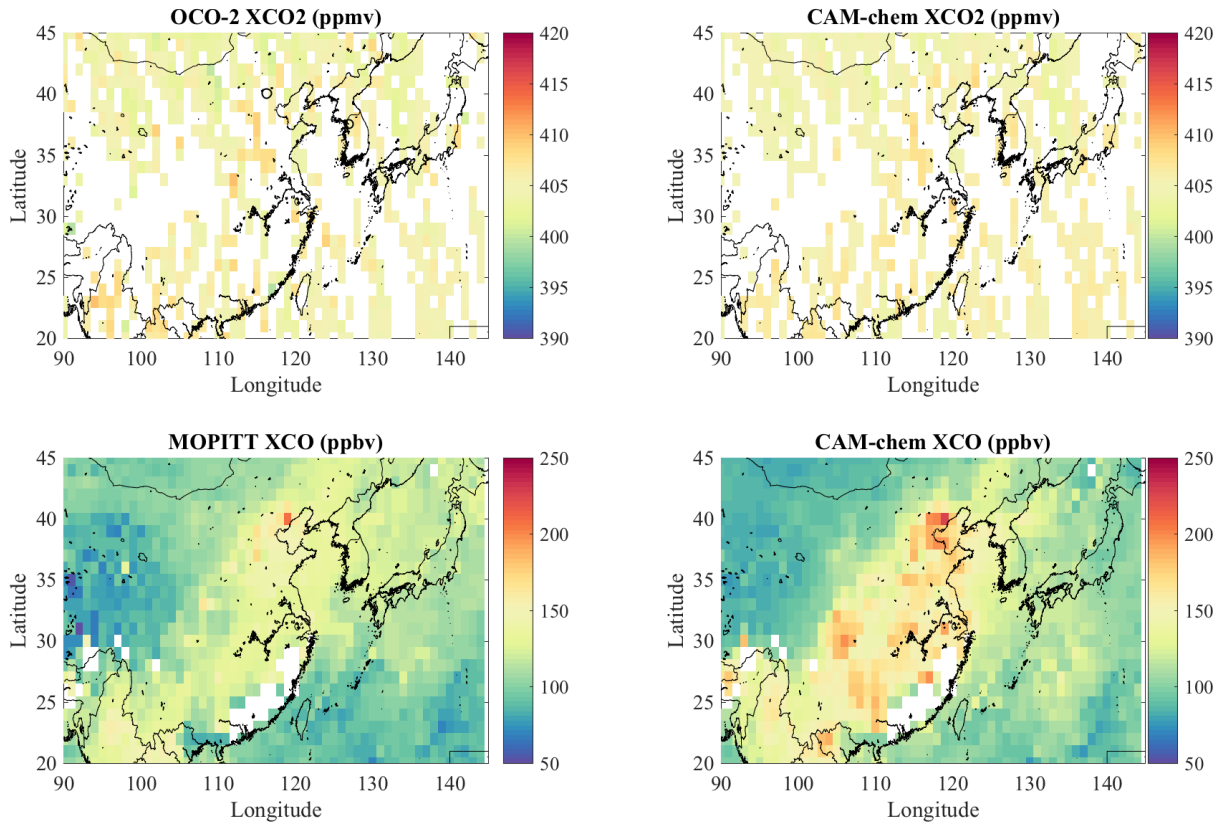

Figure E5. Comparison with CO_2 and CO satellite data. Top panels correspond to the mean OCO-2 XCO_2 column density across KORUS-AQ period (ppmv) (top left), and equivalent XCO_2 averaged across four model simulations (top right). Bottom panels correspond to MOPITT XCO column density averaged across KORUS-AQ period (ppbv), (bottom left) and equivalent XCO (bottom right).

4 Model Evaluation

Here, we evaluate the ensemble of CAM-chem CO_2 and CO simulations with observations from different platforms and/or measurement types (flask samples from surface sites, surface and space observations of column density, airborne observations). We also analyze the consistency of observational and modeled CO, CO_2, and CO-CO_2 relationships among different platforms. Results will be presented mainly for the period (May and June 2016) over East Asia (20-45°N, 90-146°E) to match the KORUS-AQ campaign. Again, the domain of the study and an overview of the ground and airborne measurements are shown on Figure E1. The overall observation and model statistics along with a summary of model evaluation statistics are presented in Table E4. We note however that this evaluation is mostly intended to check model consistency of CAM-Chem with the ensemble of inversion systems since the CO_2 flux products and initial conditions are derived from these systems (e.g., errors in implementation).

4.1 Comparison with NOAA CCGG

We show in Figure E2 the time series of CO_2 and CO from NOAA CCGG together with the model simulation results. While our study focuses on the KORUS-AQ period, we present this comparison for the entire year of 2016 to provide the seasonal context of CO_2 and CO in these sites. We show the ensemble mean (across the 4 CO_2 flux products that we used) as well as the range (in terms of minimum and maximum values) of the ensemble. We note that there are very limited observations (i.e., 4~12 observations for each site) during the KORUS-AQ period which is indicated in gray shade. This hinders us to provide robust statistical interpretation of our evaluation during this period. Correlations, mean biases, and root mean square errors (RMSEs) are calculated for the entire year instead (see Table E4). Overall, modeled CO_2 and CO are in agreement with surface CO_2 and CO at these sites (R ranges from 0.62-0.92 for CO_2 and 0.21 to 0.92 for CO; RMSE ranges from ~3 to 10 ppmv for CO_2 and ~59.0 to 178 ppbv for CO; Mean Bias ranges from ~ -3 to 1.5 ppmv for CO_2 and ~ -14 to 57 ppbv for CO). The use of posterior CO_2 fluxes has significantly improved CO_2 simulations over the AMY and LLN sites relative to the default CO_2 setting in CAM-Chem. Although not shown, the default CO_2 has higher RMSE and bias (by a factor of 2-3) and slightly lower correlation. For CO, CAM-chem performs well at the AMY and LLN sites while showing less agreement over more remote sites in WLG and UUM. This is especially the case for

the CO simulation over the WLG site, with low correlation (0.22), large bias (57 ppbv), and large RMSE (180 ppbv). This can be better elucidated by comparing the observed variability across the year. The variability in CO_2 is underestimated by CAM-Chem except in WLG while the CO variability is overestimated in the model across all sites by a factor of ~2 and even greater in WLG. Along with an overestimation of CO:CO_2 correlation in CAM-Chem, our results suggest that the coarse resolution model has difficulty resolve species transport over highly complex terrain of the Tibetan plateau.

We note that the KORUS-AQ period in May/June coincides with a slowly dropping CO2 abundance over UUM and WLG. This is not very apparent in CO although there is a strong decline in CO mixing ratio in LLN during this period. The seasonality in CO_2 is more pronounced in these sites. This is also seen in the global budget where the net change in abundance ranges from a low positive to low negative for CO2 and low negative for CO. This is expected as it is in this period that the northern hemisphere transitions from spring (CO_2 respiration and CO transport) to summer (more drawdown for CO_2, higher OH for CO). The seasonality in CO_2 and CO are reasonably captured. This is supported well with the high correlation of model CO_2 and CO with observations.

4.2 Comparison with TCCON

Column measurements of CO_2 and CO are expected to complement with corresponding surface measurements. This is not clearly the case for this study as the TCCON and CCGG sites are not collocated (except AMY). The XCO_2 and XCO from TCCON, which are mostly in Japan are associated with air downwind of Korea (except Anmyeon-do/Amy). Unfortunately, there is limited number of retrievals over the Anmyeon-do site for both TCCON (Amy) and CCGG (AMY) to assess complementarity in information content between these platforms. Hence, our comparison with TCCON should be interpreted to correspond to model performance over Japan. We will compare this performance however with satellite-derived XCO_2 and XCO in the KORUS-AQ domain in section 4.4 to add spatial context to both TCCON and CCGG.

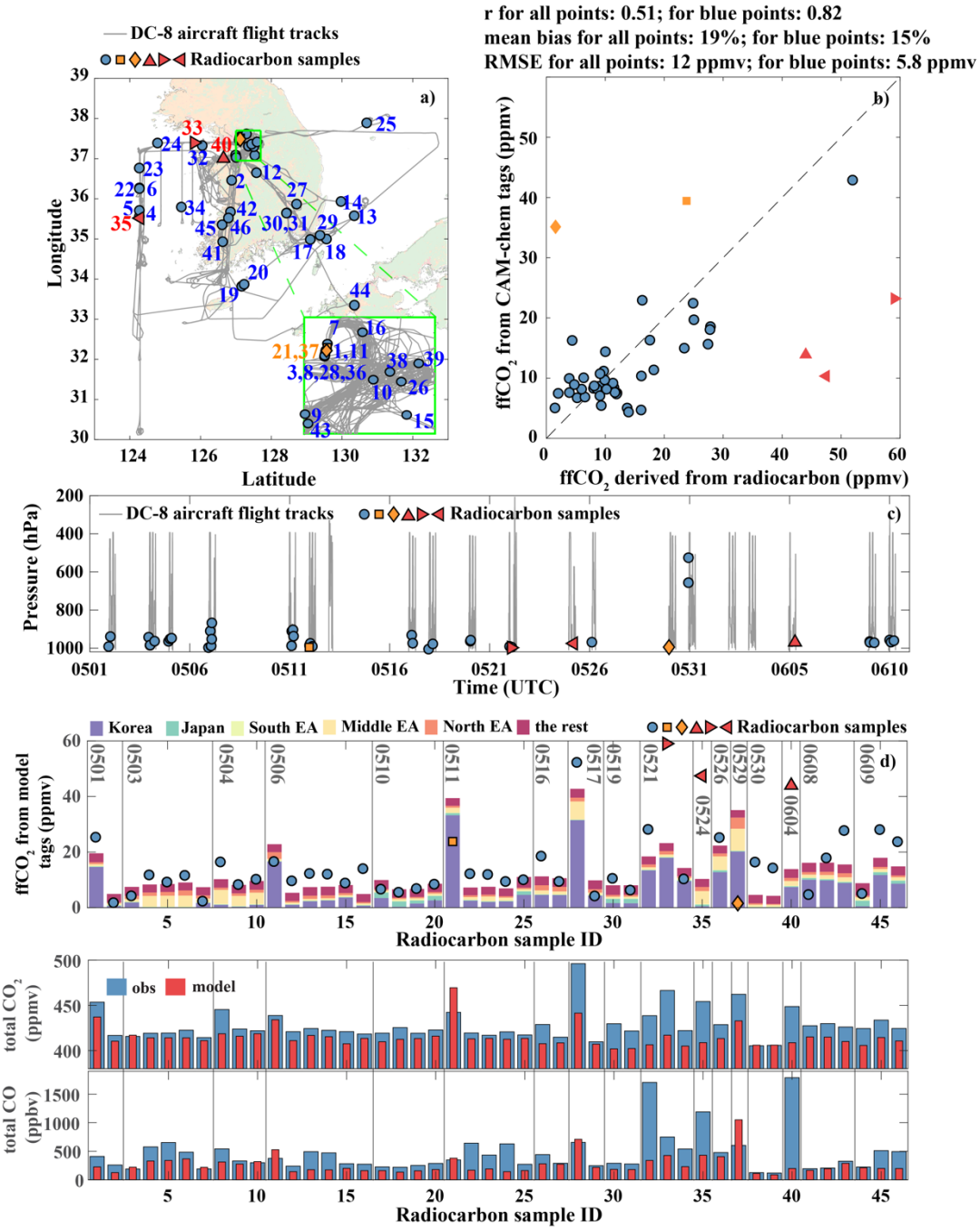

Figure E6. Comparison of $FFCO_2$ tags with radiocarbon data during KORUS-AQ. The spatial and temporal sampling of radiocarbon (colored markers) and CO_2 measurements (gray line) are shown in top left panel (a), (horizontal) and middle panel (c) (vertical and time), respectively. Data points colored in orange and red are considered outliers. The top right panel (b) correspond to a scatterplot between $FFCO_2$ from CAM-chem tags and $FFCO_2$ from radiocarbon (overall correlation is indicated for all data points and excluding outliers). Modeled regional contributions to $FFCO_2$ are shown in the bottom panel (d) along with the values of radiocarbon samples (ppmv) and corresponding CO_2 (e) and CO (f) model and data comparison for each sample.

In Figure E3, we show that simulations of CO_2 and CO in CAM-Chem are in very good agreement with TCCON in Saga, Tsukuba and Rikubetsu. The fit to the data is relatively tight especially for CO_2. The RMSE ranges from 1.1 to 1.8 ppmv for CO_2 and 12 to 16 ppbv for CO, while the mean bias ranges from 1.1 to 1.6 ppmv for CO_2 and -6.1 to 2.4 for CO (see Table E4). This translates to about 2-4% (CO_2) and 11-16% (CO) error relative to TCCON. The use of posterior CO_2 fluxes also provides a significant improvement as XCO_2 using prescribed CO_2 fields consistently underestimate XCO_2 by 3-5 ppmv. We also find that the correlation of model XCO_2 to TCCON XCO_2 (0.84 to 0.95) is consistently higher than its corresponding correlation with CCGG CO_2. This is most likely due to smoothing when model is transformed to a TCCON-like retrieval. It is also important to note that the observed variability and CO:CO_2 correlation are well captured by the model in contrast to CCGG statistics. The seasonality in CO_2 is again more pronounced in TCCON than CCGG remote sites, although we also see declining CO abundance during KORUS-AQ period (relative to late winter months) in both the retrievals and model simulations.

4.3 Comparison with NASA DC-8

Here, we will focus our evaluation on CO_2 since we have evaluated the CAM-chem simulations of CO with the measurements from the NASA DC-8 aircraft during KORUS-AQ in our previous study (Tang et al., 2019). We also place our results in context with our evaluation of CAMS CO_2 and CO forecast analysis (Tang et al., 2018). Although the models are different (and the fluxes are also not exactly the same), the modeling issues such as boundary layer mixing and synoptic transport should be similar.

We show in Figure E4 the mean vertical profiles of DC-8 measurements and model simulations in different groups of flight tracks associated with a specific spatiotemporal sampling goal during the campaign. Similar to previous comparisons (section 4.1 and 4.2), we show the ensemble mean and spread of the CO_2 simulations using the 4 flux products. Statistics for each simulation are shown in Table E4 for comparison purposes. Overall, there is a very good agreement of modeled CO_2 profile especially above 800 hPa with DC-8 regardless of flight groups. The best fit to CO_2 data is shown in the Seoul-Busan jetway where the ensemble mean is very close to DC-8 profile across all layers. There is however a systematic underestimation of about 2-5 ppbv in the boundary layer (surface to 800 hPa) except Seoul-Busan. This model performance is in contrast to CAMS CO_2

(forecast and analysis) where CAMS was shown to slightly overestimate CO_2. The fit to data is quite expected however since CO_2 flux products have already been constrained to observations. In fact, the Taylor score for CAM-Chem simulations jump from ~0.04 with default CO_2 smoothed fields to ~0.7 with these fluxes. Although the CAMS CO_2 fluxes were also calibrated (bias corrected, Agustí-Panareda et al., 2016) based on CAMS CO_2 flux product used in this study, the use of spatiotemporally explicit CO_2 fluxes that are observationally-constrained is important to capture local-to-regional scale errors in surface boundary conditions.

The modeled CO profiles are also underestimated in the lowermost troposphere during KORUS-AQ. There is indication of vertical structures that are enhanced in CO profile compared to CO_2. This is more evident in more polluted samples (over Seoul and East Asian plume transport to the West Sea) and samples aloft Seoul-Jeju jetway (which may be due to plume transport from East Asia). This suggest that CO can help constrain the simulated transport of CO_2 especially in regions where CO_2 data is lacking. Such constraints can be easily provided using data assimilation. We note however that this does not directly constrain fluxes, rather CO provide information to constrain CO_2 concentration fields. The sensitivity of flux to errors in CO_2 transport is more complicated to constrain with CO alone.

The systematic underestimation of CO_2 and CO near the surface suggest that either CO_2 and CO local sources are underestimated or that the sinks (and/or mixing) are overestimated in the region. However, the agreement in CO_2 over Seoul-Busan and the underestimation of CO across all vertical layers also suggest that CO_2 sink may be reasonably captured by the fluxes. A 'stronger mixing' argument may also be possible (albeit not a dominant driver) given the underestimation in CO profile. The DC-8 CO_2 statistics over Seoul show that the variability is within similar magnitude as CCGG AMY but the modeled CO_2 better captured the DC-8 than CCGG AMY variability and CO_2:CO correlation. This model/DC-8 correspondence is evident not only over Seoul but for all flight groups. This may be because enhancements derived from these measurements are mostly representative of pollution plumes rather than background. Nevertheless,

this comparison shows that there is clear synergy between AQ (CO) and GHG (CO_2) particularly in regions where anthropogenic combustion is dominant.

4.4 Comparison with OCO-2 and MOPITT

Spatial distributions of OCO-2 observations of CO_2 column density (XCO_2) and XCO_2 derived from modeled results during KORUS-AQ are shown in Figure E5. The model values are interpolated to the location of satellite observations prior to applying the satellite *a priori* profiles and AKs. The XCO_2 from OCO-2 and models are then gridded to a 1-degree by 1-degree map and averaged for the KORUS-AQ period. Note that even though the maps show average values over the KORUS-AQ period, each grid in the domain (20°-45°N, 90°-145°E) has only a few days of data due to the coverage of OCO-2. Specifically, 55% grids have no data, 36% grids have only one day's data, 8% grids have only two days' data, and only 1% have three days' data. The statistics of the comparisons between OCO-2 and modeled column density are also summarized in Table E4. Overall, the four simulations using posterior CO_2 fluxes agree well with OCO-2 observations during KORUS-AQ (correlation=0.46~0.68, mean bias=-0.0~0.8 ppmv, and RMSE=1.3~1.7 ppmv). Note however that in TCCON Amy site, the mean model XCO_2 is underestimated across 2016. There appears to be high XCO_2 over China in OCO-2 than the model and vice versa over Seoul. Also, XCO_2 derived from the simulation using monthly CT fluxes have higher correlation with XCO_2 from OCO-2 (0.68), lower mean bias (0.5 ppmv) and RMSE (1.3 ppmv) compared to XCO_2 derived from the simulation using 3-hourly CT fluxes (correlation=0.46, mean bias=0.76 ppmv, and RMSE=1.7 ppmv). Simulations using CTE2018 and CAMS CO_2 fluxes have smaller mean biases (0.2 and -0.0 ppmv, respectively) compared to the simulations using CT fluxes. This is true as well in the model comparison with DC-8, especially over Seoul-Busan jetway. In other words, using the same CO_2 fluxes with lower temporal resolution leads to better agreement with satellite observations. This implies that errors in diurnal variations may confound model performance.

Our comparison between XCO derived from CAM-chem and MOPITT observations of XCO are conducted in the same way as XCO_2. A more comprehensive evaluation of XCO derived from CAM-chem against MOPITT observations can be found in Tang et al. (2019). Here, we briefly summarize statistics of the CO simulation we used in this study within the context of the CO_2

statistics. XCO derived from the CAM-chem simulation have higher correlation (0.76) with satellite observations compared to those for XCO_2 (0.46~0.68). The mean bias (6.40 ppbv) and RMSE (18.47 ppbv) are both reasonably small. Note Note however that in TCCON Amy site, the mean model XCO is underestimated across 2016 (similar to XCO_2). There appears to be low XCO over China in MOPITT than the model and vice versa over Seoul. Although not shown, the correlations between modeled surface CO concentrations and modeled CO column densities are high (0.87). This indicates that MOPITT observations of column density are strongly correlated with and can be used to represent the surface concentrations. This may be related to the fact that MOPITT multispectral retrievals have improved sensitivity to the surface (Worden et al., 2010). This sensitivity is reflected by the MOPITT AKs that are applied to CAM-chem results in order to calculate column density. Overall, the XCO derived from the CAM-chem simulation used in this study agree well with MOPITT observations.

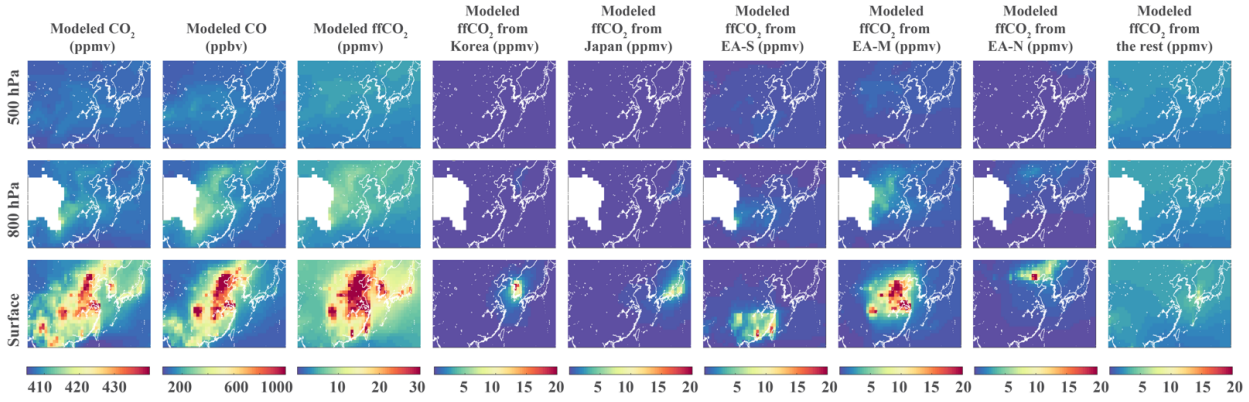

Figure E7. Spatial distribution (averaged across KORUS-AQ) of modeled total CO_2 (ppmv) and CO (ppbv), modeled $FFCO_2$ and $FFCO_2$ tags at model surface, 800 hPa, and 500 hPa.

The utility of CO in constraining $FFCO_2$ from the satellite perspective is three-fold. First, there is a larger number of retrievals for CO (and other AQ trace gases) than OCO-2 and/or GOSAT XCO_2. This provides additional information in filling the data gaps especially in combustion regions. This is shown in Figure E5 over Beijing and Shanghai. We note however that CO retrievals cannot stand alone in tracking $FFCO_2$. It has to be placed in the context of *a priori* CO_2 and strong CO_2:CO correlation. This can be done through model calibration. Second, CO retrievals provide enhanced spatial structure of combustion signature ($FFCO_2$) which cannot be easily identified with CO_2

retrievals without filtering and prior signal processing. While this can be related to coverage, enhancements of CO are stronger than CO_2 even in megacities, and in particular downwind of the source regions. In fact, the combination of NO_2 (shortest lifetime relative to CO_2 and CO) and CO (medium lifetime) provides an informative footprint of plume transport from the source and downwind. Third, sectoral emissions can also be enhanced without the addition of tracers. This is particularly the case with fires where a strong CO enhancement can be observed. All these are not evident in OCO-2/MOPITT statistics where the CO_2:CO correlation is only 0.22. This is due to the limited data of OCO-2 along with sampling bias over background regions and smoothing across KORUS-AQ period.

5. Utility of Joint CO and CO_2 Analyses

In this section, we describe in some detail the relationship between CO_2 and CO, as well as $FFCO_2$ and FFCO and their associated tags. Our aim is to elucidate the value of a joint analysis of CO_2 and CO. In particular, we illustrate three key constraints from CO on tracking $FFCO_2$: 1) consistencies in modeled and observed $FFCO_2$; 2) transport patterns of combustion-related plumes and sectoral information of $FFCO_2$; 3) consistencies in combustion efficiencies ensuing from atmospheric modeling of $FFCO_2$ emissions. We emphasize that this study focuses on substantiating these constraints in order to motivate future in-depth evaluation of their impact within the framework of tracking $FFCO_2$ using data assimilation approaches. The CO_2 and CO tagging mechanism in CAM-chem has been described in section 2.2.2. We take advantage of extensive measurements from KORUS-AQ to evaluate this tagging mechanism especially with the radiocarbon measurements for $FFCO_2$.

5.1 On $FFCO_2$

During KORUS-AQ, forty-six (46) $^{14}CO_2$ measurements from whole air samples, were collected onboard the NASA DC-8 aircraft during the KORUS-AQ campaign, along with in-situ CO_2 and CO measurements. We compare these $^{14}CO_2$ measurements with global total $FFCO_2$ emitted since Jan 1st 2016 (sum of the 12 tagged regions). We note that the modeled tag of global total $FFCO_2$ (emitted since Jan 1st 2016) is not exactly the same as $FFCO_2$ derived from the $^{14}CO_2$ measurements. However, these airborne measurements are taken closely to the fossil fuel emission sources, and hence the variations in the $FFCO_2$ tags (accumulated since Jan 1st 2016) are expected

to capture the spatial and temporal variations of $FFCO_2$ derived from $^{14}CO_2$ measurements. Figure E6 show the horizontal, vertical and temporal distributions of $^{14}CO_2$ measurements. Sample IDs are indicated in the sample location along with approximate time stamps for a group of samples. Figure E6 also shows a scatter plot of $FFCO_2$ derived from the $^{14}CO_2$ measurements and $FFCO_2$ from CAM-chem. Overall, the correlation between $FFCO_2$ derived from $^{14}CO_2$ measurements and modeled $FFCO_2$ tags is significant (r=0.51). We identified three (3) data points where $FFCO_2$ derived from $^{14}CO_2$ measurements are significantly high (> 40 ppmv). These points are marked as red colored points in Figure E6. We also identified two (2) data points where $FFCO_2$ derived from $^{14}CO_2$ measurements are significantly lower than modeled $FFCO_2$. These are marked as orange colored points in Figure E6. Without the five data points, $FFCO_2$ derived from $^{14}CO_2$ measurements and modeled $FFCO_2$ agree very well (r=0.82).

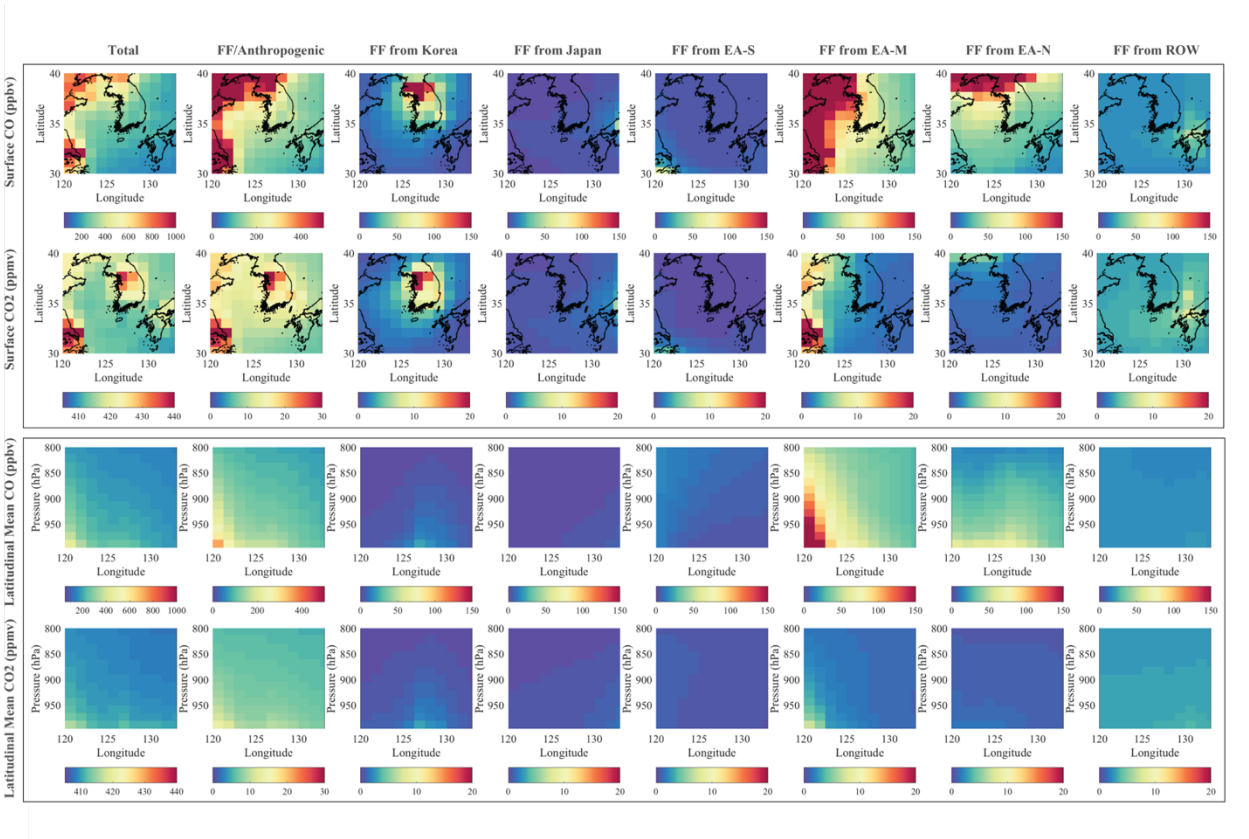

Figure E8. Spatial distribution of CO_2 and CO over Seoul and nearby regions. This is shown in the different columns for total CO_2 (or CO), its associated $FFCO_2$ (or FFCO) and regional contributions at the surface (top), along with corresponding mean zonal distributions averaged across KORUS-AQ domain (bottom).

We further analyze potential causes for disagreement between model and observations for the five data points. We note that the five data points were all sampled near surface, implying surface CO_2 fluxes may play a role in the model-observation discrepancy. The source contribution for the modeled $FFCO_2$ derived from the CAM-chem tags for the five data points are superimposed in Figure E6b. In addition, a bar plot showing source contribution for the modeled $FFCO_2$ for all the data points is presented in Figure E6d along with CO_2 and CO (Figure E6e and 6f). The $FFCO_2$ from the rest of the world (representing background $FFCO_2$ of the region) generally contribute a small portion of total $FFCO_2$ derived from CAM-chem tags while $FFCO_2$ from Korea and East Asia play a more important role. It appears that variations in the accumulated $FFCO_2$ tags since January 1, 2016 are able to capture the spatial and temporal variations of $FFCO_2$ in the region. We find that the three data points colored in red, which were sampled over the ocean, are mainly contributed by $FFCO_2$ from Korea and/or East Asia. The potential cause for these 3 data points could be: (1) high $FFCO_2$ derived from observations at the 3 points are caused by underestimation of $FFCO_2$ background (i.e., $FFCO_2$ before Jan 1st 2016 are not accounted for in these tags; (2) CT FF fluxes used in this study may be underestimated; (3) CT bio and/or ocean fluxes are too strong removing more of the tagged $FFCO_2$ than they are supposed to. On the other hand, the two points colored in orange, which were both sampled over the Seoul metropolitan area during missed approaches near surface, are dominated by $FFCO_2$ from Korea. For this case, a reasonable cause would be overestimation of CT FF fluxes in Korea. Despite the model-observation discrepancy at these five data points, we find that modeled $FFCO_2$ are reasonably consistent with $FFCO_2$ derived from $^{14}CO_2$ measurements.

We also attempted to fit the regional $FFCO_2$ tags (East Asia, Korea+Japan, and Rest of the World) with the $FFCO_2$ derived from the radiocarbon samples using a simple optimal estimation algorithm (Rogers, 2000). Excluding these outliers (i.e., $|obs - model| > 2\sigma_{obs}$), we find that $FFCO_2$ over East Asia and Rest of the World needs to be scaled up (1.61 and 1.28, respectively) while Korea+Japan $FFCO_2$ needs to be scaled down (0.84). There appears to be an underestimation of CO_2 in the boundary later over Seoul by about 2-5 ppmv in the mean sense based on DC-8. If $FFCO_2$ over Seoul needs to be decreased, (i.e., there's too much right now), then it begs the question on why there is an underestimation in total CO_2. If, on the other hand, we assume that the cause of this underestimation is that the sink is too strong over Seoul, this is still in conflict with required $FFCO_2$ scaling. Given that it has also been reported by Tang et al., (2019) that there is a

good percentage of CO from East Asia contributing to CO over Seoul (~30% near surface), it might be that the suggested increase of ~60% of $FFCO_2$ from East Asia in our regression translates to reducing the low bias in CO_2 over Seoul. We argue that the sink from the flux products are reasonably captured over Korea given that the Seoul-Busan CO_2 is significantly close to DC-8 CO_2 profile.

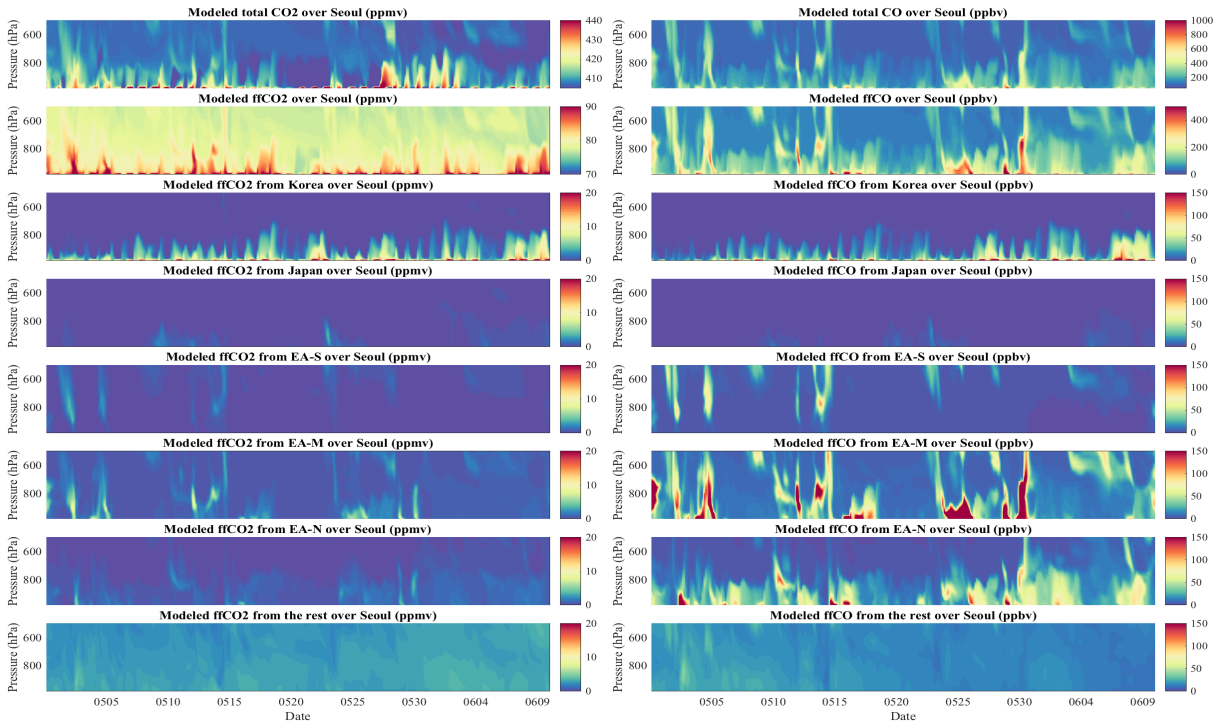

Figure E9. Time series of modeled vertical profiles of total CO_2 and CO, $FFCO_2$ and FFCO, and their associated regional contributions over Seoul.

5.2 On Regional and Sectoral Contributions

Here, we demonstrate (albeit qualitatively) that signatures of modeled CO_2 plume transport and sectoral emissions can be enhanced when modeling analysis of CO is also considered. We show in Figures 7, 8, and 9 our CO_2 and CO simulation results over the KORUS-AQ domain along with associated $FFCO_2$ tags. Our goal is to disaggregate the modeled CO_2 into regional and sectoral contributions and show complementary information when corresponding 3D CO fields are shown in conjunction with these CO_2 fields.

In Figure E7, we show that modeled CO_2 and CO have similar spatial pattern over this region. The similarity of CO_2 and CO, which is evident over areas of combustion, is even more pronounced with $FFCO_2$ and CO in both at the surface and aloft. This is consistent with the DC-8 vertical profiles where enhancements in CO can be found in some of the layers. This also supports our argument that CO can be a good tracer of $FFCO_2$. Some features in this comparison also reveals additional information from CO. There is high CO_2 signature over Seoul and EA-S that are not very apparent in CO. High CO_2 signatures are associated with mostly $FFCO_2$ (EA-M, EA-N) and fire (EA-S) emissions. It is possible therefore that either $FFCO_2$ emissions over Seoul is overestimated and fire CO_2 over EA-S is underestimated or our assumption of combustion efficiency (CE) for these regions is not accurate. These signatures can be clearly seen in Figure E8. We show a zoom-in version of Figure E8 with a side-by-side comparison of CO_2 and CO and their associated tags at the surface and also across the mean vertical profile. Again, CO_2 and CO show similar spatial patterns but emission signatures and vertical structures are more enhanced in CO. There appears to be high CO contributions from EA-M and EA-N at the surface (even towards Seoul). There is also a relatively high CO_2 and $FFCO_2$ over Seoul that is not reflected in CO and FFCO but only $FFCO_2$ from Korea. Transport of FF plumes from EA-S is more evident aloft in FFCO than $FFCO_2$ from EA-S. This is also the case for $FFCO_2$ from EA-N where higher FFCO from EA-N can be seen aloft but not in $FFCO_2$.

While the contributions in $FFCO_2$ from these regions can be elucidated by disaggregating the modeled $FFCO_2$ into regional $FFCO_2$ tags, accurate source apportionment requires sufficient data with high precision to constrain the $FFCO_2$ inverse problem. This can be complemented by calibrating (offline) modeled $FFCO_2$ using CO data especially when there is a lack of CO_2 data spatiotemporal coverage, including vertical information when column CO_2 retrievals are used. An observationally-constrained modeled CO (chemical analysis or reanalysis) can also be used to probe these contributions in conjunction with CO_2 data assimilation. This is particularly appealing to carry out with the advent of high-resolution CO retrieval products such as TROPOMI (Veefkind et al., 2012) and availability of a long record of CO retrievals from IASI (George et al. 2015) and MOPITT (Deeter et al., 2018). It should be noted, however, that such analyses cannot stand alone and a carefully design multi-species assimilation framework is required to effectively substantiate this complementary information. Here, we suggest that such joint CO_2 and CO analysis offers

some diagnostics on the fidelity of modeled $FFCO_2$, in particular regarding inconsistencies between $FFCO_2$ and CO.

Finally, we present in Figure E9 another side-by-side comparison of modeled CO_2 and CO and their associated tags, but now showing the temporal evolution of the vertical profile over Seoul during KORUS-AQ. A similar figure for Beijing and Shanghai is presented in the supplementary material (Figure ES2, ES3). Here, we can see evidence of plume signatures passing over Seoul and diurnal variations in boundary layer mixing and dilution affecting CO_2. Enhanced $FFCO_2$ can also be observed near the surface to about 800 hPa during the day. This is quite obscured by a moderate $FFCO_2$ 'background' aloft. Contributions to $FFCO_2$ from Korea (although dominant) cannot account for all $FFCO_2$. Some $FFCO_2$ are contributed by $FFCO_2$ from East Asia especially EA-M and EA-N. While most of EA-S plumes comes from fire emissions as reported in Tang et al., (2019), intermittent signatures of $FFCO_2$ plume transport from EA-S can be seen aloft. The ROW contributes as well to the background $FFCO_2$ over Seoul. These $FFCO_2$ and regional contributions can be better observed with FFCO and its associated tags. We highlight its importance especially when diagnosing the vertical extent of $FFCO_2$ without $FFCO_2$ tags in hand. Yet even with $FFCO_2$ tags, the modeled contributions of $FFCO_2$ from EA-M and EA-N, for example, appear to be low compared to CO. Note that CO over Seoul is still underestimated relative to DC-8 CO (even over the West Sea where East Asian outflow was targeted during the campaign, see Figure E4 and Table E4). In Tang et al. (2019), we investigated different emission scenarios including doubling FFCO and VOCs from EA and Korea, which is the scenario used in this study. And so, the high CO enhancements from FFCO EA-N and EA-M are not overestimated; in fact they may still be underestimated. The low $FFCO_2$ from these regions imply either an underestimation of $FFCO_2$ emissions or stronger sink (including mixing and dilution) than the actual sinks along the transect of the plumes to Seoul (see Figure E8 as well). We alluded to this underestimation in our evaluation of modeled $FFCO_2$ (section 5.1), where we suggest that $FFCO_2$ from East Asia is underestimated after a regression analysis of $FFCO_2$.

We can also investigate the modeled profiles using the $^{14}CO_2$ samples that we considered as outliers (sample 33, 35, and 40). These samples were taken over the West Sea and Seoul on May 21, 24 and June 4, respectively (see Figure E6). During May 17-22, persistent high pressure and stagnant conditions occurred while a blocking pattern occurred with no significant change in

meteorology during June 1-6 (Miyazaki et al. 2018). $FFCO_2$ is significantly underestimated in these samples. Both CO and CO_2 in these samples are also significantly low. This consistency between CO and CO_2 (as well as $FFCO_2$) are well defined in Figure E9.

5.3 On Combustion Efficiency

The use of joint CO and CO_2 analysis is typically associated with characterizing combustion efficiency for a given plume or source. This is usually quantified as enhancement ratios of CO to CO_2. Higher ratios correspond to more incomplete combustion (i.e., more CO is produced). We have investigated in detail the ratios observed during KORUS-AQ in our evaluation of CAMS forecast and analyses products (Tang et al., 2018, 2019). Briefly, we found that air from East Asia are less efficient than air from Seoul. Our finding, however, was mainly based on a few assumptions and expert classification (or flight grouping) of air samples. This approach can be problematic when ratios are used to constrain CE in operational mode (e.g., forecasting or analysis) since these ratios have significant variations from sample to sample. This was highlighted in Ammoura et al., (2016) as a limitation on the use of these ratios. Our previous work on deriving ratios based on satellite retrievals from GOSAT and MOPITT (Silva et al., 2013) also suffered a similar limitation. In fact, we reported ratios only for winter months since we found a strong seasonality of these ratios. Mixed processes can confound our findings based on regression analysis of data that exhibit non-stationarity and non-linearity. A related point was also raised by Shiga et al. (2014) that estimates of $FFCO_2$ emissions is only accurate with analysis of data during winter months while notwithstanding the fact that there are limited data available for the analysis. For our case, the use of CO and CO_2 breaks down during the summer as confounding factors (e.g., OH, biogenic sources, biospheric sinks) can influence the analysis. While we report the associated ratios in Table E4 based on NOAA CCGG, TCCON and OCO-2/MOPITT, these ratios should only be interpreted as approximate tightness on the relationship of CO and CO_2 observed at a given site or region. It does not make sense to associate these ratios with CE for a given plume or source since they are derived from an entire year of data (CCGG, TCCON) or averaged across a large domain (KORUS-AQ). In summary, the use of ratios to identify CE is strongly suggested only for near-field studies with careful consideration on the validity of non-stationary and non-linear assumptions.

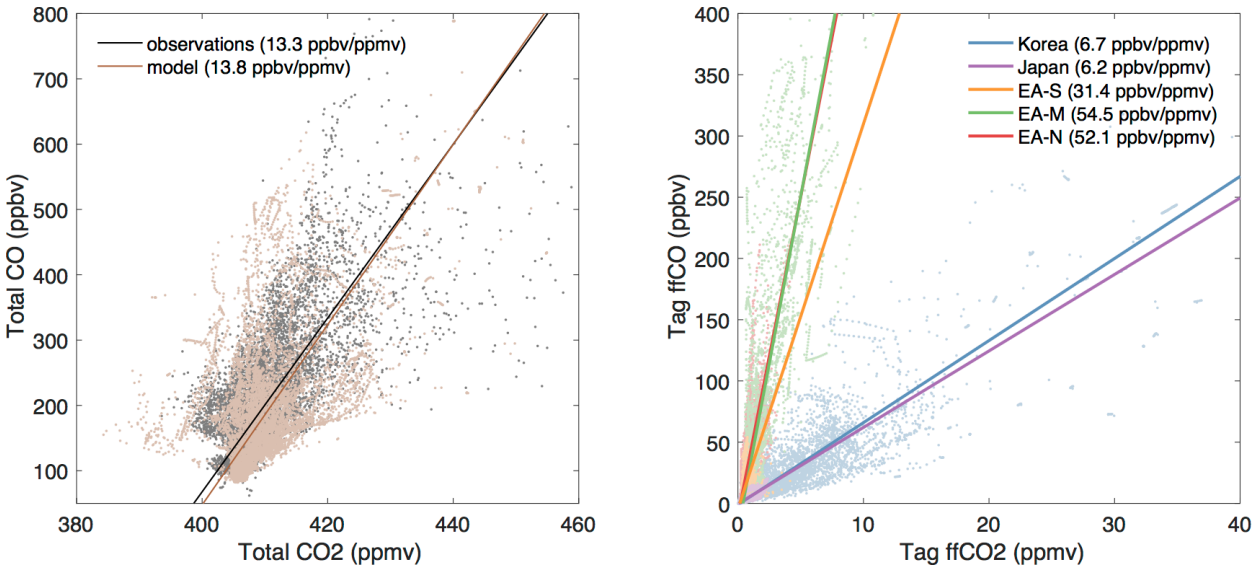

Figure E10. Comparison between observed (black) and modeled (brown) total CO_2 and CO mixing ratios (left panel) and corresponding association of modeled FFCO and $FFCO_2$ tags.

Figure E10 shows an example of an approach that may be more appropriate when applying these ratios to CE. The left panel in Figure E10 shows a scatter plot of CO_2 and CO based on DC-8 measurements and model equivalents from our CAM-Chem simulations. The overall observed dCO/dCO_2 of 13.3 ppbv/ppmv is very well captured by CAM-chem (13.8 ppbv/ppmv). This is consistent with the ratios derived from CAMS CO and CO_2 forecasts and analyses (Tang et al. 2018). Notably, this value represents air that is relatively efficient. When these ratios are broken down into flight groups, we see that this ratio is more representative of air from Seoul (~9 ppbv/ppmv) than East Asia (as represented by West Sea flight group, ~28 ppbv/ppmv). We could not have known this without classifying the data into representative flight groups. This was convenient for us since KORUS-AQ was a dedicated campaign aimed to characterize pollution plumes over Seoul and plumes entering Korea. Differentiating CE between Seoul and East Asia without such ancillary information becomes more difficult. Here, we show that this can also be done using tags of FFCO and $FFCO_2$. In particular, we show in the right panel of Figure E10 the corresponding scatter plot for FFCO and $FFCO_2$ and broken down into their associated regional tags. We find that $dFFCO/dFFCO_2$ from Korea (6.7 ppbv/ppmv) is lower than from EA-N and EA-M (~52-55 ppbv/ppmv), indicating that anthropogenic combustion in Korea has higher CE than that in East Asia. Again, this is consistent with previous studies (e.g., Suntharalingam et al., 2004; Wang et al., 2010; Turnbull et al., 2011; Silva et al., 2013). More importantly, this shows

that the overall dCO/dCO_2 is a mixture of different air masses. Assuming that the total ratio is representative of FFCO and $FFCO_2$, we can regress this data and find that the contribution of East Asia is about 15% of 13.8 ppbv/ppmv and that this ratio is mostly influenced by Korean air masses. The capability to identify the contributions in observed CE is highlighted here. We do not suggest however that this be carried out in every assimilation (or inversion) window. Note that the data we used for deriving this ratio covers the entire KORUS-AQ period with a mix of data sampled near surface and aloft). We suggest a 'model calibration' approach where $FFCO_2$ emissions is adjusted based on $FFCO_2$ and FFCO at a spatiotemporal scale that is representative of the best possible change in CE. In particular, changes in $FFCO_2$ emissions due to changes in CE (through improved technology, pollution abatement, changes in fuel mixture, process changes, or even abrupt shutdown of a power plant) do not manifest at diurnal scale or in every assimilation window (e.g., 6-hourly). Ratios derived at shorter scale can be noisy. Smoothing algorithms or a longer assimilation window should be used if CE needs to be constrained in tandem with $FFCO_2$ emission adjustments. Changes in emissions due to changes in CE is usually detectable at a far longer spatiotemporal scale. This is our suggested approach even with availability of a larger number of CO and CO_2 data constraints to minimize assimilating noisy data that may potentially lead to systematic methodological biases in emission adjustments.

In summary, we find that dCO/dCO_2 ratios can be more effectively use to diagnose inconsistencies in CE using the associated tags especially with FFCO and $FFCO_2$. We find that observed enhancement ratios are dominantly influenced by more efficient air from Korea and with a moderate contribution from less efficient air from East Asia. However, a carefully designed assimilation system is required to effectively incorporate these constraints in inverse modeling systems. If this is not feasible, we suggest a more conservative 'model calibration' approach instead to minimize misattribution or unrealistic emission adjustments.

6 Summary and Implications

In this study, we present key demonstrations on the utility of a joint CO_2 and CO analysis. Given the increasing importance in science and policy of accurately tracking and quantifying $FFCO_2$, this study is placed within the context of constraining transport models of CO_2 with observational and modeling information from CO. We use the recent KORUS-AQ field campaign as our test case

region given extensive measurements during this campaign that are focused on sampling pollution plumes over Seoul and plumes entering Korea. This study focuses on directly investigating abundance rather than emissions as this is the most tractable and natural way to link CO_2 observations with identifiable CO constraints. First, we evaluate model simulations of CO and CO_2 based on observationally-constrained surface fluxes for CO_2 and a 'best emission scenario' for CO. This is done within the atmospheric chemistry component of CESM (CAM-Chem) rather than in the land (CLM) or atmospheric component (CAM) to develop a future capability of simulating AQ and GHG in a more consistent and interactive manner. We used collocated CO_2 and CO measurements from flask sample (NOAA CCGG), ground-based remote sensing (TCCON), airborne measurements during KORUS-AQ (including $^{14}CO_2$), as well as XCO_2 and XCO retrievals from space-based remote sensing (OCO-2 and MOPITT) in order to encapsulate complementary information that can be derived from these observational platforms. We also introduce a tagging capability that we further developed for CO_2 and CO in CAM-Chem to help track sectoral and/or regional contributions to $FFCO_2$. This is similar to the approach used in previous atmospheric CO_2 Bayesian synthesis inversions. While noting that such techniques can introduce aggregation errors and are sensitive to *a priori* flux spatiotemporal distribution, we view this as an informative tool given the relatively cheaper computing cost these days of adding a number of tracers in models (albeit still expensive in terms of matrix inversions, memory, and storage). We then used these $FFCO_2$ and FFCO tags to elucidate constraints from CO in terms of identifying relative combustion efficiencies of sampled air during KORUS-AQ (including inconsistencies in $FFCO_2$) and enhancing signatures of transport and mixing of atmospheric CO_2.

Our results show that the modeled CO_2, CO, and $FFCO_2$ are reasonably consistent with measurements across platforms. Errors in simulated abundance are within the range of uncertainties of current global CO_2 transport models and inversion systems as well as global chemical transport models for CO. While this is expected considering that the fluxes and emissions have already been adjusted to match their corresponding observations (through inversions in the case of CO_2 or tuning in the case of CO), these results indicate that there are no significant systematic errors in our implementation of a 'tracer mode' version of global atmospheric CO_2 and CO modeling. Most notably, the modeled $FFCO_2$ is generally consistent with observed $FFCO_2$ derived from radiocarbon measurements during KORUS-AQ. This provides confidence on the fidelity of $FFCO_2$ in CAM-Chem. We find that simulations of regionally-tagged $FFCO_2$ and FFCO

reveal significantly higher combustion efficiency in air samples from Korea than East Asia. This is consistent with previous studies, we highlight the utility of using these tags to assess and quantify the contributions of different $FFCO_2$ sources to observed enhancement ratios. This is particularly appealing since analysis of these observed enhancement ratios suffer from lack of collocated CO_2 and CO data but more importantly from the validity of stationarity assumption especially when the analysis is applied to long observational windows. The use of these tags provides a means to calibrate the modeled abundances without needing to classify data into groups and to filter data for confounding factors. Based on our results and previous studies, we find that the modeled response (abundance) of $FFCO_2$ emissions from East Asia appears to be underestimated while the modeled response (abundance) of $FFCO_2$ emissions from Korea is overestimated. We emphasize that this result can be used to calibrate $FFCO_2$ emissions prior to data assimilation. Lastly, we show, albeit qualitatively, that signatures of plume transport and sectoral emissions of CO_2 are enhanced with CO analyses. Our intention is to show that such type of analysis can be used at first to diagnose inconsistencies in transport patterns as well as emission patterns between $FFCO_2$ and CO. The former is related to model errors in boundary layer mixing, convection, and transport of constituents in frontal systems. We recognize that this is not trivial to diagnose although CO has been used in the past as tracers of constituent transport because of its medium lifetime. We do not suggest however that this be carried out to directly adjust $FFCO_2$ emissions as it is difficult to disentangle errors in transport from errors in emissions or fluxes without messing up the other. The latter, on the other hand, is related to diagnosing combustion efficiency and monitoring emission factors in current inventories, as well as identifying non-$FFCO_2$ contributions such as fire CO_2. CO from biomass burning has been previously studied since CO is one of the main constituents in smoke.

With this, we propose that the community should start considering incorporating this type of analysis, especially to help in designing integrated observing systems for carbon monitoring. We are cognizant, however, on the limitations of incorporating these CO constraints in current inversion systems. The role of chemistry in greenhouse gas monitoring, especially for $FFCO_2$, is increasingly becoming relevant given past and on-going efforts to better quantify emissions for air quality and public health; but more importantly with the availability of a large number of complementary data (with global coverage) which can be used by the carbon community. We suggest augmenting the current carbon observing system to include AQ measurements. This is

especially the case with the advent of new missions (Geo-Carb, TROPOMI, GOSAT-2 and 3). We also suggest that AQ-related field campaigns be exploited as we have shown in this study. All these, of course, should only complement the more pressing problem in carbon community, which is to better constrain our understanding of the biospheric and oceanic CO_2 flux and their carbon dynamics.

Acknowledgements

This study is supported by NNX16AE16G and NNX17AG39G. We also thank the CESM and CAM-chem team for technical support. CESM is sponsored by the National Science Foundation (NSF) and the U.S. Department of Energy (DOE). Administration of the CESM is maintained by the Climate and Global Dynamics Division (CGD) at the National Center for Atmospheric Research (NCAR). We thank CarbonTracker, CarbonTracker-Europe, and CAMS greenhouse gases inversion team for CO2 fluxes. We thank HTAP and FINN team for the CO emission inventories. We thank the KORUS-AQ team for the measurements. We thank TCCON team for the TCCON observations. We thank NOAA ESRL Carbon Cycle Cooperative Global Air Sampling Network for the surface air flask sampling data. We acknowledge MOPITT and OCO-2 teams for CO and CO_2 data, respectively. The NCAR MOPITT project is supported by the National Aeronautics and Space Administration (NASA) Earth Observing System (EOS) Program.

References

Al-Saadi, Jassim, Gregory Carmichael, James Crawford, Louisa Emmons, Saewung Kim, Chang-Keun Song, Lim-Seok Chang, Gangwoong Lee, Jhoon Kim, Rokjin Park: KORUS-AQ: An International Cooperative Air Quality Field Study in Korea, *the KORUS-AQ white paper* (https://espo.nasa.gov/korus-aq/content/KORUS-AQ_White_Paper), 2014.

Ammoura, L., Xueref-Remy, I., Vogel, F., Gros, V., Baudic, A., Bonsang, B., Delmotte, M., Té, Y., and Chevallier, F.: Exploiting stagnant conditions to derive robust emission ratio estimates for CO2, CO and volatile organic compounds in Paris, Atmos. Chem. Phys., 16, 15653-15664, https://doi.org/10.5194/acp-16-15653-2016, 2016.

Anderson, J., Hoar, T., Raeder, K., Liu, H., Collins, N., Torn, R. and Avellano, A.: The data assimilation research testbed: A community facility. Bulletin of the American Meteorological Society, 90(9), pp.1283-1296, 2009.

Andres, R.J., Boden, T.A., Bréon, F.M., Ciais, P., Davis, S., Erickson, D., Gregg, J.S., Jacobson, A., Marland, G., Miller, J. and Oda, T.: A synthesis of carbon dioxide emissions from fossil-fuel combustion. *Biogeosciences*, 9(5), pp.1845-1871, 2012.

Andres, R.J., Boden, T.A., and Higdon, D.M.: Gridded uncertainty in fossil fuel carbon dioxide emission maps, a CDIAC example, *Atmospheric Chemistry and Physics*, 16, 14979-14995, https://doi.org/10.5194/acp-16-14979-2016, 2016.

Arellano Jr, A.F. and Hess, P.G.: Sensitivity of top-down estimates of CO sources to GCTM transport. Geophysical research letters, 33(21), 2006.

Arellano Jr, A.F., Raeder, K., Anderson, J.L., Hess, P.G., Emmons, L.K., Edwards, D.P., Pfister, G.G., Campos, T.L. and Sachse, G.W.: Evaluating model performance of an ensemble-based chemical data assimilation system during INTEX-B field mission. Atmospheric Chemistry and Physics, 7(21), pp.5695-5710, 2007.

Asefi-Najafabady, S., Rayner, P.J., Gurney, K.R., McRobert, A., Song, Y., Coltin, K., Huang, J., Elvidge, C. and Baugh, K.: A multiyear, global gridded fossil fuel CO2 emission data product: Evaluation and analysis of results. Journal of Geophysical Research: Atmospheres, 119(17), pp.10-213, 2014.

Baklanov, A., Molina, L.T. and Gauss, M.: Megacities, air quality and climate. *Atmospheric Environment*, 126, pp.235-249, 25, 2016.

Barré, J., Gaubert, B., Arellano, A.F., Worden, H.M., Edwards, D.P., Deeter, M.N., Anderson, J.L., Raeder, K., Collins, N., Tilmes, S. and Francis, G.: Assessing the impacts of assimilating IASI and MOPITT CO retrievals using CESM-CAM-chem and DART. Journal of Geophysical Research: Atmospheres, 120(19), pp.10-501, 2015.

Basu, S., Houweling, S., Peters, W., Sweeney, C., Machida, T., Maksyutov, S., Patra, P.K., Saito, R., Chevallier, F., Niwa, Y. and Matsueda, H.: The seasonal cycle amplitude of total column CO2: Factors behind the model-observation mismatch. Journal of Geophysical

Research: Atmospheres, 116 (D23), 2011.

Basu, S., Miller, J.B. and Lehman, S.: Separation of biospheric and fossil fuel fluxes of CO_2 by atmospheric inversion of CO_2 and $^{14}CO_2$ measurements: Observation System Simulations. *Atmospheric Chemistry and Physics*, 16(9), 2016.

Beirle, S., Boersma, K. F., Platt, U., Lawrence, M.G., and Wagner, T.: Megacity emissions and lifetimes of nitrogen oxides probed from space. Science, 333(6050), 1737-1739, 2011.

Berezin, E.V., Konovalov, I.B., Ciais, P., Richter, A., Tao, S., Janssens-Maenhout, G., Beekmann, M., and Schulze, E.-D.: Multiannual changes of CO2 emissions in China: indirect estimates derived from satellite measurements of tropospheric NO2 columns, Atmos. Chem. Phys., 13, 9415-9438, https://doi.org/10.5194/acp-13-9415-2013, 2013.

Berhanu, T.A., Szidat, S., Brunner, D., Satar, E., Schanda, R., Nyfeler, P., Battaglia, M., Steinbacher, M., Hammer, S. and Leuenberger, M.: Estimation of the fossil fuel component in atmospheric CO2 based on radiocarbon measurements at the Beromünster tall tower, Switzerland. Atmospheric chemistry and physics, 17(17), pp.10753-10766, 2017.

Boesch, H., Baker, D., Connor, B., Crisp, D. and Miller, C.: Global characterization of CO2 column retrievals from shortwave-infrared satellite observations of the Orbiting Carbon Observatory-2 mission. Remote Sensing, 3(2), pp.270-304, 2011.

Brioude, J., Angevine, W. M., Ahmadov, R., Kim, S.-W., Evan, S., McKeen, S. A., Hsie, E.-Y., Frost, G. J., Neuman, J. A., Pollack, I. B., Peischl, J., Ryerson, T. B., Holloway, J., Brown, S. S., Nowak, J. B., Roberts, J. M., Wofsy, S. C., Santoni, G. W., Oda, T., and Trainer, M.: Top-down estimate of surface flux in the Los Angeles Basin using a mesoscale inverse modeling technique: assessing anthropogenic emissions of CO, NOx and CO2 and their impacts, Atmos. Chem. Phys., 13, 3661-3677, https://doi.org/10.5194/acp-13-3661-2013, 2013.

Brophy, K., Graven, H., Manning, A.J., White, E., Arnold, T., Fischer, M.L., Jeong, S., Cui, X. and Rigby, M.: Characterizing uncertainties in atmospheric inversions of fossil fuel CO2 emissions in California. Atmospheric Chemistry and Physics, 19(5), pp.2991-3006, 2019.

Broxton, P.D., Zeng, X., Sulla-Menashe, D. and Troch, P.A.: A global land cover climatology using MODIS data. Journal of Applied Meteorology and Climatology, 53(6), pp.1593-1605, 2014.

Butz, A., Guerlet, S., Hasekamp, O., Schepers, D., Galli, A., Aben, I., Frankenberg, C., Hartmann, J.M., Tran, H., Kuze, A. and Keppel-Aleks, G.: Toward accurate CO2 and CH4 observations from GOSAT. Geophysical Research Letters, 38(14), 2011.

Chevallier, F., M. Fisher, P. Peylin, S. Serrar, P. Bousquet, F.-M. Bréon, A. Chédin, and P. Ciais: Inferring CO2 sources and sinks from satellite observations: method and application to TOVS data. J. Geophys. Res., 110, D24309, doi:10.1029/2005JD006390, 2005.

Chevallier, F., Ciais, P., Conway, T. J., Aalto, T., Anderson, B. E., Bousquet, P., Brunke, E. G.,

Ciattaglia, L., Esaki, Y., Fröhlich, M., Gomez, A., Gomez-Pelaez, A. J., Haszpra, L., Krummel, P. B., Langenfelds, R. L., Leuenberger, M., Machida, T., Maignan, F., Matsueda, H., Morgui, J. A., Mukai, H., Nakazawa, T., Peylin, P., Ramonet, M., Rivier, L., Sawa, Y., Schmidt, M., Steele, L. P., Vay, S. A., Vermeulen, A. T., Wofsy, S., and Worthy, D.: CO2 surface fluxes at grid point scale estimated from a global 21-year reanalysis of atmospheric measurements, J. Geophys. Res., 115, D21307, doi:10.1029/2010JD013887, 2010.

Chevallier, F.: On the parallelization of atmospheric inversions of CO2 surface fluxes within a variational framework, Geosci. Model Dev., 6, 783-790, https://doi.org/10.5194/gmd-6-783-2013, 2013.

Chevallier, F., Palmer, P.I., Feng, L., Boesch, H., O'Dell, C.W. and Bousquet, P.: Toward robust and consistent regional CO2 flux estimates from in situ and spaceborne measurements of atmospheric CO2. Geophysical Research Letters, 41(3), pp.1065-1070, 2014.

Chevallier, F., Description of the CO2 inversion production chain. CAMS deliverable CAMS73_2015SC3_D73.1.5.6_201803_CO2 inversion production chain_v1. http://atmosphere.copernicus.eu/, 2018.

Choi, Y. and Wang, Y.: Dynamics of carbon sequestration in a coastal wetland using radiocarbon measurements. Global Biogeochemical Cycles, 18(4), 2004.

Ciais, P., Paris, J.D., Marland, G., Peylin, P., Piao, S.L., Levin, I., Pregger, T., Scholz, Y., Friedrich, R., Rivier, L. and Houwelling, S.: The European carbon balance. Part 1: fossil fuel emissions. *Global Change Biology*, 16(5), pp.1395-1408, 2010.

Ciais, P., Dolman, A.J., Bombelli, A., Duren, R., Peregon, A., Rayner, P.J., Miller, C., Gobron, N., Kinderman, G., Marland, G. and Gruber, N.: Current systematic carbon-cycle observations and the need for implementing a policy-relevant carbon observing system. *Biogeosciences*, 11, pp.3547-3602, 2014.

Ciais, P., Crisp, D., Van Der Gon, H.D., Engelen, R., Janssens-Maenhout, G., Heiman, M., Rayner, P. and Scholze, M., 2015. Towards a European operational observing system to monitor fossil CO2 emissions. Final Report from the expert group, European Comission.

Cogan, A.J., Boesch, H., Parker, R.J., Feng, L., Palmer, P.I., Blavier, J.F., Deutscher, N.M., Macatangay, R., Notholt, J., Roehl, C. and Warneke, T.: Atmospheric carbon dioxide retrieved from the Greenhouse gases Observing SATellite (GOSAT): Comparison with ground-based TCCON observations and GEOS-Chem model calculations. Journal of Geophysical Research: Atmospheres, 117(D21), 2012.

Creutzig, F., Baiocchi, G., Bierkandt, R., Pichler, P.P. and Seto, K.C.: Global typology of urban energy use and potentials for an urbanization mitigation wedge. *Proceedings of the National Academy of Sciences*, 112(20), pp.6283-6288, 2015.

Deeter, M. N., Martínez-Alonso, S., Edwards, D. P., Emmons, L. K., Gille, J. C., Worden, H. M., Sweeney, C., Pittman, J. V., Daube, B. C., and Wofsy, S. C.: The MOPITT Version 6 product: algorithm enhancements and validation, Atmos. Meas. Tech., 7, 3623–3632,

https://doi.org/10.5194/amt-7-3623-2014, 2014.

Deeter, M.N., Edwards, D.P., Francis, G.L., Gille, J.C., Martínez-Alonso, S., Worden, H.M. and Sweeney, C.: A climate-scale satellite record for carbon monoxide: the MOPITT Version 7 product. Atmospheric Measurement Techniques, 10(7), pp.2533-2555, 2017.

Djuricin, S., Pataki, D.E. and Xu, X.: A comparison of tracer methods for quantifying CO_2 sources in an urban region. *Journal of Geophysical Research: Atmospheres*, 115(D11), 2010.

Dlugokencky, E.J., Lang, P.M., Mund, J.W., Crotwell, A.M., Crotwell, M.J., and Thoning, K.W.: Atmospheric Carbon Dioxide Dry Air Mole Fractions from the NOAA ESRL Carbon Cycle Cooperative Global Air Sampling Network, 1968-2017, Version: 2018-07-31, Path: ftp://aftp.cmdl.noaa.gov/data/trace_gases/co2/flask/surface/, 2018.

Duren, R.M. and Miller, C.E.: Measuring the carbon emissions of megacities. *Nature Climate Change*, 2(8), p.560, 2012.

Edwards, D.P., Emmons, L.K., Hauglustaine, D.A., Chu, D.A., Gille, J.C., Kaufman, Y.J., Pétron, G., Yurganov, L.N., Giglio, L., Deeter, M.N. and Yudin, V.: Observations of carbon monoxide and aerosols from the Terra satellite: Northern Hemisphere variability. Journal of Geophysical Research: Atmospheres, 109(D24), 2004.

Edwards, D.P., Emmons, L.K., Gille, J.C., Chu, A., Attié, J.L., Giglio, L., Wood, S.W., Haywood, J., Deeter, M.N., Massie, S.T. and Ziskin, D.C.: Satellite-observed pollution from Southern Hemisphere biomass burning. Journal of Geophysical Research: Atmospheres, 111(D14), 2006.

Eldering, A., Wennberg, P.O., Viatte, C., Frankenberg, C., Roehl, C.M. and Wunch, D.: The Orbiting Carbon Observatory-2: First 18 months of science data products. Atmospheric Measurement Techniques, 10(2), pp.549-563, 2017.

Fioletov, V.E., McLinden, C.A., Krotkov, N., Yang, K., Loyola, D.G., Valks, P., Theys, N., Van Roozendael, M., Nowlan, C.R., Chance, K. and Liu, X.: Application of OMI, SCIAMACHY, and GOME-2 satellite SO2 retrievals for detection of large emission sources. Journal of Geophysical Research: Atmospheres, 118(19), pp.11-399, 2013.

Fisher, J. A., Murray, L. T., Jones, D. B. A., and Deutscher, N. M.: Improved method for linear carbon monoxide simulation and source attribution in atmospheric chemistry models illustrated using GEOS-Chem v9, Geoscientific Model Development, 10, 4129-4144, https://doi.org/10.5194/gmd-10-4129-2017, 2017.

Folberth, G.A., Butler, T.M., Collins, W.J. and Rumbold, S.T.: Megacities and climate change–A brief overview. Environmental Pollution, 203, pp.235-242, 2015.

Gamnitzer, U., Karstens, U., Kromer, B., Neubert, R.E., Meijer, H.A., Schroeder, H. and Levin, I.: Carbon monoxide: A quantitative tracer for fossil fuel CO_2?. *Journal of Geophysical Research: Atmospheres*, 111(D22), 2006.

Gately, C.K. and Hutyra, L.R.: Large uncertainties in urban-scale carbon emissions. *Journal of Geophysical Research: Atmospheres*, 122(20), pp.11-242, 2017.

Gaubert, B., Arellano, A.F., Barré, J., Worden, H.M., Emmons, L.K., Tilmes, S., Buchholz, R.R., Vitt, F., Raeder, K., Collins, N. and Anderson, J.L.: Toward a chemical reanalysis in a coupled chemistry-climate model: An evaluation of MOPITT CO assimilation and its impact on tropospheric composition. Journal of Geophysical Research: Atmospheres, 121(12), pp.7310-7343, 2016.

Gaubert, B., Stephens, B.B., Basu, S., Chevallier, F., Deng, F., Kort, E.A., Patra, P.K., Peters, W., Rödenbeck, C., Saeki, T. and Schimel, D.: Global atmospheric CO2 inverse models converging on neutral tropical land exchange, but disagreeing on fossil fuel and atmospheric growth rate. Biogeosciences, 16(1), pp.117-134, 2019.

Gelaro, R., McCarty, W., Suárez, M.J., Todling, R., Molod, A., Takacs, L., Randles, C.A., Darmenov, A., Bosilovich, M.G., Reichle, R. and Wargan, K.: The modern-era retrospective analysis for research and applications, version 2 (MERRA-2). Journal of Climate, 30(14), pp.5419-5454, 2017.

George, M., Clerbaux, C., Bouarar, I., Coheur, P.F., Deeter, M.N., Edwards, D.P., Francis, G., Gille, J.C., Hadji-Lazaro, J., Hurtmans, D. and Inness, A.: An examination of the long-term CO records from MOPITT and IASI: comparison of retrieval methodology. Atmospheric Measurement Techniques, 8, pp.4313-4328, 2015.

Graven, H.D., Stephens, B.B., Guilderson, T.P., Campos, T.L., Schimel, D.S., Campbell, J.E. and Keeling, R.F.: Vertical profiles of biospheric and fossil fuel-derived CO2 and fossil fuel CO2: CO ratios from airborne measurements of Δ14C, CO2 and CO above Colorado, USA. Tellus B: Chemical and Physical Meteorology, 61(3), pp.536-546, 2009.

Graven, H., Hocking, T. and Zazzeri, G.: Detection of Fossil and Biogenic Methane at Regional Scales Using Atmospheric Radiocarbon. Earth's Future, https://doi.org/10.1029/2018EF001064, 2019.

Goo, T.-Y., Y.-S. Oh, V. A. Velazco.: TCCON data from Anmeyondo, South Korea, Release GGG2014R0. TCCON data archive, hosted by CaltechDATA, California Institute of Technology, Pasadena, CA, U.S.A. https://doi.org/10.14291/tccon.ggg2014.anmeyondo01.R0/1149284, 2017.

Gurney, K.R., Law, R.M., Denning, A.S., Rayner, P.J., Baker, D., Bousquet, P., Bruhwiler, L., Chen, Y.H., Ciais, P., Fan, S. and Fung, I.Y.: Towards robust regional estimates of CO2 sources and sinks using atmospheric transport models. Nature, 415(6872), p.626, 2002.

Gurney, K.R., Law, R.M., Denning, A.S., Rayner, P.J., Baker, D., Bousquet, P., Bruhwiler, L., Chen, Y.H., Ciais, P., Fan, S. and Fung, I.Y.: TransCom 3 CO2 inversion intercomparison: 1. Annual mean control results and sensitivity to transport and prior flux information. Tellus B: Chemical and Physical Meteorology, 55(2), pp.555-579, 2003.

Gurney, K.R., Law, R.M., Denning, A.S., Rayner, P.J., Pak, B.C., Baker, D., Bousquet, P., Bruhwiler, L., Chen, Y.H., Ciais, P. and Fung, I.Y.: Transcom 3 inversion intercomparison: Model mean results for the estimation of seasonal carbon sources and sinks. Global Biogeochemical Cycles, 18(1), 2004.

Gurney, K.R., Chen, Y.H., Maki, T., Kawa, S.R., Andrews, A. and Zhu, Z.: Sensitivity of atmospheric CO2 inversions to seasonal and interannual variations in fossil fuel emissions. Journal of Geophysical Research: Atmospheres, 110(D10), 2005.

Gurney, K.R., Mendoza, D.L., Zhou, Y., Fischer, M.L., Miller, C.C., Geethakumar, S. and de la Rue du Can, S.: High resolution fossil fuel combustion CO2 emission fluxes for the United States. Environmental science & technology, 43(14), pp.5535-5541, 2009.

Gurney, K.R., Razlivanov, I., Song, Y., Zhou, Y., Benes, B. and Abdul-Massih, M.: Quantification of fossil fuel CO2 emissions on the building/street scale for a large US city. Environmental science & technology, 46(21), pp.12194-12202, 2012.

Gurney, K.R., Liang, J., O'Keeffe, D., Patarasuk, R., Hutchins, M., Huang, J., Rao, P. and Song, Y.: Comparison of Global Downscaled Versus Bottom-Up Fossil Fuel CO2 Emissions at the Urban Scale in Four US Urban Areas. Journal of Geophysical Research: Atmospheres, https://doi.org/10.1029/2018JD028859, 2019.

Hakkarainen, J., Ialongo, I. and Tamminen, J.: Direct space-based observations of anthropogenic CO2 emission areas from OCO-2. Geophysical Research Letters, 43(21), 2016.

Hogue, S., Marland, E., Andres, R.J., Marland, G. and Woodard, D.: Uncertainty in gridded CO2 emissions estimates. Earth's Future, 4(5), pp.225-239, 2016.

Houweling, S., Bergamaschi, P., Chevallier, F., Heimann, M., Kaminski, T., Krol, M., Michalak, A. M., and Patra, P.: Global inverse modeling of CH4 sources and sinks: an overview of methods, Atmos. Chem. Phys., 17, 235-256, https://doi.org/10.5194/acp-17-235-2017, 2017.

Hsiao, T.C., Chen, W.N., Ye, W.C., Lin, N.H., Tsay, S.C., Lin, T.H., Lee, C.T., Chuang, M.T., Pantina, P. and Wang, S.H.: Aerosol optical properties at the Lulin Atmospheric Background Station in Taiwan and the influences of long-range transport of air pollutants. Atmospheric Environment, 150, pp.366-378, 2017.

Hurrell, J.W., Holland, M.M., Gent, P.R., Ghan, S., Kay, J.E., Kushner, P.J., Lamarque, J.F., Large, W.G., Lawrence, D., Lindsay, K. and Lipscomb, W.H.: The community earth system model: a framework for collaborative research. Bulletin of the American Meteorological Society, 94(9), pp.1339-1360, 2013.

Hutyra, L.R., Duren, R., Gurney, K.R., Grimm, N., Kort, E.A., Larson, E. and Shrestha, G.: Urbanization and the carbon cycle: Current capabilities and research outlook from the natural sciences perspective. *Earth's Future*, 2(10), pp.473-495, 2014.

Ishizawa, M., Uchino, O., Morino, I., Inoue, M., Yoshida, Y., Mabuchi, K., Shirai, T., Tohjima,

Y., Maksyutov, S., Ohyama, H. and Kawakami, S.: Large XCH 4 anomaly in summer 2013 over northeast Asia observed by GOSAT. Atmospheric Chemistry and Physics, 16(14), pp.9149-9161, 2016.

Janssens-Maenhout, G., Crippa, M., Guizzardi, D., Dentener, F., Muntean, M., Pouliot, G., Keating, T., Zhang, Q., Kurokawa, J., Wankmüller, R. and Denier van der Gon, H.: HTAP_v2. 2: a mosaic of regional and global emission grid maps for 2008 and 2010 to study hemispheric transport of air pollution. Atmospheric Chemistry and Physics, 15(19), pp.11411-11432, 2015.

Jing, Y., Wang, T., Zhang, P., Chen, L., Xu, N., and Ma, Y.: Global Atmospheric CO2 Concentrations Simulated by GEOS-Chem: Comparison with GOSAT, Carbon Tracker and Ground-Based Measurements. Atmosphere, 9(5), 175, 2018.

Kennedy, C.A., Stewart, I., Facchini, A., Cersosimo, I., Mele, R., Chen, B., Uda, M., Kansal, A., Chiu, A., Kim, K.G. and Dubeux, C.: Energy and material flows of megacities. *Proceedings of the National Academy of Sciences*, 112(19), pp.5985-5990, 2015.

Keppel-Aleks, G., Randerson, J.T., Lindsay, K., Stephens, B.B., Keith Moore, J., Doney, S.C., Thornton, P.E., Mahowald, N.M., Hoffman, F.M., Sweeney, C. and Tans, P.P.: Atmospheric carbon dioxide variability in the Community Earth System Model: Evaluation and transient dynamics during the twentieth and twenty-first centuries. Journal of Climate, 26(13), pp.4447-4475, 2013.

Konovalov, I.B., Berezin, E.V., Ciais, P., Broquet, G., Beekmann, M., Hadji-Lazaro, J., Clerbaux, C., Andreae, M.O., Kaiser, J.W. and Schulze, E.D.: Constraining CO2 emissions from open biomass burning by satellite observations of co-emitted species: a method and its application to wildfires in Siberia. Atmospheric Chemistry and Physics, 14, pp.10383-10410, 2014.

Kulawik, S., Wunch, D., O'Dell, C., Frankenberg, C., Reuter, M., Oda, T., Chevallier, F., Sherlock, V., Buchwitz, M., Osterman, G., Miller, C. E., Wennberg, P. O., Griffith, D., Morino, I., Dubey, M. K., Deutscher, N. M., Notholt, J., Hase, F., Warneke, T., Sussmann, R., Robinson, J., Strong, K., Schneider, M., De Mazière, M., Shiomi, K., Feist, D. G., Iraci, L. T., and Wolf, J.: Consistent evaluation of ACOS-GOSAT, BESD-SCIAMACHY, CarbonTracker, and MACC through comparisons to TCCON, Atmos. Meas. Tech., 9, 683-709, https://doi.org/10.5194/amt-9-683-2016, 2016.

Kuze, A., Suto, H., Nakajima, M. and Hamazaki, T.: Thermal and near infrared sensor for carbon observation Fourier-transform spectrometer on the Greenhouse Gases Observing Satellite for greenhouse gases monitoring. Applied optics, 48(35), pp.6716-6733, 2009.

Lamarque, J.F., Emmons, L.K., Hess, P.G., Kinnison, D.E., Tilmes, S., Vitt, F., Heald, C.L., Holland, E.A., Lauritzen, P.H., Neu, J. and Orlando, J.J.: CAM-chem: Description and evaluation of interactive atmospheric chemistry in the Community Earth System Model. Geoscientific Model Development, 5(2), p.369, 2012.

Lawrence, M. G., Butler, T. M., Steinkamp, J., Gurjar, B. R., and Lelieveld, J.: Regional pollution

potentials of megacities and other major population centers. Atmospheric Chemistry and Physics, 7(14), 3969-3987, 2007.

Le Quéré, C., Andrew, R. M., Friedlingstein, P., Sitch, S., Pongratz, J., Manning, A. C., Korsbakken, J. I., Peters, G. P., Canadell, J. G., Jackson, R. B., Boden, T. A., Tans, P. P., Andrews, O. D., Arora, V. K., Bakker, D. C. E., Barbero, L., Becker, M., Betts, R. A., Bopp, L., Chevallier, F., Chini, L. P., Ciais, P., Cosca, C. E., Cross, J., Currie, K., Gasser, T., Harris, I., Hauck, J., Haverd, V., Houghton, R. A., Hunt, C. W., Hurtt, G., Ilyina, T., Jain, A. K., Kato, E., Kautz, M., Keeling, R. F., Klein Goldewijk, K., Körtzinger, A., Landschützer, P., Lefèvre, N., Lenton, A., Lienert, S., Lima, I., Lombardozzi, D., Metzl, N., Millero, F., Monteiro, P. M. S., Munro, D. R., Nabel, J. E. M. S., Nakaoka, S.-I., Nojiri, Y., Padin, X. A., Peregon, A., Pfeil, B., Pierrot, D., Poulter, B., Rehder, G., Reimer, J., Rödenbeck, C., Schwinger, J., Séférian, R., Skjelvan, I., Stocker, B. D., Tian, H., Tilbrook, B., Tubiello, F. N., van der Laan-Luijkx, I. T., van der Werf, G. R., van Heuven, S., Viovy, N., Vuichard, N., Walker, A. P., Watson, A. J., Wiltshire, A. J., Zaehle, S., and Zhu, D.: Global Carbon Budget 2017, *Earth System Science Data*, 10, 405-448, https://doi.org/10.5194/essd-10-405-2018, 2018.

Lehner, F., Joos, F., Raible, C. C., Mignot, J., Born, A., Keller, K. M., and Stocker, T. F.: Climate and carbon cycle dynamics in a CESM simulation from 850 to 2100 CE. Earth system dynamics, 6(2), 411-434, 2015.

Lelieveld, J., Evans, J.S., Fnais, M., Giannadaki, D. and Pozzer, A.: The contribution of outdoor air pollution sources to premature mortality on a global scale. *Nature*, 525(7569), p.367, 2015.

Levin, I., Kromer, B., Schmidt, M. and Sartorius, H.: A novel approach for independent budgeting of fossil fuel CO_2 over Europe by $14CO_2$ observations. *Geophysical Research Letters*, 30(23), 2003.

Levin, I., Hammer, S., Kromer, B. and Meinhardt, F.: Radiocarbon observations in atmospheric CO2: determining fossil fuel CO2 over Europe using Jungfraujoch observations as background. Science of the Total Environment, 391(2-3), pp.211-216, 2008.

Levin, I., Naegler, T., Kromer, B., Diehl, M., Francey, R., Gomez-Pelaez, A., Steele, P., Wagenbach, D., Weller, R. and Worthy, D., 2010. Observations and modelling of the global distribution and long-term trend of atmospheric 14CO2. Tellus B: Chemical and Physical Meteorology, 62(1), pp.26-46.

Lindenmaier, R., Dubey, M.K., Henderson, B.G., Butterfield, Z.T., Herman, J.R., Rahn, T. and Lee, S.H.: Multiscale observations of CO2, 13CO2, and pollutants at Four Corners for emission verification and attribution. Proceedings of the National Academy of Sciences, 111(23), pp.8386-8391, 2014.

Lindsay, K., Bonan, G.B., Doney, S.C., Hoffman, F.M., Lawrence, D.M., Long, M.C., Mahowald, N.M., Keith Moore, J., Randerson, J.T. and Thornton, P.E.: Preindustrial-control and twentieth-century carbon cycle experiments with the Earth System Model CESM1 (BGC). Journal of Climate, 27(24), pp.8981-9005, 2014.

Lopez, M., Schmidt, M., Delmotte, M., Colomb, A., Gros, V., Janssen, C., Lehman, S. J., Mondelain, D., Perrussel, O., Ramonet, M., Xueref-Remy, I., and Bousquet, P.: CO, NOx and 13CO2 as tracers for fossil fuel CO2: results from a pilot study in Paris during winter 2010, Atmos. Chem. Phys., 13, 7343-7358, https://doi.org/10.5194/acp-13-7343-2013, 2013.

Miller, J.B., Lehman, S.J., Montzka, S.A., Sweeney, C., Miller, B.R., Karion, A., Wolak, C., Dlugokencky, E.J., Southon, J., Turnbull, J.C. and Tans, P.P.: Linking emissions of fossil fuel CO_2 and other anthropogenic trace gases using atmospheric $^{14}CO_2$. *Journal of Geophysical Research: Atmospheres*, 117(D8), 2012.

Miyazaki, K., Sekiya, T., Fu, D., Bowman, K.W., Kulawik, S.S., Sudo, K., Walker, T., Kanaya, Y., Takigawa, M., Ogochi, K. and Eskes, H.: Balance of Emission and Dynamical Controls on Ozone During the Korea-United States Air Quality Campaign From Multiconstituent Satellite Data Assimilation. Journal of Geophysical Research: Atmospheres, 124(1), pp.387-413, 2019.

Molod, A., Takacs, L., Suarez, M., and Bacmeister, J.: Development of the GEOS-5 atmospheric general circulation model: Evolution from MERRA to MERRA2. Geoscientific Model Development, 8(5), 1339, 2015.

Moore, J. K., Lindsay, K., Doney, S. C., Long, M. C., and Misumi, K.: Marine ecosystem dynamics and biogeochemical cycling in the Community Earth System Model [CESM1 (BGC)]: Comparison of the 1990s with the 2090s under the RCP4. 5 and RCP8. 5 scenarios. Journal of Climate, 26(23), 9291-9312, 2013.

Morino, I., T. Matsuzaki, A. Shishime.: TCCON data from Tsukuba, Ibaraki, Japan, 125HR, Release GGG2014R2. TCCON data archive, hosted by CaltechDATA, California Institute of Technology, Pasadena, CA, U.S.A. http://doi.org/10.14291/tccon.ggg2014.tsukuba02.R2, 2017a.

Morino, I., N. Yokozeki, T. Matzuzaki, A. Shishime.: TCCON data from Rikubetsu, Hokkaido, Japan, Release GGG2014R2. TCCON data archive, hosted by CaltechDATA, California Institute of Technology, Pasadena, CA, U.S.A. https://doi.org/10.14291/tccon.ggg2014.rikubetsu01.R2, 2017b.

Nassar, R., Jones, D.B., Suntharalingam, P., Chen, J.M., Andres, R.J., Wecht, K.J., Yantosca, R.M., Kulawik, S.S., Bowman, K.W., Worden, J.R. and Machida, T.: Modeling global atmospheric CO2 with improved emission inventories and CO2 production from the oxidation of other carbon species. Geoscientific Model Development, 3(2), p.689, 2010.

Nassar, R., Napier-Linton, L., Gurney, K.R., Andres, R.J., Oda, T., Vogel, F.R. and Deng, F.: Improving the temporal and spatial distribution of CO2 emissions from global fossil fuel emission data sets. Journal of Geophysical Research: Atmospheres, 118(2), pp.917-933, 2013.

Nathan, B., Lauvaux, T., Turnbull, J. and Gurney, K.: Investigations into the use of multi-species

measurements for source apportionment of the Indianapolis fossil fuel CO_2 signal. Elementa: *Science of the Anthropocene*, 6(1), 2018.

Newman, S., Xu, X., Gurney, K.R., Hsu, Y.K., Li, K.F., Jiang, X., Keeling, R., Feng, S., O'Keefe, D., Patarasuk, R. and Wong, K.W.: Toward consistency between trends in bottom-up CO_2 emissions and top-down atmospheric measurements in the Los Angeles megacity. *Atmospheric Chemistry and Physics*, 16(6), pp.3843-3863, 2016.

Niu, Z., Zhou, W., Wu, S., Cheng, P., Lu, X., Xiong, X., Du, H., Fu, Y. and Wang, G.: Atmospheric fossil fuel CO2 traced by Δ14C in Beijing and Xiamen, China: temporal variations, inland/coastal differences and influencing factors. Environmental science & technology, 50(11), pp.5474-5480, 2016.

O'Dell, C. W., Eldering, A., Wennberg, P. O., Crisp, D., Gunson, M. R., Fisher, B., Frankenberg, C., Kiel, M., Lindqvist, H., Mandrake, L., Merrelli, A., Natraj, V., Nelson, R. R., Osterman, G. B., Payne, V. H., Taylor, T. E., Wunch, D., Drouin, B. J., Oyafuso, F., Chang, A., McDuffie, J., Smyth, M., Baker, D. F., Basu, S., Chevallier, F., Crowell, S. M. R., Feng, L., Palmer, P. I., Dubey, M., García, O. E., Griffith, D. W. T., Hase, F., Iraci, L. T., Kivi, R., Morino, I., Notholt, J., Ohyama, H., Petri, C., Roehl, C. M., Sha, M. K., Strong, K., Sussmann, R., Te, Y., Uchino, O., and Velazco, V. A.: Improved retrievals of carbon dioxide from Orbiting Carbon Observatory-2 with the version 8 ACOS algorithm, Atmos. Meas. Tech., 11, 6539-6576, https://doi.org/10.5194/amt-11-6539-2018, 2018.

Oh, Y.S., Kenea, S.T., Goo, T.Y., Chung, K.S., Rhee, J.S., Ou, M.L., Byun, Y.H., Wennberg, P.O., Kiel, M., DiGangi, J.P. and Diskin, G.S.: Characteristics of greenhouse gas concentrations derived from ground-based FTS spectra at Anmyeondo, South Korea, 2018.

Osterman, G. B., Eldering, A., Avis, C., Chafin, B., O'Dell, C. W., Frankenberg, C., Fisher, B. M., Mandrake, L., Wunch, D., Granat, R., and Crisp, D.: Orbiting Carbon Observatory-2 (OCO-2) data product user's guide, operational L1 and L2 data versions 8 and 8R, Jet Propulsion Laboratory, Pasadena, CA, USA, 2016.

National Research Council: Verifying Greenhouse Gas Emissions: Methods to Support International Climate Agreements, Natl. Acad. Press, Washington, D.C, https://doi.org/10.17226/12883, 2010.

Palmer, P.I., Suntharalingam, P., Jones, D., Jacob, D.J., Streets, D.G., Fu, Q., Vay, S.A. and Sachse, G.W.: Using CO2: CO correlations to improve inverse analyses of carbon fluxes. Journal of Geophysical Research: Atmospheres, 111(D12), 2006.

Parrish, D.D., Kuster, W.C., Shao, M., Yokouchi, Y., Kondo, Y., Goldan, P.D., de Gouw, J.A., Koike, M. and Shirai, T.: Comparison of air pollutant emissions among mega-cities. Atmospheric Environment, 43(40), pp.6435-6441, 2009.

Peters, W., Jacobson, A. R., Sweeney, C., Andrews, A. E., Conway, T. J., Masarie, K., Miller, J. B., Bruhwiler, L., M. P., Pétron, G., Hirsch, A. I., Worthy, D. E. J., van der Werf, G. R., Randerson, J. T., Wennberg, P. O., Krol, M. C., and Tans, P. P.: An atmospheric perspective on North American carbon dioxide exchange: CarbonTracker, P. Natl. Acad.

Sci. USA, 104, 18925–18930, doi:10.1073/pnas.0708986104, 2007.

Petron, G., Crotwell, A.M., Lang, P.M., Dlugokencky, E.: Atmospheric Carbon Monoxide Dry Air Mole Fractions from the NOAA ESRL Carbon Cycle Cooperative Global Air Sampling Network, 1988-2017, Version: 2018-10-17, Path: ftp://aftp.cmdl.noaa.gov/data/trace_gases/co/flask/surface/, 2018.

Peylin, P., Houweling, S., Krol, M.C., Karstens, U., Rödenbeck, C., Geels, C., Vermeulen, A., Badawy, B., Aulagnier, C., Pregger, T. and Delage, F.: Importance of fossil fuel emission uncertainties over Europe for CO2 modeling: model intercomparison. Atmospheric chemistry and physics, 11(13), pp.6607-6622, 2011.

Peylin, P., Law, R.M., Gurney, K.R., Chevallier, F., Jacobson, A.R., Maki, T., Niwa, Y., Patra, P.K., Peters, W., Rayner, P.J. and Rödenbeck, C.: Global atmospheric carbon budget: results from an ensemble of atmospheric CO2 inversions. Biogeosciences, 10, pp.6699-6720, 2013.

Pfeil, B., Olsen, A., Bakker, D.C., Hankin, S., Koyuk, H., Kozyr, A., Malczyk, J., Manke, A., Metzl, N., Sabine, C.L. and Akl, J.: A uniform, quality controlled Surface Ocean CO2 Atlas (SOCAT). Earth System Science Data Discussions, 5(2), pp.735-780, 2012.

Pollack, I.B., Ryerson, T.B., Trainer, M., Neuman, J.A., Roberts, J.M. and Parrish, D.D.: Trends in ozone, its precursors, and related secondary oxidation products in Los Angeles, California: A synthesis of measurements from 1960 to 2010. Journal of Geophysical Research: Atmospheres, 118(11), pp.5893-5911, 2013.

Pommier, M., McLinden, C.A. and Deeter, M.: Relative changes in CO emissions over megacities based on observations from space. Geophysical Research Letters, 40(14), pp.3766-3771, 2013.

Quilcaille, Y., Gasser, T., Ciais, P., Lecocq, F., Janssens-Maenhout, G. and Mohr, S., 2018. Uncertainty in projected climate change arising from uncertain fossil-fuel emission factors. Environmental Research Letters, 13(4), p.044017.

Rayner, P.J., Raupach, M.R., Paget, M., Peylin, P. and Koffi, E.: A new global gridded data set of CO2 emissions from fossil fuel combustion: Methodology and evaluation. Journal of Geophysical Research: Atmospheres, 115(D19), 2010.

Reuter, M., Bovensmann, H., Buchwitz, M., Burrows, J. P., Connor, B. J., Deutscher, N. M., Griffith, D. W. T., Heymann, J., Keppel-Aleks, G., Messerschmidt, J., Notholt, J., Petri, C., Robinson, J., Schneising, O., Sherlock, V., Velazco, V., Warneke, T., Wennberg, P. O., Wunch, D.: Retrieval of atmospheric CO2 with enhanced accuracy and precision from SCIAMACHY: Validation with FTS measurements and comparison with model results, J. Geophys. Res.-Atmos., 116, D04301, doi:10.1029/2010JD015047, 2011.

Reuter, M., Buchwitz, M., Hilboll, A., Richter, A., Schneising, O., Hilker, M., Heymann, J., Bovensmann, H. and Burrows, J.P.: Decreasing emissions of NO_X relative to CO_2 in East Asia inferred from satellite observations. *Nature Geoscience*, 7(11), p.792, 2014.

Reuter, M., Buchwitz, M., Schneising, O., Krautwurst, S., O'Dell, C. W., Richter, A., Bovensmann, H., and Burrows, J. P.: Towards monitoring localized CO2 emissions from space: co-located regional CO2 and NO2 enhancements observed by the OCO-2 and S5P satellites, Atmos. Chem. Phys. Discuss., https://doi.org/10.5194/acp-2019-15, in review, 2019.

Rodgers, C.D.: Inverse methods for atmospheric sounding: theory and practice. World scientific, https://doi.org/10.1142/3171, 2000.

Saeki, T. and Patra, P.K.: Implications of overestimated anthropogenic CO2 emissions on East Asian and global land CO2 flux inversion. Geoscience Letters, 4(1), p.9, 2017.

Schneising, O., Bergamaschi, P., Bovensmann, H., Buchwitz, M., Burrows, J. P., Deutscher, N. M., Griffith, D. W. T., Heymann, J., Macatangay, R., Messerschmidt, J., Notholt, J., Rettinger, M., Reuter, M., Sussmann, R., Velazco, V. A., Warneke, T., Wennberg, P. O., andWunch, D.: Atmospheric greenhouse gases retrieved from SCIAMACHY: comparison to ground-based FTS measurements and model results, Atmos. Chem. Phys., 12, 1527–1540, doi:10.5194/acp-12-1527-2012, 2012.

Shiga, Y.P., Michalak, A.M., Gourdji, S.M., Mueller, K.L. and Yadav, V.: Detecting fossil fuel emissions patterns from subcontinental regions using North American in situ CO_2 measurements. Geophysical research letters, 41(12), pp.4381-4388, 2014.

Shiomi, K., Kawakami, S., H. Ohyama, K. Arai, H. Okumura, C. Taura, T. Fukamachi, M. Sakashita.: TCCON data from Saga, Japan, Release GGG2014R0. TCCON data archive, hosted by CaltechDATA, California Institute of Technology, Pasadena, CA, U.S.A. https://doi.org/10.14291/tccon.ggg2014.saga01.R0/1149283, 2017.

Silva, S.J., Arellano, A.F. and Worden, H.M.: Toward anthropogenic combustion emission constraints from space-based analysis of urban CO_2/CO sensitivity. *Geophysical research letters*, 40(18), pp.4971-4976, 2013.

Silva, S. and Arellano, A.F.: Characterizing regional-scale combustion using satellite retrievals of CO, NO_2 and CO_2. *Remote Sensing*, 9(7), p.744, 2017.

Stephens, B.B., Gurney, K.R., Tans, P.P., Sweeney, C., Peters, W., Bruhwiler, L., Ciais, P., Ramonet, M., Bousquet, P., Nakazawa, T. and Aoki, S.: Weak northern and strong tropical land carbon uptake from vertical profiles of atmospheric CO2. Science, 316(5832), pp.1732-1735, 2007.

Streets, D.G., Canty, T., Carmichael, G.R., de Foy, B., Dickerson, R.R., Duncan, B.N., Edwards, D.P., Haynes, J.A., Henze, D.K., Houyoux, M.R. and Jacob, D.J.: Emissions estimation from satellite retrievals: A review of current capability. *Atmospheric Environment*, 77, pp.1011-1042, 2013.

Suntharalingam, P., Jacob, D.J., Palmer, P.I., Logan, J.A., Yantosca, R.M., Xiao, Y., Evans, M.J., Streets, D.G., Vay, S.L. and Sachse, G.W.: Improved quantification of Chinese carbon

fluxes using CO2/CO correlations in Asian outflow. Journal of Geophysical Research: Atmospheres, 109(D18), 2004.

Suntharalingam, P., Randerson, J.T., Krakauer, N., Logan, J.A. and Jacob, D.J.: Influence of reduced carbon emissions and oxidation on the distribution of atmospheric CO2: Implications for inversion analyses. Global biogeochemical cycles, 19(4), 2005.

Sweeney, C., Karion, A., Wolter, S., Newberger, T., Guenther, D., Higgs, J.A., Andrews, A.E., Lang, P.M., Neff, D., Dlugokencky, E. and Miller, J.B.: Seasonal climatology of CO2 across North America from aircraft measurements in the NOAA/ESRL Global Greenhouse Gas Reference Network. Journal of Geophysical Research: Atmospheres, 120(10), pp.5155-5190, 2015.

Tang, W., Arellano, A. F., DiGangi, J. P., Choi, Y., Diskin, G. S., Agustí-Panareda, A., Parrington, M., Massart, S., Gaubert, B., Lee, Y., Kim, D., Jung, J., Hong, J., Hong, J.-W., Kanaya, Y., Lee, M., Stauffer, R. M., Thompson, A. M., Flynn, J. H., and Woo, J.-H.: Evaluating high-resolution forecasts of atmospheric CO and CO_2 from a global prediction system during KORUS-AQ field campaign, *Atmospheric Chemistry and Physics*, 18, 11007-11030, https://doi.org/10.5194/acp-18-11007-2018, 2018.

Tang, W., Arellano, A. F., Gaubert, B., Miyazaki, K., and Worden, H. M.: Satellite Data Reveals a Common Combustion Emission Pathway for Major Cities in China, *Atmospheric Chemistry and Physics*, https://doi.org/10.5194/acp-2018-1121, 2019.

Tang, W., Emmons, L. K., Arellano, A. F., Gaubert, B., Knote, C., Tilmes, S., Buchholz, R. R., Pfister, G. G., Diskin, G. S., Blake, D. R., Blake, N. J., Meinardi, S., DiGangi, J P., Choi, Y., Woo,J., He, C., Schroeder, J. R., Suh, I., Lee, H., Jo, H., Kanaya, Y.,Jung, J., Lee, Y., and Kim, D.: Source contributions to carbon monoxide concentrations during KORUS-AQ based on CAM-chem model applications, J. Geophys. Res. Atmos., 10.1029/2018JD029151, 2019.

Turnbull, J.C., Miller, J.B., Lehman, S.J., Tans, P.P., Sparks, R.J. and Southon, J.: Comparison of $14CO_2$, CO, and SF6 as tracers for recently added fossil fuel CO_2 in the atmosphere and implications for biological CO_2 exchange. *Geophysical research letters*, 33(1), 2006.

Turnbull, J., Rayner, P., Miller, J., Naegler, T., Ciais, P. and Cozic, A.: On the use of 14CO2 as a tracer for fossil fuel CO2: Quantifying uncertainties using an atmospheric transport model. Journal of Geophysical Research: Atmospheres, 114(D22), 2009.

Turnbull, J. C., Tans, P. P., Lehman, S. J., Baker, D., Conway, T. J., Chung, Y. S., Gregg, J., Miller, J. B., Southon, J. R., and Zhou, L. X.: Atmospheric observations of carbon monoxide and fossil fuel CO_2 emissions from East Asia, *Journal of Geophysical Research: Atmospheres*, 116, D24306, https://doi.org/10.1029/2011JD016691, 2011.

Turnbull, J.C., Sweeney, C., Karion, A., Newberger, T., Lehman, S.J., Tans, P.P., Davis, K.J., Lauvaux, T., Miles, N.L., Richardson, S.J. and Cambaliza, M.O.: Toward quantification and source sector identification of fossil fuel CO_2 emissions from an urban area: Results from the INFLUX experiment. Journal of Geophysical Research: Atmospheres, 120(1),

pp.292-312, 2015.

United Nations: World urbanization prospects: The 2014 revision. United Nations Department of Economics and Social Affairs, Population Division: New York, NY, USA, 2015.

van der Laan-Luijkx, I. T., van der Velde, I. R., van der Veen, E., Tsuruta, A., Stanislawska, K., Babenhauserheide, A., Zhang, H. F., Liu, Y., He, W., Chen, H., Masarie, K. A., Krol, M. C., and Peters, W.: The CarbonTracker Data Assimilation Shell (CTDAS) v1.0: implementation and global carbon balance 2001–2015, Geosci. Model Dev., 10, 2785-2800, https://doi.org/10.5194/gmd-10-2785-2017, 2017.

Vay, S.A., Choi, Y., Vadrevu, K.P., Blake, D.R., Tyler, S.C., Wisthaler, A., Hecobian, A., Kondo, Y., Diskin, G.S., Sachse, G.W. and Woo, J.H.: Patterns of CO2 and radiocarbon across high northern latitudes during International Polar Year 2008. Journal of Geophysical Research: Atmospheres, 116(D14), 2011.

Veefkind, J.P., Aben, I., McMullan, K., Förster, H., De Vries, J., Otter, G., Claas, J., Eskes, H.J., De Haan, J.F., Kleipool, Q. and Van Weele, M., 2012. TROPOMI on the ESA Sentinel-5 Precursor: A GMES mission for global observations of the atmospheric composition for climate, air quality and ozone layer applications. Remote Sensing of Environment, 120, pp.70-83.

Vogel, F., Hamme, S., Steinhof, A., Kromer, B. and Levin, I.: Implication of weekly and diurnal ^{14}C calibration on hourly estimates of CO-based fossil fuel CO_2 ata moderately polluted site in southwestern Germany. *Tellus B: Chemical and Physical Meteorology*, 62(5), pp.512-520, 2010.

Wang, Y., Munger, J. W., Xu, S., McElroy, M. B., Hao, J., Nielsen, C. P., and Ma, H.: CO_2 and its correlation with CO at a rural site near Beijing: implications for combustion efficiency in China, *Atmospheric Chemistry and Physics*, 10, 8881–8897, https://doi.org/10.5194/acp-10-8881-2010, 2010.

Wang, Y., Broquet, G., Ciais, P., Chevallier, F., Vogel, F., Kadygrov, N., Wu, L., Yin, Y., Wang, R. and Tao, S.: Estimation of observation errors for large-scale atmospheric inversion of CO2 emissions from fossil fuel combustion. Tellus B: Chemical and Physical Meteorology, 69(1), p.1325723, 2017.

Warner, J. X., Wei, Z., Strow, L. L., Barnet, C. D., Sparling, L. C., Diskin, G., and Sachse, G.: Improved agreement of AIRS tropospheric carbon monoxide products with other EOS sensors using optimal estimation retrievals, Atmos. Chem. Phys., 10, 9521–9533, https://doi.org/10.5194/acp-10-9521-2010, 2010.

Wofsy, S.C.: HIAPER Pole-to-Pole Observations (HIPPO): fine-grained, global-scale measurements of climatically important atmospheric gases and aerosols. Philosophical Transactions of the Royal Society A: Mathematical, Physical and Engineering Sciences, 369(1943), pp.2073-2086, 2011.

Worden, H. M., Deeter, M. N., Edwards, D. P., Gille, J. C., Drummond, J. R., and Nédélec, P.:

Observations of near-surface carbon monoxide from space using MOPITT multispectral retrievals. Journal of Geophysical Research: Atmospheres, 115(D18), 2010.

Wunch, D., Toon, G. C., Blavier, J. F. L., Washenfelder, R. A., Notholt, J., Connor, B. J., Griffith, D. W., Sherlock, V., and Wennberg, P. O.: The total carbon column observing network, *Philosophical Transactions of the Royal Society A*, 369, 2087–2112, 2011.

Wunch, D., Toon, G. C., Sherlock, V., Deutscher, N. M., Liu, C., Feist, D. G., and Wennberg, P. O.: The total carbon column observing network's GGG2014 data version. Carbon Dioxide Information Analysis Center, Oak Ridge National Laboratory, Oak Ridge, Tennessee, USA, available at: doi, 10, 2015.

Wunch, D., Wennberg, P. O., Osterman, G., Fisher, B., Naylor, B., Roehl, C. M., O'Dell, C., Mandrake, L., Viatte, C., Kiel, M., Griffith, D. W. T., Deutscher, N. M., Velazco, V. A., Notholt, J., Warneke, T., Petri, C., De Maziere, M., Sha, M. K., Sussmann, R., Rettinger, M., Pollard, D., Robinson, J., Morino, I., Uchino, O., Hase, F., Blumenstock, T., Feist, D. G., Arnold, S. G., Strong, K., Mendonca, J., Kivi, R., Heikkinen, P., Iraci, L., Podolske, J., Hillyard, P. W., Kawakami, S., Dubey, M. K., Parker, H. A., Sepulveda, E., García, O. E., Te, Y., Jeseck, P., Gunson, M. R., Crisp, D., and Eldering, A.: Comparisons of the Orbiting Carbon Observatory-2 (OCO-2) XCO2 measurements with TCCON, Atmos. Meas. Tech., 10, 2209–2238, https://doi.org/10.5194/amt-10-2209-2017, 2017.

Yang, K., Dickerson, R.R., Carn, S.A., Ge, C. and Wang, J.: First observations of SO2 from the satellite Suomi NPP OMPS: Widespread air pollution events over China. Geophysical Research Letters, 40(18), pp.4957-4962, 2013.

Zhu, Q., Peng, X. and Wu, K.: Calculation and decomposition of indirect carbon emissions from residential consumption in China based on the input–output model. *Energy Policy*, 48, pp.618-626, 2012.

Supporting Information

Figure ES1. Global average atmospheric CO_2 mixing ratios in 2016 from CT2017 mole fraction fields (black line) and CAM-chem simulations of CO_2 (colored lines).

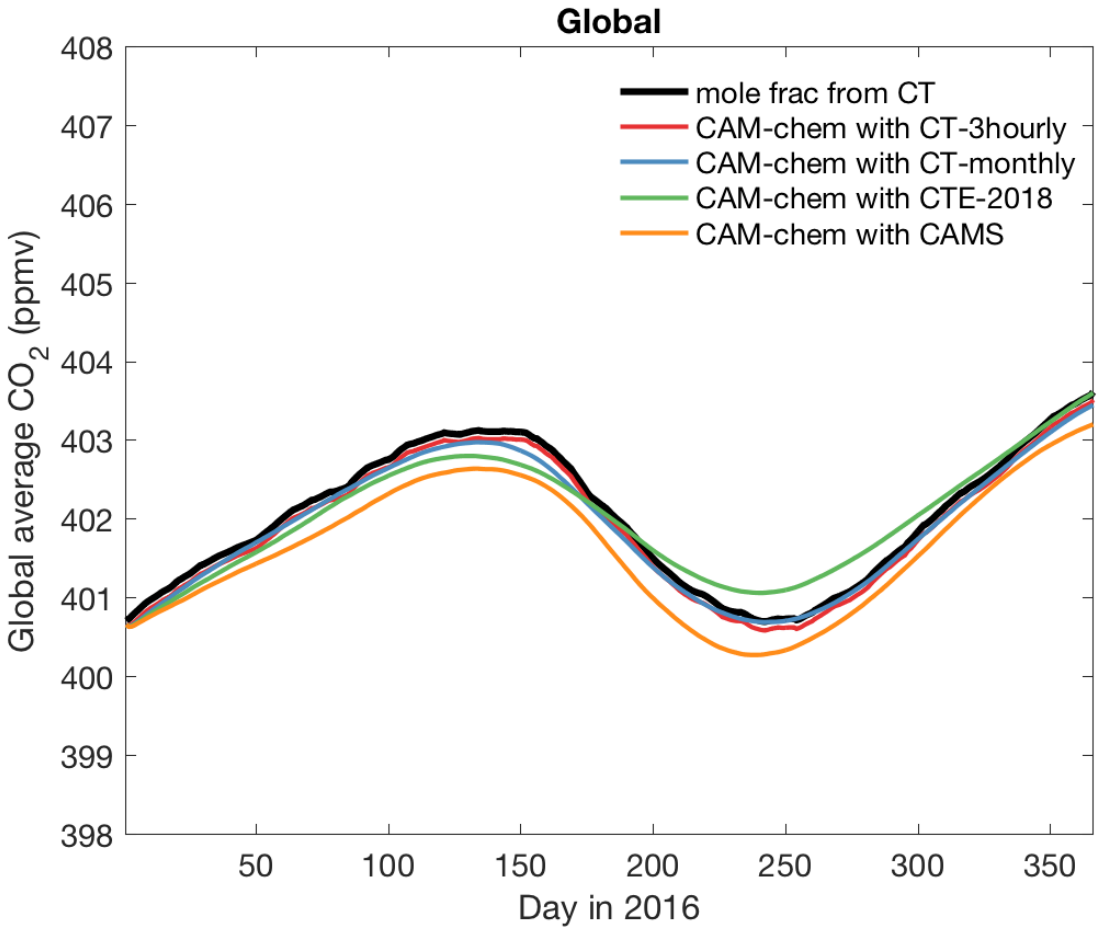

Figure ES2. Similar to Figure 9 but over Beijing. Three-hourly time series of modeled vertical profiles of total CO_2 and CO, $ffCO_2$ and ffCO, and their associated regional contributions over Beijing.

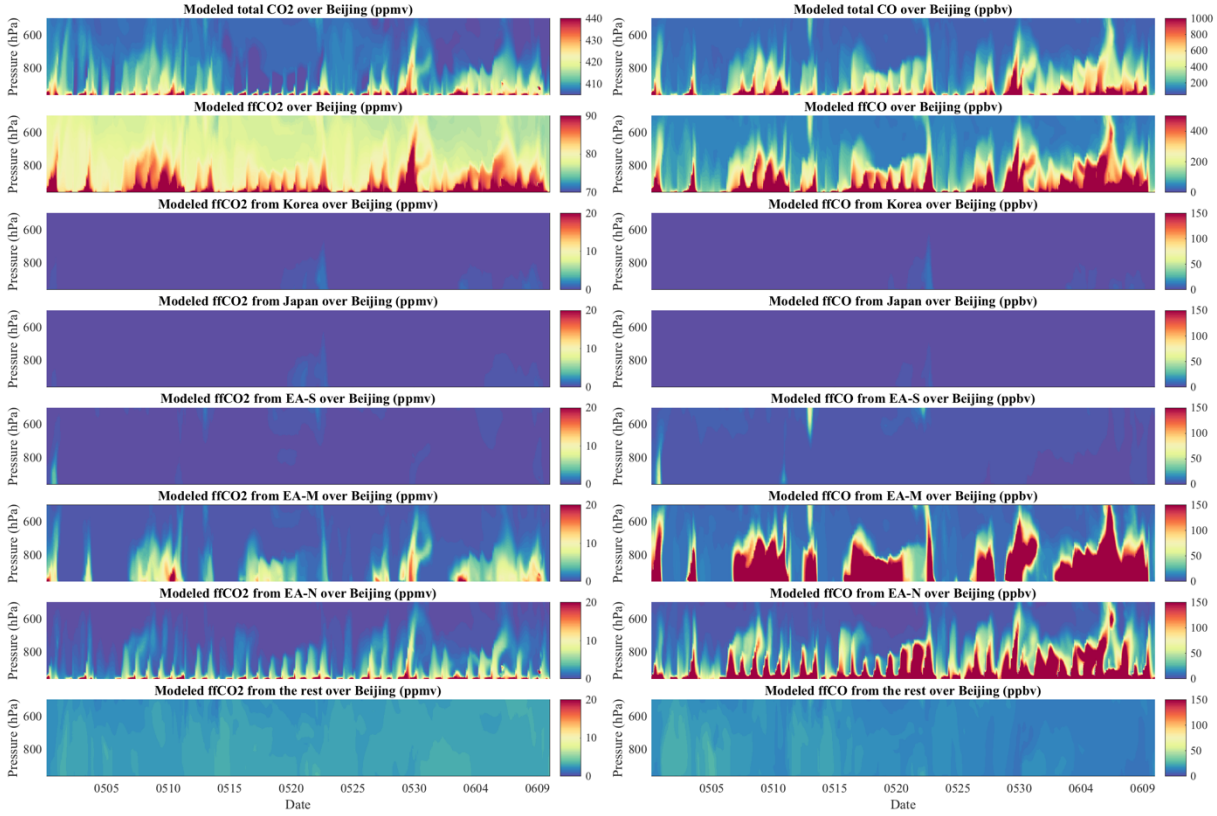

Figure ES3. Similar to Figure S2 but over Shanghai. Three-hourly time series of modeled vertical profiles of total CO_2 and CO, $ffCO_2$ and ffCO, and their associated regional contributions over Shanghai.